UNIVERSITÀ DEGLI STUDI DELL'AQUILA

DIPARTIMENTO DI INGEGNERIA INDUSTRIALE
E DELL'INFORMAZIONE E DI ECONOMIA

Dottorato di Ricerca in Ingegneria Industriale e dell'Informazione e di Economia

Curriculum Ingegneria Meccanica, Energetica e Gestionale

XXXV ciclo

Titolo della tesi

Thermal Management of Internal Combustion Engines. Theoretical and experimental analysis of innovative pumps for engine cooling.

SSD ING-IND/09

Dottorando

Ing. Giammarco Di Giovine

Coordinatore del corso

Prof.ssa Katia Gallucci

Tutor

Prof. Roberto Cipollone

a.a. 2021/2022

To my Family

Abstract

Global warming has become one of the biggest deal human mankind has to tackle to avoid unprecedented environmental disasters. As widely proved by the scientific community, this issue has been caused by anthropogenic CO_2 emissions, which have been rising seamlessly since the beginning of the industrialization era. The reason of such emissions is the use of fossil fuels as primary energy source. To face this problem, several international agreements have been concluded between Countries. So far, a cap of 450 ppm for the maximum concentration of CO_2 in the atmosphere has been set to limit global warming at 2°C. This requires urgent actions in all sectors, considering that already 417 ppm have been reached in 2022.

The transport sector is one of the main contributors to CO_2 emissions, with about the 26% in Europe, the 71% of which coming from road transport. The main reason is the use of Internal Combustion Engines (ICEs) as propulsion systems in road vehicles, which are mainly based on fossil fuels as energy vector. In addition, combustion engines produce pollutant emissions, which impact locally on the health of people and environment.

To limit the emissions of road vehicles, progressively stringent regulations have been implemented over the years, although with a non-uniform regulatory framework among different Countries. Historically, pollutants have been addressed first, due to their high tangible impact on a small space-time scale. Instead, CO_2 emissions have become to be seriously limited only in the recent years. Generally, these regulations define emission limits for each gas or pollutant, to be complied within specific laboratory test procedures. Moreover, in the EU regulation, also Real Driving Emissions (RDE) tests have been introduced recently, to consider more realistic emission values than those measured only with a laboratory test.

In any cases, currently the main driver of the regulations in the road transport sector is the reduction of CO_2 emissions. A valid contribution in this sense can be given by electric vehicles, which are gradually gaining market shares. However, costs and operability concerns are still limiting their large scale diffusion. Furthermore, Life-Cycle Analysis (LCA) studies show that the actual CO_2 emissions of an electric vehicle depend strictly on the carbon intensity associated with electricity generation, which varies strongly with the considered Country. Consequently, further improvements of ICE vehicles are still necessary to actually reduce CO_2 and pollutant emissions in the road transport sector.

At a vehicle level, significant benefits have been introduced by aerodynamic and lightweight vehicle bodies, as well as by electrified powertrain systems. These latter include simply micro-hybrid solutions (with the start/stop technology), up to full hybrid plug-in vehicles, which can be declined in a wide variety of powertrain architectures (from P0 to P5).

Also the engine efficiency has been strongly maximized over the years, thanks to a wide range of solutions. Downsized high power density engines, as well as overexpanded thermodynamic cycles with Variable Valve Actuation (VVA) systems, allow now to reach high efficiencies both at part and high load conditions. Moreover, advanced combustion strategies

are capable to optimize the combustion efficiency by combining together spark and compression ignition concepts, thanks to innovative port and direct fuel injection systems. In addition, high-efficiency technologies (exhaust gases recirculation systems, variable compression ratio and cylinder deactivation strategies, etc.), as well as waste energy recovery systems (turbochargers, turbocompounding, ORC-based power units), offer a valid contribution in reducing fuel consumption and emissions.

In this context, the optimization of the Engine Thermal Management represents one of the most promising strategies. In fact, the engine temperature impacts strongly on fuel consumption, due to its influence on engine oil viscosity and thus on friction losses, as well as on pollutant formation. Hence, the engine thermal needs have to be suitably managed during driving, to let the engine reach quickly, and maintain safely, a certain nominal temperature after start-up. Typically, this is accomplished by a cooling system, designed to remove the waste heat of the engine under extreme conditions, as well as to manage other thermal needs (oil cooling, cabin heating, etc.). Such system has still room for improvement, because it generally uses basic fail-safe components (a wax thermostat valve and a mechanically actuated cooling pump), that do not allow any optimization of the engine thermal state under many common driving conditions (such as in the warm-up phase). Moreover, the oversizing of the cooling pump reduces its efficiency when operating at low loads, resulting in a waste of energy during everyday driving.

Hence, many technologies have been developed over time to optimize the engine functioning at nominal and warm-up conditions. In fact, thanks to precision cooling strategies, the nominal temperature can be adjusted to maximize thermodynamic efficiency, while keeping under control pollutants emissions, knock phenomena, and after- or over-cooling issues. Moreover, the engine warm-up time can be minimized by optimizing cooling and lubricant systems. Possible solutions range from low-volume circuits to reduce the engine thermal inertia, up to innovative layouts with bypass valves or split-flow strategies, capable to better manage flow rates among heat exchangers and engine head and block. Recently, also active control systems on coolant and oil pumps have been introduced to regulate more precisely flow rate, eventually even by means of an electric actuation.

All these systems require high-efficiency pumps to reduce the energy spent to cool or lubricate the engine. Volumetric pumps can offer a valid contribution in this sense, due to their high efficiency also when operating far from the design point, as usual on-board of a vehicle. Although they are a well-established technology as engine oil pumps, they have been studied for cooling applications only recently, especially as sliding vane rotary pumps.

In this thesis, screw-type volumetric pumps have been studied when used as cooling pumps in ICEs. In fact, being volumetric machines, these pumps have a generally high and stable efficiency, which fits well for this type of application, never considered before in literature.

Hence, a novel zero-dimensional mathematical model capable to predict the volumetric, indicated and mechanical performances of screw pumps has been developed. The model

considers a triple-screw pump with a manufacture oriented to low cost, as generally requested by the road transport sector. Specifically, this pump has a single driver screw aligned with only one bearing, and two idler screws simply entrained inside cylindrical supports. Such layout does not prevent screws misalignments, whose effects on pump performances had to be considered.

The developed model offers a good prediction of the volumetric and mechanical performances compared with the experimental values. In particular, by giving as inputs pressure head and pump speed, the model calculates flow rate and mechanical power as main outputs, with a mean error equal to 0.6% and 6.1%, respectively.

Once validated, the model has been used to optimize the design of screw pumps for engine cooling applications. Firstly, the potential benefits deriving by their use in the cooling system of an engine have been assessed theoretically. Compared with a standard centrifugal pump, a screw pump operating over a homologation cycle allows to reduce the energy spent to cool the engine by about 13.8%.

In light of this significant result, a novel model-based methodology for the design of screw-type engine cooling pumps has been proposed. After identifying a suitable design point for a specific engine cooling application, the performances of a wide set of screw pump's geometries have been studied, in order to identify the geometric proportions which maximize the pump efficiency. Moreover, the effects of the aspect ratio on the triple-screw pump's performances have been investigated, finding that finger shaped geometries allow to reach efficiencies up to 60% in a typical engine cooling application. Then, the so-designed pump has been compared with the standard centrifugal one when operating on a reference driving cycle. The results show a strong energy reduction (about 56%), and thus a significant CO_2 emissions saving (2.08 g_{CO2}/km).

These promising results suggested to build a physical prototype of the so-designed triple-screw pump. For the same application, also an equally optimized centrifugal pump has been designed through a corresponding model-based approach, and a prototype built to compare experimentally the performances of both pumps. Even in this case, the results show significant energy (-21%) and emissions (-0.28 g_{CO2}/km) savings when using a screw pump instead of a centrifugal counterpart optimized for the same application.

The prototyped triple-screw pump introduced also an innovative idler screws' axis support, designed to reduce friction, wear and vibration phenomena during pump operation. Hence, to predict more accurately the performances of this new pump layout, the mathematical model has been refined. Specifically, the volumetric sub-model has been suitably modified to catch also blow-hole backflows, and the mechanical one to predict the reduced friction phenomena induced by the new screws' arrangement. The experimental validation of the so-modified model showed average errors in the flow rate and mechanical power calculations equal to 1.9% and 3.5%, respectively. Then, this model has been used to calculate the performances of the prototyped pump when operating under extreme conditions, difficult to measure experimentally. The results show efficiencies higher than 20% also when operating with low

pressure heads (0.3 bar) and high pump speeds (4000 rpm), or vice versa (5 bar and 1000 rpm, respectively). This testifies the good versatility of this type of pumps, of great interest also for other tough cooling applications.

The availability of a screw pump prototype allowed to investigate experimentally also the indicated cycle of this type of machine. Hence, additional pressure sensors have been installed on the pump case to measure the fluid pressure during pump operation. Simultaneously, the chamber volumes evolution over the screws' rotation angle has been theoretically derived. In this way, the indicated cycle of the machine has been reconstructed for several operating points. The results show that the pump is able to process more chamber volumes simultaneously through a smooth pumping process, i.e. without significant pressure peaks. Moreover, the suction and discharge phases take place with slight under and over pressure conditions, respectively, which depend on the pump speed, rather than the pressure head.

Finally, the thermal management of a passenger vehicle propelled by a spark ignition engine has been investigated experimentally. The aim was to measure the impact of the engine thermal state on CO_2 and pollutant emissions under real driving conditions, and to identify any strategies to speed-up the engine warm-up phase. To this end, the vehicle was equipped with a Portable Emissions Measurement System (PEMS), and with additional sensors to characterize completely the thermal dynamics of coolant, oil and engine block.

Hence, the same road test has been realized staring with different initial temperatures of the engine. The results show a significant reduction of fuel consumption (-3.9%), CO_2 (-5.9%) and CO (-30.6%) emissions when starting with the engine already warmed up. Instead, higher NO_x emissions (+21.6%) have been measured, although they remain below the limit allowed by the current EU Regulation. Moreover, in this specific engine, the thermal dynamics of the block's metallic masses evolves almost simultaneously with that of the coolant. This is of great scientific interest if a variable-speed cooling pump wants to be implemented. In fact, the engine block temperature could be used as a reference value to actuate the cooling pump only when necessary, thus reducing the warm-up time, as well as the energy spent to cool the engine.

In conclusion, this study offers a deep understanding of the potential benefits related to the use of screw pumps for engine cooling applications, thus filling a gap in literature. Furthermore, it provides useful information to develop advanced cooling pumps for the optimization of the engine thermal management, especially during the warm-up phase.

Index

Summary

The improvement of Internal Combustion Engines is still necessary to fulfill CO_2 and pollutant emission limits imposed by the current regulations in the road transport sector. The optimization of the engine thermal management can offer a valid contribution in this sense, due to the high impact of the engine temperature on fuel consumption and emissions, especially during the warm-up phase. Typically, the engine thermal needs are managed by a cooling system, which uses basic fail-safe components designed to guarantee the engine cooling under extreme conditions. Such system has plenty of room for improvement in terms of efficiency and flexibility of operation. In fact, the cooling pump is generally oversized and mechanically actuated by the crankshaft, resulting in long engine warm-up times, as well as in a waste of energy during everyday driving.

This thesis is focused on the study of screw-type volumetric pumps for engine cooling applications. In fact, this type of pumps has a high efficiency also when operating far from the design point, as always happens on-board of a vehicle. This feature allows to reduce the energy spent to cool the engine, and it is particularly useful also if an electric actuation of the pump wants to be implemented to improve the engine thermal management.

Hence, a mathematical model capable to predict the performances of screw pumps has been developed and experimentally validated. The model allowed to verify theoretically the benefits of screw pumps in terms of energy absorbed to cool the engine, compared with standard centrifugal pumps. Moreover, the model has been used to optimize the design of such pumps for engine cooling applications. In this way, an optimized prototype has been designed and built for a specific case study. The performances of this pump have been compared experimentally with those of a centrifugal pump optimized for the same application. The results showed once again a significant energy saving. Subsequently, the mathematical model has been refined considering the optimizations introduced by the prototyped screw pump. This model has been used to predict its performances when operating under extreme conditions, difficult to measure experimentally. Furthermore, the availability of a screw pump prototype allowed to investigate experimentally the indicated cycle of this type of machines, which has been reconstructed for several operating points.

Finally, the impact of the engine warm-up phase on emissions has been investigated experimentally over on-the-road tests. To this end, a passenger vehicle was equipped with a Portable Emissions Measurement System (PEMS), and with additional sensors to characterize completely the thermal dynamics of coolant, oil and engine block. A significant reduction of fuel consumption and emissions (except for NO_x) has been measured over the same road test when starting with the engine already warmed-up. Moreover, a simultaneous evolution of the thermal dynamics of engine block and coolant has been found. This will be particularly useful in case more advanced control strategies of the cooling pump want to be implemented to optimize the thermal management of this specific engine, especially during the warm-up phase.

The contents of the manuscript have been divided in the following way:

- In Chapter 1, an introduction on global warming and on the regulatory framework developed worldwide to limit the emissions of road vehicles has been presented. A special focus has been given to the regulations in force in EU and USA to limit CO_2 emissions in the automotive sector.
- In Chapter 2, a state of the art of the main technologies capable to improve the efficiency of passenger vehicles propelled by Internal Combustion Engines has been presented. Specifically, these technologies have been outlined distinguishing between those acting on the vehicle system, from those effective at an engine level.
- In Chapter 3, a thorough review of most relevant studies on engine thermal management has been proposed. These studies have been distinguished between those aimed at improving the engine thermal state at nominal conditions, from those focused on the speed-up of the engine warm-up phase. Moreover, the main researches realized on volumetric pumps for engine cooling applications have been presented.
- In Chapter 4, the mathematical model developed to predict the performances of screw-type volumetric pumps has been described in detail. Moreover, the two progressively more complex steps followed to validate the model have been outlined, along with a description of the test bench used to characterize experimentally the pumps.
- In Chapter 5, the optimization of screw pumps for engine cooling applications has been discussed. Firstly, the energy saving they can introduce compared with standard centrifugal pumps has been evaluated theoretically. Then, their geometrical optimization for engine cooling systems has been described, and the model-based design approach followed to build a physical prototype for a specific application has been presented. Finally, the actual energy saving of the prototyped pump relative to a centrifugal pump optimized for the same application has been evaluated experimentally.
- In Chapter 6, the refinements introduced in the mathematical model to predict more accurately the performances of the prototyped screw pump have been presented, along with their experimental validation. Then, the performances of the pump when operating under extreme working conditions have been analyzed theoretically.
- In Chapter 7, the indicated cycle of the prototyped screw pump has been derived experimentally. Starting from the description of the experimental setup developed to measure the pressure of the fluid inside the machine, the steps followed to reconstruct the indicated cycle have been outlined. Moreover, the results obtained at different pump operating points have been compared together, and the influence of pressure head and pump speed on the indicated cycle has been analyzed in detail.
- In Chapter 8, the experimental study on the engine thermal management of a passenger vehicle has been presented. Firstly, the specific vehicle and engine, as well as the experimental setup implemented on them, have been described. Then, the results of the

road tests executed at cold and warm engine starting conditions have been presented and compared together. Specifically, they have been discussed distinguishing among those relative to the engine performances, the engine thermal dynamics, fuel consumption, and CO_2 and pollutant emissions.

1 Introduction

1.1 Global warming and CO_2 emissions

Global warming is one of the worst issue that has to be faced by human mankind. Variations of the global surface temperature have always happened during the past, but from 1850 up to nowadays a rapid increase of that temperature has started [1], as represented in Figure 1-1.

To understand the reason of global warming, it is important to observe the atmospheric concentration of carbon dioxide during the last decades. Since the beginning of the industrial era (1750), human activities have raised CO_2 concentration by about 50%, leading to 417 ppm in 2022 [2]. This is represented in Figure 1-2 (a), where CO_2 levels during the last three glacial cycles (as reconstructed from ice cores) up to nowadays are reported.

Although the relation between global warming and anthropogenic activities is still a matter of debate [3], the influence of CO_2 emissions on the global surface temperature through the greenhouse effect is scientifically proved [4]. Therefore, an increase of CO_2 emissions, and more in general of Greenhouse Gas (GHG) emissions, leads necessarily to an increase of the global surface temperature. This is clearly represented in Figure 1-2 (b), where the temperature increase (relative to 20th century average) and the global carbon dioxide concentrations are overlapped together, showing both an increasing trend.

This global warming is unprecedented in at least the last 2000 years, and could lead to severe consequences on climate [1]. In fact, the increase of global surface temperature influences the melting of ice caps, determining an increase of the sea level, as well as an increase of the ocean acidification. These phenomena change the global climate on a wide space-time scale, with an intensification of extreme weather events such as floods and heat waves, which determine environmental and biological imbalances worldwide. The more GHGs will be emitted, the more these effects will be severe, as demonstrated by different scenarios in Figure 1-3 and Figure 1-4.

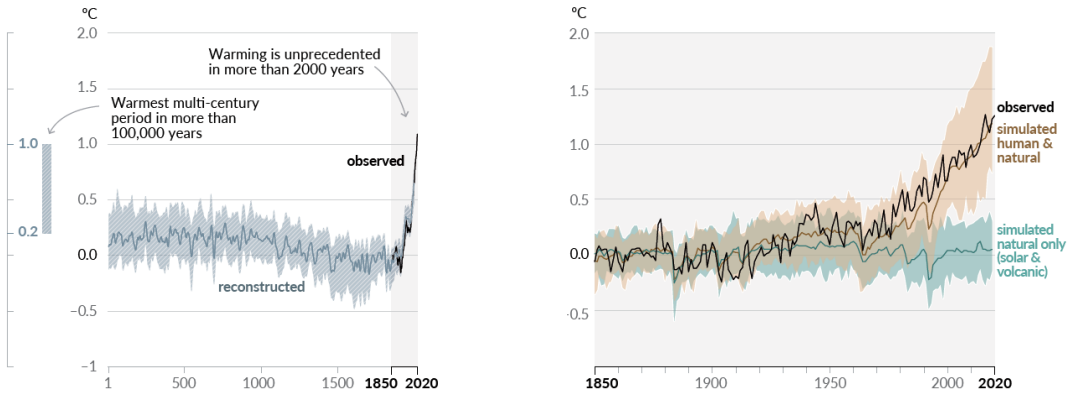

(a) (b)

Figure 1-1. Changes in global surface temperature relative to 1850–2020: (a) decadal average as reconstructed (1-2000) and observed (1850-2020); (b) annual average as observed and simulated (1850-2020) [1].

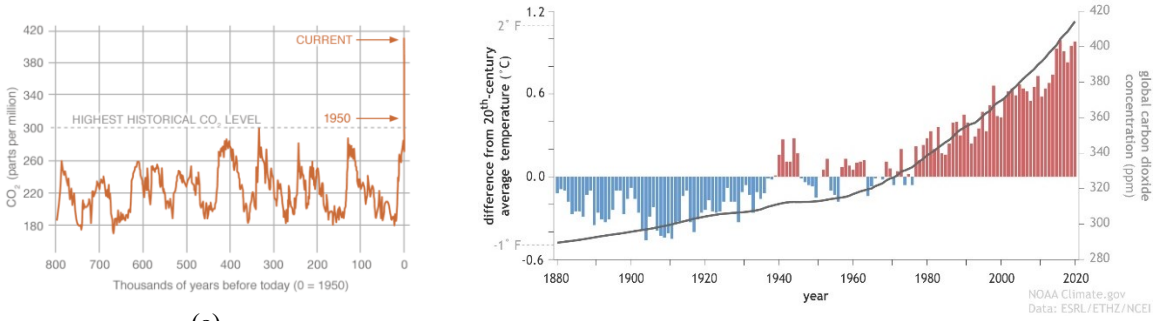

(a) (b)

Figure 1-2. (a) CO_2 levels during the last three glacial cycles [5]; (b) global atmospheric carbon dioxide and surface temperature (1880-2020) [6].

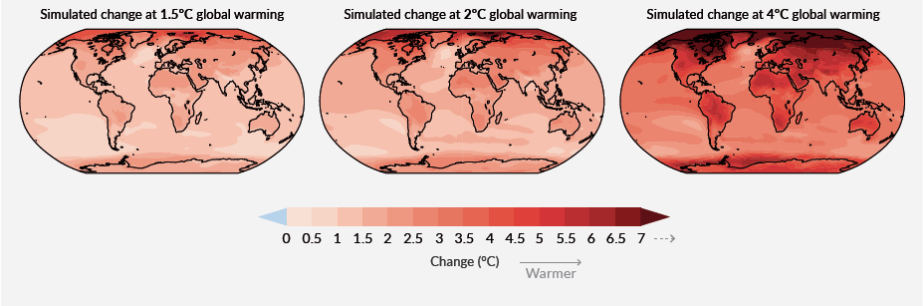

Figure 1-3. Annual mean temperature change (°C) relative to 1850-1900. Land areas warm more than ocean areas, and the Artic and Antarctica warm more than the tropics [1].

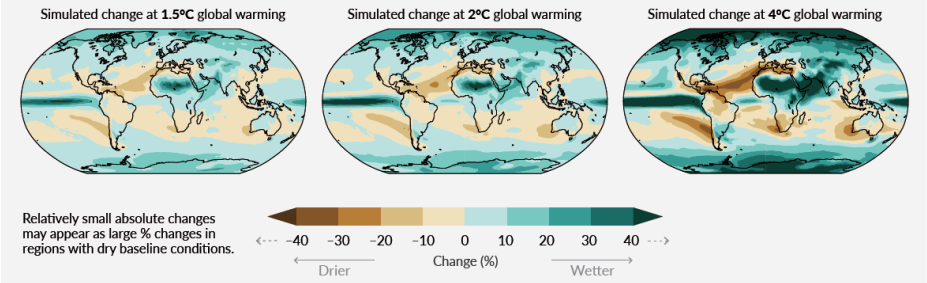

Figure 1-4. Annual mean precipitation change (%) relative to 1850-1900. Precipitation is projected to increase over high latitudes, the equatorial Pacific and parts of the monsoon regions, but decrease over parts of the subtropics and in limited areas of the tropics [1].

Global warming is likely to reach 1.5°C (compared to pre-industrial levels) between 2030 and 2052 if it continues to increase at the current rate [7]. According to the Intergovernmental Panel on Climate Change (IPCC), limiting global warming under 1.5 °C could minimize the impact on water and land ecosystems, as well as the adaptation needs of human and natural systems, compared to a 2°C warming. To keep global warming below 1.5°C, global net anthropogenic CO_2 emissions must decline by about 45% from 2010 levels by 2030, reaching net zero around 2050. Instead, if CO_2 emissions decline by about 25% by 2030 and reach net

zero around 2070, global warming reaches to 2°C, increasing climate-related risks to health, livelihoods, food security, water supply, human security, and economic growth.

1.2 International Agreements

The warnings launched by the scientific community on the potentially catastrophic consequences of global warming have been simulating the international community to take urgent actions in reducing CO_2 emissions. To this end, several international agreements and cooperation have followed over the years (Figure 1-5).

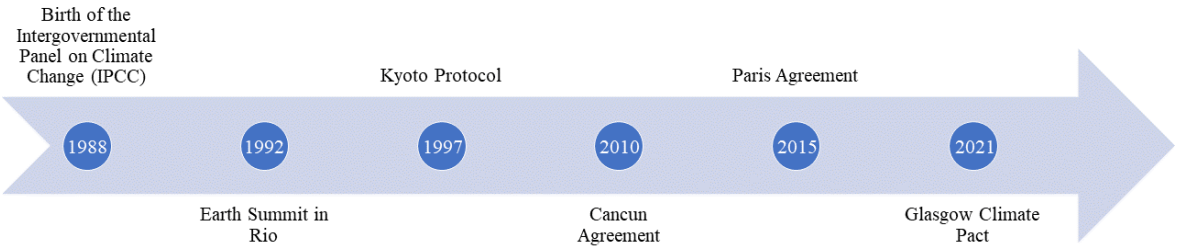

Figure 1-5. Timeline of the most relevant Climate Change Negotiations [8].

After the institution of the IPCC in 1988, the first treaty stating the need to reduce GHGs emissions has been the United Nation Framework Convention on Climate Change (UNFCC), adopted in 1992 by multiple parties at the Earth Summit in Rio. However, only with the Kyoto Protocol in 1997 legally binding emissions reduction targets have been set. This Protocol became effective later in 2005, after debates over the most appropriate levels and timings. Most of the adhering nations respected their limits, also because of the economic crisis of 2009, but global GHGs emissions continued to increase up to 30% in the same time span. The first document setting the limit of average temperature increase at 2°C was redacted with the Cancun Agreement in 2010 during the 16th Conference of Parties (COP), where also a periodical review of the process toward the long-term global goal has been established. The subsequent important milestone has been the Paris Agreement, signed by 196 Parties during COP21 in 2015 [9]. It represents the first-ever universal, legally binding global climate deal. The objective of the agreement is to maintain the increase in global temperatures well below 2°C above pre-industrial levels, pursuing efforts to limit the increase to 1.5°C. The agreement aims to ensure global GHG emissions peak as soon as possible, and to balance emissions and removals of GHGs in the second half of this century. Furthermore, the agreement addresses the adaptation to climate change, and the financial support for developing Countries in technology transfer, capacity building, and damages mitigation.

By limiting the temperature to 2°C, also the maximum CO_2 concentration admissible in atmosphere has been limited to a value of 450 ppm [7]. This aspect introduces an important

concept, called “Carbon Budget”, which represents the maximum quantity of Carbon which can be emitted in the atmosphere to stay below 450 ppm. According to IPCC estimates [1], the atmosphere can absorb, calculated from the beginning of 2020, no more than 400 Gt of CO_2 if we are to stay below the 1.5°C threshold. Annual emissions of CO_2 - from burning fossil fuels, industrial processes and land-use change - are estimated to be 42.2 Gt per year, the equivalent of 1337 tons per second. With emissions at a constant level, the budget would be expected to be used up in less than 8 years from now. The budget for staying below the 2°C threshold, for its part, of 1150 Gt, would be exhausted in about 25 years [10]. These numbers show how little time is left for political decision-makers to take action.

The last COP 26 held in Glasgow in 2021 introduced the Glasgow Climate Pact, which calls for Countries to reduce coal use and fossil fuel subsidies - both firsts for a UN climate agreement - and urges governments to submit more ambitious emissions-reduction targets by the end of 2022. In addition, delegates finally established rules for a global carbon market. Smaller groups of Countries made notable side deals on deforestation, methane emissions, coal, and more. But analysts noted that even if Countries follow through on their pledges for 2030 and beyond, the world’s average temperature will still rise 2.1°C.

1.3 Global primary energy demand and impact of transport sector

A huge effort will be required by developed and developing Countries to meet the targets set by the international agreements, as the world economy has been substantially fossil fuel based. As Figure 1-6 (a) shows, global primary energy consumption has begun to increase strongly since 1850, when the industrial era got started, and it is continuing to rise, due to the economic growth of developed and developing Countries. In 2019, the total amount of primary energy consumption reached 173340 TWh: this huge amount of energy has come mainly from fossil fuels, i.e. coal, oil and natural gas. In 2019, about 84% of global primary energy consumption came from fossil fuels (Figure 1-6 (b)): specifically, 33% from oil, 27% from coal and 24% from gas. The remaining part was covered by hydropower, nuclear and removable energies (wind, solar, biofuels and others) in gradually smaller amounts, about 6%, 4% and 3%, respectively.

Fossil fuels are responsible for CO_2 emissions, since their chemical energy is made available through combustion. Emissions of CO_2, and more in general of GHGs, can be broken down relatively to the type of final energy use. Figure 1-7 shows the historical trend of global GHGs emissions by sector from 1990 to 2018. Electricity and heat production are the largest contributor to global emissions (about 15 billion tCO_2e in 2018), followed by transport (8 billion tCO_2e), manufacturing and construction (6 billion tCO_2e), and agriculture (5 billion tCO_2e). It is worth to notice that the breakdown of GHG emissions by sector depends greatly on the considered geographical area. As an example, after electricity and heat use, transport is the second larger contributor (5.39 tCO_2e per capita per year) to GHG emissions in United

States (Figure 1-8 (a)), while in China the majority of emissions come from manufacturing and industry sectors (Figure 1-8 (b)).

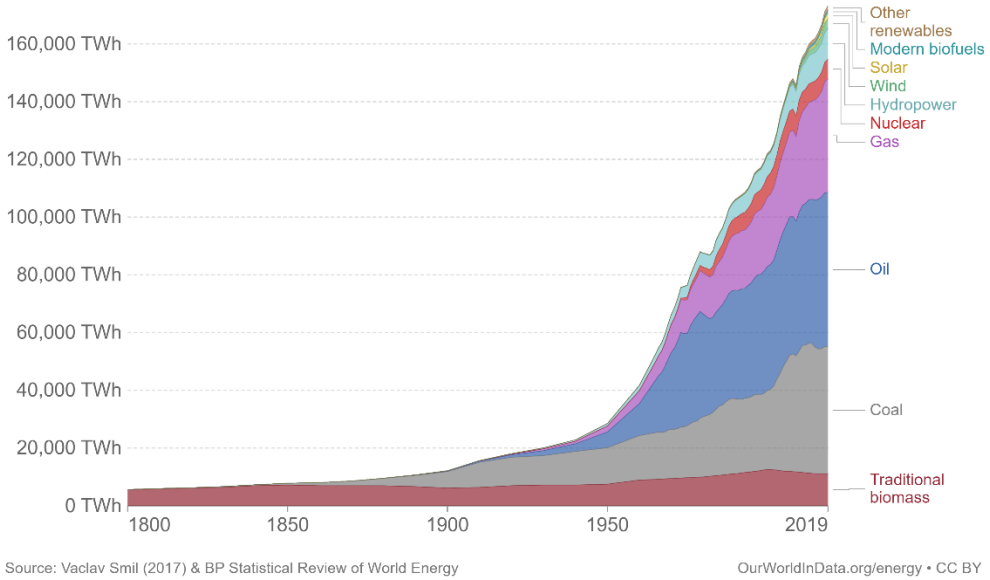

(a)

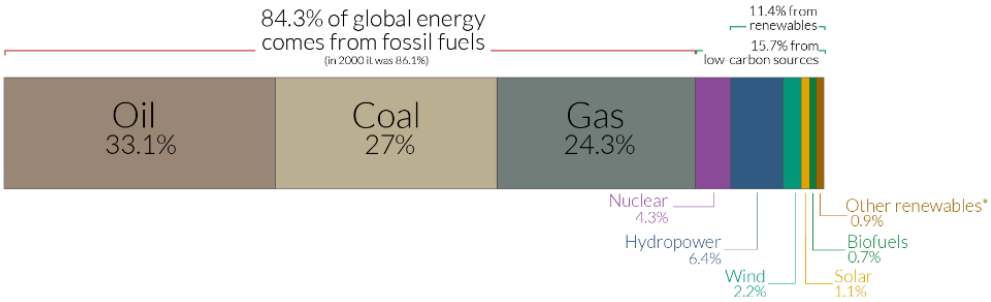

(b)

Figure 1-6. Global primary energy consumption by source: historical trend up to 2019 (a) and breakdown by source based on global primary energy for 2019 (b) [11].

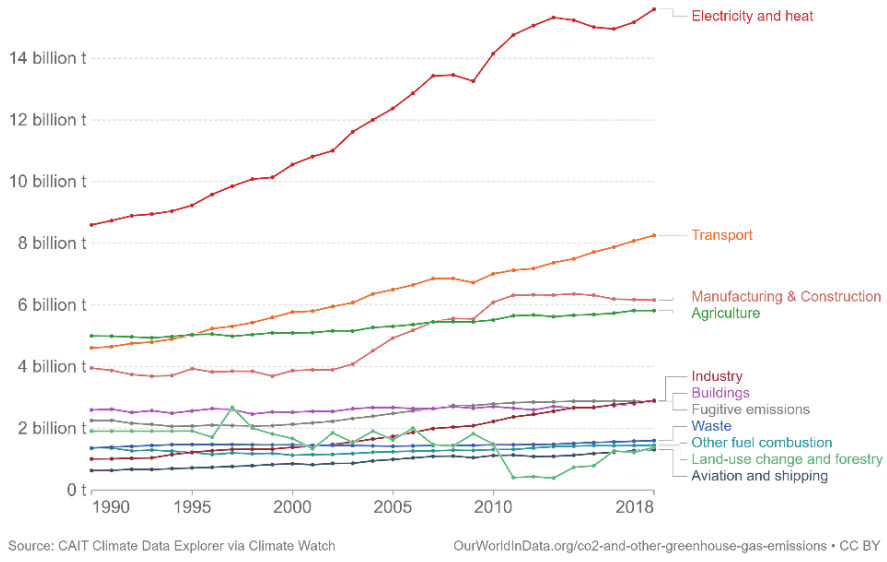

Figure 1-7. Global Greenhouse gas emissions by sector from 1990 to 2018. GHG emissions are measured in tons of carbon dioxide-equivalents (CO_2e) [12].

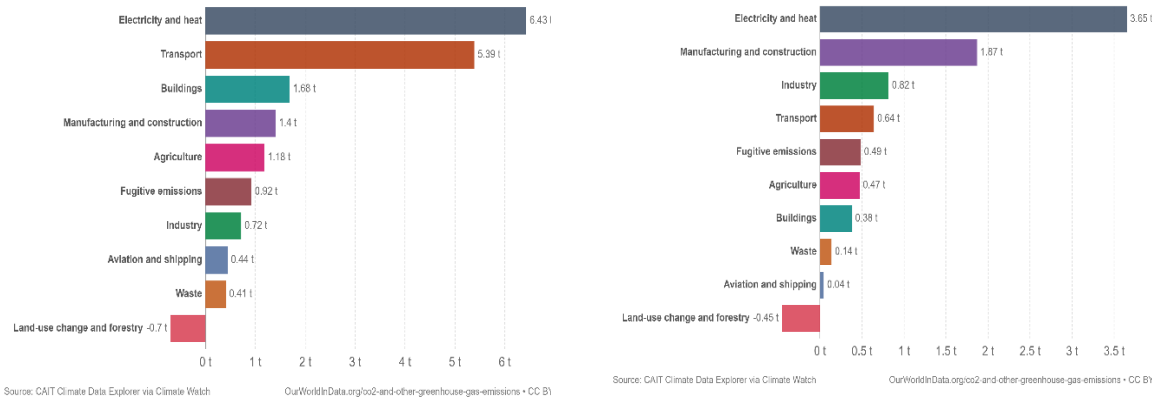

(a) (b)

Figure 1-8. Per capita GHG emissions by sector: relative to United States (a) and China (b) [12].

To reduce CO_2 emissions, the current primary energy covered by fossil fuels will have to derive from carbon-free energy sources. This means that all sectors must move towards CO_2-free technologies, and that this transition should involve all the Countries worldwide, starting from the most emitting ones.

In this thesis, a special focus is paid to the transport sector, which represents about 16% of global GHG emissions, whereas almost the 12% is emitted from the road transport sector (Figure 1-9 (a)). Again, these percentages depend widely on the considered geographic area: for the European Union Countries, transport sector contributes for almost 26% to GHG emissions (Figure 1-9 (b)), the 71% of which is due to road transportation (Figure 1-9 (c)).

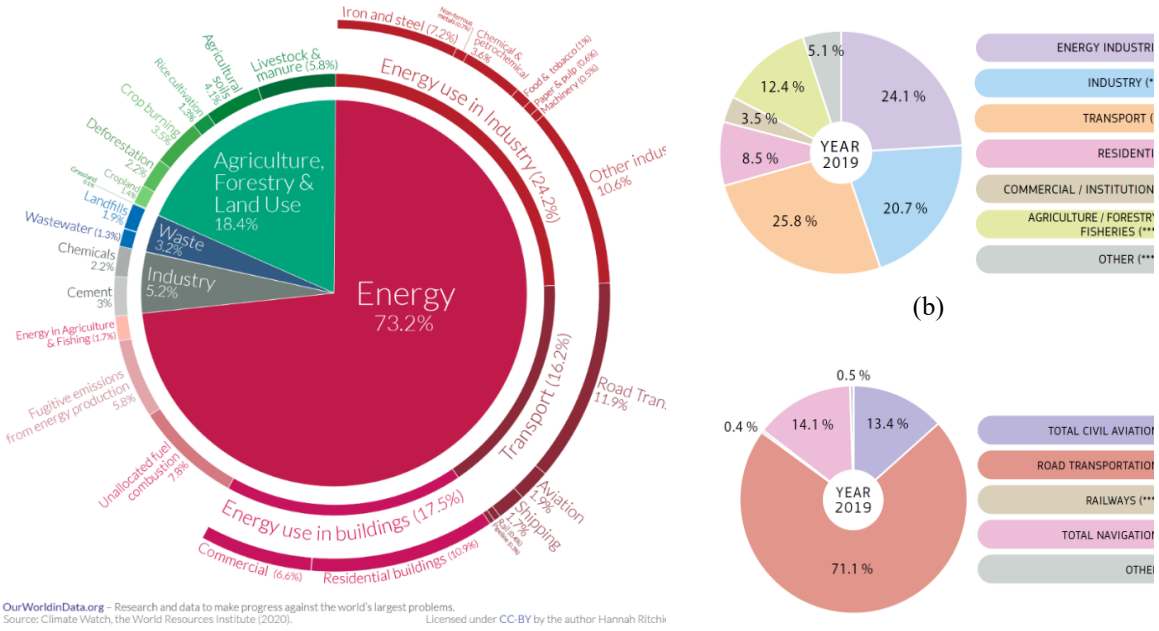

(a) (b) (c)

Figure 1-9. Greenhouse gas emissions by sector: Global (relative to 2016) [12] (a), in EU relative to 2019 (b), and breakdown of transport sector contributions [13] (c).

These data confirm that transport sector is surely one of the main causes of global GHG emissions, although also industrial, agricultural and buildings sectors contribute with higher shares, about 24.2%, 18.4% and 17.5% respectively (Figure 1-9 (a)). However, the transport sector has been object of increasingly stricter regulations during the last decade, especially after the Volkswagen emissions scandal also known as “Dieselgate”, begun in 2015 in USA. Approximately 590000 diesel motor vehicles sold from 2009 to 2016 were equipped with “defeat devices", i.e. computer software systems designed to cheat on federal emissions tests [14]. The major excess pollutant at issue was oxides of nitrogen (NO_x), dangerous for human health, as well as for the environment. Although NO_xs act as a greenhouse gas indirectly, Volkswagen violations increased public concern on the damages caused by transport sector emissions, leading to increasingly strict regulations also on CO_2 emissions.

1.4 Regulations in the road transport sector

Road transport sector has been object of emissions legislations since 1960s, when the first standard regulating emissions from vehicles was introduced in California due to severe smog events experienced in Los Angeles during that period. Since then, the negative effects of tailpipe emissions on health and environment became evident, pushing legislators towards increasingly stricter regulations.

Generally, tailpipe emissions can be limited by controlling vehicle emissions, as well as fuel quality standards. This latter approach gave some of the biggest improvements in emissions reduction in the early stages of vehicle emissions regulations, because the substances contained into the fuel determine directly the nature of the emitted pollutant. Examples are the removal of lead from gasoline since 1970s due to its negative effects on health and catalytic converters, and the removal of sulfur from automotive fuels due to the environmental issues (acid rain) determined by sulfur dioxide (SO_2), which has been reduced up to 15 ppm and 80 ppm in USA [15] for diesel and gasoline, respectively.

Beside this approach, vehicle emissions regulations have been established to limit tailpipe emissions and fuel consumption. It is worth to notice that this regulatory field is continuously updating as new technologies become available on the market, which introduce different test procedures depending on the energy vector used to produce propulsion power (Figure 1-10).

Historically, the main pollutants controlled by vehicle regulations have been Nitrogen Oxides (NO_x), Unburned Hydrocarbons (UHC), Carbon Monoxide (CO), Particulate Matter (PM) and, recently, also Particulate Number (PN). In addition, since 1978 also CO_2 emissions (fuel economy) from vehicles have been limited, starting with USA and Canada legislations.

Vehicle emissions regulations exert their potential by setting upper limits for these emissions, and defining the test procedures to be followed to measure them. In fact, the same emission limit can be achieved or not by a vehicle depending on the test procedure imposed to

it, being its efficiency and emission peculiarities strictly dependent on its operating point variations.

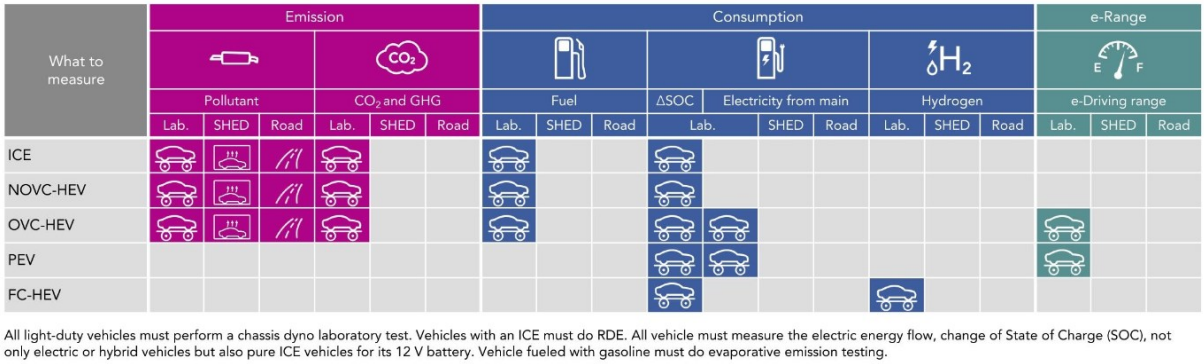

Figure 1-10. Different test types and measurements to be performed depending on the type of powertrain and energy source, from pure internal combustion engine vehicles (ICE) to pure electric vehicles (PEV) [16].

Therefore, after introducing the main emissions regulations adopted worldwide, an overview of the test procedures will be presented, focusing the attention on the reasons that determined their evolution over time. Subsequently, the emission limits imposed by past and current legislations will be underlined, giving a special focus on the CO_2 emissions regulations of some relevant Countries, specifically EU and USA.

1.4.1 Overview of emissions regulations for passenger cars

In the past, there were pure "Pollutant Emissions Legislations", which had some provisions to measure and report CO_2 emissions and fuel consumption, although little attention was paid to the test procedure used to measure them. Currently, all modern legislations have been converted into an "Emission and Energy legislation", which regulate both pollutants and fuel consumption (i.e. CO_2 emissions), including test procedures for all types of powertrains. These legislations are constituted by 6 main elements [16]:

- not-to-exceed pollutant emissions limits;
- Real Driving Emissions (RDE) requirements;
- CO_2 or Fuel Consumption targets;
- test cycle;
- test procedures and specifications;
- equations to calculate the results.

The first three of them are important to define the degree of environment protection and the requirements for powertrain engineering. Instead, the remaining three define the requirements for planning and operating a testbed. While older emission legislation covered all parts in one document, the latest legislation split it up into two documents, one focused on the environmental

and engineering relevant requirements, and the other defining the test procedures and its specifications, as well as the test and measurement systems to be used and the requirements that must be fulfilled. In Europe, this approach is called the "split-level approach": the limits are specified by EU regulations, while the technical specifications are adopted from the UN-ECE Global Technical Regulations (GTR). Instead, in USA different "standard setting parts" for different engine applications define the emission limits, the test cycles, and "technical regulations", in which the test and measurement procedures and specifications are explained.

Generally, Countries could set their own standards, or follow one of the established standards, most often EU or US. Figure 1-11 summarizes the emissions regulations for passenger cars of some important Countries, underlining for each of them how reference emissions limits and technical regulations updated over time. It is worth to notice that since 2018 emissions have been controlled also through Real Driving Emissions (RDE) tests, to overcome the mismatch between laboratory tests results and emissions during real driving conditions (see Section 1.4.2.2). The phase-in of RDE tests began in Europe with progressively lower conformity factors (CF), which is going to be followed by China, India and Japan, whereas USA has not planned to introduce them yet. Moreover, pollutant and CO_2 emissions are monitored in all the considered Countries, but their limits and reference cycles are not completely harmonized.

Looking at a global scale (Figure 1-12), it can be observed that Countries where emissions are legislated most often follow EU or US established standards. The majority of them (Europe, Asia, Africa, Australia) follow the Euro standards in some form, often with a time lag. Instead, Canada and Latin American Countries adopt US-based legislations. In addition, there are plans for ECOWAS (Economic Community of West African States) and SADC (Southern African Development Community) covering western and southern Africa, to implement Euro 4 standards in the 2021–2022 timeframe [15].

Figure 1-12 shows also that some Countries do not have direct emissions legislation, and even more than 100 Countries worldwide have no vehicle emission standards at all [17], often without any domestic vehicle manufacturers. These Countries typically apply restrictions to the age of vehicles being imported as a surrogate to emissions legislation (Table 1-1). According to a recent UN report [17], 86 out of the 146 surveyed Countries have "weak" or "very weak" (according to the report metrics) legislation, regulation, or policies around the importation of used vehicles.

Country	Topic	2012	2013	2014	2015	2016	2017	2018	2019	2020	2021	2022	2023	2024	? 2025 ff	Notes
EU	Limits	EU-5b			EU-6b			EU-6d temp		EU-6d					EU-7	01/2019 Euro 6d-TEMP-ISC 09/2019 Euro 6d-TEMP-EVAP
	RDE					Monitoring		CF 2.1/1.5		CF 1.43/1.5					CF 1	CF NOx/PN
	CO_2	phase in			130 g CO_2/km					95 g CO_2/km					-15%	
	Tech. Reg.	UNR-83 (NEDC)						GTR-15 (WLTC)							UNR-154	

Country	Topic	2012	2013	2014	2015	2016	2017	2018	2019	2020	2021	2022	2023	2024	2025 ff	Notes
USA	EPA Limits	EPA Tier 2					EPA Tier 3									
	CARB Limits	CARB LEV II			CARB LEV III, phase in of 1 mg/mi PM											
	RDE															PEMS used for detection of defeat devices
	CO_2	GHG 263 → 225 g CO_2/mi					GHG 212 → 143 g CO_2/mi									
	Tech. Reg.	40 CFR Part 86			phase in of 40 CFR 1066				40 CFR Part 1066							

Country	Topic	2012	2013	2014	2015	2016	2017	2018	2019	2020	2021	2022	2023	2024	2025 ff	Notes
China	National	China 4					China 5			China 6a			China 6b			China 6, fuel independent limits
	Cities	Beijing 5							China 6b							China 6, fuel independent limits
	RDE									Monitoring			RDE			Altitude 0-700-2400 m
	CO_2	Fuel consumption Stage 2				6.9 l/100 km (~161 g CO_2/km)				5 l/100km (~117 g CO_2/km), NEDC					4 l/100 km	
	Tech. Reg.	GB 18352.3-2005 (NEDC)					GB18352.5-2013 (NEDC)			GB 18352.6-2016 (WLTP)						maybe a new cycle

Country	Topic	2012	2013	2014	2015	2016	2017	2018	2019	2020	2021	2022	2023	2024	2025 ff	Notes
Japan	Limits	Post New Long Term							Post Post New Long Term							
	RDE											RDE CF NO_x 2				only Diesel
	CO_2	Fuel Economy Targets			Fuel Economy Targets 2015					Fuel Economy Targets 2020						
	Tech. Reg.	TRIAS (JC08)							TRIAS (WLTC)							

Country	Topic	2012	2013	2014	2015	2016	2017	2018	2019	2020	2021	2022	2023	2024	2025 ff	Notes
India	Limits	Bharat III / Bharat IV in large cities						Bharat IV		Bharat VI						Bharat stage is like EU stage
	RDE									Monitoring		RDE				
	CO_2					5.5 l/100 km (~130 g CO_2/km)					4.7 l/100 km (~113 g CO_2/km)					
	Tech. Reg.	UNR-83 with 90km/h NEDC (MoRTH / CMVR / TAP-115/116 AIS137)														WLTP expected 2028

Country	Topic	2012	2013	2014	2015	2016	2017	2018	2019	2020	2021	2022	2023	2024	2025 ff	Notes
Korea	Limits	K-LEV II 2014: Euro 6 Diesel				K-LEV III (Gasoline), Euro 6 (Diesel)										
	RDE							RDE CF NO_x 2.1		RDE CF NO_x 1.5						Diesel only
	CO_2	17 km/l or 140 g CO_2 /km						phase in		24.3 km/l or 97 g CO_2/km						
	Tech. Reg.	40 CFR-86 (Gasoline) + UNR-83 (Diesel)						40 CFR-1066 (Gasoline) + WLTP (Diesel)								

Country	Topic	2012	2013	2014	2015	2016	2017	2018	2019	2020	2021	2022	2023	2024	2025 ff	Notes
Brazil	Limits	PROCONVE L5		PROCONVE L6						PROCONVE L7						5 Star classification
	RDE											Monitor		RDE		in discussion
	CO_2	Energetic Consumption EC in (MJ/kg)														Energy consumption classification A to E
	Tech. Reg.	FTP-75 cycle, Regulation based on 40 CFR-86														

Country	2012	2013	2014	2015	2016	2017	2018	2019	2020	2021	2022	2023	2024	2025 ff	Notes
ASEAN	ASEAN countries are from EU-2 up to EU-5 levels, based on UNR-83														
Mexico	EPA Tier 2 / CARB LEV II / Euro-4 or equivalent														
Argentina	Euro-5 or equivalent														
Chile	EPA Tier 2 / Euro-5														
Russia and Eurasia	Euro-5 or equivalent														
Australia, New Zealand	Euro-6 or equivalent														
Africa	from EU-1 to EU-4 or equivalent, but several countries don't have any emission standard														

Figure 1-11. Overview of emissions regulations for passenger cars for different Countries (EU, USA, China, Japan, India, South-Korea and Brazil) [16].

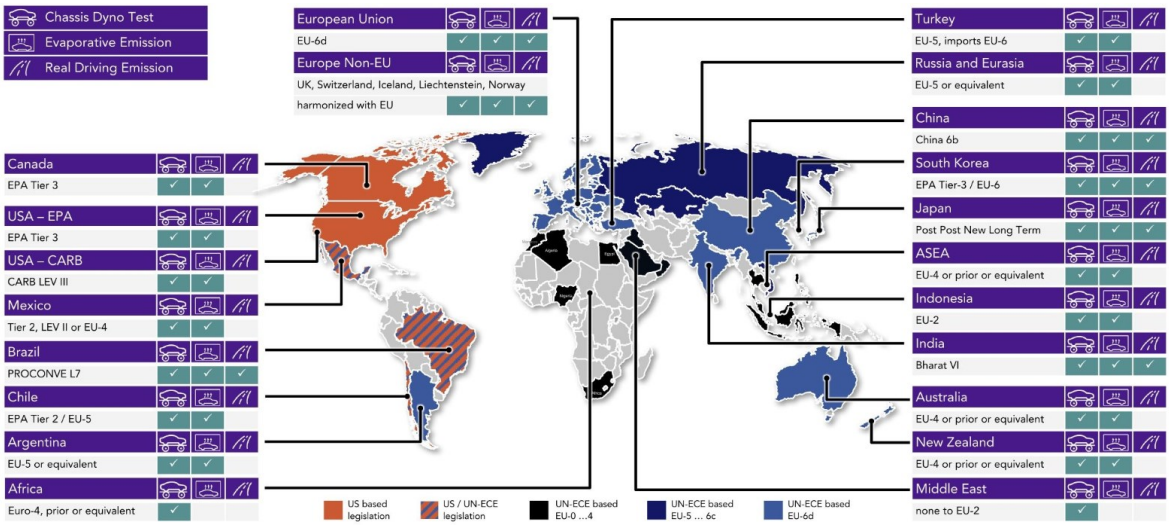

Figure 1-12. Map of emissions regulations for passenger cars used worldwide for the period 2018-2025 (expected) [16].

Ban on used vehicles	Egypt, Morocco, South Africa, Sudan
Ban on vehicles older than 5 years	Algeria, Angola, Chad, Egypt, Gabon, Libya, Mauritius, Morocco, Mozambique, Niger, Seychelles, Tunisia
Ban on vehicles older than 10 years	Benin, Cameroon, Congo, DRC, Eritrea, Guinea, Kenya, Lesotho, Mauritius, Namibia, Nigeria, Reunion, Senegal
No age restrictions	Botswana, Burkina Faso, Burundi, Cape Verde, Central African Republic, Cote d'Ivoire, Djibouti, Equatorial Guinea, Ethiopia, Gambia, Ghana, Guinea Bissau, Lesotho, Madagascar, Malawi, Mali, Rwanda, Somalia, South Sudan, Tanzania, Togo, Uganda, Zambia, Zimbabwe
Roadworthiness test	Benin, Burkina Faso, Cameroon, Chad, Cote d'Ivoire, DRC, Ethiopia, Gabon, Gambia, Ghana, Guinea Bissau, Guinea, Kenya, Liberia, Mali, Mauritania, Mauritius, Mozambique, Niger, Senegal, South Africa, Sudan, Tanzania, Togo, Tunisia, Uganda, Zambia, Zimbabwe
Tax based on age	Cape Verde, Cote d'Ivoire, Gambia, Ghana, Guinea Bissau, Kenya, Liberia, Malawi, Mali, Rwanda, Sao Tome and Principe, Sierra Leone, South Africa, Tanzania, Tunisia, Uganda, Zimbabwe
Tax based on engine capacity	Angola, Benin, Cameroon, Cote d'Ivoire, Egypt, Ethiopia, Ghana, Guinea Bissau, Kenya, Malawi, Mauritius, Mozambique, Rwanda, Tanzania, Togo, Tunisia, Zambia, Zimbabwe
Tax incentives for cleaner vehicles	Gambia, Mauritius, South Africa, Zimbabwe

Table 1-1. Global vehicle import restrictions, used as emissions regulation [15,18].

Finally, it is worth noting that all but a very few (less than ten) Countries worldwide also have fuel standards as ways of controlling emissions, and that many Countries follow the European fuel quality standards, going alongside the Euro emissions standards, without implementing the emissions part of those standards.

1.4.2 Test procedures to measure emissions

As mentioned above, an essential part of any legislation is the definition of driving and testing conditions under which the emissions limits must be met. Therefore, several laboratory testing procedures have been set up over time to compare emissions of different vehicles on a common basis, while representing suitably real driving conditions generally experienced on the road. Laboratory tests uses standardized drive cycles and test procedures to measure emissions. However, recently also Real Driving Emissions tests have been introduced in many Countries (Figure 1-11), to consider the discrepancies on vehicle emissions introduced by the randomness of real driving conditions.

1.4.2.1 *Drive cycles*

Basically, drive cycles define a vehicle speed over time, to be followed by a vehicle operating on a chassis dyno, after defining also accelerations, decelerations and idling conditions. A drive cycle can be developed in three different ways [16]:

- Assuming the real recording of one single driving conducted in a typical road context. This is the case of the FTP-72 drive cycle, which was developed by the California Air Resources Board (CARB) in the 60's and 70's. This cycle is also known as LA-4 cycle,

as it was the 4th route selected among those recorded along the streets of Los Angeles. It is currently used by USA legislation despite being downscaled at that time due to the impossibility for the chassis dyno of the CARB laboratory to accommodate the recorded faster accelerations.

- Developing a driving cycle based on local vehicle traffic statistics. The New European Drive Cycle (NEDC) is an example, being it built on traffic data of Rome and Paris. This cycle has low speeds and an unrealistic geometric shape, which are mainly due to the uncontrolled traffic situations in the 70's and the adopted statistical approach.
- Developing a drive cycle based on a large database of real street data. Here belongs the World harmonized Light Duty Vehicle Test Cycle (WLTC). Starting from 2009, real street data from instrumented vehicles tested along 450000 km in Europe, 153000 km in USA and 98000 km in Asia have been collected and processed together. The output was a set of 4 different drive cycles, one for each corresponding vehicle class.

A drive cycle represents driving on different types of roads (urban streets, rural roads and highways), as well as the time the vehicle is in idle or stopped. The type of road is typically not defined by location, but by the speed range. In order to test a vehicle on a chassis dyno, the road loads of the vehicle must be simulated, as it would be on the road. This is realized through coast-down tests [19] which determine the speed/time points of a specific car when "coasted down" by freewheeling after being accelerated up to 140 km/h on a flat street.

The main characteristics of present and old legal light-duty drive cycles, and of specific R&D cycles, are summarized and compared together in Table 1-2. The test time has an influence on the results, even if they are average emissions over the driven distance in g/km. In fact, longer test times tend to determine lower pollutant emissions compared to shorter tests. The reason is that the high cold start emissions are less significant for a longer test, when referred to a specific unit of distance travelled. All world harmonized cycles are 30 min long, light- as well as heavy-duty. Similarly, lower emission results are determined by longer distance cycles due to less significance of cold start. The average speed plays a not proportional role for CO_2, fuel and energy consumption. In fact, a low-speed cycle can turn out to have higher CO_2 emissions than a cycle with a higher average speed, because pure ICEs operating at low speed have poor efficiency. Moreover, low-speed cycles may also have lower exhaust temperatures, which can reduce the efficiency of the catalytic converter. Instead, higher speed cycles determine higher engine speed and thus higher exhaust flow, resulting in larger exhaust aftertreatment system volume. Going forward, positive accelerations define the required amount of energy, which correlates directly with CO_2 emissions. Finally, Battery Electric Vehicles (BEVs) and Hybrids are affected positively by decelerations, which define the potential of energy recuperation during the test [20]. In fact, cycles typically do not require heavy breaking with the mechanical brake, maximizing the use of the recuperation system of electrified powertrains.

Drive Cycle Overview	Characteristics	NEDC	WLTC 3b	RDE Example	AVL R&D RDE Gleisdorf Runde
Test parameter	Time [min]	20	30	104	66
	Distance [km]	11	23	86	54
	average Speed [km/h]	34	47	52	49
	max. Speed [km/h]	120	131	124	132
	max.pos.Accel. [km/h/sec]	4	6	20	10
Power/Energy of mid-size car	max. Power [kW]	30	36	109	51
	Energy for driving [kWh]	1,1	2,8	8,9	6,9
	Energy for driving [kWh/100km]	10	12	10	13
e-Mobility	Recuperation potential [%]	16%	14%	14%	10%
Idle / Stop	v = 0	25%	13%	9%	18%
Urban	0 > v ≤ 10	6%	3%	4%	6%
	10 > v ≤ 20	10%	12%	7%	7%
	20 > v ≤ 30	5%	12%	9%	7%
	30 > v ≤ 40	18%	8%	10%	8%
	40 > v ≤ 50	15%	10%	18%	6%
	50 > v ≤ 60	2%	9%	7%	14%
Rural	60 > v ≤ 70	10%	7%	5%	10%
	70 > v ≤ 80	1%	5%	8%	5%
	80 > v ≤ 90	1%	4%	9%	3%
Highway	90 > v ≤ 100	4%	5%	2%	3%
	100 > v ≤ 110	1%	3%	6%	1%
	110 > v ≤ 120	2%	3%	7%	0%
	120 > v ≤ 130	0%	4%	0%	1%
	130 > v ≤ 140	0%	0%	0%	11%
extended	140 > v ≤ 150	0%	0%	0%	0%
	150 > v ≤ 160	0%	0%	0%	0%
German Autobahn	v > 160	0%	0%	0%	0%

(a) Drive cycles (part I).

ARTEMIS 150km/h	RTS95	FTP-75 w/o soak	EPA 5-Cycle w/o soak	Japan JC08 w/o soak	China CLTC-P w/o soak
52	15	31	95	23	30
52	13	18	71	10	14
59	53	34	44	27	29
150	134	91	128	82	114
10	10	6	13	6	7
60	70	29	71	18	33
7,5	2,2	1,9	8,0	1	1
14	17	10	11	10	10
12%	21%	21%	17%	24%	21%
11%	7%	19%	15%	27%	23%
6%	9%	6%	5%	7%	7%
6%	8%	6%	5%	10%	15%
6%	10%	10%	8%	14%	13%
9%	11%	17%	13%	11%	11%
10%	11%	21%	16%	8%	10%
8%	7%	9%	9%	11%	9%
7%	6%	1%	3%	5%	4%
5%	5%	3%	7%	5%	3%
6%	3%	7%	9%	1%	1%
3%	3%	2%	6%	0%	1%
5%	6%	0%	2%	0%	1%
4%	6%	0%	2%	0%	1%
8%	6%	0%	0%	0%	0%
2%	2%	0%	0%	0%	0%
3%	0%	0%	0%	0%	0%
0%	0%	0%	0%	0%	0%
0%	0%	0%	0%	0%	0%

Actual legal cycles | Old legal cycles, but still be in use in some countries | Specific cycles

(b) Drive cycles (part II).

Table 1-2. Overview of Light-Duty drive cycle and of their main characteristics ((a) and (b)) [16].

Among the drive cycles summarized in Table 1-2, the most important are NEDC, WLTC and US FTP-75 drive cycles.

The European emissions legislations for light duty vehicles employed the New European Drive Cycle (NEDC) (Figure 1-13) until 2019. It coincides with the type 1 test cycle as defined in UNECE regulation 83 [21], and consists of 4 repeats of the ECE-15 urban driving cycle (representative of urban driving), which cover about 4 km in total. The urban cycle is followed by one extra-urban (i.e. highway) driving cycle to account for more aggressive high-speed driving. Overall, it covers a distance of 11.03 km in 1180 s (just under 20 minutes) with an average and a maximum speed of 33.6 km/h and 120 km/h, respectively. It was used also to provide the fuel economy figures for vehicles sold in EU. The emissions are expressed as g/test cycle and are measured from the instant the engine starts.

The ineffectiveness of the NEDC was firstly stated in 2011 by the research body of the European Commission, the Joint Research Center (JRC), which highlighting the large and growing discrepancies between laboratory and on-road emissions, especially for NO_x emissions from diesel cars [22]. Many factors contribute to this issue. Among all, the moderate transients and constant-pedal zones of the cycle, as well as the presence of not completely defined boundary conditions of the test procedure [23] [24]. In fact, the NEDC is a light-load cycle, which means that, in most cars, the engine never reaches its highest torque and power. Moreover, the very slow accelerations and decelerations of the NEDC are not representative of real-world driving. Additionally, it does not take into account the extras that modern cars have, such as HVAC (heating, ventilation, and air conditioning) systems and electrical load from onboard computers. This is reflected also in the differences between advertised fuel consumption figures and those experienced by consumers. In fact, the discrepancy between CO_2 emissions obtained with type-approval tests and everyday driving tests has become wider during the years, increasing on average from 7% in 2001 to 30% in 2013 (Figure 1-14).

To overcome these shortcomings, the NEDC cycle was replaced in 2019 by the Worldwide Harmonized Light Vehicles Test Procedure (WLTP). The WLTP is a procedure published as UNECE Global Technical Regulation No 15 (GTR-15) [25], that defines WLTC test cycles and all the specifications needed to type approve a vehicle. This procedure was developed by the European Union, Japan, and India (USA ultimately did not participate) under the auspices of the United Nations Economic Commission for Europe (UNECE) World Forum for Harmonization of Vehicle Regulations. The WLTP divides vehicles into three Classes based on their power-to-weight ratio (PWr), and there is a different cycle for each Class. Since most European mid-market vehicles have a PWr of around 50-100 kW/ton, the 34 kW/ton lower limit for Class 3 (the highest class) effectively mandates its use for all European passenger vehicles. Instead, Class 1 might include very small vehicles driven in India, and Class 2 includes small vehicles driven in India and Japan.

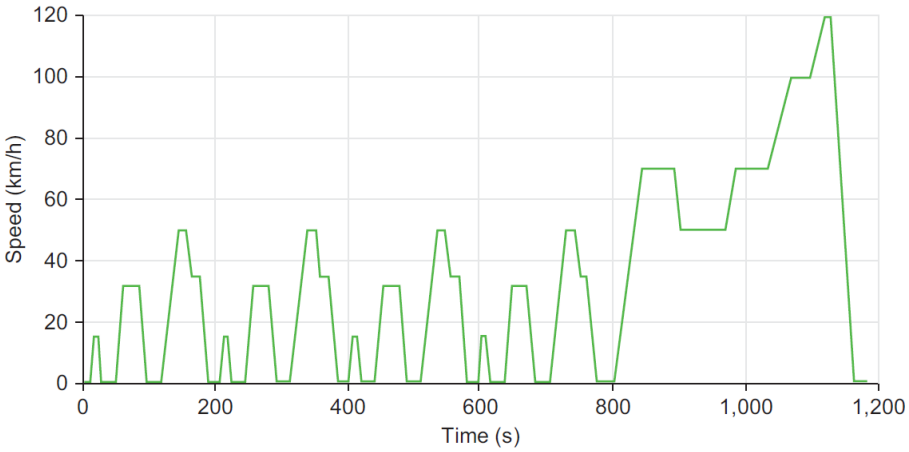

Figure 1-13. New European Drive Cycle (NEDC) speed-time trace [15].

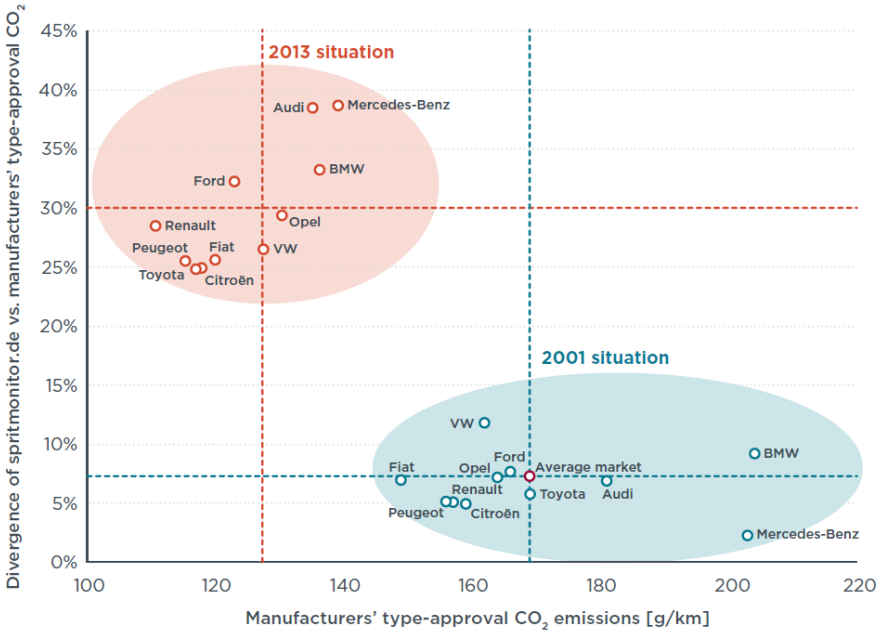

Figure 1-14. Sales-weighted CO_2 emissions in g/km, and discrepancy between the values collected by spritmonitor.de, and those deriving from type-approval tests, considering the selected manufacturers in 2001 and 2013 [26].

As Figure 1-15 shows, the speed-time trace of WLTC Class 3 is far less smooth than the NEDC one (Figure 1-13). Higher accelerations and decelerations shares substitute constant driving phases (Table 1-3 (c)), and stricter limits are imposed on various parameters that influence the test, including road load (i.e., uphill versus downhill), gear changes, and total car mass (i.e. cargo and passengers). The WLTP includes special provisions for testing of various categories of hybrid-electric and electric vehicles. Specifically, Off-Vehicle Chargeable Hybrid Electric Vehicles (OVC-HEVs), Not Off-Vehicle Chargeable Hybrid Electric Vehicles (NOVC-HEV) and Pure Electric Vehicles (PEV) are classified as Class 3 vehicles. Emissions and other parameters proper of these vehicles are tested over the respective Class 3 (3a or 3b) cycle, in both charge-depleting and charge-sustaining modes (Table 1-3 (a) and (b)). Moreover,

WLTC city cycles, composed of low and medium speed phases only, are considered for the testing of the All Electric Range (AER) and of the Recharged Energy (E_{AC}).

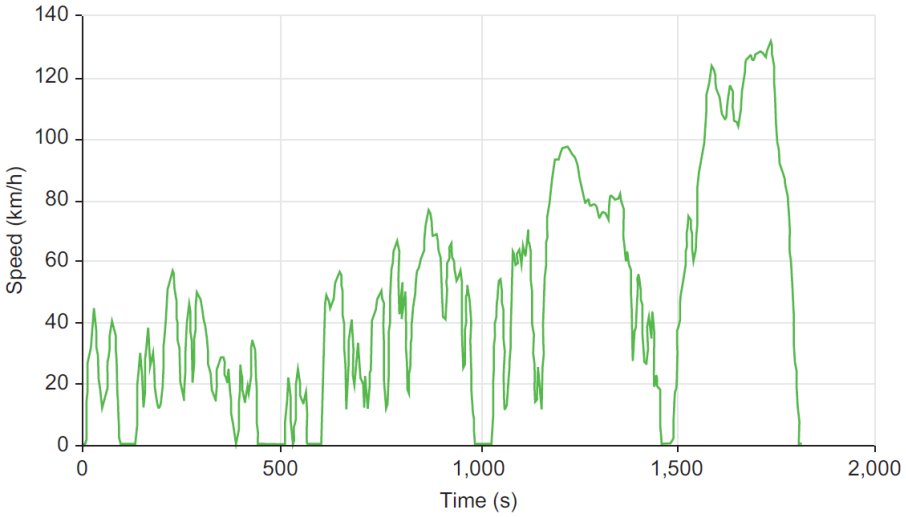

Figure 1-15. Speed-time trace of the WLTP Class 3 drive cycle [15].

		WLTP		WLTP city
		Charge-depleting	Charge-sustaining	Charge-depleting
		Criteria Emissions, FC, CO_2, AER, EAER, R_{CDC}, R_{CDA}, E_{AC}	*Criteria Emissions, FC, CO_2*	*AERcity, E_{AC}city*
OVC-HEV	Class 3a	Low 3 + Medium 3-1 + High 3-1 + Extra High 3	Low 3 + Medium 3-1 + High 3-1 + Extra High 3	Low 3 + Medium 3-1
	Class 3b	Low 3 + Medium 3-2 + High 3-2 + Extra High 3	Low 3 + Medium 3-2 + High 3-2 + ExtraHigh 3	Low 3 + Medium 3-2
NOVC-HEV	Class 3a	--	Low 3 + Medium 3-1 + High 3-1 + ExtraHigh 3	--
	Class 3b	--	Low 3 + Medium 3-2 + High 3-2 + Extra High 3	--
PEV	Class 3a	Low 3 + Medium 3-1 + High 3-1 + Extra High 3	--	Low 3 + Medium 3-1
	Class 3b	Low 3 + Medium 3-2 + High 3-2 + Extra High 3	--	Low 3 + Medium 3-2

(a)

Abbreviations:
AER - All-electric range
EAER - Equivalent all-electric range
E_{AC} - Recharged energy
FC - Fuel consumption
NOVC-HEV - not off-vehicle charging hybrid electric vehicle
OVC-HEV - off-vehicle charging hybrid electric vehicle
PEV - pure electric vehicle
R_{CDA} - Charge-depleting actual range
R_{CDC} - Charge-depleting cycle range

(b)

Parameters	NEDC	WLTC
Duration (s)	1180	1800
Distance (km)	11.03	23.27
Average speed (km/h)	33.6	46.5
Maximum speed (km/h)	120.0	131.3
Stop duration (%)	23.7	12.6
Constant driving (%)	40.3	3.7
Acceleration (%)	20.9	43.8
Deceleration (%)	15.1	39.9
Average positive acceleration (m/s^2)	0.59	0.41
Maximum positive acceleration (m/s^2)	1.04	1.67
Average positive "speed*acceleration" (m^2/s^3)	1.04	1.99
Maximum positive "speed*acceleration" (m^2/s^3)	9.22	21.01
Average deceleration (m/s^2)	-0.82	-0.45
Minimum deceleration (m/s^2)	-1.39	-1.50

(c)

Table 1-3. Characteristics of WLTP: WLTP provisions for the testing of hybrid and electric vehicles [27] (a) and corresponding explanation of the abbreviations (b); comparison between the main parameters of NEDC and WLTC driving cycles [28].

WLTP does not apply in USA, whereas several certification cycles are used: the US06, the SC03, and the FTP-75 cycle (Figure 1-16), as defined by the Environmental Protection Agency (EPA) [29]. The FTP-75 (Federal Test Procedure) cycle is derived from the FTP-72 by adding a 3rd phase of 505 s, identical to the first phase of FTP-72 but with a hot start, starting after the engine is stopped for 10 minutes. Thus, the entire FTP-75 cycle consists of a cold start transient phase (with the ambient temperature at 20-30°C) till 505 s, followed by a stabilized phase up to 1372 s; then, a hot soak lasting between 540 and 660 s precedes the last 505 s hot start transient phase. Therefore, without considering the hot soak, the total duration is 1874 s, and being the average speed equal to 21.2 mph (34.12 km/h) with a maximum value of 56.7 mph (91.25 km/h), the total distance traveled by the vehicle is 11.04 miles (17.77 km).

The FTP-75 is only one of the procedures necessary for emissions certification in the USA, which will be detailed in Section 1.6.

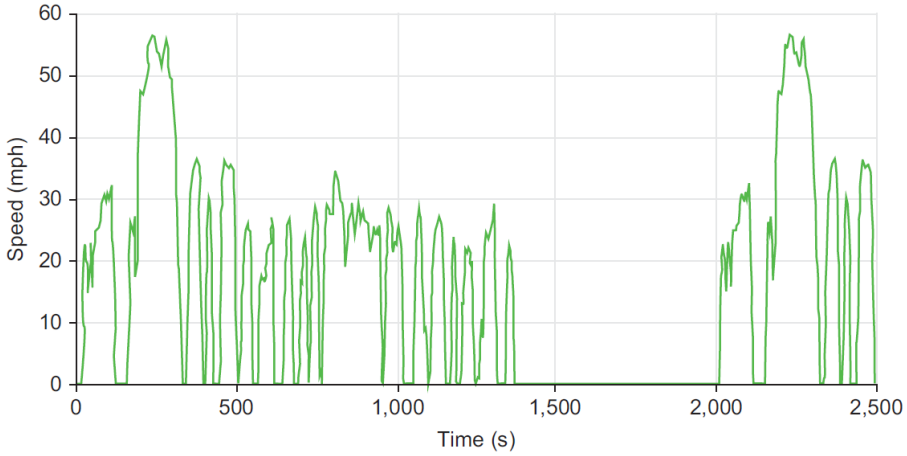

Figure 1-16. The US FTP-75 drive cycle speed-time trace [15].

Similarly to WLTP, the cycles used in USA emissions regulations include sharper accelerations than those of the NEDC, that are more representative of real-world driving and lead to higher fuel consumption and emissions. However, a gap always remains between laboratory and real driving emissions, which is one of the reasons that led to the introduction of Real Driving Emissions tests.

1.4.2.2 Real Driving Emissions (RDE) tests

To close the gap between real emissions and emissions over the certification drive cycles, besides the adoption of transient drive cycles, Real Driving Emissions (RDE) tests have been firstly introduced in Europe since 2017 through the Euro 6d-Temp legislation, and are being taken by many Countries (such as China, India, Japan) except the USA (Figure 1-11). This was

possible thanks to the creation of Portable Emissions Measurement Systems (PEMS), which allow to measure emissions on the road in real traffic conditions (Figure 1-17).

The RDE tests have been regulated by the European Commission [30–34], although a new Global Technical Regulation (GTR) and UNECE Regulation have been under development since 2018 [35]. The EU RDE legislation has been divided into four legislative packages, for enactment over several years:

- The 1st package was voted on in May 2015 and published in March 2016 [30]. It applied to Euro 6c vehicles (NEDC approved) starting from April 2016. It introduced the basic features of RDE test, i.e. trip characteristics, description of data evaluation tools, technical requirements of PEMS equipment, and reporting obligations. It was only intended for monitoring and reporting gaseous emissions, especially NO_x emissions, which have been under special surveillance after "Dieselgate" [14]. The test data could be evaluated through a moving average window method or a power binning method.
- The 2nd package was voted on in October 2015 and published in April 2016 [31]. It defined Not-To-Exceed (NTE) limits on NO_x and a RDE implementation timetable. NTE limits are defined through a Conformity Factor (CF), whose value is being progressively diminished to one. Moreover, technical limits on boundary conditions and GPS analysis were introduced.
- The 3rd package was voted on in December 2016 and published in June 2017 [33], coinciding with the introduction of WLTP. A Particulate Number (PN) measurement protocol and associated CF was introduced from September 2017, as well as procedures for including cold starts, regeneration events and hybrid vehicles testing.
- The 4th package was voted on in March 2018 and published in November 2018 [34]. A stricter NO_x CF was adopted, and In-Service Conformity (ISC) and surveillance tests were introduced, along with specific provisions for light commercial vehicles (vans). Furthermore, the data evaluation mode was modified to provide suitable correction factors for high CO_2 emitting vehicles.

Since the implementation of the 2nd RDE package, all of the pollutants that are regulated by laboratory-based cycle testing are also regulated by RDE, and Not-To-Exceed (NTE) limits had to be complied with. These limits are defined by multiplying the Euro 6 emission limits with a Conformity Factor (CF) (Eq. 1-1).

$$NTE_{pollutant} = CF_{pollutant} \cdot EURO\ 6_{limit} \qquad \text{Eq. 1-1}$$

The CF is a number greater than one, granted for some pollutants as an interim measure. It allows a margin for increased emissions over the laboratory procedure, to account for the variability induced by real traffic conditions and the lower measurement accuracy of PEMS compared to lab instrumentation. RDE CFs for the respective pollutants are summarized in

Table 1-4. There are two conformity factor phases for NO_x emissions: a temporary phase with a value of 2.1 (Euro 6d-TEMP, i.e. from September 1, 2017), and a final phase for which the conformity factor is the margin of uncertainty of the PEMS measurement (Euro 6d, i.e. from January 1, 2020). This margin was initially set at 0.5, and then updated at 0.43 with the 4th RDE package, leading to a NO_x CF equal to 1.43. Instead, PN CF has been set at 1.5 since Euro 6d-TEMP, thus considering a 50% margin of uncertainty of the PEMS measurement.

This means that the Euro 6 NO_x emission limit of 80 mg/km for diesel passenger cars translates into a 168 mg/km RDE limit for the Euro 6d-TEMP, and into a ~114 mg/km RDE limit for the Euro 6d (note that the RDE limits are tighter for gasoline vehicles, which have an Euro 6 NO_x emission limit equal to 60 mg/km) [36].

The legislation allows for an annual revision of CFs, in order to take into account the technical progress of PEMS devices. The aim is to eliminate them, as the EU parliament vote expressed in October 2020.

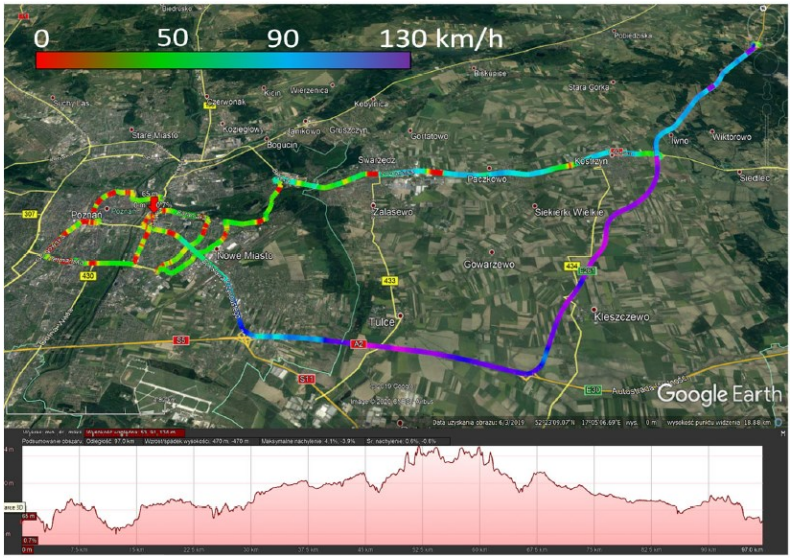

(a)

(b)

Figure 1-17. Example of a RDE test route (a) [37] and of a vehicle instrumented with AVL PEMS™ (b) [38].

	NOx CF	PN CF	CO
Euro 6d-TEMP	2.1	1.5 = 1 + margin PN, margin PN = 0.5	CO is to be measured and recorded
Euro 6d	1.43 = 1 + margin, margin = 0.43		

Table 1-4. Summary of RDE Conformity Factors [39].

The NTE limits have to be met for the whole RDE trip as well as for the urban part separately. This can be expressed by Eq. 1-2, where k is a subscript indicating total trip (t) or urban portion (u), and $M_{RDE,k}$ is the measured specific emission.

$$M_{RDE,k} \leq NTE_{pollutant} \qquad \text{Eq. 1-2}$$

$M_{RDE,k}$ is the final RDE distance-specific mass of gaseous pollutants [mg/km] or particle number [#/km] after correcting for the RDE/WLTP CO_2 ratio. The correction is expressed in Eq. 1-3, where $m_{RDE,k}$ is the distance-specific mass of gaseous pollutant or particle number over the RDE trip prior to CO_2 ratio correction, and RF_k is the result evaluation factor calculated for the RDE trip. This latter depends on the ratio of the distance specific CO_2 emissions during the RDE test over that of the WLTP (Figure 1-18).

$$M_{RDE,k} = m_{RDE,k} \cdot RF_k \qquad \text{Eq. 1-3}$$

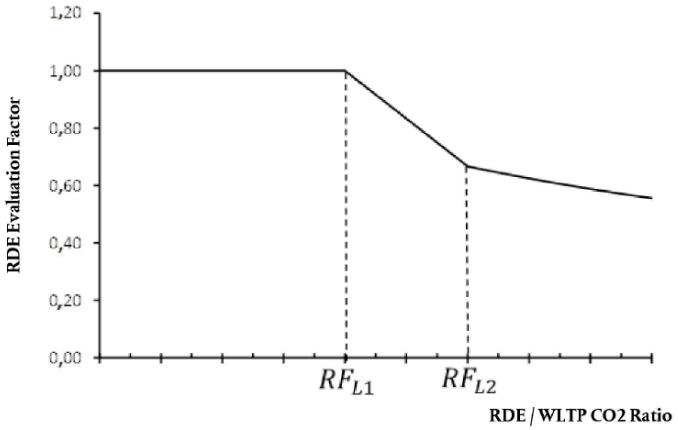

Figure 1-18. Function to calculate the result evaluation factor [34].

Thus, the measured distance specific result is equal to the test result unless the distance specific CO_2 emissions during RDE testing are more than 20% - 30% higher than during WLTP testing [39]. In this latter case, a correction less than 1 can be applied.

To be valid, an RDE trip must meet several specifications (Table 1-5). The test must last between 90 and 120 minutes with urban, rural, and motorway driving accounting for about one-third of the route each. These driving phases are distinguished referring purely to the vehicle speed: urban conditions occur for speeds up to 60 km/h, then rural conditions from 60 to 90 km/h, and finally motorway conditions above 90 km/h.

In addition to trip specifications, other defined boundary conditions must be met by the RDE test to be valid, which include ambient conditions, altitude, stop times, maximum speed, and dynamic boundary conditions (Table 1-6 and Figure 1-19).

Ambient conditions in terms of altitude and temperature are divided into “moderate” and “extended” (Table 1-6). If a data point falls within the extended conditions, the emissions measured have to be divided by a factor of 1.6. Any data point falling outside of the boundary conditions makes the whole trip invalid. In any cases, the cumulative positive elevation gain over a trip is limited to 1200 m/100 km, and no more than a 100-m-altitude difference between start and finish must be exceeded.

Trip specifics		Provision set in the legal text
Total trip duration		Between 90 and 120 min
Distance	Urban	>16 km
	Rural	>16 km
	Motorway	>16 km
Trip composition	Urban	29%[13] to 44% of distance
	Rural	23% to 43% of distance
	Motorway	23% to 43% of distance
Average speeds	Urban	15 to 40 km/h
	Rural	Between 60 km/h and 90 km/h
	Motorway	>90 km/h (>100 km/h for at least 5 min)

Table 1-5. Distance and speed specifications for each urban, rural, and motorway part of the RDE test [36].

Parameter		Provision set in the legal text
Payload		≤90% of maximum vehicle weight
Altitude	Moderate	0 to 700 m
	Extended	Between 700 and 1300 m
Altitude difference		No more than a 100-m-altitude difference between start and finish
Cumulative altitude gain		1200 m/100 km
Ambient temperature[14]	Moderate	0°C to 30°C
	Extended	From –7°C to 0°C and 30°C to 35°C
Stop percentage		Between 6% and 30% of urban time
Maximum speed[15]		145 km/h (160 km/h for 3% of motorway driving time)
Dynamic boundary conditions	Maximum metric	95th percentile of *v*a* (speed * positive acceleration)
	Minimum metric	95th percentile of RPA (relative positive acceleration)
	Curves shapes shown in Figure 2.	
Use of auxiliary systems		Free to use as in real life (operation not recorded)

Table 1-6. Boundary conditions for RDE tests [36].

Driving that could be regarded as "too smooth" or "too aggressive", based on indicators such as speed and acceleration, must be discarded. Figure 1-19 shows high and low dynamic boundary conditions through the limit curves as a function of speed, of the speed (v) multiplied by acceleration (a), and the Relative Positive Acceleration (RPA), respectively. To be valid, each urban, rural, and motorway section of an RDE trip must be below the line showing the v·a speed dependency, and above the line showing the RPA one.

Prior to the 4th RDE package, two evaluation tools were independently developed and included as part of RDE Regulation 2016/427 [30] for processing data collected during an RDE trip: the moving-average window method and the power-binning method.

The moving-average window method was developed by the European Commission JRC. It divides the measured data into windows and uses "normal" windows to calculate the test result.

One associated software is called EMROAD. Instead, the power-binning method was developed by the Technical University of Graz. It adjusts the measured result according to bins corresponding to instantaneous power at the wheels. One associated software offered is called CLEAR.

Both tools use trip data on engine power or CO_2 emissions or both to decide whether a particular driving situation was relatively demanding. The tools then mathematically correct or weigh the measured exhaust emission levels upward or downward based on that driving situation [36].

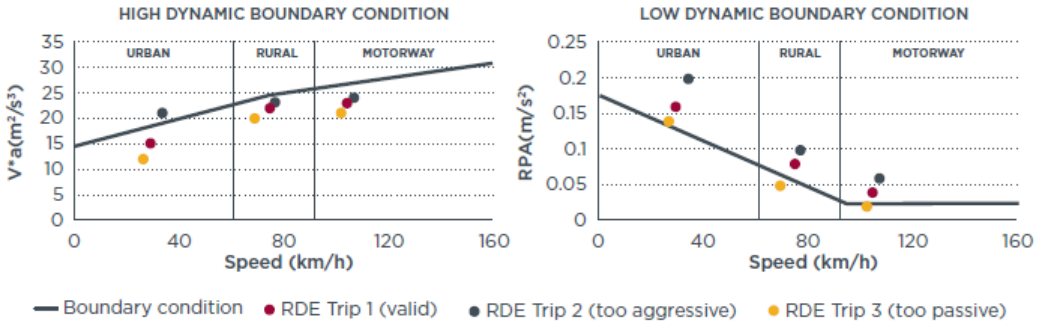

Figure 1-19. Dynamic boundary conditions with three illustrative RDE trips [36].

The 4th RDE package also includes a requirement to report the maximum NO_x and PN values for the urban portion and the entire trip in the certificate of conformity. These "Declared Maximum RDE Values" are used for In-Service Conformity, in which vehicles must comply with their emission limits throughout their defined "normal life". The legislation defines "normal life" as five years or 100000 km. Note that this is much shorter than the average age of cars in the EU, which is 11.8 years [40].

RDE tests have been forcing the development of more robust NO_x aftertreatment systems and strategies on diesel engines and the widespread use of gasoline particulate filters (GPF) on gasoline cars [39]. The resulting positive effects have been stated by many studies. Since the introduction of the RDE legislation, a two-to-three-fold (50–66%) decrease in NO_x emissions compared to vehicles certified under the immediately preceding legislation (Euro 6b) has been reported [41]. Moreover, a variety of studies found even more significant decreases in NO_x emissions, with reductions of 77–99% [42,43]. The compliance with legislative limits has been found also testing vehicles under challenging test cycles on the road [44], and has been achieved efficiently also by diesel engines [45], which have shown the potential to reduce both CO_2 and NO_x simultaneously [46].

The positive effects of the introduction of WLTP/RDE-based legislations reflect also in the reduction of CO_2 emissions. In fact, the variance between published CO_2 emissions and real-world values has fallen from 30-38% to 1-10% shifting from NEDC to WLTP/RDE standards [47,48].

1.4.3 Emission limits

Once having presented the driving and testing conditions referred to by emission legislations, pollutant and CO_2 emission limits imposed over time can be detailed. As described in Section 1.4.1, generally there are two main emission legislative approaches followed by Countries worldwide, i.e. the EU-type and the US-type approaches, each regulating both pollutants and fuel consumption limits.

For what concerns CO_2 emissions, 10 governments, representing around 40 Countries, have introduced corresponding legislations. These legislations follow the outcomes of the Paris Agreement, which covers not just the transportation sector, but all sources of Greenhouse Gases (GHGs) emissions (see Section 1.2). Considering passenger cars, fuel consumption can be limited by imposing restrictions on the vehicle fuel economy itself, or on CO_2 emissions, being internal combustion engines based on the combustion process. However, while EU standards regulate only CO_2 emissions, USA standards regulate also other GHG emissions, specifically CH_4, N_2O, and R-134a [15].

In Countries adopting the EU-type legislative approach, CO_2 standards are set as g/km. Initially, these were tested over the NEDC, and since 2017, over the WLTP (completing the transition from NEDC to WLTP in 2021), with RDE compliance also required. Conversely, in Countries adopting the US-type legislative approach, CO_2 standards are set as fuel consumption standards (mpg) and typically tested over the legislative drive cycles, with parallel legislations regulating GHG emissions (see Section 1.6 for further details).

In all jurisdictions, manufacturers are required to ensure that their total sales meet the legislated level on average, according to a specific fleet-average approach (e.g., Corporate Average Fuel Economy, or CAFE, in the USA). Consequently, manufacturers with diverse portfolios (e.g., GM™, VW™, and Ford™) will find it easier to meet this fleet-average approach than those specialized in larger vehicles (e.g., Ferrari™ and Aston Martin™), because larger vehicles can emit above the limit as long as smaller ones do not exceed it.

Moreover, legislations consider emissions only from the tailpipe. Therefore, purely electric vehicles are considered “zero emissions vehicles”, and in some places they entitle their manufacturer to CO_2 credits sellable to high emitting ones (as in the case of Tesla™). If this legislative approach encourages the production of electric vehicles, it neglects completely any life-cycle analysis of electric vehicles, which could give equivalent CO_2 emissions also higher than those of ICEs, depending on the considered geographical context [49].

A worldwide outlook of the CO_2 emissions limits imposed by passenger vehicle legislations over time is reported in Figure 1-20 (a). The current legislation runs out to about 2030, depending on the jurisdiction, and only approved legislations (not just planned) have been considered. The permitted CO_2 emissions from vehicles have decreased by approximately 50% in the decade from 2010 to 2020. Moreover, the EU has the strictest CO_2 legislation, permitting only 59 g/km by 2030. On the other hand, generally the USA has permitted the highest CO_2

emissions, also considering future legislations. However, in addition to the CO_2 emissions, the USA legislation also controls N_2O and CH_4, regulated at a rate of 6.2 and 18.6 mg/km over the FTP-75 cycle, respectively. Both of these limits are significantly more stringent than the regulations for CO_2 in any jurisdiction, even considering the GWPs of N_2O and CH_4, equal to 300 and 32 respectively.

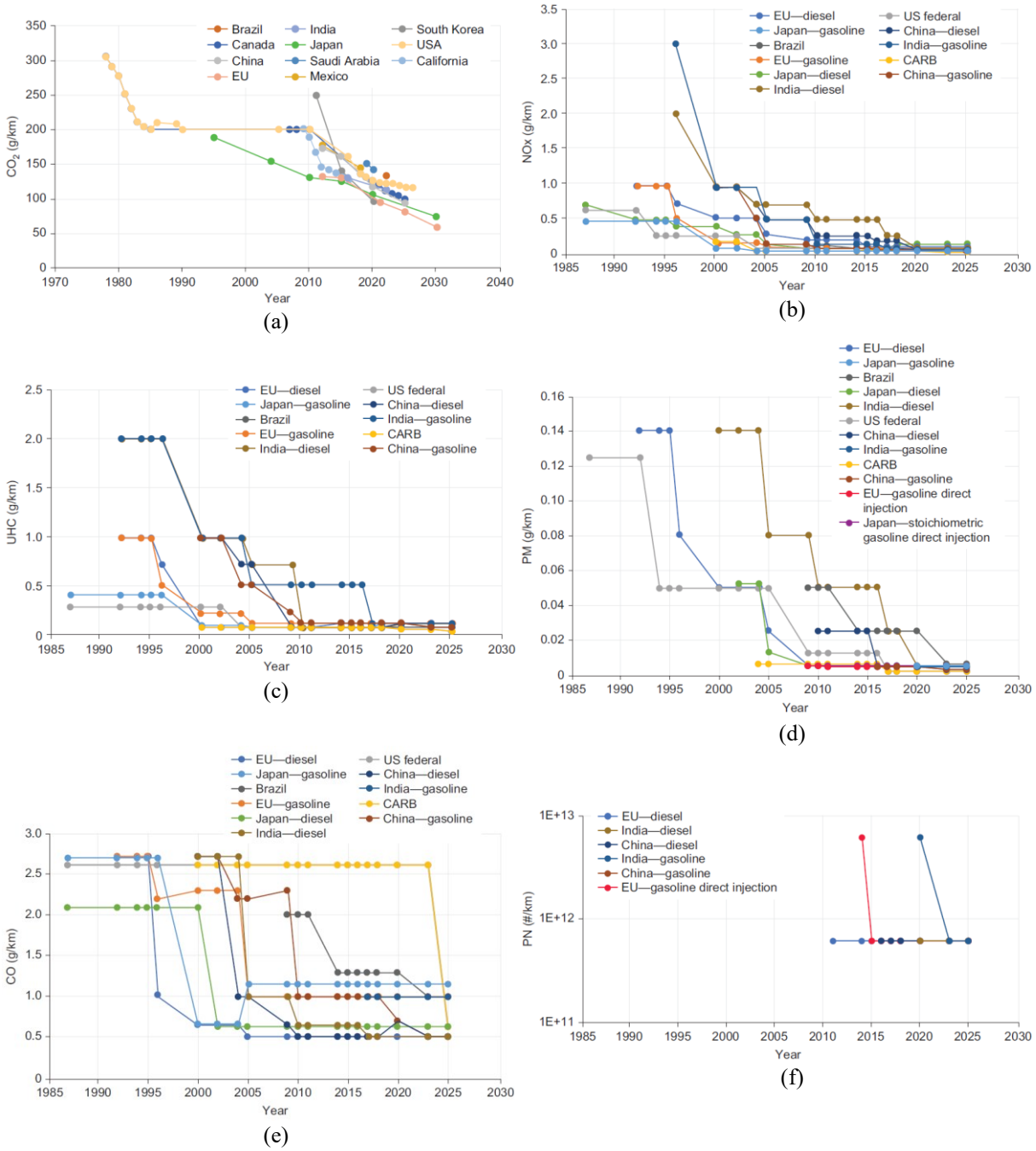

Figure 1-20. Global light-duty emissions legislations: (a) CO_2 limits, expressed as g/km emitted over the NEDC; (b) NO_x limits, showing at least a ten-fold decrease since the first limits; (c) UHC limits, showing at least a five-fold decrease since the first limits; (d) PM limits, showing at least a 25-fold decrease since the first limits; (e) CO emissions limits, showing at least a five-fold decrease since the first limits; (f) PN limits, expressed in a logarithmic scale [15].

It is worth to notice that these limits are expressed referring to the NEDC rather than other drive cycles more representative of real driving conditions. This was necessary because there is not sufficient information available to move to another metric yet [15].

As mentioned in Section 1.4.1, pollutant emissions from vehicles are regulated more widely than GHGs, being about 70 Countries restricting these emissions (Figure 1-12). Most Countries follow the EU-type or US-type legislation, which differ for the test cycle (WLTP versus FTP-75) and the inclusion of PN among regulated emissions.

The evolution over time of the global pollutant emissions standards (converted in g/km) are reported from Figure 1-20 (b) to Figure 1-20 (f).

Firstly, considerable differences in the levels that were deemed acceptable existed among legislations worldwide. With time, these levels converged, and now they are substantially coincident. Specifically, the standards have become far more stringent since they were firstly introduced in the 1990s, and most pollutants can now be emitted at less than 5% of the first legislated standard. Beginning in the period 2017–2020, permissible pollution levels from vehicles converged at about 0.05 g/km for NO_x and UHC emissions (Figure 1-20 (b) and (c)), and at 0.005 g/km for PM emissions (Figure 1-20 (d)). Instead, CO emissions still have different limits, ranging from 0.5 to 1.3 g/km (Figure 1-20 (e)).

Different considerations can be made for PN emissions (Figure 1-20 (f)). Still few jurisdictions regulate them: since 2011, the EU has regulated PN, followed by China and India, while in contrast the USA decided not to. Currently, the limit is set at $6 \cdot 10^{11}$ particles per kilometer, and counts particles as small as 23 nm. With the forthcoming Euro 7, particles with diameter equal to 10 nm are expected to be counted [50], making the compliance with this limit even harder. The EU PN legislation has rendered the PM one practically obsolete for most vehicles (particularly for gasoline direct injection vehicles), being stricter than that. The aim is to reduce the particulate matter exposure, whose negative health effects seem to be dependent on the number of particles and their size rather than their mass.

It is worth to notice that many Countries have adopted different standards for different vehicle technologies: gasoline, diesel, and, in the case of the Japanese PM legislation, a stoichiometric gasoline direct injection engine (Figure 1-20 (d)). This derives in part from industry lobbying, and in part from uncomplete technology neutrality in legislation [15].

Similar considerations can be made for pollutant and CO_2 emissions legislations of light-duty vehicles.

As Figure 1-21 shows, the global trend of historical and enacted CO_2 emissions limits for light duty trucks is decreasing, although higher limits are allowed compared to passenger vehicles (Figure 1-20 (a)). Again, the EU legislation is the stricter one, whereas the USA ones have tended to be more permissive.

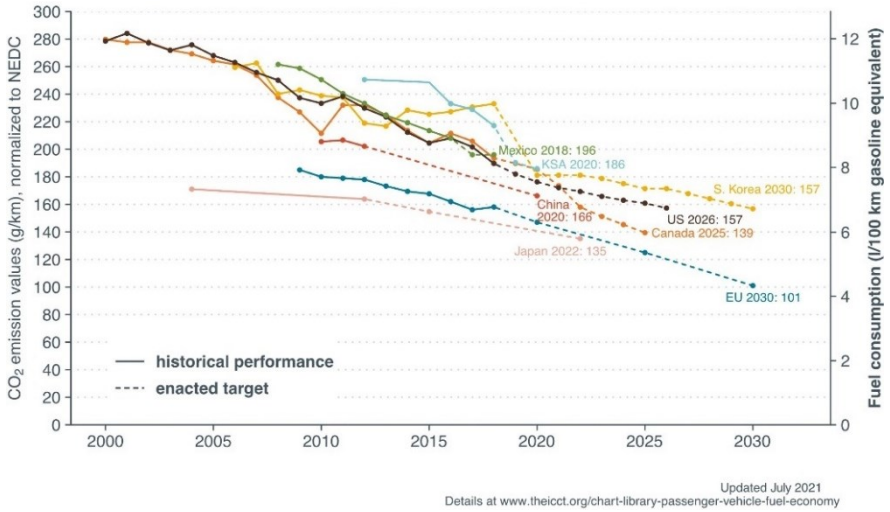

Figure 1-21. Light truck CO_2 emissions and fuel consumption, normalized to NEDC [51].

1.5 CO_2 emissions legislation in EU

European Union has always paid a high attention in reducing CO_2 emissions deriving from road transport sector. Regulation (EU) 2019/631 [52] sets CO_2 emission performance standards for new passenger cars and light duty vehicles (vans). Specifically, this regulation sets EU fleet-wide CO_2 emission targets applying from 2020, 2025 and 2030, and it includes a mechanism to incentivize the spread of zero- and low-emission vehicles. For the period 2020-2024, this regulation confirms the EU fleet-wide CO_2 emission targets set under the previous Regulations (EC) No 443/2009 [53] and (EU) No 510/2011 [54], equal to 95 gCO_2/km and 147 gCO_2/km for cars and vans, respectively. These target levels refer to the NEDC emission test procedure, but the new WLTP emission test procedure is mandatory since 2021.

Specific emission targets are set annually for each manufacturer, depending on the EU fleet-wide targets and the average mass of the manufacturer's new vehicles registered in a given year. The specific emission targets are identified using a limit value curve, which is set so that the targets for the EU fleet-wide average emissions are achieved. Only in 2020, emissions targets applied to the 95% of the least emitting new cars of each manufacturer, passing to the 100% since 2021.

Considering passenger cars, the specific emissions of CO_2 (g/km) in 2020 were determined in accordance with the following formula [52]:

$$CO_{2\ specific\ emissions} = 95 + a\ (M - M_0) \qquad \text{Eq. 1-4}$$

Where:

- M is the mass in running order of the vehicle in kilograms (kg);

- M_0 is a constant equal to 1379,88 kg;
- a is a constant coefficient equal to 0,0333;

Thus, each manufacturer in 2020 calculated its specific emissions target as the average of the specific emissions of CO_2 determined according to Eq. 1-4 of each new passenger car registered in that calendar year.

Instead, since 2021 the specific emissions reference target for a manufacturer has been calculated as follows:

$$WLTP_{reference\ target} = \left(WLTP_{CO_2} \cdot \frac{NEDC_{2020\ target}}{NEDC_{CO_2}} \right) \quad \text{Eq. 1-5}$$

Where:

- $WLTP_{CO_2}$ is the average specific emissions of CO_2 in 2020 in the WLTP;
- $NEDC_{CO_2}$ is the average specific emissions of CO_2 in 2020 in the NEDC;
- $NEDC_{2020\ target}$ is the 2020 specific emissions target calculated as in Eq. 1-4.

Once known the specific emissions reference target, the specific emissions target for a manufacturer is calculated as follows:

$$Specific\ emission\ target = \\ = WLTP_{reference\ target} + a\left[(M_\Phi - M_0) - (M_{\Phi,2020} - M_{0,2020})\right] \quad \text{Eq. 1-6}$$

Where:

- $WLTP_{reference\ target}$ is the 2021 WLTP specific emissions reference target calculated in accordance with Eq. 1-5;
- a is 0,0333;
- M_Φ is the average of the mass in running order (in kilograms) of the new passenger cars of the manufacturer registered in the relevant target year;
- M_0 is 1379,88 kg in 2021, and for the years 2022, 2023 and 2024 it will be adjusted according to the average mass in running order of all new passenger cars registered in the three previous years (further details can be found in [52]).
- $M_{\Phi,2020}$ is the average of the mass in running order (in kilograms) of the new passenger cars of the manufacturer registered in 2020;
- $M_{0,2020}$ is 1379,88 kg.

Eq. 1-6 shows clearly that manufacturers of heavier cars are allowed higher average emissions than manufacturers of lighter cars. Moreover, since 2021 new fleet wide reference targets will be evaluated based on WLTP measurements.

For the subsequent period 2025-2030 and beyond, stricter EU fleet-wide CO_2 emission targets will be set, which are defined as a percentage reduction from the 2021 starting points. Specifically, a 15% reduction from 2025 on will be adopted for both cars and vans, while a 37.5% and 31% reduction will be necessary from 2030 on for cars and vans, respectively.

Table 1-7 shows the fleet average CO_2 emissions relative to 2021 of some of the main car manufacturers, and the gap with their emission target. On average, passenger car manufacturers complied with the emission target with 4 g/km left (114 g/km of average CO_2 emissions against 118 g/km as emission target), i.e. with a safety factor equal to 3%. A key element for ensuring compliance for some manufacturers was to form a pool with other manufacturers. The most striking example is Tesla, which joined with Honda and JRL to ensure compliance for the latter two companies. Pooling can be realized only between manufacturers of the same vehicle class, i.e. it is not possible between car and van manufacturers. Moreover, it must respect the rules of competition law. It is worth to notice that the target gaps are evaluated considering also bonuses, i.e. CO_2 credits for eco-innovations and super credits for low emissions vehicles, which have been introduced by the aforementioned regulations.

	Target gap	New car fleet average CO_2 (in g/km)								
		Dec 2021		2021		Compliance credits		Status 2021	Target 2021	Target gap
		WLTP	NEDC	WLTP	NEDC	EC	SC	WLTP	WLTP	WLTP
Tesla-Honda-JLR	-54%	31	26	65	54	0.0	0.0	65	143	-78
Volvo	-23%	77	64	102	85	0.0	0.0	102	132	-30
BMW Group	-6%	98	84	116	99	0.2	0.0	116	124	-8
Mercedes-Benz	-5%	105	94	116	103	0.0	0.0	116	122	-6
Kia	-4%	91	78	105	91	0.0	0.0	105	110	-5
Ford	-4%	110	89	120	97	0.2	5.7	115	120	-5
AVERAGE	-3%	101	84	115	95	0.0	0.6	114	118	-4
Hyundai	-2%	96	83	107	92	0.0	0.0	107	110	-3
Renault-Nissan-Mitsubishi	0%	94	80	110	94	0.0	0.0	110	111	-1
VW Group	0%	110	92	119	99	0.0	0.0	119	120	-1
Stellantis	0%	109	86	119	93	0.0	0.3	118	118	0
Mazda-Subaru-Suzuki-Toyota	0%	117	93	119	95	0.0	2.6	116	116	0

Notes: EC = eco-innovations, SC = super-credits; all CO_2 values are estimates, see methodology section.

Table 1-7. New passenger car fleet average CO_2 emission level, by manufacturer pool [55].

CO_2 regulatory compliance credits have been provided since 2020 to help manufacturers comply with their target. Specifically, a super-credits system applies for passenger cars with emissions of less than 50 gCO_2/km (NEDC) in the years from 2020 to 2022. These vehicles, called Zero- and Low- Emission Vehicles (ZLEV), are counted multiple times for the calculation of the average specific emissions of a manufacturer: as 2 vehicles in 2020, as 1.67 vehicles in 2021, and as 1.33 vehicles in 2022 [52]. A cap on the super-credits is set at 7.5 g/km per car manufacturer over the three years, and each ZLEV will count as 1 passenger car since 2023. No super-credits system is in place for vans.

From 2025, a different ZLEV crediting system is introduced for both car and van manufacturers. It allows for the relaxation of a manufacturer's specific emission target, if its share of new ZLEVs (vehicles with emissions below 50 g CO_2/km (WLTP)) registered in a given year exceeds 15% from 2025 on and 35% from 2030 on for cars, and 15% from 2025 on and 30% from 2030 on for vans. The target relaxation is capped at maximum 5%, and specific rules apply for calculating the ZLEV share in a manufacturer's fleet, as detailed in [52].

Besides super-credits, eco-innovations is an incentive mechanism introduced to promote innovative technologies that produce real-world CO_2 savings beyond what is measured over the standardized test cycle during vehicle type approval. In this sense, these technologies are also referred as "off-cycle". Both manufacturers or component suppliers can apply to obtain eco-innovations certifications. Novel technologies must pass positively the following approval procedure to be eligible as eco-innovations:

- Technologies may not be currently part of the EU Commission strategies to reduce CO_2 emissions from light-duty vehicles. This restriction prevents air conditioning systems, tire pressure monitoring systems, tire rolling resistance measures, gear shift indicators, and bio fuels from qualifying as eco-innovations.
- Technologies must be novel. The novelty is established considering its market penetration, which should not exceed 3% in 2009.
- Technologies must contribute to the safety or performance of the vehicle. Thus, nonessential comfort technologies are not eligible as eco-innovations.
- Technologies must determine measurable CO_2 savings (greater than 1 g/km in a statistically significant manner) during repeated tests.
- Functionally similar eco-innovations can be bundled in technology packages in order to meet the 1 g/km CO_2 saving threshold, measured using one testing methodology.
- Only the CO_2 savings obtained outside the type-approval conditions can be counted as eco-innovation emission reductions.
- Technologies which depend on the driver behavior cannot be considered eco-innovations, unless statistical evidence can be provided.

The total contribution of those technologies in reducing the average specific emissions of CO_2 of a manufacturer may be up to 7 gCO_2/km. The applicants propose their own method to calculate the CO_2 savings from eco-innovations, following the technical guidelines provided by the EU Commission. Basically, the procedure must quantify the difference in CO_2 emissions between identical vehicles with and without the eco-innovation technology installed. To this end, firstly the tests are conducted under modified type-approval conditions, which should trigger the activation of the technology. Then, the tests are repeated under standard type-approval conditions: any CO_2 savings are subtracted from those obtained under modified conditions to avoid double counting. Lastly, the result is multiplied by a usage factor, to consider how often that technology is used in real conditions.

A summary of the main types of approved eco-innovations up to 2017 is reported in Table 1-8. Innovations involve a wide spectrum of technologies, belonging from the alternator to the thermal subsystem of the vehicle. Moreover, only 9 of the 25 approved eco-innovations were installed in passenger cars in 2017, and less than 3% of new cars were equipped with eco-innovation technologies. Thus, even if the CO_2 savings per vehicle reached 1.5 g/km, the fleet-average CO_2 savings were sensibly lower, due to the low market penetration of the technologies.

Type	Approved eco-innovations	Installed eco-innovations	Vehicle registrations	Average CO_2 savings (g/km)	Fleet-average CO_2 savings (g/km)
Alternator	10	5	304,986	1.4	0.028
Kinetic	3	1	1	4.1	<0.001
Lights	7	1	20,109	1.0	0.001
Solar	3	0	0	–	0
Thermal	2	2	8,540	1.2	0.001
Multiple	–	–	28,140	2.7	0.005
Unknown	–	–	17,711	1.3	0.002
Total	**25**	**9**	**379,487**	**1.5**	**0.040**

Table 1-8. Summary of approved eco-innovations by type: number of approved eco-innovations to date; number of eco-innovations installed in cars in 2017; number of vehicles with eco-innovations registered in 2017; average CO_2 savings in vehicles with eco-innovations in 2017; fleet-average CO_2 savings in 2017 [56].

Globally, the effects of CO_2 regulatory compliance credits can be observed in Figure 1-22, which shows the average type approval CO_2 emissions of the new passenger car fleet in the 27 EU Member States, Iceland, Norway and the UK, and the regulatory target values. Until 2019, the CO_2 fleet average ranged well below the fleet average target for all manufacturers, set at 130 g CO_2/km (NEDC), with the low point of 118 g/km reached in 2016. In 2020, when a sharply reduced fleet-wide emission standard of 95 g CO_2/km came into force, average CO_2 emission values decreased significantly to 97 g CO_2/km (NEDC). This drop is largely the result of more BEVs and PHEV registrations in 2020, constituting 11% of all new passenger cars compared to 3% in 2019. In 2020, excluding BEVs and PHEVs and regulatory compliance credits (super-credits for electric vehicles, eco-innovation credits, and phase-in credits), the average CO_2 emission level of the total new passenger car fleet would have been about 22 g/km higher in 2020 (about 119 g CO_2/km, NEDC) (yellow line in Figure 1-22). Instead, by including electric vehicles and regulatory compliance credits, manufacturers were largely able to comply with their respective 2020 CO_2 emission targets and avoid paying penalties.

Generally, a penalty must be paid by the manufacturer whose fleet average CO_2 emissions exceed its specific emission target in a given year. The fee is 95 € per g/km of target exceedance for each of its vehicles newly registered in that year. The correspondence between the CO_2 emissions recorded in the certificates of conformity and the CO_2 emissions of vehicles in-service must be ensured by manufacturers. This correspondence will be verified by type-approval authorities, which will report any deviations to the EU Commission.

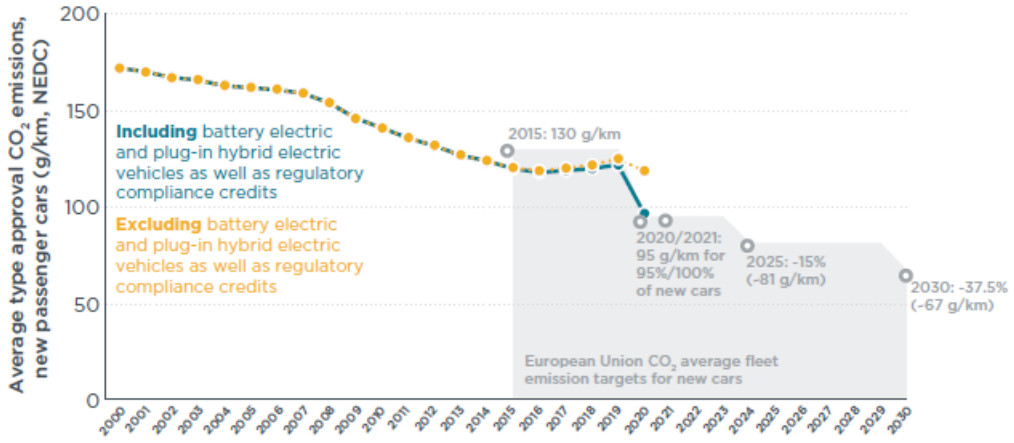

Figure 1-22. Average type approval CO_2 emission levels (NEDC) of new passenger cars in the 27 EU Member States, Iceland, Norway and the UK since 2000, including regulatory target values [57].

1.6 CO_2 emissions legislation in USA

Efficiency standards of US federal passenger vehicle are set through two regulations, issued by the National Highway Traffic Safety Administration (NHTSA) and the Environmental Protection Agency (EPA). In addition, regulations by the California Air Resources Board (CARB) affect about one third of the U.S. fleet [58], and they have typically preceded federal action.

The NHTSA is an agency of the U.S. federal government, part of the Department of Transportation, whose aim is to set Federal Motor Vehicle Safety Standards (FMVSS) as well as regulations for motor vehicle fuel economy, as part of the Corporate Average Fuel Economy (CAFE) system. Since the oil embargo by the Organization of Petroleum Exporting Countries (OPEC) in 1973, CAFE standards have been set out to reduce oil imports, by making the US passenger vehicle fleet more fuel efficient. This reduces indirectly the emissions of carbon dioxide, although the CAFE regulations do not directly target CO_2, neither other GHGs or "conventional" pollutants.

Instead, carbon dioxide emissions from vehicles, and other GHGs, are regulated under the Clean Air Act (CAA) by the EPA, which has the authority to regulate them since 2007. Although fuel consumption and GHG emissions are closely linked together, the increasing presence of alternative-fuel vehicles, most of all hybrid and electric vehicles, has determined the need of suitable GHGs emissions standards. The up-to-date one regulates not only CO_2 emissions, but also CH_4, N_2O, and air-conditioning refrigerants (typically R-134a). This fuel-to-carbon link has led NHTSA and EPA to develop standards jointly since 2010, although EPA has assisted NHTSA on the CAFE regulation since the beginning. The cooperation between them, as well as with CARB and federal agencies, ensures automakers to develop a single fleet of vehicles complying with all relevant regulations nationwide.

The NHTSA and EPA rules regulate passenger vehicles with a gross vehicle weight of up to 8500 lb (about 3856 kg) and medium-duty SUVs and passenger vans up to 10000 lb (about 4536 kg) produced for sale in the U.S. These regulations define annual corporate average standards, or targets, for fuel economy (in miles per gallon) and CO_2 emissions (in grams of CO_2 per mile), based on the U.S. Federal Test Procedure (FTP), which is weighted by 55% city driving and 45% highway driving. Specifically, they specify:

- how an individual corporate standard will be determined for every auto manufacturer, for every year that the regulation applies;
- a baseline and an annual rate of improvement in fuel efficiency, by type and size, for all vehicles sold in the U.S.;
- the means by which manufacturers can meet their annual targets.

The corporate standard depends on the average size of a manufacturer fleet, and on the mix of cars and light trucks it sells in a given year. Consequently, the target will differ from an automaker to another, and for each manufacturer from year to year. Moreover, CAFE/GHG regulations do not set a target for the U.S. light-duty fleet as a whole, but apply targets to the average efficiency of all the cars and light trucks a manufacturer sells in a year, assuming for it a mix of vehicles that will be sold in that year.

Between 2021 and 2022, EPA and NHTSA issued the final role of GHG and CAFE standards, for passenger cars and light trucks of Model Years (MY) 2023-2026 and MYs 2024-2026, respectively [59]. The rates of annual improvement of fleet average GHG emissions and fuel economy are different under the two rules, but the levels of stringency in the two standards are roughly the same in 2026.

The standards set separate numerical targets according to the vehicle “footprint”, i.e. the vehicle size given by wheelbase and average track width. The system uses piecewise linear functions between vehicle footprint and test-cycle GHG emissions or fuel economy rate. The targets are sales-weighted based on each manufacturer production to determine the overall standards that the manufacturer must meet for its passenger cars and light trucks. Exemptions can be asked to EPA and NHTSA, respectively, from manufacturers with less than 5000 or 10000 annually sold vehicles.

GHG emissions targets as a function of vehicle footprint are given by Eq. 1-7, where the coefficients *A*, *B*, *C* and *D* are defined in Figure 1-23 (a) as a function of MYs 2023–2026. The resulting standard curves are reported in Figure 1-23 (b) and (c) for passenger and light trucks, respectively.

$$GHG_{target} = \min\left(B, \max(A, C \cdot Footprint + D)\right) \qquad \text{Eq. 1-7}$$

Minimum and maximum footprints are considered in the compliance target equation. The minimum footprints are 41 square feet for both cars and light trucks, and the maximum

footprints are 56 square feet for cars and 74 square feet for light trucks. For vehicles exceeding these limits, the CO_2 standards are leveled off as flat lines from the minimum footprint down or maximum footprint up.

		A (g/mile)	B (g/mile)	C (g/mi/ft²)	D (g/mile)
Passenger car	2023	145.6	199.1	3.56	-0.4
	2024	138.6	189.5	3.39	-0.4
	2025	130.5	179.4	3.26	-3.2
	2026	114.3	160.9	3.11	-13.1
Light truck	2023	181.1	312.1	3.97	18.4
	2024	172.1	296.5	3.77	17.4
	2025	159.3	277.4	3.58	12.5
	2026	141.8	254.4	3.41	1.9

(a)

		a (mpg)	b (mpg)	c (gal/mi/ft²)	d (gal/mile)
Passenger car	2024	55.44	41.48	0.000405	0.00144
	2025	60.26	45.08	0.000372	0.00133
	2026	66.95	50.09	0.000335	0.00120
Light truck	2024	44.48	26.74	0.000452	0.00395
	2025	48.35	29.07	0.000416	0.00364
	2026	53.73	32.30	0.000374	0.00327

(d)

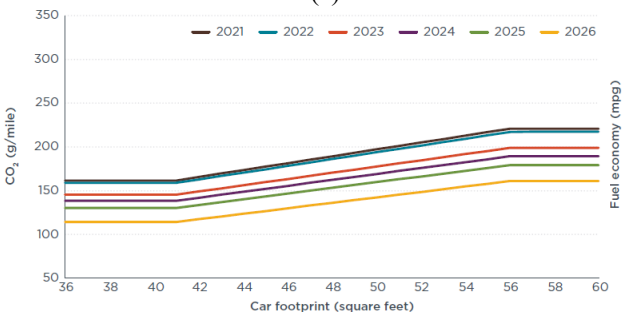

(b)

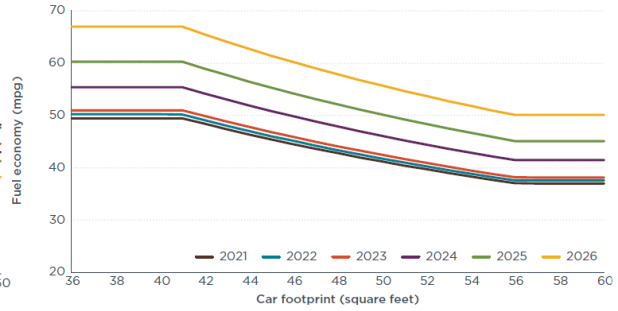

(e)

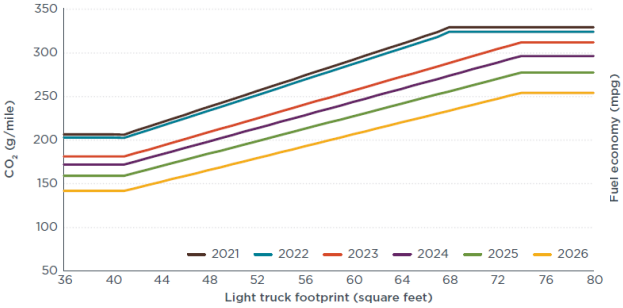

(c)

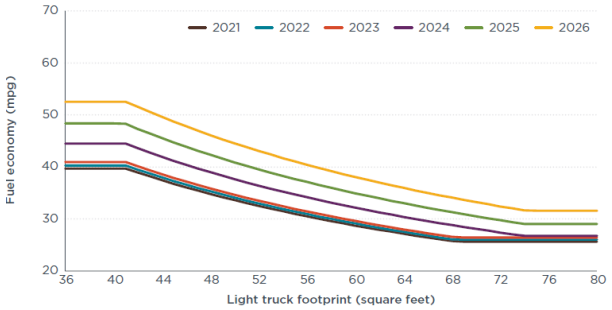

(f)

Figure 1-23. GHG and fuel economy targets: (a) parameters for GHG emission targets (MYs 2023–2026); passenger car (b) and light truck (c) GHG standard curves; (d) parameters for the fuel economy targets (MYs 2024-2026); passenger car (e) and light truck (f) corporate fuel economy standards [59].

Similarly, fuel economy targets as a function of vehicle footprint are given by Eq. 1-8, where *a*, *b*, *c* and *d* are defined in Figure 1-23 (d) as a function of MYs 2024-2026. Thus, the corporate fuel economy standards are represented in Figure 1-23 (e) and (f), for passenger and light trucks, respectively.

$$Fuel\ Economy_{target} = \frac{1}{\min\left(\max\left(c \cdot Footprint + d, \frac{1}{a}\right), \frac{2}{b}\right)} \qquad \text{Eq. 1-8}$$

In this way different sized vehicles can have different standards in the sloped portion, but the largest vehicles are constrained at the upper bend, whereas vehicles below the lower bend are incentivized.

Both EPA and NHTSA have established flexibilities, or incentives, in their regulations to ease the manufacturers transition toward more stringent emission and fuel economy standards.

To this end, EPA provided several types of flexibilities in the final MY 2023–2026 rule, summarized as follows:

- credit banking, trading, and transfer;
- multiplier incentives for advanced technology vehicles;
- full-size pickup truck incentives;
- off-cycle credits;
- air-conditioning system credits.

EPA calculates flexibilities through the definition of emissions credits in Megagrams (Mg), obtained by multiplying the CO_2 emission rate (g/mile), with the applicable vehicle production volume, and the expected vehicle miles traveled (VMT) for those vehicles (Eq. 1-9). The VMT is specified as 195264 miles for cars and 225865 for light trucks [60], and the reversed equation is used to calculate g/mile value from Mg of credits.

$$Credits\ (Mg) = \frac{CO_2 \cdot VMT \cdot Production}{1000000} \quad \text{Eq. 1-9}$$

Firstly introduced in 2010 through the Averaging, Banking and Trading (ABT) program, credits can be used as follows:

- credit carry-forward, i.e. saving over-compliant credits for future use;
- credit carry-back, i.e. using credits to offset a deficit in meeting fleet standard in prior model years;
- credit transfer, i.e. transferring unlimited credits between car and trucks in each manufacturer fleet within the allowable carry-forward and backward years;
- credit trading, i.e. trading credit across manufacturers within the allowable years.

In the final MYs 2023–2026 rule, EPA allows credits to be carried forward for five years and carried back for three years, extending time credits by one year to be carried forward for MY 2017 and MY 2018. Moreover, advanced technology vehicles (battery electric vehicles (BEVs), plug-in hybrid vehicles (PHEVs), fuel cell vehicles (FCVs), and natural gas vehicles (NGVs)) are incentivized through multipliers, which count each of them as more than one. The multiplier is 1.5 for BEVs and FCVs, and 1.3 for PHEVs, and is applicable for only MYs 2023–2024 under the EPA MYs 2023–2026 final rule. Caps and exceptions are provided to multiplier credits, as specified in [61].

Among the wide range of incentives, noteworthy are off-cycle credits, which recognize and incentivize technologies that provide real-world emission reductions which are not captured in the two-cycle (city and highway) EPA FTP laboratory tests used for GHG compliance

verification. For MYs 2023–2026, each manufacturer has off-cycle credits from a detailed list of preapproved technologies, distinguished for cars and light duty trucks (Table 1-9). A cap ranging from 10 g/mile (combined car and truck fleet average per year) to 15 g/mile is provided, meaning that the cumulative menu-based credits for the manufacturer fleet may not exceed the specified off-cycle maximum credit (10 or 15 g/mile).

Technology	Credit for cars (g/miles)	Credit for trucks (g/mile)
High efficiency alternative (at 73%; scalable)	1.0	1.0
High efficiency exterior lighting (at 100W)	1.0	1.0
Waste heat recovery (at 100W; scalable)	0.7	0.7
Solar roof panels (for 75W; battery charging only)	3.3	3.3
Solar roof panels (for 75W, active cabin ventilation plus battery charging	2.5	2.5
Active aerodynamic improvement (scalable)	0.6	1.0
Engine idle start-stop with heater circulation system	2.5	4.4
Engine idle start-stop without heater circulation system	1.5	2.9
Active transmission warm-up (no longer allow systems that capture heat from coolant circulating in the engine block)	1.5	3.2
Active engine warm-up (no longer allow systems that capture heat from coolant circulating in the engine block)	1.5	3.2
Solar/thermal control	Up to 3.0	Up to 4.3
Glass or glazing	Up to 2.9	Up to 3.9
Active seat ventilation	1.0	1.3
Solar reflective paint	0.4	0.5
Passive cabin ventilation (only methods that create convective airflow)	1.7	2.3
Active cabin ventilation	2.1	2.8

Table 1-9. Off-cycle technologies and credits for car and light trucks [59].

Manufacturers can collect off-cycle technology credits and exceed the menu-based cap through two pathways.

The first one allows manufacturers to use five-cycle testing to demonstrate and justify their off-cycle technologies and submit the test data to EPA. The five-cycle tests include three additional tests, designed to address fuel consumption related to aggressive and high-speed driving, air-conditioning use, and cold temperature driving. In fact, as mentioned in Section 1.4.2.1, five cycles need to be performed for emission certification and fuel economy testing of light-duty vehicles in the USA (Figure 1-24):

- the FTP-75 (Federal Test Procedure), which is composed by a city test with no heating, ventilation, and air conditioning (HVAC) operation;
- the HWFET (Highway Fuel Economy Test Cycle), which is a highway test with no HVAC operation;
- the US06 SFTP (Supplemental Federal Test Procedures), which is a more aggressive high speed test with no HVAC operation;
- the SC03 SFTP, which is a hot test at 95°F (35°C) and HVAC set to cool the cabin;
- the cold temperature FTP-75, which is a cold test performed at a lab temperature of 20°F (-6.7°C) and HVAC set specifically for heat and defrost.

Since 2008, EPA has been using the five-cycle methodology to label fuel economy on vehicle window stickers, calculating the results as specified in [61].

Similarly, for what concerns emission certification, from model year 2000 vehicles have to be additionally tested on the US06 SFTP and the SC03 SFTP to suitably represent the effects of aggressive high speed driving, and the effects of using air conditioning, respectively.

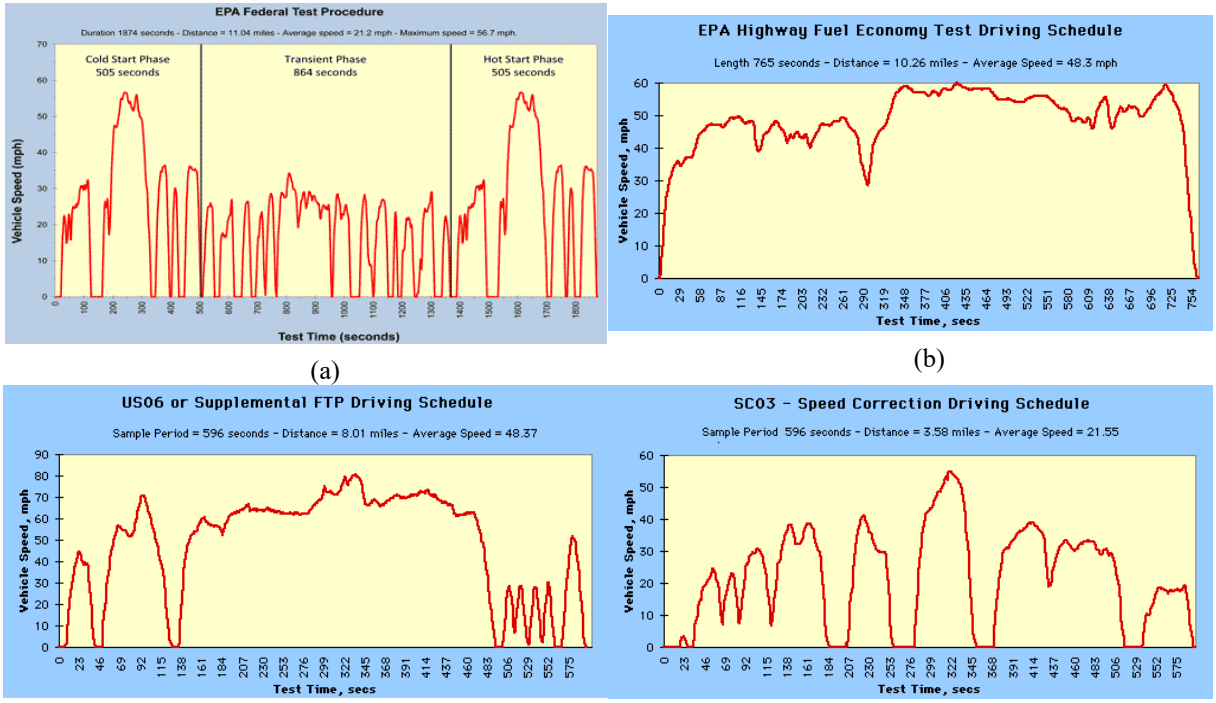

Figure 1-24. EPA five-cycle testing: (a) FTP-75, run in regular (68°F ÷ 86°F) and cold (20°F) temperature conditions; (b) EPA HWFET driving schedule; (c) US06 SFTP driving schedule; (d) SC03 SFTP driving schedule [62].

The other pathway to collect off-cycle technology credits allows manufacturers to use an alternative methodology other than the menu-based and five-cycle tests. Manufacturers have to prove that the five-cycle approach is not adequate in representing the benefits of the technology, and EPA has to approve the proposed methodology.

Similar incentives and flexibilities are included also in NHTSA CAFE standards, although with some minor differences [59].

Civil penalties must be paid by manufacturers not complying with the EPA GHG standards. EPA considers a variety of factors to determine the appropriate penalties. Specifically, it takes into account the history of the manufacturer and all its previous violations. Based on the latest operative statutory civil monetary penalties for violations, for assessment on or after December 23, 2020, but before January 12, 2022, the penalties are up to $48762 per vehicle for violations of various acts, as adjusted for inflation since the first 1970 Clean Air Act penalty.

Penalties are also set by NHTSA for the CAFE standards. Since March 25, 2022, the civil penalty for not complying with CAFE standards is $14 (beginning with MY 2019, and accounting for annual adjustment afterward) per tenth of an mpg under the target value times the total volume of vehicles manufactured for the given model year.

Finally, it is worth to notice that the discrepancies in the two standards are going to be eliminated by NHTSA in 2026, because it is imposing higher annual improvements in CAFE standards to compensate the delays relative to GHG standards (Table 1-10). Specifically, fuel economy will increase at a rate between 8% and 10% per year for both cars and light trucks from 2024 to 2026, whereas GHG emissions will reduce on average by 5% to 10% per year from 2023 to 2026.

	EPA (regulatory agency)				NHTSA			
Fleet	2023	2024	2025	2026	2023	2024	2025	2026
Passenger cars	166	158	149	132	197	181	166	150
Light trucks	234	222	207	187	274	253	233	210
Overall fleet	202	192	179	161	238	219	201	181

(a)

	EPA				NHTSA (regulatory agency)			
Fleet	2023	2024	2025	2026	2023	2024	2025	2026
Passenger cars	54	56	60	67	45.2	49.2	53.4	59.4
Light trucks	38	40	43	48	32.4	35.1	38.2	42.4
Overall fleet	44	46	50	55	37.4	40.6	44.2	49.1

(b)

Table 1-10. Projected average targets for USA legislation: GHG targets in g/mile (a); CAFE targets in mpg (b) [59].

Table 1-10 includes the projection from the regulatory agency and the equivalent estimation from the other agency. NHTSA adjusts its targets considering also the exclusion of AC direct emission credits, which would have made these two programs roughly aligned if included.

1.7 Conclusions

This introduction Chapter gave an overview of the main regulations adopted worldwide in the road transport sector to limit both pollutants and CO_2 emissions. Specifically, the crucial aspects that led to the development of current test procedures have been outlined, along with the description of their main features. Moreover, an international outlook on the emissions limits followed over time was provided, in order to understand how strict they have become over the years, and how challenging will be to comply with them in the future.

Finally, a special focus was dedicated to CO_2 emissions legislations. Specifically, the key aspects of EU and USA legislations have been summarized, being them the reference point for all other regulations adopted worldwide.

In this regulation framework, the sustainable improvement of Internal Combustion Engines (ICEs) is absolutely necessary, being them still extensively used as propulsion systems in the road transport sector. Hence, the state of the art of the technologies that allow such enhancement will be outlined in the next Chapters, with a special focus on the optimization of the engine

thermal management. This is necessary to introduce the core of the research activity, that is the study of innovative screw-type volumetric pumps for engine cooling applications.

2 Internal combustion engines for road vehicles

2.1 Overview

In the last decades, the tightening of emissions regulations in road transport sector, especially regarding CO_2 emissions, is encouraging the development of carbon-free technologies for the vehicle propulsion system. In this sense, full electric vehicles have been usually assumed by policy makers as the best technological solution, due to the absence of tailpipe emissions. If this is true for criteria pollutants, the same cannot be stated for CO_2 emissions, being electricity an energy vector rather than an energy source. However, today's propulsion legislation considers only the in-use phase when assessing emissions, benefiting de facto electric vehicles. A broader approach should consider a Life-Cycle Analysis (LCA) to evaluate suitably the actual CO_2 emissions of an electric vehicle [15]. This methodology is also referred to as cradle-to-grave analysis, because it includes also the GHGs emitted during the well-to-tank (WTT) stage, as well as during all the stages necessary for the production and disposal of vehicle components. All LCAs studies show that the actual GHG emissions of an electric vehicle depends strictly on the carbon intensity associated with electricity generation, which depends strongly by the considered Country [49,63,64]. Moreover, LCAs depend largely on the assumptions and datasets considered for the analyses, resulting in conflicting conclusions among different studies. This aspect has been shown by the consultancy Frontier Economics, which conducted a meta-analysis of more than 80 LCAs [65]. A wide variability on LCA results was found (Figure 2-1), making not possible to determine univocally which is the best propulsion technology in terms of GHG emissions yet.

Besides LCA considerations, several aspects are still limiting a complete phase-out of ICE vehicles. Firstly, the electric vehicle costs are still much higher than those of a traditional vehicle, despite incentives aimed at reducing this gap [66]. Moreover, technological limitations still exist, mainly related to the limited battery range and the high charging times, which are exacerbated by a still not capillary recharging network. Added to these, there are issues related to the need of precious and rare materials for batteries and electric motors (such as cobalt, lithium and nickel), which pose social and political concerns, as well as performance degradation problems over extreme weather conditions [67].

Similar considerations apply to hydrogen vehicles (both fuel-cells and hydrogen ICEs), since hydrogen is an energy vector rather than an energy source. Additionally, cost, infrastructure, technical, storing and safety concerns related to the on-board use of hydrogen need still to be solved [68,69].

A further consideration in favor of Internal Combustion Engines (ICEs) regards carbon-neutral fuels. Currently, more than 95% of energy for transportation is provided by liquid fuels from fossil sources [70]. However, fuels can be produced also through sustainable methods,

which have a neutral (or even negative) overall balance in terms of CO_2 emissions. Two categories of carbon-neutral fuels can be distinguished: biofuels and e-fuels (Figure 2-2).

Figure 2-1. LCA results obtained grouping together many relevant LCA studies [65].

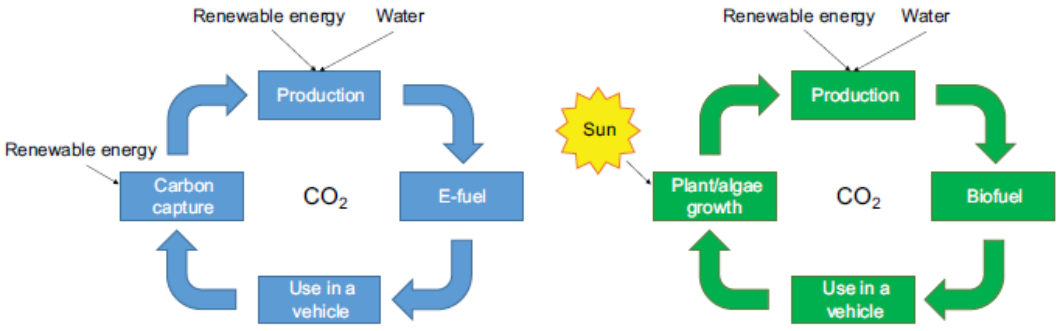

Figure 2-2. Carbon cycles of e-fuels (left) and biofuels (right) [15].

Biofuels capture CO_2 from the atmosphere through photosynthesis in plants or algae. Then, biodiesel and bioethanol are obtained mainly through transesterification and fermentation, respectively. Instead, e-fuels (also called power-to-liquid fuels, e-gasoline, renewable synthetic fuels, syn-fuels, e-diesel, and electro-fuels) can be obtained by the CO_2 captured from rich exhaust or the atmosphere. Once captured, electrolysis of water, reverse water-gas shift reaction, and hydrogenation process (or alternatively hydrocarbon synthesis from syngas) need to be performed to obtain hydrocarbons similar to fossil fuels [15]. These processes are highly energy-intensive, but can be sustainable environmentally and economically if electric energy from renewable sources is used and subsidized [71]. Carbon-neutral fuels are generally compatible with existing fleet, and therefore may help in decarbonizing transport sector in the short-mid term, as the average age of vehicles in EU is about 11.8 years [40].

For these reasons, ICEs are still necessary for the years to come in the road transport sector, as they have been so far [70]. In fact, about 2 billion ICEs have been produced since they were invented in order to satisfy transport and other power needs [72], and over 2 billion new ICE vehicles will be sold over the next 30 years according to the ICCT forecasts [73]. With these numbers, the advancement of ICEs is reasonable and appropriate, also due to the room for improvement they can still achieve, especially in terms of efficiency [74].

Typically, the road transport sector uses four-stroke cycle ICEs as propulsion systems, the 80% of which are Spark-Ignition (SI) gasoline engines for light-duty vehicles [75]. These engines have already been object of a deep optimization process since their first implementation on-board of a vehicle.

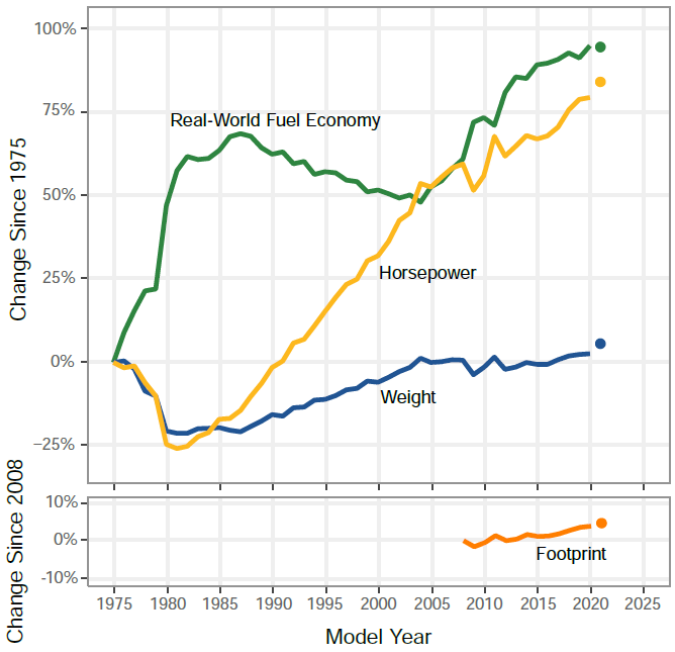

Figure 2-3. Percent changes since 1975 of fuel economy, weight, horsepower and footprint of light-duty vehicles in the USA [60].

The effects of this optimization can be observed in Figure 2-3, where the simultaneous growth of power and real-world fuel economy testifies the efforts in improving both efficiency and performance of the engine, and thus of the overall vehicle.

Many aspects have been involved in ICEs optimization. Firstly, the fuel delivery system has been deeply innovated, in order to guarantee a strictly stoichiometric air-fuel ratio over all operating conditions (for spark-ignited (SI) engines), and generally a more precise control of fuel quantities inside each cylinder. This has been successfully achieved by substituting carburetors with fuel injection systems, which evolved from single-point injection, to port fuel injection (PFI) and direct injection (DI) systems, so much that Gasoline Direct Injection (GDI) engines represent today over half of the US market share [60].

Other important innovations have involved the air delivery system, with the implementation of forced induction methods to maximize engine breathing. This can be achieved through supercharging or turbocharging, as well as through Variable Valve Timing (VVT) systems, which allow to increase the amount of air brought into the engine, improving both power and efficiency. Specifically, turbocharged Compression Ignition (CI) engines offer up to 50% higher specific power and torque, and about 10% better fuel economy than naturally aspirated CI engines of approximately equal torque capability [76].

Moreover, the evolution of the ignition system has played a fundamental role in maximizing the energy output from the combustion process. Besides gasoline engines based on spark ignition, diesel engines based on compression ignition have been developed since the early stages of the automotive history, reaching a wide success especially in Europe between 1990 and 2015 with the introduction of Common Rail [77]. Their higher compression ratios necessary for fuel autoignition have enabled higher efficiencies, reducing CO_2 emissions by 5% to 15% compared to gasoline engines [15].

The main driver of these innovations has been the reduction of criteria pollutants and, more recently of fuel consumption, while improving the vehicle performance. Although the ICE vehicles (ICEVs) of today can achieve very low criteria pollutants, the GHG problem still remains. To reduce CO_2 emissions even further, innovative technologies capable to improve both the efficiency of the engine and of the overall vehicle system are necessary. In the following, a comprehensive review of the main technological advancements currently under investigation in this sense is presented, in order to introduce the potentialities in CO_2 reduction of improved engine thermal management systems.

2.2 Technologies to enhance the vehicle efficiency

Reaching the targets imposed by emissions regulations requires the improvement of the overall vehicle efficiency. Commonly, the efficiency of ICEVs ranges between 12% and 45%, although an overall vehicle efficiency of 80% is theoretically possible, with an ICE efficiency

of 60% [15]. This can be achieved by implementing advanced combustion concepts, together with hybridization, careful thermal management, and other vehicle-level optimizations.

Currently, a typical mid-size gasoline vehicle operating in a combined city/highway driving presents the energy losses summarized in Figure 2-4. Only the 16% - 25% of the fuel chemical energy is converted into mechanical energy to the wheels, where it is dissipated roughly in equal parts as wind and rolling resistances, and breaking losses. The remaining energy losses are mainly thermal engine losses (about one third of fuel energy goes to exhaust gases and cooling system, each), and auxiliaries and drivetrain losses (4%-8% and 3%-5%, respectively).

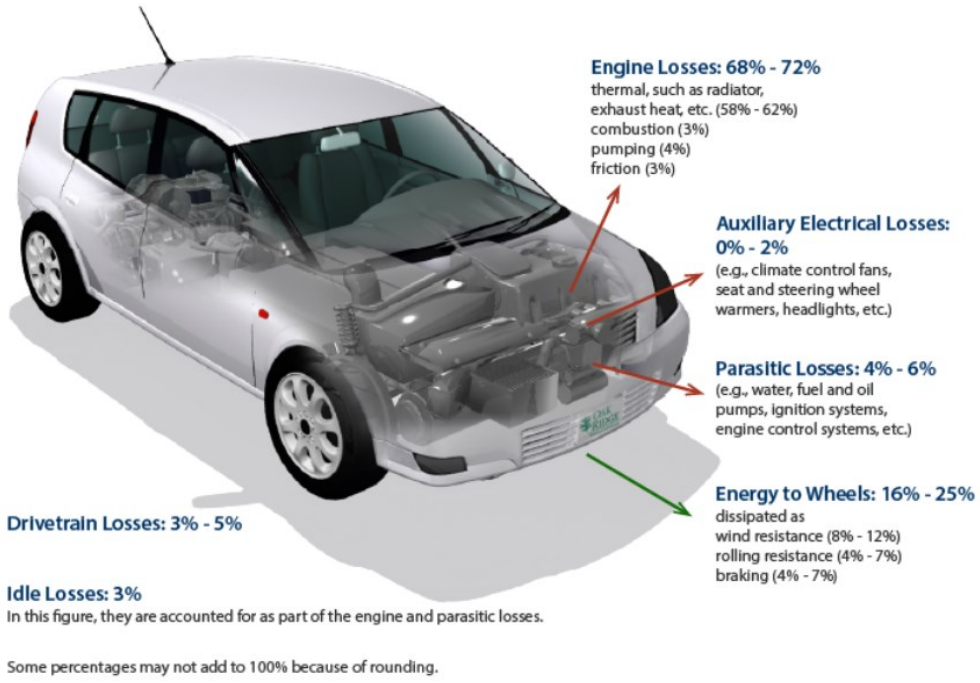

Figure 2-4. Energy requirements for combined city/highway driving for a typical gasoline vehicle [78].

It follows that, besides the reduction of engine thermal losses, technologies capable to reduce the vehicle propulsion power have an immediate potential in reducing fuel consumption. These technologies can act on the reduction of vehicle mass and friction, as well as on the energy recovery during driving.

Before diving into a deeper description of these topics, it is worth to analyze the approach currently adopted by institutions and vehicle manufacturers to enhance the vehicle efficiency.

Figure 2-5 illustrates the technology progression for a representative passenger car for increased efficiency in the 2025 time frame, as proposed by U.S. EPA in 2016 [79]. Specifically, incremental vehicle cost and CO_2 reduction potential with respect to model year 2008 have been assessed for each technology. Results show that a first 28% emissions reduction can be reached at less than 500 $ additional cost by simply reducing engine friction, tire rolling resistance (-10%), aerodynamic drag (-10%), vehicle weight (-5%), and improving transmission and auxiliaries efficiency. Moreover, additional CO_2 savings up to almost 60% can be reached

with an incremental cost around 4000 $. This requires the further reduction of mass, engine friction, tire rolling and aerodynamic resistances, as well as powertrain hybridization and methods to increase the engine efficiency (turbocharging and innovative thermodynamic cycles).

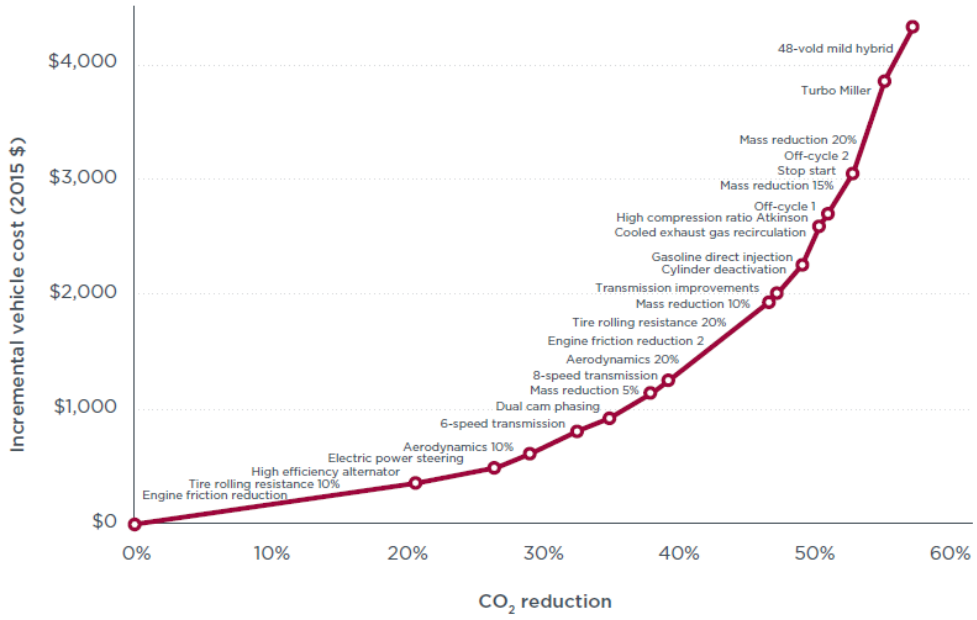

Figure 2-5. Lowest cost efficiency technology progression for CO_2 reduction in passenger cars, based on U.S. EPA 2016c [79].

The effective application of these innovations on the vehicle market depends largely on the specific manufacturer. Figure 2-6 (a) gives an overview of the main technologies adopted in passenger vehicles for model year 2020. On average, 7+ gears transmissions and non-hybrid Stop&Start solutions, as well as Gasoline Direct Injection engines, are adopted together with a technology share of 52%, 46% and 57%, respectively, followed by turbocharging (35%), continuous variable transmission CVT (28%) and cylinder deactivation (15%) systems. Almost all German automotive companies make use of GDI, turbocharging and start/stop systems with 7+ gears, whereas CVT is preferred by Japanese and Korean companies. In both cases, the aim is to increase the number of gears (theoretically infinite in CVTs) to allow the engine operation near peak efficiency. Noteworthy is also the diffusion of Hybrid and Electric vehicles. If on average they represent only 5% and 2% of technology share respectively, they have entered rapidly and consistently in the market during the last decade. In fact, the production rate of plug-in hybrids and full electric vehicles (mainly Battery Electric Vehicles rather than Fuel Cell Vehicles) has risen from almost zero in 2010 up to 4% in 2021 (Figure 2-6 (b)), also thanks to the emergence of new battery electric vehicles manufacturers (Tesla). Hybrid vehicles assume a strategic role in large companies such as Toyota and Mercedes (13% each), and Stellantis (10%), because they allow to optimize both the engine and the vehicle system during highly

transient operating conditions (urban driving). Also GDI engines have known a rapid expansion in the last decade, passing from a technology share of 2.3% in 2008 to 55.6% in 2021.

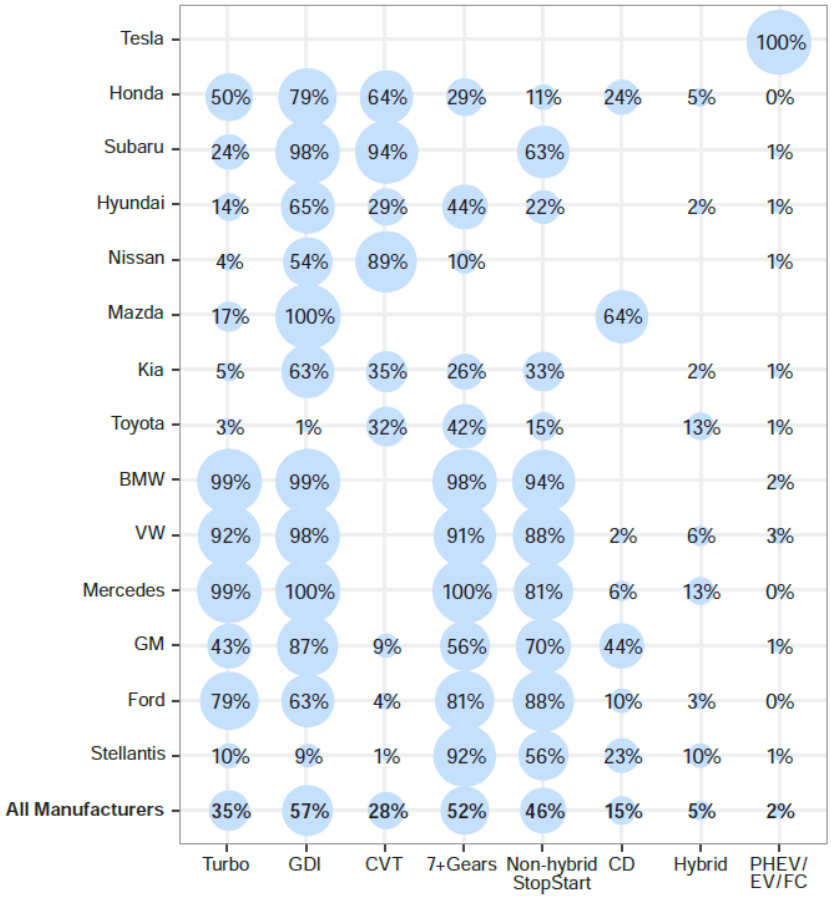

(a)

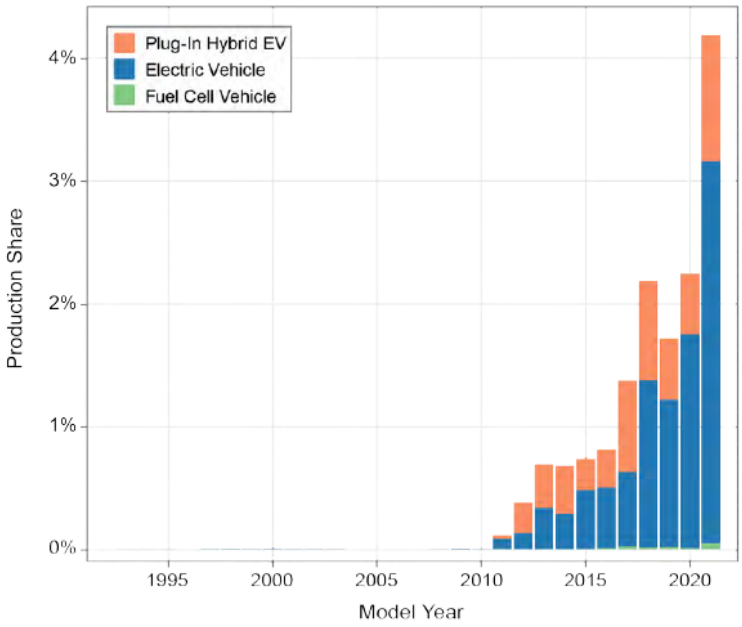

(b)

Figure 2-6. Technologies for vehicle efficiency improvement: (a) manufacturer use of emerging technologies for model year 2020; (b) production share of EVs, PHEVs, and FCEVs [60].

Regardless the engine propulsion type, the vehicle mass and friction phenomena affect greatly its CO_2 emissions, and thus they need to be reduced as much as possible. As Figure 2-7 (a) shows, since 1978 a strong reduction of CO_2 emissions has been obtained by reducing the vehicle mass, and lighter vehicles still emit on average 50% less than the heaviest. Further improvements can be achieved in this sense, as more performing materials (such as carbon fiber composites) will become more affordable [80].

Frictional losses in vehicles outside of the engine include aerodynamic drag and rolling resistance, determined by the tire/road interface and by the friction in rotating components, such as axles and transmission. These losses are determined experimentally through coast-down tests, in which velocities and times of the vehicle are measured when decelerating from a constant speed (e.g. 130 km/h) on a flat and straight road, with engine and gearbox decoupled.

Aerodynamic drag can be mitigated by reducing the car frontal area, replacing side-mirrors with cameras, and using thin, high-pressure tires, among other techniques. An evaluation of the vehicle aerodynamics is given by the drag coefficient. This parameter decreased sensibly over the years, reaching values below 0.26 also for series vehicles (Figure 2-7 (b)).

Rolling resistance is due to both tire properties and mechanical driveline. This latter contributes for 14% and 21% share of total rolling resistance in a single-axle and two-axle driven vehicle, respectively [81]. Therefore, rolling resistance is mainly determined by the tire/road interface through the Rolling Resistance Coefficient (RRC), i.e. the ratio between the force necessary to pull the axle of a tire horizontally, and the vertical load on the tire. The rolling resistance historical trend is reported in Figure 2-7 (c), which shows an average annual decline of 1.3% considering the time span 2004-2014. These data are derived from the EPA database, and are lower than the current EU market average, although high performance tires with just 6 kg/t of RRC are already available on the market. Higher performances can be achieved by increasing stiffness and decreasing plasticity of tires.

Besides the reduction of weight and frictional losses, the energy recovery during driving has a high potential in increasing the efficiency of the overall vehicle. In fact, traditional ICE vehicles use friction brakes to decelerate during driving, wasting mechanical energy into heat. This energy can be recovered partially through regenerative braking systems. There are a variety of approaches to this energy recovery. An advanced method is surely the Kinetic Energy Recovery System (KERS), which has been used in some larger vehicles (like buses) and F1 cars. Typically, it is a flywheel-type system which allows to recover the vehicle kinetic energy mainly during braking operations into mechanical energy available in a flywheel, to be used immediately after during the vehicle acceleration. There are also other types of KERS, which use pneumatic or hydraulic, as well chemical storage systems, to recover energy even from the vehicle vertical oscillations. Many configurations have been developed for KERS, including spring based systems embedded in a Continuous Variable Transmission (CVT) [82].

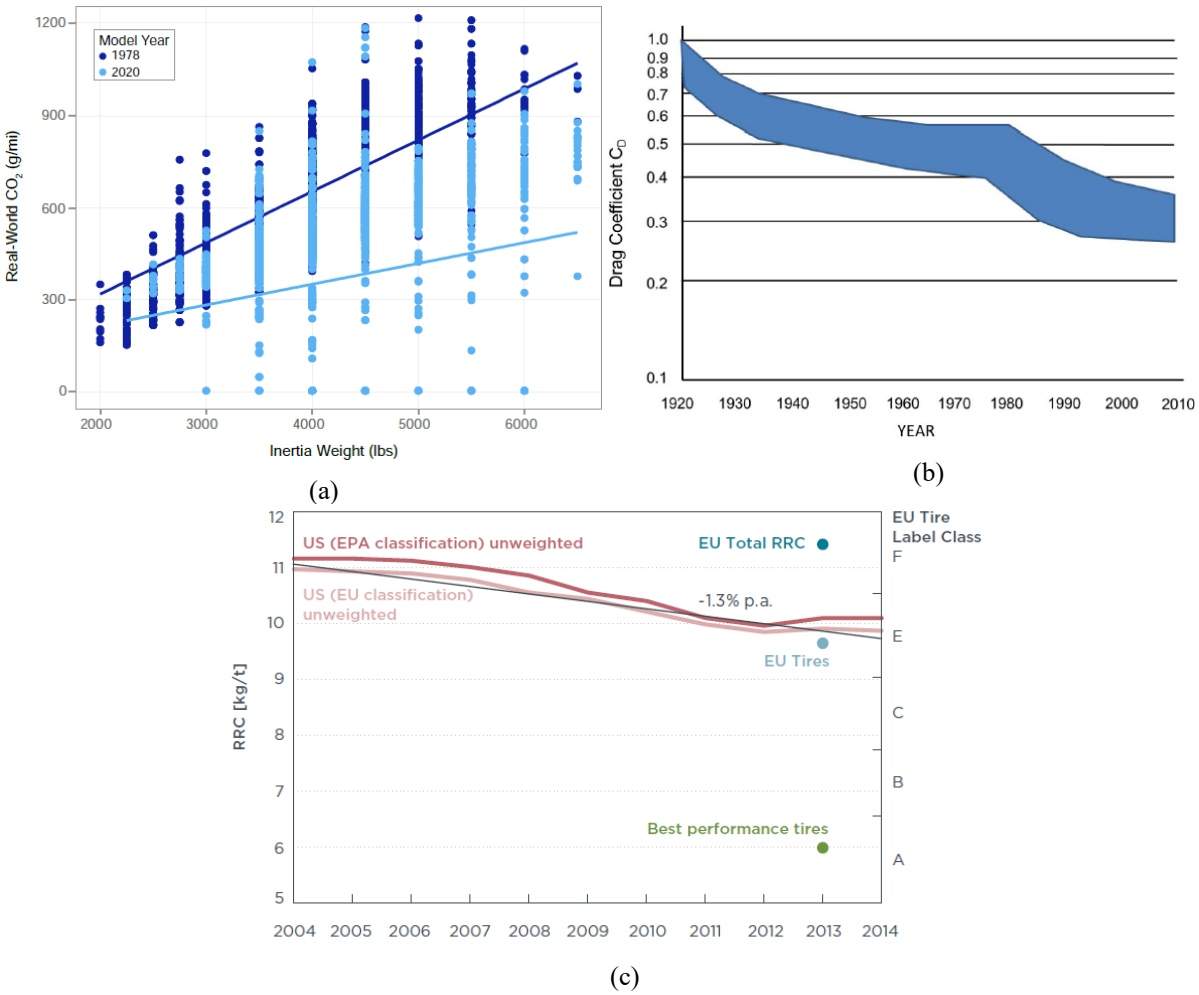

Figure 2-7. Reduction of weight and drag in light-duty vehicles: (a) relationship between inertia weight and CO_2 emissions [60]; (b) trend in passenger car drag reduction [83]; (c) rolling resistance of U.S. car fleet considering EU and EPA classifications [84].

Nevertheless, the most widespread energy recovery system uses electrical machines operating as electric generators. Part of the vehicle kinetic energy is converted during deceleration into electric energy through the electric generator, and then stored into chemical energy inside the batteries. These systems are typically used in Hybrid and Battery Electric Vehicles, which have electrified powertrains capable to expand the vehicle efficiency even beyond the potential of energy recovery during decelerations.

These vehicles include a wide range of powertrains, depending on their degree of electrification. Table 2-1 and Figure 2-8 give an overview of the main acronyms used to distinguish them and their main classification in ascending order of electrification. At the opposite ends, there are Internal Combustion Engine Vehicles (ICEVs), which are 0% electrified in their powertrain, and Electric Vehicles intended as Battery Electric Vehicles (BEVs) or Fuel-Cell Electric Vehicles (FCEVs), which are 100% electrified, i.e. no ICE is used on-board to produce energy. Note that FCEVs use a hydrogen fuel cell to produce electricity, and therefore they can't be referred to as "Plug-ins" in Figure 2-8, because they need a hydrogen refueling station instead of a charging station.

In the middle, there are hybrid vehicles, which use also an ICE to produce the energy necessary to move the vehicle. The simplest configuration is that of Micro Hybrid Electric Vehicles (μHEVs), in which an integrated starter/generator shuts down the engine when in idle conditions, and starts it again when releasing the brake. This system can reduce fuel consumption up to 10% during city driving [85].

The next degree of electrification is given by Mild Hybrid Electric Vehicles (MHEVs), which incorporates a 48 V battery and an electric motor/generator, that runs in a parallel hybrid configuration in conjunction with the ICE. In this way, these vehicles can store the energy recovered during braking and use it for acceleration assistance, providing fuel efficiency increases up to 20% compared to ICEVs [86].

Electric driving is possible starting from Full Hybrid Electric Vehicles (FHEVs). The ICE and the electric motor run in a parallel hybrid configuration, meaning that both devices can drive the wheels individually or simultaneously. The aim is to use the electric motor during highly transient driving conditions, i.e. in urban areas, recharging the batteries through regenerative braking and ICE operation at high efficiency points (for this reason they are also referred to as "self-charging" vehicles). Thus, the electric driving is limited to a small range (3-4 km), enough to cover brief accelerating phases alone (in the city driving) or in conjunction with the ICE (in the highway driving). This hybrid system enables high fuel savings (up to 30%) in urban driving compared to ICEVs, whereas the reduction is substantially negligible at high and constant speed driving [87].

A step further towards powertrain electrification is made by Plug-in Hybrid Electric Vehicles (PHEVs), which are similar to FHEVs except that the battery can be charged from the grid. This allows to extend the electric driving range at about 40 km (which is within the medium range of everyday driving in the US [88]), while maintaining the flexibility of the ICE for longer distance trips. The ICE and the electric motors can be run in either serial or parallel hybrid mode. If the serial only mode is adopted, the PHEV is referred to as Extended Range Electric Vehicle (EREV), because driving is electrically powered and the ICE is only used as a generator to recharge the batteries. The extra-weight of PHEVs and EREVs determined by the larger electrical components (mainly the battery pack) makes these vehicles fuel efficient compared with FHEVs only when charging the battery pack from the grid [89]. In this case, a fuel consumption saving up to 60% compared to conventional ICE vehicles can be reached [90]. It is worth mentioning again that this fuel consumption is limited to the vehicle consumption, without considering fuel consumption, and thus emissions, associated with the grid energy mix, as allowed by current regulations (Section 1.4). The main characteristics of the different types of hybrid vehicles at their current status are summarized in Table 2-2. It is worth to notice that micro hybrids can also have a 24V battery (either NiMH or Li-ion), and that FHEVs need high voltage systems to manage the higher electric power of the powertrain. Moreover, electrical power and CO_2 reduction potential are likely to increase in the near future for MHEVs [86].

Type	Acronym	Features	Includes an ICE?
Internal combustion engine vehicle	ICEV	Full internal combustion engine driving	Yes
Micro hybrid electric vehicle	µHEV	Stop/start technology	Yes
Mild hybrid electric vehicle	MHEV	µHEV + regenerative braking for energy recovery and electric torque assistance (assist acceleration from stop)	Yes
Full hybrid electric vehicle	FHEV	MHEV + electric driving with battery charged from the ICE	Yes
Plug-in hybrid electric vehicle	PHEV	FHEV + electric driving with battery charged from the grid	Yes
Extended range electric vehicle	EREV	PHEV, but the ICE is only used as a generator to recharge the battery	Yes
Battery electric vehicle	BEV	Full electric driving with battery charged from the grid	No
Fuel-cell electric vehicle	FCEV	Full electric driving with hydrogen fuel cell producing electricity	No

Table 2-1. Vehicles classification according to their degree of electrification [15].

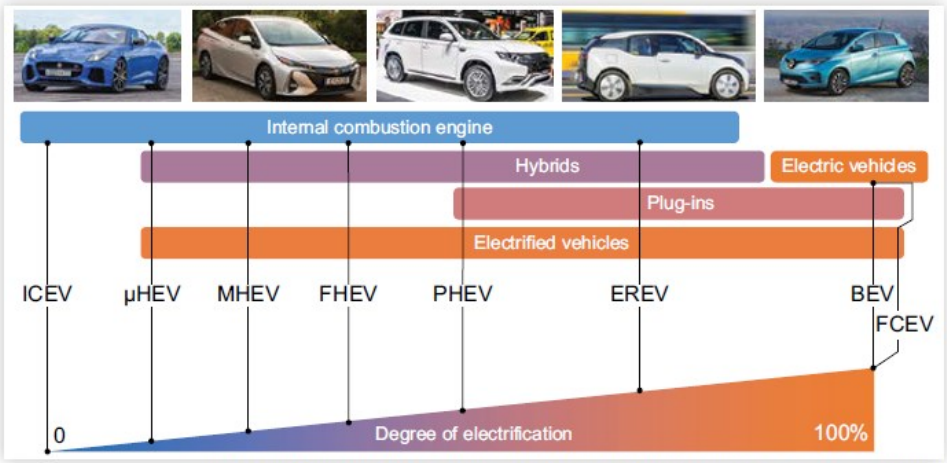

Figure 2-8. Degrees of electrification of road vehicles [15].

Type of hybrid vehicles	Battery type	HV battery voltage	Electrical power	CO_2 reduction potential
Micro hybrid	Lead-acid	12V	<5 kW	~3%
Mild hybrid	Li-ion	24-48V	5-20 kW	up to 15%
Full hybrid	Li-ion	200-400V	20-80 kW	15-30%

Notes: The CO_2 reduction potential refers to chassis dynamometer type-approval tests, not real-world driving.

Table 2-2. Main characteristics of the different types of HEVs [86].

As mentioned above, the main goal of hybridization is the improvement of fuel efficiency, as well as the reduction of pollutant emissions. Several functionalities during various phases of vehicle driving can be implemented thanks to the electrified powertrain. The engine start-stop functionality can be extended in order to allows short distances with stopped engine, such as when the vehicle is decelerating at low vehicle speeds. Moreover, the regenerative braking can be enhanced by managing the degree of energy recuperation associated to gas and brake pedals.

The combustion engine efficiency can be increased by shifting the load point towards higher efficiency (Figure 2-9 (a)) and the powertrain performance can be increased by using the torque assist of the electric motor (Figure 2-9 (b)). Depending on the operating conditions, the almost instantaneous torque of the electric motor can cover the ICE torque deficit during the first seconds of a harsh acceleration (torque fill), or increase the maximum system torque especially at the low engine speed range (torque boost). In addition, coasting phases can be covered with ICE switched off, and even extended taking advantage of the electric motor extra torque (active coasting). Finally, limited pure electric driving can be performed at low vehicle speeds, depending on the battery state of charge (SOC).

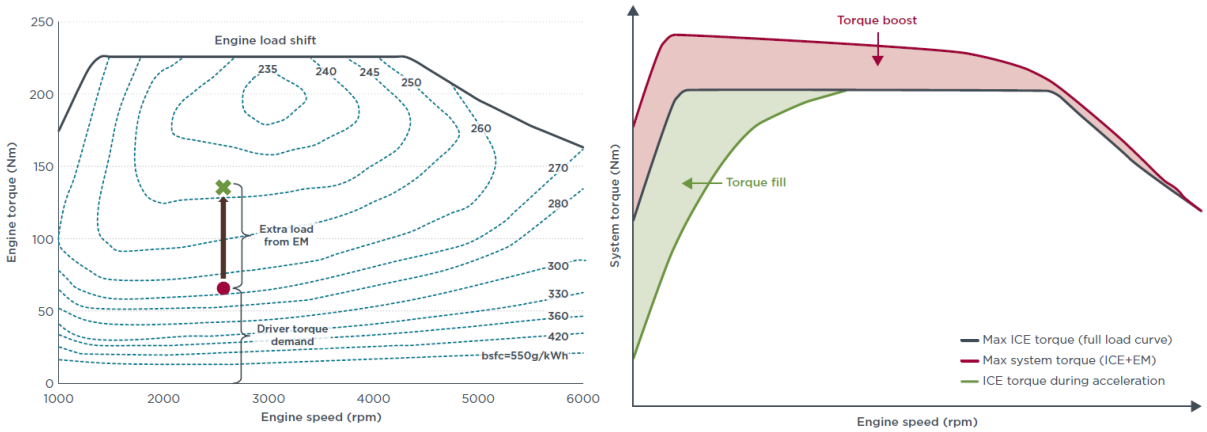

Figure 2-9. Fuel efficient functionality available on HEVs: (a) engine load shift strategy; (b) torque assist of the electric motor [86].

However, the applicability of these functionalities depends on the ability of the powertrain architecture to manage the mechanical power requested by the vehicle. According to the way the ICE is connected to the powertrain, hybrid-electric vehicles can be categorized by three main types (Figure 2-10):

- Series hybrid, in which the vehicle is propelled only by the electric motors (EMs), while the ICE is only used to charge the battery or to power directly the electric motors through a generator. Regenerative braking is maximized, and ICE operation at its optimal efficiency and emissions point is allowed, being decoupled from the vehicle power demand. However, this system requires at least two EMs increasing weight and cost, and introduces energy losses from converting the ICE mechanical energy to electricity and then back to motive power.
- Parallel hybrid, in which both the ICE and the EM are connected to the drive shaft and can thus power the vehicle individually or simultaneously. Typically, the ICE powers the wheels at higher speeds where it is most efficient, and only one EM acting as both a motor or generator is used.
- Power-split hybrid, which combines the parallel and series configurations. The ICE and the EMs are connected to a planetary gearbox, which acts as a power split device by

distributing the motive power between the ICE, the generator, and the traction motor as needed, according to the applied energy management strategy. This hybrid type allows for maximum efficiency, power, and driving comfort, although it requires two EMs, resulting in increased weight and cost, and more a sophisticated control system.

Currently, the most common type of HEV is the parallel powertrain, followed by the power split type implemented mainly by Toyota. Instead, the series layout is used in EREVs and few PHEVs [86].

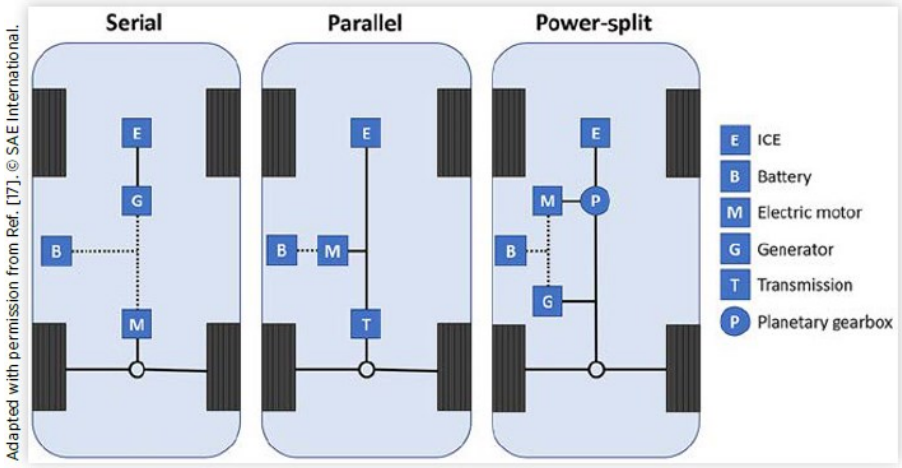

Figure 2-10. Schematics of serial, parallel and power-split hybrid systems [15].

Parallel hybrids can be further distinguished according to the position of the electric machines, which leads to the architectures categorized from P0 to P5 (Figure 2-11), each of which enables the hybrid functions summarized in Table 2-3:

- The P0 architecture, also called belt starter generator (BSG) or belt alternator starter (BAS), has the EM permanently connected to the ICE in the front-end accessory drive (FEAD). It enables start and stop, regenerative braking, coasting and torque assist with low cost solutions, but with low efficiency, because the EM cannot be decoupled from the ICE resulting in high friction losses due to the high-tension belt link.
- The P1 architecture, also called integrated starter generator (ISG), crankshaft motor generator (CMG), or crankshaft starter generator (CSG), has the EM attached directly to the ICE crankshaft in front of the clutch. Compared to P0, increased belt friction is avoided and higher torque can be transferred during torque assist and energy recovery. Moreover, pure electric driving is theoretically possible, but with low efficiency.
- The P2 architecture, also called transmission motor generator (TMG), has the EM as in P1 but coupled through an additional clutch with the ICE. Thus, the EM can be decoupled from the ICE, increasing the efficiency of the system in all hybrid functionalities. Depending on the EM positioning in the transmission (coaxial or off-axis design), engine re-start could require optimization strategies to enhance drivability.

- The P3 architecture has the EM attached to the output shaft of the transmission, i.e. permanently connected to the wheels. It enhances the energy recuperation potential, but it cannot benefit from the variable transmission gear ratio to optimize the EM operating point, and it cannot be used for engine stop/start operation.
- The P4 architecture, also called "e-axle", has the EM connected to the axle that is not driven by the ICE. It allows the vehicle to operate in all-wheel drive (AWD) mode, improving also the energy recovery potential. However, it usually requires an additional clutch or transmission to suitably operate the EM at high vehicle speeds, as well as a specific system (P0 or P1) to enable engine start/stop.
- The P5 architecture, also called "e-wheel", has two EMs integrated in the wheel hubs, directly acting on the wheels. It enables individual control of the non-driven wheels and maximizes all the hybrid functions, except the engine start/stop which must be managed by a supplementary system. However, increased cost, larger unsprung masses and safety risks still represent downsides of this configuration.

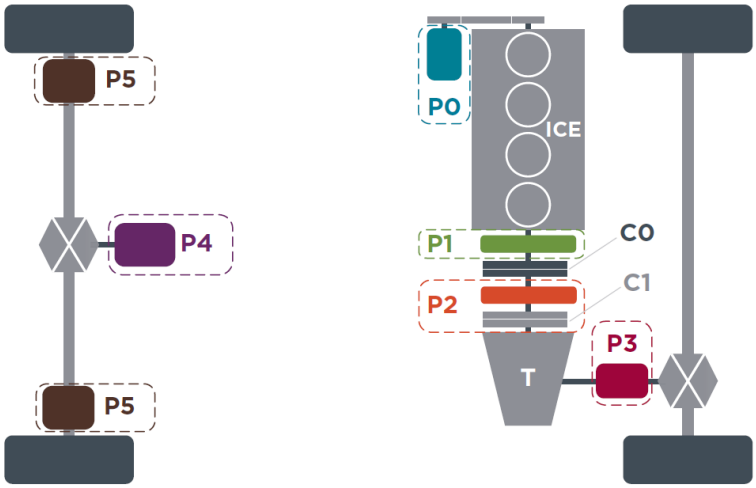

Figure 2-11. Different types of architectures (P0 to P5) for parallel hybrid powertrains [86].

Functionality	MHEV powertrain architecture					
	P0	P1	P2	P3	P4	P5
Engine stop/start (extended)	●	●	coaxial: ● off-axis: ○	×	n/a	n/a
Recuperation during coasting and regenerative braking	○	○	●	●	●	●
Engine load shift	●	●	●	○	○*	○*
Torque assist	●	●	●	●	●	●
Active coasting	○	○	●	●	●	●
Pure electric drive	×	○	●	●	●	●
Electric all-wheel-drive	n/a	n/a	n/a	n/a	●	●

●: possible; ○: possible but less efficient; ×: not possible; n/a: not applicable
* Potentially associated with control and stability challenges.

Table 2-3. Overview of hybrid functions theoretically possible for the different MHEV powertrain architectures [86].

These vehicle level-improvements, together with a suitable thermal management of the whole hybrid powertrain (engine, batteries and components of the electric system), can significantly reduce the energy use of the vehicle. Estimations refer to 43-47% fuel consumption reductions [45,91], notably larger than the engine-level improvements possible [15]. In addition, investing in vehicle-level improvements will benefit all propulsion technologies. In fact, for BEVs these improvements would provide range increases equivalent to that percentage, assuming a constant battery size.

2.3 Technologies to enhance the engine efficiency

Currently, the 99.8% of global transport is powered by internal combustion engines (ICEs) [45], and credible projections suggest that by 2035 about the 45% of EU vehicles will be still powered by ICEs [92]. Therefore, the improvement of ICEs is still necessary to reduce the local and global environmental impact of road transport.

Table 2-4 summarizes some advanced technologies which allow to improve the engine efficiency. Specifically, the CO_2 reduction potential of each technology can be evaluated assuming as baseline a turbocharged stoichiometric GDI engine, which can be considered as the "standard" today [15]. This table shows that high CO_2 emissions savings are still possible for ICEs by implementing innovative combustion strategies (up to 30% for Reactivity Controlled Compression Ignition - RCCI) or engine layouts (up to 35% for two-stroke opposed-piston diesel).

Engine technology	CO_2 reduction potential
Turbocharged stoichiometric GDI	Baseline
Advanced stop/start	2–5%
Atkinson cycle (& VVT)	3–5%
Water injection	5–10%
Variable compression ratio	10%
Dynamic cylinder deactivation + mild hybrid or Miller cycle	10–15%
Lean-burn GDI	10–20%
GCI	15–25%
Homogeneous lean	15–20%
DEGR	15–20%
RCCI	20–30%
Octane-on-demand	20–30%
Two-stroke opposed-piston diesel	25–35%

Table 2-4. Overview of advanced engine technologies to reduce CO_2 emissions [15].

To analyze systematically the benefits of these engine-level improvements, the approaches generally followed by vehicle manufacturers to enhance engine efficiency and thus reduce fuel consumption have to be described. Two dominant pathways can be distinguished [93]. One is the High Power Density (HPD) path, which aims to decrease the engine displacement through engine downsizing, allowing more efficient engine operating conditions. The other is the Lower Power Density (LPD) path, which aims to use an overexpanded Atkinson or Miller cycle to increase the peak engine efficiency.

In the HPD path, the increase of power density can be accomplished by increasing the maximum engine load or the maximum engine speed, as well as through a combination of these. Engines with brake mean effective pressures (BMEPs) more than 15 bar or speeds above 7000 rpm are considered high-load or high-speed concepts, respectively. Currently, engine downsizing combined with direct injection (DI) fueling and boosting through turbochargers is the most common solution used as high load strategy, which is preferred over the high-speed one due to its intrinsic friction penalties. Engine downsizing can be quantified by the downsizing factor (Eq. 2-1):

$$DF = \frac{V_{d,NA} - V_{d,Downsized}}{V_{d,NA}} \quad \text{Eq. 2-1}$$

Where $V_{d,NA}$ is the displacement volume for comparably-powered naturally-aspirated (NA) engines, and $V_{d,Downsized}$ is the one of the downsized engine. DFs up to 40% have been reached in current production vehicles, and downsized boosted engines have increased rapidly since 2005, passing from 1.7% to 35% of market share in 2020 [60].

In the LPD path, overexpanded engine cycles combined with high compression ratios r_c deliver peak efficiencies higher than those of downsized engines, although the power densities are lower because of the not fully utilized displacement volume. Generally, DI engines with high r_c based on Atkinson or Miller cycles have been used by vehicle manufacturer. Some of these engines also utilize cooled EGR (Exhaust gas recirculation) or intake valve actuation strategies (early or late intake valve closing - EIVC or LIVC) to increase the engine efficiency at part load. Some examples are:

- the 2014 Mazda 2.0 L SKYACTIV-G engine, with a very high r_c (13:1), and consequently a high peak efficiency (37.9%), although with significantly lower power density (57.5 kW/L) than the boosted HPD engines [94].
- the 1.8 L Toyota engine, with high levels of cooled EGR dilution (25%), and consequently high efficiency (40%) but low specific power outputs (39.4 kW/L) [95].
- the 2.5 L Toyota engine, with LIVC and 25% cooled EGR dilution, which achieved the same high efficiency (40%) of the 1.8 L, but with a higher power density (60 kW/L) [96].

It is worth to notice that both the HPD and LPD pathways offer an efficiency benefit, but from different portions of the load range. This characteristic can be observed by comparing the brake thermal efficiency as a function of torque of a baseline 2.4 L naturally aspirated (NA) PFI engine, with a boosted downsized 1.5 L Honda engine, and an Atkinson cycle 2.5 L Toyota engine (Figure 2-12). At the lightest engine loads, the downsized boosted engine results to be more efficient than the NA baseline engine and the overexpanded engine. Contrarily, at higher engine loads, the overexpanded engine results to be the most efficient solution, with the boosted

engine being less efficient even than the baseline. Thus, the benefits of each engine types depend also by transmission pairing and vehicle duty cycle.

Some engines have been designed to combine the two efficiency pathways. An example is the Audi 2.0 L TFSI (turbo fuel stratified injection) engine. It is a turbocharged DI engine using a Miller cycle, which is similar to Atkinson cycle, but with forced induction using a turbocharger or supercharger. The extension of the expansion phase up to 25%, together with others friction-related measures, resulted in 8 g/km less CO_2 emissions compared to Audi previous 1.8 TFSI, when tested in the Audi A4 over the NEDC [97].

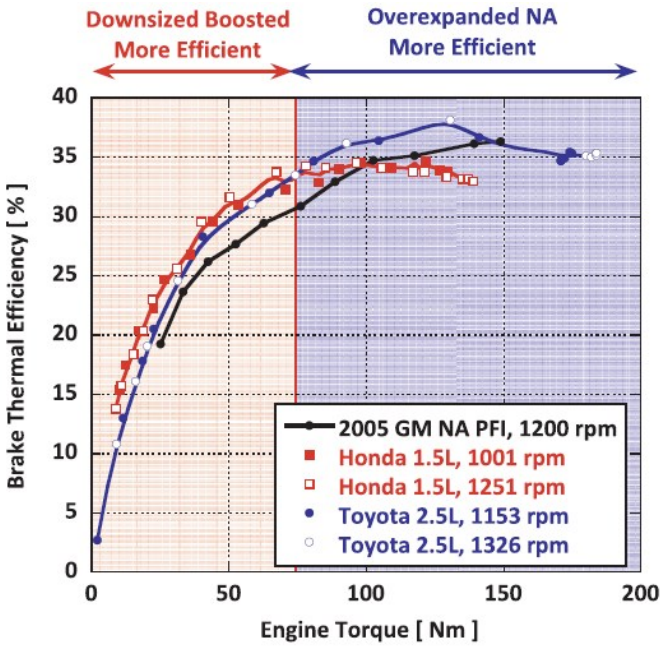

Figure 2-12. Brake thermal efficiency as a function of torque for a baseline 2.4 L NA PFI engine, a boosted downsized 1.5 L Honda engine, and an Atkinson cycle 2.5 L Toyota engine [93].

Prior to deepen the main engine technologies that are being deployed by engine manufacturers to improve efficiency, it is worth to recall the thermodynamic basis for efficiency in ICEs. According to [93], the brake thermal efficiency η_b may be broken down into component efficiencies, each representing a different energy loss identifiable inside the engine (Eq. 2-2).

$$\eta_b = \eta_{mech}\,\eta_{comb}\,\eta_{GE}\,\sigma_{HT}\,\eta_{ideal}\,\sigma_{ideal} \qquad \text{Eq. 2-2}$$

Table 2-5 summarizes the expressions of each component efficiency present in Eq. 2-2.

$\eta_{mech} = \frac{BMEP}{IMEP_n}$	Eq. 2-3	$\eta_{comb} = \frac{Q_{HR}}{Q_{fuel,total}}$	Eq. 2-4
$\eta_{GE} = 1 + \frac{PMEP}{IMEP_g}$	Eq. 2-5	$\sigma_{HT} = 1 - \frac{Q_{HT}}{Q_{HR}}$	Eq. 2-6
$\eta_{ideal,Otto} = 1 - r_c^{1-\gamma}$			Eq. 2-7
$\sigma_{ideal} = \frac{1}{\eta_{ideal,Otto}\, Q_{HR}} \int_{SOC}^{EOC} \left(1 - \left(\frac{V_d + V_c}{V(\theta)}\right)^{1-\gamma}\right) \frac{dQ_{HR}}{d\theta} d\theta$			Eq. 2-8

Table 2-5. Component efficiencies of the engine brake thermal efficiency η_b.

The difference between indicated (net indicated mean effective pressure - $IMEP_n$) and brake work (brake mean effective pressure - BMEP) is taken into account by the mechanical efficiency η_{mech} (Eq. 2-3), also referred to as organic efficiency. It can be attributed to engine friction losses and energy absorbed by the engine auxiliaries (such as water, fuel and oil pumps).

The combustion losses are quantified through the combustion efficiency η_{comb} (Eq. 2-4), which is the ratio between the total amount of energy released through combustion Q_{HR}, and the amount of useful fuel energy $Q_{fuel,total}$ (typically, the fuel lower heating value - LHV).

The gas exchange losses are accounted by η_{GE} (Eq. 2-5), where PMEP is the pumping mean effective pressure, and $IMEP_g$ is the gross mean effective pressure. It is worth noting that PMEP is a negative quantity for naturally aspirated engines, but it can be positive for boosted engines, for which η_{GE} can be larger than unity [93].

The proportion of total heat release available after wall heat losses Q_{HT} have removed energy from the system, is expressed by σ_{HT} (Eq. 2-6). Moreover, the efficiency of the ideal working cycle η_{ideal} (in the case the Otto cycle) is expressed by Eq. 2-7, in which r_c is the geometric compression ratio of the engine, and γ is the ratio of specific heats for the working fluid.

Finally, the degree of constant volume combustion σ_{ideal} can be expressed by Eq. 2-8, where: SOC and EOC are start and end of combustion, respectively; V_d and V_c are displacement and clearance volume of one cylinder, respectively; and $V(\theta)$ is the crank angle (θ) dependent volume (V) of one cylinder.

Thus, the main technologies for the improvement of engine efficiency can be analyzed, underlying their contribution on each component efficiency distinguished in Eq. 2-2. Generally, many of them are used to increase r_c within acceptable knock limitations, thus maximizing η_{ideal}, or to minimize pumping work, thus maximizing η_{GE}.

All SI ICEs must deal with knock phenomena, occurring over the high-load portion of their operating range. Figure 2-13 (a) shows speed-load operating points over two different engine driving cycles, and which of those are knock-limited, considering a typical midsize sedan in the U.S. market. Clearly, the majority of driving conditions on both schedules are not knock-limited, being under the approximate knock limit curve. In fact, engines are designed to

maximize r_c, while still being able to achieve their maximum load at a predetermined level of knock mitigation.

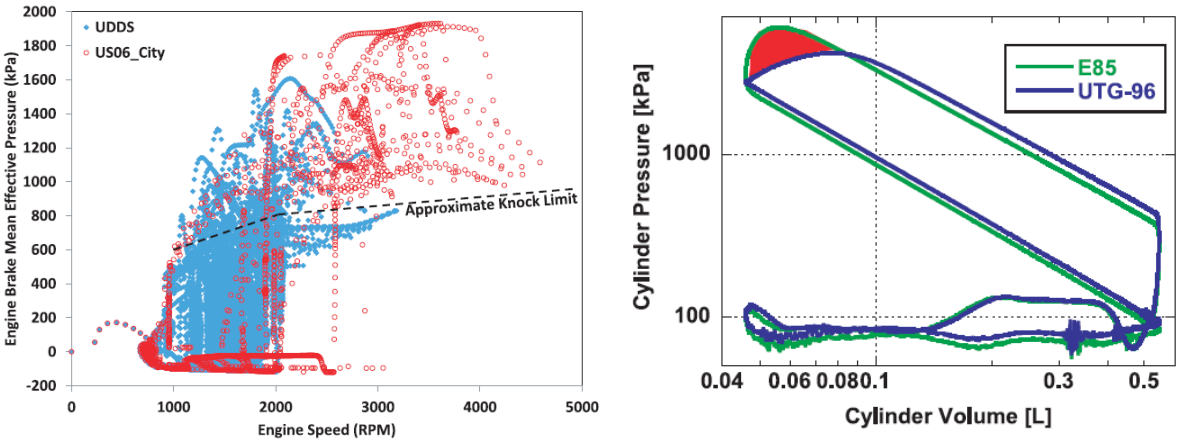

(a) (b)

Figure 2-13. Knock limitations in SI ICEs: (a) engine operating conditions over UDDS and US06-city driving cycles; (b) lost work from the engine cycle due to retarded combustion phasing for knock mitigation [93].

At loads higher than the knock limit, the most common solution is spark ignition delay, which allows to reduce pressure and temperature of the unburned gas prior to the consumption of the end-gas, slowing the autoignition reactions that cause knock. However, this late combustion phasing decreases σ_{ideal}, because moves the heat release away from the point of minimum cylinder volume. This results in lost work, as shown by the red area in Figure 2-13 (b), obtained by comparing the indicated cycle of a not knock-limited fuel (E85) with that of a knock-limited fuel (UTG-96).

For what concerns pumping work reduction at light engine load, several strategies can be used depending on the engine type. HPD boosted engines can limit the mass of air trapped into cylinders at light loads by simply reducing the intake manifold pressure below the ambient value, thus diminishing the use of intake throttling.

Instead, LPD engines utilize several strategies to maximize η_{GE} at the lightest operating loads. Typically, overexpanded engine cycles and cylinder deactivation help reaching this goal by reducing the effective engine displacement under part-load conditions. Moreover, cooled EGR dilution maximizes the in-cylinder mass for a given load condition without varying the air mass. In addition, EIVC and LIVC strategies allow to use only a portion of the displacement volume of the intake stroke, reducing pumping losses and thus enhancing η_{GE}. EIVC consists in closing intake valves during the intake stroke, reducing the trapped air and fuel mass without requiring throttling. Similarly, LIVC delays the intake valve closure by drawing in the full cylinder charge, and then expelling a portion of it back into the intake manifold during the compression stroke. Both these strategies have a net benefit in the pumping work, as shown in the indicated cycles in Figure 2-14.

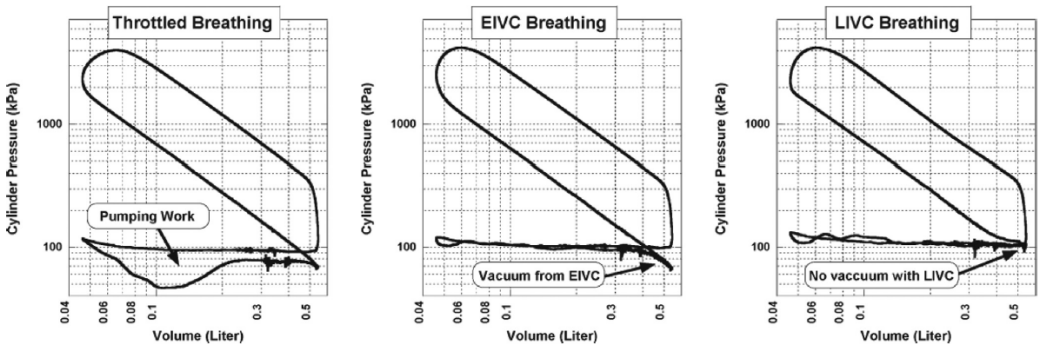

Figure 2-14. Effects of conventional throttled operation, EIVC and LIVC valve strategies on the pressure-volume diagram of an engine operating at 1500 rpm and 8 bar BMEP [93].

EIVC and LIVC can be realized through many mechanical solutions, going from multiple cam profiles to cam-in-cam arrangements. Finally, it is worth to notice that they enable a higher mechanical r_c (up to 13:1 in numerous production engines), since the compression stroke is only partially utilized, reducing the effective r_c [93].

In light of these considerations, generally the de-throttling effect of HPD boosted engines makes them more efficient than LPD engines at the lightest operating loads, as shown clearly in Figure 2-12.

2.3.1 Advanced combustion strategies

Traditionally, spark ignition and compression ignition have been the two combustion options for engines. However, new promising concepts have been introduced, some of them already available in the market. The combustion strategy inside an engine is defined by the architecture of fuel delivery and ignition systems.

Direct Injection (DI) systems deliver fuel directly into the combustion chamber through fuel injectors, substituting Port Fuel Injection (PFI) systems in SI engines, which introduce the fuel upstream of the combustion chamber.

DI enables several advantages compared with PFI. Firstly, it allows for a more precise control of fuel quantities inside each cylinder even during highly transient engine operating conditions, enabling a proper functioning of the after-treatment devices for emissions abatement: in fact, in SI engines, it helps maintaining strictly stoichiometric combustion conditions, necessary for the proper functioning of the three-way catalyst (TWC).

Moreover, DI fueling is advantageous for knock mitigation, because the heat of vaporization (HoV) of the fuel cools the air-fuel mixture, reducing the in-cylinder temperature. This allows to mitigate knock and increase r_c. Furthermore, combustion duration can be reduced thanks to the increased in-cylinder turbulence, thus enhancing σ_{ideal}. Finally, fuel-wall interactions can be limited, increasing the fuel available for combustion and, consequently, η_{comb} [98].

DI fueling can be coupled with different ignition strategies, depending on used fuel and combustion types to be realized. Generally, three main categories of ignition systems can be distinguished: Spark Ignition (SI), Compression Ignition (CI), and Advanced Compression Ignition (ACI) [99]. In SI engines, the mixture is ignited with a spark plug, which creates an electrical discharge between two electrodes delivering to the gas about 30 mJ [100]. This establishes a core of high-temperature plasma, that develops into a propagating flame front. Contrarily, in CI engines the mixture is ignited by fuel autoignition at high pressure and temperature conditions (end of compression stroke), and premixed and diffusive combustion types coexist. CI typically refers to Diesel-cycle based engines, but CI concepts not using diesel fuel also exist. Therefore, Conventional Diesel Combustion (CDC) engines can be distinguished from Advanced Compression Ignition (ACI) engines.

The potentialities of ACI engines can be observed in Figure 2-15, which offers an overview of the NOx and soot formation zones on the equivalent ratio (φ) – combustion temperature (T) chart. For SI combustion, the air-fuel mixture is homogeneous (φ=1) for PFI engines, and combustion temperatures locate them in the NO_x zone, although GDI engines can enter the soot formation zone in case of relatively poor air-fuel mixing. Instead, CDC engines cover a wide range of the φ-T map, overlapping with both the soot and NO_x formation zones depending on the air to fuel ratio (AFR), which in turn depends on engine load.

ACI concepts try to operate in zones of the φ-T map without formation of soot or NO_x, in order to reduce the use of aftertreatment devices. These concepts can be schematized as in Figure 2-16, and allow to increase σ_{ideal} as well as η_{comb}, while limiting pollutant emissions.

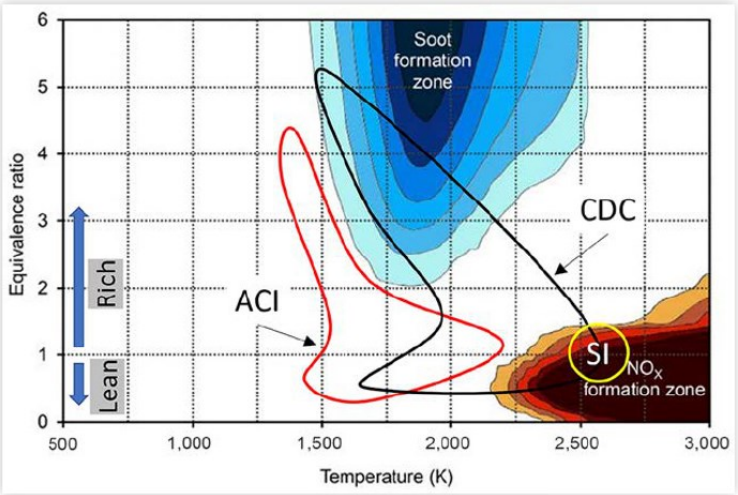

Figure 2-15. Plot of Equivalence Ratio - Temperature space, with locations of various combustion concepts [99].

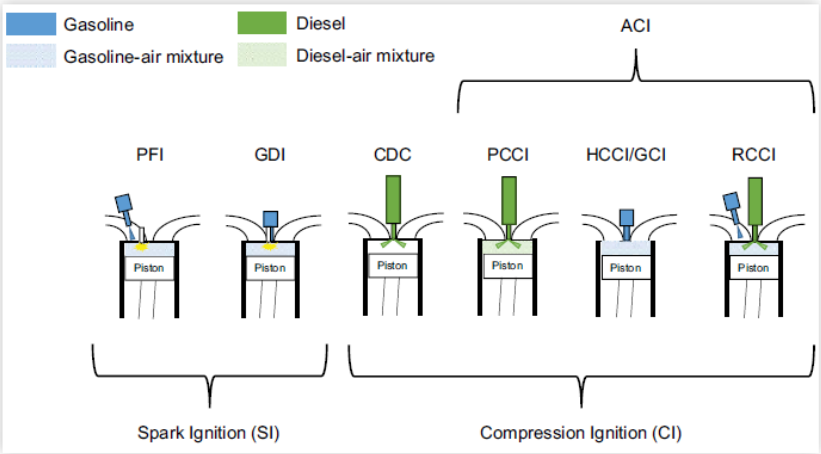

Figure 2-16. Overview of SI, CI and ACI concepts [15].

Homogeneous charge compression ignition (HCCI) engines work by injecting fuel during the intake stroke, and then compressing the uniform air-fuel mixture until it all ignites simultaneously. This strategy is difficult to be realized for the entire speed-load range of the engine, although some applications already exist on the market, even if with some modifications. It is the case of the Mazda SKYACTIV-X, a gasoline engine which employs a concept called "spark assisted compression ignition (SACI)", also known as "spark plug controlled compression ignition (SPCCI)" [101]. A spark plug is used to control combustion when HCCI is not possible, and a "smart mode-switching" allows to switch between the spark and compression ignition modes. This engine allows to reduce fuel consumption by 20-30% compared to the previous SKYACTIV-G gasoline engine.

A variation on the HCCI concept is the gasoline compression ignition (GCI) [42]. In GCI engines, the air-fuel (gasoline) mixture is ignited via compression in a diesel-type combustion mode, thus removing completely the spark plug. Low-octane gasolines are good fuels for this technology, and efficiency improvements up to 25% have been shown, with less expensive engine components (high-pressure fuel injection not required) and aftertreatment devices compared to those of diesel engines [102,103].

To overcome some of the control and operating range constraints of HCCI, premixed charge compression ignition (PCCI) have been developed. In this case, the homogeneous mixture is ignited by an additional injection of the same fuel when the piston is near the top of its stroke. It is an intermediary combustion technique between HCCI and CDC, which offers some of the advantages of HCCI without its control and operating range issues [104].

Similar to PCCI, RCCI uses two different fuels to increase knock resistance and reduce ignition delay. Specifically, a high-octane fuel is added through port fuel injection, while the direct injection occurs for a high-cetane fuel. RCCI results in high efficiencies, up to 57% on a gross indicated basis [105], but it requires two fuel injection systems, increasing cost and complexity as well [106].

Besides ACI strategies, there are other technologies to improve engine efficiency and reduce emissions. Among all, water injection is a promising technique to reduce the in-cylinder and exhaust temperature, mitigate combustion knock, and decrease NO_x emissions [107]. Moreover, high thermal efficiency (up to 35%) can be reached if advanced spark timing is implemented, due to a better combustion phasing and shorter combustion [108]. However, this system requires a separate water thank, which adds weight and uncomfortable operation for consumers [15].

Lean operation of the engine has great potentialities to increase engine efficiency, because it increases the ratio of specific heats in the expansion ratio [45]. Furthermore, excess air mitigates knock phenomena, enabling higher compression ratios and thus higher efficiency, and decreases NO_x emissions thanks to lower combustion temperatures. On the other hand, ignition is challenging, and requires novel ignition technologies, such as the pre-chamber ignition. In this system, the spark plug is placed inside the pre-chamber (therefore called "pre-chamber spark plug - PCSP"), which is a small region connected to the combustion chamber through nozzle holes. The air-fuel mixture is ignited in the pre-chamber, where pressure and temperature rise rapidly, causing gas or flame-jets to penetrate into the main combustion chamber through the nozzle holes and ignite the mixture in several spots simultaneously (Figure 2-17 (a)). In addition to the ignition of highly diluted mixtures, this approach allows to speed up the combustion process in the main chamber. However, cold operation at low loads and mixture preparation with active operation (in which the fuel is introduced in the pre-chamber separately through a fuel-metering device) still represent an issue [109]. Fuel saving potentials up to 9% in WLTC have been demonstrated [110], and advanced concepts have been developed, as the Maserati Nettuno™ engine (Figure 2-17 (b)). It is a 3L 6-cylinder twin-turbo engine, with pre-chambers, lateral spark plugs, and a twin injection system incorporating both GDI and PFI. The lateral spark plugs allow to stabilize combustion at light load, whereas the PCSPs allow the engine to run at high boost pressures while increasing knock resistance.

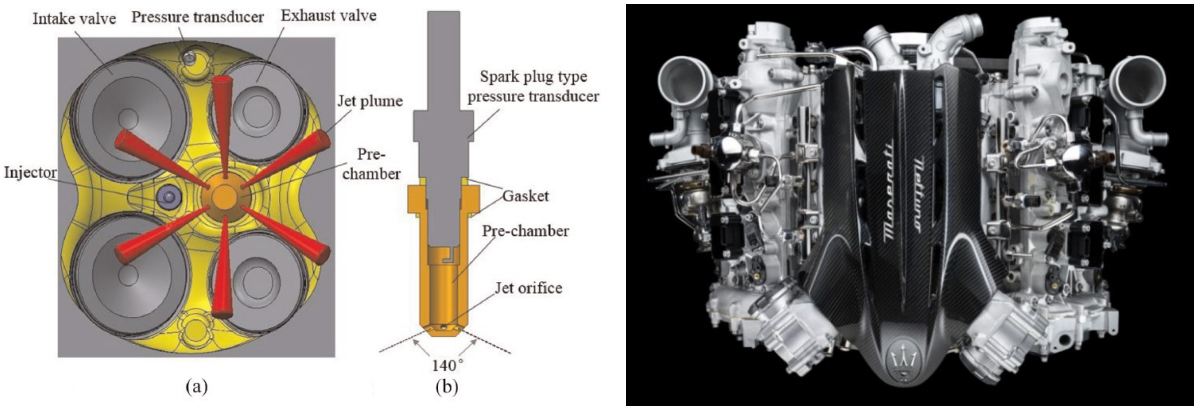

(a) (b)

Figure 2-17. Pre-chamber ignition: (a) schematic diagram of passive pre-chamber jet ignition [111]; (b) Maserati Nettuno™, an example of engine with PCSPs [112].

Many other advanced ignition systems have been studied, mainly trying to extend the stability range of an engine, as seen for pre-chamber ignition. Among them, laser ignition, corona discharge ignition, plasma jet and rail plug ignition systems can be mentioned [93]. The scope is to run an engine leaner, and thus more efficiently, by performing a faster initial burn rate.

Finally, another combustion strategy is the octane-on-demand system, which alternates the use of a high-octane and a low-octane fuel to maximize peak engine efficiency. To avoid refueling of two different fuels, a fuel with oxygenate components (such as E10 gasoline) can be used, whose high- (i.e., ethanol-rich) and low- (i.e., ethanol-lean) octane components can be separated through an onboard system. A 20-30% decrease in fuel consumption has been reached by using this process in passenger cars and light-duty vehicles [113], and additional advantages can be achieved if combined with GCI [114].

2.3.2 High-efficiency engine technologies

Besides advanced combustion strategies, many engine technologies have been developed to enhance its efficiency, some of them widely established on the market.

Cooled EGR consists in recirculating part of the exhaust gases towards the intake manifold, after having cooled them in a dedicated heat exchanger. Apart from reducing NO_x emissions, this technology increases the engine efficiency η_b, although it affects the component efficiencies in Eq. 2-2 differently. The additional mass added by the EGR increases the manifold pressure without increasing the intake oxygen flow, thereby maintaining a stoichiometric charge while decreasing engine pumping especially at part-load conditions, benefiting η_{GE} [93]. Moreover, EGR dilution decreases the adiabatic flame temperature, diminishing heat transfer and thus enhancing σ_{HT}. The reduced in-cylinder temperature mitigates knock propensity, allowing to increase r_c, and thus η_{ideal}, which also benefits from the increased ratio of specific heats (γ). On the other hand, EGR decreases the laminar flame speed of the fuel, adversely impacting the σ_{ideal}, and worsens cycle to cycle combustion variability, as well as combustion efficiency, affecting adversely η_{comb}.

Many technological variations of EGR concept also exist, such as the dedicated EGR (DEGR) [115]. It is a 4-cylinder engine, in which one cylinder is run with rich mixture, and its exhaust gases are fed into the other three cylinders, which can run stoichiometrically or lean. The first cylinder generates syngas, which mixes with CO_2 in the EGR prior to feed the other cylinders, helping to mitigate knock and improve burn rate. This allows to increase r_c (benefiting η_{ideal}) and to reduce emissions across engine operating conditions.

The compression ratio r_c can be increased also mechanically through variable compression ratio (VCR) technologies, as long as the knock limit is not exceeded. This can be realized by varying the position of the crankshaft relative to the engine head, or the linkage distance

between crankshaft and piston, in order to vary the clearance volume at top dead center without changing the engine stroke. Many design solutions have been developed to allow the r_c mechanical adjustment, ranging from variable-length connecting rod, to eccentric crankshaft support [93], or multi-link crankshaft rotation mechanisms (Figure 2-18 (a)). Moreover, continuous or step-manner actuation strategies can be implemented, offering fuel savings up to 3.7% [116].

Engine displacement can be varied through cylinder deactivation, which consists in stopping fuel injection, as well as intake and exhaust valve actuation, to one or more engine cylinders. This allows to decrease pumping work at part load operation, thus increasing η_{GE}, while maintaining stoichiometric conditions for the proper functioning of the TWC. In fact, for the same demanded power, the remaining cylinders have to increase their net power, reducing throttling losses and thus operating more efficiently (η_b enhanced generally by about three percentage points [117]). On the other hand, transient control and noise, vibration, and harshness (NVH) constraints have been limiting their diffusion. However, Dynamic Skip Fire technologies have helped mitigating these issues [118], and in 2020 almost 15% of gasoline vehicles in the U.S. were equipped with cylinder deactivation technologies [60].

Many engine concepts have also been developed with the aim of reducing thermal losses. An example is represented by opposed-piston engines (Figure 2-18 (b)). The engine layout is composed of two pistons arranged opposite one another, which reciprocate against each other. This architecture allows to reduce heat losses significantly, thus increasing η_{comb} and σ_{HT}. In heavy-duty applications, brake thermal efficiencies up to 55% have been achieved, enabling substantial reductions in CO_2 emissions [119], which can be further improved by combining this technology with GCI [103].

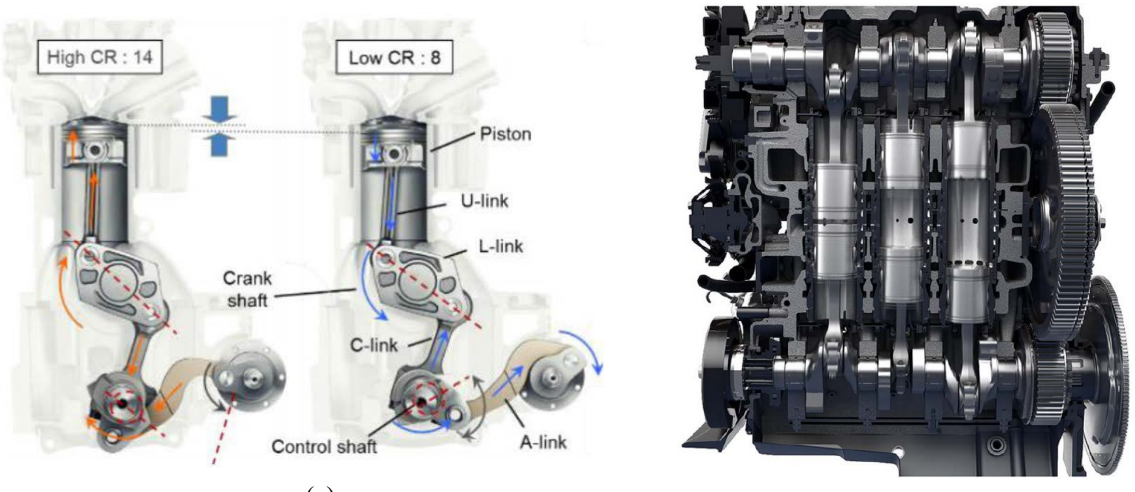

(a) (b)

Figure 2-18. High-efficiency engine technologies: (a) multi-link crankshaft VCR with r_c from 8:1 to 14:1 [120]; (b) opposed-piston two-stroke engine, from Achates Power™ [119].

2.3.3 Waste energy recovery

Generally, waste energy from exhaust gases plays a fundamental role in engine efficiency improvement, since about one third of the fuel chemical energy is wasted through their enthalpy [121]. Energy recovery can be realized both directly or indirectly, by taking advantage of their high pressure or temperature, respectively.

Direct energy recovery solutions take advantage of exhaust gases high pressure (compared to ambient conditions) to produce additional mechanical power. A typical method is represented by turbocharging systems, which belong to the category of engine boosting technologies.

Boosted engine operation is a key solution for HPD downsized engines. By compressing intake air, a higher air mass can be inducted, allowing to satisfy the same load operation with a smaller displacement [122]. Consequently, r_c increases, with obvious benefits on η_{ideal}. Moreover, engine operation of partial loads results optimized, enabling higher η_{GE} than naturally aspirated SI engines [93]. Intake manifold pressure can be increased through turbocharging or supercharging. In the first case, the high pressure of exhaust gases is used to drive a turbine directly linked to a compressor located along the suction line of the engine. Instead, supercharging uses part of the crankshaft mechanical power to drive the compressor. Consequently, turbocharging results to be more efficient, as it recovers waste energy from exhaust gases. This is one of the main aspects making them the state-of-the-art technology for boosted engines, which represent almost 35% of the gasoline market share in the U.S. [60].

In addition to turbocharging, turbocompounding is surely a promising technology to further enhance the direct waste energy recovery from ICEs. Turbocompound engines can be categorized as low-pressure (LP) and high-pressure (HP) systems, and many configurations can be distinguished according to the energy recovery strategy (Figure 2-19).

In LP turbocompounding, a power turbine (PT) is added in the exhaust line to extract energy from the wasted exhaust coming out the turbocharger turbine (T). The PT operates at low pressure ratios, and the recovered power may be linked to the engine mechanically or converted in electric energy through a generator. In mechanical turbocompounding, fixed ratio gears or continuously variable transmission (CVT) can be adopted. Depending on turbines arrangement, series and parallel configurations can be distinguished (Figure 2-19 (a) and (b), respectively).

Alternatively, HP turbocompounding makes use of a single turbine that operates at higher pressure ratios and produces more power than that required by the compressor. The surplus power is transmitted to the engine or to an electric generator. Various arrangements have been studied. Superturbo is a turbocharger with an integrated CVT (Figure 2-19 (c)), which functions as a supercharger at low engine speeds, by taking energy from the crankshaft to drive the compressor, or as a turbocompound at high engine speeds and loads, by giving to the crankshaft the surplus power extracted from the turbine. In an electric turbocharger, the surplus power from the turbine is converted into electricity by a generator mounted on the turbocharger shaft (Figure 2-19 (d)). The electric machine is also able to run the turbocharger compressor when

its power requirement cannot be met by the turbine. Turbocompounding can be even done with separated turbine and compressor (without turbocharger). Both can be connected to the engine crankshaft mechanically (Figure 2-19 (e)) or electrically, i.e. with an electric generator or motor, respectively (Figure 2-19 (f)).

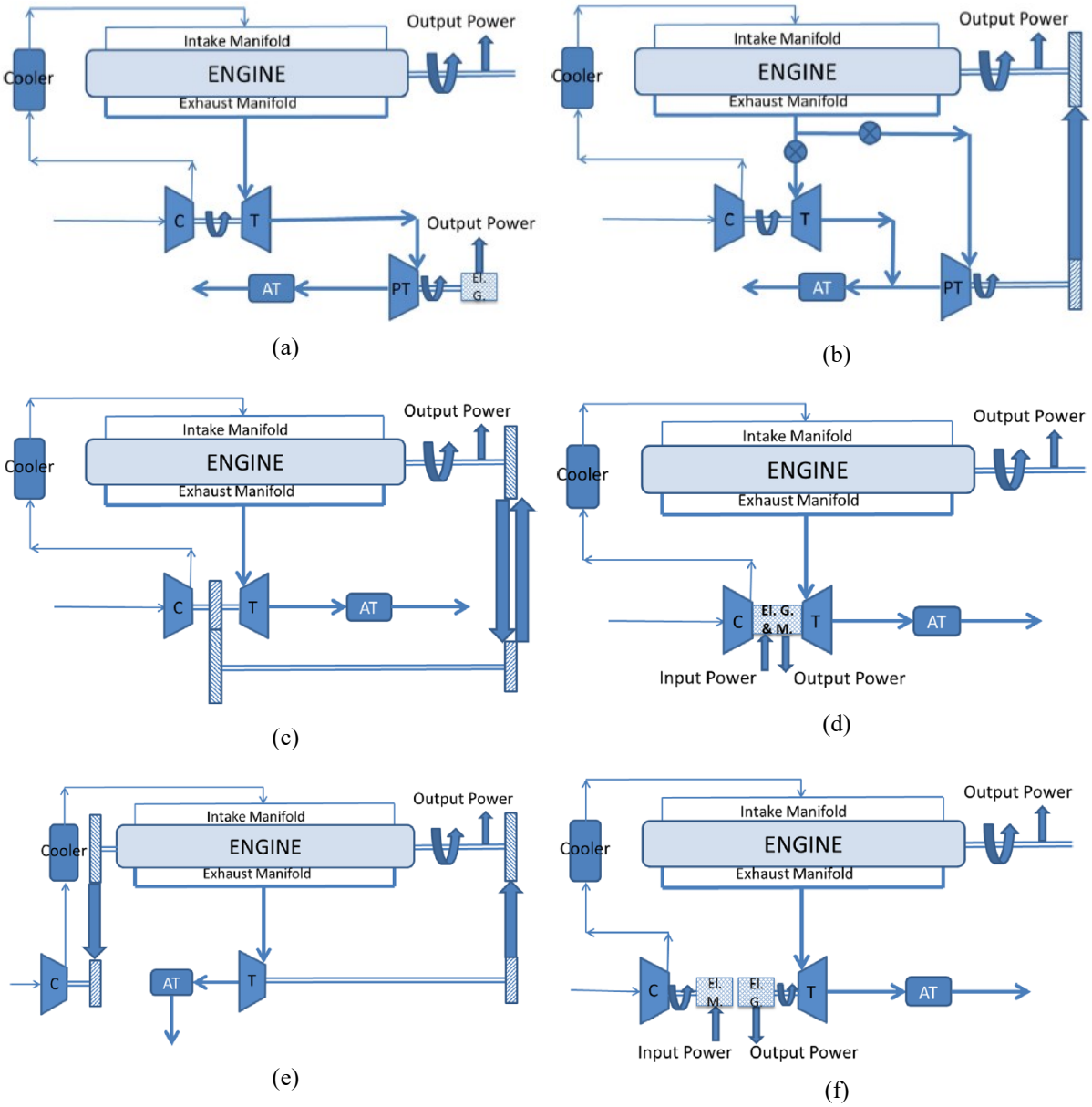

Figure 2-19. Turbocompounding configurations: (a) LP series; (b) LP parallel; (c) HP superturbo; (d) HP electric turbocharger; (e) HP with separated turbine and compressor; (f) HP with separated turbine and compressor and corresponding electric machines (AT=exhaust after-treatment) [123].

Depending on the driving cycle, fuel savings of 1% to 6% have been demonstrated through electric turbocharging systems [124], and even a 10.9% improvement in overall efficiency of a LP turbogenerator have been reached [125]. However, several aspects still limit their diffusion on the market. Firstly, the high back-pressure in the exhaust manifold, which hinders the expelling of burned gases, resulting in more pumping losses, as well as increased residual gases,

delayed combustion, increased heat transfer in the cylinder, and disruption of global engine thermo-dynamic balance [123]. Moreover, improvements are still required regarding the efficiency of power turbines in low load regions, and the thermal management of electric turbochargers.

Exhaust gases are also an attractive source of waste heat, which can be recovered through indirect energy recovery systems. Many technologies have been investigated in order to convert this exhaust heat into mechanical power. According to their physical principles, thermo-electric generators and recovery units based on bottoming thermodynamic cycles can be distinguished.

Thermo-electric generators convert heat into electric energy through the Seebeck effect, a phenomenon which determines a voltage difference between two semiconductors, proportional to the temperature difference they are subjected. They are composed of several thermo-electric modules constituted by elements made of p and n semiconductor materials. Thermically, these elements are connected in parallel from, while they are connected in series electrically [126]. The hot source is represented by exhaust gases or engine cooling fluid. Thermo-electric generators does not have moving parts, they are easy to install, and space and volume requirements can be fulfilled by a wide range of geometries [127]. On the other hand, back-pressure issues can raise when the exhaust gases are used as hot source, and the conversion efficiency does not exceed 5% with electrical power output under 1 kW [128].

The other approach involves recovery units based on bottoming thermodynamic cycles to produce mechanical power and, eventually, electric power available on-board. Several cycles have been investigated for waste heat recovery applications: Kalina cycles, Stirling engines, Inverted Brayton Cycles (IBC) [129,130], and Organic Rankine Cycles (ORC). ORC-based power units represent a well-established technology for stationary applications and a wide range of nominal power (from hundreds kW to MW), and are considered a promising solution for vehicle applications. This is mainly due to their high thermodynamic potential, flexibility and low complexity of components [131], as well as their efficiency higher than other alternatives for a wide range of hot source temperatures [132].

A suitable choice of the working fluid allows to recover heat from different waste streams, as the ICEs cooling system, the exhaust gases, or intercooler and EGR systems [121]. Especially exhaust gases are a promising waste heat source. The quality of the available thermal power in terms of temperature and flowrate defines strictly the thermodynamic conversion efficiency. This efficiency is limited by the temperature level of exhaust gases, as well as their typical large-gradient temperature drop. The cycle efficiency of ORC itself can reach even 11%, but 6% can be considered a real value, if the negative impacts of added back pressure, weight and ORC off-design operation are taken into account [133].

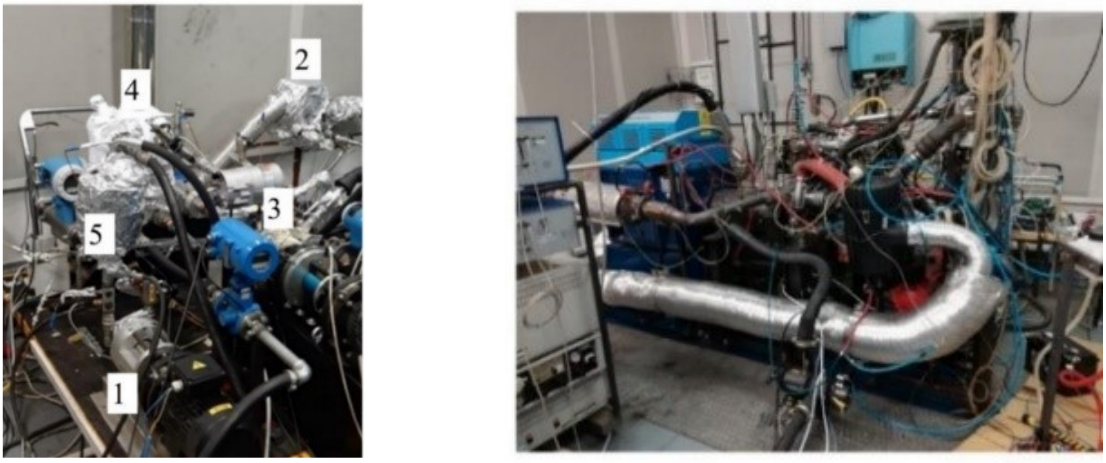

(a)

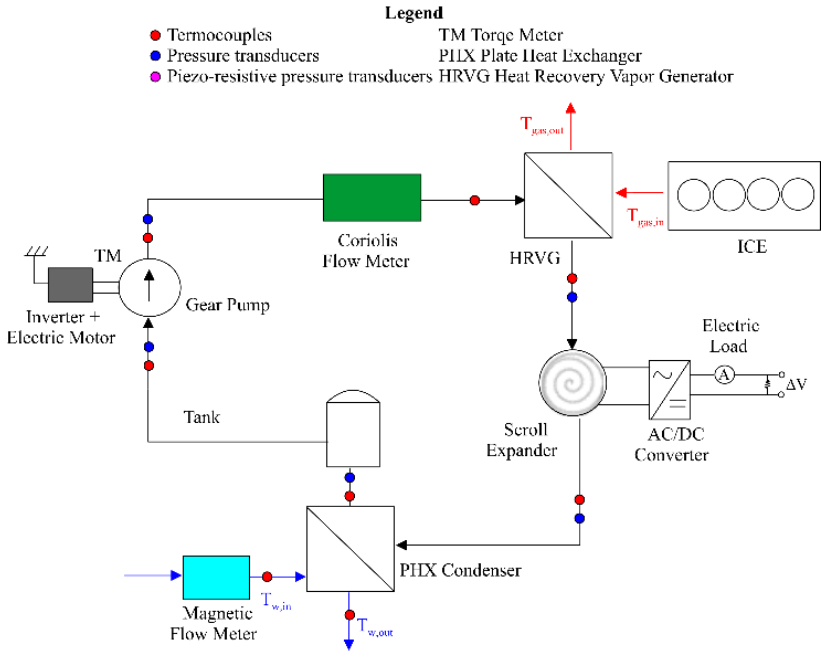

(b)

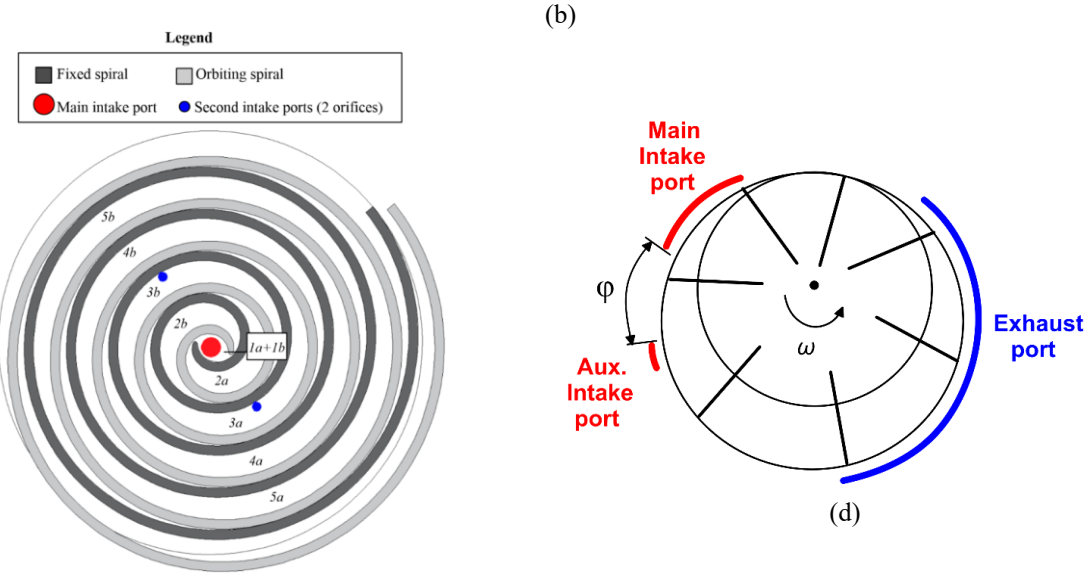

(c) (d)

Figure 2-20. (a) ORC test bench of the University of L'Aquila; (b) Scheme of ORC-based power unit; (c) DIP concept in SVRE; (d) DIP concept in Scroll expander [134,135].

Nevertheless, the full development of this technology on the market has been delayed by several issues: the increase of engine back-pressure caused by the heat recovery vapor generator (HRVG), not to mention the increase in weight and size produced by the recovery unit, are well known limiting factors, which still need to be addressed [136]. In addition, ICE operation during driving determines intrinsic transient conditions of the heat source (exhaust gases), which leads the ORC-based unit to operate in strong off-design conditions [134,137]. Thus, besides the development of a robust and reliable control system [138], it is fundamental that the components of the recovery unit are properly chosen and designed to ensure operating flexibility [139]. In this sense, the expander plays a fundamental role. Generally, volumetric-type machines are preferred, due to their capacity to deal with time-varying thermo-fluid dynamic inlet properties. This capability can be further extended through innovative strategies, such as the expander dual-intake-port (DIP) technology. DIP widens the expander permeability, enabling a higher mass flow rate of working fluid, for the same intake pressure. This technology has been applied to sliding rotary vane expander machines (SVRE), as well as to Scroll expanders, and promising results have been demonstrated. Figure 2-20 (a and b) shows the ORC test bench of the University of L'Aquila used to verify experimentally the proposed solutions. DIP in Scroll expanders (Figure 2-20 (c)) can increase mechanical power up to 25% with respect to the baseline machine, without modifying the in-out pressure ratio [135,140]. Instead, DIP in SVREs (Figure 2-20 (d)) allows to reach higher power boosts (up to 83%), but the DIP Scroll results to be more efficient (50-60%) when compared to the DIP SVRE case (40%) [141,142].

2.4 Conclusions

This Chapter gave an overview of the main vehicle and engine level technologies developed so far for the improvement of the overall vehicle efficiency. In fact, the first approach to reduce fuel consumption and emissions is to reduce the energy consumption of the vehicle. This can be done by reducing weight and friction, as well as by electrifying the propulsion system, which allows to optimize the energy management among different drive systems, depending on the specific driving condition.

However, the effectiveness of electrified propulsion systems relies on efficient ICEs, which still have room for improvement in this sense. Hence, the state of the art on the main technologies developed to improve the efficiency of ICEs has been outlined in this Chapter, ranging from advanced combustion strategies, to waste recovery systems on the exhaust gases.

In this research field, a high potential is offered also by the optimization of the engine thermal management. As this is the main topic of this thesis, a comprehensive review of the most advanced thermal management strategies will be presented in the next Chapter 3, followed by the presentation of the research activity conducted in this field.

3 Engine Thermal Management

3.1 Overview

As known, an ICE requires suitably designed cooling and lubrication systems to function properly over its entire operating range. The primary scope of the coolant system is to keep the lubricant and component materials within acceptable service temperatures, whereas the lubricant system prevents metal on metal contact between moving components, thereby reducing friction and wear.

Cooling and lubrication systems play a fundamental role in defining engine efficiency and pollutant emissions. In fact, they interact strongly with the combustion process, impacting directly on pollutant emissions. In addition, they determine the friction conditions realized in the main mechanical couplings of the engine, thereby affecting fuel consumption and thus CO_2 emissions. The optimal design of these systems is challenging, because they must deal with continuous and greatly variable operating conditions of the engine, commonly experienced during real driving conditions, as well as homologation cycles. This goal is even more difficult to achieve if cost and reliability requirements must be met, as usual in the automotive sector.

A typical layout of these systems is shown in Figure 3-1. Basically, the cooling system (Figure 3-1 (a)) is constituted by a centrifugal pump (3), which allows the circulation of the coolant fluid (a water-glycol mixture) towards the internal passageways of engine block and head (1). Then, the fluid flows back to the pump through the bypass path (9) or the radiator (6) depending on the thermostat valve (8) opening. A secondary cooling circuit can be designed to realize charge air cooling (CAC) through a dedicated heat exchanger (11), served by a secondary pump (10) and radiator (7).

Similarly, the lubricant system (Figure 3-1 (b)) is composed by an oil sump (1) collecting the oil returning from the engine, and a volumetric pump (3), which sucks the oil through a suction head (2) and drives it towards the oil filter (6), the oil cooler (7) and then the internal passages of engine head and block. Specifically, these passages are composed by the main oil gallery (9), from which several tunnels branches off, feeding main (12) and pin (11) bearings, piston pins and rings (13), turbocharger (16), valve train (18) and MultiAir™ system (20). Moreover, a set of valves (present in (5) and (3)) and a feedback-bypass tunnel (14) allow the regulation of the oil flow, avoiding high pressures inside the oil circuit.

It is worth noting that typically both coolant and oil pumps are mechanically coupled with the crankshaft, which therefore fixes their speed according to a predetermined gear ratio. Moreover, the standard flow control of both systems is realized thermo-mechanically, being assigned to a wax-based thermostat for the cooling flow distribution among bypass and radiator branches, and to one or more overpressure valves for the oil flow recirculation.

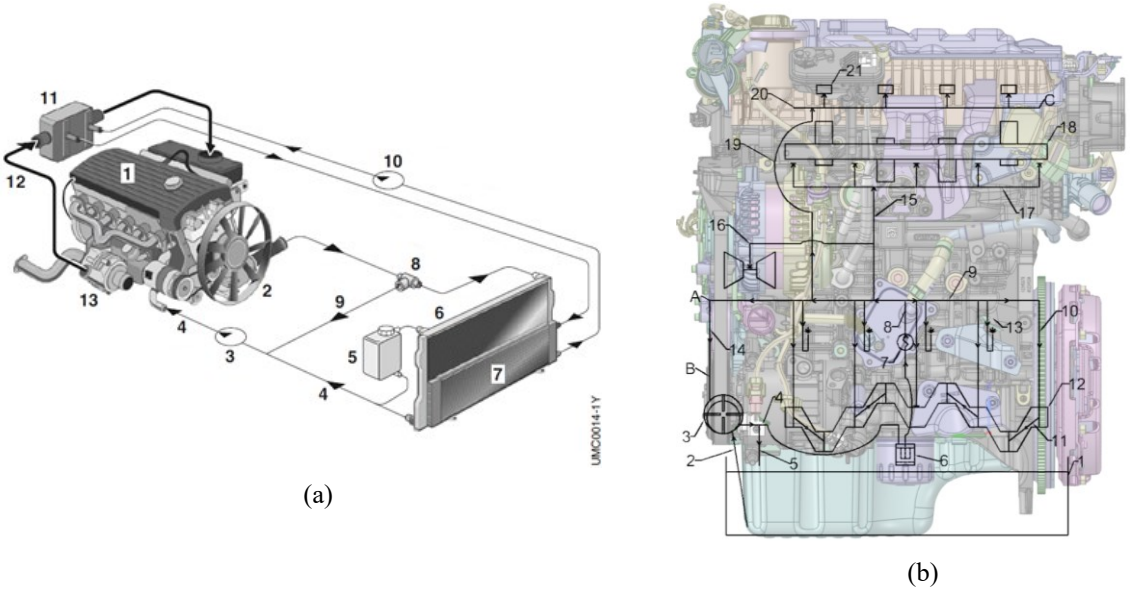

(a) (b)

Figure 3-1. (a) Passenger car cooling system with intercooling [143]; (b) lubrication system of the Firefly™ T4 engine (University of L'Aquila).

Traditionally, these systems are designed to operate under extreme conditions (uphill trailer tow), and as such they operate excessively at most other driving conditions [144]. An example is the motorway driving, where the engine speed is high: this causes high coolant pump loads, which however are unnecessary due to the large cooling power available over the vehicle radiator. Consequently, both excessive pumping work and overcooling of the engine occur [145]. Moreover, the simple layout and control strategies commonly used on cooling and lubricant systems (pump speed fixed with the crankshaft one, simple regulating valves, etc.) limit strongly engine performances in terms of power output, pollutant and CO_2 emissions during start-up transients (especially cold starts), where the engine operates far from its design temperature, requiring a warm-up period to reach it.

In light of these considerations, there is a large potential for improving cooling and lubricant systems in an ICE, in order to reduce the excessive power consumption of these units, as well as their negative effects on engine thermal state and, thus, on engine performance and emissions. This potential can be carried out by following two strands [144]:

- optimizing cooling and lubricant systems to adjust the engine operating temperature both in the steady state and during warm-up, in order to reduce emissions and fuel consumption;
- improving the efficiency of cooling and lubricant systems, i.e. reducing the pumping work required by the corresponding pumps.

Prior to explore both these strategies, a preliminary remark about the interactions of coolant and oil with the engine is necessary.

Commonly, coolant temperature is assumed to be representative of the engine metal temperatures, but this holds true only at steady state conditions, and for a particular operating

speed and load. In fact, the temperature of the metal and coolant varies from one point to another in the engine structure, giving a non-uniform temperature distribution, and this is exacerbated by the continuously variable operating points of the engine imposed by the driving load. Therefore, the coolant flow inside the engine must always guarantee that the most vulnerable regions, such as the exhaust-valve bridge area, never exceed the maximum temperature permissible for the specific material, in order to avoid engine failure [146]. In addition, knock protection must be ensured in SI engines, and the coolant flow distribution inside head and block must be designed to prevent this issue [147].

Simultaneously, engine lubrication should be always guaranteed in order to reduce friction and wear of engine moving components. Friction is strongly linked to the thermo-fluid-dynamic conditions experienced by the lubricating oil, which in turn depend on oil temperature. Generally, three different lubrication regimes can occur between two contacting surfaces:

- Boundary lubrication, in which the surfaces are in contact and rubbing against each other, and friction depends on the surface properties of the two materials.
- Hydrodynamic lubrication, in which an oil film builds up between the two surfaces and completely separates them. In this case, the friction is only a result of the shearing of the fluid and is highly dependent on the oil viscosity.
- Mixed-lubrication regime, in which the oil film may break down, enabling some direct contact between the two surfaces.

The Stribeck diagram (Figure 3-2) helps visualizing these lubrication regimes by plotting the friction coefficient as a function of the Hersey number (N_H), which depends on the oil dynamic viscosity (μ), the entrainment speed (N), and the normal load per length of tribological contact (P) (Eq. 3-1).

$$N_H = \frac{\mu N}{P} \qquad \text{Eq. 3-1}$$

Inside an ICE, different lubrication regimes occur depending on the specific mechanical coupling. The piston skirt acts in the hydrodynamic region throughout the engine cycle, while the piston rings have a more complex operation: in fact, hydrodynamic lubrication occurs when the piston is midstroke, whereas mixed and boundary-lubrication regimes occur as the piston approaches the top or bottom dead centers (TDC or BDC) [148]. Overall, piston friction occurs mainly in the hydrodynamic regime, thus resulting highly sensitive to the lubricant viscosity. Similarly, the main bearings operate in the hydrodynamic regime, although there are claims of mixed lubrication during peak cylinder pressures [149]. Instead, valvetrain operates in boundary lubrication regime, so resulting unchanged or even increased for reduced oil viscosity [150].

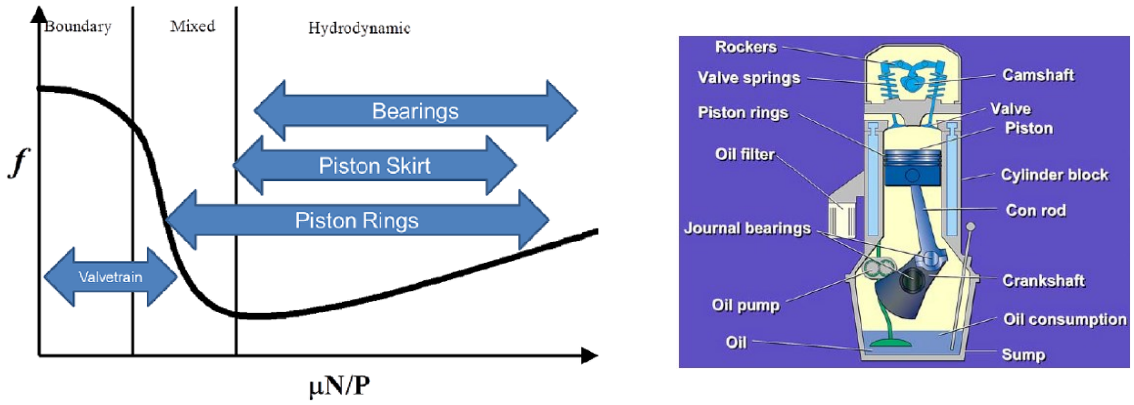

Figure 3-2. The Stribeck curve and different lubrication regimes applying on the main engine components [149].

Overall, the effect of engine temperature on engine friction is shown in Figure 3-3. Increasing the oil temperature causes a drop in the oil dynamic viscosity, which results in a reduction of the overall engine friction, measured through the Friction Mean Effective Pressure (FMEP). Therefore, the hydrodynamic lubrication regime appears dominant in ICEs, and thermal management strategies promoting low-viscosity oil should be preferred.

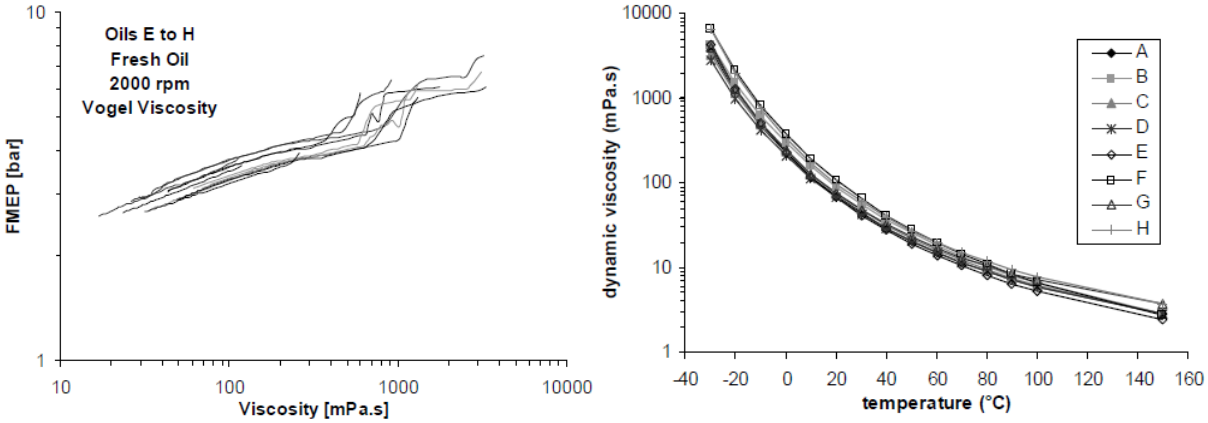

(a) (b)

Figure 3-3. (a) Measured engine FMEP as a function of the oil viscosity; (b) oil dynamic viscosity as a function of the oil temperature [151].

Another important aspect to consider when dealing with engine thermal management is the proper functioning of the after-treatment system of exhaust gases. Over the years, increasingly complex after-treatment devices have been developed for both SI and CI engines to reduce pollutant emissions. Depending on the specific engine, three-way catalysts (TWCs), diesel oxidation catalysts (DOCs), selective catalytic reduction (SCR) systems, and diesel or gasoline particulate matter filters (DPFs or GPFs), have been successfully implemented [152]. However, these systems offer good pollutant abatement performances only if the exhaust gases temperature exceeds the so-called light-off temperature (about 250°C [152]). Moreover, regeneration issues of DPFs and GPFs may occur in conditions of low exhaust temperature. On

the other hand, prolonged operation of after-treatment devices under high exhaust gases temperature could determine overheating and thermal sintering issues, resulting in irreversible catalyst damage [153,154]. Therefore, a suitable design of the engine exhaust line, as well as of the thermal management strategies for emissions abatement, must be performed in order to optimize the conversion efficiency of the after-treatment devices, without affecting negatively fuel consumption or system safety.

It follows that, if fuel and emissions savings want to be achieved, cooling and lubricant systems should be designed to maximize engine, as well as exhaust after-treatment devices, operation at their optimal temperature for as long as possible during driving. Therefore, the main strategies developed so far for engine steady-state and warm-up optimization will be presented in the next Sections, followed by the description of the potentialities offered in this sense by volumetric pumps when used as cooling pumps in ICEs.

3.2 Improving the engine thermal state

The cooling system plays a fundamental role in setting the engine operating temperature under design conditions. Once the limits on the temperature of the exhaust-valve bridge area are known, this temperature set point can be shifted, upward or downward, to improve the performance of the engine and the cooling system. However, care must be paid when tuning this set-point, because an attempt to solve one problem may result in a deterioration of another performance.

The increase in operating temperature raises the oil temperature, lowering frictional losses in the engine, thus reducing fuel consumption. Moreover, higher metal temperatures improve the effectiveness of the heat-transfer process in engine and radiator, allowing a lower coolant flowrate for a given power condition. This reduces the power consumption of the auxiliary system, which is particularly significant at part-load conditions [146] (see Section 3.4). Many concepts have been developed to reduce coolant pump power by improving heat transfer in the engine. Precision cooling enhances heat transfer in the critical areas of block and head by adjusting coolant velocity to the local heat flux. Coolant velocity is increased where more heat needs to be extracted, thus reducing the coolant flowrate requirements. The velocity can be varied by sizing suitably the engine coolant jacket (Figure 3-4 (a)). This results in a lower flow rate but a higher pressure drop in the cooling circuit, which overall yields a reduction of the coolant pump power consumption up to 54% [155]. Moreover, heat transfer can be enhanced by allowing the boundary layer of the coolant jacket to operate at its boiling temperature. This strategy, called nucleate boiling, is viable as long as saturated boiling does not occur, and allows to reduce flow requirements thanks to the high heat transfer coefficients reached with higher wall temperatures (Figure 3-4 (b)). However, nucleate boiling is often used as a safety margin rather than a nominal operating condition, because of its potential to evolve into saturated boiling, which would result in catastrophic failure [144]. The main concern of raising engine

operating temperature is its impact on the formation of pollutant emissions, due to the increase of NO_x emissions.

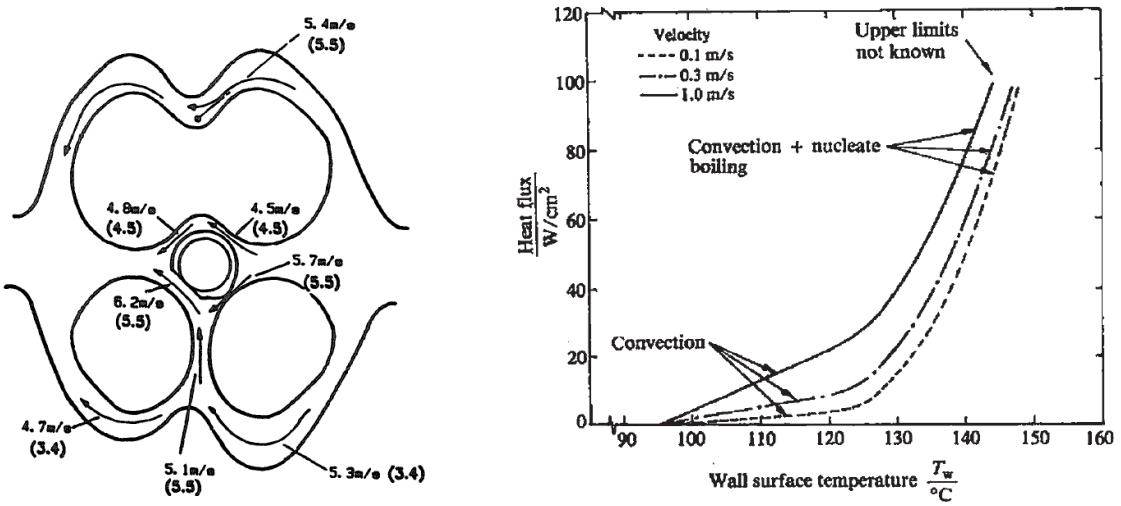

(a) (b)

Figure 3-4. (a) Coolant fluid flow in precision cooling [155]; (b) effects of nucleate boiling on heat flux [144].

Contrarily, engine temperature set-point can be shifted downward, enabling different advantages. By reducing the coolant temperature feed to the head, knock protection improves, allowing to increase compression ratio, which in turn leads to better fuel consumption and emissions if spark timing if suitably recalibrated [156]. Moreover, volumetric efficiency results improved due to the lower charge temperature, and life of engine components can be extended [146]. A lower coolant temperature in engine head can be obtained through reverse cooling or split cooling systems. Reverse cooling involves pumping coolant through the head and then through the block, as opposed to conventional systems. In this way, heat transfer is increased in the head, thanks to the higher temperature difference between engine walls and coolant. Moreover, heat transfer in the block is reduced, which can therefore be kept at a higher temperature, with benefits in terms of friction reduction. However, as vapor bubbles escape naturally towards the top of the engine, issues may rise due to the reverse coolant flow direction [144]. This issue can be overcome by split cooling systems, where head and block are cooled through independent circuits. Consequently, head and block can be run cooler and warmer than standard conditions, respectively. This allows to keep both advantages of low and high engine temperature set-point. Specifically, a cooler head determines higher volumetric efficiency, compression ratio and lower charge temperature, which allows a more rapid and complete combustion, reducing CO, HC, and NO_x formation, while increasing the output power. In addition, the higher block temperature reduces frictional losses, due to the lower oil viscosity, and indirectly diminishes the peak in-cylinder pressure and temperature, which as a strong association with NO_x formation [146]. The effectiveness of this strategy has been demonstrated by several studies [156–158], and many concepts have also been patented [159,160]. In [156]

the compression ratio was raised from 9:1 to 12:1 thanks to the head fed with coolant temperature at 50°C, while maintaining the block temperature feed at 80°C. This yielded to 5% and 7% improvement in fuel consumption at part-load and idling conditions, respectively, while increasing the peak wide open throttle (WOT) engine output by 10% relative to the baseline engine. Similarly, in [157] the coolant temperature was set at 50°C for the head and at 150°C for the block. This reduced fuel consumption by 4-6% and HC by 20-35% at part-load conditions, whereas at WOT a comprehensive improvement on fuel consumption, power output and emissions was obtained by setting a milder coolant temperature (90°C) for the engine block. More recently, the benefits of split cooling systems in terms of warm-up time reduction have also been investigated, as will be described in detail in Section 3.3.

Engine thermal state can be improved also through innovative systems which allow an active control of the cooling circuit. This is commonly realized by introducing electrified components in the cooling system, such as electric coolant pumps, electronic thermostat valves, electric fans and electric shutters to control the airflow over the radiator [144]. Specifically, the electric coolant pump allows to disengage its speed from the crankshaft one, enabling high potential gains in terms of engine operability, safety and thermal management requirements. In fact, it helps preventing under or overcooling issues [161], as well as knock phenomena [162] or after-boiling problems after prolonged high-load operation [163], which may arise under common driving conditions with standard passive control cooling systems.

Similarly, electronic thermostat valves, or more generally smart thermostats, allow to optimize engine cooling, thus reducing fuel consumption by about 1-2% if actuated through suitably defined map-controlled strategies [164]. In addition, variable-speed electric radiator fans can further reduce the power consumption by using only the required amount of power and also by avoiding over-cooling of the coolant [165]. Moreover, active grille shutters can limit the air drawn into the engine compartment at high vehicle speeds. If optimally controlled, this system allows to reduce sensibly engine under-cooling (especially during warm-up) and vehicle drag [166,167], with benefits in terms of fuel consumption up to 2.6% [168].

All these systems can be combined together to maximize engine thermal management [169]. This requires the development of integrated control systems, which have been developed for both warm-up and fully warmed engine thermal states [170], reaching in this latter case significant results in terms of coolant flow rate reduction [171].

As guessed, active control of engine cooling, and all the strategies for engine thermal state improvement, offer a high potential in enhancing engine performance also during the warm-up phase. Due to its relevance and connections with other engine systems (oil circuit and after-treatment devices), the technologies related to engine warm-up improvement will be detailed in the following Section 3.3.

3.3 Improving the engine warm-up performance

During common driving conditions as well as homologation cycles, the engine must always go through an initial warm-up phase, which is necessary to reach its nominal operating temperature (about 90°C referring to coolant temperature [172]) for which it has been optimized and designed. This warm-up phase constitutes a critical period of the engine operation, since its emissions and performances are sensibly degraded compared to the nominal ones, due to the deviation from nominal thermal conditions. In fact, a large portion of engine-out CO_2 and harmful pollutants emissions are largely induced during cold start-up [173,174], and in the first 75% of engine homologation cycles [175]. Specifically, about 60-80% of total emissions occurs in the engine cold start during the first 300 s of the NEDC and US FTP 75 cycles [176,177]. As a result, HC and CO emissions can be 60% higher than those in the hot engine phase [178,179], and a diesel engine may emit up to 7 times more particulate matter during cold operation than under warm conditions, coupled also to a prolonged period of unacceptable smoke emissions [180].

As described in Section 3.1, this is mainly due to the higher engine internal frictional losses, ineffective combustion [181], and low efficiency of catalytic converters, which derive from a not optimal temperature of engine and exhaust line components during warm-up. The negative effects of cold engine operation can be caught by observing Figure 3-5 (a), which gives an overview of the energy balance at the combustion chamber during the warm-up phase. About 53% of fuel chemical energy is transferred as heat to the cylinder walls, where it contributes to the heating of engine metal masses (32%), as well as coolant (12%) and oil (4%), whereas the biggest part is lost directly to the environment (52%).

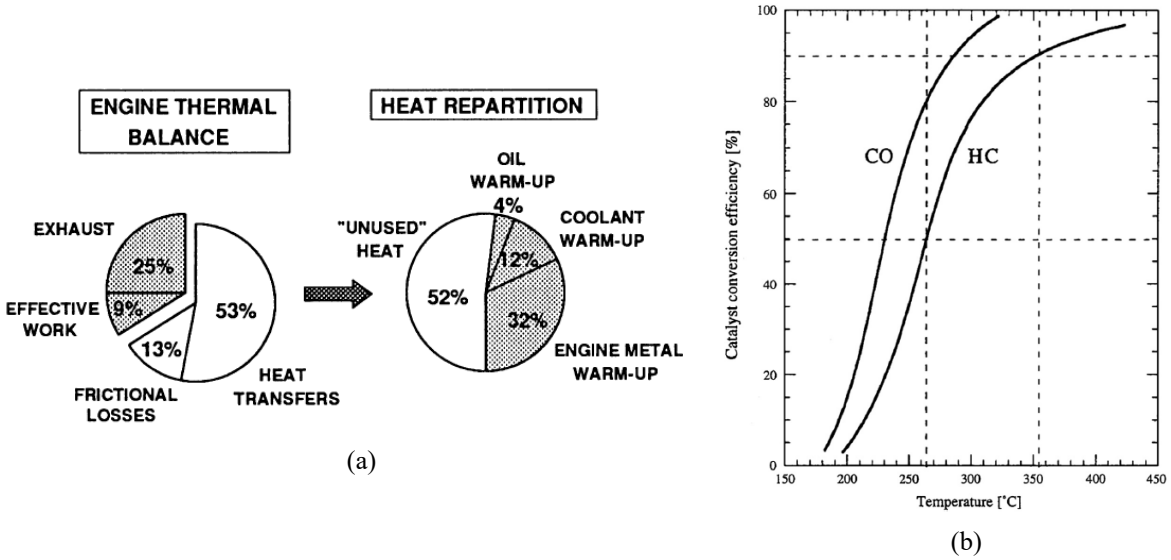

Figure 3-5. (a) Energy thermal balance during warm-up of a 4 cylinder 1.7 L SI engine operating at 2000 rpm and 10 Nm [182]; catalytic converter efficiency as a function of operating temperature for HC and CO emissions [183].

In addition, cold operation affects negatively also the after-treatment system, whose efficiency is defined as in Eq. 3-2 for each pollutant, where $\dot{m}_{pollutant}$ is the mass flow rate incoming or outcoming the device. Figure 3-5 (b) shows the conversion efficiency of a typical catalytic converter as a function of temperature, considering HC and CO emissions. The light-off temperature, to which corresponds 50% conversion efficiency, is in the range 220-270°C, and only above 400°C the catalytic converter reaches almost unitary conversion efficiencies.

$$Conversion\ efficiency = \frac{\dot{m}_{pollutant,in} - \dot{m}_{pollutant,out}}{\dot{m}_{pollutant,in}} \qquad \text{Eq. 3-2}$$

In summary, three primary effects co-exist during engine cold-starts [184]:

- the lubricant viscosity is increased, resulting in high frictional losses;
- the engine cylinder walls are excessively cold, resulting in poor combustion and increased piston/liner friction;
- the catalytic converter temperature is not high enough to offer satisfactory conversion efficiencies of exhaust pollutants.

In light of these considerations, any strategy or technology capable to reduce the warm-up time of the engine and of its after-treatment system has a high potential in reducing overall CO_2 and pollutant emissions. Several solutions have been developed in this sense (Table 3-1).

	Lubricant warm-up	Combustion warm-up	Catalytic converter functionality	Vehicle integration	Overall effect on fuel economy	Overall effect on emissions quality
Exhaust gas energy recovery (Section 6.1)	■	■	□	□	■	▨
Use of TBCs (Section 6.2)	▨	■	■	■	■	■
Standard insulation (Section 6.3)	■	■	■	□	■	■
Pre heated coolant (Section 6.4.1)	■	■	■	□	■	■
Coolant flow control (Section 6.4.2)	□	■	■	■	■	■
Lubricant flow diversion (Section 6.4.3)	■	▨	▨	■	■	■
Stop start technology (Section 6.4.4)	□	□	□	■	■	▨
Phase change material (Section 6.5)	□	□	□	■	▨	▨

Key

■ Positive effect
▨ Neutral effect
□ Negative effect

Table 3-1. Summary of the main potential solutions to engine cold-start issues and their effects on the vehicle sub-systems [184].

Each of them can have a different (positive, negative or neutral) impact on the main vehicle sub-systems. For example, energy recovery from exhaust gases can potentially improve lubricant and combustion warm-up, with positive effects on fuel economy and neutral effects on emissions, but affects negatively the catalytic converter functionality and is generally difficult to implement. Moreover, lubricant and coolant flow controls maximize fuel economy

and emissions abatement, without affecting negatively the catalytic converter efficiency. Similarly, engine insulation, thermal barrier coatings (TBC) and pre-heated coolant offer good potentialities, although with some issues relative to their integration on-board of vehicles. Instead, stop-start technology and phase change materials may have negative effects on the catalytic converter functionality and almost neutral effects on fuel consumption.

Among these solutions, the optimization of the engine cooling and lubricant systems is particularly interesting, due to their easy and cost-effective implementation, along with significative fuel and emissions gains. Therefore, they deserve an in-depth study, which will be presented in the following sections.

3.3.1 Optimization of the engine lubricant system

During the engine warm-up phase, three thermal masses interacts with each other, namely the main engine block, the lubricant and coolant (Figure 3-6). The coolant is the fastest to respond, due to its temperature being closely coupled to that of the combustion gases. Contrarily, lubricant and block temperatures are generally much slower, because of the large thermal inertia of the block, and the less straightforward bonding between lubricant temperature and combustion process, respectively [184].

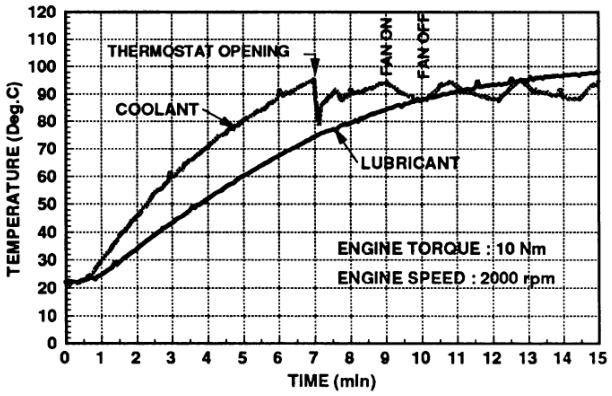

Figure 3-6. Lubricant and coolant temperatures during engine warm-up (with constant speed and torque) [182].

When lubricant is cold, its viscosity is much higher than at regime conditions, determining the engine FMEP to be about 25% higher during the cold phase with respect to the hot stabilized phase, and even up to 400% in worse cold-start scenarios [151]. To speed-up oil warm-up, the heat flow network between oil and surrounding components must be priorly understood. In fact, in the early phases of engine running, oil is heated primarily from frictional dissipation in the engine systems (such as the main bearings), rather than the combustion process [182]. This has been demonstrated by observing that the lubricant heating rate is positively correlated with engine speed (hence bearing surface speed) rather than engine load (hence combustion) [185]. Consequently, the heat generated from bearing friction disperses through lubricant flow or

through conduction into the surrounding metallic structures, resulting the first heat source for lubricant oil during early warm-up phase (Figure 3-7).

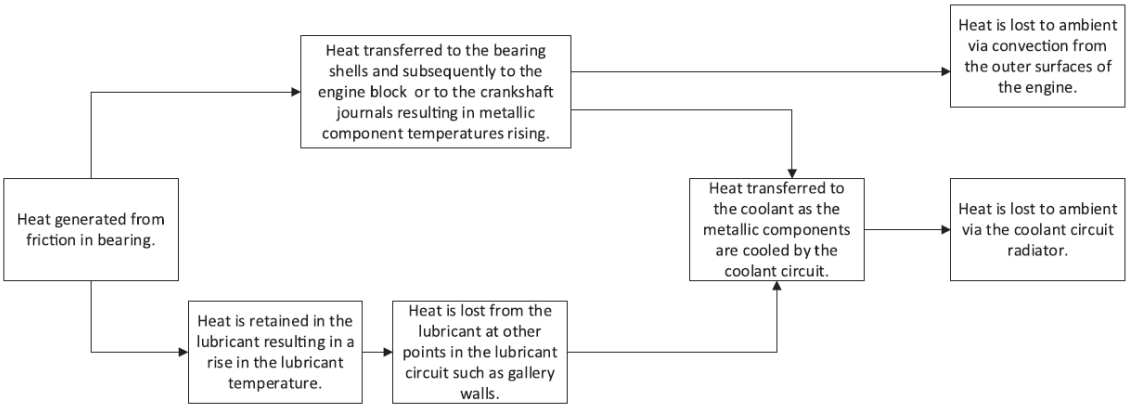

Figure 3-7. Schematic heat flow network representing bearing heat to oil [184].

These considerations agree with those shown in Figure 3-5 (a), and suggest that an attempt to improve engine warm-up could be the re-apportion of its thermal balance during that phase. Specifically, the 52% of heat wasted into ambient, as well as the 25% and 13% of heat wasted though exhaust gases and frictional losses, respectively, could be redirected to raise lubricant temperature more quickly, thus reducing engine friction.

Exhaust gases have a high potential in improving engine warm-up, since they leave the ICE at about 300-900°C, depending on engine load [172]. First assessments of their effectiveness for warming up the lubricant oil can be retrieved from [186,187]. In [188], by heating up oil directly through exhaust gases, fuel consumption and CO emissions have been reduced by 7% and 27%, respectively, over a 22°C NEDC. Similarly, in [189] an oil heat exchanger has been introduced after the catalytic converter, and its effects have been evaluated through an integrated numerical model of the engine; results show a strong reduction of the oil warm-up time (from 875s to 335s), with CO_2 emissions reduced by 1.32% over the NEDC. Moreover, the effects of an engine oil heater using EGR have been evaluated in [190]: fuel economy improvements of 1.08% at 28°C and 2.78% at -7°C, with an NO_x emission penalty of 40.3% and 11.5%, respectively, have been demonstrated through the numerical model of a full size sedan operating over a NEDC. A comprehensive assessment of CO_2 and pollutant emissions savings achievable with oil warm-up through heat recovery on exhaust gases has been realized for a light-duty diesel engine in [191]. The heat exchanger requirements have been evaluated according with the unsteady behavior of exhaust gases, and the need of limiting engine backpressure, without exceeding size constraints of the exhaust line. With respect to the standard situation, a 3.6% drop in fuel consumption was achieved, together with a great reduction on primary pollutants emissions (-7.2% of CO, -3.7% of NO_x, -3.5% of HC, and -1.7% of Soot).

Therefore, the heating of oil with exhaust gases can be considered significatively beneficial in terms of CO_2 and harmful emissions savings. However, the main issue is still the engine backpressure induced by the additional heat exchanger introduced in the exhaust line: in [192], a pressure loss close to 180 mbar for a gas flow rate of 0.08 kg/s was obtained, producing a fuel consumption increase of about 2.9% and thus reducing the net benefit at 0.7%. Moreover, catalyst light-off time could be increased [152,193], affecting negatively pollutant emissions.

Oil dynamics interacts continuously with cooling fluid dynamics through the oil heat exchanger, impacting on the overall engine warm-up. This interaction has been deeply investigated in [194], where the fuel consumption contributes of lubricant and coolant temperatures have been split. Specifically, engine performances at cold start (i.e. cold engine and oil), pre-heated oil (i.e. cold engine and hot oil), and fully warmed conditions (i.e. hot engine and hot oil), have been studied experimentally and numerically through modifications in the oil circuit layout. Results show that oil dynamics is faster than cooling fluid dynamics due to the reduced flow rates, and oil heat exchanger by-pass allows to reduce warm-up time of about 40-45%.

Other strategies for oil warm-up concern the introduction of additional heat sources to heat up the oil in the early stages of cold-starts, such as oil-sump heaters [195] or thermal storage systems using waste heat resulting from a previous engine usage [175,196,197]. However, in this case side effects on fuel consumption (oil-sump heaters) or operability (thermal storages) should be taken into account. This latter strategy has been investigated in [198], where a 5 L insulated tank of water provides heat to the lubricant oil. The water is warmed by a previous utilization of the engine, and re-heated by exhaust gases as soon as they can sustain the tank temperature level. A reduction of the oil warm up time is achieved in about 100s, which leads to a faster warm up of the coolant (-60s) and of the engine itself, allowing to reach -1.7% of fuel consumption over the NEDC, and so -4.4 g/km of CO_2 emissions.

In addition, lubricant flow diversions and active control systems (including electric oil pump or electronic valves) have been investigated [199]. An example is the oil sump volume modification, as that designed and tested in [200]. A standard oil sump was divided into two chambers, one always active and a closed one, connected through a thermostatic valve (Figure 3-8 (b)). During cold operation, the valve is closed and the pump aspirates only the oil in the active chamber. As the oil warms up, the valve opens, connecting the two chambers and restoring the total amount of lubricant oil. By reducing the remixing oil volume, this system reduces the oil temperature dynamics, with positive effects on friction and fuel consumption, diminished by 1% compared to the standard configuration.

A review of some of the most promising methods for lubricant oil warm-up has been realized in [201]. Five different techniques have been assessed experimentally (Figure 3-8 (a)): the positioning of the oil/water heat exchanger in the radiator coolant branch, and its complete bypassing by means of a temperature actuated valve in the oil circuit; the exhaust gases thermal

energy recovery; the sump heating by an external source; and the oil sump volume modification (Figure 3-8 (b)).

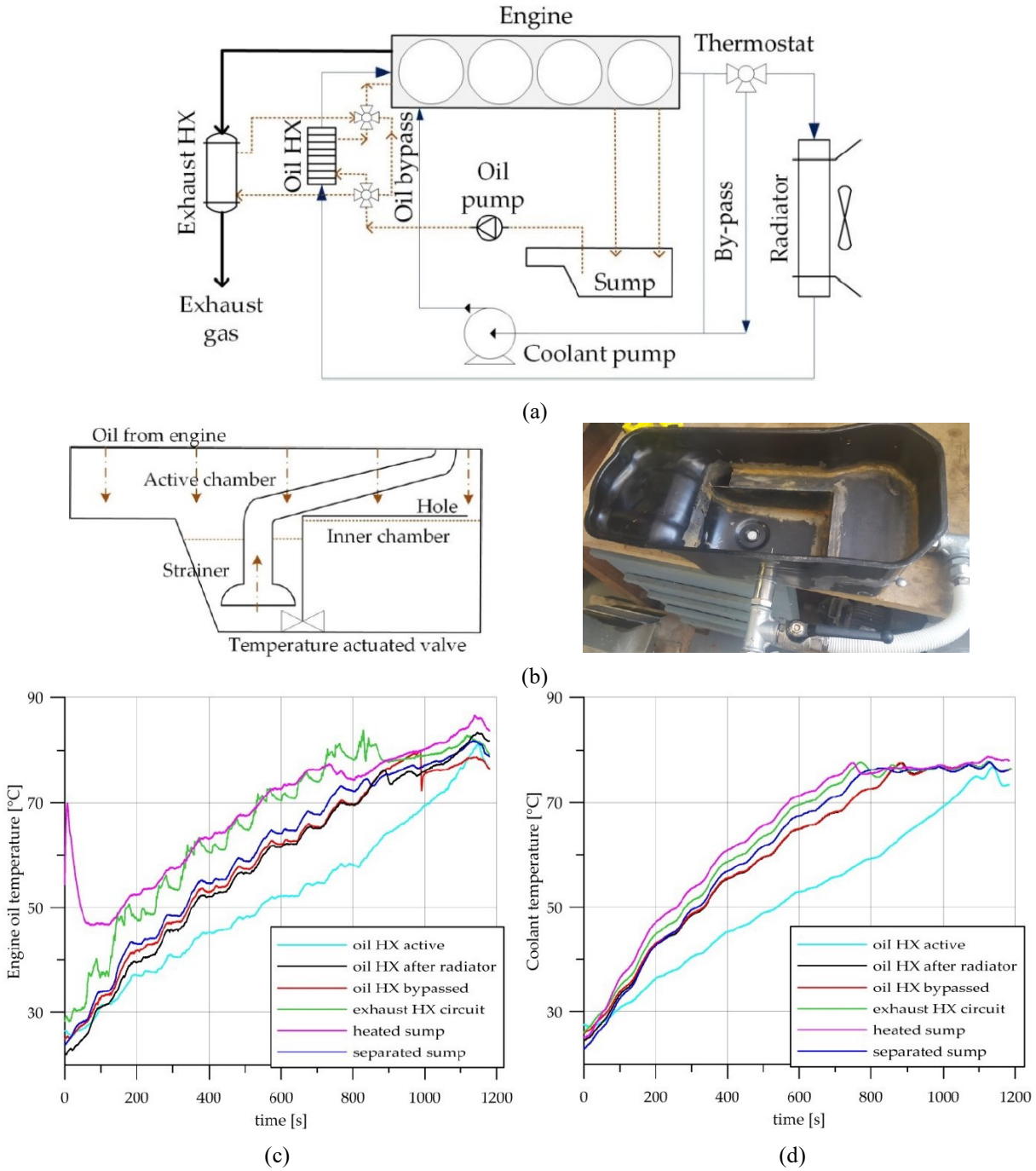

Figure 3-8. (a) Oil circuit layouts for engine warm-up; (b) separated oil sump; (c) oil temperature at the engine inlet; (d) coolant temperature at the engine outlet [201].

The effects on warm-up time of lubricant oil and coolant are summarized in Figure 3-8 (c) and (d), respectively. A first great benefit can be obtained by placing the oil cooler in the coolant radiator branch. Starting from this, it is clear that the oil heat exchanger bypass and the oil sump partitioning do not introduce further significant benefits on oil warm-up time, whereas the heat recovery from exhaust gases and the oil sump pre-heating enable the highest benefits. These

can be observed also in the coolant temperature, where each improvement contributes almost equally to coolant warm-up. In terms of fuel consumption, the introduction of the oil heat exchanger in the radiator branch brings the highest benefit (-4% of fuel consumption). Relative to this layout, the heated sump allows a further reduction of 1.8%, if the consumption of the external energy source is not considered. Moreover, exhaust heating and oil sump separation showed a reduction of 1.3% and 0.7%, respectively, whereas bypass of the oil-coolant heat exchanger does not produce significant benefits.

Other systems involving phase change materials and thermoelectric generators (TEGs) have been studied over the years, although efficiency, operability and cost issues still remain unsolved [184]. Anyway, fast oil warm-up performances can be reached through TEGs, as demonstrated in [202]. In that study, a TEG has been used in engine warm-up (EWP) mode (using the Peltier effect) to speed up oil heating during the beginning of the NEDC. Then, the TEG has been switched in waste heat recovery (WHR) mode (using the Seebeck effect) to recover heat from exhaust gases when the engine oil warm-up was finished. Results showed the oil temperature rising by 7°C in the first 100s, with partial compensation of the energy used in EWP with that produced in the later WHR mode.

3.3.2 Optimization of the engine cooling system

Another way to improve engine warm-up phase is to optimize its cooling system. Similarly to the lubricant system, innovative circuit layouts and renewed components, along with suitable control strategies, can be easily implemented with a good ratio between expected costs and CO_2 emissions saving (less than 50$ for each 1% reduction in fuel consumption [203]). Each strategy interacts differently with the other engine subsystems (lubricant, after-treatment devices, etc.), and a net benefit can be achieved only adopting a comprehensive approach.

During cold starts, the cylinder liner temperatures are below their nominal values, influencing negatively both combustion process and piston/liner friction phenomena. This temperature is very closely coupled to that of the coolant, which can therefore be used to speed up the cylinder liner heating.

Typically, during the warm-up phase, the thermostat valve is not open and heat is not being rejected by the radiator. However, coolant flow is maintained inside the engine to reduce the buildup of hot spots [184], thus cooling the cylinder liners. Coolant flow depends on pump speed, which is determined by the crankshaft speed through a fixed gear ratio. As a consequence, during periods of warm-up the cooling system is over specified [204].

Variable speed coolant pumps can help overcoming this issue. The effects of coolant flow rate on cylinder liner temperatures can be observed in Figure 3-9.

At steady state conditions, the mid-liner position is the coolest of all the locations, and pump speed has a strong influence on liner temperatures (Figure 3-9 (a)). This occurs also during warm-up (Figure 3-9 (b)). However, the benefit on fuel consumption is limited, with a saving

of 0.5-1% over the NEDC, and can be attributed largely to the reduction of pumping work, provided by the electric motor rather than the auxiliary drive.

In [205], the coolant pump was turned off during a NEDC until the coolant outlet temperature had reached 60°C, then on for 30s, and after off again for 60s (with this cycle being repeated). The top liner region was found to be most effective, with temperatures 10°C higher than with normal flow, whereas the lower liner did not vary significantly. This pulsed coolant flow strategy resulted in an approximately 6% reduction in HC emissions in the first 250s. Instead, the fuel consumption reduced less than 1%, primarily thanks to the reduced pumping work, rather than any thermal benefit.

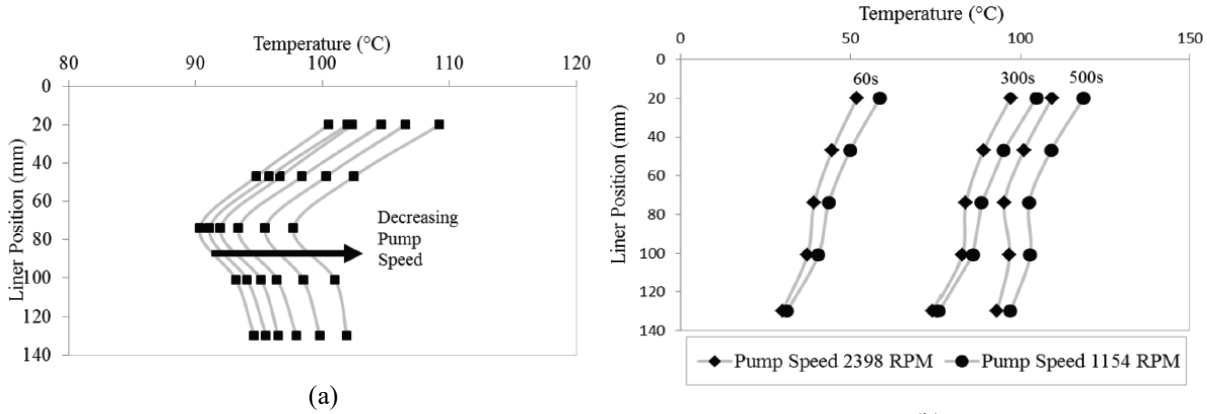

Figure 3-9. Effects of changing coolant pump speed on cylinder liner temperature: at steady state conditions (a); and during warm-up at 60s, 300s and 500s after start up (b) [206].

Other strategies have aimed at pre-heating the coolant before engine starting. In [207], a 3 kW electric heater preheated the coolant to 90°C in the coolant tank of a secondary circuit. Then, the coolant was streamed into an oil filter cooler assembly (FCA) to heat the lubricant oil during engine warm-up. As the coolant began to flow, the main gallery lubricant temperature increased from 20°C to 40°C, whilst only a 5°C increase was registered in the bearings. This demonstrates that the local lubricant temperature is highly sensitive to that of the surrounding metal. Nonetheless, this slight increase in lubricant temperature resulted in a significant reduction in its viscosity, and an 8% reduction in main bearings friction work was estimated relative to the standard case. Similarly, in [205] pre-heated coolant was circulated directly through either the block or the head, and tests were run by circulating the coolant 20s before the engine was fired, as well as since engine starting. No benefits were observed in the pre-circulating test relative to the simultaneous one. However, the friction levels were reduced relative to the situation with no preheating, with benefits of 5% and 9% on FMEP observed for block and head pre-heating, respectively.

Coolant can be heated during warm-up also using the thermal energy of exhaust gases, which reach suitable temperatures soon after engine start (about 150°C after 200s [191]). The effects of a coolant-to-exhaust-gases heat exchanger have been investigated already in [208]. The

warm-up time was reduced by up to 1 min, resulting in a fuel consumption reduction equal to 2.2%, although no details about emissions were offered. This fuel saving has been likely a result of reducing the piston liner friction rather than any dramatic increase in lubricant temperature, because of the weak thermal interaction between exhaust gases and lubricant [184]. To increase this interaction, in [193] enhanced lubricant/coolant and coolant-to-exhaust-gases heat exchangers were implemented in a 1.4 l S.I. engine. The first one aimed at improving the heat transfer between coolant and lubricant during warm-up, as this latter always follows the coolant temperature with a certain time delay (Figure 3-6). In addition, the second heat exchanger helps heating the coolant during cold starts, which in turn heats the lubricant oil with the first heat exchanger. At constant brake power, the first heat exchanger reduced coolant temperature by 10°C and increased the oil one by 6°C within the first minute, resulting in a 6% improvement in brake specific fuel consumption (BSFC). By adding also the second heat exchanger, coolant and oil temperatures increased by 20°C and 12°C, respectively, resulting in a 16% peak improvement of BSFC.

In contrast with the outcomes of these research, [188] claimed the ineffectiveness of coolant as a medium for heat recovery from exhaust gases to the lubricant. This study suggests a transfer efficiency of 32% when recovering exhaust heat directly to the lubricant, as opposed to an efficiency of 0.8% when using the coolant circuit as an intermediate heat transfer system. However, the effectiveness of exhaust-to-coolant heat recovery in reducing warm-up time has been demonstrated also more recently [209], and even in very cold starting conditions, in combination [210] or not [211] with phase change materials as energy storage medium.

The optimization of engine warm-up can be realized also by rearranging the engine thermal needs managed by the cooling system. A viable solution could be the splitting of the cooling circuit into two circuits operating at different temperature levels, in order to better match heat sources and sinks during warm-up, as well as steady state operations. This concept has been investigated in [212]. The standard cooling circuit of a small diesel engine (Figure 3-10 (a)) has been substituted by a double circuit (Figure 3-10 (b)), one serving the high temperature thermal needs (engine, oil cooler, EGR cooler, first stage intercooler), and the other the low thermal ones (second stage intercooler, cabin heater, A/C condenser). Each circuit has its own pump, and the low temperature loop does not require a thermostat, being its equilibrium reached among the different thermal requirements. Compared to the standard layout, this system has been proven numerically to reduce sensibly the coolant warm-up time, up to 50% over a NEDC if a liquid charged air intercooling is considered (Figure 3-10 (c)). Moreover, the double circuit produces a decrease in the mass flow rate necessary to cool the engine (Figure 3-10 (d)), thus reducing pumping work and warm up times of oil and engine. Finally, the presence of a low temperature cooling circuit allows to integrate also the A/C condenser, which can be operated with lower condensation temperatures, producing an energy saving close to 5%.

The cooling system can be optimized also for what concerns the cooling flow passages inside the engine. In [213], the benefits introduced by the split cooling between engine head and block

on warm-up time reduction have been investigated. Starting from the standard layout (Figure 3-11 (a)), two cooling layout options have been conceived and theoretically studied. The first one (SC1) considers a full flow that cools first all the cylinder heads (in sequence) and, then, the engine block, with a short circuiting path managed by a valve between head and block circuits (Figure 3-11 (b)). The second one (SC2) adds to the first option the capability to recirculate part of the coolant flow leaving the engine into the block, thanks to a different arrangement of coolant pump and by-pass valve (Figure 3-11 (c)). The aim is to reduce head temperature, while increasing the block one, without important modifications on the actual engine. This goal has been reached, being the engine head colder that the engine block of about 8-10°C. Moreover, the second split cooling concept can effectively reduce coolant warm-up time by 10%, whereas the first one does not show significative improvements (Figure 3-11 (d)).

Both the concepts of a double cooling circuit operating at different temperature levels, and of an engine head and block split cooling system, can be combined together to maximize the overall benefits in terms of engine warm-up time reduction. This has been realized efficiently in [214], through a physically consistent mathematical model capable to describe the main phenomena about heat transfer on engine cooling circuits. Specifically, the cooling sequence has been reversed so that a single stream cools the head and after returns inside the engine to cool the block. Moreover, low and high engine thermal needs have been split among two cooling circuits, as in Figure 3-10 (b). The combined system shows a 6°C reduction in the mean head temperature during a WTLP cycle, as well as a 2°C increase in the block temperature. In addition, the two circuits guarantee a lower mechanical power absorption by the cooling pumps, due to the lower coolant flow rate crossing the engine, and to the increase of the mean pumps efficiency. Furthermore, similarly to [212], the warm-up time has been reduced up to 50%, and the repositioning of the A/C condenser in the low temperature circuit allowed an energy saving up to 3.5% over the WLTC.

Another strategy to improve engine warm-up can be the introduction in the cooling circuit of other thermal needs, which can enhance the heat transferred to the coolant, producing a faster temperature increase. One of these is the liquid charge air cooler (CAC), which provides heat from compressed intake air almost immediately. In [215], a comprehensive engine cooling model has been developed to predict the benefits of the addition of a CAC in the cooling system reported in Figure 3-10 (a). Results show that, for the specific application, the mean thermal power exchanged in the CAC over the NEDC is equal to 6 kW, which is capable to reduce the coolant warm up time of about 60%. Moreover, the pressure drop introduced by the CAC does not vary dramatically the working point of the coolant pump, which increases its power absorption less than 2% of the mean propulsive power over the NEDC.

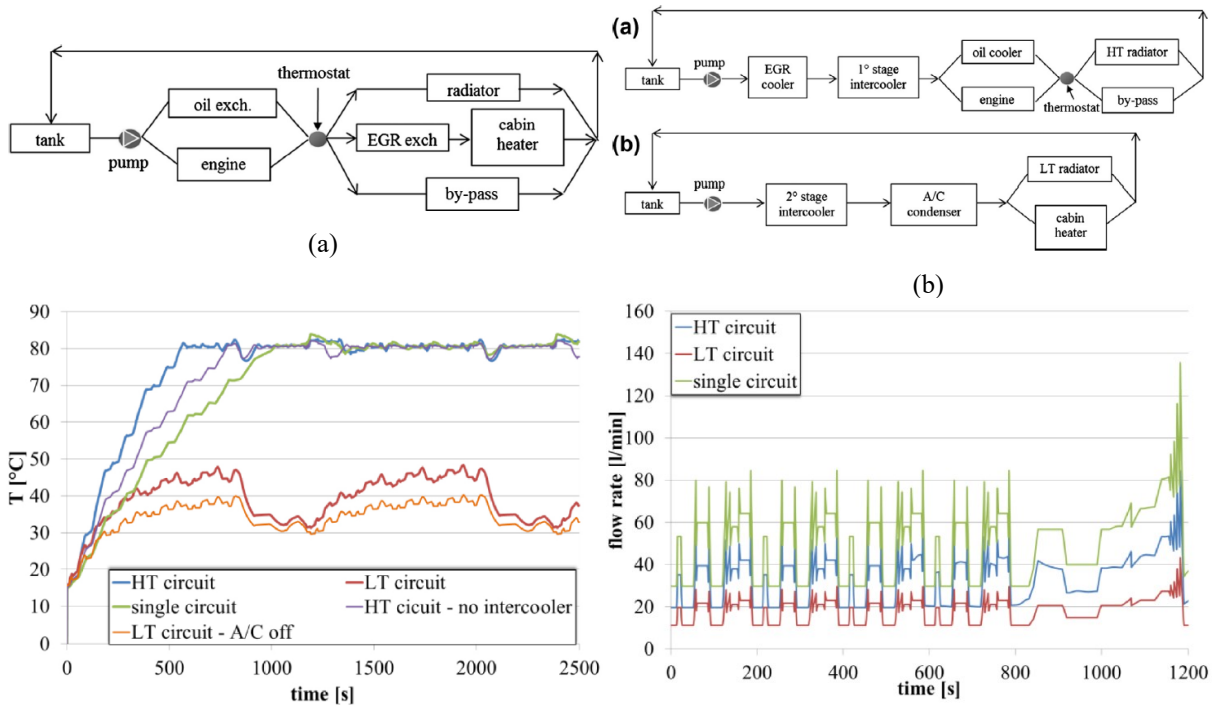

Figure 3-10. Double cooling circuit at two temperature levels: (a) original circuit; (b) modified circuit; (c) benefits on coolant temperature, and on coolant flow rate (d), during the NEDC [212].

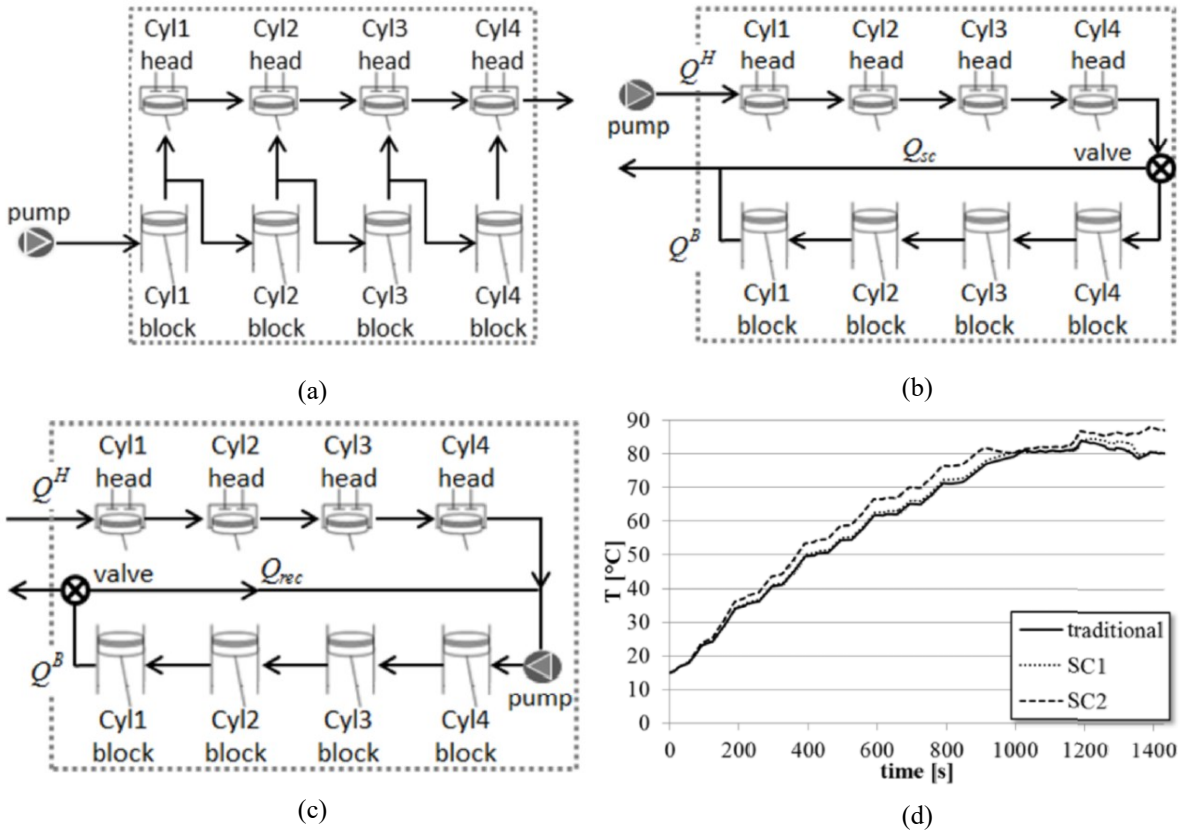

Figure 3-11. Head and block split cooling: (a) traditional hydraulic layout; (b) first split cooling system, with short circuit at the block; (c) second split cooling system, with by-pass on the block; (d) coolant temperature during the NEDC [213].

A different, and in some ways simpler, approach to optimize engine warm-up is the reduction of the volume of the hydraulic circuits. This has been successfully simulated in [216]. Results show that, by reducing both coolant and lubricant oil volumes by 90%, a fuel saving up to 1.2% can be reached during the warm-up phase of a WLTC in ambient boundary conditions. Moreover, the reduction of just the coolant volume by 45% yields to savings in warm-up time and fuel consumption equal to 7% and 0.4%, respectively. The impact is even higher for cold conditions (-7°C), where these values rise up to 13% and 0.5%, respectively.

Similarly, the reduction of the thermal inertia of head and block is crucial for the engine warm-up optimization. A recent study [217] demonstrated that the heat cumulated in the engine structure is about 37% at the initial stage of a cold start WLTC, before moving towards 5% at the end of the cycle. The choice of the engine materials plays a fundamental role in this sense: by changing the head material from cast iron to aluminum, a warm up time reduction of 15% has been demonstrated over a NEDC [212].

Many advanced smart cooling systems have been also developed. Typically, they use electrically actuated cooling pumps, smart thermostats, electric fans and grille shutters, managed through active control units to optimize the overall engine operation. In [218], a variable position electromagnetic thermostat (VPEMT) and an electric coolant pump (EWP) have been implemented in the cooling system of a light duty diesel engine. Results show a 28.5% warm-up time saving over a NEDC, along with a strong reduction of THC, CO and CO_2 cumulated emissions (-31.4%, -22.6%, and -34.9%, respectively), but a slight increase of NO_x emissions. Similarly, the benefits of introducing an EWP in combination with heated thermostat and electrical fan have been assessed in [219], in which an intelligent control program has been modeled too. In this way, savings in terms of fuel consumption, HC and CO emissions up to 1.1%, 5.3% and 6.1%, respectively, have been demonstrated over a NEDC compared to a conventional cooling system. Advanced thermal management systems (TMS) including combined control strategies for both coolant and lubricant oil circuits have been also investigated [220]. During engine warm-up, fan and valves were kept closed, and coolant and oil pumps remained at their minimum flow rates for engine reliable operation. Then, the electrical pumps and fan were controlled by a feedforward and feedback control strategy, and the electrical valves through a feedback approach. The comparison with conventional system showed a 57% reduction of the TMS total power consumption over the European Transient Cycle (ETC). These strategies can be combined also with split cooling concepts [221]. In this case, an EWP and a servo motor valve have been used to manage the cooling flows between head and block circuits. This improved the warm-up time by more than 35%, thanks to the significant reduction of coolant flow rate.

When dealing with electrically driven pumps, a suitable controller for the management of coolant flow rate must be developed in order to properly manage nucleate-boiling [222], after-boiling [163] and knock (for SI engines) phenomena [162]. This has been accomplished successfully in [170]. A model predictive control approach for electric pumps has been set up

to operate the cooling system around the onset of nucleate boiling, in order to take advantage of the associated high transfer coefficients. Experimental tests provided that it is effective in decreasing the warm-up time and in reducing the coolant flow rate under fully warmed conditions as compared to a standard configuration with pump speed proportional to engine speed. Specifically, a 60% reduction in coolant flow rate in the early part of the NEDC was obtained, and wall and oil temperatures reached their reference values (120°C and 90°C, respectively) about 3 minutes earlier [223]. In terms of fuel consumption saving, a reduction of about 2-3% and 1-2% can be achieved during engine warm-up and fully warmed operations, respectively, with the engine operating at constant speed and torque (2000 rpm and 2-4 bar, respectively) [224]. Over the NEDC, fuel-savings up to 8% can be achieved by implementing high boiling level control strategies, thanks to the strong reduction of coolant flow rate, especially under part-load conditions [225].

Clearly, in all the solutions above mentioned, the efficiency of the coolant pump affects significantly that of the whole cooling system. Therefore, innovative solutions have been proposed also for what concerns the improvement of cooling pumps for ICE vehicles. Being one of the main topics of this thesis, they will be detailed in the following Section 3.4.

3.4 Volumetric pumps for engine cooling

Focusing on the engine cooling system, conventional technologies adopt a centrifugal pump to move the cooling fluid into the circuits, which is mechanically linked to the crankshaft. These systems have two weak points: (a) the pump is driven at variable speed, and this prevents a high pump efficiency, which is very sensible to the impeller speed; (b) the cooling fluid circulates also when the engine cooling requests are not needed, as it happens during engine warm-up phase. Indeed, the pump Best Efficiency Point (BEP) is located at high flow rate and rotational speed, corresponding to the maximum engine mechanical power. This operating point is distant from those commonly experienced by the pump, as happens during real driving or type-approval cycles. Therefore, pump efficiency is usually very low, between 15% and 20%, producing a power absorbed not negligible compared to the propulsion one [226]. By disengaging the pump from the crankshaft and driving it with an electric motor, the cooling flow rate can be modulated to shorten warm-up time, but the problem of a reduced pump efficiency still remains unsolved.

Many strategies have been investigated to improve centrifugal pumps efficiency [227,228], even when operating at very high speed applications (up to 12000 rpm) [229,230]. This latter solution is particularly interesting for HEVs, because it allows to downsize both the pump and the electric motor, easing the on-board positioning. Moreover, many different pump actuation systems have been studied, mainly aimed at varying pump speed without renouncing to the intrinsic benefits of a mechanical link with the crankshaft (fail safe, cost effective and reliable). For example, in [231] the effects of two mechanical pump technologies have been evaluated on

an engine cooling system: a planetary gear centrifugal pump, which could reduce the revolution speed up to 65% through a pulley, and an on/off centrifugal pump, which could completely stop the rotation of the impeller. The performances of the two devices were assessed through warm-up tests (target coolant temperature of 80°C) and along the NEDC. The warm-up test of the planetary gear pump was 7.3% faster than a conventional water pump, while the one of the on/off centrifugal pump was 24.7% faster. For the NEDC test, the result was an improvement rate of fuel consumption up to 1.7% and 4%, respectively.

On the other hand, rotary volumetric pumps represent a viable solution for engine cooling. In fact, they are less efficiency sensitive to revolution speed, flow rate and head, preventing in this way a lower efficiency when working far from the design point. Moreover, they have a linear relationship between revolution speed and coolant flow rate, which is particularly useful in automotive applications, where the engine operating point changes constantly, and so an albeit minimal control strategy of the auxiliary pumps should always be implemented.

Due to these important properties, volumetric pumps are widely used in lubricating applications, and recently they are gaining interest also for what concerns engine cooling. Among different solutions, sliding vane rotary pumps (SVRPs) have shown a high potential in substituting standard centrifugal cooling pumps. In [232,233], a SVRP has been designed for an existing engine cooling circuit, starting from the study of vane rotary compressors. The pump has been built and extensively tested, and its performance maps have been introduced in a comprehensive mathematical model reproducing both the engine and the vehicle operating conditions over a homologation cycle. This allowed to compare its performances with those of the standard centrifugal pump. It was found that the proposed SVRP absorbs about 15% less mechanical energy over a NEDC. This translates into CO_2 emissions savings varying between 0.3-0.5 g/km and 0.6-1 g/km, depending whether the SVRP is mechanically linked to the engine, or managed by keeping the same flow rates and heads of the centrifugal pump, respectively.

Following this topic, the control of coolant flow rate in SVRPs has been investigated in [234], where the effects of a variable eccentricity actuation on pump performance have been evaluated though a model-based approach developed for sliding vane rotary compressors [235]. In fact, a fixed eccentricity SVRP has a global efficiency less sensitive with the revolution speed than a standard centrifugal pump, resulting in higher coolant flow rates, and thus hydraulic power, if actuated with the same speed profile. To overcome this issue, a variable flow rate SVRP was proposed. This system modifies continuously the pump geometry through a change of the eccentricity between stator and rotor, in order to vary the pump displacement according to the coolant flow rate requested by the engine. In this way, the mechanical energy requested by the SVRP over a WLTC decreased by 22% than that requested by the centrifugal pump, with higher benefits at lower engine loads. This translates into a CO_2 emissions reduction of about 0.5 g/km.

These studies on SVRPs with variable eccentricity for flow control purposes have opened the way to further investigations about their geometrical optimization. In [236], a novel model-based design procedure was developed to optimize pump ports and shape. A mathematical model capable to predict the pump performances was experimentally validated considering an original equipment manufacturer (OEM) SVRP. Then, it was used to design inlet and exhaust ports, and to determine the machine's optimal aspect ratio. Specifically, starting from the OEM configuration (Figure 3-12 (a)), an improved ports (IP) pump was obtained by replacing the original axial intake port with a larger radial one, and by adding a radial port at the exhaust (Figure 3-12 (b)). This mitigated the mismatch between intake and exhaust ports, improving the indicated efficiency by 50% with respect to the OEM SVRP. Subsequently, the IP configuration was considered in a disk-shaped (DS) (Figure 3-12 (c)) and finger-shaped (FS) (Figure 3-12 (d)) arrangements. The IP-DS configuration achieved higher efficiencies (up to 55%) than FS and OEM machines, thanks to its generally higher volumetric and mechanical efficiencies. Finally, the optimized IP-DS SVRP was operated on a specific test bench to reproduce the operating points of a centrifugal pump used in the cooling circuit of a turbocharged diesel engine. The flow rate was controlled over a WLTC by an electric actuation or by a continuous modification of the eccentricity. In the first case, the pump operated with a significantly higher mean efficiency (43.5%) than that of the centrifugal pump (31.5%), determining a 30% reduction in the absorbed mechanical energy, and CO_2 emissions savings up to 1.5 g/km.

When designing a SVRP for an engine cooling application, the choice of revolution speed and displaced volume plays a fundamental role on the overall pump performances. In fact, they affect differently the various efficiency components (volumetric, indicated and mechanical), making necessary to find a suitable trade-off among them. This aspect has been deepened in [237,238], where a comprehensive mathematical model capable to predict even the indicated diagram of SVRPs has been experimentally validated and used as a model-based design tool.

Generally, there are multiple combinations of revolution speed (ω) and volumetric displacement (V_{disp}) capable to fulfill the flow rate request (Q), which can be expressed as a function of them through the volumetric efficiency (η_{vol}) (Eq. 3-3).

$$Q = \eta_{vol}\, \omega\, V_{disp} \qquad \text{Eq. 3-3}$$

However, each combination of ω and V_{disp} affects differently the pump efficiency. In fact, higher revolution speeds lead to a higher volumetric efficiency, whereas mechanical and indicated efficiencies result penalized. This effect is mainly determined by the interaction between blades and stator inner surface. Indeed, when the revolution speed grows, the centrifugal force acting on the blades increases as well, pushing them against the stator inner surface. This reduces the clearance gaps between blades and stator, thus diminishing the backflow inside the machine, with obvious benefits on the volumetric efficiency. On the other

hand, the friction force between blade tips and stator inner surface increases, thus depleting the mechanical efficiency. In addition, under and over-pressure issues occurring during intake and exhaust phases respectively, as well as pressure peaks during pump rotation, worsen, affecting negatively the indicated efficiency.

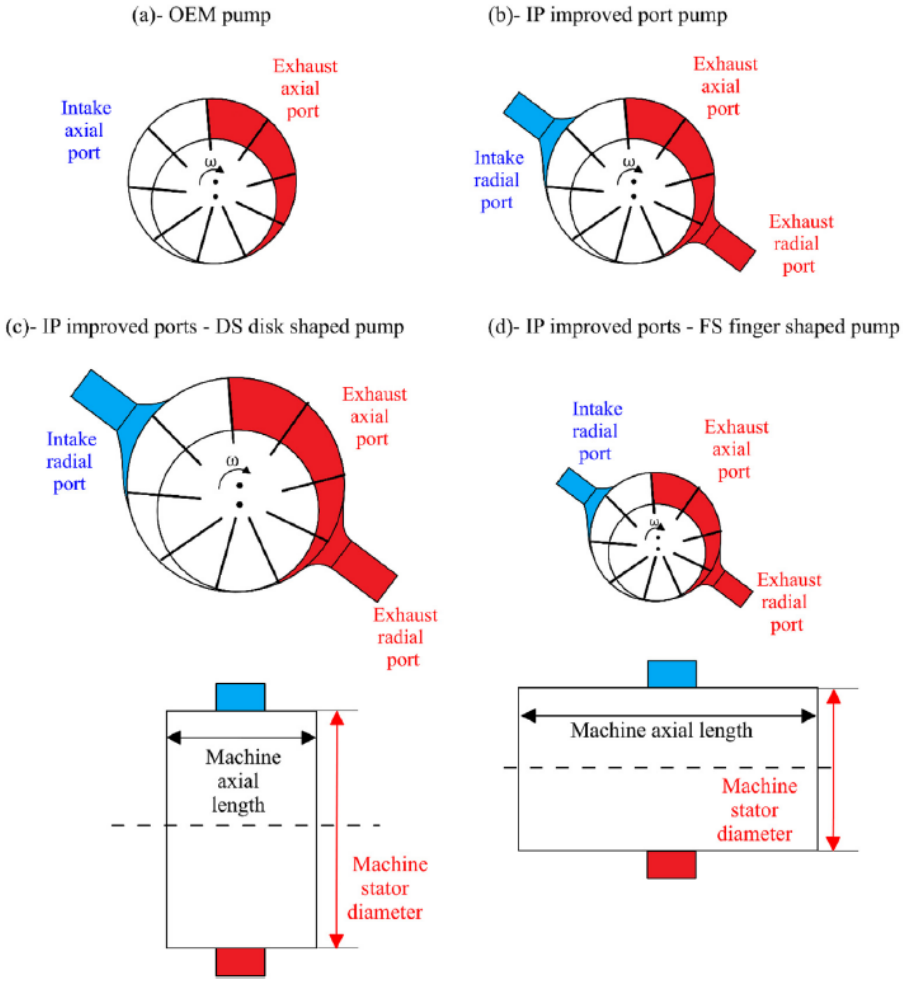

Figure 3-12. OEM (a), IP (b), IP-DS (c), and IP-FS (d) configurations for SVRPs [236].

Overall, higher pump speeds determine lower global efficiencies, but at the same time they allow to minimize the volumetric displacement, and thus the pump dimensions, which is always requested in on-board applications. Fortunately, a trade-off can be reached by taking advantage of the specific aspect ratio of these machines. In fact, a slight increase of the pump radial dimension (+3%) can produce a sensible growth of the displaced volume (+25%), allowing to reduce significantly the revolution speed for the same design flow rate to be delivered [237]. In addition, an axial design of intake and exhaust ports facilitates filling and emptying processes of the chamber volumes, increasing the indicated efficiency. As a result, this strategy can enable very high efficiencies (up to 60%), with only a slight efficiency penalty when operating far from the design point.

Further improvements on the design of SVRPs for engine cooling applications have been investigated in [238], thanks to a detailed modeling of the fluid-dynamic and mechanical losses occurring during pump operation. Light-weight materials for the blades (such as graphite) have been proven to be effective in reducing the blade centrifugal force, and thus the friction force acting on the stator inner surface. Moreover, the direct measurement of the pressure inside the chamber volumes allowed to trace the indicated cycle. This showed the occurrence of pressure spikes during pump rotation, mainly due to the closed volume transformation happening in correspondence of the intake end phase and the start of the exhaust one (black lines in Figure 3-13). In fact, due to the limited fluid compressibility, slight volume reductions during vane rotation can produce significant pressure increases, which can seriously damage the pump. In addition, the higher is the revolution speed, the higher are these pressure spikes (Figure 3-13 (a-c-e)). This issue can be successfully overcome by modifying the intake and exhaust phase angular extents, in order to prevent closed volume compression. The proposed solution realized a slight port overlap, whose angular extent was predicted through the above mentioned model-based design tool. The effects on the indicated cycle are noteworthy and show a substantial elimination of severe pressure spikes (red lines in Figure 3-13).

Putting together all these aspects, the design of SVRPs should be oriented towards a reduction of revolution speed, which can be easily obtained through the enhancement of the displaced volume without a significative increase of the overall pump dimensions. This alone could improve efficiency up to 25% with respect to a SVRP designed to operate at higher revolution speeds, reaching peak efficiencies over 60%. Moreover, blades made of light-weight materials should be preferred to further reduce mechanical losses, along with dual axial intake and exhaust ports to mitigate fluid-dynamic losses. Finally, closed volume transformations should be definitely limited to avoid pressure spikes and prevent an early failure of the machine.

Another promising technology of volumetric pumps for engine cooling is represented by screw pumps. They share with SVRPs many of the concepts above introduced about operating principle and physical phenomena defining their performances. The research activity conducted on screw pumps is one of the main topics of this thesis, and so it will be described in detail in the next Chapter 4.

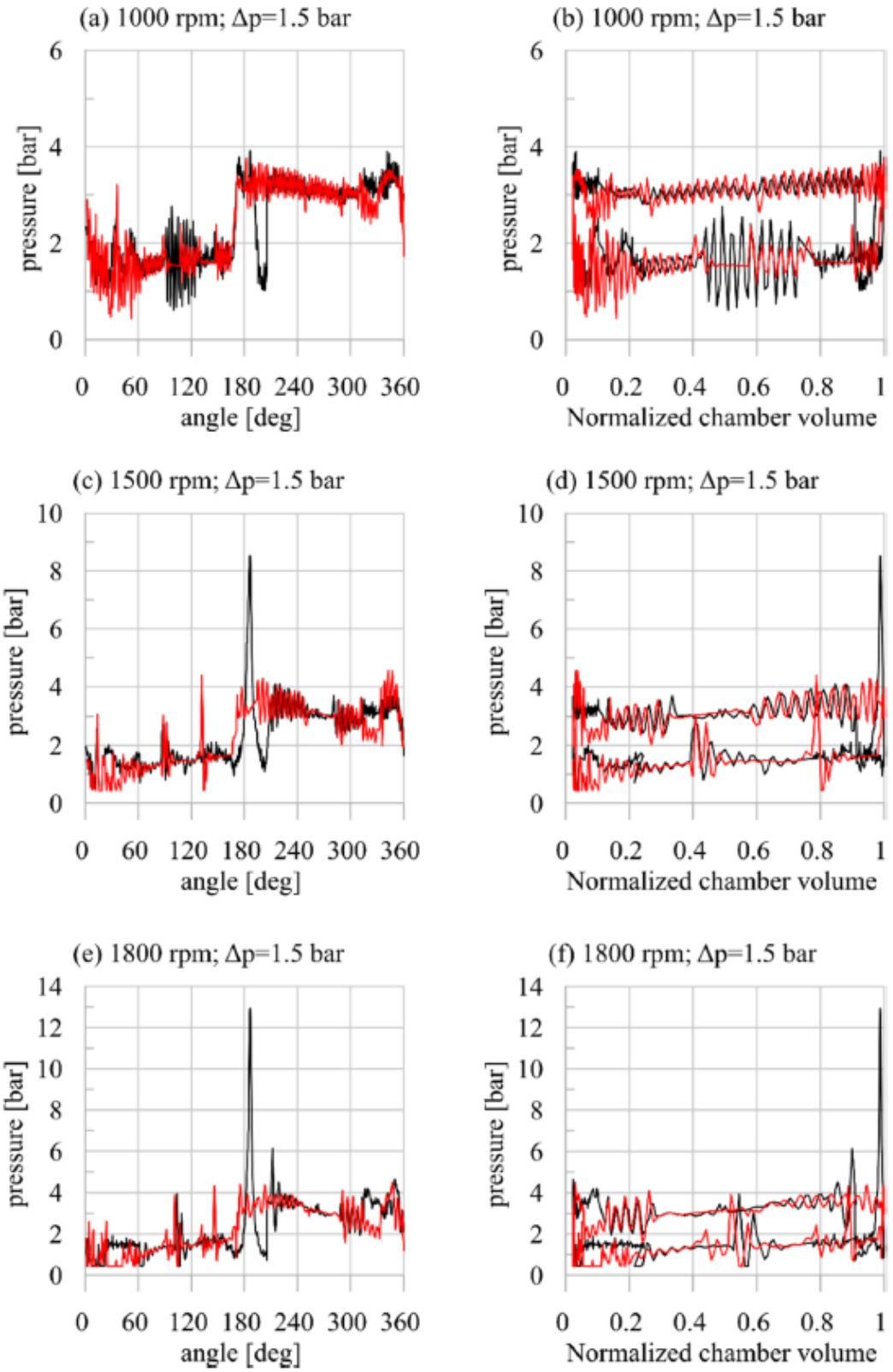

Figure 3-13. Comparison between the indicated cycles of experimental (black) and optimized SVRP (red) as function of angle and volume for 1000 RPM (a-b), 1500 RPM (c-d) and 1800 RPM (e-f). [238].

3.5 Conclusions

This Chapter summarized the most advanced technologies related to the optimization of the engine thermal management. Specifically, those concerning the performance improvement in steady state conditions, as well as during the warm-up phase, have been thoroughly reviewed. It appears clear that the possible solutions embrace many different engine sub-systems, such as the lubricant, cooling and aftertreatment apparatus, which are all intimately connected each other. Hence, further technical advancements should be implemented assuming a holistic approach, in order to minimize both fuel consumption and pollutant emissions.

Among the reviewed solutions, those related to the improvement of the engine cooling system have been object of a closer research. Specifically, innovative screw-type volumetric pumps for engine cooling have been proposed. In fact, this technology can potentially reduce the mechanical energy necessary to cool the engine, which is particularly useful if an efficient electrification of the auxiliaries wants to be performed.

Therefore, Chapters 4, 5, 6 and 7 will discuss the experimental and theoretical analysis developed on screw pumps for engine cooling applications. Then, Chapter 8 will present the experimental activity realized on a passenger vehicle available in the laboratories of the University. The aim is to investigate experimentally potential solutions to optimize the engine warm-up phase.

4 Screw-type volumetric pumps for engine cooling

4.1 Overview

The basic functional principle of positive displacement pumps is to use a volume variation to create suction and pressurize a fluid. Specifically, they move volumes of liquid for each operating cycle, and pressurization happens when the fluid is discharged into the receiving circuit.

Among volumetric pumps, screw pumps are widely used in the industrial and in the oil & gas sector. They have higher efficiency, head capacity and reliability than other types of pumps in these applications. Moreover, they have important advantages, such as small hydraulic pulses, smooth transmission and low noise [239]. They are commonly designed to work with high viscosity fluids, such oils, and to guarantee high levels of pressure delivered. Generally, friction between rotor and stator, and among screws, introduces mechanical losses, which decrease efficiency. Increasing clearances between these elements can improve the mechanical performance, but leads to a volumetric efficiency decrease. Therefore, a balance between these two factors should be reached.

The screw machines have been considered widely in literature, in terms of thermodynamic model and fluid flow processes [240]. New advanced rotor profiles were extensively studied [241,242], more referred to screw compressors, where the contacts between driver and idler have been optimized in order to reduce wear and friction. The effects of the temperature on the effective clearance of an oil free compressor have also been investigated [243].

Screw pumps have been studied to improve their performance, mainly when operating with clean and lubricating fluids [244]. The rotor profile plays a crucial role in the screw pump performance [245], due to the influence on friction and, definitively, on pump efficiency. Therefore, the screw profile needs to be optimized to reduce both friction and blow hole backflow. This optimization can be realized by varying the blunting of the screw profile, as well as the screw shape.

Among the blunting methods, an elliptic arc was developed in [246] for the rotor of a three-screws pump. Comparing with the existing profiles, this method significantly reduces the blow hole of the screw pump, improving volumetric efficiency. The screw shape was studied in [247], where the screw's angle was optimized to maximize the overall efficiency of a twin-screw oil pump: a prototype was built, validated with a CFD method and experimentally characterized.

The screw machines optimization has been studied also in vacuum applications. A smoothly-connected eccentric involute screw rotor was developed for a twin-screw vacuum pump in [248]. This enabled continuous, smooth and short spatial contact curve, no leakage gaps and a better inter-stage sealing performance. The design of an optimized rotor profile for a timed and

oil-free twin-screw vacuum pump was developed in [249], while in [250] a profile of claw-type rotor by means of the theory of gearing was designed to improve sealing and reduce carryover.

CFD analyses are the most used approach to predict performances of screw pumps. A full design platform for screw machines having many features for design [251], as well as an automatic numerical mapping method for arbitrary screw compressor geometries [252], have already been developed. Thus, the difference in performance of a 2-3 lobe combination of a twin-screw pump with different rotor profiles was investigated by use of a 3D CFD analysis [245].

The effective prediction of the real performances of screw pumps also requires the study of the effects induced by construction imperfections and operating conditions. The effects of manufacturing deviations on the pressure pulsation of three-screws pumps were studied in [253]. In fact, even though they are theoretically low-noise and pulsation-free, low viscosity fluids and low rotating speeds can induce dynamic instabilities of the idler screws [254]. The structural bending of the idler screws due to the pressure load, which needs to be overlaid to the rigid body displacement, was shown numerically and experimentally in [255].

It is known that zero-dimensional approaches (lumped parameter models) are lighter than CFD methods, in terms of computational cost and overall modeling complexity, but they require correlations that have a physical consistency. They have a great engineering interest, helping in understanding the processes and, when experimentally validated, they can be used as virtual platform to support design among different choices.

A complete parametrical analytical model of a triple-screw pump for an aerospace application has been developed in [256], where the boundary-layer theory [257] was adapted for the prediction of the backflow and the viscous losses. The thermodynamic model of a twin-screw multiphase pump was developed and validated in [258], while a mathematical model of the end face profiles of a triple-screw pump was studied in [259], in which a new geometry for the screws, minimizing wear, was validated experimentally. The theoretical and the real flow rate of a three-screws pump was analyzed in [260], in which the trade-off between friction reduction and leakages was discussed. The same authors in [261] elaborated a method for the calculation of pressure loads acting on the rotors, and in [262] simulated the loads, validating the results experimentally.

Among the studies which treat the modeling in a lumped parameter form, a need for a modeling updating is requested for a series of new applications of screw pumps never considered before. The cooling sector of ICEs opens potentially a new massive interest, for which a more refined lumped parameter model is suggested. The prediction of the volumetric efficiency of the pump, for instance, must be reassessed considering different contributions (clearances between idler/driver screws and stator, and between idler and driver through the so-called blow-how line), described in a more engineering way through models which could be experimentally identified. This also applies to the treatment of the dry contacts that happens between driver and idler screws, stressing the viscous flow losses model. In addition, the

manufacturing of this class of pumps, which could be considered interesting for engine cooling applications, is more oriented to simplicity and low cost than to the adoption of solutions that certainly would improve their performances. An example could be the manufacture of three-screws pumps with only one bearing on the driver fixing in some way its axis, and the absence of bearings on the other two idler screws, whose axis is thus not constrained. This opens to the occurrence of dry contacts, whose presence should be modeled. It is also true that most part of these aspects could be neglected when oil or viscous fluids are considered, as it happens for existing applications.

In this study, a novel zero-dimensional mathematical model has been formulated to predict the performances of triple-screw pumps, in terms of volumetric, indicated and mechanical efficiency (Section 4.2). A wide experimental activity has been realized, confirming the validity of the model, and the need to identify some phenomena on the base of models having a wide engineering use (Section 4.3). In fact, the pump considered for the development of the model has a manufacture oriented to simplicity and low cost, which is the right environment for engine cooling applications. Particularly, the driver screw is aligned with only one bearing, and the other two idler screws are simply entrained inside a cylindrical cavity, without any sustaining support. The developed model catches this intrinsic simplicity, offering a prediction of the volumetric and mechanical efficiencies satisfactorily, in spite of the intrinsic uncertainties related to the real, partly unknown, behavior.

Subsequently, the mathematical model has been used to optimize the design of screw pumps when used in the engine cooling system of a vehicle (Chapter 5).

Firstly, thanks to the model, the performances of a screw pump operating in an automotive engine over a homologation driving cycle have been evaluated. The comparison with the performances of the standard centrifugal pump confirms the expectations to obtain a net benefit in terms of pump efficiency when moving from a dynamic-type to a volumetric-type pump.

This has opened the way to the development of a model-based design approach of screw-type pumps for engine cooling applications, which allowed to identify the best geometric features of the screws capable to maximize the pump efficiency. Hence, an optimized pump concept has been proposed and prototyped, and its performances compared experimentally with those of an equally optimized centrifugal counterpart. Once again, the results verify the actual benefit introduced by screw-type volumetric pumps in terms of mechanical energy saved to cool the engine, which translates into significant values of fuel and CO_2 emissions savings.

Subsequently, the mathematical model has been refined in order to suitably represent also the performances of screw pumps with advanced screws' axes supports, as those introduced by the specific prototype to reduce friction and improve durability (Chapter 6). This allowed to extend the validity of the model also to un-conventional construction solutions. Moreover, it enabled a comprehensive theoretical analysis on the performance of this type of pumps when operating beyond the operating points commonly experienced in an engine cooling application.

This allowed to better understand the main physical phenomena influencing each component of the pump efficiency.

Finally, an extensive experimental campaign to measure the indicated cycle of the prototyped screw pump has been realized (Chapter 7). In this way, the complex physical phenomena defining the fluid pressure inside the machine during the pumping process have been investigated. The results allowed to understand the relation between the pump operating point and the indicated cycle, as well as to verify the model accuracy in predicting the indicated power absorbed by the pump.

4.2 Mathematical modeling

Triple-screw pumps, or three-screw pumps, are rotary positive displacement pumps, in which three rotating screws move the fluid along their axial direction. The fluid stands inside chambers defined by the screws' profiles and the stator. The three screws rotate at the same angular velocity. The central screw (driver) gives the motion to the others (idlers) which rotate oppositely. As displacement pumps, they do not increase pressure during displacement, but simply move fluid from the inflow to the outflow plenums, leaving the pressurization when the chambers are opened toward the exhaust end and the hydraulic circuit. Triple-screw pumps can be classified according to a pump series, which is a set of four numbers: three of them represent the proportions between the Driver Screw Outer Diameter (D_1), the Idler Screw Outer Diameter (D_2) and the Tooth Height (t), and the last one is the Number of Stages (n_{STAGE}). Once defined the pump series, a scale factor f modifies in absolute way the real dimensions (further geometrical details are summarized in Appendix A).

In more advanced solutions, screws are sustained by bearings according to different arrangements (one or two for each screws). In most simple solutions, a single bearing fixes the axis of the driver, being the other two screws simply entrained without any specific device that fixes their axis other than a simple cylindrical cradle for supporting the shaft. This certainly makes more complex the modeling of the pump, considering that shaft misalignments are possible, and they make more severe friction modeling and the occurrence of mechanical interferences.

The present mathematical model refers to these simple solutions and would offer a way for a model-based design. Therefore, volumetric (Section 4.2.1), indicated (Section 4.2.2), and mechanical (Section 4.2.3) efficiencies have been theoretically represented considering the specificity of these simple manufactured pumps. This allowed to obtain a comprehensive mathematical model capable to predict the performances of this type of pumps, starting from a specified set of input parameters.

4.2.1 Volumetric sub-model

The volumetric efficiency calculation requires both the ideal and the actual flow rate modeling. The ideal flow rate Q (Eq. 4-1) is expressed by the product between the cross sectional flow area A_{PUMP} (Eq. 4-2), the screw pitch length L, and the revolution speed N.

$$Q = A_{PUMP}\, L\, N \qquad \text{Eq. 4-1}$$

$$A_{PUMP} = A_{CASE} - (A_{DRIVER} + n_{IDLER}\, A_{IDLER}) \qquad \text{Eq. 4-2}$$

The flow area A_{PUMP} depends on the geometrical modeling, which considers the cross-sectional area of the pump casing and of the driver and idler screws. Their expressions have been reported from Eq. A. 5 to Eq. A. 7 in Appendix A. The product between A_{PUMP} and L is also the pump displacement V.

The real flow rate (Eq. 4-3) delivered by the pump has been calculated by considering the backflow S_{TOT} due to internal leakages produced by the opposing pressure gradient during flow motion.

$$Q_{REAL} = Q - S_{TOT} \qquad \text{Eq. 4-3}$$

From a physical point of view, the overall backflow S_{TOT} depends on three terms (Figure 4-1), i.e. the backflow across:

- the clearance between the driver-screw's tooth tips and the pump casing (S_{DRIVER});
- the clearance between the idler-screws' tooth tips and the pump casing (S_{IDLER});
- the contact regions between the driver screw and the idler screws, where the motion is transferred. In fact, the fluid escapes through a blow-hole line following the pressure gradient, which is opposite to the fluid motion inside the pump ($S_{DR/IDL}$).

Thus, the overall backflow (Eq. 4-4) can be calculated by adding these three contributions:

$$S_{TOT} = S_{DRIVER} + S_{IDLER} + S_{DR/IDL} \qquad \text{Eq. 4-4}$$

Figure 4-1 shows a typical axial cross section of a triple-screw pump. The driving screw is sustained by only one bearing. The two idlers are entrained by the screw profile of the driver, which matches with the ones on the idlers. These idlers are not sustained by any bearing, being simply supported in two cylindrical cavities on the stator. Their axes are free to reorient according to that of the driver.

The fluid from the inlet pipe fills a chamber dissipating its kinetic energy, and it is entrained by volumes which are realized by the rotation of the screws. The geometry of the screws realizes only one closed chamber during rotation, except for leakages: so, leakage flow proceeds from the discharge plenum to the closed volume, and from it to the inlet plenum. A kind of labyrinth flow is realized: when the fluid passes through the clearance, a nozzle flow is dominant with a negligible loss. Proceeding with it, when the fluid moves from the clearance passage to the volume defined by the two screws, kinetic energy is lost (sudden enlargement) and static

pressure is kept constant. This two-stages flow is repeated from the volume between screws and the inlet plenum. In Figure 4-1 the three contributions to leakages are highlighted.

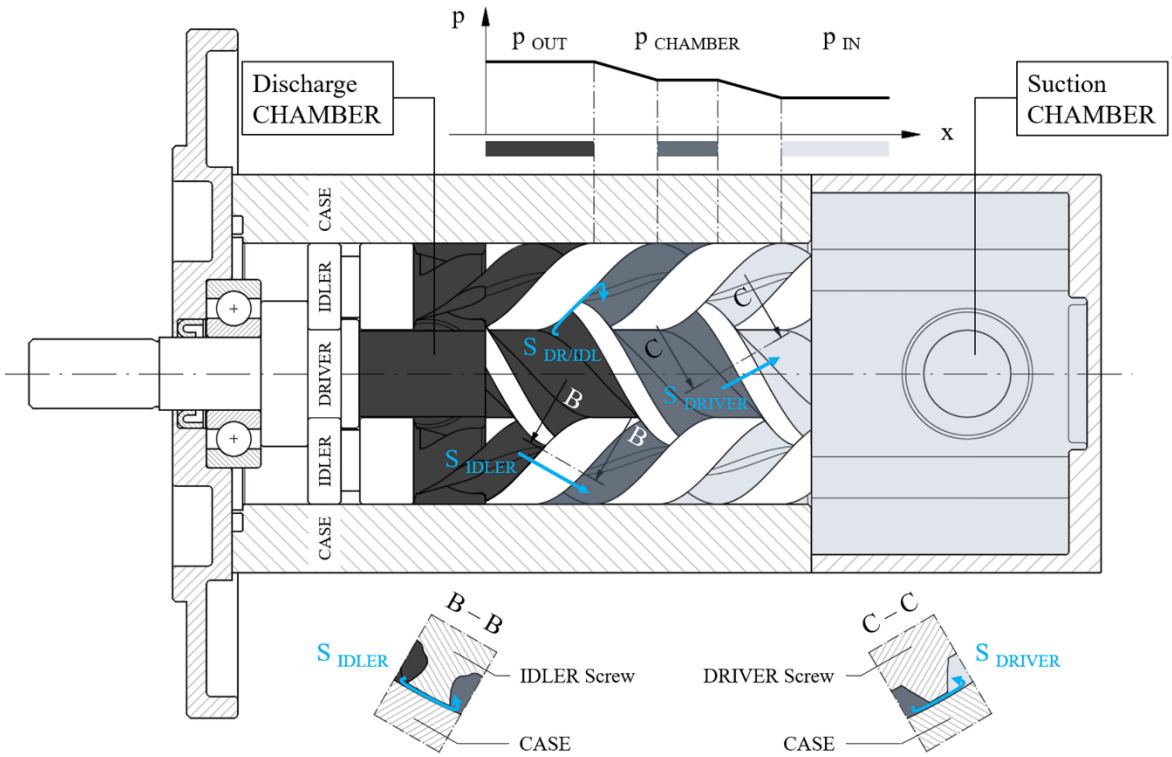

Figure 4-1. Main leakage paths for the backflow inside the triple-screw pump. The B-B section shows the backflow S_{IDLER} which happens across the idler-screw tooth tips and the pump casing, while the C-C section shows the backflow S_{DRIVER}, across the driver-screw tooth tips and the pump casing. The pressure profile of leakages reports the value inside the discharge (p_{OUT}) and intake (p_{IN}) volumes, and inside the unique closed chamber ($p_{CHAMBER}$) produced by the screws.

The theoretical evaluation of the backflow contributions is complex and, partly, unknown. Clearances around rotating parts and casings, as well as among rotating parts, involve many aspects for which simplifications are strongly required if a lumped parameter model of these leakages is adopted. In this analysis, S_{DRIVER} and S_{IDLER} have been treated using a simple approach represented by a suitably redefined Poiseuille-Couette modeling [257].

The Poiseuille-Couette model solves the Navier-Stokes equations representing the fluid flow that happens in a thin space, defined between a fixed and a sliding surface, due to a pressure gradient. A simplified perpendicular section of the leakage path has been considered (Figure 4-2), in which the pump casing and the tooth tip have been represented by a fixed and a sliding surface, respectively.

The curvature of both the tooth tips and the pump case has been approximated by a flat surface with a length equal to $\Delta\bar{x}$, in order to simplify the resolution of the equations. The symbol δ identifies the clearance between fixed and sliding surfaces. The clearance separates the i-th and the (i+1)-th chambers, which have different pressures, assuming $p_{(i+1)}>p_i$.

Rotating chambers force the fluid from inlet to outlet, transferring it without increasing pressure and leaving the pressurization to the discharge chamber. Instead, leakage moves from the (i+1)-th cell to the i-th cell, according to the pressure gradient. The cross-sectional area through which fluid moves is generated by multiplying the clearance between fixed and sliding surfaces (δ) and the perimeter of the pump case, whose development depends on driver and idler radii. The versus of $\vec{v}$ is opposite to that of the leakage flow, which moves in accordance with the pressure gradient inside adjacent chambers.

Moreover, the boundary condition considered in the calculation is that of no-slip wall, which assumes that the fluid velocity is equal to that of the solid boundary. In this way, the fluid in contact with the fixed surface has no speed, while the fluid in contact with the sliding surface moves with a velocity equal to $\vec{v}$. From a qualitative point of view, the fluid velocity field has been reported in Figure 4-2. The magnitude of the vector $\vec{v}$ depends on the screw radius, as it is a circumferential velocity.

The definition of the length $\Delta\bar{x}$ and the clearance tip δ requires a suitable approach. The length $\Delta\bar{x}$ corresponds to the minimum distance that the fluid can tread, which follows the geometry of the helix, and it depends on the screw angle σ. Since the geometries of the idler and the driver screws are different, Appendix A presents the mathematical expression of both $\Delta\bar{x}_s$.

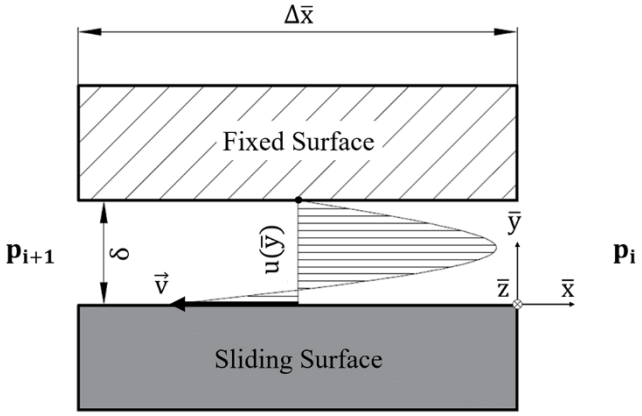

Figure 4-2. Perpendicular simplified cross section of the leakage path between tooth tips and pump case.

The clearance between the driver screw and the pump case, δ_{DRIVER}, does not have the same value of the clearance between the idler screw and the pump case, δ_{IDLER}. Considering that both leakages are treated with the same equivalent model, an equivalent clearance δ (Eq. 4-5) has been defined as a linear combination of the driver and the idler clearances, weighted considering two dimensionless parameters $f_1 = p_{DRIVER}/p$ and $f_2 = p_{IDLER}/p$ (being n_{IDLER}, p_{DRIVER}, p_{IDLER} and p defined as in Appendix A).

$$\delta = f_1\,\delta_{DRIVER} + n_{IDLER}\,f_2\,\delta_{IDLER} \qquad \text{Eq. 4-5}$$

Pressure along the screws' axis increases from the suction to the discharge section of the pump, and it can be assumed to be step varying, as the i-th chamber establishes a mean pressure between that of the (i-1)-th and the (i+1)-th. In screw pumps, this pressure increase is very limited, because the volume variation during chamber motion in the axial direction is very small. The pressure inside the chambers (only one chamber in the case under study) is the result of fluid motion from inlet to outlet chambers, and of the backflow that proceeds in the opposite versus.

As already observed, according to the labyrinth seals theory [263], when fluid leakage approaches the clearance, moving from the chamber at higher pressure, the conservation equation applies. Then, when it enters the chamber at lower pressure, the kinetic energy is completely lost due to a sudden enlargement produced inside the chamber. Moreover, the pressure drop due to the indicated losses (Section 4.2.2) must be considered. Therefore, being $n_{CHAMBERS}$ the number of sealed chambers and $\Delta p_{ind} = p_{OUT} - p_{IN}$, the i-th chamber-to-chamber pressure drop can be calculated as follow:

$$\Delta p_i = \frac{\Delta p_{ind}}{n_{CHAMBERS} + 1} \qquad \text{Eq. 4-6}$$

Since, in the specific case, only one sealed chamber exists between suction and discharge plenums, three pressure levels have been considered: p_{IN}, $p_{CHAMBER}$ and p_{OUT} (Figure 4-1). Thus, the chamber-to-chamber pressure drop Δp is equal to half the global outlet-inlet pressure drop Δp_{ind}. A cross section of the fluid passages inside the clearances of idler-casing and driver-casing has been sketched in Figure 4-3.

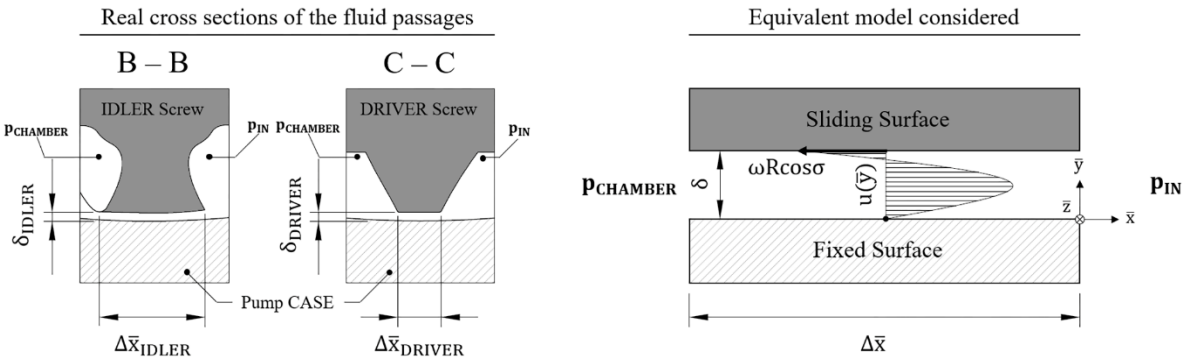

Figure 4-3. Idler and driver screw backflow contributions (see the position of the B-B and C-C cross sections in Figure 4-1).

Leakages are assumed happening under the hypotheses of the Poiseuille-Couette flow:

- $\Delta\bar{x}$ is at least ten times the clearance height δ;
- the fluid motion is 1D and, for each position along the flow, it is uniform on $\bar{z}$;
- the flow inside the clearance is laminar;
- the flow profile is uniform along the length $\Delta\bar{x}$ and it does not vary with time (steady flow).

Thus, the momentum equation can be simplified as in Eq. 4-7.

$$\frac{1}{\mu}\frac{\partial p}{\partial \bar{x}} = \frac{\partial^2 u}{\partial \bar{y}^2} \qquad \text{Eq. 4-7}$$

The equation can be analytically solved by applying the boundary conditions of no slip wall, i.e. $u(0) = 0$ and $u(\delta) = |\vec{v}|$. The $|\vec{v}|$ value depends on the radius of the sliding surface: for a general radius *R* at tip screw, the magnitude of the velocity is $|\vec{v}| = -\omega R cos\sigma$ (see Figure 4-3). According to the mentioned boundary conditions, the general solution of the differential equation Eq. 4-7 is:

$$u(\bar{y}) = \frac{1}{\mu}\frac{\partial p}{\partial \bar{x}}\frac{\bar{y}^2}{2} + \left(-\frac{\omega R}{\delta}cos(\sigma) - \frac{1}{\mu}\frac{\partial p}{\partial \bar{x}}\frac{\delta}{2}\right)\bar{y} \qquad \text{Eq. 4-8}$$

By varying $\bar{y}$ from 0 to δ, the integration of Eq. 4-8 has the following result:

$$s = \frac{1}{\mu}\frac{\Delta p}{\Delta \bar{x}}\frac{\delta^3}{12} + \frac{\omega R \delta}{2}cos(\sigma) \qquad \text{Eq. 4-9}$$

In Eq. 4-9, the parameter *s* represents the fluid leakage per unit length of the pump case perimeter *p* (Eq. A. 13 in Appendix A), which is equal to $R_1(2\pi - 2n_{IDLER}\psi)$ and $n_{IDLER}R_2(2\pi - 2\xi)$ for the driver and the idler screws, respectively. R_1 and R_2 correspond to the radius of driver and idler screws, respectively. The length $\Delta\bar{x}$ has been related to ΔX_{DRIVER} (Eq. A. 16 in Appendix A) and ΔX_{IDLER} (Eq. A. 17 in Appendix A). The final expression of the leakage flow related to the clearances of driver and idlers is:

$$S_{DRIVER} + S_{IDLER} = n_{STARTS}\left\{\left[\frac{1}{12\mu}\frac{\Delta p\,\delta^3}{\Delta X_{DRIVER}} + \frac{\omega R_1 \delta}{2}cos(\sigma)\right]R_1(2\pi - 4\psi) + \left[\frac{1}{12\mu}\frac{\Delta p\,\delta^3}{\Delta X_{IDLER}} + \frac{\omega R_2 \delta}{2}cos(\sigma)\right]n_{IDLER}R_2(2\pi - 2\xi)\right\} \qquad \text{Eq. 4-10}$$

It is important to observe the occurrence of the term n_{STARTS}, which represents the number of starts of the screws.

The third contribution $S_{DR/IDL}$ would require a more complex approach. Therefore, its effects are not considered for now, assuming that the backflow through the blow-hole line ($S_{DR/IDL}$) is negligible compared to the backflow through the screws' teeth tips and the pump casing (S_{DRIVER}+S_{IDLER}). This hypothesis holds true as long as the flow area is sufficiently high, and it can be preliminarily accepted if the good results obtained in the experimental validation of this model are taken into account (see Section 4.3). Later in Chapter 6, this assumption will be removed, and a refined model capable to predict even this contribution will be presented.

Finally, the overall backflow can be expressed according to Eq. 4-11.

$$S_{TOT} = S_{DRIVER} + S_{IDLER} \qquad \text{Eq. 4-11}$$

Once the real flow rate (Eq. 4-3) is known, the volumetric efficiency can be calculated according to Eq. 4-12.

$$\eta_v = \frac{P_h}{P_t} \quad \text{Eq. 4-12}$$

Where P_h is the hydraulic power output (Eq. 4-13), and P_t is the theoretical power output (Eq. 4-14), calculated with the pressure drop Δp_{tot} existing between discharge and suction pipes.

$$P_h = Q_{REAL}\, \Delta p_{tot} \quad \text{Eq. 4-13}$$

$$P_t = Q\, \Delta p_{tot} \quad \text{Eq. 4-14}$$

4.2.2 Indicated sub-model

The ideal indicated cycle should be represented in the p-V plane by a rectangular sequence of transformations: two of them are isobaric ones (chamber filling and emptying) and the remaining two are isochoric.

However, the real cycle is much more complex. In fact, the filling of the suction chamber imposes a pressure loss, being the pressure inside the chamber lower than the one inside the inlet pipe. Similarly, the feeding of the external circuit during the emptying of the discharge chamber requires a pressure delivered from the chamber greater than the one on the circuit. Moreover, during the fluid motion inside the machine due to the screws' rotation, the chambers' geometrical volume does not match exactly the physical volume of the fluid inside the chamber, producing pressure spikes that must be kept under control.

As a result, the chambers formed by the intermeshing screws fill at a pressure below the one at the inlet port, and they get emptied at a pressure higher than that at the exhaust port. In addition, during the displacement from suction to discharge plenums of the fluid trapped into the chambers, pressure spikes are likely to occur, being inescapable some imperfections on screws and pump case geometries.

In this Chapter, a simplified approach for indicated cycle modeling has been preliminarily proposed, in order to quantify the associated power losses with good accuracy and, at the same time, through a lean mathematical modeling. Later in Chapter 7, this topic will be further investigated, giving a deeper insight on the indicated losses occurring inside the machine.

Hence, in this analysis the pressure losses have been calculated through a simple lumped parameter model, which evaluates them as kinetic energy lost. If the fluid speeds at pump inlet and outlet pipes are c_{IN} and c_{OUT} respectively, the following pressure losses have been considered at inlet (Eq. 4-15) and at outlet (Eq. 4-16):

$$\Delta p_{IN} = \rho\, c_{IN}^2/2 \quad \text{Eq. 4-15}$$

$$\Delta p_{OUT} = \rho\, c_{OUT}^2/2 \quad \text{Eq. 4-16}$$

In fact, the fluid entering the intake volume inside the machine loses its kinetic energy, while at the exhaust the fluid must gain a kinetic energy to fill the circuit. Therefore, the intake

pressure is lower than that of the ambient, while the exhaust pressure is higher than the circuit one. Thus, the indicated power results as in Eq. 4-17:

$$P_i = Q\ \Delta p_{ind} \quad \text{Eq. 4-17}$$

Where:

$$\Delta p_{ind} = \Delta p_{tot} + \Delta p_{OUT} + \Delta p_{IN} \quad \text{Eq. 4-18}$$

Note that Eq. 4-17 underestimates the real indicated power, having considered intake and exhaust phases represented by two isobaric transformations. Finally, the indicated efficiency can be expressed as in Eq. 4-19, where P_t is given by Eq. 4-14:

$$\eta_i = \frac{P_t}{P_i} \quad \text{Eq. 4-19}$$

4.2.3 Mechanical sub-model

The mechanical sub-model calculates the mechanical losses inside the pump. These power losses can be distinguished into two contributions, i.e. viscous and friction losses. The viscous losses occur inside the fluid and are correlated with its physical properties and flow conditions. Instead, the friction losses depend on the friction conditions realized in the mechanical couplings.

4.2.3.1 Viscous losses modeling

As for the volumetric sub-model, the viscous power losses are calculated with a lumped parameter model from the solution of the flow field given by the Poiseuille-Couette theory [257] inside the clearances between the screws' tips and the pump case.

The viscous power losses are calculated defining the shear stress acting within the fluid. This stress is evaluated on the screw rotating surface, represented by the cylindrical envelope of the screws' teeth tips. In fact, the dragging of the first cylindrical layer of the fluid in contact with the moving surfaces applies a resistance to the screws' rotation. Therefore, the contribution is terms of viscous power losses can be expressed as:

$$P_{FR\,VISC} = \omega\ R\ \tau\ A \quad \text{Eq. 4-20}$$

Where τ is the shear stress of the fluid in contact with the screw, A is the action area, R is the shear force radius and ω is the screw angular speed.

The flow model for the shear stress calculation is based on assumptions analogous to those assumed for the backflow model (Section 4.2.1). However, in this case, the flat channel is identified considering the wet perimeter of the channel flow, which can be observed through the transversal section of the screw pump (Figure A. 1 in Appendix A). Therefore, the flow model is analogous to the one in Figure 4-2, in which the velocity of the fluid in contact with

the screw is assumed equal to the screw's peripheral velocity $\vec{v} = \omega R$. Moreover, the $\bar{x}$ - axis has the same direction of $\vec{v}$, which is opposite to the backflow.

Thus, the flow field $u(\bar{y})$ (Eq. 4-21) can be easily found by applying the new boundary conditions to the general solution of the differential equation (Eq. 4-7):

$$u = \frac{1}{\mu}\frac{\Delta p}{\Delta \bar{x}}\frac{\bar{y}^2}{2} + \left(-\frac{\omega R}{\delta} - \frac{1}{\mu}\frac{\Delta p}{\Delta \bar{x}}\frac{\delta}{2}\right)\bar{y} + \omega R \qquad \text{Eq. 4-21}$$

The shear stress τ can be evaluated through its definition, where the velocity gradient along the $\bar{y}$ - direction is obtained through the $\bar{y}$ - derivation of the Couette flow velocity field (Eq. 4-21). Evaluating τ at the screw's external surface, i.e. in $\bar{y} = 0$, and considering its absolute value, it follows that:

$$|\tau(0)| = \frac{\mu\omega R}{\delta} + \frac{\Delta p}{\Delta \bar{x}} \cdot \frac{\delta}{2} \qquad \text{Eq. 4-22}$$

The shear stress τ and its insisting area A, as well as the shear force radius R, can be specified for the driver and the idler screw, respectively. Moreover, the screw angle σ is considered by multiplying for the number of screw principles n_{START}, for each screw pitch n_{STAGE}. Finally, the expression of $P_{FR\ VISC}$ (Eq. 4-23) can be obtained:

$$P_{FR\,VISC} = n_{STAGE}\, n_{START}\, \omega\, [R_1\, \tau_{DRIVER}\, A_{V\,DRIVER} + n_{IDLER} R_2 \tau_{IDLER} A_{V\,IDLER}] \qquad \text{Eq. 4-23}$$

Where the driver and the idler contributions to the shear stress (Eq. 4-24, Eq. 4-25), as well as the respective action areas (Eq. 4-26, Eq. 4-27), have the following expressions:

$$\tau_{DRIVER} = \frac{\mu\, \omega\, R_1}{\delta_{DRIVER}} + \frac{\Delta p}{\alpha\, R_1}\ \frac{\delta_{DRIVER}}{2} \qquad \text{Eq. 4-24}$$

$$\tau_{IDLER} = \frac{\mu\, \omega\, R_2}{\delta_{IDLER}} + \frac{\Delta p}{\beta\, R_2}\ \frac{\delta_{IDLER}}{2} \qquad \text{Eq. 4-25}$$

$$A_{V\,DRIVER} = R_1(2\pi - n_{IDLER}\, 2\, \psi)\, \Delta x_{DRIVER} \qquad \text{Eq. 4-26}$$

$$A_{V\,IDLER} = R_2\, (2\pi - \, 2\, \xi)\, \Delta x_{IDLER} \qquad \text{Eq. 4-27}$$

4.2.3.2 Friction losses modeling

The friction power losses depend on the friction conditions realized in the mechanical couplings (Figure 4-1). Three contributions can be distinguished, according to the specific mechanical sub-element in which they occur:

1. power losses due to the friction in the contact between driver and idler screws, and between them and the pump case;
2. power losses due to the friction in the disk coupling elements between the screws;

3. power losses due to the friction in the driver screw's sealing and bearing;

As already observed, the driver is sustained by only one bearing, behaving in cantilever mode. Moreover, the two idlers are simply positioned inside a cylindrical support and, during the entrainment, they are free to orient their axis differently from that of the driver. Hence, dry contacts are present, which must be carefully modeled. In the following, each of these friction contributions will be outlined.

1. Friction in the contact between driver and idler screws

The cinematic-dynamic study of the coupled screws moves from the identification of the contact surfaces between the screws and the stator, and between the screws themselves. As already observed, radially, the driver screw is supported by the spherical bearing and by the contact with the idler screws, which are supported by the stator itself and rotate inside a cylindrical support. Axially, the idler screws are linked with the driver screw through disk coupling elements. This mechanical assembly does not ensure a fixed position for the screws' rotational axes. Therefore, dry friction phenomena can occur in some contact surfaces between the driver and the idler screws, or between the screws and the stator. Furthermore, the radial profiles of both driver and idler screws do not provide pure rolling conditions between the teeth flanks for all the rotational angles. In fact, the screws have the same angular velocity, but their contact point is not equidistant from the driver and the idler axes. Consequently, slip friction conditions occur.

The bearing theory [264] is adapted at this case-study to calculate the forces exchanged between the screws, and so the mechanical power losses due to the slip friction conditions realized at the intermeshing screws' surfaces. Firstly, the forces are calculated considering only the transversal section. This assumption is equal to assume straight-cut tooth, i.e. screw angle σ equal to 0°. The free body diagram of the idler screw is shown in Figure 4-4 (a).

The idler screws are supported radially by the stator, through a fluid film whose thickness depends on the fluid flow conditions. The contact point *A* (Figure 4-4 (a)) between the screw and the stator is assumed to be in the y-axis. The driver and idler screws are in contact in the points *B* and *C* (Figure 4-4 (a) and (b)).

The pressure differential acting at the idler's tooth flank determines the force $F_{P\ IDLER}$ (Eq. 4-28). This force is considered parallel to the y-axis and applied at the center of the tooth flank (Figure 4-4 (a)), with a lever arm $b_{IDLER} = r_2 + t/2$. The pressure force $F_{P\ IDLER}$ depends on the pressure force F_P" (Eq. 4-29), which is obtained through simple geometrical considerations (Figure 4-4 (c)), assuming Δp as in Eq. 4-6.

$$F_{P\ IDLER} = F_P" \cos(\sigma)\ sen(\sigma) \quad \text{Eq. 4-28}$$

$$F_P" = \Delta p\ [\pi R_2^2 - A_{IDLER}] \quad \text{Eq. 4-29}$$

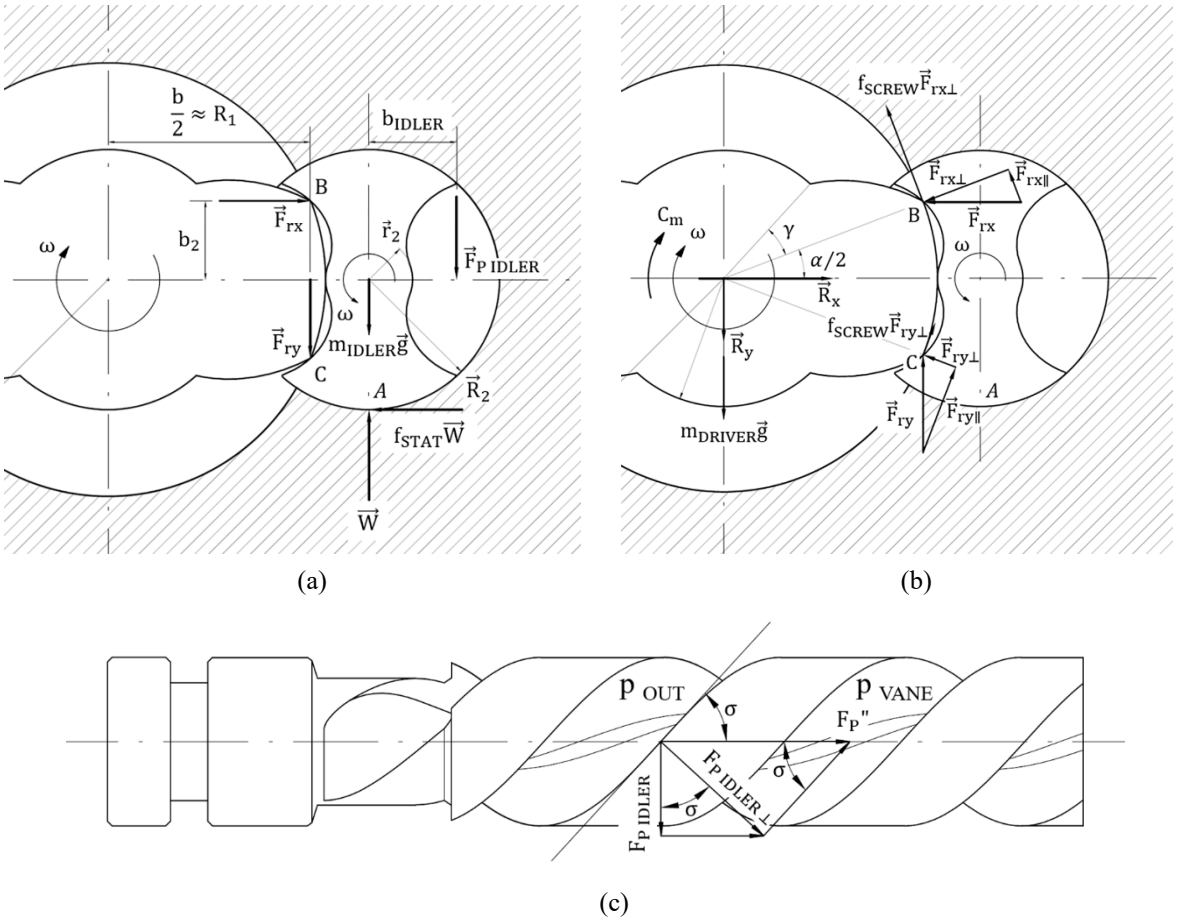

(a) (b)

(c)

Figure 4-4. Free body diagram of the right idler (a) and driver (b) screw, neglecting the effect of the axial screw angle σ. Geometrical considerations for determining the pressure forces F_P" and $F_{P\ IDLER}$ (c).

The reaction forces are applied in the contact points *A*, *B* and *C* (Figure 4-4 (a)). In point *A* there is the stator-to-idler reaction, constituted by the vertical component W and the horizontal component $f_{STAT} \cdot W$. Thus, this latter component depends on a friction coefficient f_{STAT}. In points *B* and *C*, the driver-to-idler reactions F_{rx} and F_{ry} are parallel to the x and the y axes, respectively. Moreover, their versus is chosen to balance the moment reactions (Figure 4-4 (a)). The solution of the dynamic balance of the idler screw yields the reactions F_{rx} (Eq. 4-30), F_{ry} (Eq. 4-31) and W (Eq. 4-32).

$$F_{rx} = f_{STAT}\, W \qquad \text{Eq. 4-30}$$

$$F_{ry} = W - F_{P\ IDLER} - m_{IDLER}\, g \qquad \text{Eq. 4-31}$$

$$W = \frac{F_{P\ IDLER}\,(r_2 + b_{IDLER}) + m_{IDLER}\, g\, r_2}{(r_2 - f_{STAT}\, R_2 - f_{STAT}\, b_2)} \qquad \text{Eq. 4-32}$$

Therefore, the torque due to the friction at the intermeshing screws can be obtained through the moment equilibrium related to the driver screw (Eq. 4-33, Figure 4-4 (b)):

$$C_{FR\ SCREW} = f_{SCREW}\ 2\ R_1 \left(F_{rx}\, cos\left(\frac{\alpha}{2}\right) + F_{ry}\, sen\left(\frac{\alpha}{2}\right)\right) \qquad \text{Eq. 4-33}$$

In fact, the idler-to-driver reactions F_{rx} and F_{ry} determine a radial component, $F_{rx\perp}$ and $F_{ry\perp}$ respectively. Then, the tangential components in the contact points B and C can be obtained by multiplying the radial components $F_{rx\perp}$ and $F_{ry\perp}$ for a friction coefficient f_{SCREW}. The tangential components generate the resistant friction torque $C_{FR\ SCREW}$ (Eq. 4-33).

The axial geometrical shape of the intermeshing screws needs to be considered to evaluate correctly the mechanical power losses determined by the friction torque. In fact, the meshing condition between the driver and the idler screws' teeth (Figure 4-4 (a) and (b)) is achieved axially for a certain number of times. Specifically, it is achieved two times for each screw stage (i.e. for each revolution of the screw's tooth), considering the pressure gradient along the screws' axes (Figure 4-1). Therefore, the friction power losses $P_{FR\ SCREW}$ can be calculated by multiplying the power losses associated to the friction torque, for the number of starts n_{START} and the number of stages n_{STAGE} (Eq. 4-34).

$$P_{FR\ SCREW} = n_{START}\ n_{STAGE}\ C_{FR\ SCREW\ RAD}\ \omega \qquad \text{Eq. 4-34}$$

Note that the friction coefficients f_{STAT} and f_{SCREW} depend on the local contact conditions. Their values have been experimentally identified, and they are discussed in detail in Section 4.3.

The described procedure considers straight-cut screw teeth. This assumption was necessary to simplify the free-body diagram of the screws, whose forces were considered only in the transversal section. However, the existence of a screw angle σ imposes that these forces have always an axial component. The idler screws are supported axially by the disk coupling elements. Therefore, in this analysis, these elements are assumed to be the main mechanical features supporting the axial components of the forces acting on the idler screws.

2. Friction in the disk coupling elements between the screws

The idler screws are supported axially by two disk coupling elements (Figure 4-1). These elements have also a sealing function. In fact, they separate the discharge chamber from an intermediate chamber, whose fluid is at the inlet pressure. This arrangement provides low power losses at the driver lip seal. Moreover, it helps to balance the axial forces acting on the idler screws. Here, the balancing effect of the axial forces acting on the idler screws is neglected, and a resulting force due to the pressure difference acting in the pump positive axial direction is assumed (Figure 4-1).

For these reasons, slip friction occurs at the contact surfaces between the disk elements. The power loss $P_{FR\ DISK}$ depends on the outlet-inlet pressure difference Δp_{ind} (Section 4.2.2), the contact area A_{CS} (Eq. A. 10), and the friction coefficient f_{DISK} (Eq. 4-35). The value assumed for this friction coefficient is discussed in detail in Section 4.3.

$$P_{FR\ DISK} = f_{DISK}\ (\Delta p_{ind}\ A_{CS})\ D_1\ \omega \qquad \text{Eq. 4-35}$$

3. Friction in the driver screw's sealing and bearing

In this work, only the driver screw's shaft is connected outside the pump case for the mechanical coupling with the electric motor (Figure 4-1), making necessary the use of a radial lip seal to prevent the leakage of fluid out of the pump.

Generally, the power absorption of radial lip-seals depends on several parameters. Among others, the type of lubricant and the scale of contamination play a fundamental role [265]. This specific application uses a 50% glycol-water-mixture instead of oil or grease, which increases the power absorbed by the driver lip-seal.

Moreover, the mechanical power absorbed by the pump depends also on the power losses inside the spherical bearing of the driver shaft, as well as on the friction phenomena in the driver-stator contact surfaces. In this discussion, all these contributions have been taken into account through the auxiliary power loss $P_{FR\,AUX}$ (Eq. 4-36), which is a quadratic expression of the pump speed ω (expressed in rpm).

$$P_{FR\,AUX} = a\,\omega^2 + b\,\omega + c \qquad \text{Eq. 4-36}$$

The fitting coefficients *a*, *b* and *c* depend on the specific pump layout. Therefore, they have been identified through an experimental calibration, which will be described in Section 4.3.

4.2.4 Performance analysis

Having defined all the contributions to friction losses, the total amount of friction power losses is known and equal to the sum of them (Eq. 4-37), i.e. of the viscous losses (Eq. 4-23), the power losses due to the friction in the contact between driver and idler screws (Eq. 4-34), the power losses in the disk coupling elements (Eq. 4-35), and the power losses in the sealing and bearing of the driver screw (Eq. 4-36).

$$P_{FR} = P_{FR\,DISK} + P_{FR\,AUX} + P_{FR\,SCREW} + P_{FR\,VISC} \qquad \text{Eq. 4-37}$$

Thus, the mechanical power absorbed by the pump P_m (Eq. 4-38) can be obtained by summing together these friction power losses (Eq. 4-37) with the indicated power (Eq. 4-17).

$$P_m = P_i + P_{FR} \qquad \text{Eq. 4-38}$$

This allows to calculate also the mechanical efficiency, expressed as in Eq. 4-39.

$$\eta_m = \frac{P_i}{P_m} \qquad \text{Eq. 4-39}$$

Finally, the global efficiency of the screw pump (Eq. 4-40) can be expressed as the ratio between the hydraulic power (Eq. 4-13) and the absorbed mechanical power (Eq. 4-38). This efficiency includes three contributions, which quantify the volumetric, the indicated and the mechanical efficiencies, respectively (Eq. 4-12, Eq. 4-19, Eq. 4-39).

$$\eta_g = \eta_v \, \eta_i \, \eta_m = \frac{P_h}{P_m} \qquad \text{Eq. 4-40}$$

4.2.5 Model parametrization

Once the volumetric, indicated and mechanical sub-models have been defined, the three blocks can be linked together to define how to calculate specific output parameters starting from a defined set of input constraints.

To this end, the block diagram of the mathematical model of the triple-screw pump with the construction layout shown in Figure 4-1 has been realized and reported in Figure 4-5. This diagram shows the connections between the main parameters calculated by the model, distinguishing between volumetric, indicated and mechanical sub-models.

The overall pressure difference Δp_{tot} and the speed rotation ω of the pump are the operating input parameters. Together with the geometrical and the physical parameters, they enable the calculation of the performance parameters of the screw pump. Among them, the actual flow rate Q_{REAL} and the absorbed mechanical power P_m are the main output parameters, which will be considered also in the validation process of the model.

In Figure 4-5, the input parameters, as well as the main output parameters, are displayed inside highlighted boxes. Starting from the inputs, the model calculates the theoretical flow rate Q and the indicated pressure difference Δp_{ind}. Thus, the overall backflow S_{TOT} and the real flow rate Q_{REAL}, as well as the indicated power P_i, are evaluated.

Subsequently, the four contributions of the friction power losses P_{FR} are calculated. Starting from the evaluation of the pressure forces acting on the idler screws (F_P" and $F_{P\ IDLER}$), and of the contact force between idler screw and pump case (W), the forces exchanged between idler and driver screws (F_{rx} and F_{ry}) are calculated. Therefore, the friction torque acting on the driver screw $C_{FR\ SCREW}$ is calculated, leading to the evaluation of the friction power loss between driver and idler screws $P_{FR\ SCREW}$.

Moreover, the balance of forces acting on the disk coupling elements between the screws allows to calculate the friction power loss $P_{FR\ DISK}$, while the power absorbed by the driver's sealing and bearing is calculated by $P_{FR\ AUX}$ through experimental fitting coefficients. Finally, the viscous power loss $P_{FR\ VISC}$ is calculated through the evaluation of the shear stress acting on the fluid in contact with the sliding surfaces of the screws' tooth tips, using the redefined Poiseuille-Couette model developed for the backflow calculation.

By summing together the four friction power losses ($P_{FR\ SCREW}$, $P_{FR\ DISK}$, $P_{FR\ AUX}$ and $P_{FR\ VISC}$), the friction power loss P_{FR} is calculated. Thus, the mechanical power P_m is finally evaluated by summing together the indicated power P_i and the friction power loss P_{FR}.

The model requires the definition of the screws' friction coefficients f_{STAT}, f_{SCREW} and f_{DISK} to calculate the mechanical power absorbed by the pump (Section 4.2.3). These coefficients define the friction conditions occurring in the contact surfaces between the screws themselves (f_{SCREW} and f_{DISK}) and between the idler screws and the pump case (f_{STAT}), thus determining the

friction power losses inside the pump. The simplified construction layout considered for the development of the mathematical model has the idler screws simply entrained inside cylindrical supports, without any bearing fixing their axis. This mechanical coupling does not prevent from any dry friction phenomena between the idler screws and the pump case, whose occurrence may generally vary with the pump operating point. In fact, a kind of hydrodynamic support of the idler screws is realized by the backflow interposed between them and the casing, which is very unlikely to be unsensitive to variations of pump speed and head.

These complex phenomena have been modeled through two approaches. Firstly, a simplified method has been followed, which considers constant friction coefficients, thus neglecting the effects of the pump operating point (Section 4.3.2). Subsequently, an advanced friction modeling between idlers and casing has been proposed, in order to catch the influence of the pump operating point on the friction conditions realized inside the pump (Section 4.3.3). In any cases, the friction coefficients have been identified by tuning the output performance parameters of the model to the corresponding experimental values, while verifying the validity of the obtained coefficients. This experimental calibration constituted a relevant part of the model validation. Therefore, it will be detailed in the next Section 4.3.

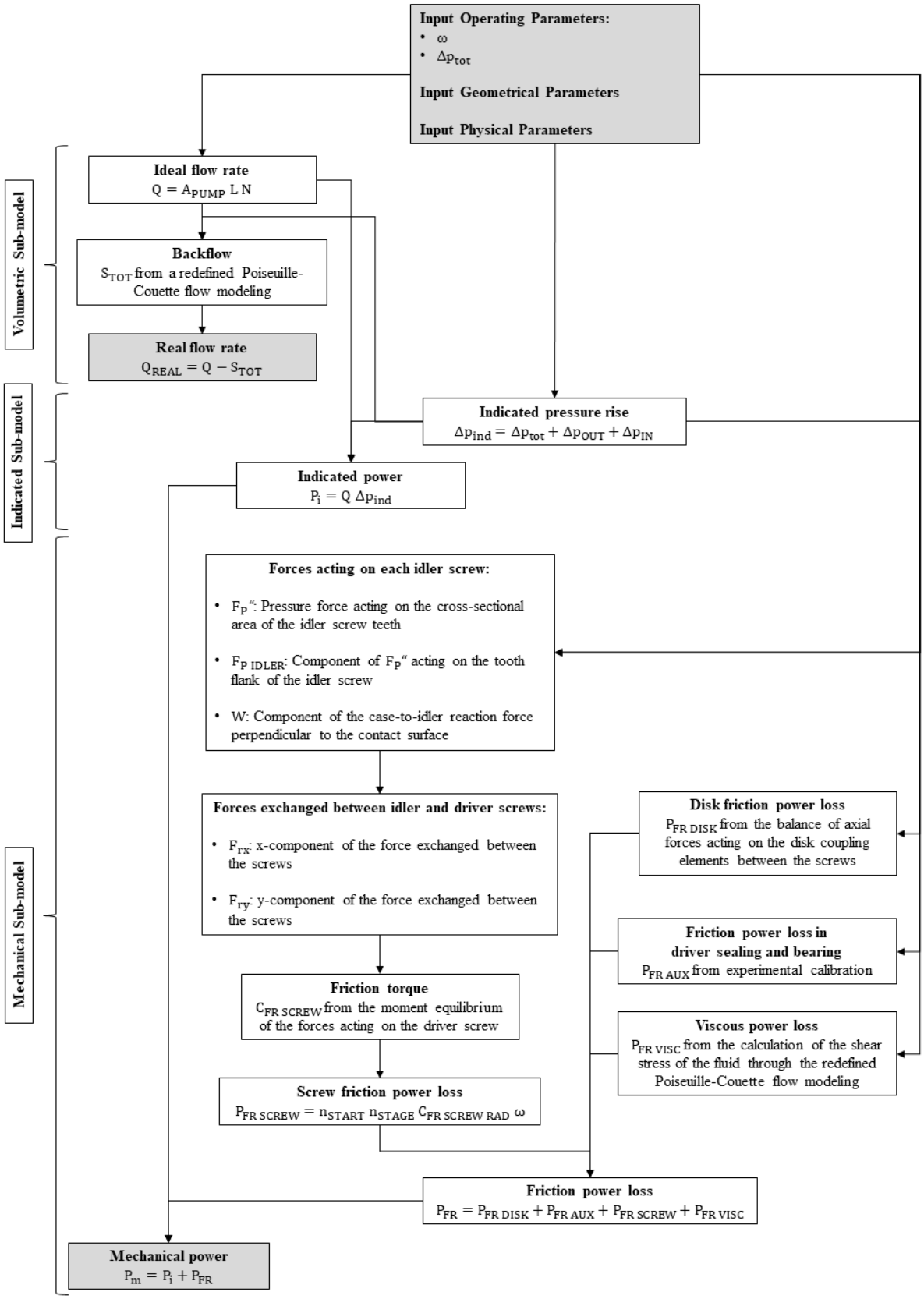

Figure 4-5. Block diagram of the mathematical model of the triple-screw pump. Starting from the input parameters, the calculated parameters are summarized and linked together, leading to the main output parameters, i.e. the real flow rate Q_{REAL} and the absorbed mechanical power P_m. Input and output parameters are reported inside highlighted boxes.

4.3 Experimental validation

4.3.1 Experimental setup

The performances of the triple-screw pump have been evaluated on an experimental test bench properly designed to acquire dynamic working points [226]. It is schematically represented in Figure 4-6, and a real image is reported in Figure 4-7.

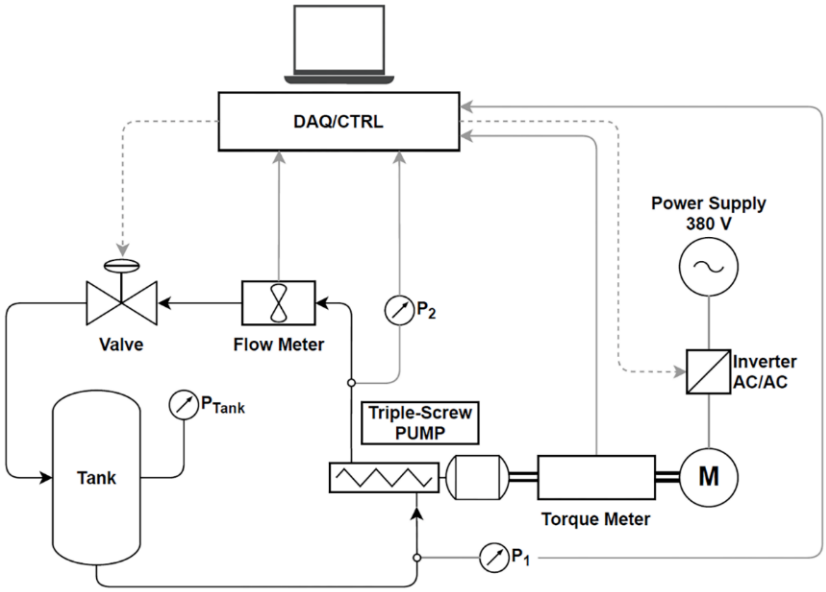

Figure 4-6. Schematic of the dynamic test bench for pumps.

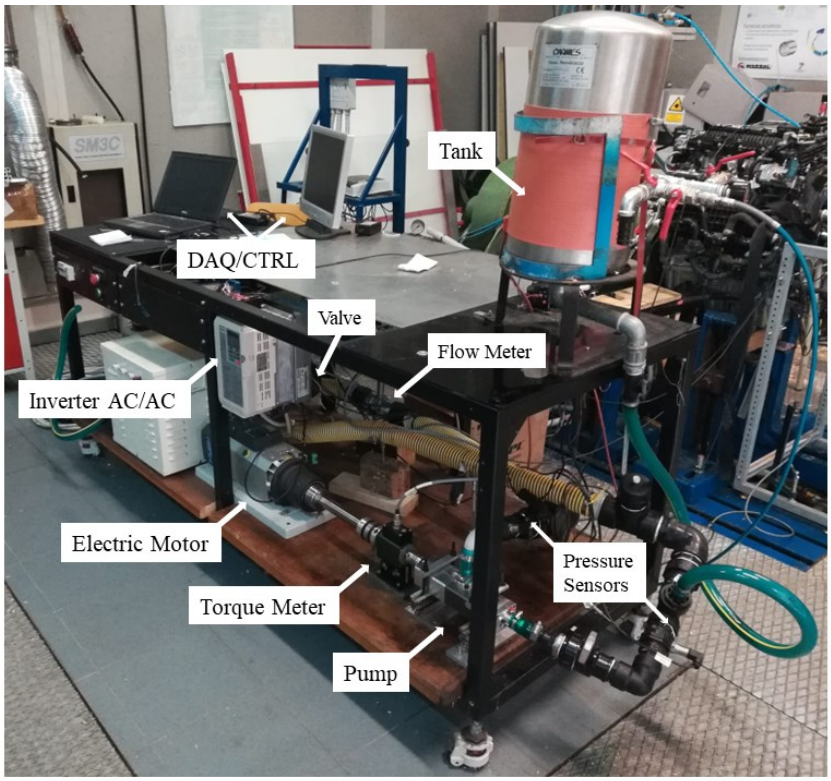

Figure 4-7. Image of the experimental test bench.

This test bench for hydraulic pumps is able to drive the pump with constant speed as input variable, as well as with a speed profile, including the WLTC class 3 homologation cycle. The resistance of the circuit can be regulated through a proportional pneumatic valve, which can be actuated in order to reproduce the hydraulic permeability imposed by the thermostat valve lift in an engine cooling circuit. Moreover, the circuit is equipped with a 24 liters tank pressurized through compressed air, which allows to adjust the hydraulic head acting on the pump to avoid cavitation phenomena during pump operation.

The measurement and acquisition system includes a magnetic flow meter, which measures the instantaneous flow rate delivered by the pump, and diaphragm pressure sensors installed before and after the pump to derive the pressure rise. In this way, the hydraulic power can be calculated. The test bench layout allows to evaluate also the actual mechanical power absorbed by the pump. In fact, the pump is driven by a three-phase electric motor controlled by an inverter, and linked to it through a torque meter. This latter measures torque and rotational speed, allowing to calculate the absorbed mechanical power, and thus the global efficiency of the pump.

Finally, a data acquisition and control unit (DAQ) manages input and output signals with an adjustable acquisition rate, which was set at 1 Hz for the purposes of this preliminary experimental characterization. In Chapter 7, an enhanced measurement and acquisition system will be presented, specifically developed to measure the indicated cycle of the triple-screw pump proposed in Section 5.3. Table 4-1 summarizes the uncertainties of the measuring instruments and of the main derived quantities.

Quantity	Instrumentation	Uncertainty
Torque	Burster torque meter	0.015 Nm
Revolution speed	Burster torque meter	0.01 %
Coolant flow rate	Riel turbine flow meter	0.15 %
Pressure	Piezo	0.003 bar
Derived quantities		
Hydraulic power		< 1.5 %
Mechanical power		< 7%

Table 4-1. Measurement uncertainties.

4.3.2 Preliminary friction modeling and experimental validation

As mentioned in Section 4.2 and detailed in Appendix A, the geometry of triple-screw pumps is defined by a specific set of geometrical parameters. The dimensions of driver and idler screws are defined by the pump series (D_1-D_2-t proportions, and number of stages n_{STAGE}) and the proportionality factor *f*. The real dimensions of D_1, D_2 and t are obtained by multiplying each number of the pump series for the scale factor *f*. The axial cross section of the screws is defined by the screw angles α, β and γ, and by the ratio A_γ/R_2^2. The angles α and β define the

angular extension of the teeth of driver and idler screws, respectively. They are calculated from their ratio β/α, and from the angle γ. The angle γ defines the angular extension of the epicycloid profile, which links inner and outer diameters of each screw. It is calculated imposing the maximum meshing angle condition, once the outer diameters of the screws (D_1 and D_2) and the tooth height (t) are known (see Appendix A).

The axial length of the screws is defined by the winding angle of the screws' teeth σ, and the number of stages n_{STAGE}. This latter parameter defines the number of axial repetition of a stage, that is a complete axial revolution of the screws' teeth. Further parameters defining the screw pump layout are the number of starts n_{STARTS}, which defines the number of teeth of each screw, and the number of idler screws n_{IDLER}, equal to two in this analysis. Finally, the clearances between the screws and the pump case are defined by δ_{DRIVER} and δ_{IDLER}, for driver and idler screws respectively.

To validate the mathematical model presented in Section 4.2, a standard triple-screw pump of the 5-3-1 series has been considered. This pump has a proportionality factor f equal to 8 and a number of stages equal to 1.31, which determine external diameters of driver and idler screws equal to 40 mm and 24 mm, respectively. Moreover, the screws are 90 mm long, determining a displacement equal to 48 cm^3.

Steel is assumed for the material of the idler screws, with a density equal to 7860 kg/m^3, and a 50% glycol-water-mixture is used as working fluid, with a dynamic viscosity equal to $8.86 \cdot 10^{-4}$ Pa·s. This selection was made in order to develop and validate the mathematical model of a triple-screw pump operating in conditions as close as possible to real on board applications, which typically use this mixture instead of pure water to prevent freezing and rusting issues. Figure 4-8 shows an image of this pump, with driver and idler screws disassembled from the pump case.

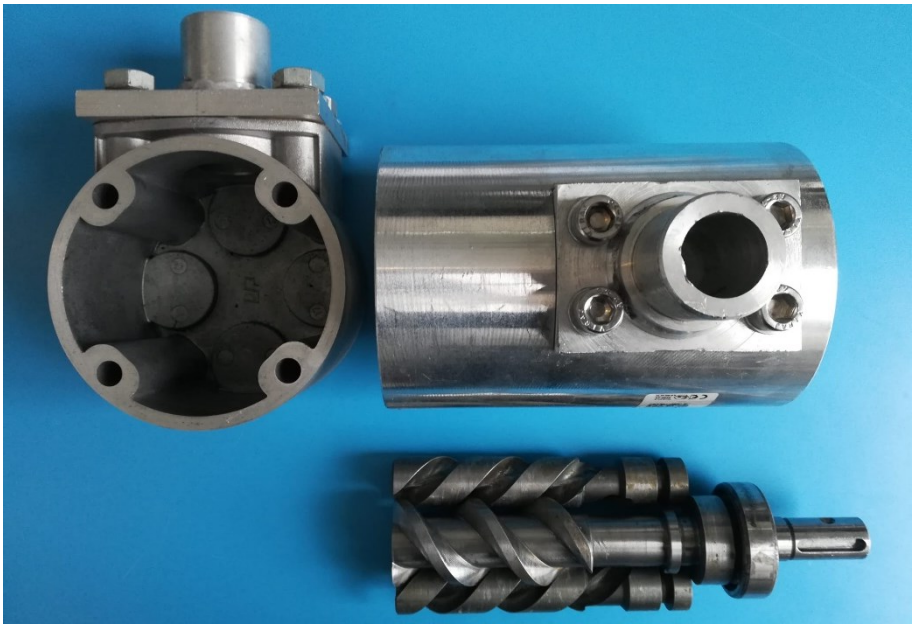

Figure 4-8. Standard triple-screw pump considered for the model validation, disassembled to show driver and idler screws.

As mentioned in Section 4.2.5, the model requires the definition of the screws' friction coefficients f_{STAT}, f_{SCREW} and f_{DISK} to calculate the mechanical power absorbed by the pump. The friction coefficients are involved in the interaction between the screws themselves (f_{SCREW} and f_{DISK}), and between the screws and the pump case (f_{STAT}). Their value is strictly correlated to the friction conditions realized in the respective contact surfaces, which generally vary with the pump operating point (speed and pressure rise). Hence, an experimental calibration is necessary to suitably catch the specificity of the friction conditions realized in the contact areas between the main components of the pump.

In this preliminary analysis, the effect of the pump operating point on the friction coefficients has been neglected, and they have been assumed to be constant during pump operation. Therefore, their values have been tuned in order to match the mechanical power actually absorbed by the pump. To this end, the standard triple-screw pump was tested through the experimental test bench reported in Section 4.3.1 over a wide operating range, measuring torque and speed in order to calculate the mechanical power effectively absorbed by the pump. Figure 4-9 shows the pump mounted on the test bench for its experimental characterization.

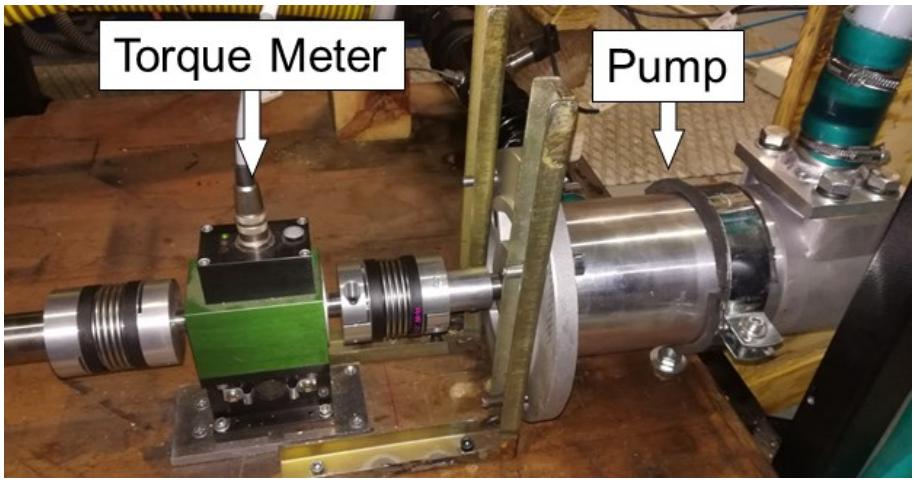

Figure 4-9. Picture of the standard triple-screw pump tested to validate the model.

Then, the friction coefficients f_{STAT}, f_{SCREW} and f_{DISK} have been varied in the range between 0.1 and 0.2, in order to minimize the mean error between measured and predicted mechanical power. This range has been chosen according to typical values known for steel-steel lubricated sliding friction coefficients [264].

The resulting coefficients are 0.16, 0.1 and 0.1 for f_{STAT}, f_{SCREW} and f_{DISK}, respectively. These values can be considered reliable if the specific pump layout is taken into account. In fact, the idler screws are simply entrained within cylindrical supports, without any specific device that fixes their axis. This mechanical coupling does not prevent from any dry contact phenomena between the idler screws and the pump case, especially for some operating conditions, as those with low pressure rise and low pump speed. Therefore, the identified friction coefficient f_{STAT}

can be expected to be higher than f_{SCREW} and f_{DISK}, as effectively found through this calibration approach.

Moreover, also the friction losses determined by the driver screw's sealing and bearing require an experimental evaluation. To this end, before characterizing the friction coefficients f_{STAT}, f_{SCREW} and f_{DISK}, the pump was tested when operating without idler screws. In these working conditions, the absorbed mechanical power was totally wasted as heat in the pump's bearing and sealing apparatus (which are those of the driver screw in the considered pump layout), without any hydraulic power produced as output. This allowed to evaluate the experimental fitting coefficients *a*, *b* and *c* mentioned in Section 4.2.3.2.

Finally, all these parameters have been set as inputs to the model represented in Figure 4-5. Table 4-2 (a), (b) and (c) summarizes the geometrical and physical parameters, and the experimental coefficients found to characterize the power lost in the pump's auxiliaries, respectively.

Parameter	Value	Units
Series	5-3-1	
f	8	-
n_{STAGE}	1,31	-
n_{STARTS}	2	-
σ	61,4	deg
β/α	2,65	-
A_γ/R_2^2	0,0265	For 5-3-1 series
n_{IDLER}	2	-
δ_{DRIVER}	120	μm
δ_{IDLER}	10	μm
Displacement	48	cm^3
$D_{SUCTION}$	24	mm
$D_{DISCHARGE}$	24	mm
V_{IDLER}	35	cm^3
b_2	6	mm

(a)

Parameter	Value	Units
μ	8.86·10-4	Pa · s
ρ_{FLUID}	1045	kg/m^3
ρ_{IDLER}	7860	kg/m^3
f_{STAT}	0.16	-
f_{SCREW}	0.1	-
f_{DISK}	0.1	-

(b)

Parameter	Value	Units
a	$7 \cdot 10^{-6}$	W/rpm^2
b	$34 \cdot 10^{-4}$	W/rpm
c	9	W

(c)

Table 4-2. Geometrical (a) and physical (b) input parameters to the model summarized in Figure 4-5; experimental fitting coefficients used to calculate the power losses $P_{FR\ AUX}$ in the driver's sealing and bearing (c).

Once tuned, the mathematical model was experimentally validated. The tests were conducted by regulating the pneumatic proportional valve, in order to vary the hydraulic head of the circuit, as well as by regulating the electric motor speed to vary the pump speed, and thus the coolant flow rate.

For the model validation, the actual flow rate Q_{REAL} and the absorbed mechanical power P_m have been considered among the output parameters. Therefore, by giving as inputs the pump speed ω, the overall pressure rise Δp, and the geometrical and physical parameters, the output values predicted by the model have been compared with the measured counterparts, and the corresponding errors have been evaluated.

The pressure rise as a function of the flow rate is graphed in Figure 4-10, where calculated and measured values are compared for a specified range of pump speeds, i.e. from 750 to 3000 rpm. The flow rate ranges between 30 l/min and 140 l/min, while the maximum pressure rise does not exceed 3 bar. The model shows a good agreement with the experimental values, resulting in a good representation of the volumetric performance of the tested three-screws pump. The errors in the calculated flow rate can be observed qualitatively along the horizontal axis, being the pressure rise one of the model input parameters. Quantitatively, the flow rate is calculated with an absolute average error equal to 0.6% (Figure 4-11 (a)). This error is mainly caused by the approximations adopted for the backflow modeling (Section 4.2.1). However, it is also influenced by the error in the ideal flow rate calculation. In fact, the ideal flow section is slightly approximated due to the particular shape of the screws' tooth profile (see Appendix A).

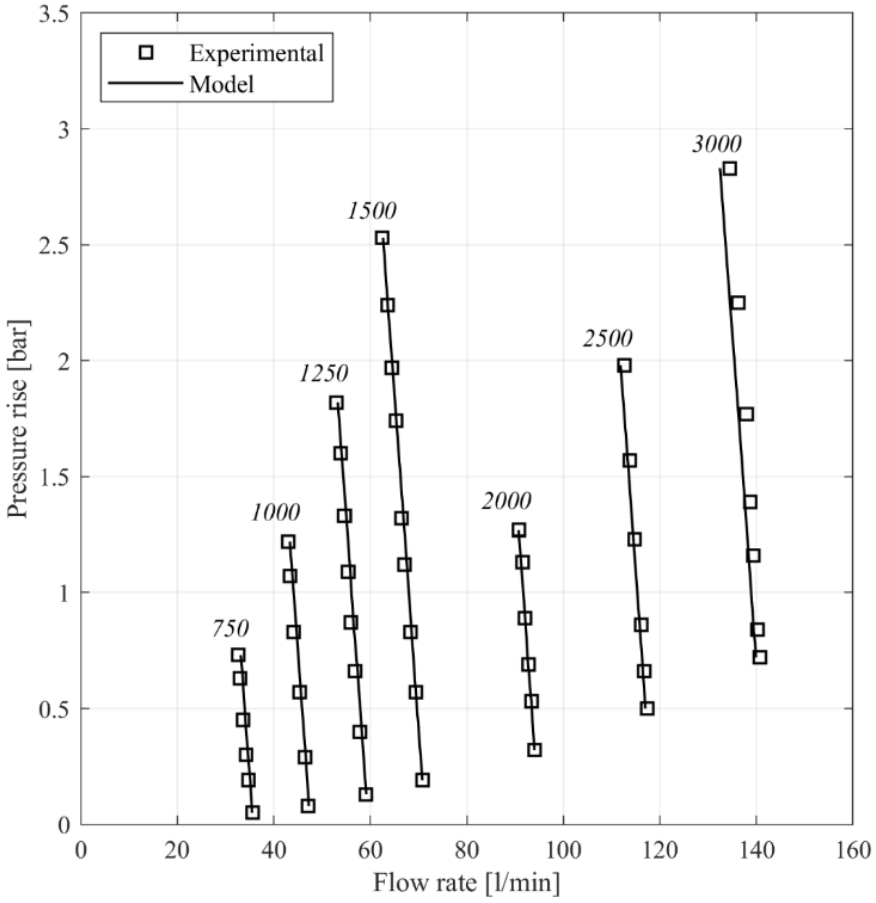

Figure 4-10. Pressure rise as a function of the flow rate calculated by the model (continuous lines), compared with the measured values (points), varying the pump speed from 750 to 3000 rpm.

The volumetric efficiencies calculated by the model are compared to the corresponding values obtained from experimental data in Figure 4-11 (b). The backflow calculated by the model yields to a good estimation of the volumetric efficiency of the pump. In fact, calculated and measured values are substantially aligned, and the overall mean error in the volumetric efficiency calculation is equal to 0.6%. Moreover, the volumetric efficiency is always above 87%, and reaches the 98% for low speeds and low pressure rises.

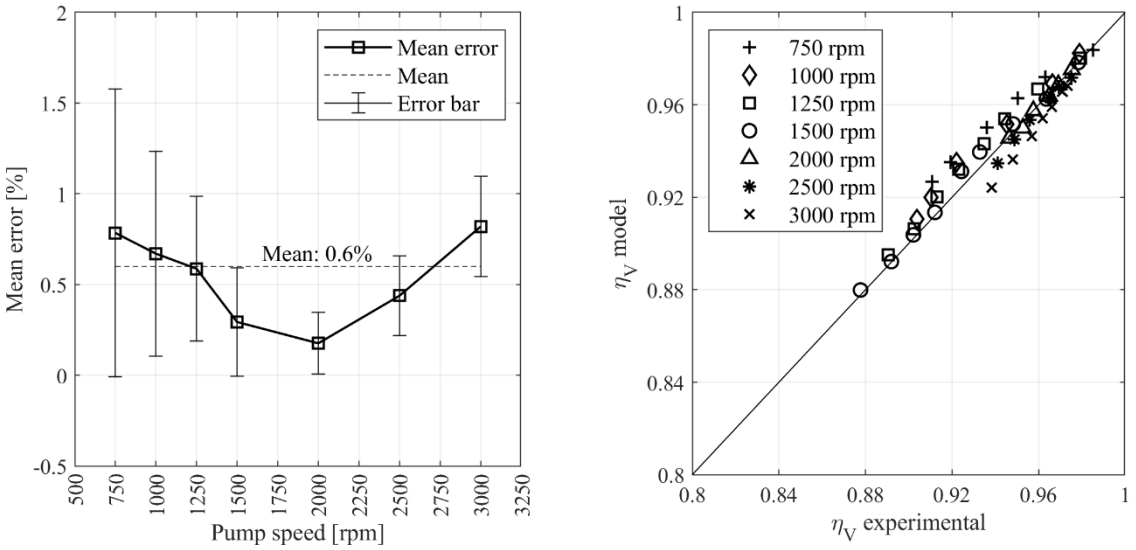

(a) (b)

Figure 4-11. Errors in the calculation of the actual flow rate Q_r for each tested pump speed (a); volumetric efficiency calculated by the model and from the experimental data (b).

Similarly, the mechanical power as a function of flow rate is graphed in Figure 4-12, where calculated and measured values are compared for the same range of pump speeds. The tested mechanical power absorbed by the pump reaches 970 W at 3000 rpm. The distance between calculated curves and measured points represents qualitatively the error in the mechanical power and the flow rate calculations. The overall absolute mean error in the mechanical power calculation is 13.5%. This is a reasonable value considering the simplicity of the model. Indeed, the friction power losses in the contact surfaces between the screws are calculated assuming a simplified free body diagram for the screws, in which friction coefficients independent from the pump operating point have been preliminarily assumed. Moreover, the indicated power is evaluated considering an ideal indicated cycle, which neglects any pressure spikes occurring during nominal operating conditions. Furthermore, similarly to the backflow calculation, the viscous power losses are calculated considering simplified Poiseuille-Couette flow conditions in the clearances between the screws' teeth tips and the pump case. Finally, the uncertainty in the measured mechanical power is about 7% (Table 4-1), confirming the order of magnitude of the experienced error and the dispersion of the data due to operating issues of the pump during tests (high revolution speeds, no lubrication, low pressurization).

The global efficiency achieved experimentally is up to 70%. It is worth to notice that this value is significantly higher than the one usually experienced in centrifugal pumps of the same

size. This makes screw pumps interesting for engine cooling applications, as will be described in Chapter 5.

However, the global efficiency calculated by the model suffers of the same inaccuracy observed for the mechanical power. Therefore, a deeper knowledge of the complex friction phenomena occurring inside screw pumps is suggested, and a possible solution will be proposed in the next Section 4.3.3.

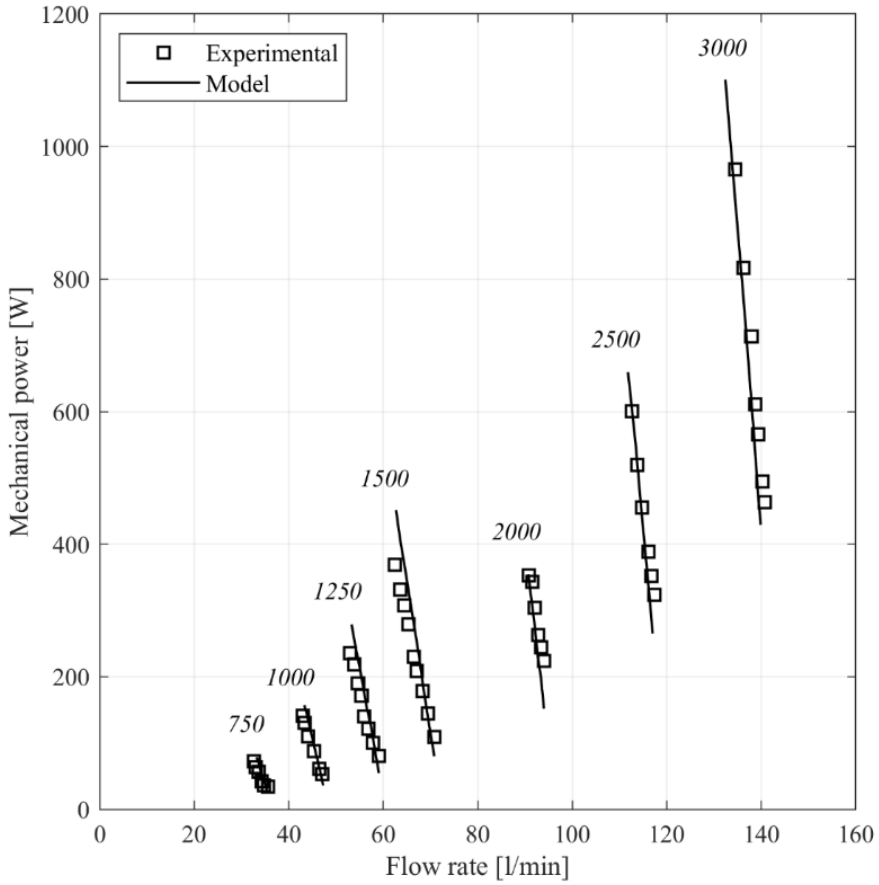

Figure 4-12. Mechanical power as a function of the flow rate calculated by the model (continuous lines), compared with the measured values (points), varying the pump speed from 750 to 3000 rpm.

4.3.3 Advanced friction modeling and experimental validation

The mechanical sub-model presented in Section 4.2.3 requires the definition of the friction coefficients f_{STAT}, f_{SCREW} and f_{DISK} to calculate the mechanical power absorbed by the pump. These friction coefficients have been preliminarily identified by varying them within typical ranges for steel-steel contact, and assuming them to be insensitive to the pump operating conditions, i.e. pump speed and pressure head (Section 4.3.2). Specifically, the values reported in Table 4-2 (b) were found, in order to match the mechanical power absorbed by the pump measured during the experimental activity, with the one predicted by the model.

The main limits of this model are related to the impossibility to represent correctly the effects of dry friction phenomena when the pump operating point varies. In fact, the above mentioned

friction coefficients implemented in the model were assumed to be constant, neglecting their dependency with pressure head and pump speed. This simplified modeling was reflected on the error between experimental and calculated power absorbed by the pump, which ranged between 10% and 15%, contrarily to the few percentage points error observed in the flow rate calculation.

In this section, a deeper study of these friction coefficients used to calculate the friction power losses is conducted, developing a mechanical model capable to predict their value when the pump operating point varies. Specifically, a more detailed mathematical model for the estimation of the friction coefficient between idler screws and pump case (f_{STAT}) has been proposed, while keeping the same values of the preliminary friction modeling for the coefficients involved in the interactions between driver and idler screws (f_{SCREW} and f_{DISK}).

In fact, the idler screws shafts are not supported by any bearings, being simply entrained inside a cylindrical support bordered by the pump case and the driver screw. This layout simplifies the pump manufacture, as generally requested by automotive applications, but enables axes misalignments, and thus occasional dry friction phenomena between idlers and casing during pump operation. Surface damages, in fact, are often found after operation, and the occurrence that the fluid operated is a mixture of water and glycol (instead of being a more conventional oil for oil dynamic applications) increases the risks of damages. Therefore, a dedicate discussion about the values assumed by the friction coefficient f_{STAT} during pump operation is necessary to improve the mechanical model effectiveness.

Hence, a relation between the friction coefficient f_{STAT} and the pump operating point has been developed, referring to the journal bearing theory [264].

In fact, the motion of the idler screw inside its cylindrical support can be analyzed as a shaft journal rotating inside a bushing element. That mechanical coupling is described by Petroff's equation, which gives a linear relation between the coefficient of friction f and the bearing characteristic number $\mu N/p$, where μ, N and p are the dynamic viscosity of the fluid, the shaft speed and the pressure inside the lubrication film, respectively. Therefore, the bearing number defines the hydrodynamic conditions of the lubricating film supporting the shaft, which determine the friction coefficient of the journal bearing.

Similarly, the idler screw rotating inside the pump case is supported hydrodynamically by the film of fluid entrained in the clearance existing between these two elements. The flow conditions of this thin film of fluid are determined by pump speed and pressure rise. For a given pump speed, the higher is the pressure rise across the screws, the higher is the backflow occurring through the clearances between idler and casing, and thus the higher is the hydrodynamic support of the screw. Consequently, a lower friction coefficient should be observed. Moreover, this effect should decrease for high pump speeds, because the idler screw is more subjected to the gyroscopic effect, which tends to stabilize its rotational axis. This behavior can be expressed by Eq. 4-41 and Eq. 4-42, which show the friction coefficient f_{STAT} as a function

of the bearing number $\mu N/p$, through a proportionality factor $k(N)$, which is inversely proportional to the pump speed N.

$$f_{STAT} = k(N)\ \frac{\mu\, N}{p} \qquad \text{Eq. 4-41}$$

$$k(N) = \frac{a}{N} + b \qquad \text{Eq. 4-42}$$

These relations have been introduced in the mechanical sub-model developed in Section 4.2.3, and the coefficients a and b in Eq. 4-42 have been identified by minimizing the error between the mechanical power calculated by the model and the one measured experimentally. To this end, the experimental data used in the preliminary validation of the model (presented in Section 4.3.2) have been considered. The obtained values of a and b are reported in Table 4-3.

Parameter	Value	Units
a	$1.12 \cdot (10^9)$	rpm
b	$2.09 \cdot (10^5)$	-

Table 4-3. Parameters defining the proportionality factor k, used to calculate f_{STAT}.

The friction coefficients identified during the minimization process of the error in the absorbed power calculation, and the model defined by Eq. 4-41 and Eq. 4-42 with a and b as in Table 4-3, are represented as a function of the dimensionless quantity $\mu N/p$ in Figure 4-13. The mechanical model is a bundle of straight lines passing through the origin, with a slope decreasing with the idler screw speed, and minimum and maximum values fixed at 0.05 and 0.2, respectively. The friction coefficients optimized for each working point are arranged along these lines, confirming the validity of this modeling approach.

Thus, these trends show that, for a given pump speed N, a decrease in the average pressure p of the fluid, supporting hydro-dynamically the rotating idler screw, determines an increase of the friction coefficient f_{STAT}, which has a maximum value equal to 0.2. Vice versa, an increase in the average pressure determines a decrease down to 0.05 for this friction coefficient. The physical meaning of these trends is that the higher is the pressure of the backflow fluid, passing through the clearance between the idler screw and the pump case, the more the idler screw is supported hydrodynamically by the fluid, and thus the less is the probability of dry contact conditions with the pump case, i.e. the friction coefficient f_{STAT} assumes smaller values. Therefore, these trends offer a simple modeling of the undefined type of contact conditions realized between the unconstrained idler screws and the pump case when the pump operating point (speed and pressure) changes: contacts tending towards dry conditions are modelled with higher friction coefficients, and vice versa.

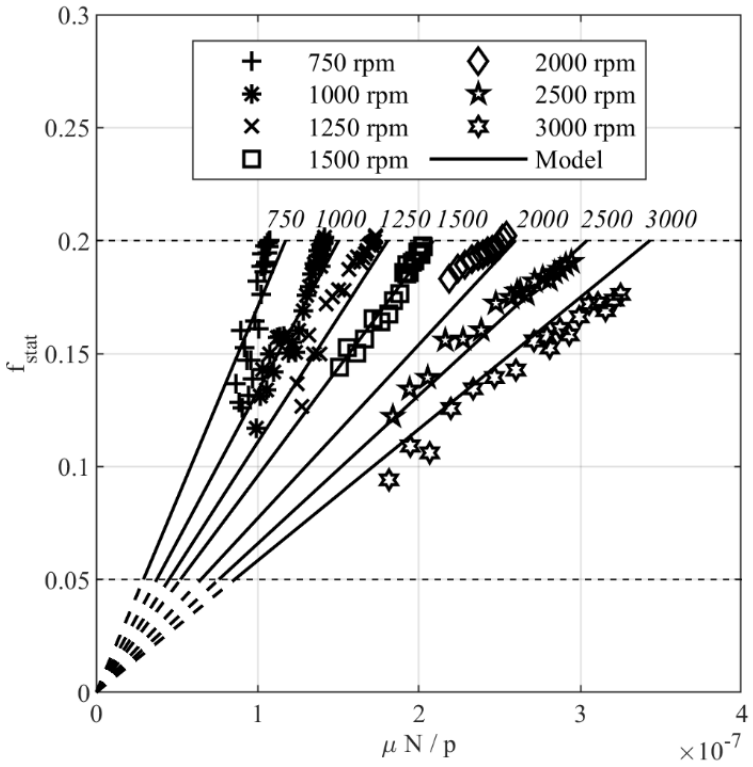

Figure 4-13. Friction coefficient between idler screw and pump case f_{STAT}, as a function of the dimensionless quantity $\mu N/p$. The symbols represent the values minimizing the error in the mechanical power calculation for each working point. Instead, the lines represent the values calculated by the mechanical model.

Finally, the friction model defined by Eq. 4-41 and Eq. 4-42, with *a* and *b* specified by the values reported in Table 4-3, can be introduced in the mechanical sub-model presented in Section 4.2.3. This allows to calculate a friction coefficient f_{STAT} between idler and casing which varies with the pump operating point. In this way, the friction losses are supposed to be predicted more accurately, enabling a reduction of the error in the mechanical power calculation.

The reliability of the redefined overall model has been assessed through a dedicated experimental validation, again conducted on the triple-screw pump described in Section 4.3.2 with the test bench described in Section 4.3.1.

The pump speed was varied between 750 rpm and 3000 rpm, and the hydraulic permeability of the circuit was varied to reach a pressure rise across the pump up to 3 bar. In these conditions, the screw pump delivers a flow rate ranging between 20 l/min and 150 l/min, absorbing up to about 1 kW at 3000 rpm.

The validation is realized by comparing the flow rate Q_{REAL} and the absorbed mechanical power P_m calculated by the model, with the corresponding measured values, giving as inputs the measured values of pump speed ω and overall pressure rise Δp.

As expected, the flow rate Q_{REAL} is calculated with a mean error of the same order of magnitude of that obtained in Section 4.3.2, being unchanged the volumetric model of the triple-screw pump.

On the other hand, the mechanical power absorbed by the pump P_m is calculated with a mean error equal to 6.1%, and a standard deviation equal to 7.4%. This result shows the benefits obtained considering the friction coefficient between idler screws and pump case f_{STAT} variable with pump speed and output pressure. In fact, in Section 4.3.2 the mean error in the mechanical power calculation was 13.5%, with a standard deviation of the same order of magnitude. Therefore, the advanced friction modeling hereby proposed allows to reduce the error by 50% with respect to the previous simpler model. Moreover, it is worth to consider the accuracy of this result also in relation to the uncertainty of the measured mechanical power. In fact, it is equal to 7% (Table 4-1), due to the absolute uncertainty in the torque measure.

The positive effects introduced by this friction modeling can be observed also in the global efficiency. In fact, it is estimated with an overall mean error equal to 6.8%. The pump model shows a good agreement with experimental values, and the real trends are reproduced correctly (Figure 4-14). This can be observed well in Figure 4-15, where calculated and measured values are substantially aligned.

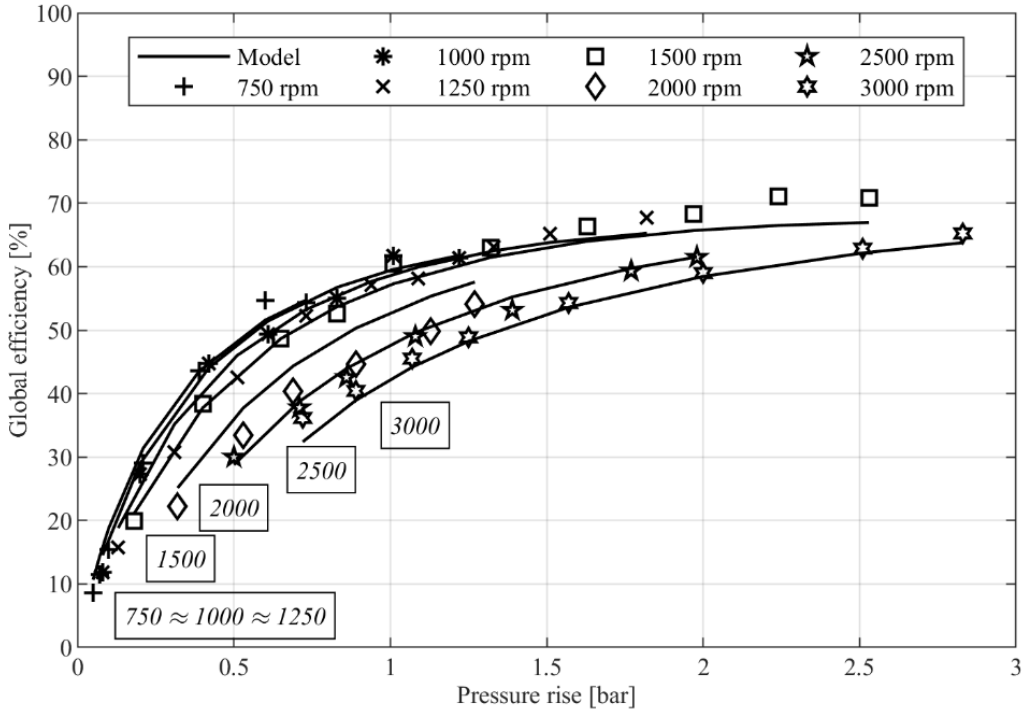

Figure 4-14. Global efficiency, as a function of pressure rise, calculated by the model (continuous lines), and from the measured values (symbols), varying the pump speed from 750 to 3000 rpm.

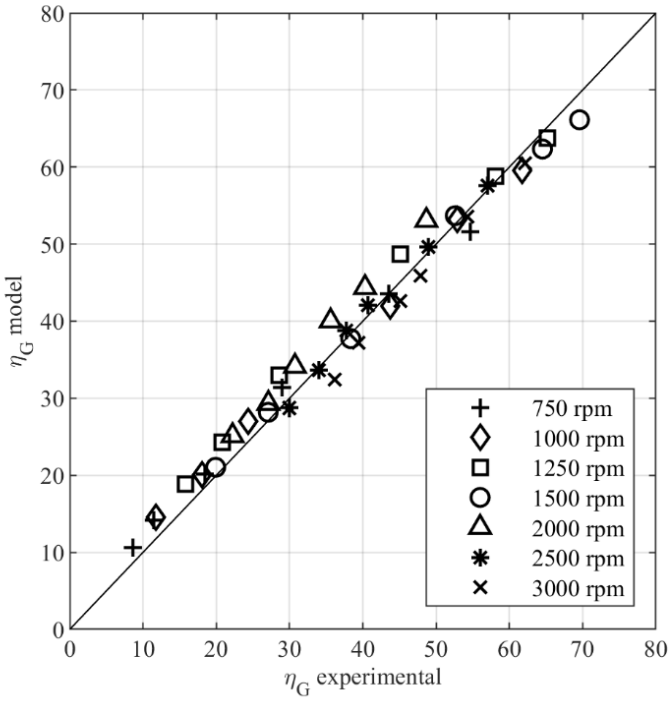

Figure 4-15. Global efficiency of the triple-screw pump calculated by the model and from the experimental data.

It is important to observe the maximum global efficiency reached by this pump, about 70% at 1500 rpm and 2.5 bar (i.e. low speed and high pressure rise), and its slight variation when the operating point of the pump varies. These values are unreachable with a centrifugal pump, especially regarding the capacity to keep the global efficiency high for a wide range of operating conditions, as clearly shown in Figure 4-14. In the transport sector, this characteristic can reduce the energy spent for engine cooling, which is of great interest nowadays due to the environmental and economic value of CO_2.

Finally, thanks to this advanced friction modeling, the mathematical model of triple-screw pumps with unconstrained idler screws presented in Section 4.2 can be considered validated, and it can be used for further analyses on the optimization of this type of pumps for engine cooling applications, as will be discussed in the next Chapter 5.

4.4 Conclusions

In this Chapter, a comprehensive zero-dimensional mathematical model of screw pumps has been developed. The model is capable to predict the volumetric and mechanical performances of these machines, once specific geometrical and operating input parameters have been defined. In particular, it calculates the flow rate and the mechanical power absorbed by the pump, by giving pressure head and pump speed as inputs.

More specifically, the model is composed by three sub-models, each of which describes the volumetric, indicated and mechanical performances of the pump, respectively:

- The volumetric sub-model calculates the actual flow rate by estimating the backflow occurring inside the machine through a suitably redefined Poiseuille-Couette flow modeling.
- The indicated sub-model calculates the indicated power by considering the pressure losses occurring during the suction and discharge phases of the plenums at the boundaries of the screws.
- The mechanical sub-model calculates the mechanical power by estimating both the viscous and dry friction power losses. These latter required a dedicated modeling of the friction conditions realized inside the machine. This was necessary due to the simple layout of the considered triple-screw pump, which does not prevent the occurrence of dry friction phenomena between the screws and the pump case. Hence, two progressively more difficult friction modellings have been proposed: one with constant friction coefficients, and the other with a specific modeling for the friction coefficient between the idler screws and the pump case, based on a suitably redefined Petroff's equation.

In this way, the model has been validated experimentally, and it is capable to calculate the flow rate and the mechanical power with a mean error equal to 0.6% and 6.1%, respectively.

In the following Chapter 5, the proposed modeling will be used as a model-based design platform to optimize the design criteria of screw pumps when used in the engine cooling system of a passenger vehicle. This will lead to the design and prototyping of a triple-screw pump optimized for a real application, whose characteristics will be assessed both theoretically and experimentally.

5 Optimization of screw pumps for engine cooling

In the previous Chapter 4, a comprehensive mathematical model capable to predict the performances of screw-type volumetric pumps has been developed and validated. This model considers a simple layout with a single driver screw and two symmetrical idler screws simply entrained inside cylindrical supports machined in the pump casing, which represents a reliable and cost effective solution also for the automotive sector.

In this Chapter, firstly the potential benefits in terms of energy and CO_2 emissions savings introduced by screw pumps when used in the cooling system of automotive ICEs have been evaluated. Specifically, the proposed mathematical model has been used to predict their performances when operating over a homologation cycle, which was assumed as a reference mission profile useful to compare them with standard centrifugal pumps. This comparison allowed to catch also possible improvements on the design of screw pumps for this type of application, which have thus been investigated through a model-based design approach. The main geometrical parameters improving the pump performances have been identified, and an optimized triple-screw pump has been proposed for a specific engine cooling system. Subsequently, that design has been prototyped, embedding also some construction improvements suggested by the outcomes of the advanced friction modeling proposed in Section 4.3.3. The experimental testing of the proposed pump will show very promising results compared with those obtained with an equally optimized centrifugal counterpart, corroborating the hypothesis that screw pumps could represent a viable solution to reduce the energy spent to cool the engine.

5.1 Comparison with centrifugal cooling pumps

The mathematical model developed in Chapter 4 can be used to simulate the performances of a screw pump when used in the cooling system of an ICE of the automotive sector. This allows to understand if any benefits can be obtained compared with standard centrifugal pumps, as theoretically expected due to the high and stable efficiency generally attributed to screw-type machines. In fact, volumetric pumps efficiency is less dependent on rotational speed and pressure head compared to that of centrifugal pumps. This aspect has been observed also for the triple-screw pump tested in this thesis to validate the model (Figure 4-14). Its overall efficiency ranges between 50% and 70%, which are unconventional values in the automotive sector. Moreover, low pump speeds allow to reach higher values of efficiency, which remains almost constant for a wide range of pressure heads. Therefore, for a given automotive application, the screw pump's geometry should be chosen in order to keep the pump speed as low as possible.

To evaluate all these aspects, a real engine cooling system embedding a triple-screw pump has been studied. Specifically, an IVECO F1C™ diesel engine for a light duty application was

considered [194], assuming the two permeability curves reported in Figure 5-1, corresponding to closed and open thermostat configurations, respectively.

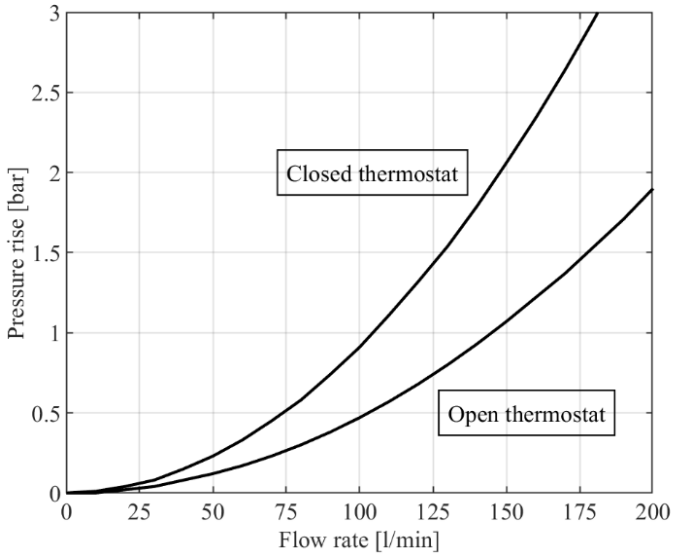

Figure 5-1. Permeability curves of the diesel engine cooling circuit.

The original system adopts a centrifugal pump mechanically linked with the crankshaft. This pump is designed to deliver 240 l/min and 2.8 bar at 4000 rpm of engine speed, with a maximum efficiency equal to 46%, which is the Best Efficiency Point (BEP).

In order to investigate the screw pump's performances for this engine cooling application, the mathematical model developed in Chapter 4 has been utilized to design a specific pump for this engine. The output of the design was a screw pump with the same geometric proportions of the pump used for the model validation (Table 4-2 (a)), but with a 50% increase of its displacement (from 48 cm^3 to 72 cm^3). This displacement was identified in order to keep the revolution speed of the pump lower than 3500 RPM. This maximum value is reached when the flow rate approaches 240 l/min, which is the flow rate at the BEP of the centrifugal pump, i.e. the maximum cooling request of the engine operating at peak power. The maximum speed has been chosen close the highest values experienced during the experimental campaign of the pump considered for the model validation (Section 4.3), in order to avoid vibration and wear issues which could likely appear at high revolution speeds. At the same time, this value allows to keep the pump size within the maximum dimensions imposed by the specific application.

Moreover, the triple-screw pump was assumed to be actuated by an electric motor, considering an average electric efficiency equal to 0.9. This allows to vary the pump speed independently from the crankshaft, delivering the right amount of flow rate requested by the engine during a driving cycle, that is the flow rate provided by the standard centrifugal pump.

Hence, the performances of the triple-screw pump have been evaluated over the class-3b WLTC homologation cycle, by using the mathematical model schematized in Figure 4-5. Specifically, the pump speed has been regulated to match the flow rate delivered by the standard

centrifugal pump, whereas the same pressure head of the OEM pump has been given as input. In this way, efficiency and energy consumptions of the two pumps have been compared together. The results are presented from Figure 5-2 to Figure 5-5.

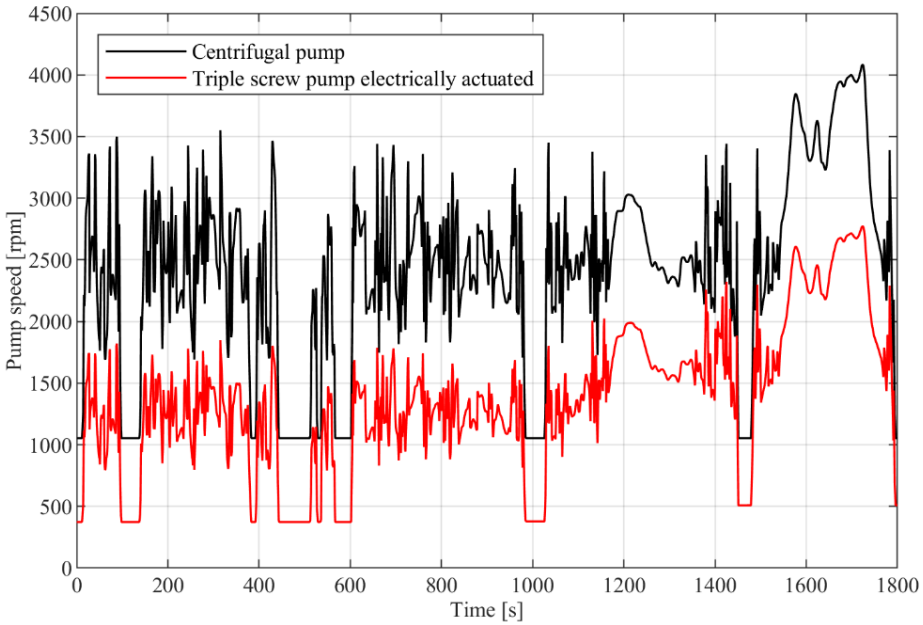

Figure 5-2. Speed of the centrifugal pump during a WLTC, compared with that of the electrically actuated triple-screw pump.

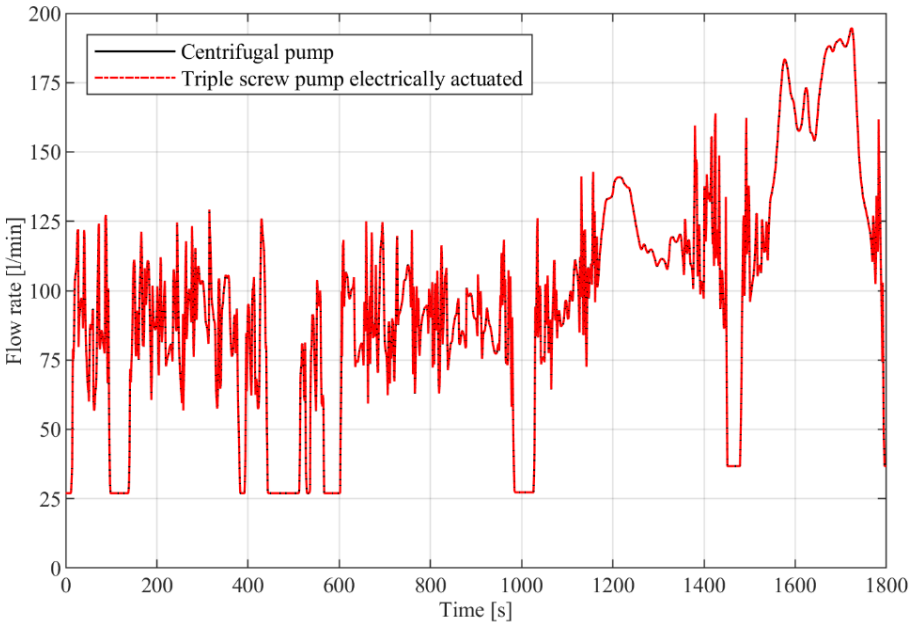

Figure 5-3. Flow rate delivered by the centrifugal pump during a WLTC, compared with that of the electrically actuated triple-screw pump. The two curves are substantially coincident.

The speed profiles of the two pumps during the WLTC are compared in Figure 5-2. The electric screw pump follows its own path, being disengaged from the crankshaft speed and simultaneously regulated to satisfy the engine cooling requirements, which coincide with the flow rate delivered by the centrifugal pump (Figure 5-3). This latter was calculated by knowing the hydraulic characteristics of the circuit (with the thermostat opened or closed, Figure 5-1) and the revolution speed of the OEM pump, which is mechanically linked to the engine crankshaft. Specifically, the mathematical model built in [228] has been used to calculate flow rate and mechanical power of the OEM pump, for a given velocity profile, circuit hydraulic resistance, and pump performance map. In particular, a vehicle equipping that engine was considered. Then, the engine shaft's speed profile was calculated, considering the gear ratios of the transmission system and assuming the exact speed for each gear-change. Hence, by knowing the experimental performance map of the OEM pump, its instantaneous speed, flow rate and absorbed power over the homologation cycle were determined, considering the circuit impedance according to the thermostat valve position assumed during the WLTC.

The mean speed of the centrifugal pump during most of the cycle is about 2500 rpm, while the corresponding value of the electric triple-screw pump is sensibly lower, about 1250 rpm. This allows to deliver about 90 l/min of flow rate, which varies during the cycle from a minimum of 27 l/min to a maximum of 195 l/min.

The global efficiency of the centrifugal pump is compared with that of the electrically actuated triple-screw pump in Figure 5-4. The efficiency of the electric screw pump takes into account also the efficiency of the electric motor, which is assumed constant during the cycle and equal to 0.9.

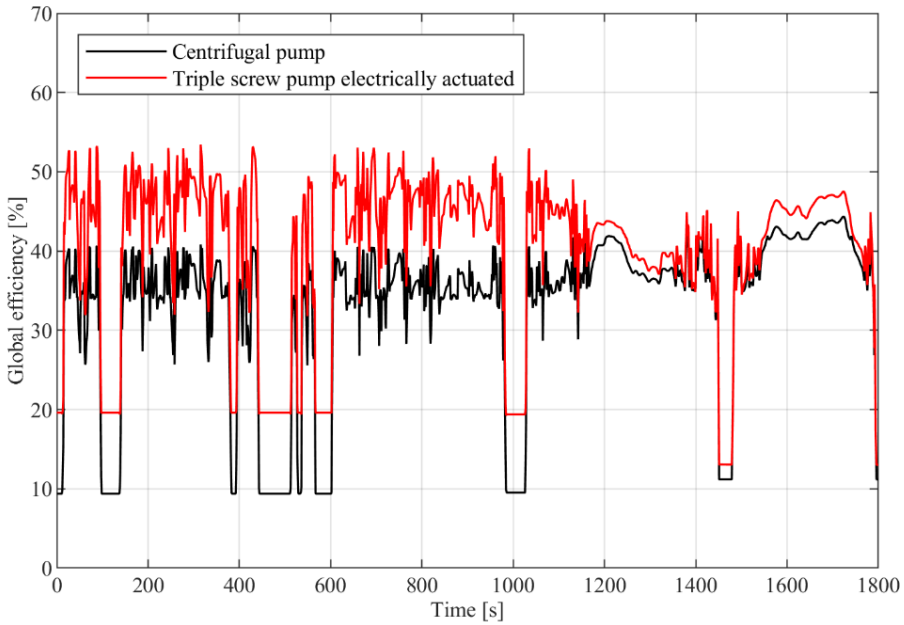

Figure 5-4. Global efficiency of the centrifugal pump during a WLTC, compared with that of the electrically actuated triple-screw pump.

The electrical screw pump shows a global efficiency higher than that of the centrifugal pump, although this advantage is progressively reduced after the thermostat valve opening, which happens at about 1200 s. This is due to the lower efficiency of the electric screw pump when it operates with higher pump speeds, which are reached in the second part of the cycle, after the thermostat valve opening. Instead, the centrifugal pump increases its efficiency after 1200 s, because it moves towards operating points with high flow rate, closer to its BEP.

The cumulative energy absorbed by the two pumps during the cycle is reported in Figure 5-5. The electric triple-screw pump absorbs 562 kJ of cumulated energy during the WLTC, against 652 kJ absorbed by the traditional centrifugal pump, leading to a 13.8% reduction of energy requested by the pump to cool the engine. This result is due to the improved efficiency of the triple-screw pump, which keeps higher values even when the pump speed varies, despite the adverse effect on the global efficiency introduced by the electric drive.

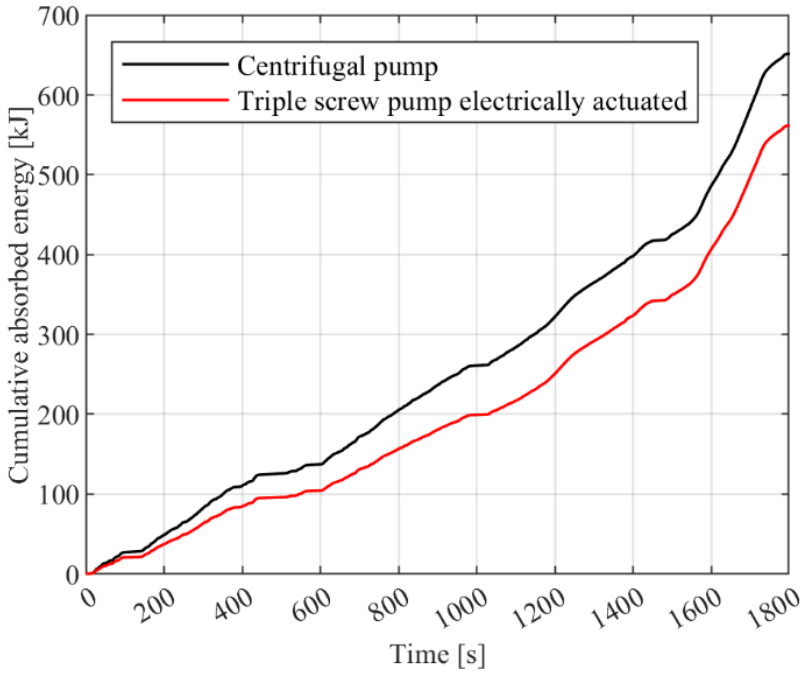

Figure 5-5. Cumulative energy absorbed by the centrifugal pump during a WLTC, compared with that of the electrically actuated triple-screw pump.

Even greater energy savings could be achieved if the displacement of the volumetric pump is further increased, resulting in a lower revolution speed for a given flow rate to be delivered. In fact, low revolution speeds always increase the efficiency of a volumetric pump. However, this is accomplished by higher displacements, which produce a dimension increase too.

Hence, a trade-off between space availability under the hood and pump efficiency (i.e. energy reduction) should be found. To this end, the effects on pump performances induced by variations of its geometric proportions have been analyzed in the next Section 5.2. The aim is to identify the best geometric arrangement optimizing the pump efficiency for a given operating point to be satisfied.

5.2 Model-based design for engine cooling applications

The mathematical model developed in Chapter 4 has been utilized to define the design criteria of screw pumps when used as cooling pumps of internal combustion engines.

Engine cooling applications require reliable and compact cooling pumps, capable to ensure coolant flow rate during all operating conditions. Typically, the operating point with maximum power output, i.e. maximum thermal power to be removed from the engine, is used as the design point of the coolant pump. However, this point is never reached by the engine during homologation cycles, as well as during typical real driving conditions. Therefore, in this analysis, the design point of the screw pump has been determined considering the maximum flow rate requested by the engine during a WLTC, while verifying that the pump is capable to deliver the maximum flow rate requested by the engine operating at maximum power. This approach optimizes the design point itself, allowing to reach an enhanced efficiency gain during the WLTC, as already demonstrated in [228].

To this end, the cooling circuit of a small turbocharged gasoline engine has been considered. That engine type was chosen because it has been the object of a deep energy optimization on the auxiliaries, which also belongs the electrification of the water pump. The standard application uses a centrifugal pump mechanically actuated through an Oldham joint, linked to the timing chain of the engine. This pump delivers a maximum flow rate equal to 50 l/min at 1.5 bar during the WLTC, which has been considered as the design point of the triple-screw pump.

Hence, the mathematical model developed in Chapter 4 has been used to evaluate the performances of a set of triple-screw pumps with different combinations of displacement and design speed, considering an operating point with 50 l/min of flow rate and 1.5 bar of pressure rise. The aim is to investigate the performances of screw pumps with different size and geometric proportions by regulating the design speed to deliver the flow rate of the design point, in order to find the geometry that allows to maximize the pump efficiency. In fact, for a given application, a trade-off between design speed and geometric proportions (i.e. displacement) needs to be found, in order to maximize the pump efficiency without exceeding size constraints given by the specific on-board layout.

5.2.1 Sensitivity analysis on pump geometry and efficiency

The displacement of triple-screw pumps can be varied acting on suitable geometric parameters, while ensuring the correct intermeshing between driver and idler screws. This can be achieved by maintaining a certain ratio between driver screw diameter D_1, idler screw diameter D_2, teeth height t and screw's axial angle σ (i.e. the pump series). To ensure correct intermeshing between driver and idler screws, five different series commonly used for triple-screw pumps have been considered [256]: the 5-3-1, 9-5-2, 13-7-3, 17-9-4, 21-11-5 series.

Then, for each pump series, the scale factor *f* has been incremented from 1 to 10 with a 0.5 step, to investigate the performance of different screw pump sizes of the same pump series.

The dependency of the displacement as a function of the scale factor for each pump series is shown in Figure 5-6 (a). Each circle identifies a specific pump geometry, and thus a certain displacement. For a given pump series, the increase of the scale factor determines an increase of the pump displacement. Moreover, different pump displacements can be achieved with the same scale factor, depending on the pump series. The maximum displacement has been limited to 500 cm^3, which was assumed as a reasonable limit value for an on-board application.

Subsequently, the performances of these pump geometries have been evaluated through the developed model. The pump speed has been regulated to let the pump deliver 50 l/min of flow rate at 1.5 bar of pressure rise, which have been chosen as hydraulic targets. Thus, larger screw pumps are expected to rotate with lower speeds to deliver the same flow rate. This trend can be observed in Figure 5-6 (b), where the dependency of the design speed as a function of the scale factor for each pump series is shown. For a given pump series, the increase of the scale factor determines a decrease in the design speed. Moreover, the same scale factor determines different design speeds, depending on the pump series. The maximum design speed has been limited at 5000 rpm to limit vibration and wear issues of the screws.

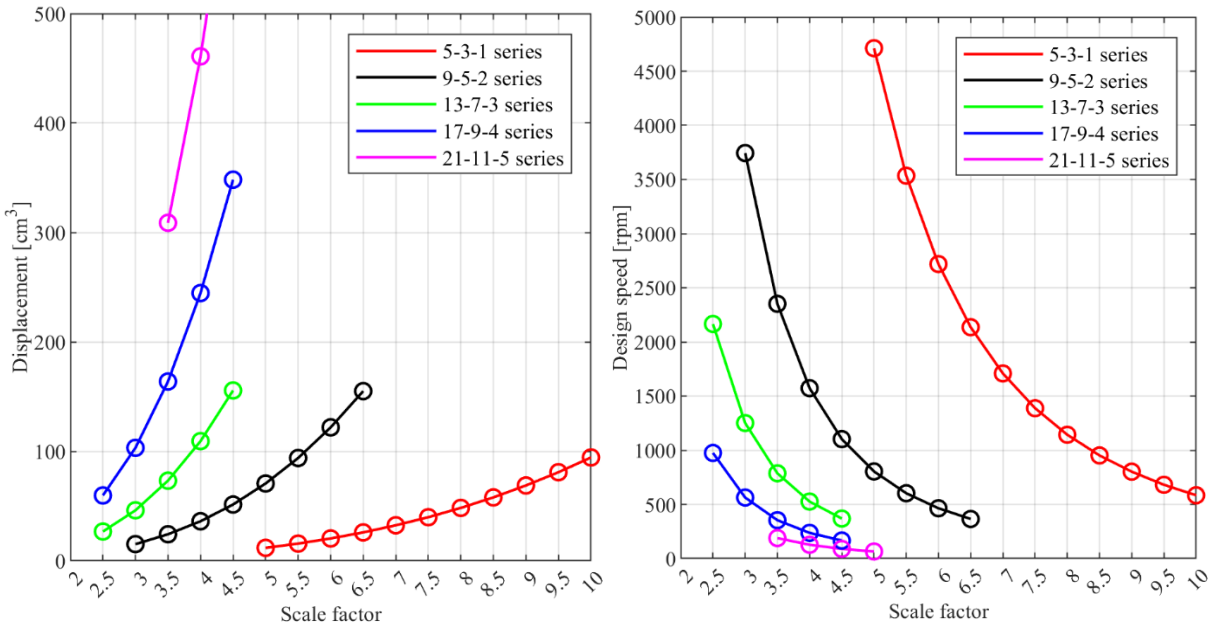

(a) (b)

Figure 5-6. (a) Displacement of the triple-screw pump as a function of the scale factor, distinguishing between different pump series. (b) Design speeds (determined for a given operating point) as a function of the scale factor, distinguishing between different pump series.

Displacement and design speed obtained with the same pump series and scale factor can be plotted together, obtaining the design map reported in Figure 5-7 (a). Each colored curve is relative to a pump series, and each circle identifies a couple of values {displacement; speed} which satisfies the hydraulic target of 50 l/min and 1.5 bar. The map shows that a decrease in

the displacement produces an increase of the design pump speed, as expected for volumetric machines. Moreover, the same couple of values of displacement and design speed can be achieved with different pump series by suitably setting the scale factor, as the curves are partially overlapped together.

Once the design map of triple-screw pumps is obtained, the global efficiency of each design point can be evaluated through the mathematical model. The efficiency map is reported in Figure 5-7 (b). Each curve is relative to a pump series, and each circle corresponds to one of the design points reported in Figure 5-7 (a). For a given design speed (and thus displacement), the map shows that the 5-3-1 series enables higher efficiency values. Specifically, the efficiency of a 5-3-1 series can rise up to 70% if the design speed is 580 rpm and the displacement is 94 cm^3. Moreover, the increase of the design speed always determines a reduction of the screw pump's efficiency. In fact, for the 5-3-1 series, the efficiency decreases from 70% to 33% when the design speed increases from 580 rpm to 4700 rpm, and the displacement decreases from 94 cm^3 to 11 cm^3.

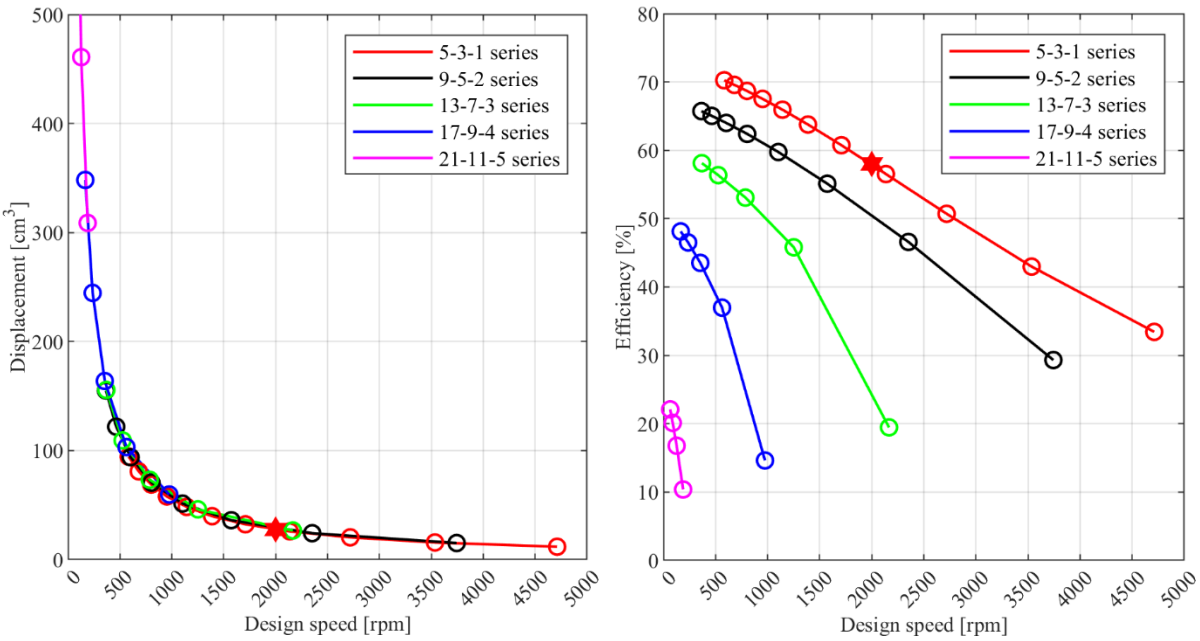

(a) (b)

Figure 5-7. Design (a) and efficiency (b) maps of triple-screw pumps. Each circle identifies the couple displacement-design speed which satisfies the hydraulic target. The highlighted star is the design point chosen for the specific engine cooling application.

Therefore, these results suggest that the design of triple-screw pumps should be oriented to the geometries of the 5-3-1 series. Moreover, a trade-off between displacement and design speed must be achieved to maximize the pump efficiency. In fact, the pump speed should be minimized, and thus large displacement pumps should be designed, without exceeding the space available in an on-board application.

5.2.2 Performance optimization

Once the overall design criteria of triple-screw pumps, when used as cooling pumps of internal combustion engines, have been defined, the performance optimization of these pumps has been realized. To this end, the influence of the aspect ratio on the pump efficiency has been investigated.

Therefore, the design and efficiency maps reported in Figure 5-7 have been used to identify the geometry series, displacement and design speed of a screw pump suitable for the engine cooling application under investigation, which has a flow rate equal to 50 l/min and a pressure rise equal to 1.5 bar at the design point.

A triple-screw pump of the 5-3-1 series has been chosen, being the efficiency of this series higher than that of the others. Moreover, a displacement equal to 27 cm^3 and a design speed equal to 2000 rpm have been selected (star point highlighted in Figure 5-7). These design features have been defined considering the space available under the hood of the specific application. Moreover, they help keeping the pump speed higher than 500 rpm during common operating conditions, which has been assumed as a lower limiting value for technological reasons, especially in case of a mechanical actuation linked to engine crankshaft.

The aspect ratio of triple-screw pumps has been defined as the ratio between the total length of the screws L_{tot} and the external diameter of the driver screw D_1. The screws' length is determined by the axial screw angle σ. An increase of σ determines a decrease of L_{tot} (Figure A. 4).

The performances of the selected pump have been studied by varying the driver diameter D_1 between 30 mm and 35 mm, and finding the screw's axial angle σ through the mathematical model in order to match the same displacement and speed chosen in the design phase. The screw angle σ was varied in the range between 50° and 65°, to ensure the meshing conditions between driver and idler screws. This led to a variation of the aspect ratio L_{tot} / D_1 from 3 to 1.94.

Thus, the performances of the designed triple-screw pump with different aspect ratios have been evaluated through the mathematical model developed in Chapter 4. The volumetric, indicated, mechanical and global efficiencies as a function of the aspect ratio are reported in Figure 5-8.

The increase of the aspect ratio determines an increase of both the volumetric and mechanical efficiencies, while no effects can be observed in the indicated efficiency. Consequently, the global efficiency of the screw pump increases from 56.7% to 59.9% when the aspect ratio rises from 1.9 to 3.

These trends can be explained thanks to the model. The increase of the aspect ratio determines a finger-shaped screw pump, which offers higher hydraulic resistance to the backflow occurring inside the pump, increasing the volumetric efficiency. Moreover, higher aspect ratios determine smaller diameters of the screws relatively to their length, reducing the friction torque and thus increasing the mechanical efficiency of the pump. Instead, the indicated

efficiency is not influenced by the aspect ratio, being calculated independently from the screws' geometry. As a result, finger-shaped screw pumps allow to reach higher efficiencies and should be preferred over disk-shaped ones.

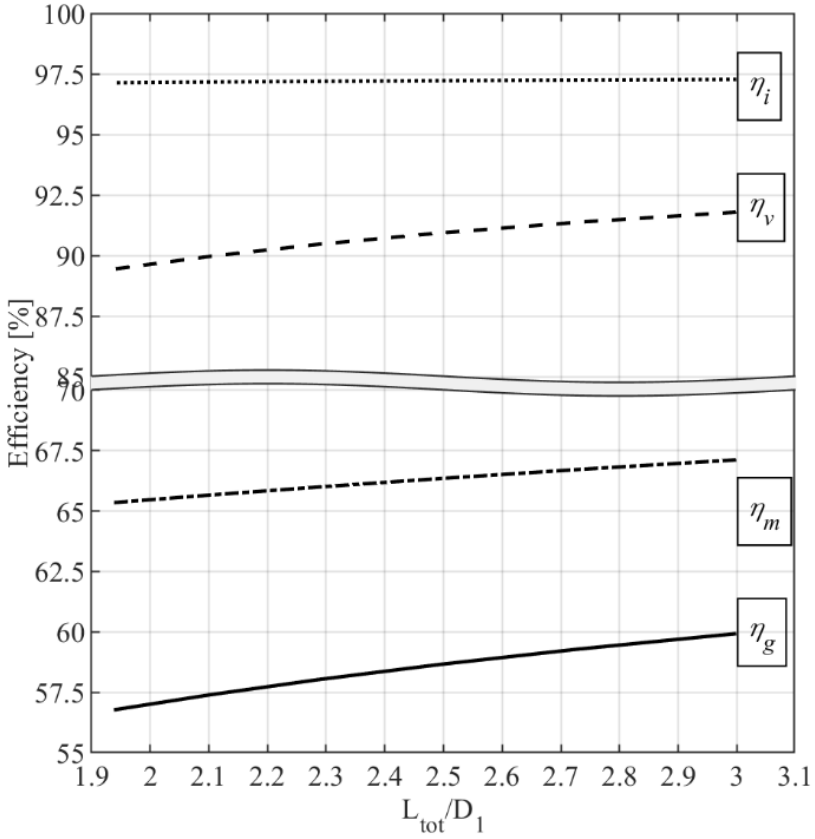

Figure 5-8. Efficiency of the designed triple-screw pump with different aspect ratios. Finger-shaped screw pumps allow to reach higher efficiencies.

5.2.3 Theoretical results on engine cooling

In Sections 5.2.1 and 5.2.2, the main design and performance optimization criteria for screw pumps used in engine cooling applications have been identified. In light of those considerations, a triple-screw pump for the cooling system considered to realize this optimization study has been proposed.

The design output is a 5-3-1 series triple-screw pump, with a displacement equal to 27 cm^3 and an aspect ratio equal to 3, obtained as the ratio between the length of the screws (equal to 90 mm) and the driver external diameter (equal to 30 mm). This geometry allows to reach the highest pump efficiency (about 60%) at the design point considered for this application, chosen as the one with maximum flow rate requested by the engine during the WLTC (50 l/min at 1.5 bar).

Thus, the performance of this pump can be evaluated when used as the cooling pump of the small turbocharged gasoline engine hereby considered, operating in a class 3b WLTC.

Furthermore, these results can be compared with those of the standard OEM centrifugal pump, which have been determined as in Section 5.1. Specifically, fully opened thermostat has been considered, which is the thermostat valve position more frequently assumed during the WLTC.

Therefore, the flow rate profile delivered by the OEM centrifugal pump has been assumed as that required by the engine, and it has been used as a target to calculate the rotational speed of the triple-screw pump. At the same time, the capability of the screw pump to deliver the maximum flow rate requested by the engine operating at maximum power was verified.

Results are shown in Figure 5-9. In particular, Figure 5-9 (a) shows the difference between the speeds of OEM and triple-screw pumps. It is evident that the designed volumetric pump must work at lower speeds to deliver the required flow rate. Anyway, this can be done easily by changing the pulley ratio between the engine crankshaft and the pump itself.

Furthermore, thanks to the model, it has been possible to compare the overall mechanical energy absorbed by the two pumps during the WLTC. Figure 5-9 (b) shows the results. The flow rate delivered is the same for the two pumps and, so, pressure rise and hydraulic power, sharing the same cooling circuit. The efficiency of the OEM centrifugal pump is very low, being traditional pumps designed for a working point with high speed and flow rate (corresponding to maximum engine power). The mechanical energy absorbed by the OEM centrifugal pump is 264 kJ, while the energy absorbed by the optimized triple-screw pump is 113 kJ. Therefore, the energy absorbed by the triple-screw pump is about 56.5% less than the OEM centrifugal one.

This strong reduction has a double origin:

a) the screw pump has been designed in the highest operating point reached during the WLTC (which represents common daily operation), instead of the maximum flow rate requested by the engine (in which the OEM centrifugal pump is designed), having verified that the screw pump is capable to deliver it. This allows to have the Best Efficiency Point very close to the most common operating points;
b) the screw pump has an efficiency independent on the revolution speed, which definitively can be higher than the centrifugal one, which suffers of low efficiency when it works far from the design point.

In other words, the triple-screw pump, besides being optimized in terms of efficiency in an optimized design point, keeps a higher efficiency also when it operates far from it, contrary to what happens with the OEM centrifugal pump. This translates directly into a strong reduction of the energy required to cool the engine, which in turn reduces fuel consumption and CO_2 emissions.

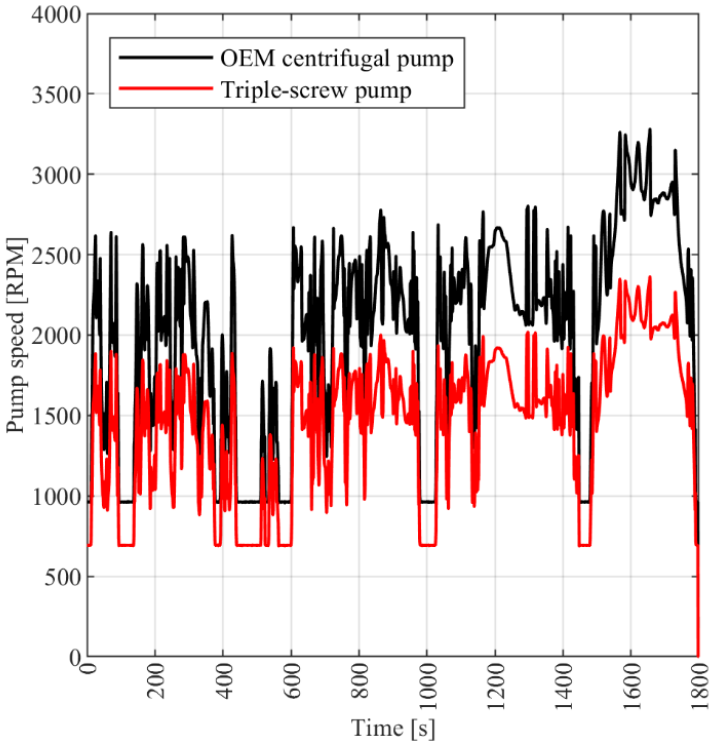

(a)

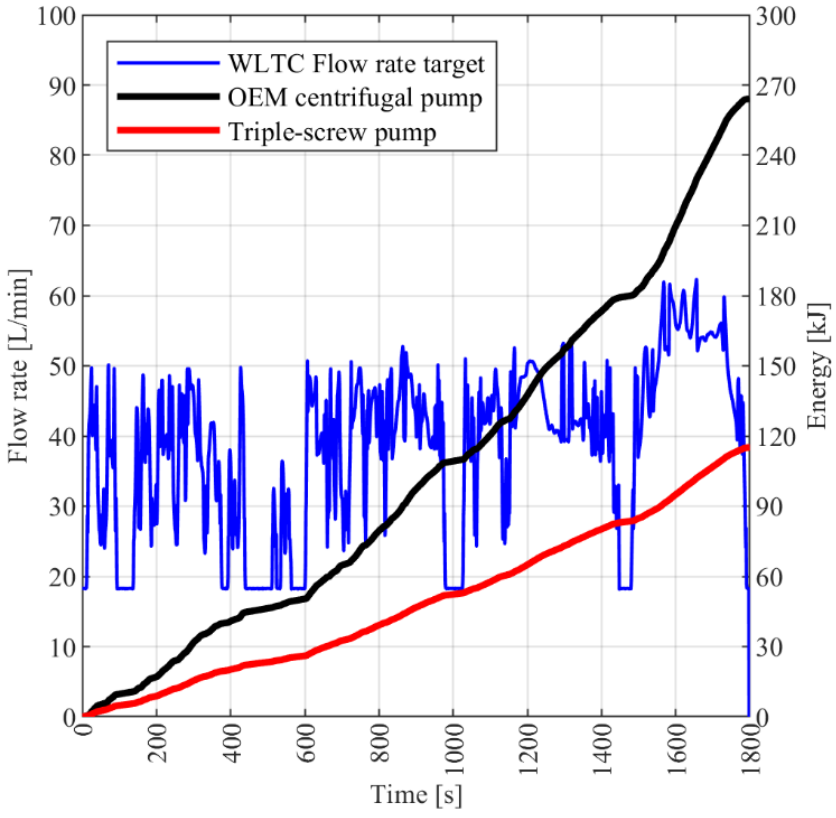

(b)

Figure 5-9. (a) Velocity profile of triple-screw pump and OEM centrifugal pump during the WLTC. (b) WLTC flow rate target and overall energy absorbed: OEM centrifugal pump vs. triple-screw pump.

Consequently, the CO_2 emissions saving can be evaluated by assuming the mean performances of an ICE over the WLTC. In fact, considering an average thermal efficiency of 22% [236], the associated fuel chemical energy needed to drive the two water pumps during the WLTC can be calculated. Then, the amount of saved fuel can be estimated, assuming 43.93 MJ/kg as the lower heating value of gasoline and 800 kg/m^3 as its density.

In this way, a reduction of 0.83 ml/km has been achieved, being known the total distance of a WLTP class 3b cycle (with $v_{max} \geq 120$ km/h). This translates into a reduction of CO_2 emissions equal to 2.08 g/km, assuming an emission factor for gasoline equal to 3.14 $kgCO_2$ / $kg_{gasoline}$ [266]. This significant CO_2 reduction is worthy of attention, considering the fines imposed in Europe to automobiles companies for exceeding the targets, and it confirms the validity of the proposed model-based design approach.

To the best of author's knowledge, these results give a first-in-literature understanding of the model-based design of screw pumps for engine cooling applications. Thus, the availability of such a reliable modeling platform has been the hint to the design and prototyping of a screw pump for the engine cooling system object of study. The aim is to prove experimentally the effectiveness in reducing the energy necessary to cool the engine. Moreover, the experimental characterization of a prototype can be extended also to the measurement of the indicated cycle of the machine, in order to better understand the complex fluid dynamic phenomena occurring inside the pump during the screws' rotation. This can be the chance also to refine the mathematical model developed so far, and possibly increase the optimization of this type of machines even more. All these researches will be presented in the following sections.

5.3 An optimized triple-screw pump for engine cooling

Thanks to the model-based design analysis presented in Section 5.2, an optimized triple-screw pump has been designed and prototyped for an engine cooling application. Specifically, the cooling system is that of a small turbocharged gasoline engine, the same considered in the previous section to assess theoretically the benefits introduced by a screw pump suitably optimized for this type of application. As mentioned in Section 5.2, the OEM centrifugal pump of this cooling system was designed considering the coolant flow rate requested by the engine when operating at maximum power, as usual in on-board applications. However, this design approach is extremely conservative, being that operating point almost never reached during typical real driving conditions neither during homologations cycles. In fact, these operating conditions impose the pump to operate far from the BEP, resulting in low pump efficiency and high energy consumption.

Therefore, similarly to what done in Section 5.2, a design point more representative of common driving conditions has been considered, while verifying the capability of the pump to guarantee the cooling flow rate requested by the engine operating at full load. Specifically, in this case the design point has been chosen as the average of the maximum values of flow rate

requested by the engine during a WLTC, considering the pressure rise determined by an intermediate impedance curve representative of the mean hydraulic permeability of the cooling circuit. In fact, generally the thermostat valve position varies continuously during driving, and this shifts the impedance curve of the cooling circuit between those with closed and open thermostat depending on the engine thermal state. Therefore, this criterion led to 54,2 l/min as flow rate and 1,65 bar as pressure rise. In this way, the pump can operate more frequently closer to its BEP, reducing the energy consumption during a homologation cycle and, above all, in real driving conditions.

Hence, the optimization criteria underlined in Section 5.2 have been used to design a triple-screw pump under these specific hypotheses. In addition, a centrifugal pump optimized in the same design point has been proposed, in order to assess if volumetric screw-type pumps can produce an effective advantage over the more conventional centrifugal ones. In other words, the aim is to verify experimentally the potential benefits in terms of efficiency of screw pumps over centrifugal pumps, when both have been optimized and designed for the same operating point.

5.3.1 Design procedure

The cooling pumps under investigation are a centrifugal and a screw-type volumetric pump. These pumps have been optimized and designed through a model-based design approach, which has been possible thanks to the corresponding mathematical models capable to predict their performances. Specifically, the centrifugal pump has been designed through the modeling approach presented in [229,230], whereas the triple-screw pump with the one presented in Section 5.2. Thus, corresponding design procedures have been implemented to find iteratively the optimal geometry maximizing the pump efficiency at the design operating point.

A schematic of the model-based design procedure followed to develop the optimized centrifugal pump is represented in Figure 5-10. Starting from the design specifications in terms of flow rate, pressure rise and revolution speed at the design point, a semi-empirical mathematical model has been used to calculate the main dimensions of the pump. This model has two main sections: the first one optimizes the design of the impeller, while the second optimizes the design of the volute in accordance with the free-vortex law. The model varies iteratively the dimensions of impeller hub and pump casing to maximize the volumetric efficiency, calculating also the hydraulic efficiency in the main cycle. At the end of the design iterative procedure, the model gives the main dimensions of the designed pump, in terms of hub and shroud angles, blade heights, volute diameters and spiral radiuses. Thus, the performances of the pump in off-design conditions have been verified through a CFD model, capable to catch important real phenomena (3D analysis) and also cavitation phenomena particularly relevant at high revolution speeds. Thanks to some geometrical adjustments done with a CFD model, an optimized geometry for the specific application has been assessed.

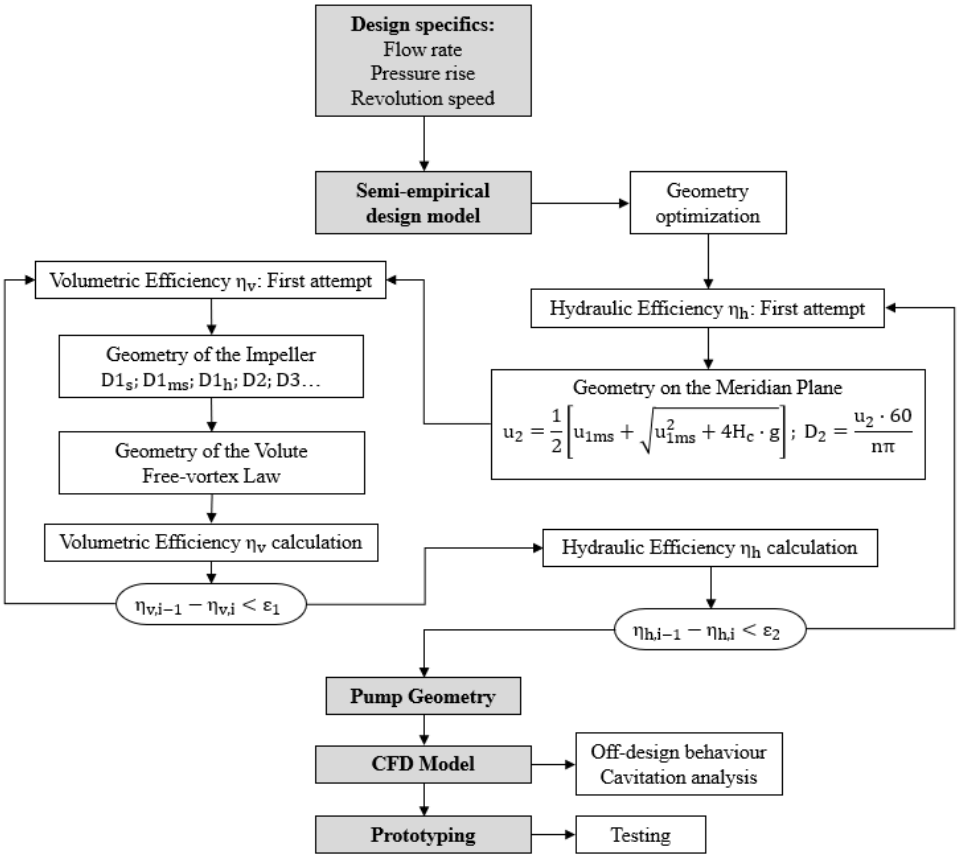

Figure 5-10. Schematic of the model-based design procedure followed to develop the optimized centrifugal pump.

Similarly, the schematic of the model-based design procedure followed to develop the triple-screw pump is represented in Figure 5-11. Given the design specifics in terms of flow rate, pressure rise and revolution speed, the 0D mathematical model presented in Chapter 4 has been used to calculate the main dimensions of the pump. The model optimizes the screws' geometry to maximize the pump efficiency, while satisfying the desired flow rate and pressure rise at the design speed. Retracing briefly the model structure, the volumetric, indicated and mechanical sub-models follow one another during calculation. The volumetric sub-model calculates the overall backflow occurring inside the pump through the suitably redefined Poiseuille-Couette flow modeling, allowing to evaluate the actual flow rate delivered by the pump, as well as its theoretical and hydraulic powers. Then, the indicated sub-model estimates the pressure losses intrinsic in the filling and emptying processes of suction and discharge chambers respectively, enabling the calculation of the indicated cycle and of the indicated power. Subsequently, the mechanical sub-model schematizes viscous and friction phenomena through a lumped-parameter and semi-empirical approach, calculating the overall mechanical power absorbed by the pump and its global efficiency. Thus, the screws' geometry optimizing the efficiency of the triple-screw pump at the same design point considered for the centrifugal pump has been assessed for the specific application.

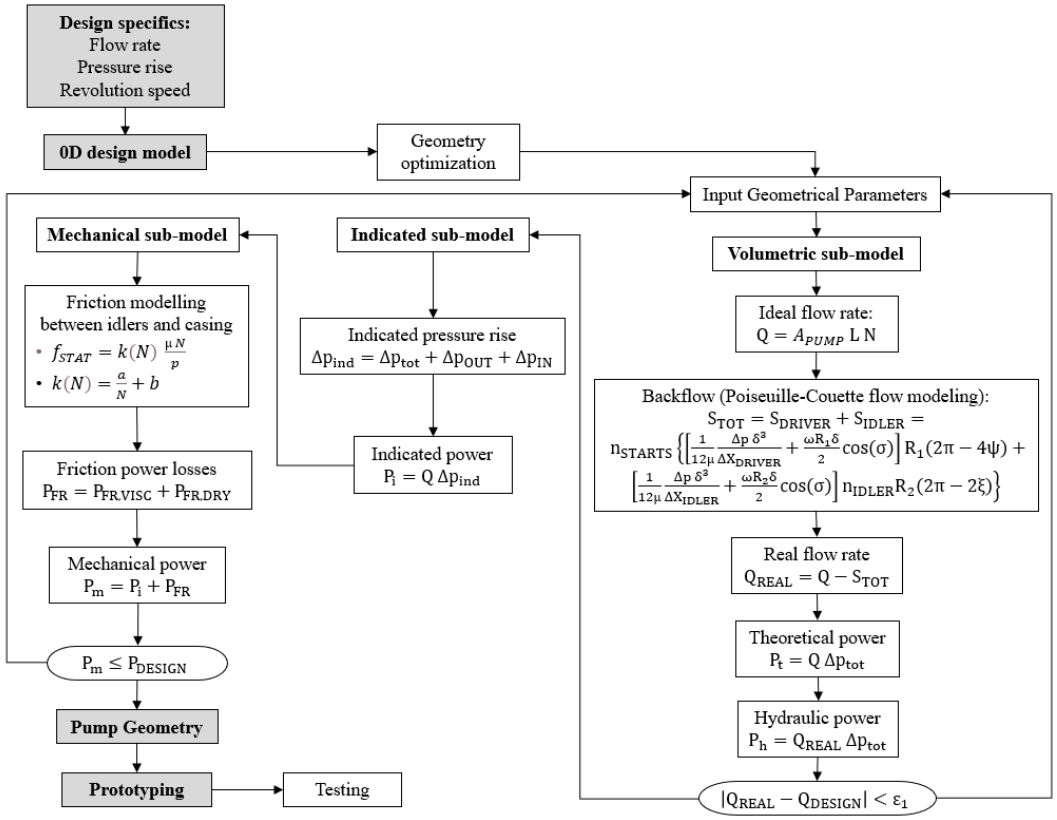

Figure 5-11. Schematic of the model-based design procedure followed to develop the triple-screw pump.

At the design point, the pump speed needs to be defined as an input constraint. The centrifugal pump speed has been set at 7000 rpm, while 3000 rpm was that chosen for the triple-screw pump. These values have been identified considering the consequences they impose on the pump size and on the worst cooling condition the pump must meet. In fact, they represent a trade-off value between pump dimensions and maximum speed necessary to deliver the peak flow rate requested by the engine operating at maximum power. This trade-off depends on the under-hood dimensions, and thus it refers to a specific on-board vehicle application of the engine considered for this study.

5.3.2 Pump prototyping and testing

The two so-designed pumps have been prototyped thanks to the technical support of the company Metelli Group S.p.a.™. Figure 5-12 presents an image of them when disassembled, in order to show their main internal components.

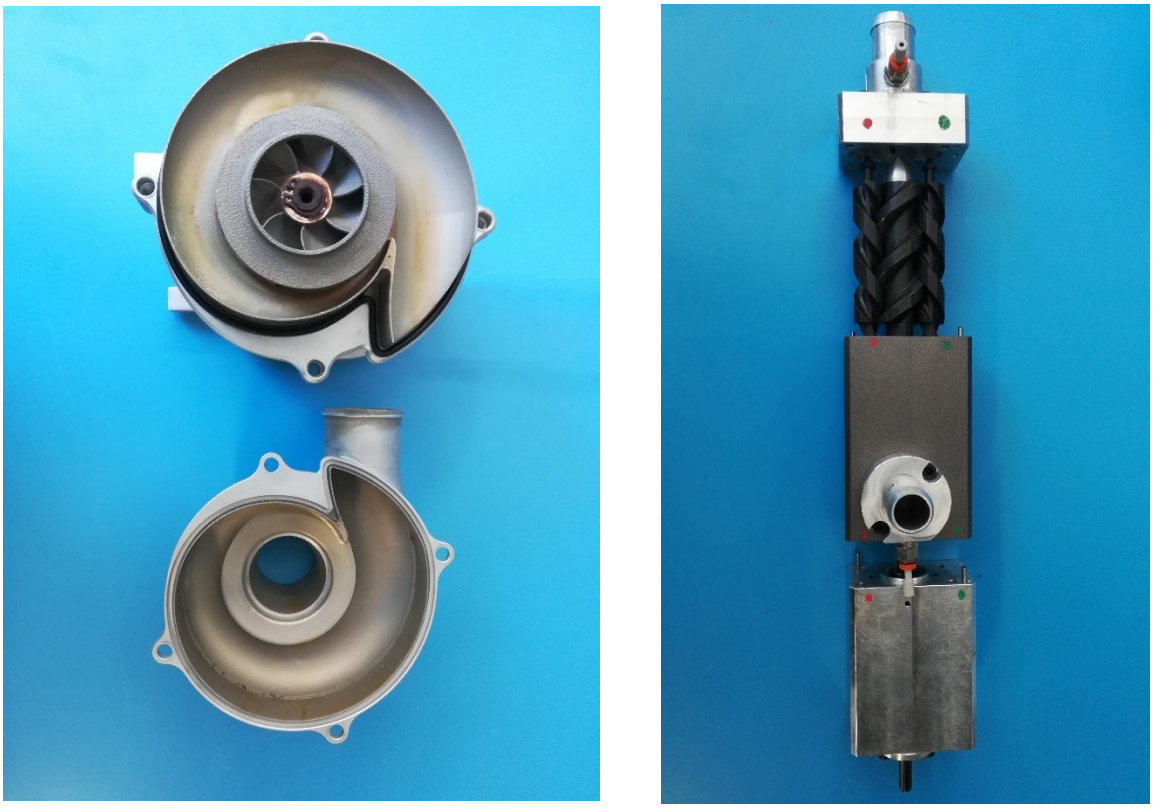

(a) (b)

Figure 5-12. Pumps prototyped after the design and optimization process: centrifugal pump (a) and triple-screw pump (b).

Their rotating elements have been deeply optimized also from a manufacturing and operational point of view. In fact, especially for the screw pump, wear and vibration represent serious issues, particularly dangerous at high revolution speeds, as experienced during the experimental characterization of the pump considered for the model validation (Section 4.3). Therefore, several measures have been introduced in this concept to limit their negative effects, mostly regarding the mechanical support of the idler screws. This technical innovation improved significantly performance and durability of the pump, and determined many other advantages, which will be discussed later in Chapter 6.

Once prototyped, the two pumps have been experimentally characterized through the test-bench described in Section 4.3.1.

Their performance maps in terms of efficiency as a function of pressure rise and flow rate have been derived experimentally for a wide range of operating conditions (centrifugal pump in Figure 5-13, and screw pump in Figure 5-14). In these figures, also the hydraulic permeability curves of the engine cooling circuit when the thermostat valve is open and closed have been represented, in order to underline important features of the two types of prototypes.

Firstly, it is worth to notice that the design point chosen for their optimization (BEP_{des}) does not coincide exactly with the Best Efficiency Point experienced during the performance tests (BEP_{exp}), although this latter remains near the hydraulic permeability curve on which the design point lies. This result can be accepted if the effects of the mechanical efficiency on the global

efficiency of the pump, as well as those related to measurement uncertainties, are considered. In fact, especially for the triple-screw pump (Figure 5-14), the power losses due to friction phenomena can determine significative variations with regard to the mechanical power, deviating the effective BEP from the design point.

These performance maps show also the high performance reached by both pumps over a wide range of operating conditions, which include those experienced during a homologation cycle, as well as during real driving. In fact, they have a high efficiency at their experimental BEP (BEP_{exp}), which is equal to 47.7% for the centrifugal pump, and 61% for the triple-screw pump.

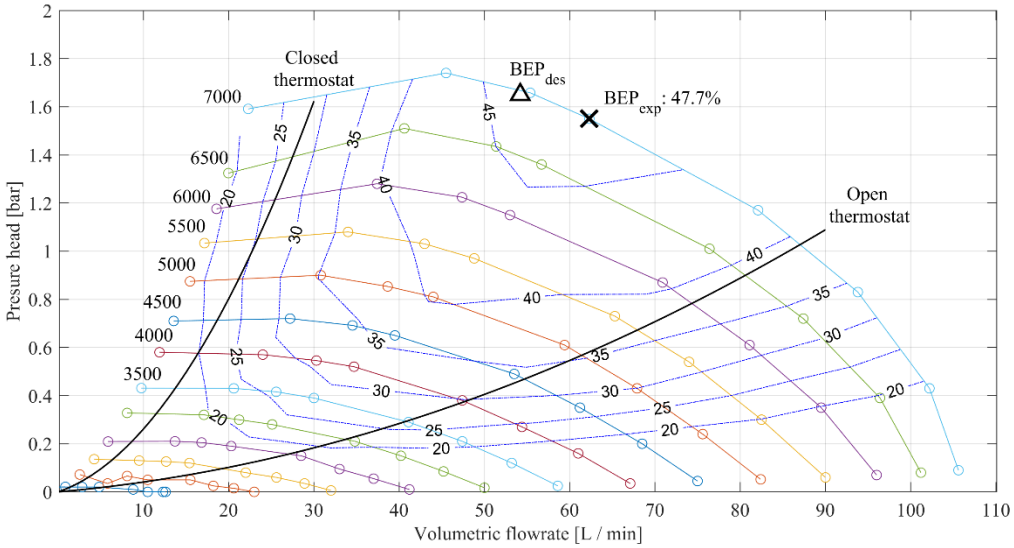

Figure 5-13. Experimental performance map of the prototyped centrifugal pump, and hydraulic permeability curves of the engine cooling circuit with open and closed thermostat. BEP_{des} is the design point, while BEP_{exp} is the experienced BEP.

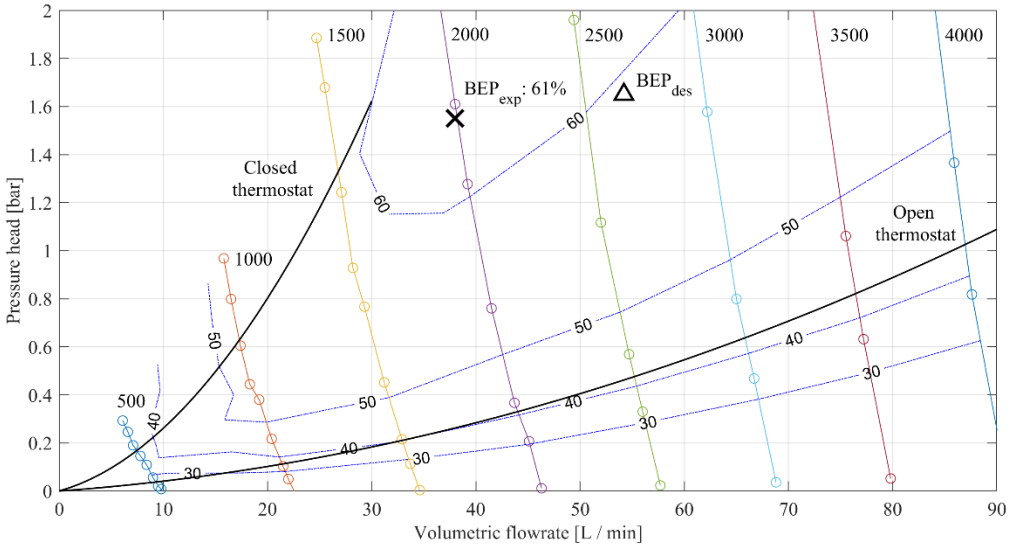

Figure 5-14. Experimental performance map of the prototyped triple-screw pump, and hydraulic permeability curves of the engine cooling circuit with open and closed thermostat. BEP_{des} is the design point, while BEP_{exp} is the experienced BEP.

However, the trends of the iso-efficiency curves show an intrinsic difference between these two types of machines, widely known in literature. In fact, the triple-screw pump keeps high values of efficiency also when operating far from its BEP, whereas the centrifugal pump efficiency decreases sensibly. This feature has strong consequences on the performance of both pumps when their operating point varies, which always happens during driving due to changes in pump speed or in the hydraulic permeability of the engine cooling circuit, imposed by variations of the crankshaft speed or of the thermostat valve position, respectively.

Therefore, the operating conditions imposed by an engine cooling application suggest to evaluate the performance of both pumps when operating on a continuously varying operating point. In order to consider a common reference testing condition, the performances of both pumps have been tested over a typical homologation cycle, which will be discussed in the next Section 5.3.3.

5.3.3 Experimental results on engine cooling

Once experimentally characterized, the prototyped centrifugal and triple-screw pumps have been studied when operating as the cooling pumps of the small gasoline engine under investigation. Their performances have been evaluated experimentally by reproducing a Class-3b WLTC homologation cycle through the experimental test bench described in Section 4.3.1., which allows to replicate the hydraulic impedance of the engine cooling circuit.

The flow rate requested by the engine during the homologation cycle has been used as a target for both pumps to be followed by varying their speed. This actuation strategy was necessary to suitably compare the performances of two pumps, whose operating principle is intrinsically different, despite they have been optimized and designed considering the same design point. In fact, the triple-screw pump is a volumetric machine, and thus it has a volumetric efficiency which diminishes less than that of the centrifugal pump when the pressure head increases. Therefore, it needs to be operated at lower speeds in order to keep the pressure inside the cooling circuit within acceptable values.

The target flow rate has been assumed to be equal to the flow rate delivered by the OEM centrifugal pump equipping the engine, which has already been evaluated in Section 5.2.3.

For what concerns the engine cooling circuit, the thermostat valve has been considered fully open. This assumption was necessary due to the lack of knowledge about the thermal dynamics of the specific engine during the warm-up phase. However, it can be considered acceptable, being the open thermostat position the one more frequently assumed during the WLTC. Supporting this assumption is also the fact that generally the power absorbed by the pump during the warm-up phase is negligible compared to that absorbed during the phase with open thermostat, which is thus more suitable when comparing the performances of different pumps over a homologation cycle. Therefore, the operating points of each pump lie on the hydraulic permeability curve of the circuit with open thermostat, determining a lower efficiency

compared to the BEP (Figure 5-13 and Figure 5-14). This leads to a conservative estimation of the performances of both pumps, which could be increased if the engine thermal dynamics are taken into account.

The target flow rate and the pressure rise determined by the circuit are reported in Figure 5-15. The flow rate ranges between 18 l/min and 62 l/min, while the pressure rise between 0.1 bar and 0.6 bar.

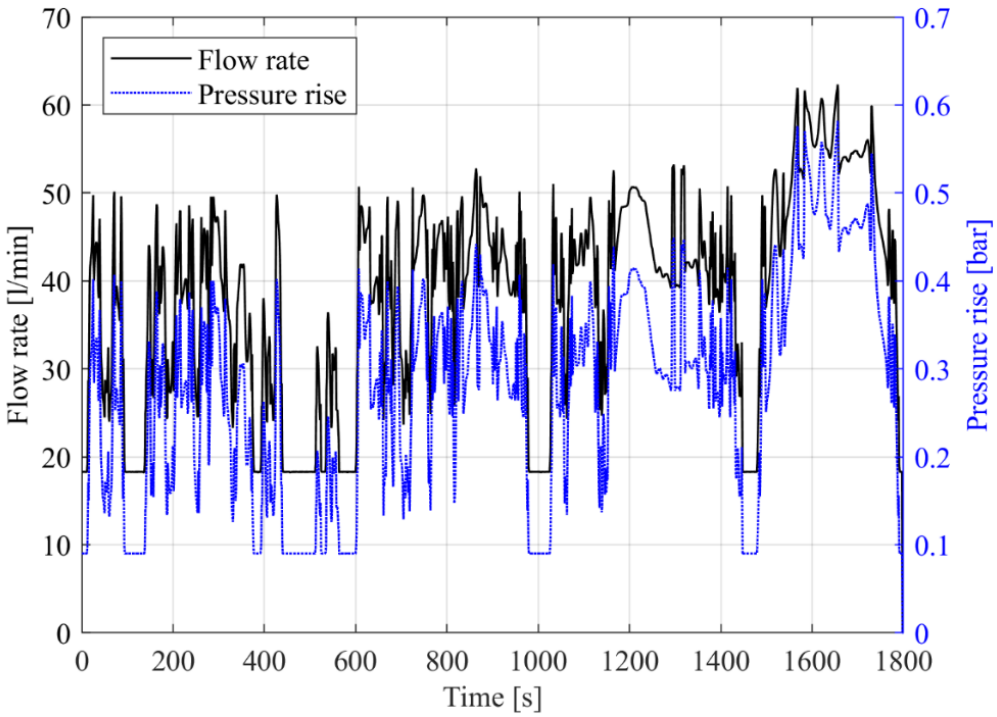

Figure 5-15. Flow rate delivered by the OEM centrifugal pump over a WLTC class 3b, and pressure rise determined by the hydraulic circuit with fully open thermostat. The flow rate is the same reported also in Figure 5-9 (b).

Thus, the speed of the prototyped pumps has been varied in order to match this target flow rate, obtaining the speed profiles represented in Figure 5-16. Each of these speed profiles could be achieved on-board of a vehicle by disengaging the pump axis from the crankshaft, and actuating it through an electric motor. It can be observed that the triple-screw pump operates at lower speeds (860-2800 rpm) than the centrifugal pump (1900-5100 rpm). This is due to the different operating principle of the two pumps. In fact, the triple-screw pump needs to be designed to operate at lower speeds compared to those of the centrifugal pump, to maximize efficiency and reduce wear.

The performances of the prototyped pumps can be observed in Figure 5-17 and Figure 5-18. The efficiency of the triple-screw pump results always higher and less variable than that of the centrifugal pump (Figure 5-17). In fact, it ranges between 25% and 38%, whereas the centrifugal pump has a more variable efficiency, ranging between 11% and 36%.

The effects of the lower efficiency of the centrifugal pump can be observed also in its energy absorbed over the WLTC (Figure 5-18). This pump absorbs 131 kJ at the end of the cycle, whereas the triple-screw pump absorbs 103 kJ, i.e. about 21% less energy.

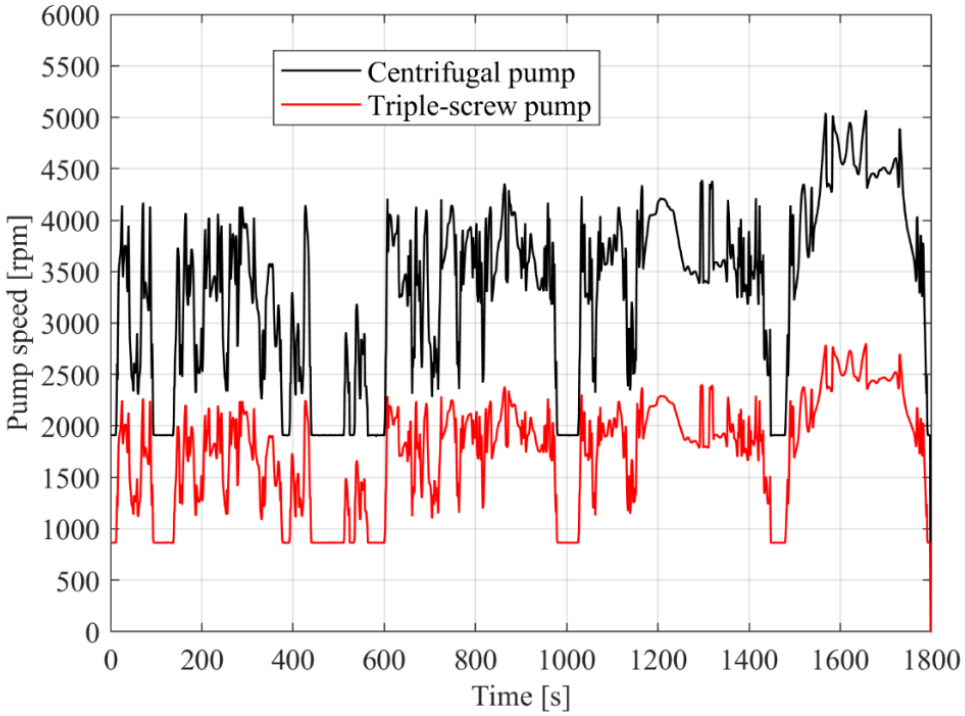

Figure 5-16. Speed profiles of the prototyped centrifugal and triple-screw pumps over a WLTC class 3b.

This energy reduction is due to intrinsic differences between the two pumps, which let the triple-screw pump to be more efficient over a WLTC compared to the centrifugal one, despite having optimized both on the same design point. In fact, the triple-screw pump belongs to the category of volumetric-type machines, which generally have an efficiency slightly variable with the operating point. This attitude is verified also for the one prototyped in this work, which keeps high values of efficiency also when operating far from the design point, for which it has been optimized. On the other hand, centrifugal pump suffers more of operating point variations, operating with a lower mean efficiency over a homologation cycle.

Moreover, these results can be compared with the performances of the OEM centrifugal pump, already evaluated in Section 5.2.3, which showed a sensibly higher energy absorption over the cycle, equal to 264 kJ. This means that the prototyped triple-screw pump enables a 61% energy saving, whereas the prototyped centrifugal pump a 50% one. This strong energy improvement achieved with both pumps is the result of the deep optimization process followed to design them through the model-based design approach presented in Section 5.3.1.

Hence, the use of the triple-screw pump instead of the centrifugal pump could contribute significantly in reducing the CO_2 emissions of the vehicle. To estimate this reduction, the mean brake efficiency of the ICE over the WLTC must be known. This requires several assumptions

on the specific vehicle application, because the engine operating point depends on the vehicle dynamics through the specific transmission system layout.

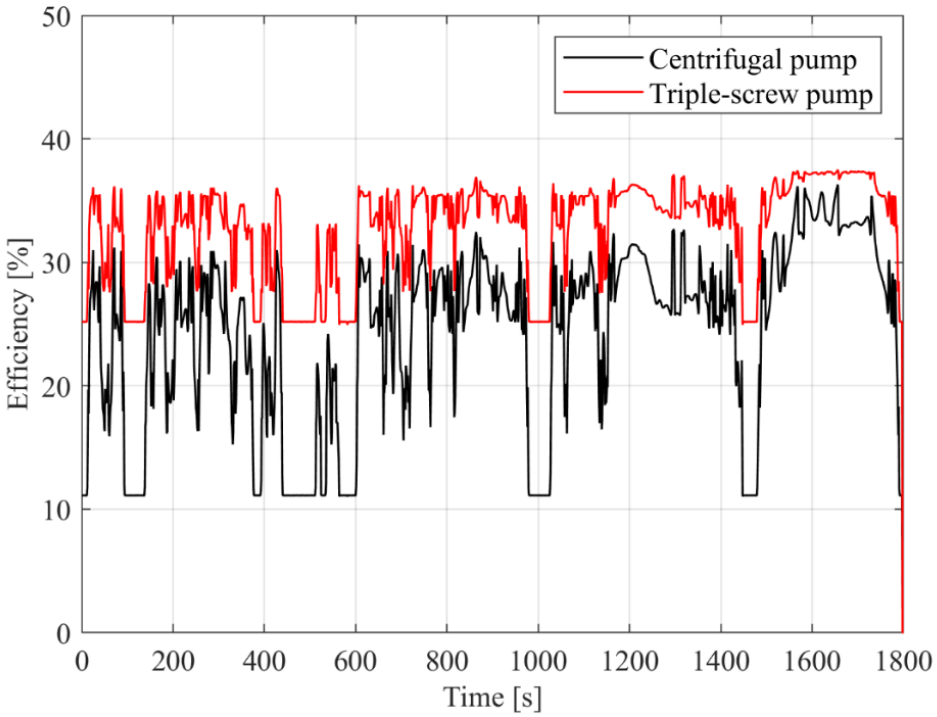

Figure 5-17. Efficiency of the prototyped centrifugal and triple-screw pumps over a WLTC.

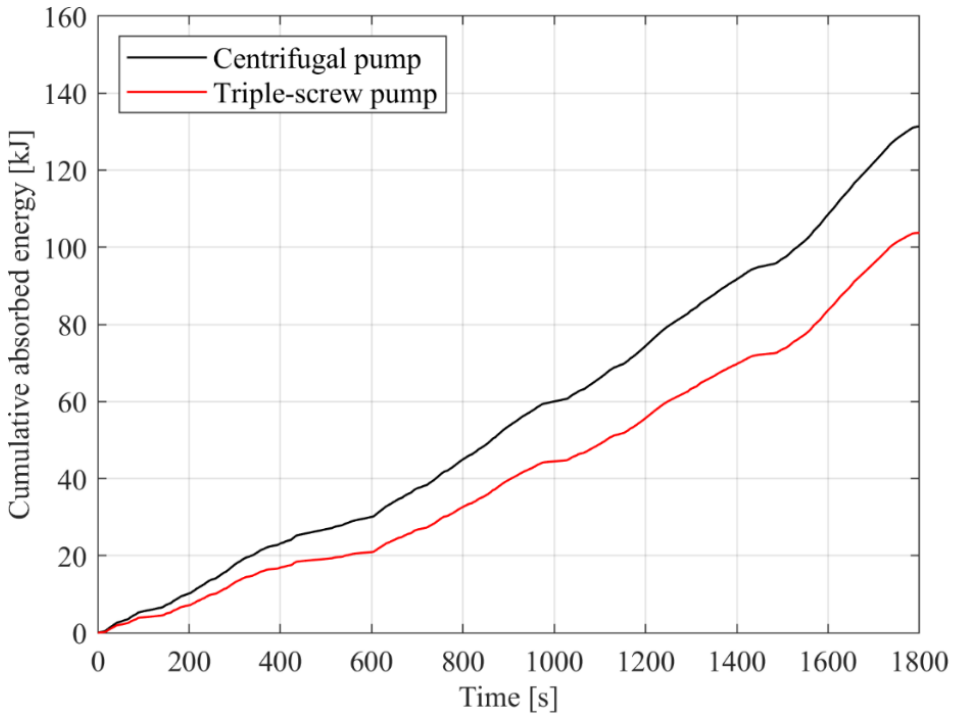

Figure 5-18. Overall energy absorbed by the prototyped centrifugal and triple-screw pumps over a WLTC.

To this end, a mean brake efficiency of the engine equal to 30% has been assumed, considering the numerical results of a similar-sized gasoline engine equipped on a small passenger vehicle tested over a WLTC [217]. Moreover, typical values for the thermo-physical properties of gasoline, as well as an emission factor equal to 3.14 $kg_{CO2}/kg_{gasoline}$ [266], have been considered. Being known the specifications in terms of total distance and duration of the WLTP Class-3b cycle (with $v_{max} \geq 120$ km/h), CO_2 emissions savings obtained through the prototyped pumps have been compared with those obtained with the OEM centrifugal pump.

Considering 16.03 km/l as fuel consumption over the WLTC, this specific vehicle determines about 156.7 g/km of CO_2 emissions, the 1.73% of which (i.e. 2.71 g/km) is due to the energy absorbed by the OEM centrifugal pump.

By knowing the energy absorbed by the prototyped pumps over the cycle (Figure 5-18), the corresponding CO_2 emissions can be calculated considering this engine example. These values are 1.06 g/km and 1.34 g/km for the prototyped triple-screw and centrifugal pump, respectively.

Therefore, the use of the prototyped triple-screw pump instead of the OEM pump allows to reduce CO_2 emissions over the WLTC by 1.05% (i.e. 1.64 g/km in absolute terms), whereas the prototyped centrifugal pump reduces them by 0.87% (i.e. 1.36 g/km). Consequently, the triple-screw pump prototyped in this work appears to be the most efficient solution for engine cooling, allowing to further reduce CO_2 emissions by 0.28 g/km compared with the prototyped centrifugal pump, optimized for the same application.

These results are significant if the choice of the cooling pump technology is considered important to insure the CO_2 emission limits. In fact, the severe fines imposed in Europe for each gram exceeding the limit (95 Euro/g_{CO2}) redefine the environmental value of the component.

5.4 Conclusions

In this Chapter, the main design criteria optimizing the performances of triple-screw pumps for engine cooling applications have been identified through a model-based design approach.

To this end, firstly the potential benefits in reducing the energy spent to cool the engine have been evaluated theoretically. Considering a light-duty application, a screw pump allows a 13.8% energy saving over a homologation cycle, compared with a standard centrifugal pump.

Hence, the design criteria optimizing the screw pumps' efficiency have been investigated. It was found that the efficiency can be maximized by adopting a low design speed with a finger shaped geometry and the proportions of the 5-3-1 series, compatibly with the size constraints given by the specific on-board application. In this way, an optimized triple-screw pump has been designed for a specific engine, and its performances compared theoretically with those of the OEM centrifugal pump over a homologation cycle. The energy spent to cool the engine reduced by 56.5%, which on turn reduced CO_2 emissions by about 2.08 g_{CO2}/km.

These encouraging results suggested to build a physical prototype of the pump. This prototype was characterized experimentally, and its performances were compared with those of

a centrifugal pump optimized for the same design point. The experimental results confirmed the effectiveness of screw pumps to reduce the energy spent to cool the engine (-21%), as well as CO_2 emissions (-0.28 g_{CO2}/km), even respect to an equally optimized centrifugal counterpart.

The prototyped triple-screw pump introduces several construction features, which improve significantly the pump durability and reliability. The adjustments involve mainly an innovative idler screws' axis support, designed to reduce friction, wear and vibration phenomena during pump operation. The next Chapter 6 will be dedicated to the discussion of the effects introduced by this new screws' support on the pump performances through a suitably redefined mathematical modeling. Moreover, an experimental analysis on the indicated cycle of this pump will be presented in Chapter 7, in order to deeply investigate the complex fluid dynamic phenomena taking place inside this type of machine during the pumping process.

6 Model refining for optimized screw pumps

6.1 Improved modeling for performance prediction

A comprehensive mathematical model of a triple-screw pump has already been developed in Chapter 4. That pump had a simple layout, with the idler screws simply entrained inside cylindrical supports, without any bearing fixing their axis. This design architecture was chosen to fulfill simplicity criteria generally requested by automotive manufacturers, typically oriented towards reliable and low-cost solutions. However, it required a suitable modeling of the friction phenomena occurring between idler screws and pump case (Section 4.3.3), which enabled a first study on the model-based design of triple-screw pumps for automotive engine cooling (Section 5.2).

In this Chapter, that mathematical model has been refined to predict more accurately the performance of the triple-screw pump proposed in Section 5.3. Specifically, the volumetric and the mechanical sub-models have been suitably modified to catch blow-hole backflows, as well as reduced friction phenomena induced by the specific layout of the proposed pump.

The block diagram of that mathematical model has been reported in Figure 6-1, where the blue boxes identify the sections of the model that have been refined. They can be summarized as follows:

1. Backflow modeling: the contribution to the backflow due to the blow-hole area has been modeled in detail, considering the screws geometry of the prototyped triple-screw pump.
2. Friction modeling: the friction phenomena acting on the screws have been modeled considering the effects of the bearings supporting the idler screws' axes, introduced in this prototype. Moreover, the power losses induced by the pump sealings and bearings have been calibrated experimentally, due to the lack of manufacturer's data on the power absorbed by these elements.

Hereafter, each of these refinements will be described in detail in Section 6.1.1 and Section 6.1.2, respectively.

It is worth noticing that this modeling improvement does not invalidate the previous model presented in Chapter 4. Instead, it represents its logical development towards a more complex pump layout, for which some simplifying hypotheses previously assumed (as the negligible blow-hole backflow) can no longer be applied. Thus, the hereby proposed mathematical model can predict the performances of an even broader spectrum of screw pumps layouts.

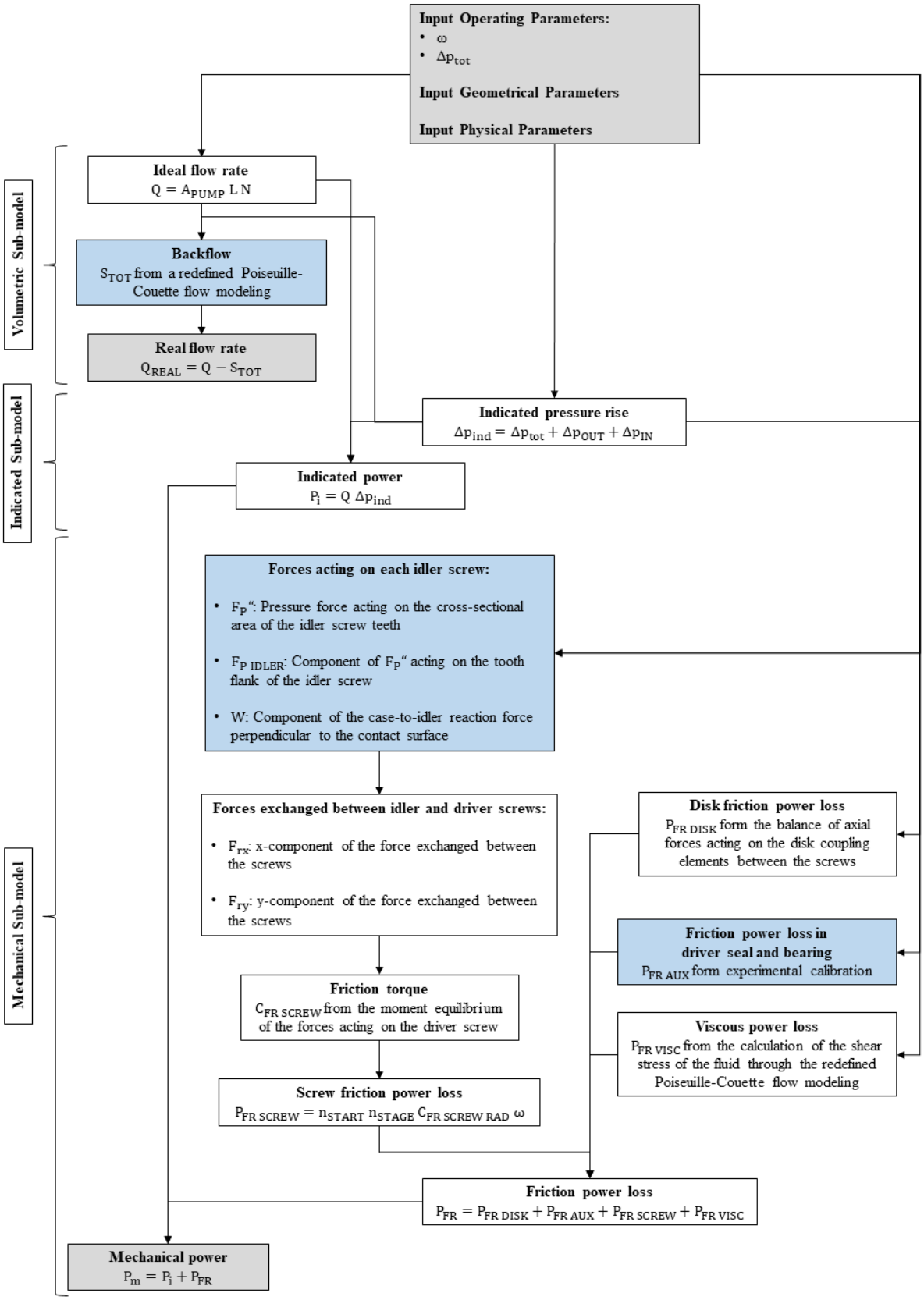

Figure 6-1. Block diagram of the mathematical model of the triple-screw pump developed in Chapter 4. The gray boxes identify input and output parameters. The blue boxes identify the sections of the model refined in the present Chapter.

6.1.1 Backflow modeling

The existence of clearances between driver and idler screws, as well as between each screw and the pump case, determine a backflow occurring during nominal operation, which negatively affects the volumetric efficiency of the pump. Therefore, the flow rate delivered by the pump Q_{REAL} is lower than the ideal flow rate Q of an amount equal to the backflow S_{TOT} (Eq. 4-3). The backflow S_{TOT} can be divided into three contributions, depending on the flow area through which they occur (Eq. 4-4):

- the backflow between the driver-screw tooth tips and the pump case (S_{DRIVER});
- the backflow between the idler-screw tooth tips and the pump case (S_{IDLER});
- the backflow through the blow-hole area, i.e. between driver and idler screws ($S_{DR/IDL}$).

In the mathematical model developed in Section 4.2.1, the overall backflow S_{TOT} was calculated considering only the effects of the backflows between the screws tooth tips and the pump case (S_{DRIVER} and S_{IDLER}), while neglecting the effects of the backflow through the blow-hole area ($S_{DR/IDL}$). This hypothesis was adopted due to the assumption that this latter contribution is smaller than the first ones as long as the flow area is sufficiently high.

However, the backflow through the blow-hole area always exists in screw-type machines, and therefore it needs to be modeled to calculate properly the backflow also for small-size triple-screw pumps.

Thus, in this Chapter, the backflow $S_{DR/IDL}$ occurring through the blow-hole area has been analyzed in detail, while the backflows S_{DRIVER} and S_{IDLER} have been calculated through the redefined Poiseuille-Couette flow modeling already presented in Section 4.2.1.

Before introducing the backflow occurring between driver and idler screws, the blow-hole pathways existing inside the pump need to be identified. These pathways exist due to geometrical features, assembly needs and manufacturing imperfections intrinsic to the specific machine. In fact, ideally, a triple-screw pump would have the following features:

- driver and idler screws, as well as pump case, with sharp edges without manufacturing imperfections;
- driver and idler screws perfectly coupled inside their housing in the pump case, without any clearance or assembly error;
- the driver screw giving the motion to the idler screws through an ideal and continuous contact line, without forming clearances or contact interruptions.

Instead, in reality a triple-screw pump deviates from the ideal case due to the following aspects:

- driver and idler screws need to have blunt edges to reduce friction phenomena occurring during rotation; moreover, also the pump case has blunt edges due to manufacturing imperfections;

- driver and idler screws are not perfectly coupled inside their housing in the pump case, determining clearances between each screw and the pump case;
- the contact between the screws is not a continuous ideal line, but a discontinuous area which allows clearances between the screws themselves.

These deviations from the ideal case introduce backflow pathways which depauperate the flow rate actually delivered by the pump. The backflows occurring between the screws and the pump case have already been modeled in Section 4.2.1, and they represent the main contribution to the overall backflow. However, some backflows occur also in the blow-hole pathways existing between the screws.

In this analysis, three blow-hole pathways have been identified (Figure 6-2). They can be observed considering the axial section A-A (Figure 6-2 (b)) located in a region of the blunt edges of the pump case, as represented in Figure 6-2 (a). The existence of a clearance between driver and idler screws determines a blow hole area, BH1, for each idler screw, extended along the screw's axis direction for the whole ideal contact line lying on the idler screw external surface (Figure 6-2 (b)). Moreover, the blunt edges of driver and idler screws, as well as those of the pump case, determine four symmetrical small blow-hole areas, BH2: among them, the one lying in section A-A is represented in section B-B (Figure 6-2 (c)). Finally, the blunt edges of the rear disk-shaped coupling elements and of the pump case determine other four symmetrical small blow-hole areas, BH3: among them, the one lying in section A-A is represented in section C-C (Figure 6-2 (d)).

Thus, the backflow $S_{DR/IDL}$ has been calculated as the sum of three contributions (Eq. 6-1), each of which flows through the corresponding blow-hole areas represented in Figure 6-2.

$$S_{DR/IDL} = S_{BH1} + S_{BH2} + S_{BH3} \quad \text{Eq. 6-1}$$

Basically, each of these backflows has been calculated as the product between the blow-hole area and the speed of the fluid flowing through it. This latter has been calculated assuming an ideal expansion of the fluid, which spontaneously flows backwards through the blow-hole according with the pressure gradient inside the pump.

As shown in Figure 6-2 (b), the backflow S_{BH1} occurs through the blow-hole area BH1 determined by the clearance $\delta_{DR/IDL}$ existing between the driver screw and each of the two side idler screws. This backflow has been calculated by multiplying together the number of idler screws n_{IDLER}, the blow-hole area A_{BH1}, and the speed u_1 of the fluid flowing through it (Eq. 6-2).

$$S_{BH1} = n_{IDLER}\, A_{BH1}\, u_1 \quad \text{Eq. 6-2}$$

$$A_{BH1} = P_{IDLER}\, \delta_{DR/IDL} \quad \text{Eq. 6-3}$$

$$u_1 = \sqrt{\frac{2\,\Delta p_{IND}}{\rho}} \qquad \text{Eq. 6-4}$$

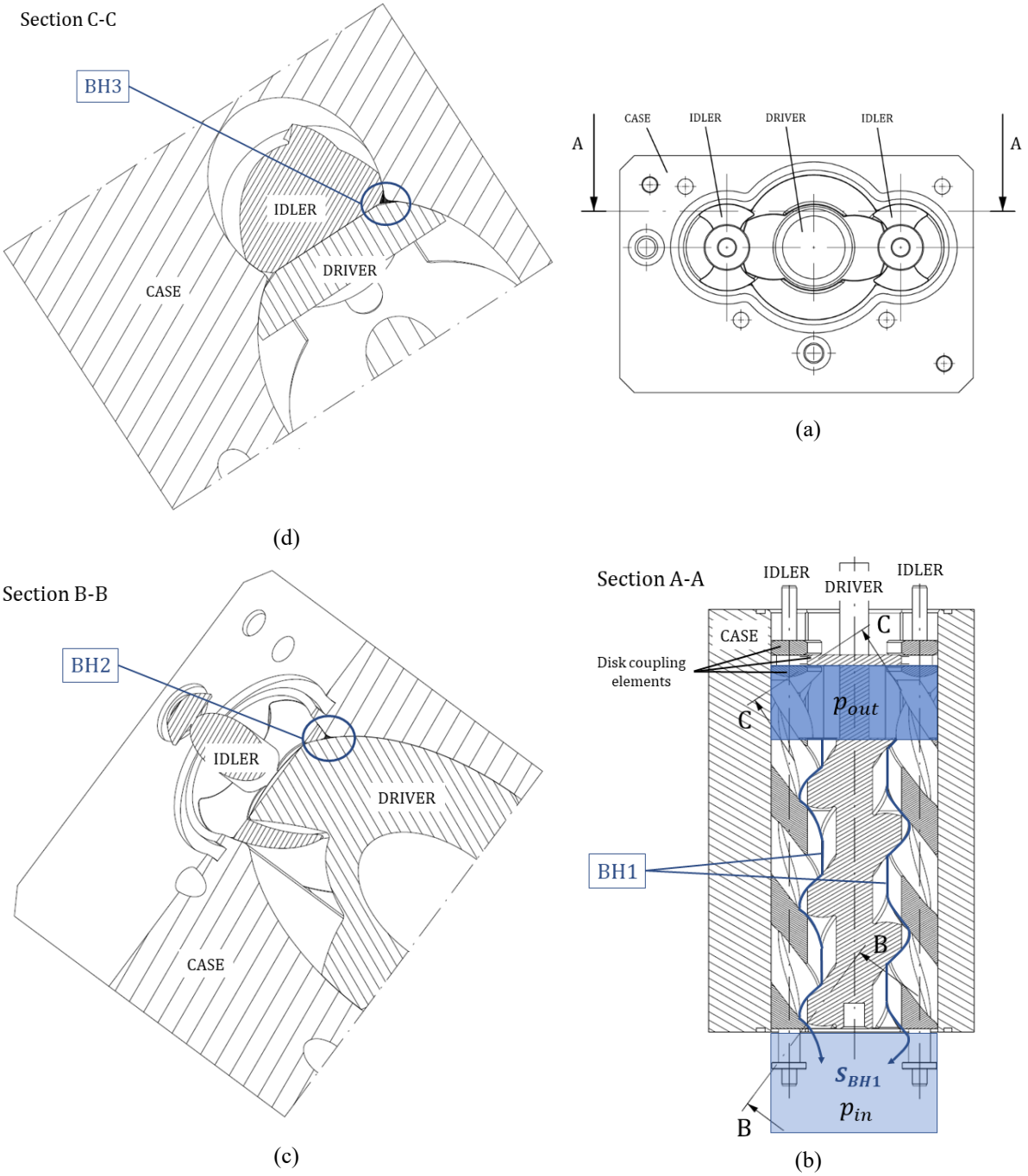

Figure 6-2. Blow-hole pathways between the screws. Considering section A-A as positioned in the frontal view of the pump (a), there are: the BH1 path, between driver and idler screws (b); the BH2 path, through the blunt edges of the screws and the pump case (c); the BH3 path, through the blunt edges of the rear disk-shaped coupling elements and the pump case (d).

The blow-hole area A_{BH1} can be obtained by multiplying the perimeter of the idler screw P_{IDLER} by the clearance $\delta_{DR/IDL}$ between driver and idler (Eq. 6-3). This assumption is justified by the fact that, during a complete revolution of the screws, the ideal contact point between

driver and idler runs along the entire perimeter of the cross section of each idler screw. Therefore, the existence of a clearance between driver and idler screws determines a blow-hole area in the screws cross section, which is assumed to be approximately equal to the perimeter of the idler screw P_{IDLER} multiplied by the clearance between driver and idler $\delta_{DR/IDL}$. The perimeter P_{IDLER} is calculated analytically through the geometrical equations summarized in Appendix B.

Moreover, the fluid speed u_1 has been calculated through Eq. 6-4, considering the entire pressure difference Δp_{IND} existing between discharge and suction chambers, which are directly connected through the BH1 path (Figure 6-2 (b)), and the constant density ρ of the incompressible fluid.

The overall blow-hole backflow $S_{DR/IDL}$ is determined also by the remaining two contributions, S_{BH2} and S_{BH3}. The backflow S_{BH2} occurs through the blow-hole area BH2 enclosed between the blunt edges of the screws and those of the pump case (Figure 6-2 (c)). It has been calculated by multiplying together the number of these holes n_{BH2}, their area A_{BH2} and the speed u_2 of the fluid flowing through them (Eq. 6-5).

$$S_{BH2} = n_{BH2}\, A_{BH2}\, u_2 \qquad \text{Eq. 6-5}$$

$$u_2 = \sqrt{\frac{2\,\Delta p_i}{\rho}} \qquad \text{Eq. 6-6}$$

$$\Delta p_i = \frac{\Delta p_{ind}}{n_{CHAMBERS} + 1} \qquad \text{Eq. 6-7}$$

The blow-hole area A_{BH2} is determined by the degree of the edge blunting. It has been estimated as a percentage of the flow area, resulting approximately equal to the 0.06% of it for the triple-screw pump prototyped in this work (Section 5.3.2).

The fluid speed u_2 has been calculated assuming an ideal fluid expansion through the blow-hole BH2 (Eq. 6-6). In this case, the fluid flows according to the i^{th} chamber-to-chamber pressure drop Δp_i, which can be calculated by knowing the overall pressure difference Δp_{IND} and the number of sealing chambers $n_{CHAMBERS}$ (Eq. 6-7). As an example, in the pump layout represented in Figure 6-2, only one sealing chamber exists, leading to a pressure difference (Δp_i) halved compared to the overall one (Δp_{IND}). Moreover, there are four BH2-type blow-holes (i.e. $n_{BH2} = 4$), which generate and move periodically from suction to discharge chambers as the screws rotate.

Finally, the backflow S_{BH3} occurs through the blow-hole area BH3 enclosed between the blunt edges of the rear disk-shaped coupling elements of the screws, and those of the pump case (Figure 6-2 (d)). Similarly, this backflow can be calculated by multiplying together the number of these holes n_{BH3}, their area A_{BH3} and the speed u_3 of the fluid flowing through them (Eq. 6-8).

$$S_{BH3} = n_{BH3}\, A_{BH3}\, u_3 \qquad \text{Eq. 6-8}$$

$$u_3 = \sqrt{\frac{2\,\Delta p_{BAL}}{\rho}} \qquad \text{Eq. 6-9}$$

In this case, the area A_{BH3} of the four BH3-type blow-holes (i.e. $n_{BH3} = 4$) has been estimated to be approximately equal to the 0.15% of the flow area. Moreover, the fluid speed u_3 has been calculated considering the pressure difference Δp_{BAL} existing between the discharge chamber and the rear balancing chamber. This pressure difference has been verified to be approximately equal to the overall pressure difference Δp_{IND}, being the balancing chamber directly connected to the suction chamber to balance the axial forces acting on the idler screws due to the pressure gradient existing inside the pump (Figure 6-2).

6.1.2 Friction modeling

The triple-screw pump proposed in Section 5.3 introduces some design improvements capable to enhance the efficiency of the pump, as well as its durability. Specifically, the idler screws have been constrained through a bearing support linking their axis with the pump case, instead of simply housing them inside cylindrical supports without any bearing fixing their axis, as usual in simpler pump layouts, as the one considered in Chapter 4. Adding these bearings modifies the friction conditions existing between each idler screw and the pump case, reducing the friction power losses and thus enhancing the pump efficiency, with positive effects also on the pump durability.

Therefore, the mathematical model summarized in Figure 6-1 needs to be refined to predict suitably the mechanical performances of triple-screw pumps adopting idler screws with such bearings supporting their axes.

The overall model includes a mechanical sub-model, which calculates the mechanical power P_m as the sum of the indicated power P_i and the friction power losses P_{FR} (Eq. 4-38).

The friction power losses P_{FR} have been modeled as the sum of four contributions (Eq. 4-37):

- the power losses due to the friction in the disk coupling elements between the screws ($P_{FR\ DISK}$);
- the power losses due to the friction in the driver screw sealing and bearing ($P_{FR\ AUX}$);
- the power losses due to the friction in the contact between driver and idler screws ($P_{FR\ SCREW}$);
- the viscous power losses ($P_{FR\ VISC}$);

As discussed in Section 4.2.3, the mechanical model which allows to determine these contributions is based on a lumped-parameter approach, which calculates the resistant torque acting on the driver screw due to the friction phenomena induced by the pressure gradient

present inside the pump. In fact, the idler screws push towards the driver screw due to the pressure difference existing between discharge and suction chambers, generating friction during the screws' rotation. This resistant torque is calculated through the free body diagrams of idlers and driver screws, involving friction coefficients for the main contact zones existing between the relative-rotating parts of the pump. The contact zones identified within this model are (Figure 6-2):

- between the disk coupling elements of the screws;
- between the screws, along their ideal contact line;
- between the idler screws and their radial support.

The contact between idler screws and pump case depends on the type of technical solution used for fixing their axis, which determines also the forces acting on each idler screw, and thus the resistant torque acting on the driver screw due to friction.

In this Chapter, the free-body diagram of the idler screws has been adjusted to the new pump layout, to consider the effects of the bearings supporting their axis. Moreover, following the approach adopted in Section 4.3.2, the friction coefficients defined in the model have been calibrated to minimize the overall absolute mean error in the mechanical power calculation. Similarly, the power losses due to the pump sealings and bearings ($P_{FR\ AUX}$) has been calibrated considering the power absorbed by the pump at low pressure head.

The free body diagram of the idler screw is reported in Figure 6-3 (a). It differs from the one presented in Figure 4-4 (a) for the support reaction acting on the idler screw at point A. In fact, this point is now positioned in the contact zone between the idler screw and the bearings supporting its axis, whereas, without these bearings, point A was located between the idler screw tooth tip and the pump case. Thus, the dynamic balance of the idler screw is now expressed by Eq. 6-10, Eq. 6-11 and Eq. 6-12, where b_3 is the lever arm (Eq. 6-13) of the y-component of the driver-to-idler reaction force F_{ry} (Figure 6-3).

$$F_{rx} = f_{STAT}\, W \qquad \text{Eq. 6-10}$$

$$F_{ry} = W - F_{P\ IDLER} - m_{IDLER}\, g \qquad \text{Eq. 6-11}$$

$$W = \frac{F_{P\ IDLER}\,(b_3 + b_{IDLER}) + m_{IDLER}\, g\, b_3}{\left(b_3 - f_{STAT}\, r_{supp} - f_{STAT}\, b_2\right)} \qquad \text{Eq. 6-12}$$

$$b_3 = (R_1 + r_2) - R_1\, cos\frac{\alpha}{2} \qquad \text{Eq. 6-13}$$

These equations are obtained considering the effect of the pressure force $F_{P\ IDLER}$ on the idler tooth profile, which is balanced through the reactions carried out by the driver screw (F_{rx} and F_{ry}) and the idler axis support (W). The pressure force $F_{P\ IDLER}$ is obtained through simple geometrical considerations from the axial force F_P'' acting on the idler tooth profiles due to the pressure gradient existing inside the pump (Figure 4-4 (c)).

The reactions exchanged between the screws (F_{rx} and F_{ry}) can be considered also under the free body diagram of the driver screw (Figure 6-3 (b)), which allows to express the friction torque $C_{FR\ SCREW}$ and the corresponding power losses $P_{FR\ SCREW}$ as already seen in Section 4.2.3 (Eq. 4-33 and Eq. 4-34, respectively).

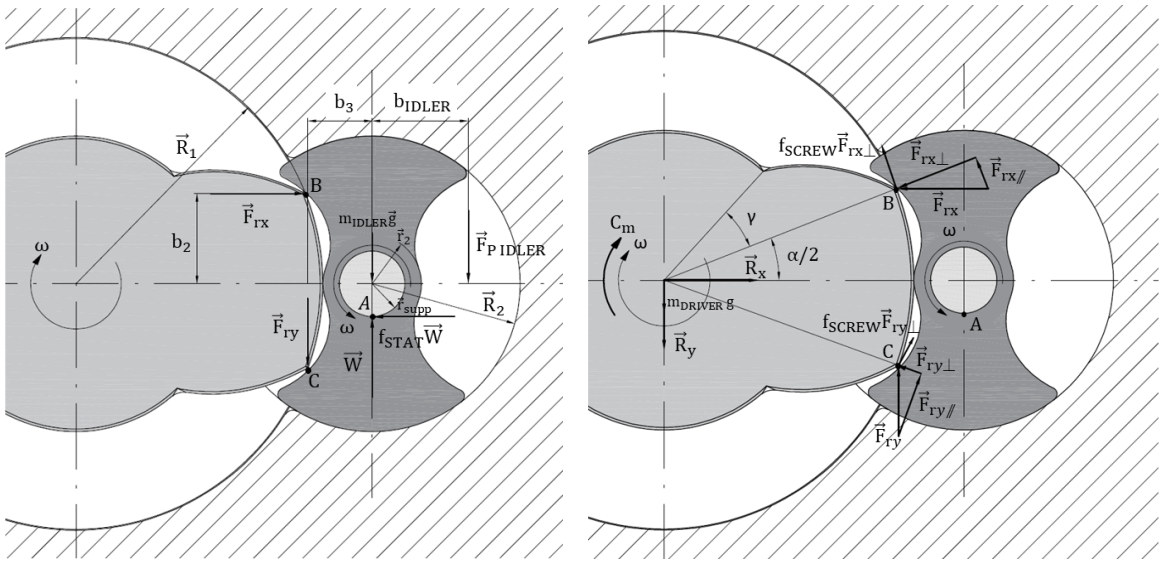

(a) (b)

Figure 6-3. Free body diagram of the right idler (a) and driver (b) screws of the prototyped triple-screw pump.

Once updated the dynamic model of the screws, the other power losses contributions ($P_{FR\ VISC}$, $P_{FR\ DISK}$ and $P_{FR\ AUX}$) can be calculated through the same equations used in Section 4.2.3 (Eq. 4-23, Eq. 4-35 and Eq. 4-36, respectively), because the new pump layout with bearings supporting the idlers axes does not affect that modeling approach. However, the friction coefficients describing the contact conditions between the screws (f_{SCREW} and f_{DISK}), and between the idler screws and their support (f_{STAT}), as well as the power absorbed by the auxiliaries ($P_{FR\ AUX}$), need to be calibrated experimentally to suitably represent the specificity of the new pump layout. In fact, materials, surface quality and lubricating conditions of the specific application affect these parameters. The results of this calibration activity and the experimental validation of the model will be described in the next Section.

6.2 Experimental validation

The mathematical model presented in Section 6.1 needs to be calibrated prior to be validated. In fact, the friction phenomena between its relative-rotating components depend strictly on the lubricating conditions allowed by the specific application.

Therefore, the friction coefficients introduced in the mechanical sub-model (f_{SCREW}, f_{DISK} and f_{STAT}) and the power absorbed by the auxiliaries ($P_{FR\ AUX}$) have been calibrated experimentally, following the approach presented in Section 4.3.2.

Specifically, to determine the friction coefficients, an acceptable range of values (0.01-0.2) for this type of application was assumed. This range deals with a steel-steel contact condition with a water-glycol mixture as lubrication fluid, which is the type of contact realized between the screws themselves, and between them and their support.

Thus, by knowing the experimental performance of the prototyped triple-screw pump (Section 5.3.2), the friction coefficients have been varied within this range to minimize the overall absolute mean error in the mechanical power calculation. In this way, 0.047 for all the friction coefficients was found.

Similarly, the power losses due to the driver screw sealing and bearing ($P_{FR\ AUX}$) have been calibrated experimentally. To this end, the pump was tested when operating at low pressure heads. In these conditions, the main contribution to friction losses is represented by $P_{FR\ AUX}$, whereas the other contributions ($P_{FR\ VISC}$, $P_{FR\ SCREW}$, $P_{FR\ DISK}$) can be considered negligible due to the low pressure difference across the pump (Eq. 4-37). Therefore, the friction power losses have been calculated by subtracting the indicated power, calculated through the model (Figure 6-1), to the mechanical power, measured directly through the torque meter (Eq. 4-38). The results showed a parabolic relation with the pump speed, as expected theoretically by Eq. 4-36. This relation can be suitably approximated assuming a equal to $9.3 \cdot 10^{-6}$ and b equal to $-5.1 \cdot 10^{-3}$, whereas c is negligible in this case.

Once calibrated, the mathematical model has been validated experimentally. To this end, the prototyped pump was tested through the experimental test bench described in Section 4.3.1 over a wide range of operating conditions. Specifically, the pump speed was varied from 1000 to 4000 rpm, where the maximum flow rate of 90 l/min was delivered, absorbing up to 1100 W at 5.5 bar as pressure head.

These operating points have been considered to validate the model developed in Section 6.1. It uses pump speed and pressure head as input parameters, returning as outputs, among the others, flow rate and mechanical power. The results are summarized from Figure 6-4 to Figure 6-7.

The model shows a good matching with the experimental results. In Figure 6-4, both the experimental and modeled performance maps in terms of pressure head and flow rate are presented. The curves calculated by the model are substantially overlapped on the experimental points, and the flow rate is predicted with an average error equal to 1.9%.

It is worth noting that, at low pressure heads, the experimental results show a nonlinear relationship between the pressure difference across the pump and flow rate. This is due to the backflow occurring through the blow-hole passages ($S_{DR/IDL}$), which is predominant on the other backflow contributions (S_{DRIVER} and S_{IDLER}) at low pressure heads. This behavior is well reproduced by the model, which gives also an analytical understanding of such nonlinearity. In fact, the square root relation of $S_{DR/IDL}$ with the pressure difference (Eq. 6-4) prevails on the linear relation of S_{DRIVER} and S_{IDLER} (Eq. 4-10) at these low head operating points. In addition, among the blow-hole backflow components, the one occurring through BH1 prevails on the

others (Figure 6-2), meaning that clearances between the screws should be carefully managed if good volumetric performances want to be achieved also with poor pressure heads.

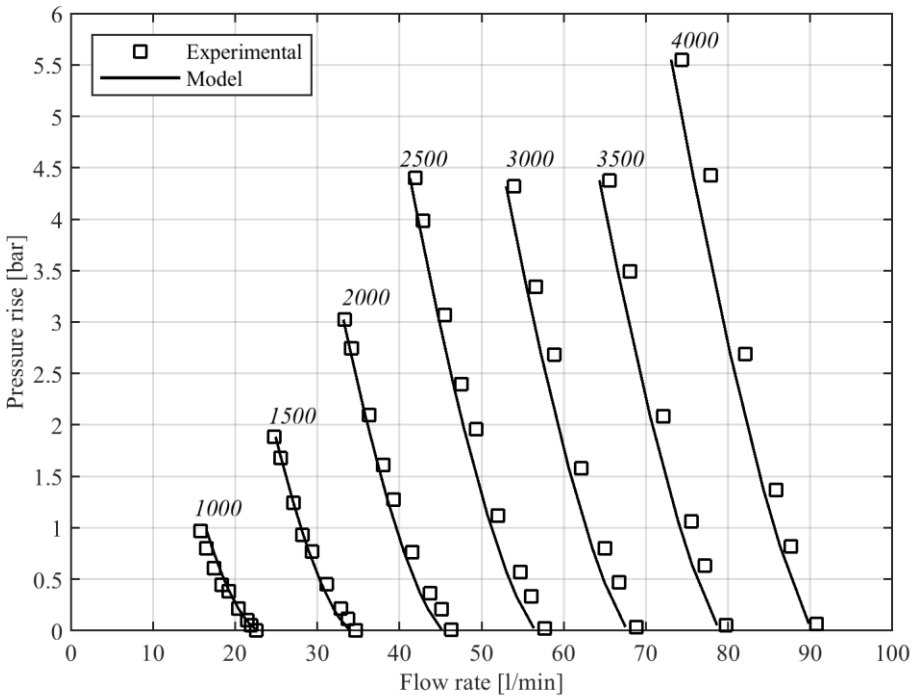

Figure 6-4. Performance map of the prototyped triple-screw pump, in terms of pressure rise VS flow rate. The continuous lines are calculated by the model, whereas the points are the experimental values. The pump speed was varied from 1000 to 4000 rpm.

Similarly, the mechanical power is predicted by the model with a good accuracy. Figure 6-5 shows experimental and model results of the mechanical power as a function of flow rate for different pump speeds. The curves calculated by the model are substantially overlapped on the experimental points, and the mechanical power is predicted with a mean error equal to 3.5%. Also in this case, the experimental mechanical power shows a nonlinear dependency with the flow rate at low pressure heads. This is related to the contribution of the blow-hole backflow on the overall one, and thus on the actual flow rate (Eq. 4-3), which in turn impacts the mechanical power required by the machine (Eq. 4-17, Eq. 4-38).

The reliability of the model to predict the performances of the prototyped pump can be observed also in Figure 6-6. The global efficiencies calculated by the model are substantially aligned with those calculated using the experimental data, with a mean error equal to 5.2%. In addition, the points are thickened towards the best efficiency point of the pump, which is about 63%. This aspect can be observed more clearly in Figure 6-7, where experimental and modeled global efficiencies are reported as a function of pressure rise and pump speed.

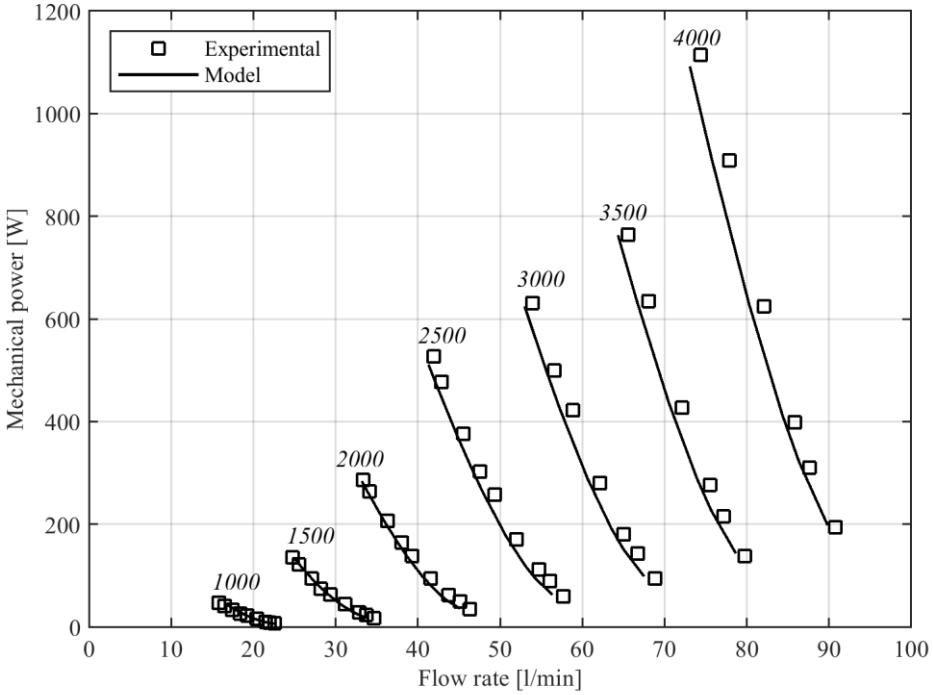

Figure 6-5. Performance map of the prototyped triple-screw pump, in terms of mechanical power VS flow rate. The continuous lines are calculated by the model, whereas the points are the experimental values. The pump speed was varied from 1000 to 4000 rpm.

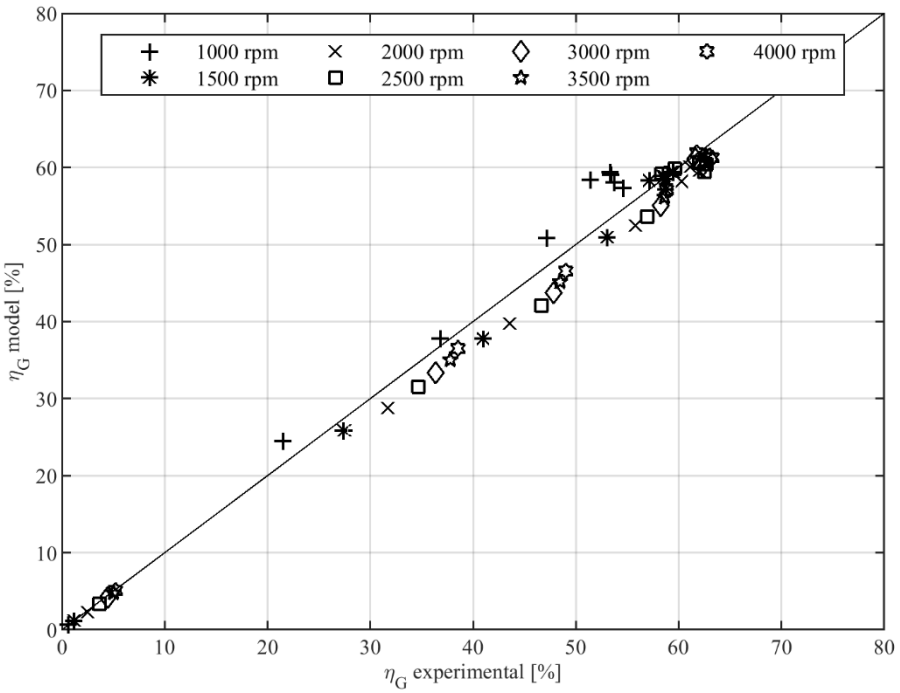

Figure 6-6. Global efficiency of the prototyped triple-screw pump calculated by the model and from the experimental data.

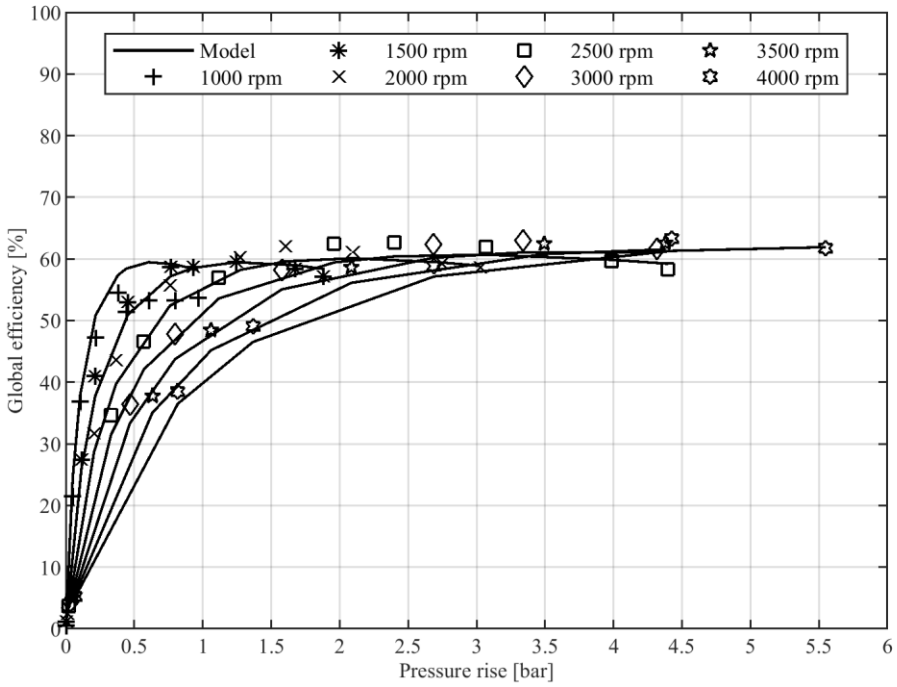

Figure 6-7. Global efficiency as a function of pressure rise and pump speed. The continuous lines are calculated by the model, whereas the points are the experimental values. The pump speed was varied from 1000 to 4000 rpm.

Distinctly, the pump can operate with high efficiencies close to the maximum value (about 63%) for a wide range of pressure heads (from 0.5 to 5.5 bar). Moreover, the slower is the pump speed, the faster the efficiency reaches its maximum, i.e. with lower pressure heads.

Generally, these results agree with those found when studying the triple-screw pump with the simpler layout (Chapter 4). However, slight variations can be observed when comparing together Figure 6-7 and Figure 4-14. In fact, the prototyped pump keeps the efficiency high for a wider range of operating conditions, although with a lower maximum value. Specifically, it has an efficiency equal to 60% already at 0.5 bar and 1000 rpm, whereas the simpler-layout pump efficiency does not exceed 50% at the same operating point, and reaches 60% only when overcoming 1 bar. On the other hand, the prototyped pump efficiency reaches 63% at most, against the 70% achieved by the simpler-layout pump.

These results can be understood if the design criteria followed to develop the triple-screw pump in Chapter 5 are considered. In fact, this pump was designed to operate in the cooling system of an ICE, which typically imposes low pressure heads on the pump, due to the early opening of the thermostat valve and the low power operation during the warm-up phase. Therefore, a steadier efficiency of the pump has been preferred over a very high peak value, which is almost never reached in an engine cooling application.

Finally, it is worth remarking that the experimental validation discussed in this Section reinforces the model robustness to predict even the performances of small displacement triple-

screw pumps. In fact, for what concerns the volumetric sub-model, it includes the modeling of the blow-hole backflows, which were neglected in the previous model discussed in Chapter 4. That assumption was justified by the higher size of the pump considered for the experimental validation of that model. The higher pump displacement allowed to validate the model even if neglecting the blow-hole backflow, due to its relatively small impact on the overall backflow compared to that of the other two contributions, i.e. those occurring between the screws and the pump case. However, that assumption still represents a good approximation for high displacement screw pumps, as those required in the engine cooling system of a heavy-duty vehicle.

Similarly, also the refined modeling of the idler screws' axis support turned out to be validated by the experimental results. This allows to expand the applicability of the model on a wider range of screw pump layouts, benefiting the generality of the model.

6.3 Performance analysis

The availability of a comprehensive fully validated model allows to study more deeply the effects of the pump operating point on its efficiency. In fact, thanks to the model, the analysis can be extended also to critical working points, difficult to measure experimentally. Even if they are far to be experienced by the pump in a typical engine cooling application, their investigation can help to understand which are the main physical phenomena influencing each component of the pump efficiency. This is important also to find out if any further technological improvements still exist.

To this end, the efficiency of the triple-screw pump prototyped in Section 5.3 has been calculated through the model on a wide range of operating conditions. Specifically, two pump speeds (1000-4000 rpm) and two pressure heads (1-5 bar) have been considered as extreme operating boundaries. Among them, the global efficiency (η_g) and its sub-components, i.e. the volumetric (η_v), indicated (η_i) and mechanical (η_m) efficiencies, have been calculated thorough the model validated in Section 6.2. The results are presented in Figure 6-8 and Figure 6-9.

The efficiencies of the pump as a function of pressure head have been reported for two rotational speeds, 1000 rpm and 4000 rpm, in Figure 6-8 (a) and Figure 6-8 (b) respectively. Generally, for a given pump speed, an increase of the pressure head determines a decrease of the volumetric efficiency (η_v), but an increase of the indicated (η_i) and mechanical (η_m) efficiencies. These trends can be explained considering both the mathematical model and the physical phenomena occurring inside the pump. In fact, a higher pressure difference across the screws produces a higher backflow (Eq. 4-10, Eq. 6-4, Eq. 6-6, Eq. 6-9), diminishing the flow rate actually delivered by the pump, and thus its volumetric efficiency. On the other hand, for the same pump speed, the fluid-dynamic losses in the filling and emptying processes of the chambers inside the machine remain unchanged (Eq. 4-18). Therefore, their relative impact on the pressure head becomes less significant if this latter increases, so benefiting the indicated

efficiency. Similarly, the mechanical efficiency increases, because the higher backflow (caused by a higher pressure head) reduces the friction coefficients among relative rotating components (Eq. 4-41), thus lowering the friction power losses.

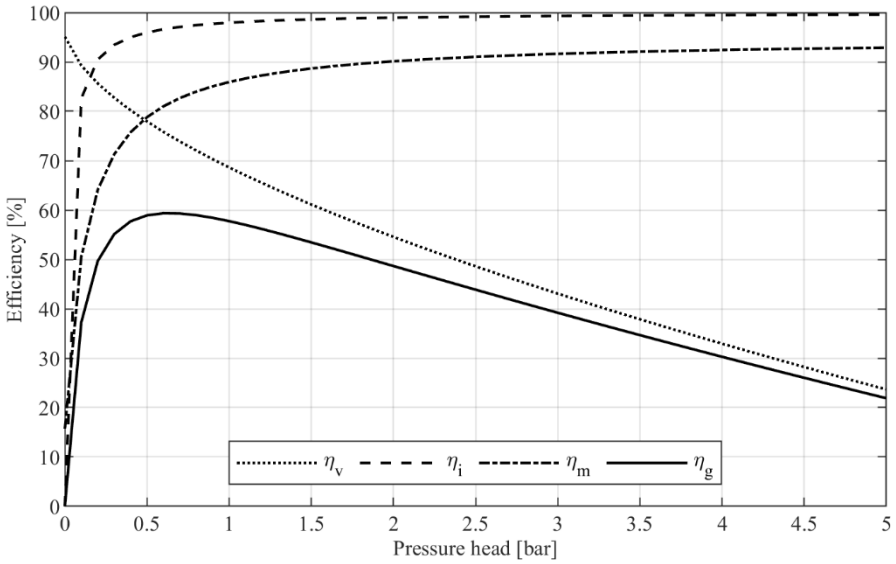

(a)

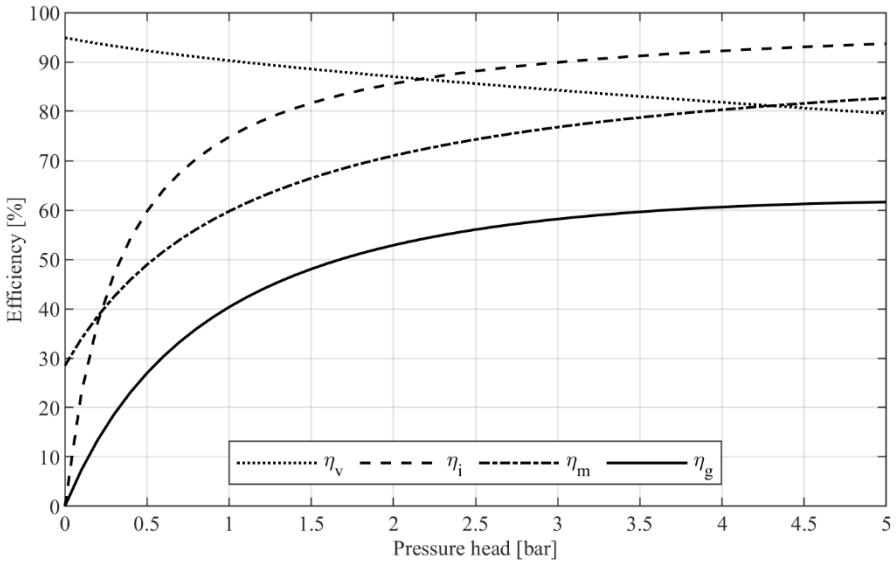

(b)

Figure 6-8. Efficiency of the triple-screw pump as a function of pressure head with pump speed at 1000 rpm (a) and 4000 rpm (b).

As a result, the global efficiency (η_g) has a maximum value, in this case about 60%. Moreover, the higher is the pump speed, the higher is the pressure head corresponding to the best efficiency point. This behavior depends on the balance between the opposite effects of volumetric, indicated and mechanical efficiencies, which have a nonlinear relation with pressure head and pump speed. In fact, in this specific case, the maximum efficiency is reached

at about 0.7 bar when the pump rotates at 1000 rpm (Figure 6-8 (a)), whereas more than 5 bar are needed at 4000 rpm (Figure 6-8 (b)).

A similar trend can be observed when calculating the efficiencies as a function of pump speed, which have been reported for two pressure heads, 1 bar and 5 bar, in Figure 6-9 (a) and Figure 6-9 (b) respectively.

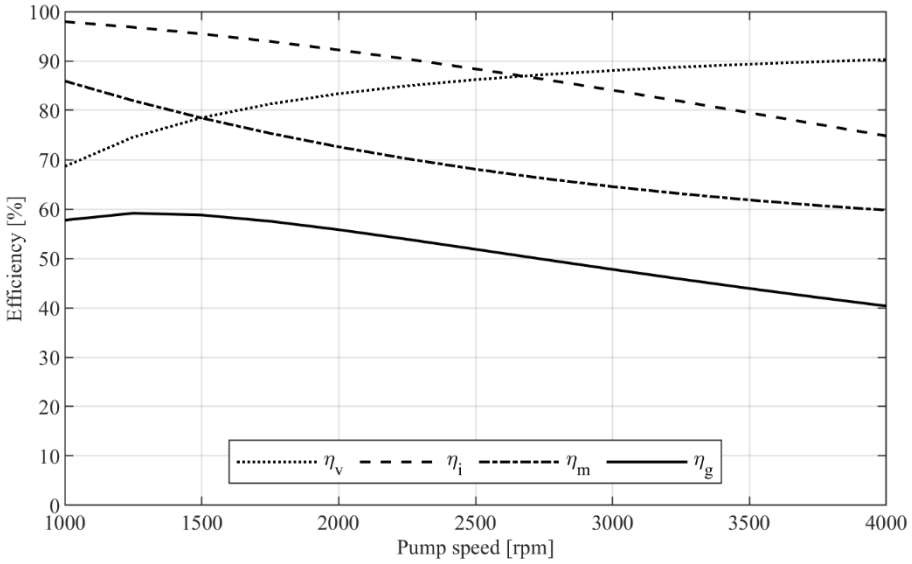

(a)

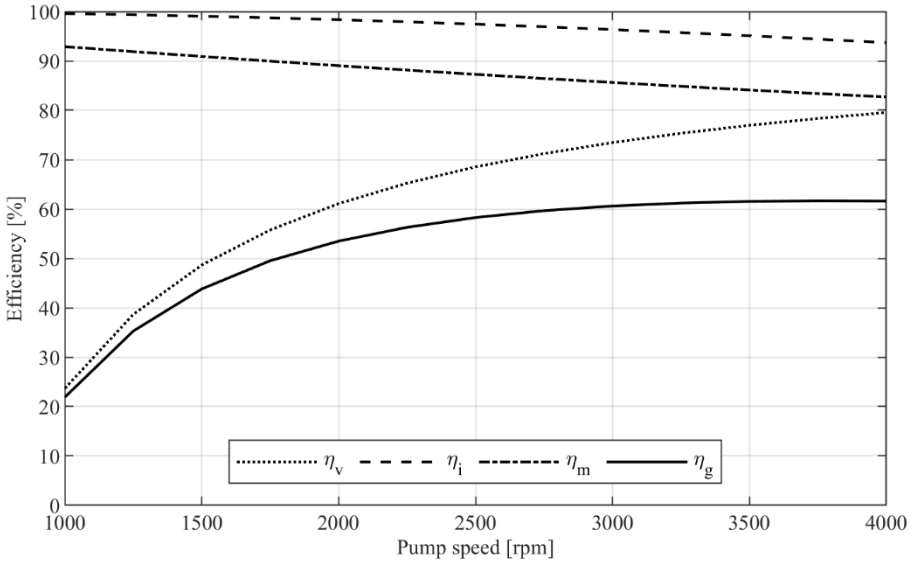

(b)

Figure 6-9. Efficiency of the triple-screw pump as a function of pump speed with a pressure head equal to 1 bar (a) and 5 bar (b).

Generally, for the same pressure head, an increase in the pump speed determines a decrease of the indicated (η_i) and mechanical (η_m) efficiencies, but an improvement of the volumetric efficiency (η_v). In fact, a higher rotational speed imposes a higher fluid velocity, which in turn worsens the fluid-dynamic losses occurring during chambers' filling and emptying, thus

depleting the indicated efficiency (Eq. 4-15, Eq. 4-16). Similarly, also the mechanical efficiency is affected negatively by the rotational speed, which increases directly the friction power losses (Eq. 4-23, Eq. 4-34, Eq. 4-35, Eq. 4-36). Instead, for the same pressure head, the volumetric efficiency improves if the pump speed increases. This happens because the backflow remains substantially unchanged, whereas the ideal flow rate increases, thus mitigating the negative impact of the backflow on the actual flow rate (Eq. 4-1).

Overall, the global efficiency (η_g) has a maximum value also in this analysis. Again, the higher is the pressure head, the more the best efficiency point is shifted towards higher pump speeds. In any cases, the efficiency is almost steady around the maximum value for a significant range of operating points. This is a particularly desired property when highly variable working conditions occur, as happens in a vehicle cooling application. In fact, in an engine cooling system, pressure heads and pump speeds have typically low values, so that the efficiency can remain higher than 50% for a very wide operating range (see Figure 6-9 (a)).

In conclusion, this theoretical analysis on the performances of screws pumps has shown the great advantage of this pump technology, which is to keep a high efficiency even when varying the pump operating point. This is especially true for engine cooling applications, where typical variations in pressure head and pump speed remain within a range that does not depauperate significantly the pump efficiency.

6.4 Conclusions

In this Chapter, the mathematical model developed in Chapter 4 has been refined to predict even the most complex phenomena occurring inside a screw pump during its operation. Specifically, the volumetric sub-model now takes into account also the backflow occurring through the blow-hole area. To this end, the main blow-hole passageways have been identified, and the backflow taking place through them has been calculated with a lumped parameter approach. Moreover, the mechanical sub-model has been suitably modified to predict the friction conditions induced by the innovative idler screw support proposed in the pump prototype. In particular, the free body diagrams of the screws have been adapted to the new construction layout, which has the idler screws' axes supported by dedicated bearings. Moreover, the friction modeling has been simplified, being the new screws arrangement capable to avoid complex dry friction phenomena between the idler screws and the pump case.

In this way, the mathematical model has been validated experimentally. The results show low average errors for the output parameters, which are now equal to 1.9% for the flow rate, and 3.5% for the mechanical power.

Thanks to this comprehensive mathematical model, the performances of the triple-screw pump have been investigated over a wide range of operating conditions. This study confirmed the high stability of the pump efficiency within the pressure heads and pump speeds commonly experienced in an engine cooling application. Moreover, it allowed to quantify the efficiency

of this pump when operating at critical working points, in order to better understand the main physical phenomena influencing each component of the pump efficiency.

The availability of a real prototype allowed also to develop a dedicated experimental campaign to measure the indicated cycle of the pump. Due to the important implications related to this topic, the experimental indicated cycle will be discussed in detail in the next Chapter 7.

7 Indicated cycle analysis

The availability of a screw pump prototype suggested to further investigate experimentally also the indicated cycle of this type of machine. In fact, in Section 4.2.2 a simplified modeling of the indicated losses was proposed. That modeling approach considers only the pressure losses occurring during the filling and emptying phases of suction and discharge plenums, respectively, while neglecting those occurring when displacing each chamber volume among such plenums. Hence, a deeper investigation on these losses has been conducted experimentally, in order to evaluate any discrepancies between the modeled cycle and the actual one.

7.1 Experimental setup

To measure the indicated cycle of the prototyped screw pump, the experimental test bench presented in Section 4.3.1 was modified. Specifically, a Kistler^{TM} measuring system was installed and suitably connected with the original DAQ, previously developed to measure the overall performances of the pump (Figure 7-1). This system includes three piezoresistive pressure sensors installed on the pump case (Figure 7-2 (a)), and a signal conditioning block to suitably manage the pressure signals coming from these sensors (Figure 7-2 (b)). This latter embodies two microprocessors, each composed by a 2-channel amplifier with an analog signal conditioning. This amplifier is particularly recommended for high-accuracy measurements with a high sample rate, such as the injection pressure or the inlet/exhaust pressures of combustion engines. This is also the case of the pumping process object of study, for which the sample rate has been set at 500 Hz due to limitations of the maximum value admissible for the basic DAQ system, with whom the Kistler^{TM} signal conditioning block needs to interact.

The piezoresistive pressure sensors installed on the pump case measure the pressure of the water-glycol mixture through a silicon load cell via a thin steel diaphragm and via oil as transmission medium. The load cell contains implanted piezoresistive resistors connected to provide a Wheatstone measuring bridge. This bridge is unbalanced due to the action of pressure, producing an output voltage signal that is proportional to the pressure. Two out of the three pressure sensors have a measuring interval ranging from 0 to 10 bar, whereas one has a measuring interval ranging from 0 to 20 bar, although in both cases the output voltage ranges between 0 and 10 V. Table 7-1 summarizes the main technical data of these pressure sensors.

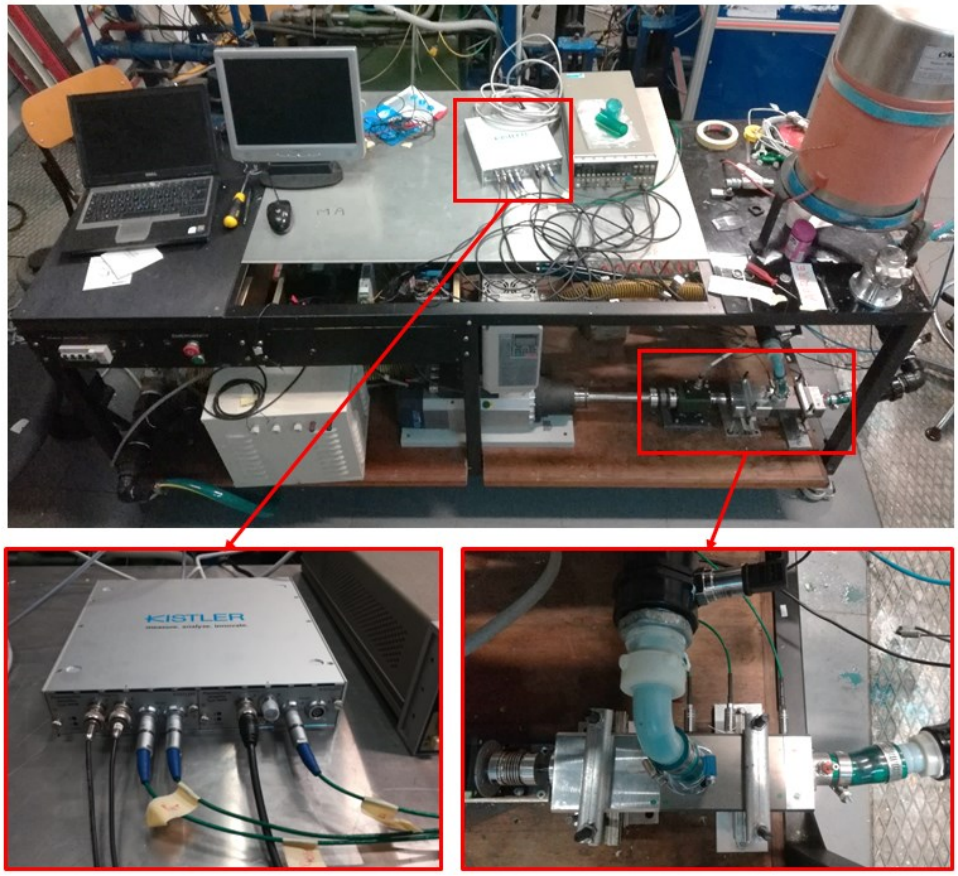

Figure 7-1. Pump test bench equipped with the Kistler™ acquisition system for the measurement of the indicated cycle of screw pumps.

(a) (b)

Figure 7-2. Piezoresistive pressure sensor installed on the pump case (a), and Kistler™ signal conditioning system (b).

The three piezoresistive pressure sensors have been mounted directly on the pump case (Figure 7-3). They have been positioned in three different points along the screws' axis, in order to measure the fluid pressure during the entire pumping process. Specifically, two of them (those measuring up to 10 bar) face the suction and discharge plenums, whereas one (the 20 bar sensor) is located at an intermediate position along the screws' axis, chosen according with the considerations that will be discussed in the next Section 7.2.

Parameter	Unit	Value	
Measuring ranges	bar	0 ... 10	0 ... 20
Overload	bar	25	50
Power supply		Integrated in amplifier	
Reference temperature (T_{ref})	°C	15	
Sensor temperature, min./max.	°C	– 40 / 180	
Temperature compensation		digital	
Temperature compensation range	°C	–20 … 120	
Max. deviation, pressure	%FSO	< ±0.5	
Max. deviation, temperature	°C	< ±3	
Linearity at (T_{ref}) (LSQ)	%FSO	< ±0.1	
Media compatibility		Fluids and gases compatible with stainless steel	

Table 7-1. Technical data of the piezoresistive pressure sensors.

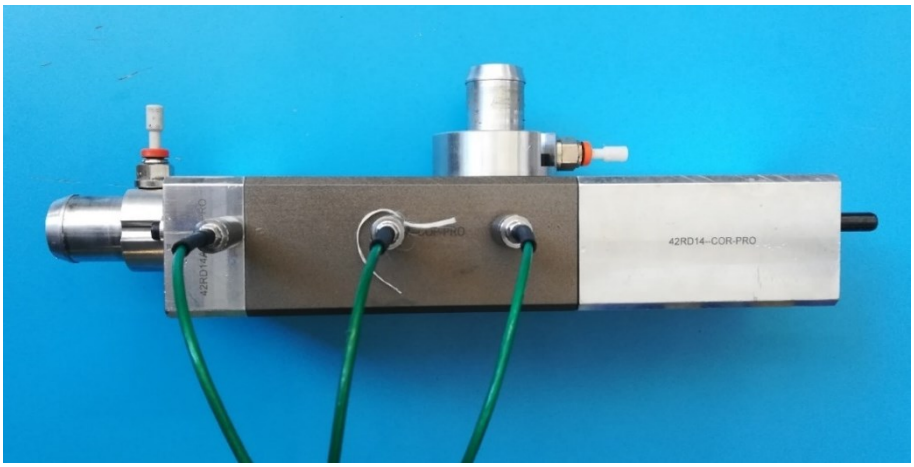

Figure 7-3. Piezoresistive pressure sensors installed on the pump case to measure the indicated cycle.

7.2 Chamber volumes' definition

To identify the indicated cycle of screw pumps, the evolution of the chamber volumes generated by the screws' rotation must be known. To this end, it is worth mentioning that a screw pump is a rotary positive displacement machine, which simply moves fluid from a low-pressure environment to a higher pressure one, without increasing pressure during displacement. In fact, as the screws rotates, two symmetrical chambers are generated periodically, whose effect is to transfer fluid from the suction to the discharge plenum. The fluid just increases its pressure when it is discharged to the end-plenum of the pump, which is connected with the high-pressure side of the hydraulic circuit.

Overall, the pumping process of a screw pump can be schematized as the sequence of three phases applying on each chamber volume, i.e. suction, displacement and discharge phases. During the suction phase, the screws' rotation generates a chamber, which increases its volume up to a maximum value, drawing in fluid from the suction plenum (Figure 4-1). Then, this

chamber is displaced along the screws' axis, as long as it does not open towards the end-plenum of the pump, where the discharge phase occurs, reversely compared with the suction one.

The evolution of the chamber volume during the pumping process has been represented qualitatively in Figure 7-4. Specifically, this figure shows the suction (from 0° to 360°) and the displacement (from 360° to 360°+Δθ) phases, whereas the discharge phase is omitted, being it equal and opposite to the suction one. Clearly, a complete revolution of the screws is necessary to realize the entire suction phase. During this phase, the chamber volume increases up to a constant value, given by the sum of two symmetric volumes, one of which is shown in Figure 7-4. It is worth noting that this value corresponds to half the pump displacement. In fact, the full one is given also by the contribution of the remaining chambers enclosed between the pump case and the screws within the screw pitch length L (see Section 4.2.1).

Then, as the screws continue rotating, the chamber closes to the suction plenum and moves towards the discharge one along the screws' axis. This displacement phase takes place for a rotation Δθ, corresponding to a certain screws' length ΔL. As the screw angular position approaches 360°+Δθ, the chamber volume opens towards the discharge plenum, starting the discharge phase, which again lasts one entire screws revolution.

As a result, the entire pumping process of each chamber volume takes place in an overall angle equal to (2·360°+Δθ), corresponding to two complete screws revolutions, with the addition of the rotation Δθ, necessary to realize the displacement phase.

As mentioned above, due to the symmetrical shape of the screws, two identical chambers evolve simultaneously and symmetrically during pump rotation, forming a couple of moving chambers. One couple is generated after each half revolution of the screws, and thus each couple is 180° phase-shifted with the previous one. Hence, as a new fluid volume is beginning the suction phase, the one previously generated is still completing this phase. This can be clearly observed by comparing together the initial position θ=0° with the one at θ=180° in Figure 7-4.

Consequently, being (2·2π+Δθ) the total angular rotation of the screws necessary to complete the entire pumping process of each couple of volumes, more than one couple is evolving simultaneously inside the machine, even considering the same axial position. This can be observed in Figure 7-5, which represents the curves of the chamber volumes over the rotation angle. Each curve corresponds to one couple of symmetrical chambers, and it is composed by three segments. The rising and decreasing ones represent the suction and discharge phases, respectively. Instead, the constant segment corresponds to the displacement phase, which lasts for a screw rotation equal to Δθ. The constant volume during the displacement phase is equal to half the pump displacement V, being it equal to the sum of the two π-phased volumes V_{ch1} and V_{ch2}, each of which is the volume of one couple of symmetrical chambers evolving simultaneously inside the pump. Moreover, the screw rotation Δθ is directly linked to the extra-length ΔL of the screws relative to the screw pitch length L, which in turn is linked to one complete revolution of the screws (see Appendix A).

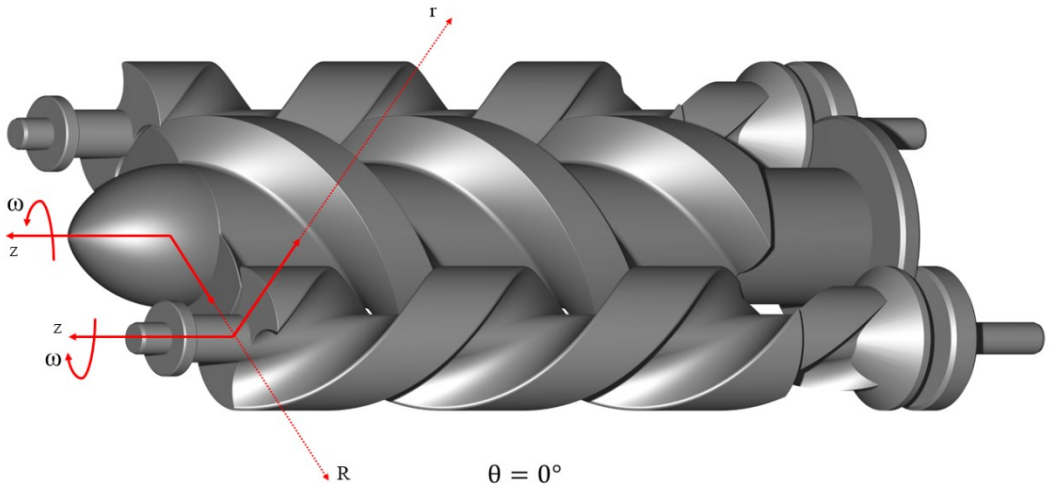

θ = 0°

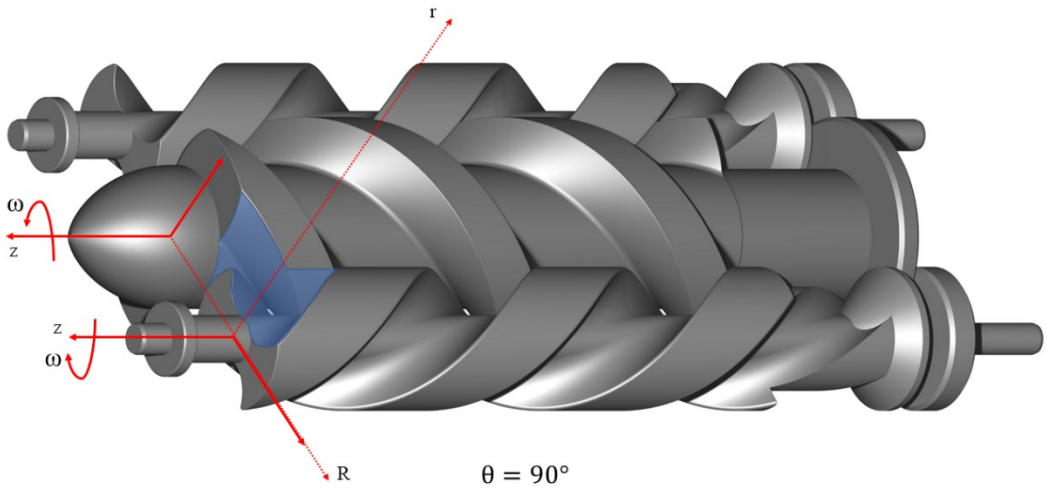

θ = 90°

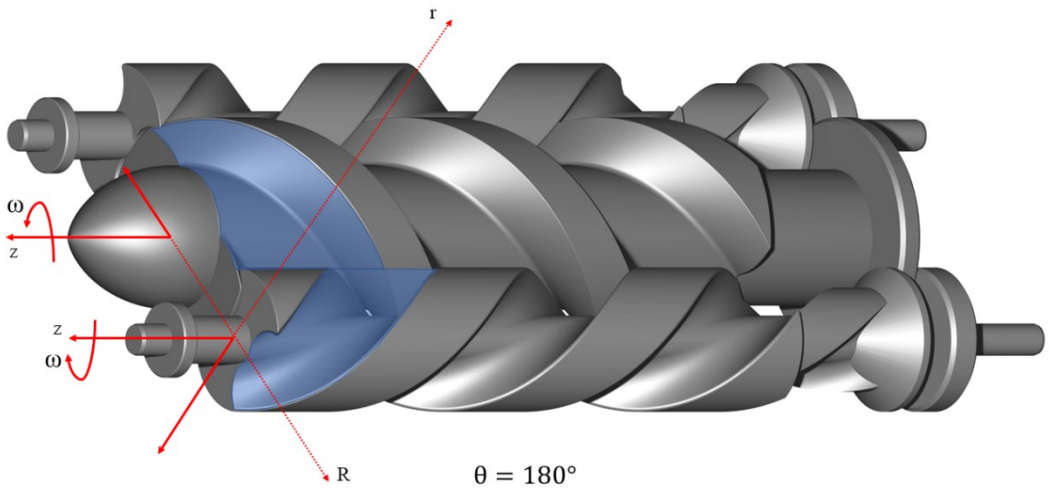

θ = 180°

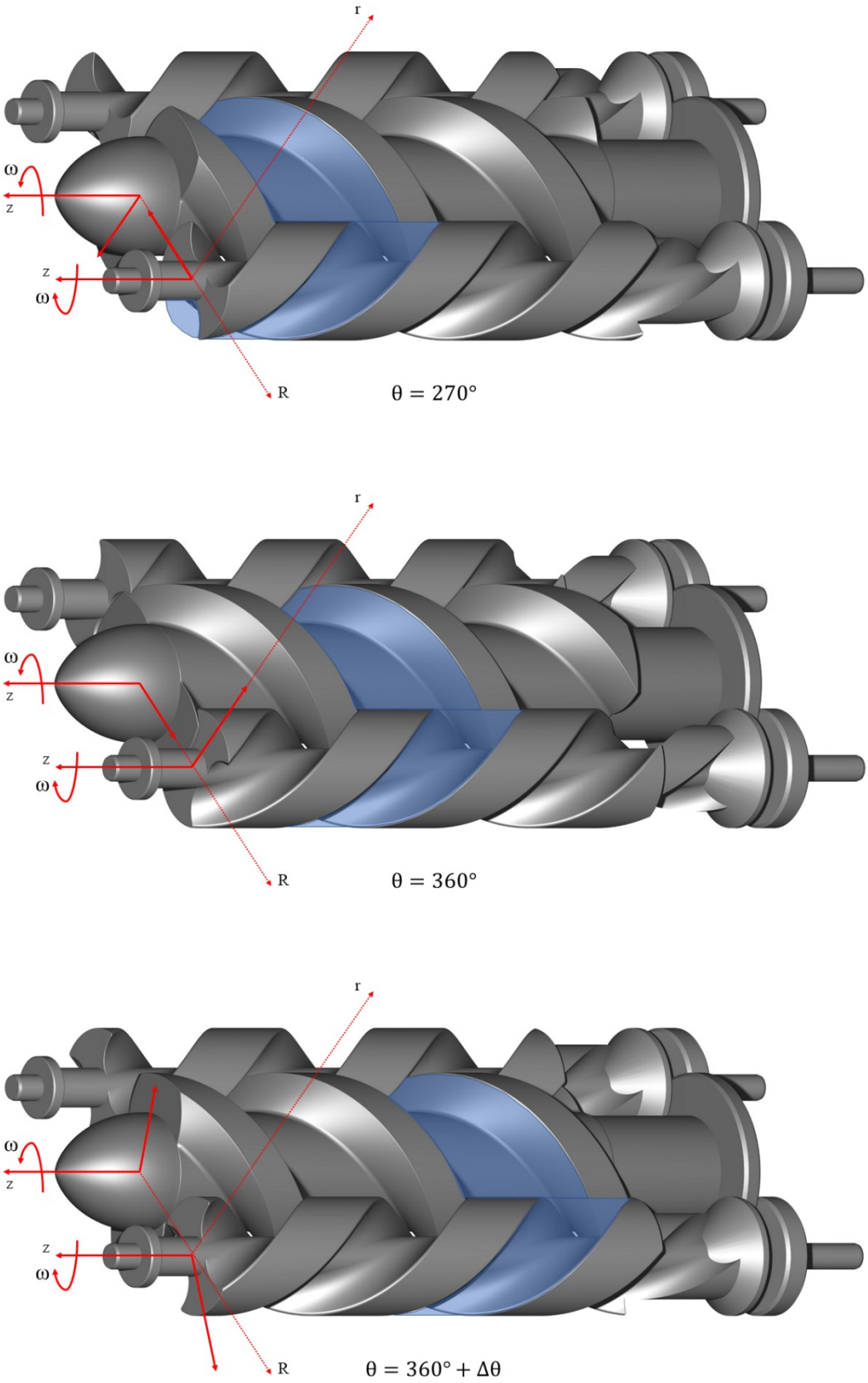

Figure 7-4. Evolution of the chamber volume (depicted in blue) during the suction phase (from 0° to 360° with 90° as angular increment), and the displacement phase (from 360° to 360°+Δθ).

It is worth remarking that after each turn of the screws (2π), the sequence of the two π-phased volumes (V_{ch1} and V_{ch2}) repeats over again, but the pumping process of the first two chambers is still ongoing, being its angular duration equal to (2·2π +Δθ). Hence, this type of volumetric pump is able to process more fluid volumes simultaneously, making the pumping process smoother, and thus delivering a low-fluctuating flow rate. Moreover, the curve trend of suction and discharge phases has been assumed to vary linearly with the rotation angle θ.

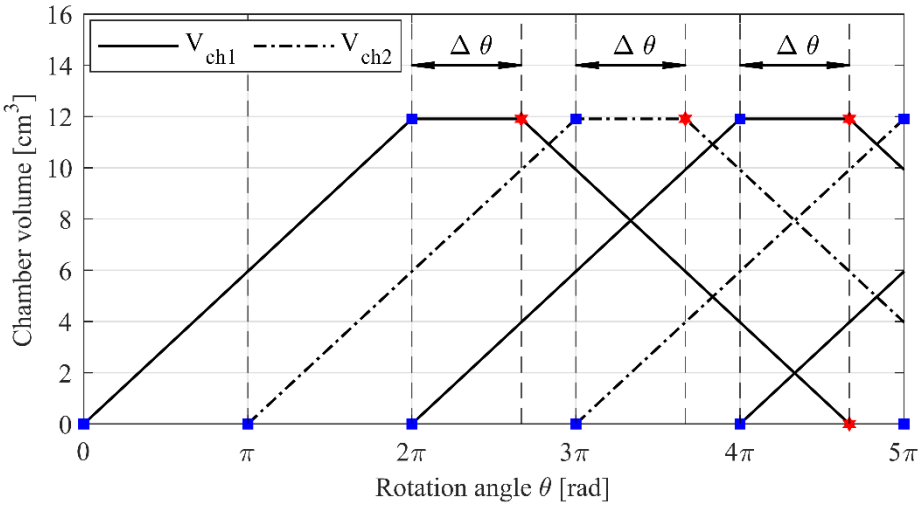

Figure 7-5. Chamber volume curves inside the pump. The blue squares indicate starting and ending points of the suction phase, whereas the red stars define the discharge phase. The displacement phase lasts for a screw rotation equal to Δθ. Each 2π rotation of the screws, the two π-phased volumes (V_{ch1} and V_{ch2}) repeat over again.

The knowledge of how the chambers follow each other during screws' rotation allows to define the axial points where to measure the chamber pressure. These points have been represented in Figure 7-6. At least three pressure sensors are necessary to reconstruct the chamber pressure during the pumping process. Two of them measure the pressure in the suction and discharge plenums, and the third is installed in a suitable position along the screws' axis.

Specifically, this position has been identified in order to measure the pressure of the intermediate chambers during the displacement phase, as well as during the beginning of the discharge phase. To this end, the relation of the chamber volumes with the screw rotation angle represented in Figure 7-5 must be considered. In fact, the displacement phase occurs within an angular rotation equal to Δθ, i.e. within an axial length equal to ΔL. At the same time, a sensor mounted along the screws' axis faces a sequence of chambers phased each other with an angle equal to π. Moreover, each chamber is divided from the subsequent by the screw's tooth, which has an angular extension equal to β (see Appendix A). As a result, for each half revolution of the screws (π), the intermediate sensor measures the pressure of the fluid enclosed inside the chamber for a rotation equal to $(\alpha+2\gamma)$, while it measures the pressure of the fluid enclosed inside the clearance between the pump case and the idler screw's tooth tip for a rotation equal to β. Hence, this sensor measures the chamber pressure only for the angular rotation $(\alpha+2\gamma) <$

π, during which the fluid enclosed in this chamber can experience the suction, the displacement or the discharge phase, depending on the axial position where the sensor is installed.

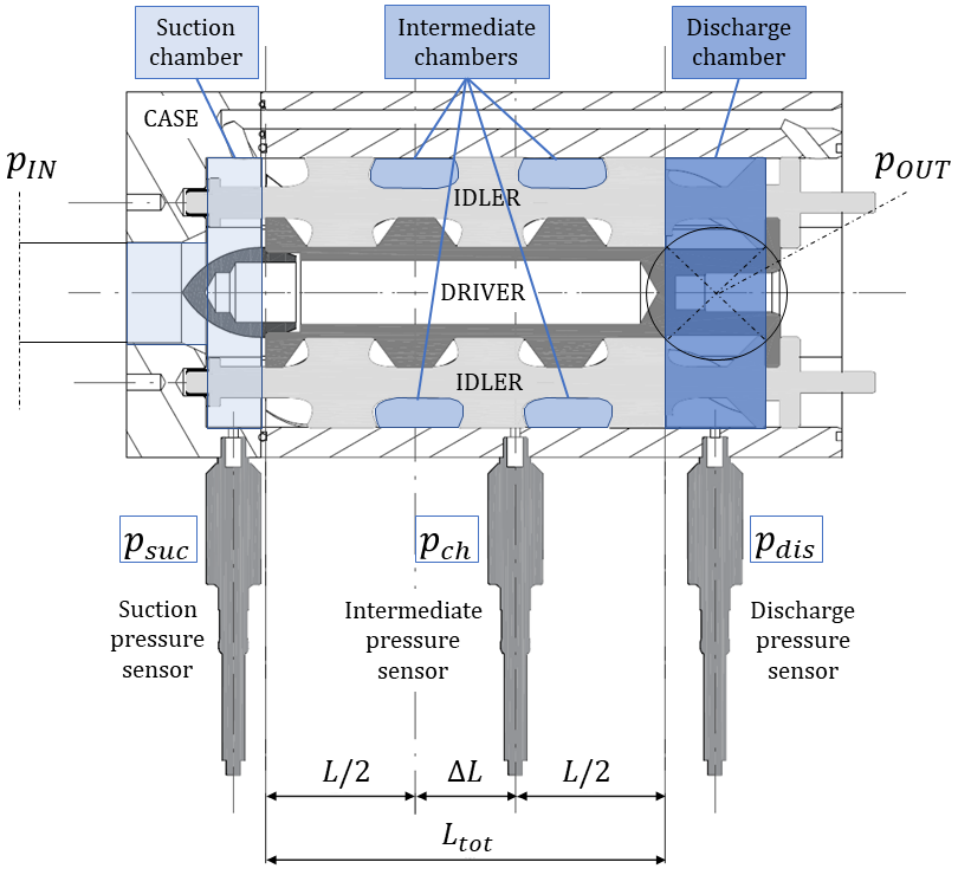

Figure 7-6. Positions of the piezoresistive pressure sensors installed on the pump case along the screws' axis.

In light of these considerations, the intermediate pressure sensor has been installed at an axial distance from the suction chamber equal to ($L/2+\Delta L$), where L is the screw pitch length and ΔL is the axial length corresponding to $\Delta\theta$. In fact, in this position the sensor is able to measure, for each chamber, both the displacement phase, and the beginning of the discharge phase. This is possible thanks to the tridimensional symmetrical shape of the double-toothed screws, and to the possibility to measure the chamber pressure only at one side of the pump. As a result, from the sided position where the sensor could be installed, both the suction and the discharge phases have an axial extension equal to half the screw pitch length, i.e. $L/2$. In fact, during the first π rotation of the screws, each of the two π-phased volumes V_{ch1} and V_{ch2} is hided to the side where the sensor is installed. Hence, this sensor can measure only the pressure for the subsequent π rotation, during which each of these volumes faces the external side of the pump.

Moreover, the suction and discharge phases are spaced each other by the displacement phase, which has an axial extension equal to ΔL. This length does not need to be halved, because the displacement phase occurs at constant volume and with one tooth of the idler screw geared with

that of the driver screw. Thus, as the screws rotate by an angle $\Delta\theta$, the volume of fluid is simply shifted forward by a length ΔL, thanks to the helical shape of the screws' teeth. Therefore, when observed from one side of the pump, the displacement phase is not influenced by the number of teeth of the screws, contrarily to what happens for the suction and discharge ones.

Finally, it is worth noting that the installation of the intermediate pressure sensor in a position that allows to measure also the beginning of the discharge phase was necessary due to the limitations on the maximum sample rate admissible for the DAQ system available on the test bench (Section 7.1). In fact, in this way the pressure signals acquired by the three piezoresistive sensors can be synchronized together and suitably linked with the chamber volume curves, in order to identify the indicated cycle of this specific screw pump. All these aspects related to the measurement and post-processing of the experimental data, as well as the main outcomes of this study, will be discussed in the next Section 7.3.

7.3 Experimental results

After the installation of the piezoresistive pressure sensors on the screw pump case, an experimental campaign has been realized on the test bench described in Section 7.1 to measure experimentally the indicated cycle of this prototype.

To this end, the pump was operated under steady state conditions on suitably defined working points, where both the overall performance of the pump (flow rate, pressure head, torque and speed), and the pressures inside the machine (through the three piezoresistive sensors) have been measured.

Specifically, flow rate, pressure head, torque and speed have been measured with a 1 Hz sample rate, as in all the experimental campaigns conducted for the model validation (Section 4.3 and 6.2). Instead, the pressures inside the machine have been acquired with the maximum sample rate allowed by the specific DAQ system, which is limited at most at 500 Hz and must be divided by the number of sensors measuring simultaneously.

Therefore, each piezoresistive signal has been acquired separately from the other two, in order to take advantage of the maximum sampling rate, leaving to a second stage the synchronization of all the three pressure signals. In any case, a test with all the three sensors measuring simultaneously was conducted for each pump operating point, in order to have experimental results useful when aligning the three signals manually during the post-processing phase.

Moreover, the maximum speed considered for the experimental characterization of the indicated cycle has been set at 1500 rpm. This value allows to have a minimum of 10 points within the period of the pressure signal coming out from each piezoresistive sensor. In fact, due to the chamber volume curves reported in Figure 7-5, each sensor experiences the same volume variation for each half revolution of the screws, to which corresponds necessarily a pressure variation, being the working fluid incompressible. As a result, the frequency of the pressure

signals inside the machine is expected to be doubled compared with the revolution frequency of the screws.

In light of these considerations, a first test was conducted by fixing the operating point of the pump at 1500 rpm and 0.5 bar as pressure head, measuring separately the pump performances (flow rate, pressure head and torque) and the internal pressures acquired by each piezoresistive sensor. At this point, the pump delivers 32 l/min, absorbing 54 W, and thus operating with an efficiency equal to 50%.

The pressure signals acquired by the three piezoresistive sensors are reported in Figure 7-7, together with the chamber volume curves defined in the previous Section 7.2.

To draw these curves, a mean time-variant pressure curve within the main period of the signal was derived for each sensor. Then, this mean pressure curve was expressed as a function of the screws' rotation angle, in order to have a time-invariant pressure signal easily comparable with those acquired in other pump operating points.

At this stage, the assumption relative to the π period of each pressure signal appeared verified. This allowed to compare each pressure curve with the chamber volume curves on a common angle basis, in order to suitably phase shift the pressure signals. This procedure has been indicated through the colored marks reported on the pressure and volume curves in Figure 7-7 (a) and (b), respectively.

Specifically, the starting and ending points of the suction phase have been marked with the blue squares. Among these points, each chamber volume increases from zero to the maximum value, which is half the pump displacement, in light of the considerations discussed in Section 7.2. As the chamber volume increases, the pressure in the suction chamber is expected to decrease, due to the vacuum effect induced by the filling of the chamber generated by the screws' rotation. This effect can be observed in the curve of the suction pressure signal, which looks as the typical pumping losses occurring in the suction phase of an internal combustion engine. Consequently, the pressure signal measured by the suction pressure sensor was phase shifted in order to align the maximums of this signal with the starting points of the suction phase, i.e. the minimum values of the chamber volumes.

Similarly, the red stars delimit the discharge phase. During this phase, the chamber volume decreases from the maximum to zero, draining out fluid to the discharge chamber. This produces an overpressure at the screws outlet, which can be clearly observed in the pressure signal acquired by the discharge sensor. Hence, this pressure signal was phase shifted in order to match its maximum values with the starting points of the discharge phase, where the chamber volume begins to decrease towards zero.

Concerning the displacement phase, a more complex discussion must be made. On the chamber volume curves, it is represented by the constant line at maximum volume between the blue and the red markers. As shown in the figure, this phase lasts for a screw rotation equal to $\Delta\theta$, which is shorter than the angular window observed by the intermediate pressure sensor, equal to π. As a consequence, this sensor will not only measure the fluid pressure during the

displacement phase, but also during the beginning of the discharge phase, considering the position where it has been installed (Figure 7-6). In addition, part of the measurement is disturbed by the crossing of the idler screw teeth in front of the sensor, each of which has an angular duration equal to β. During the teeth crossing, the sensor measures the pressure of the fluid trapped inside the clearance between the screw tooth tip and the pump case, which is moving backwards due to the pressure gradient existing inside the pump. This produces rapid pressure variations, which must be distinguished from the pressure signal relative to the fluid enclosed in the moving chamber, which lasts for an angular extension equal to $(\alpha+2\gamma)$.

As a consequence, the pressure of the fluid experiencing the displacement and part of the discharge phase can be identified within the angle $(\alpha+2\gamma)$.

Reasonably, at the beginning of the discharge phase, the pressure signal of the intermediate sensor should reach that of the discharge sensor, being the intermediate chamber opened towards the discharge one.

Moreover, during the displacement phase, an intermediate pressure between the discharge and the suction ones should be observed inside the moving chambers. In fact, the main phenomenon defining this pressure is the backflow occurring from the discharge to the suction plenum. As known, the backflow fluid approaching the clearance between the idler screw tooth tip and the pump case accelerates due to the smaller flow area defined by this gap. Then, the fluid loses pressure, due to the sudden section enlargement encountered when flowing back from the clearance towards the intermediate chamber. Consequently, the pressure in this chamber is expected to be lower than that in the discharge plenum.

Similarly, the pressure in the intermediate chamber has to be higher than that in the suction one, due to the existence of another screw tooth dividing these two chambers. Moreover, pressure spikes during the displacement phase should not occur because the clearances existing between the screws themselves, and between them and the pump case, create way outs for the fluid trapped in the moving chambers in case of undesired volume restrictions caused by geometrical imperfections of the pump.

In light of these considerations, the pressure signal of the intermediate sensor has been phase shifted in order to match the beginning of the discharge phase. Specifically, two orange markers have been placed on two points limiting the lowest part of the signal. Then, the one right before the increasing segment of the curve has been aligned with the point indicating the beginning of the discharge phase. In this way, within the angle $(\alpha+2\gamma)$ the intermediate sensor measures a small part of the displacement phase, corresponding to the minimum values of the signal, and part of the discharge phase, corresponding to the rising part of the curve.

Moreover, as the rotation angle approaches $(\alpha+2\gamma)$, a pressure spike is registered. This part of the curve occurs for an angular duration equal to β, and therefore it can be reasonably attributed to the crossing of the screw tooth in front of the intermediate pressure sensor.

Hence, in each π-period of the intermediate pressure signal, the sensor measures the pressure of the fluid trapped in the clearance between the screw tooth tip and the pump case for the first

β angle. Then, it measures the pressure of the fluid enclosed in the intermediate chamber for the subsequent $(\alpha+2\gamma)$. There, the first part is relative to the displacement phase, measured for an angular extension given by $(\Delta\theta-\beta)$, i.e. during the period not disturbed by the tooth crossing. Instead, the second part is relative to the beginning of the discharge phase, measured for an angular extension given by $(\pi-\Delta\theta)$, i.e. for the remaining period after the displacement phase where the sensor still faces the fluid enclosed in the intermediate chamber.

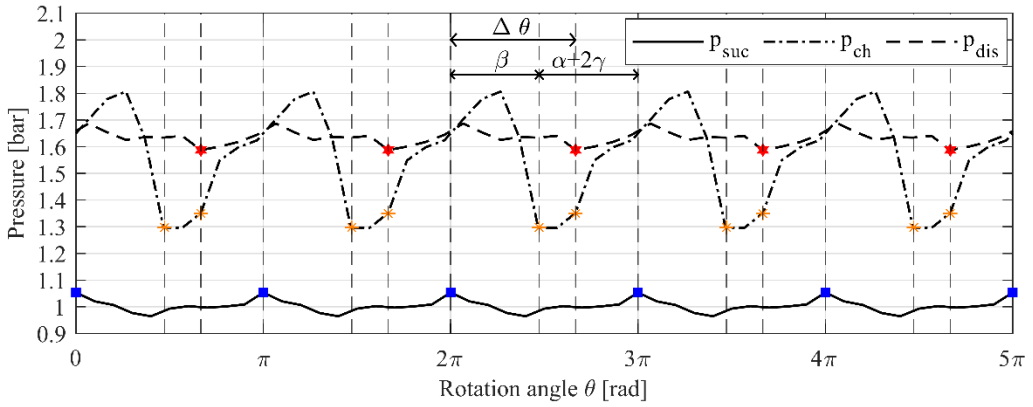

(a)

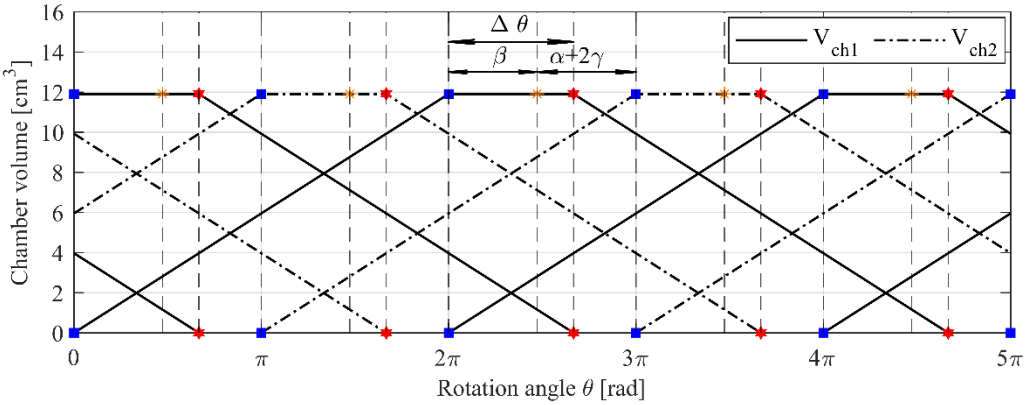

(b)

Figure 7-7. Suction, chamber and discharge pressures (a), and chamber volume curves (b), as a function of the screw rotation angle, with the pump operating at 1500 rpm and 0.5 bar as pressure head. The blue, orange and red marks indicate starting and ending points of suction, displacement and discharge phases, respectively.

Finally, it is worth mentioning that these criteria followed to phase shift the intermediate pressure signal have been verified experimentally, within the maximum sample rate settable on the experimental test bench. In fact, a test acquiring simultaneously the intermediate and the discharge pressure sensors was made, which showed how the maximum values of both signals occur almost for the same angular extension, corroborating the hypothesis assumed so far to phase shift the pressure signal of the intermediate sensor in order to match the beginning of the discharge phase.

Overall, the three pressure signals have a frequency doubled compared with the revolution one (Figure 7-7 (a)). The suction and discharge pressures have smooth oscillations around an

average value. Instead, the intermediate signal measures a mean pressure among those at the discharge and suction plenums, disturbed by pressure spikes occurring when the screw teeth face the sensor. In addition, the periodicity of the pressure curves matches that of the chamber volume curves supposed theoretically (Figure 7-7 (b)). In fact, the measured pressures verify the capability of the pump to process more chambers simultaneously, phased each other by an angle equal to π, and each taking more than two screws revolutions to complete the entire pumping process.

Once realized the phase alignment of the three pressure sensors, the pressure of a single chamber volume for an entire pumping cycle can be derived (Figure 7-8 (a) and (b), respectively). To this end, among the curves reported in Figure 7-7 (b), the chamber volume V_{ch1} starting from θ=0° has been considered. Then, its pressure has been identified by picking up the pressure signal corresponding to the specific phase experienced by the volume, among the three pressures represented in Figure 7-7 (a). Specifically, when the rotation angle θ passes from zero to 2π, the chamber volume experiences the suction phase (1-2), and thus the chamber pressure has been assumed equal to the suction one (p_{suc}). Then, between 2π and 2π+Δθ, the displacement phase (2-3) occurs. During this period, the intermediate pressure sensor measures the actual chamber pressure only for the last Δθ-β angle, being it covered by the screw's tooth for the first β rotation. There, the tooth crossing determines a pressure spike which is not representative of the pressure inside the moving chamber. Therefore, between 2π and 2π+β the chamber pressure has been assumed to rise linearly from the maximum value of the suction pressure (p_{suc}) to the minimum of the intermediate pressure (p_{ch}), and then it follows the intermediate pressure curve (p_{ch}) up to 2π+Δθ. This assumption is supported by the fact that the backflow occurs through a labyrinth-like path, i.e. from the discharge chamber to the previous ones through small clearances between the screws and the pump case. This backflow produces pressure losses, which determine a pressure gradient inside the pump that has to connect necessarily the upstream and downstream pressure levels at the boundaries of such path.

As the screws' rotation angle approaches 2π+Δθ, the discharge phase (3-4) begins, and thus the chamber pressure has been assumed to be equal to that measured by the discharge sensor (p_{dis}).

As a result, the chamber pressure follows the step-like curve reported in Figure 7-8 (a). It can be observed how the suction (1-2) and discharge (3-4) phases (each lasting an entire screw revolution) occur with slight oscillations around an average value. Moreover, the displacement phase (2-3) increases the chamber pressure from the suction to the discharge ones without any pressure spikes, having filtered those induced by the tooth crossing in front of the intermediate sensor, which are not representative of the chamber pressure during this phase. This smooth rising trend of the chamber pressure is another important positive aspect of this type of machines.

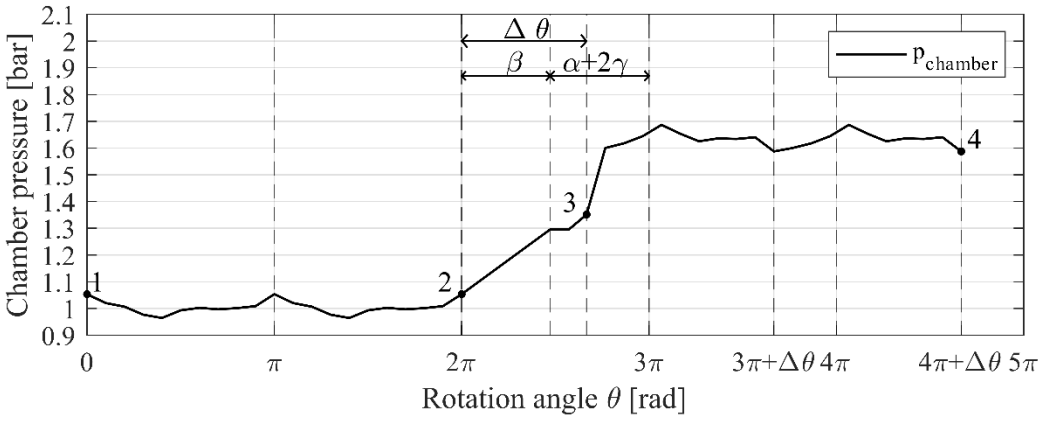

(a)

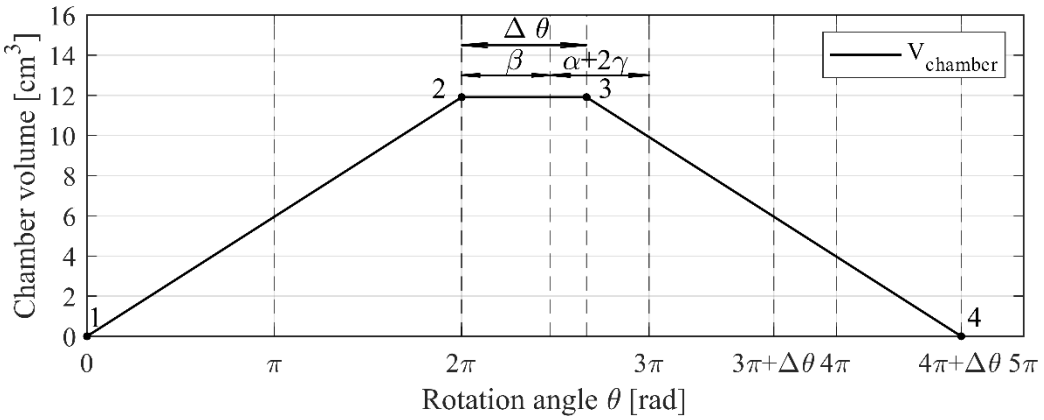

(b)

Figure 7-8. Pressure (a) and volume (b) curves of a single chamber as a function of the screw rotation angle, with the pump operating at 1500 rpm and 0.5 bar as pressure head.

The knowledge of the chamber pressure allows to represent also the indicated cycle of the pump. This has been obtained by suitably rearranging in a p-V diagram the volume and pressure values relative to a single chamber (reported in Figure 7-8). In this way, the experimental indicated cycle represented in Figure 7-9 (black line) has been obtained. This has been compared with the ideal one (red line) and with the cycle calculated by the mathematical model presented in Section 4.2.2 (blue line).

The ideal cycle represents the indicated cycle of a pump which does not have any pressure losses during the suction, displacement and discharge phases. Therefore, it is composed by two isochoric and two isobaric transformations, these latter with the pressures measured at the inflow and outflow pipes of the pump. In this operating point, the pressure difference (Δp_{tot}) between these two isobaric transformations is equal to 0.5 bar, given by a measured downstream pressure (p_{OUT}) equal to 1.52 bar, and an upstream one (p_{IN}) equal to 1.02 bar.

The indicated cycle measured experimentally inside the machine shows some discrepancies relative to the ideal one, especially for what concerns the suction and discharge phases.

Specifically, the suction phase (1-2) takes place in slight under-pressure conditions ($\Delta p_{IN,exp}$) compared to the pressure at the pump inlet (p_{IN}). This is due to the vacuum effect induced by the increasing volume of the chambers generated by the screws' rotation, which drain fluid inside the suction plenum, determining pressure losses. However, these losses remain limited, being the experimental suction curve almost overlapped to the ideal one, with slight oscillations around it. In particular, two oscillations occur with an amplitude equal to 0.1 bar, and around a mean value ($p_{SUC,exp,m}$) almost coincident with the inlet pressure (p_{IN}). In fact, after each π rotation of the screws, a new chamber volume begins the suction phase, while the previous one is still completing this phase, which requires one entire screws revolution to be completed (Figure 7-8 (b)).

Similarly, the discharge phase (3-4) occurs in over-pressure conditions ($\Delta p_{OUT,exp}$) compared to the pressure at the pump outlet (p_{OUT}). In fact, as the screws pour the chamber volumes to the discharge plenum, the pressure rises slightly in this plenum, generating flow rate towards the hydraulic circuit. This pressure increase is due to the need to push an incompressible working fluid from the chamber to the outflow pipe, which inevitably introduces pressure losses in the fluid. Moreover, the pressure measured at the discharge chamber shows two oscillations with an amplitude equal to 0.1 bar around a mean value $p_{DIS,exp,m}$, higher than p_{OUT}.

Although with almost the same oscillations, the over-pressure occurring during the discharge phase appears to be higher than the under-pressure measured during the suction one. This is due to the shape of the discharge plenum, which introduces more pressure losses than those at the suction plenum. In fact, it is linked to the outflow pipe through a 90° bend, contrarily to what happens in the suction side, where the inlet pipe and the suction chamber are straightforwardly connected (Figure 7-6).

It is worth noting that no pressure spikes have been observed during the displacement phase (2-3). As mentioned above, this is due to the backflow occurring during this phase, which imposes an intermediate pressure among those at suction and discharge plenums. Moreover, the presence of clearances between the screws and the pump case creates easy way outs for the fluid trapped in the moving chambers in case of undesired volume restrictions, preventing the onset of pressure spikes.

Finally, Figure 7-9 represents also the indicated cycle calculated by the model (blue line). As described in Section 4.2.2, this cycle has been schematized as the ideal one, i.e. with two isochoric and two isobaric transformations. However, the isobaric ones are suitably spaced each other in order to take into account the pressure losses occurring during the suction and discharge phases. Specifically, the suction pressure p_{SUC} is given by the inlet pressure p_{IN} minus the suction losses Δp_{IN}, calculated as in Eq. 4-15. Similarly, the discharge pressure p_{DIS} is calculated by adding the discharge losses Δp_{OUT} (Eq. 4-16) to pressure p_{OUT} measured at the outlet section.

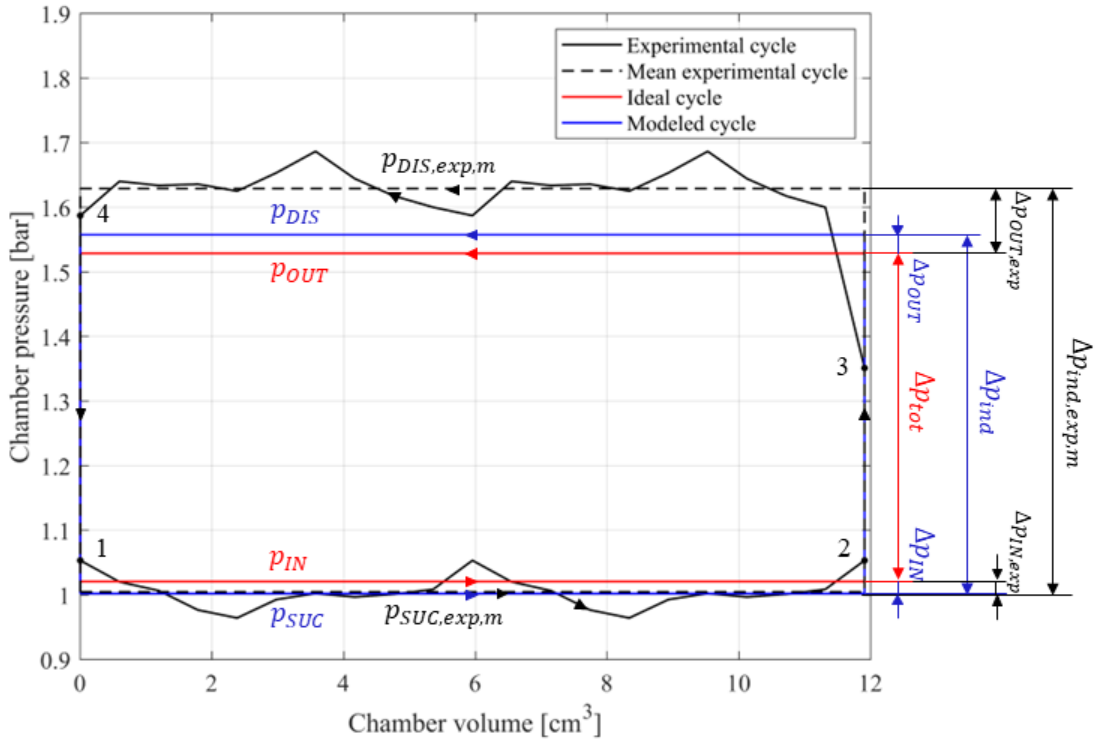

Figure 7-9. Experimental indicated cycle of a triple-screw pump operating at 1500 rpm and 0.5 bar as pressure head, compared with the ideal and the modeled ones.

Consequently, the model calculates a pressure difference (Δp_{ind}) among the suction-discharge plenums higher than that measured at the in-out sections of the pump (Δp_{tot}). However the actual mean pressure difference among such plenums measured experimentally ($\Delta p_{ind,exp,m}$) is higher than that calculated by the model (Δp_{ind}). The main discrepancy regards the discharge phase (3-4), where the measured chamber pressure shows a higher mean value ($p_{DIS,exp,m}$) compared with the calculated pressure (p_{DIS}). In fact, the model does not consider the effect of the 90° bend path that the fluid experiences going from the discharge plenum to the outlet pipe. Instead, the pressure p_{SUC} calculated by the model is almost coincident with the mean pressure measured during the suction phase ($p_{SUC,exp,m}$). In fact, in this case the fluid path from the pump inlet pipe to the suction plenum is more straightforward and without any abrupt bends, determining less actual pressure losses compared with those modeled theoretically.

The availability of the indicated cycle measured experimentally allows to calculate also the indicated work, and thus the indicated power, actually absorbed by the pump.

The indicated work L_{IND} (Eq. 7-1) is the area enclosed within the experimental indicated cycle (black line in Figure 7-9), which has been calculated through a trapezoidal numerical integration. Moreover, it can be expressed also as the product between the chamber volume experiencing the indicated cycle, and the corresponding mean pressure difference. In this case, the indicated cycle measured experimentally is relative to one of the two π-phased couple of

chambers evolving inside the machine. In other words, the pressure profile reconstructed in Figure 7-8 (a) is relative to a chamber with half the pump displacement *V* as maximum volume. Hence, the indicated work is given also by the product between half the pump displacement (*V/2*), and the mean pressure difference measured experimentally ($\Delta p_{ind,exp,m}$).

The time spent to realize this counter-clockwise cycle is expressed by T_{IND} (Eq. 7-2), which in turn is half the time necessary to complete an entire revolution of the screws. In fact, since a volume of fluid equal to the pump displacement is drained to the discharge plenum every complete revolution of the screws, half revolution is necessary to deliver half the pump displacement. Consequently, the time necessary to complete the indicated cycle of one chamber is half the time required by the entire pump displacement.

Finally, once known the indicated work L_{IND} and the time T_{IND} necessary to realize it, the indicated power P_{IND} can be calculated as the ratio between them (Eq. 7-3).

$$L_{IND} = \oint p\, dV = \frac{V}{2}\, \Delta p_{ind,exp,m} \qquad \text{Eq. 7-1}$$

$$T_{IND} = \frac{1}{2\left(\frac{\omega}{60}\right)} \qquad \text{Eq. 7-2}$$

$$P_{IND} = \frac{L_{IND}}{T_{IND}} \qquad \text{Eq. 7-3}$$

For this operating point, the experimental indicated power P_{IND} is equal to 37 W, whereas the indicated power P_i calculated by the model through Eq. 4-17 is equal to 33 W. Consequently, the model estimates the indicated power with an error equal to 11%. This error can be attributed mostly to the simplified modeling of the discharge phase, which occurs with higher pressure losses than those predicted by the model (expressed by Eq. 4-16).

Another way to calculate the indicated power is to calculate the indicated work within a certain angular range, considering the contribution of each chamber volume evolving simultaneously in this range, and the time necessary to cover it. The situation is represented in Figure 7-10, which is a detailed version of Figure 7-7 (b). In the angular range between 0 and $(2 \cdot 2\pi + \Delta\theta)$, the entire pumping process of one chamber volume (A) takes place. Specifically, from 0 to 2π the suction phase occurs, followed by the displacement phase up to $2\pi+\Delta\theta$, and by the discharge phase for the subsequent 2π rotation of the screws.

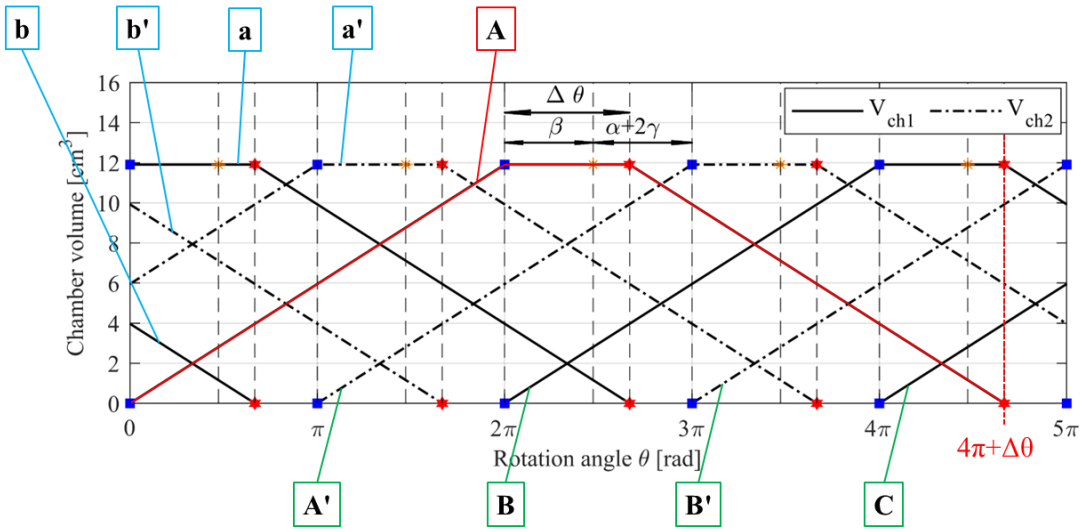

Figure 7-10. Chamber volume curves as a function of the screw rotation angle. The red one is the reference volume, the cyan ones the previous, and the green ones the subsequent volumes. The blue, orange and red marks indicate starting and ending points of suction, displacement and discharge phases, respectively.

Simultaneously, other volumes experience at least one of the three phases composing the pumping process, thanks to the symmetrical shape of the screws, which allows to process more chamber volumes at the same time, phased each other by π.

Specifically, within the angle (2·2π+Δθ), four previous volumes (a, a', b and b') have already started the pumping process. Two of them (a and a') have experienced completely the displacement and discharge phases, with (a') also the last π part of the suction phase. The remaining two (b and b') experience only part of the discharge phase, for Δθ and π+Δθ, respectively.

Moreover, other four volumes (A', B, B' and C) begin the pumping process after the volume taken as reference. Progressively, the first (A') realizes up to half the discharge phase, the second (B) up to the displacement phase, and the remaining two (B' and C) up to the suction phase for an angular extension equal to π+Δθ and Δθ, respectively.

Since the displacement phase occurs without any pressure spikes (Figure 7-8 (a)), the indicated work can be calculated by considering only the portion of suction and discharge phases experienced by each of the concurrent volumes. Specifically, within the angle (2·2π+Δθ), three volumes (A, A' and B) complete the entire suction phase (2π), while other three (a', B' and C) experience only part of it, i.e. up to π, π+Δθ and Δθ, respectively. Similarly, within this range, three volumes (A, a' and a) complete the discharge phase, while other three (A', b' and b) only part of it, for the same angular extensions seen for the suction phase.

Overall, considering the mean suction and discharge pressures measured experimentally ($p_{SUC,exp,m}$ and $p_{DIS,exp,m}$, respectively), the indicated work L_{IND} can be expressed as in Eq. 7-4, written in order to be a positive quantity. This work is absorbed by the pump in a time interval equal to that necessary to complete the entire pumping process of the volume taken as reference

(A) in Figure 7-10, as well as the partial pumping processes of the other simultaneous volumes (a', a, b', b and A', B, B', C). Hence, the time cycle T_{IND} can be calculated as the ratio between the angle $\theta_{chamber}$ (equal to $2 \cdot 2\pi + \Delta\theta$) necessary to pump one chamber volume, and the frequency necessary to do it, written as a function of the pump speed ω (Eq. 7-5).

$$L_{IND} = \left(p_{DIS,exp,m} - p_{SUC,exp,m}\right)(8\pi + 2\Delta\theta)\frac{(V/2)}{2\pi} \quad \text{Eq. 7-4}$$

$$T_{IND} = \frac{\theta_{chamber}}{2\pi\left(\frac{\omega}{60}\right)} \quad \text{Eq. 7-5}$$

In this way, the indicated power P_{IND} can be calculated with Eq. 7-3, obtaining the same result reached using the indicated work and time defined by Eq. 7-1 and Eq. 7-2, respectively.

It is worth to notice that the same P_{IND} can be achieved also considering different angular intervals, as long as the right number of phases experienced by the simultaneous volumes and the corresponding time cycle are adapted to the specific angular range taken as reference.

7.4 Comparison with other operating points

In the previous Section, the indicated cycle of the prototyped screw pump operating at 1500 rpm and 0.5 bar as pressure head has been derived. In this Section, a further analysis is discussed, in order to identify any relationship between the indicated cycle and the pump operating point. To this end, two other operating points have been analyzed: one with the same pump speed but with lower pressure head, and the other with the same pressure head but with lower pump speed.

7.4.1 Same pump speed but lower pressure head

Specifically, the first case considers 1500 rpm as pump speed and 0.13 bar as pressure head, i.e. the same pump speed but with less than half the pressure head of the case analyzed in Section 7.3. At this point, the pump delivers 34 l/min, absorbing 32 W, and thus operating with an efficiency equal to 22.6%. The results related to the indicated cycle are reported from Figure 7-11 to Figure 7-13.

Following the same procedure described in the previous Section, the pressure signals acquired with the three piezoresistive sensors have been phase shifted according with the chamber volumes evolution over the screws' rotation angle assumed theoretically (Figure 7-11 (a) and (b), respectively).

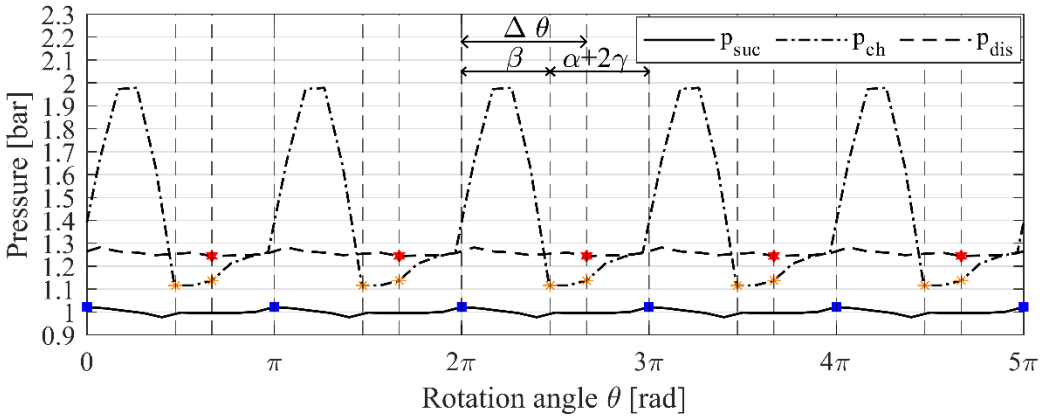

(a)

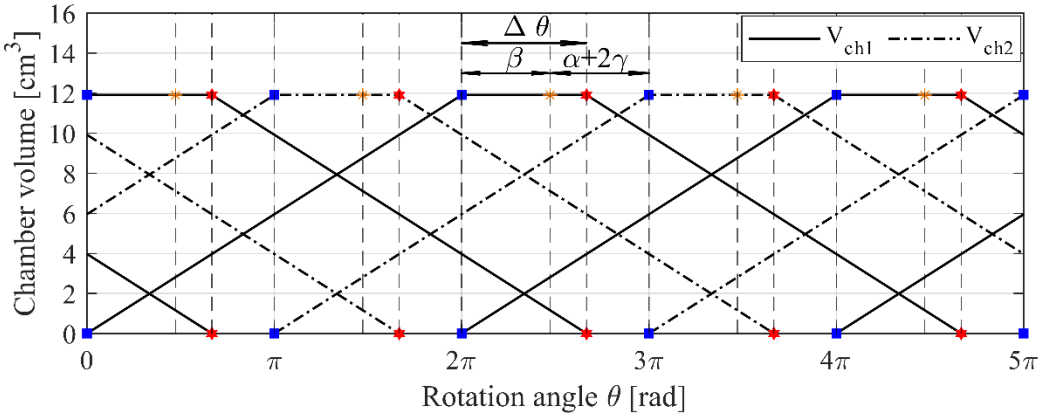

(b)

Figure 7-11. Suction, chamber and discharge pressures (a), and chamber volume curves (b), as a function of the screw rotation angle, with the pump operating at 1500 rpm and 0.13 bar as pressure head. The blue, orange and red marks indicate starting and ending points of suction, displacement and discharge phases, respectively.

In this case, higher pressure spikes due to the idler screw's teeth facing the intermediate sensor have been registered periodically for an angle β. This behavior has been investigated also for other pump speeds. In all cases, a relation between the pressure head and these pressure spikes has been observed. Specifically, as the pressure head rises, lower pressure spikes are measured, until the pressure acquired during the tooth crossing falls in the range between the intermediate pressure and the maximum pressure measured at the discharge plenum (see the case in Figure 7-14 (a)).

A possible explanation of such phenomenon could be found considering the effect of pressure head on the backflow occurring inside the pump. As the pressure head rises, the backflow increases as well, as pointed out also by the mathematical modeling proposed in Chapter 4 (Eq. 4-10). This is due to the effect of the pressure gradient, which pushes the working fluid to flow back to the suction plenum, forcing it to pass through the clearances existing between the screws and the pump case. Hence, the more the pressure difference across the screws is higher, the more the fluid trapped between the screws' teeth tips and the pump case

is forced to escape backwards. Instead, at low pressure heads, this effect is less pronounced, and the fluid enclosed within these thin gaps may experience more likely over-pressure conditions induced by the screws' rotation. This happens clearly in the case reported in Figure 7-11 (a), i.e. with 1500 rpm and 0.13 bar, although less pronounced pressure spikes can be identified also in Figure 7-7 (a), with the same pump speed but higher pressure head (0.5 bar).

Except for the higher pressure spikes, the other features measured by the three pressure sensors in Figure 7-11 (a) are the same observed also in Figure 7-7 (a). Briefly, the pressure signals have a period equal to π, and have been phased in order to match the beginning of suction and discharge phases identified on the chamber volume angular profile. Specifically, the suction pressure has the maximums aligned with the beginning of the suction phase. Instead, the discharge and intermediate pressures have the minimums aligned with the beginning of the discharge phase.

Starting from the angular phased pressure signals, the pressure profile over the screws' rotation angle of one chamber volume has been derived (Figure 7-12).

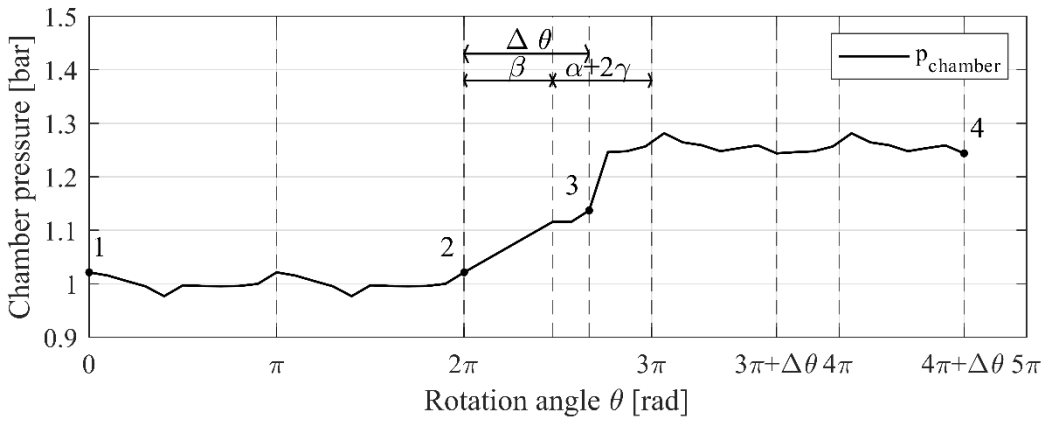

(a)

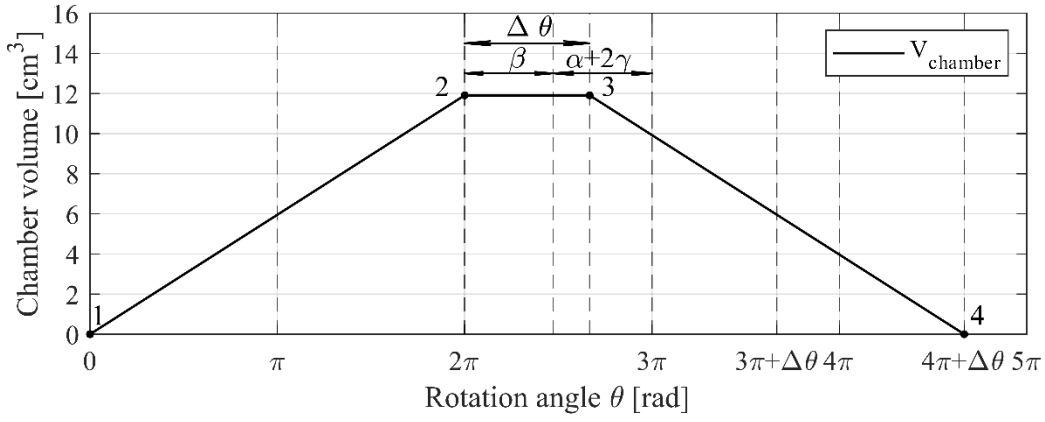

(b)

Figure 7-12. Pressure (a) and volume (b) curves of a single chamber as a function of the screw rotation angle, with the pump operating at 1500 rpm and 0.13 bar as pressure head.

This profile is not influenced by the pressure spikes registered by the intermediate sensor, because they are not representative of the actual pressure of the fluid during the displacement phase. In fact, these spikes occur periodically within the angle β, which is exactly the angular extension of the idler screw tooth. Therefore, the chamber pressure has been assumed to vary linearly within the angle β, in order to link the maximum value of the suction pressure, with the minimum of the intermediate one. Then, the chamber pressure follows the signal measured by the intermediate sensor for the range Δθ-β, the only one effectively representative of the displacement phase.

Overall, the three phases can be distinguished in the pressure and chamber volume profiles in Figure 7-12 (a) and (b), respectively. The suction one (1-2) takes place in slight under-pressure conditions relative to the inlet pressure for a complete screws' revolution. Then, the displacement phase (2-3) occurs for an angle Δθ, during which the chamber pressure rises progressively towards the discharge one. Finally, the discharge phase (3-4) takes place in slight over-pressure conditions relative to the outlet pressure for the subsequent 2π rotation, oppositely compared with the suction one.

Once known the volume and pressure profiles relative to one chamber, the indicated cycle has been derived (Figure 7-13). Here, also the ideal (red line) and modeled (blue line) cycles have been reported, together with the mean experimental one (dashed black line).

Similarly to the case discussed in Figure 7-9, the mean pressures measured during the suction and discharge phases ($p_{SUC,exp,m}$ and $p_{DIS,exp,m}$) are respectively lower and higher than the pressures measured at the pump in/out sections (p_{IN} and p_{OUT}), due to the pressure losses ($\Delta p_{IN,exp}$ and $\Delta p_{OUT,exp}$) occurring during these phases.

The model calculates these losses (named Δp_{IN} and Δp_{OUT}) with Eq. 4-15 and Eq. 4-16, respectively, and identifies the pressures p_{SUC} and p_{DIS} at suction and discharge plenums by suitably adding the quantities Δp_{IN} and Δp_{OUT} to the pressures measured at the pump in/out sections (p_{IN} and p_{OUT}). While the model offers a good accuracy in representing the suction phase, it underestimates the pressure losses at the discharge plenum, being the calculated pressure p_{DIS} lower than the mean pressure $p_{DIS,exp,m}$ measured experimentally. This is due to the approximation of the 90° bend shape of the discharge plenum, as already discussed in Section 7.3.

Hence, in this case the indicated power P_{IND} calculated on the experimental cycle through Eq. 7-3 is equal to 15 W, whereas the corresponding value calculated on the modeled cycle is equal to 10 W, with an error of about 30%.

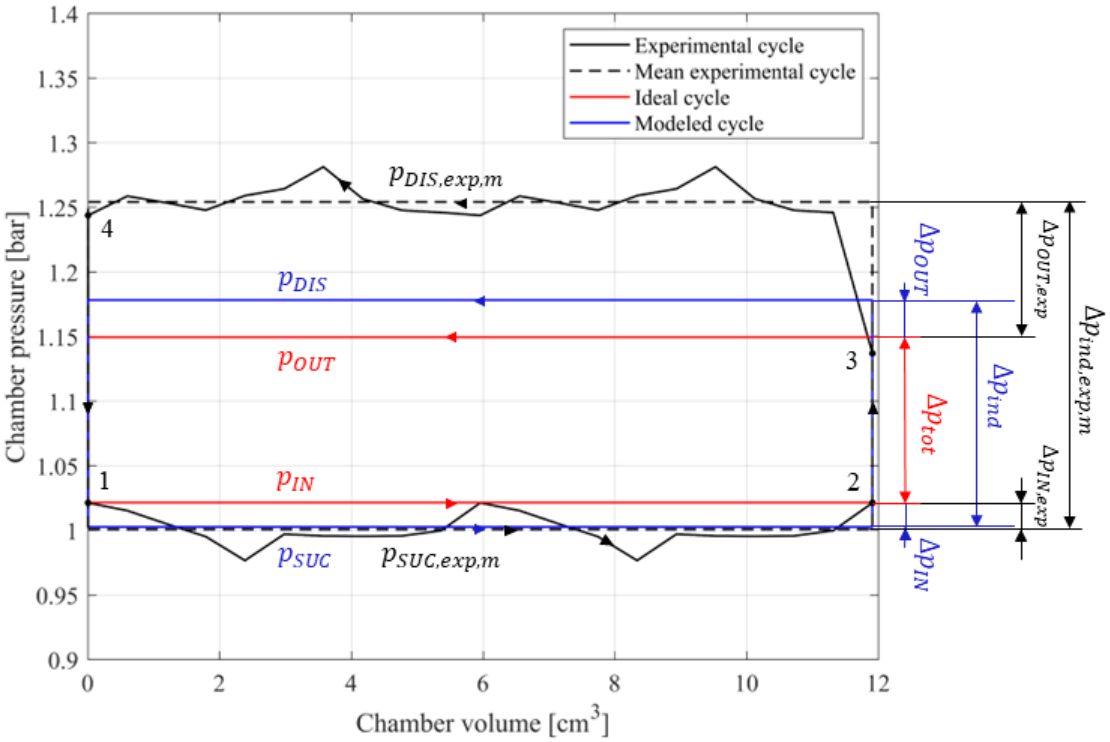

Figure 7-13. Experimental indicated cycle of a triple-screw pump operating at 1500 rpm and 0.13 bar as pressure head, compared with the ideal and the modeled ones.

This error can be explained by comparing together the indicated cycles derived for this operating point (Figure 7-13), with those derived when the pump operates with the same speed (1500 rpm) but higher pressure head (0.5 bar), represented in Figure 7-9.

Clearly, the pressure losses occurring during the discharge phase appear to be substantially insensitive on the pressure head. In fact, both cases have about the same pressure difference $\Delta p_{OUT,exp}$ (about 0.1 bar) between the mean value measured at the discharge plenum ($p_{DIS,exp,m}$) and the pressure measured at the outlet pipe (p_{OUT}). Only a slight difference on the amplitude of the pressure oscillations at the discharge chamber can be noticed, being now equal to 0.04 bar, against the 0.1 bar amplitude found in the case with 0.5 bar as pressure head.

Similarly, the pressure difference $\Delta p_{IN,exp}$ between the mean pressure measured at suction plenum ($p_{SUC,exp,m}$) and at the inlet pipe (p_{IN}) is almost the same in both cases (about 0.02 bar). Moreover, the variation in the oscillations' amplitude is analogous to that observed for the discharge phase when passing from 0.5 bar to 0.13 bar as pressure head.

This substantial stability of suction and discharge pressure losses when operating the pump with the same speed but lower pressure head, can be explained considering the physical phenomena which define the pressure losses of a liquid flow from a plenum to a duct, and vice versa. As known, for a fixed speed, the pump delivers almost the same flow rate also when varying the hydraulic permeability of the circuit, and thus the pressure head acting on the pump.

If the discharge phase is taken as reference, this means that almost the same volume of fluid per unit time has to be drawn out of the discharge plenum and sent to the high pressure side of the circuit. This process occurs with some pressure losses, which depend on the amount of fluid to be evacuated per unit time, beside its physical properties (incompressibility) as well as the geometry of the path followed to empty the discharge chamber. Being the pump able to deliver almost the same flow rate also when the pressure head varies, the volume of fluid per unit time to be moved from the discharge plenum to the circuit does not change. Hence, the pressure losses occurring during the discharge phase are not significantly influenced by the pressure head acting on the pump.

Similarly, the suction pressure losses depend on the amount of fluid moved per unit time from the low-pressure side of the circuit to the suction plenum. Again, being the screw pump a volumetric machine, this volume of fluid depends largely on the pump speed and not on the pressure head imposed by the circuit. Hence, the pressure losses occurring during the suction phase remain almost the same when decreasing the pressure head while keeping the same pump speed.

This behavior is also underlined by the mathematical model used to calculate the indicated cycle (Eq. 4-15 and Eq. 4-16), which shows clearly as the pressure losses related to the suction and discharge phases (Δp_{IN} and Δp_{OUT} respectively) depend only on the fluid speed, and thus on flow rate, which in turn is fixed by the pump speed.

A different discussion can be made for the pressure oscillations measured at both the suction and discharge chambers. Taking as reference the discharge phase, slight variations on the volume of the discharge plenum always occur during pump rotation, mainly due to the π phased sequence of the volumes that begin the discharge phase. These volume variations determine pressure oscillations, which are likely to increase if the pump head rises, due to the incompressibility of the working fluid.

Finally, it is worth remarking that the independence of the discharge pressure losses from pressure head is the main reason that causes the error between the indicated cycle calculated by the model and the experimental one. In fact, if the difference between the mean pressure measured at the discharge plenum ($p_{DIS,exp,m}$) and the one calculated by the model (p_{DIS}) remains unchanged with pressure head while keeping the same pump speed, then this discrepancy will impact more on the error when the pressure head is low, i.e. when p_{IN} and p_{OUT} measured at the in/out sections of the pump are closer. This can be clearly observed by comparing together the experimental (black) and modeled (blue) indicated cycles represented in Figure 7-13 (0.13 bar as pressure head), with those represented in Figure 7-9 (0.5 bar as pressure head).

7.4.2 Same pressure head but lower pump speed

The second case considers the indicated cycle of the screw pump when operating with the same pressure head (0.5 bar) of the case discussed in Section 7.3, but with a lower pump speed (750 rpm instead of 1500 rpm). At this point, the pump delivers 14.2 l/min, absorbing 24 W, and thus operating with an efficiency equal to 50%. The results concerning the indicated cycle are reported from Figure 7-14 to Figure 7-16.

In this case, the lower pump speed allows to have a more detailed reconstruction of the pressure profiles measured inside the pump (Figure 7-14 (a)), having kept the maximum sample rate allowed by the test bench, i.e. 500 Hz (see Section 7.1).

Similarly to the other two cases, these pressure signals have been phase shifted in order to match the beginning of suction and discharge phases, thanks to the chamber volume profiles derived theoretically as a function of the screws' rotation angle (Figure 7-14 (b)). Again, the pressure profiles show a period equal to π, with under and over pressure conditions at suction and discharge plenums respectively and, most of all, the absence of pressure spikes during the displacement phase. In fact, due to the position where the intermediate sensor has been installed (Figure 7-6), the corresponding pressure (p_{ch}) oscillates smoothly between the pressures at suction and discharge plenums. Moreover, contrarily to the other two operating points, the idler screw's teeth crossing in front of the intermediate sensor does not produce any pressure peaks. Instead it determines a smooth decreasing trend from the pressure measured in the moving chamber during the beginning of the discharge phase (which occurs for an angle π-$\Delta\theta$), to the pressure measured during the displacement phase (which occurs for an angle $\Delta\theta$-β).

The explanation of such trend is the same already discussed in Section 7.4.1. For each pump speed, as the pressure head rises, the pressure spikes produced by the screws' teeth crossing in front of the intermediate sensor tend to be mitigated, until they fall between the discharge pressure (p_{dis}) and the minimum of the intermediate chamber pressure (p_{ch}). In other words, for high pressure heads, the teeth crossing does not produce pressure peaks, as those observed when the pump operates at 1500 rpm and 0.13 bar or 0.5 bar as pressure head (Figure 7-7 and Figure 7-11, respectively). Instead, high pressure heads eliminate any pressure spikes within the angle β, as happens in this case with the pump operating at 750 rpm and 0.5 bar (Figure 7-14 (a)). This is due to the combined effect of pressure head and screws' rotation on the backflow crossing the clearances between the screws and the pump case. If the pressure head is high enough, the fluid enclosed within these thin gaps escapes backwards more easily, preventing over pressure conditions induced by the screws' rotation.

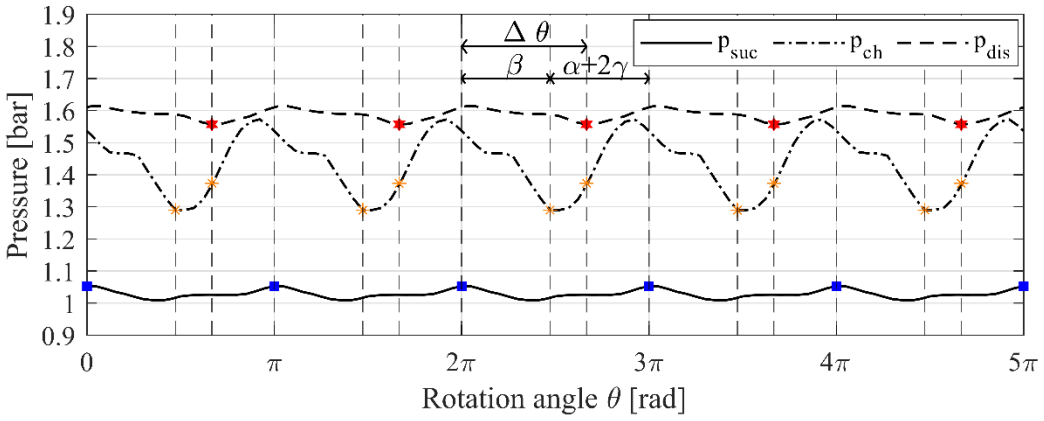

(a)

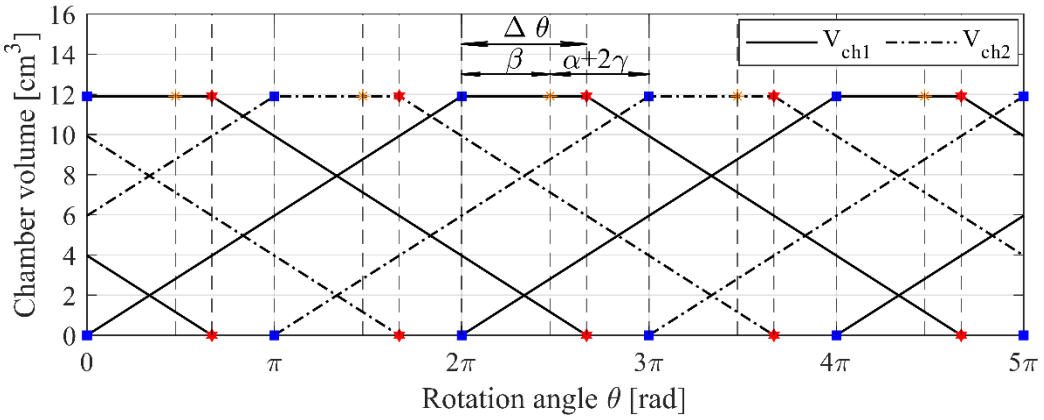

(b)

Figure 7-14. Suction, chamber and discharge pressures (a), and chamber volume curves (b), as a function of the screw rotation angle, with the pump operating at 750 rpm and 0.5 bar as pressure head. The blue, orange and red marks indicate starting and ending points of suction, displacement and discharge phases, respectively.

The knowledge of the pressure profiles measured along the screws' axis allows to derive the pressure profile over the screws' rotation angle of one chamber volume (Figure 7-15). Here, the three phases of the pumping process can be clearly distinguished. The suction phase (1-2) takes place during the first complete revolution of the screws (2π), during which two periodic under-pressure conditions are experienced by the fluid, due to the vacuum effect induced by the screws' rotation. Then, the displacement phase occurs (2-3). There, the pressure of the fluid rises smoothly towards the pressure level at the discharge section. The first segment (lasting for a rotation angle equal to β) is a linear interpolation between the maximum suction pressure and the minimum intermediate pressure. This assumption was necessary in order to filter the pressure measured by the intermediate sensor when the screw's tooth crosses in front of it, which is not representative of the actual pressure of the fluid enclosed in the chamber volume during the displacement phase. Instead, the displacement pressure is effectively measured for the subsequent Δθ-β angular range, after which the discharge phase (3-4) takes place, oppositely compared with the suction one.

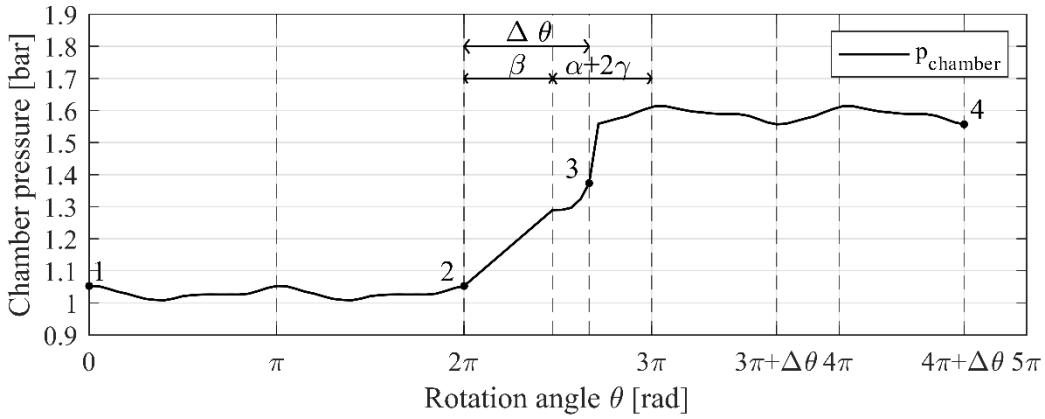

(a)

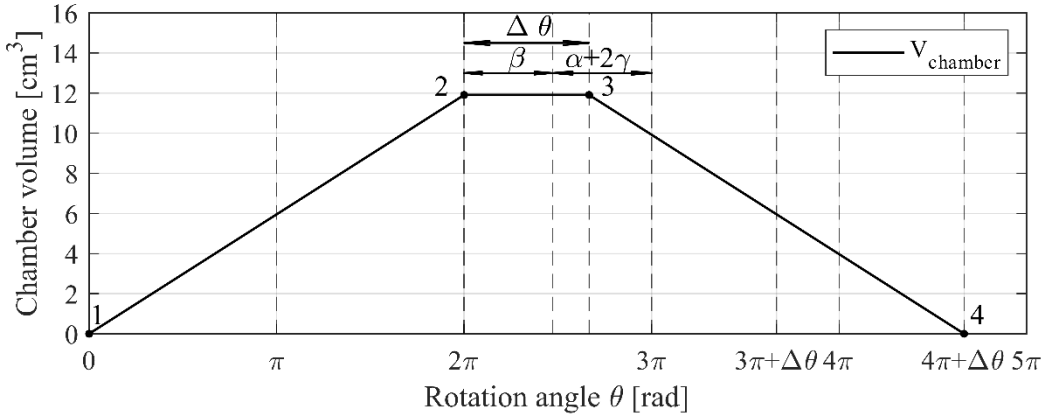

(b)

Figure 7-15. Pressure (a) and volume (b) curves of a single chamber as a function of the screw rotation angle, with the pump operating at 750 rpm and 0.5 bar as pressure head.

By suitably combining together the pressure and volume angular profiles of one chamber, the experimental indicated cycle of the screw pump can be obtained. This is represented along with the ideal (red line), the modeled (blue line), and the mean experimental (dashed black line) cycles in Figure 7-16.

Even in this operating point, the experimental cycle differs from the ideal one, especially during the discharge phase (3-4). In fact, the mean pressure measured at the discharge plenum ($p_{DIS,exp,m}$) is higher than the one measured at the outlet pipe (p_{OUT}), due to the pressure losses $\Delta p_{OUT,exp}$ occurring during the discharge phase. These losses have been modeled through (Eq. 4-16), and turn out to be substantially negligible in this case ($\Delta p_{OUT} \approx 0$, i.e. $p_{OUT} \approx p_{DIS}$). In fact, the model considers only the fluid velocity at the outlet pipe to calculate the discharge pressure losses Δp_{OUT}, neglecting the additional losses induced by the 90° bend shape of the discharge plenum.

Instead, for what concerns the suction side, the experimental mean pressure ($p_{SUC,exp,m}$) is substantially coincident with the ideal (p_{IN}) and modeled (p_{SUC}) ones. This is mainly due to the almost straightforward shape of the suction plenum, which induces lower pressure losses

compared with those at the discharge side, especially in this case with a relatively low pump speed (750 rpm).

Overall, in this case the indicated power P_{IND} calculated on the experimental cycle through Eq. 7-3 is equal to 16.5 W, whereas the corresponding value calculated on the modeled cycle is equal to 15 W, with an error of about 8%.

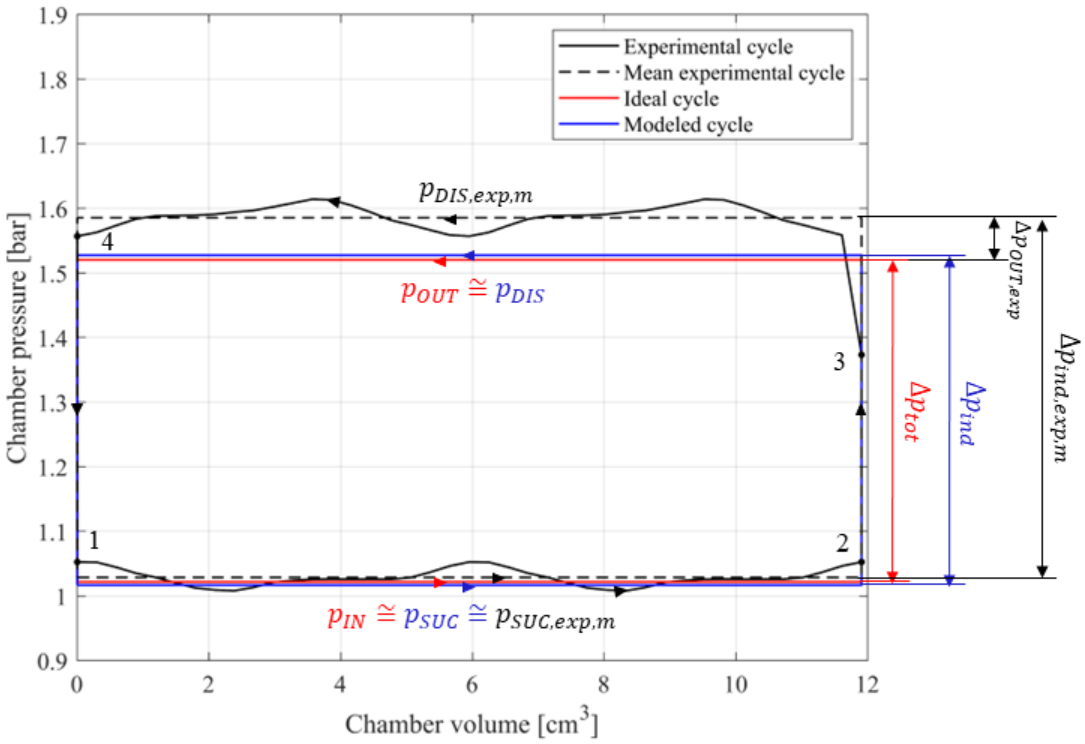

Figure 7-16. Experimental indicated cycle of a triple-screw pump operating at 750 rpm and 0.5 bar as pressure head, compared with the ideal and the modeled ones.

To better understand this error, these results (Figure 7-16) can be compared with those obtained when the pump operates with the same pressure head (0.5 bar) but with a higher speed (1500 rpm) (Figure 7-9).

Clearly, a lower pump speed determines lower pressure losses. This is especially true during the discharge phase, where the experimental losses $\Delta p_{OUT,exp}$ are about 0.06 bar in the case with 750 rpm, against 0.1 bar registered with 1500 rpm. A similar reduction is observed also in the amplitude of the pressure oscillations measured during the discharge phase, which passes from 0.1 bar at 1500 rpm, to 0.06 bar at 750 rpm, if the same pressure head (0.5 bar) is maintained.

Lower pressure losses can be observed also during the suction phase. In fact, the experimental losses $\Delta p_{IN,exp}$ passes from 0.02 bar with 1500 rpm, to less than 0.01 bar with 750 rpm. Moreover, also the amplitude of the pressure oscillations measured during the suction phase results to be almost halved.

This dependency of the pressure losses with the pump speed can be explained following the same reasoning already discussed in Section 7.4.1. Being the screw pump a volumetric machine, it delivers a flow rate substantially independent on pressure head and almost proportional with the pump speed. Moreover, the pressure losses occurring during suction and discharge phases depend on the volume of fluid per unit time to be moved from a pipe to a plenum (and vice versa), as well as on the fluid physical properties and the geometry of the fluid path. Hence, if the pump speed is reduced, a lower volume per unit time will experience the suction and discharge phases, resulting in lower pressure losses. This is especially true if the pressure head is kept constant. In fact, in this way the flow rate variation is only due to the pump speed, without any influence of the volumetric efficiency, which still depends on pressure head, albeit slightly.

For what concerns the pressure oscillations, similar considerations can be drawn. As the screws rotate, slight variations in suction and discharge chamber volumes are produced, which in turn determine slight pressure oscillations, exacerbated by the fluid incompressibility. If the pump speed decreases, a smaller volume per unit time suffers from these volume variations, determining pressure oscillations with lower amplitude.

All these considerations explain also why the modeled cycle allows to calculate the indicated power P_{IND} (Eq. 7-3) with a smaller error when considering an operating point with lower pump speed but same pressure head. This can be clearly observed by comparing together the experimental (black) and modeled (blue) indicated cycles represented in Figure 7-16 (with 750 rpm and 0.5 bar as pressure head), with those represented in Figure 7-9 (with 1500 rpm and the same pressure head).

In fact, the mathematical model proposed in Section 4.2.2 calculates the pressure losses during suction (Δp_{IN}) and discharge (Δp_{OUT}) phases considering the fluid velocity, which depends on flow rate and thus on pump speed. Hence, for a lower pump speed, the model calculates lower pressure losses. Moreover, a similar reduction is observed also for the pressure losses measured experimentally ($\Delta p_{IN,exp}$ and $\Delta p_{OUT,exp}$). By combining together the reductions of experimental and modeled pressure losses, the difference between the pressures measured at suction or discharge plenums ($p_{SUC,exp,m}$ or $p_{DIS,exp,m}$) and those calculated by the model (p_{SUC} or p_{DIS}) decreases. Consequently, the indicated power is calculated with a smaller error when decreasing the pump speed while keeping the same pressure head.

In conclusion, the experimental measurement of the pressures inside the prototyped triple-screw pump allowed to identify specific features of the indicated cycle of this type of machines.

Firstly, no pressure spikes occur during pump operation and, more specifically, during the displacement phase of the chamber volumes. In fact, the pressure peaks measured by the intermediate sensor are related to the idler screw's teeth crossing in front of the sensor, and thus are not representative of the actual pressure of the fluid enclosed inside the moving chambers.

Moreover, a dependency of the indicated cycle with the pump operating point (speed and pressure head) has been found. Specifically, the pressure losses measured during suction and

discharge phases appear to be independent from the pressure head, but dependent only on the pump speed. Consequently, screw pumps operating at high pressure head and low speeds should maximize the indicated efficiency. In fact, in these conditions, the impact of suction and discharge pressure losses on the overall pressure head turns out to be minimized. These experimental results agree with the those predicted by the model (Figure 6-8 and Figure 6-9), which therefore can be considered reliable also for what concerns the mathematical modeling of the indicated cycle of this type of machines.

7.5 Conclusions

In this Chapter, the indicated cycle of screw pumps has been investigated experimentally. Specifically, the triple-screw pump prototyped in Section 5.3 has been instrumented with three piezoresistive sensors, in order to measure the pressure of the fluid inside the machine during the pumping process. Simultaneously, the chamber volumes' evolution over the screws' rotation angle has been theoretically derived. This allowed to reconstruct the indicated cycle of the machine, and to calculate the indicated power actually absorbed by the pump.

Results show a smooth pumping process of each chamber volume, as well as of the overall pump displacement. In fact, the pump is able to process more chamber volumes simultaneously, phased each other by an angle π, and each with a pumping process lasting more than two complete revolutions of the screws ($4\pi+\Delta\theta$). Suction and discharge phases take place with slight under and over pressure conditions, respectively. Instead, the pressure during the displacement phase does not show any spikes, thus remaining at an intermediate value among those measured at suction and discharge plenums.

The only pressure peaks registered by the intermediate sensor are due to the screw's teeth crossing. This has been verified by comparing together the angular duration of each pressure peak, with the angular amplitude of the idler screw's tooth. Moreover, by increasing pressure head for a given pump speed, the pressure peaks decreased, until they fell within the discharge and intermediate pressures. This behavior has been attributed to the compression effect exerted by the screws' rotation on the backflow fluid enclosed between the screws' teeth tips and the pump case, which tends to be significant for low pressure heads and high pump speeds. In any cases, these pressure spikes are not representative of the fluid enclosed in the moving chambers during the displacement phase, which then occurs smoothly.

Finally, the indicated cycle was measured for different operating points: one having the same pump speed of the first measurement (1500 rpm) but lower pressure head (0.13 bar against 0.5 bar), and the other with the same pressure head (0.5 bar) but lower pump speed (750 rpm). The results show that suction and discharge pressure losses depend on pump speed, but not on pressure head. Specifically, the higher is the pump speed, the higher are pressure losses. Consequently, their negative impact on the indicated power (i.e. on the indicated efficiency) is higher for low pressure heads and high pump speeds. This behavior has been predicted also by

the model in Chapter 6, although it shows a good agreement with the experimental cycle as long as the pump speed is low and the pressure head is high.

So far in this thesis, screw-type volumetric pumps for engine cooling applications have been investigated both theoretically and experimentally. In the following Chapter 8, the engine cooling system of a passenger vehicle will be characterized experimentally. The aim is to evaluate the actual impact of the engine warm-up phase on fuel consumption and emissions over on-the-road tests. This will enable future researches on possible solutions to speed-up this phase, thus reducing CO_2 and pollutant emissions.

8 Experimental study on engine warm-up

8.1 Objectives

As outlined in Chapter 3, the engine thermal state has a strong influence on fuel consumption and pollutant emissions. In fact, the engine temperature defines the friction conditions between relative moving components, which impact on the FMEP, and thus on fuel consumption. Moreover, it influences the combustion efficiency, as well as the efficiency of the after-treatment devices, affecting strongly pollutant emissions.

Hence, the engine is designed to operate at a certain temperature, typically above the ambient conditions, i.e. about 90°C if the coolant temperature is taken as reference. This thermal state guarantees the optimal engine performance and the lowest emissions, without compromising engine durability, nor even its safe operation.

Typically, the engine cooling system is designed to keep the coolant temperature close to its design value during driving, but does not provide any significant devices or strategies to accelerate engine warm-up. Therefore, the engine warm-up phase follows its own time evolution, defined by the thermal balance between ambient conditions and engine dynamics, this latter depending on the instant mechanical power required by the wheels. Unfortunately, the warm-up phase still represents a significant portion of homologation cycles, causing about 60-80% of total emissions [176,177]. Thus, any viable effort in speeding up this phase is of great scientific interest.

In this Chapter, the warm-up phase of a passenger vehicle propelled by a spark ignition engine has been investigated experimentally. Specifically, the effects of the engine thermal state on fuel consumption and pollutant emissions have been measured over on-the-road tests. To this end, the vehicle has been instrumented with a Portable Emission Measurement System (PEMS), which allowed to measure the main pollutant emissions under real driving conditions. Moreover, the parameters acquired by the engine ECU have been supplemented with additional transducers installed in the engine cooling system, which include thermocouples to measure the temperature of the engine block.

Hence, a comprehensive outlook on the vehicle's performances and emissions has been provided when operating both in cold and warm start conditions. This has allowed to verify experimentally the actual benefit of a short warm-up phase on the engine emissions. Moreover, important suggestions to define suitable actuation strategies for the cooling pump have been provided thanks to the additional transducers installed in the engine. This will be particularly useful for future researches aimed at substituting the standard centrifugal cooling pump currently mounted in the engine, with more advanced variable-speed solutions. Such improvement would allow to speed-up the engine warm-up phase, with significant benefits in terms of fuel economy and pollutant emissions.

8.2 Case study

8.2.1 Vehicle: Jeep Compass with Firefly T4 engine

The passenger vehicle object of study is the Jeep Compass™, which is equipped with the FireFly™ T4 engine (Figure 8-1 and Figure 8-2, respectively).

Figure 8-1. Image of the Jeep Compass™, equipped with the FireFly T4™ engine.

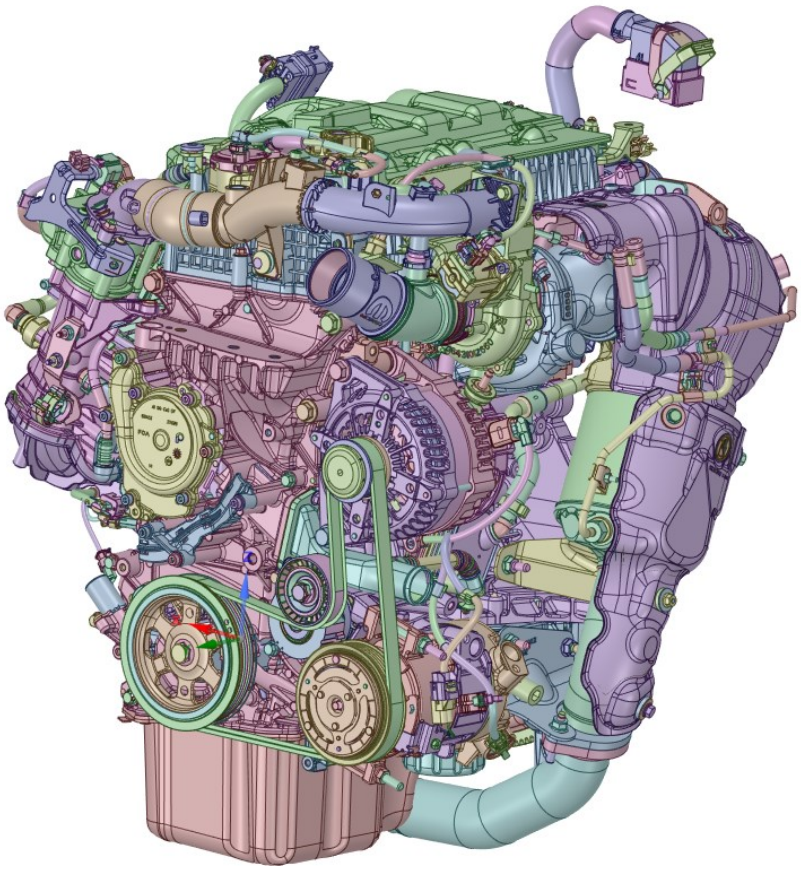

Figure 8-2. CAD image of the FireFly T4™ engine.

Both the engine and the vehicle are designed and produced by the automotive company Stellantis™. This specific vehicle is proposed with different powertrains. In this case, it is propelled by a 1.3 litres, 4-cylinders turbocharged gasoline engine, with a maximum power of 150 hp at 5250 rpm. The engine propels the front wheels through a 6 gears, dual-clutch (DCT) automatic transmission.

The main technical features of the vehicle has been summarized in Table 8-1, whereas those relative to the engine and the transmission are reported in Table 8-2 and Table 8-3, respectively.

Vehicle	Jeep Compass
Kerb Weight	1430 kg
Length	4404 mm
Width with mirrors folded	1874 mm
Height	1629 mm
Wheelbase	2636 mm
Ride height (ground clearance)	198 mm
Trunk (boot) space - minimum	438 l
Fuel tank capacity	55 l
Drive wheel	Front wheel drive
Tires size	215/60 R17

Table 8-1. Main technical specifications of the Jeep Compass [267].

Engine	FireFly T4
Number of cylinders	Inline 4-cylinders
Engine location	Front, Transverse
Displacement	1332 cm^3
Bore and stroke	70 mm and 86,5 mm
Valves per cylinder	4
Compression ratio	10,5:1
Maximum power	110 kW (150 cv) @ 5250 rpm
Maximum torque	270 Nm @ 1850 rpm
Injection system	FGT – GASOLINE DIRECT INJECTION
Fuel Type	Gasoline

Table 8-2. Main technical specifications of the FireFly™ T4 engine [268].

Transmission	dual-clutch automatic transmission (DCT)
Number of gears	6
Gear ratios 1°	4,154
2°	2,360
3°	1,435
4°	0,978
5°	0,755
6°	0,622
Reverse	4,000
Axle ratio	4,438

Table 8-3. Main technical specifications of the transmission [269].

The FireFly™ belongs to a broader family of engines designed and produced by Stellantis™, called Global Small Engines (GSE). These engines have been optimized in order to achieve a high efficiency in terms of fuel consumption and pollutant emissions, along with low weight and size. More specifically, the combustion efficiency has been maximized, thanks to an unconventional shape of the combustion chamber, together with the direct injection of fuel at about 200 bar and the ultimate VVA system MultiAir™ III. This latter allows to vary the compression ratio from 10,5:1 to about 9:1 [268], enhancing the engine efficiency also when operating at low loads. The main performance specs declared by the vehicle manufacturer are summarized in Table 8-4.

Maximum speed	200 km/h
Acceleration 0 - 100 km/h	9.2 sec
Emission standard	Euro 6d-Final
CO_2 emissions	152-159 g/km
Fuel consumption (economy) - urban	6.6 l / 100 km (15.15 km/l)
Fuel consumption (economy) - extra urban	5 l / 100 km (20 km/l)
Fuel consumption (economy) - combined	6.6-7 l / 100 km (15.15 - 14.29 km/l)

Table 8-4. Performance specs declared by the vehicle manufacturer [267].

8.2.2 Engine cooling system

The cooling system of the FireFly T4 engine equipped on the Jeep Compass is represented schematically in Figure 8-3. It is constituted by two closed loops: a high temperature coolant loop (the red line), and a low temperature one (the green line). In the figure it is also represented the Heating, Ventilation and Air Conditioning (HVAC) system (the blue line), which includes also the pressure and temperature sensors standardly equipped on this system.

The high temperature coolant loop (red line) cools the engine head and block. Starting from the cooling pump (1), the coolant flows to the engine block and head (2). At the engine out, a thermostat valve (3) splits the flow into two branches depending on the coolant temperature. If the engine is cold, i.e. the coolant temperature is below a certain temperature (about 70°C in this case), the thermostat valve is still completely closed, and the coolant is sent back to the pump (1) passing through the front heater core (4) and the engine oil cooler (5). As the engine warms-up, the thermostat valve begins to open, sending progressively more fluid to the engine radiator (6) in order to cool the coolant fluid. Then, the two fluid streams are gathered together at the pump inlet (1), and to loop starts again. Moreover, a coolant tank (7) is linked to the thermostat and the low temperature segment of the circuit, in order to pick-up eventual coolant bubbles evaporated inside the engine and send them back in the circuit.

It is worth noting that the primary coolant pump (1) is mechanically linked to the engine, which then fixes its speed. Therefore, the flow regulation is managed only by the thermostat valve, which splits the flow among the bypass branch or the radiator branch depending on the

coolant temperature. Moreover, this coolant pump is a typical centrifugal pump, actuated directly from the timing chain through an Oldham joint.

Instead, the low temperature coolant loop (green line) is used only to cool the compressed charge air aspirated by the engine. Specifically, a secondary on/off electric centrifugal pump (1') sends the coolant to a water charge air cooler (2'), and then to a low temperature radiator (3'), placed in front of the main one. Moreover, at the secondary pump outlet, a small portion of fluid is sent to the turbocharger (4'), and then collected into the coolant tank (7), which is linked also to the branch coming out of the water charge air cooler (2'). Consequently, the high and low temperature loops use the same coolant fluid, although they have two separate pumps and radiators.

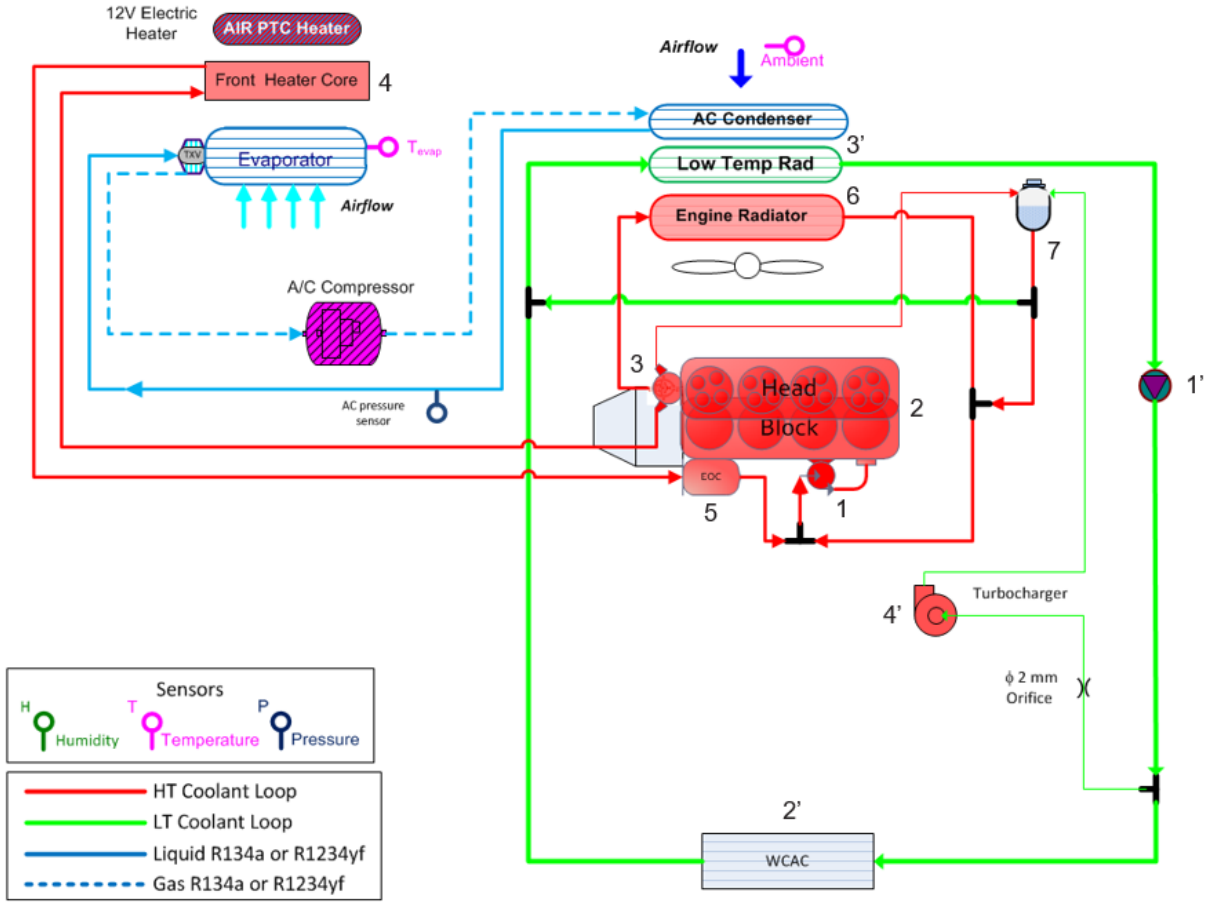

Figure 8-3. Layout of the engine cooling system of the Jeep Compass (internal source).

In Figure 8-4 (a) a detail of the internal coolant flow passages of the engine block has been reported. The geometry of these flow pathways has been studied to determine where thermocouples could be installed inside the engine block in order to measure the temperature of its metallic masses. The main aspect worth of noting is that only the first cavities facing the cylinder liners are actually wetted by the coolant, whereas the other hollows are used to link different portions of the lubricant circuit or have manufacturing purposes. This topic will be

further discussed in Section 8.3.1, where the exact installation position of each thermocouple will be presented.

In Figure 8-4 (b) is also reported an image of the coolant thermostat valve. This device includes the standard coolant temperature sensor equipped on the engine, whose signal is sent to the engine control unit (ECU). Moreover, it has an electric heating system, controlled by the ECU to better manage critical cooling conditions. An example could be to delay the thermostat closing or to anticipate the thermostat opening in order to help preventing engine under cooling situations.

In this thesis, the high temperature loop of the cooling system of the FireFly T4 engine has been object of a closer study. The research conducted on it will be discussed in Section 8.3.1.

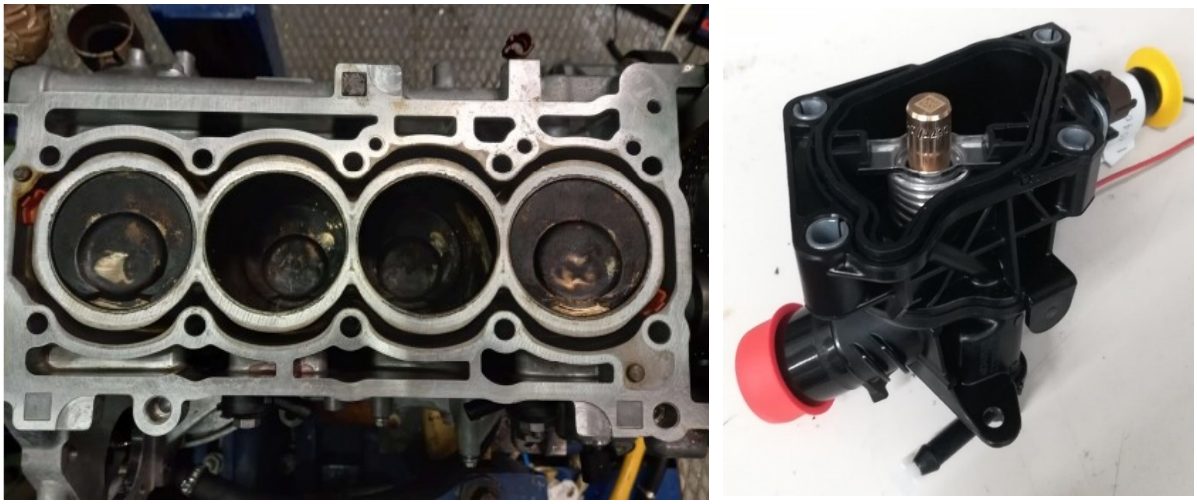

(a) (b)

Figure 8-4. Image of the internal coolant flow passages of the engine block (a), and of the coolant thermostat valve (b).

8.2.3 Engine lubricant system

To better understand the engine thermal management of the FireFly T4 equipped on the Jeep Compass, it is worth to describe briefly also the lubricant system of this engine, which has been represented schematically in Figure 8-5 (a).

In this engine, a sliding vane rotary pump (3) aspirates the oil collected by the sump (1) through the suction head (2), and sends it to the filter (6). Then the oil flows towards the engine oil cooler (7) and the main oil gallery (9) through a duct housed directly inside the engine block (8). From the main oil gallery, the oil is drained towards the bearing pins of the crankshaft and of the connecting rods (10-11-12), and to four nozzles (13) necessary to cool and lubricate the bearing pins of the connecting rods facing the pistons.

Moreover, a duct (15) links the main oil gallery to the turbo-compressor bearing (16), and to the secondary oil gallery (17), which feeds the lubrication of the camshaft bearing pins and of the intake and exhaust valves' actuation system (18).

Similarly, a duct (19) allows the oil to flow from the main oil gallery to the MultiAir^{TM} system in the upper part of the engine, which is constituted by a main central gallery (20), and a volume for each of the four cylinders (21).

The oil flow is regulated by an overpressure valve (5), which limits the maximum flow rate to be sent to the circuit, depending on the force exerted by the oil pressure on the valve. Moreover, a hydraulic control system of the sliding vane pump's displacement is realized through a control duct (14). Specifically, this duct connects the main oil gallery to control plenums embedded directly on the pump stator. In this way, as the pressure in the main oil gallery rises, the oil pressure on the stator increases, and the pump eccentricity is reduced. Hence, for a given pump speed (fixed by the crankshaft), the oil flow rate reduces as well.

It is worth noting that, in reality, the control system of the oil flow rate is constituted by many hydraulic subcomponents (as suggested by Figure 8-5 (b)), whose detailed description goes beyond the scope of this thesis, and thus it has been omitted.

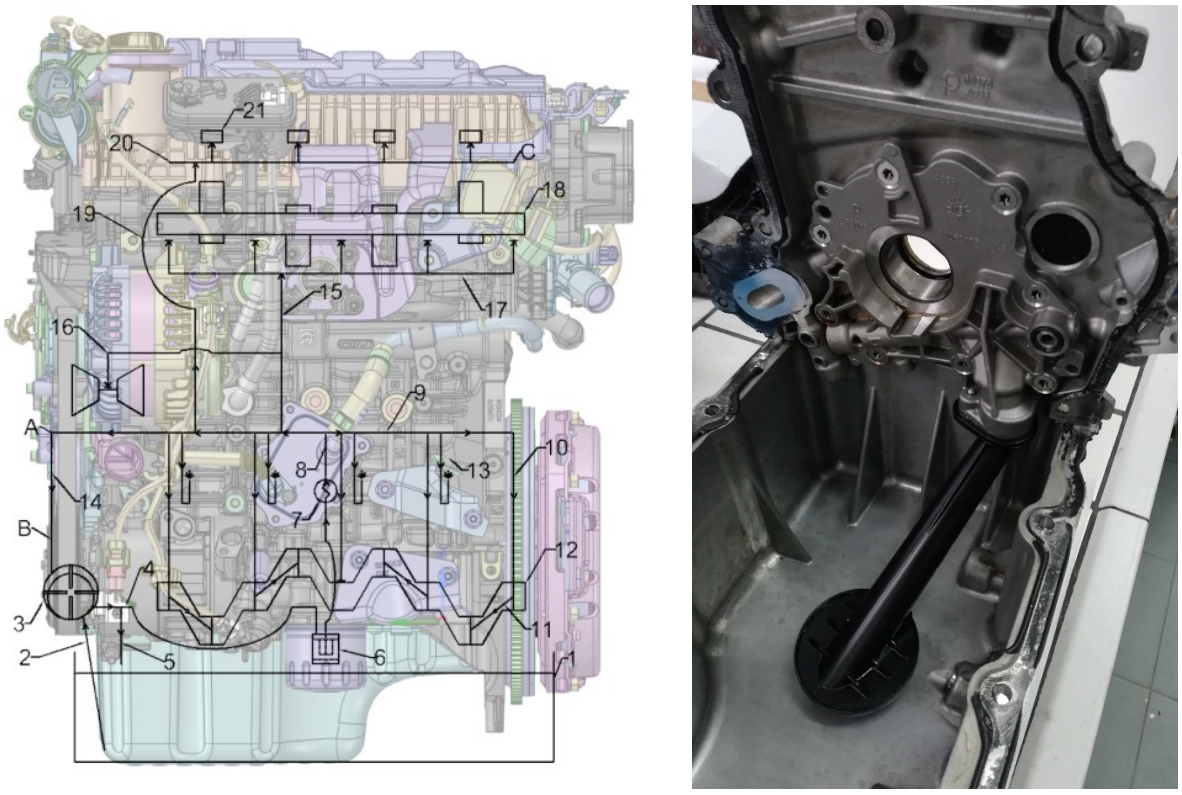

(a) (b)

Figure 8-5. Schematic of the engine lubricant circuit (a), and of the suction head facing the oil sump (b).

Finally, the standard system includes a pressure sensor (A), which sends a signal of the oil pressure inside the main oil gallery to the engine ECU. Moreover, a pressure regulator (B) bypasses part of the oil flowing to the pump control system (14) towards the engine timing chain, allowing its lubrication. Finally, a sensor (C) measures the temperature of the oil at the VVA system. As will be described in Section 8.3.1, other sensors will be installed in the engine

lubricant system, in order to characterize completely also the thermal dynamics of the engine oil.

8.3 Vehicle experimental setup

8.3.1 Instrumentation of the cooling system

In order to measure the thermal dynamics of the engine during the warm-up phase, its cooling system (the high temperature coolant loop in Figure 8-3) has been instrumented with additional sensors compared to those standardly equipped on the engine. Moreover, some thermocouples have been installed also in the lubricant circuit and in the engine block. The aim is to provide a comprehensive understanding of the interaction between coolant fluid, lubricant oil and metallic masses in defining the thermal inertia of the entire system during the warm-up period. This is also necessary to identify any correlation with the emissions measured through the PEMS system, which will be described later in Section 8.3.3.

A schematic of the additional sensors installed in the engine cooling system is reported in Figure 8-6. Specifically, there are seven thermocouples and five pressure transducers.

Among the seven K-type thermocouples, two of them have been installed in each of the two branches of the cooling circuit: specifically, one (T_5) after the oil-cooler in the by-pass loop (coolant side), and another after the engine radiator (T_6). Moreover, one thermocouple has been fitted inside the engine oil dipstick, in order to measure the temperature of the oil in the sump ($T_{oil,sump}$).

The remaining four thermocouples have been installed directly in the engine block (T_1, T_2, T_3 and T_4). Their exact position is shown in Figure 8-7. Specifically, T_1 and T_2 are the closest to the combustion chamber, being them placed in the cylinder liner of the second cylinder, i.e. in the metallic wall diving the combustion gases from the coolant flow. In particular, T_2 is at the top of the combustion chamber, whereas T_1 at the bottom of the cylinder liner. Finally, the thermocouple T_3 is installed at the external wall of the coolant flow passage, and T_4 at the external cover of the engine block, which is in contact with the ambient air.

These positions have been chosen in order to have a clear view of the thermal gradient existing inside the engine block. In fact, T_2 is expected to measure the highest temperature, due to its proximity with the combustion gases, whereas T_4 will likely measure the lowest one, being the outermost sensor. More difficult is to imagine the temperatures measured by T_1 and T_3, which will depend on the specific local heat exchange phenomena with the coolant fluid, especially during the warm-up phase.

It is worth noting that these four thermocouples have been placed at a distance equal to 1 mm from the internal wall of the cylinder liner (T_1 and T_2), the coolant flow passage (T_3) and the external block cover (T_4). Moreover, they have a rigid probe with a 1.5 mm diameter, and have been sealed with the engine block by using a high temperature resistant adhesive. A

detailed drawing of the position of the thermocouples in the engine block was omitted for reasons of confidentiality.

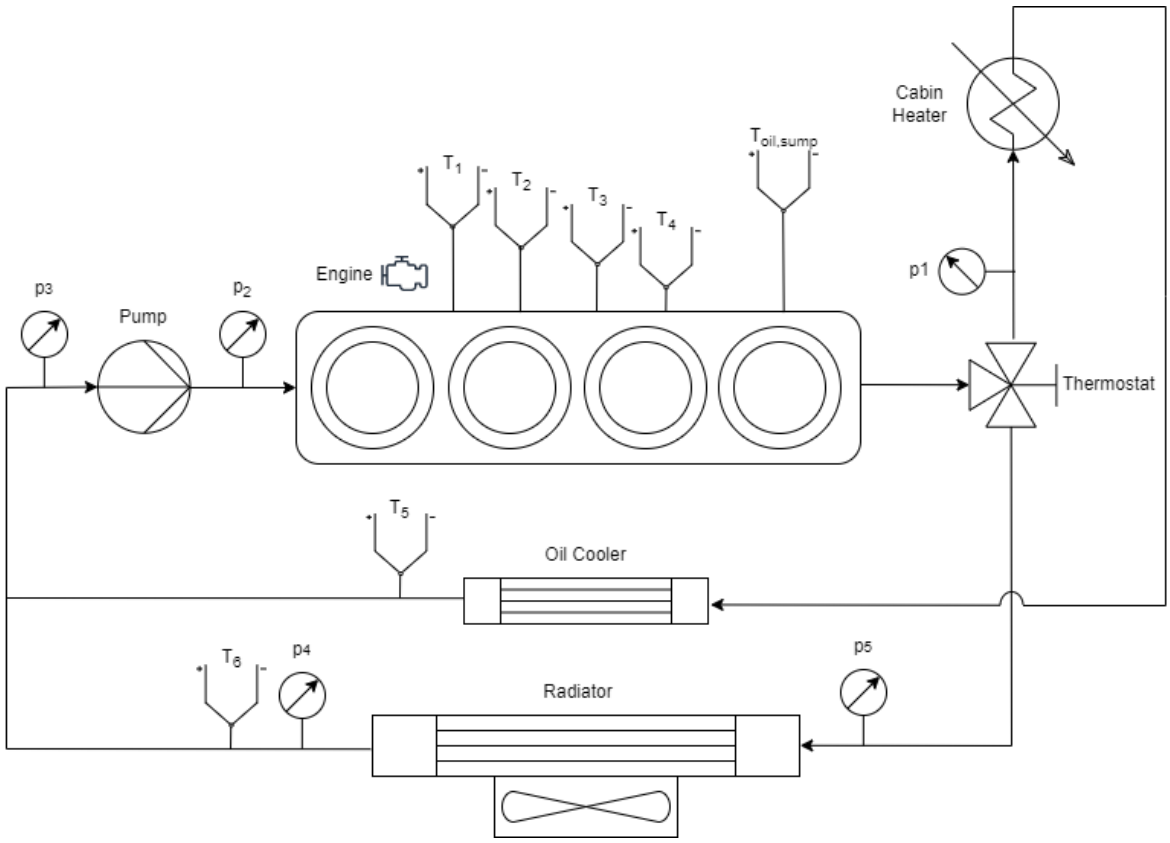

Figure 8-6. Scheme of the sensors introduced in the engine cooling system.

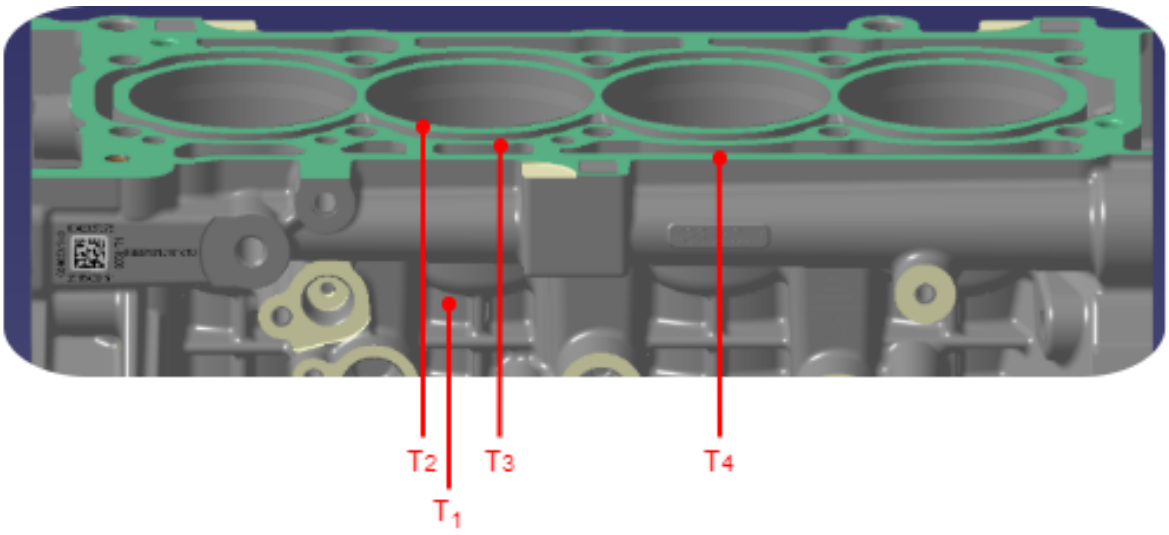

Figure 8-7. Position of the thermocouples installed in the engine block.

An image of the thermocouples installed in the FireFly T4 engine under the hood of the Jeep Compass is reported in Figure 8-8. In particular, the oil sump ($T_{oil,sump}$), the engine block (T_1, T_2, T_3 and T_4) and the oil-cooler (T_5) thermocouples can be observed. An enlargement of the

engine block thermocouples and of the oil cooler one is reported in Figure 8-9 (a) and (b), respectively.

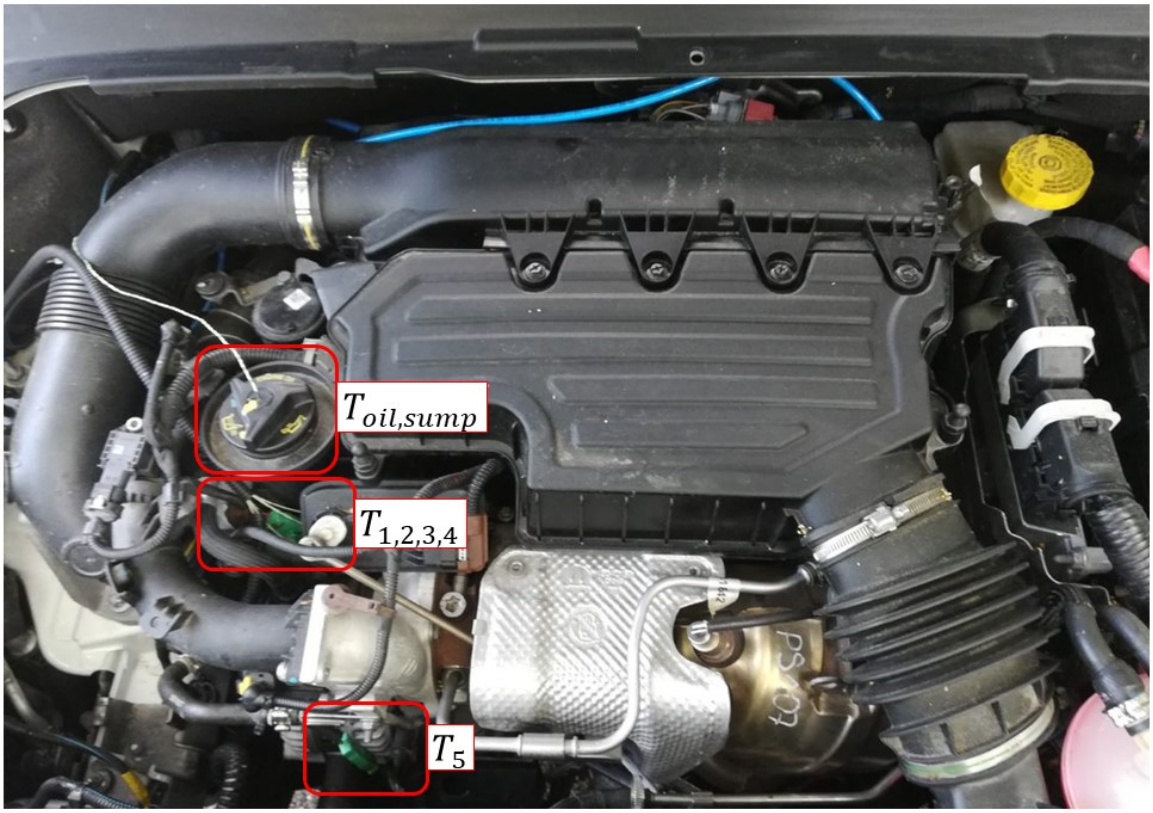

Figure 8-8. Image of the FireFly T4 engine under the hood of the Jeep Compass, with some of the additional sensors installed: specifically, the thermocouples in the oil sump ($T_{oil,sump}$), engine block (T_1, T_2, T_3 and T_4) and oil cooler (T_5).

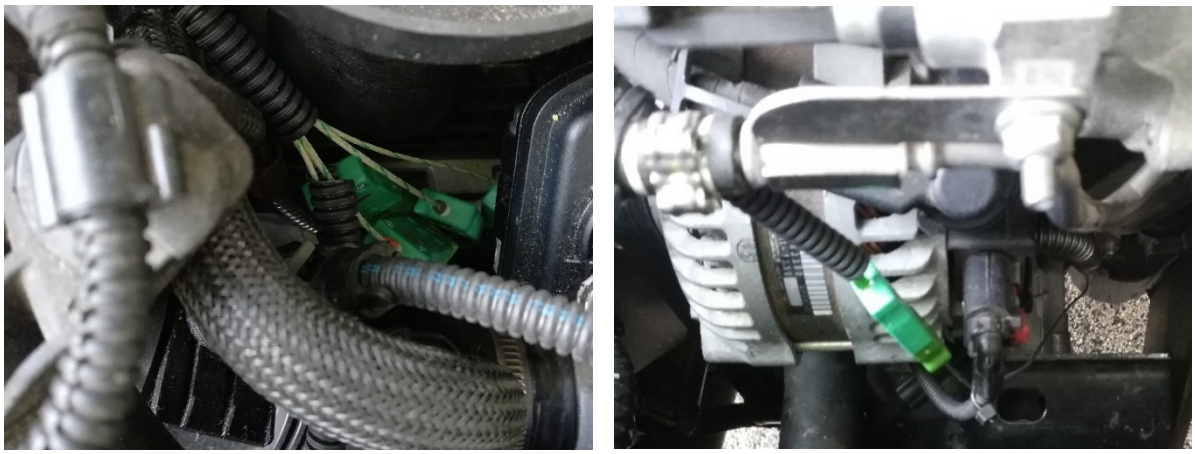

(a) (b)

Figure 8-9. Details of the some of the thermocouples installed in the engine cooling system: specifically, in (a) the thermocouples mounted in the engine block (T_1, T_2, T_3 and T_4), and in (b) the one at the oil cooler outlet (T_5).

For what concerns the five pressure transducers, they have been installed in different positions along the cooling circuit. The aim is to have an experimental evidence of how the

coolant flow is divided among the bypass and the radiator branches. In fact, the thermostat valve is characterized by a typical hysteresis loop, and its position (which depends on the coolant temperature) is not monitored during engine functioning. Hence, if a pressure difference among either ends of one branch is measured, it means that part of the coolant fluid flows in it.

Following this principle, two pressure sensors have been installed at the in/out pipes of the engine radiator (p_5 and p_4, respectively), and another one (p_1) along the bypass branch, between the thermostat and the cabin heater. Moreover, other two pressure sensors have been positioned at the suction (p_3) and discharge (p_2) sections of the coolant pump, in order to measure the pump head during engine operation.

Due to the small interstices available on the engine for the installation of the sensors, small diameters tubes (with an internal diameter equal to 5 mm) have been attached directly in the most accessible points of the engine cooling circuit. Then, the tubes have been arranged around the engine to transfer the pressure signal to the pressure transducers, which have been poisoned in the left-upper part of the hood, where more space for their housing was available (Figure 8-10 (a)). Finally, the electric signals have been passed to the DAQ system placed inside the cabin through a hole realized at the passenger side, together with the extensions of the thermocouples (Figure 8-10 (b)).

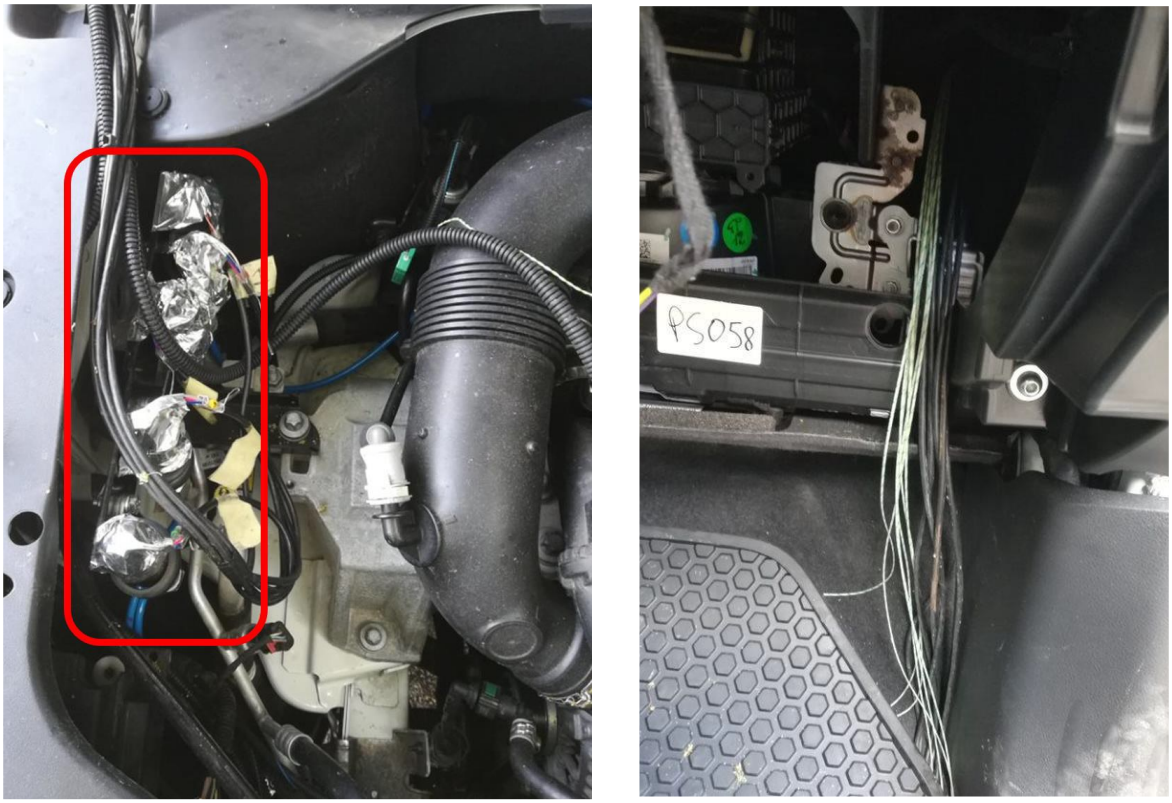

(a) (b)

Figure 8-10. Pressure sensors housed in the left part of the hood and connected in different points of the cooling circuit (a); tunnel realized to make way for the cables passing from the hood to the cabin (b).

The pressure transducers are the model type *TK* produced by the company *Gefran* (Figure 8-11). They are diaphragm pressure sensors, suitable for applications where the transducer is far from the measuring point, as in this case. The main features of these transducers are (further information can be found in [270]):

- measuring range: 0 – 5 bar;
- output signal: 0 – 10 V in DC;
- power supply: 10 – 30 V in DC.

Figure 8-11. Detail of the pressure transducer used to measure the pressure of the cooling fluid.

8.3.2 DAQ system

The data acquisition (DAQ) system implemented in the vehicle cabin is an INCA-ETAS™ DAQ system, suitably tailored for the aim of this experimental study.

It is composed by hardware components, i.e. ETAS modules, and by the software INCA installed on a personal computer (PC), to manage the in/out signals. Specifically, several ETAS modules have been connected together in order to manage simultaneously in an INCA environment both the signals coming from the sensors installed in the engine cooling system, and those registered by the engine ECU. This system allows to produce also output signals, which could be used to control electric devices, such as an electric cooling pump.

The following ETAS modules have been used:

- ES930.1, which is the main module for the acquisition of the additional sensors installed on the engine;
- ES413.1 and ES421.1, which are extension modules to increase the number of input signals registered by the main module ES930.1;
- ES582.1, which is used to acquire the quantities registered by the OBD system.

Figure 8-12 shows the DAQ system seen from the vehicle cabin. In this figure, the OBD module ES582.1, the extension modules ES413.1 and ES421.1 and the PC used to run INCA can be distinguished, whereas the main module ES930.1 is hidden by the passenger seat. In the following Section, each of these modules will be described in detail.

Figure 8-12. Image of the cabin equipped with the INCA-ETAS DAQ system.

8.3.2.1 Hardware

The ES930.1 Multi-I/O Module is a compact, robust and powerful metrology module with numerous input and output channels. The module can be used for a variety of measuring tasks, or for the control of additional hardware in the development, application and validation of electronic vehicle systems.

Overall, the ES930.1 module features 16 input and 10 output channels, as well as other channels for the sensors' power supply. More specifically:

- 4 thermo inputs;
- 8 analog inputs;
- 4 digital inputs;
- 4 analog outputs;
- 4 sensor supplies;
- 6 digital outputs, which also provide the control signals for the half-bridge switches;
- 6 half-bridge switches with current measurement.

(a)

(b)

Figure 8-13. Front (a) and rear (b) views of the ETAS ES930.1 module [271].

Since the power stages are integrated in the ES930.1 module, the pressure transducers are powered directly by the module, which in turn is powered through the IN port (Figure 8-13 (b)) from the 12 V cabin plug. Moreover, this module communicates with the PC via Ethernet through the same IN port, and it is integrated in the measuring setup within the decentral ETAS Ethernet topology (called *daisy chain*). Hence, the number of channels can be expanded by connecting several ES930.1 modules to a chain, which includes other measuring modules. As will be described later in this Section, the ES413.1 or ES421.1 extension modules were added to carry on this study, in order to manage all the sensors installed in the engine.

The front side of the ES930.1 module (Figure 8-13 (a)) features the connections summarized in Table 8-5. Moreover, four LEDs are featured. The LEDs U1 and U2 can be configured by the user in the application software, whereas the LEDs ER and ON indicate the operating states of the module summarized in Table 8-6.

Instead, the rear side of the ES930.1 module (Figure 8-13 (b)) features the connections summarized in Table 8-7. Specifically, the connections with the *daisy chain* can be

distinguished, which are used to power and connect the main module to the PC (IN port), as well as to connect the extension modules ES413.1 and ES421.1 (OUT port).

Name	Connection	Meaning
TH1-4	Thermo channel	Thermo measurement (channel 1 to channel 4)
PS	Power stages	Power stages (6 Half-bridges with current measurement) and external supply
DO	Digital outputs	Digital output channels (channel 1 to channel 6)
DI	Digital inputs	Digital input channels (channel 1 to channel 4)
AO	Analog outputs	Analog output channels (channel 1 to channel 4)
AI 5-8	Analog inputs	Analog input channels (channel 5 to channel 8); sensor supply channels (channel 3 and channel 4)
AI 1-4	Analog inputs	Analog input channels (channel 1 to channel 4); sensor supply channels (channel 1 and channel 2)

Table 8-5. Legend of the channels available at the front of the ES930.1 module [271].

LED ER	LED ON	Operating state	Comment
Off	Off	Module off	No power supply, power supply defective
Off	Green	Normal	Module on, no error
Red	Off	Hardware error	Internal error
Red	Green	LED test	Briefly during initialization of the module
Red	Green	Internal error	Module features no valid calibration. Measurements are possible in principle. The measuring accuracy is out of specification. Send the module to ETAS for calibration/repair.
Red, flashing	Green	Update process	Update of firmware

Table 8-6. Legend of the operating states of the ES930.1 module indicated by LED ER and LED ON [271].

Name	Connection	Meaning
IN	Daisy chain In	Input; Ethernet connection to the previous module or the PC, power supply of the module
OUT	Daisy chain Out	Output; Ethernet connection and power supply of the succeeding module
SERVICE	Service	Reserved; for ETAS-internal application only; no provision of functions for the customer

Table 8-7. Legend of the connections available at the rear of the ES930.1 module [271].

Figure 8-14 shows an image of the ES930.1 module housed under the passenger seat, with the connections actually used in this experimental activity. Clearly, the input channels available in this module are not enough to acquire all the signals coming from the additional sensors mounted on the engine (Figure 8-6). In fact, the main module manages only four out of seven thermocouples (T_1, T_2, T_3 and T_4, set as thermo inputs), and four out of five pressure transducers (p_1, p_2, p_3 and p_4, set as analog inputs). Hence, two extension modules have been added in the *daisy chain*, as will be described in the following.

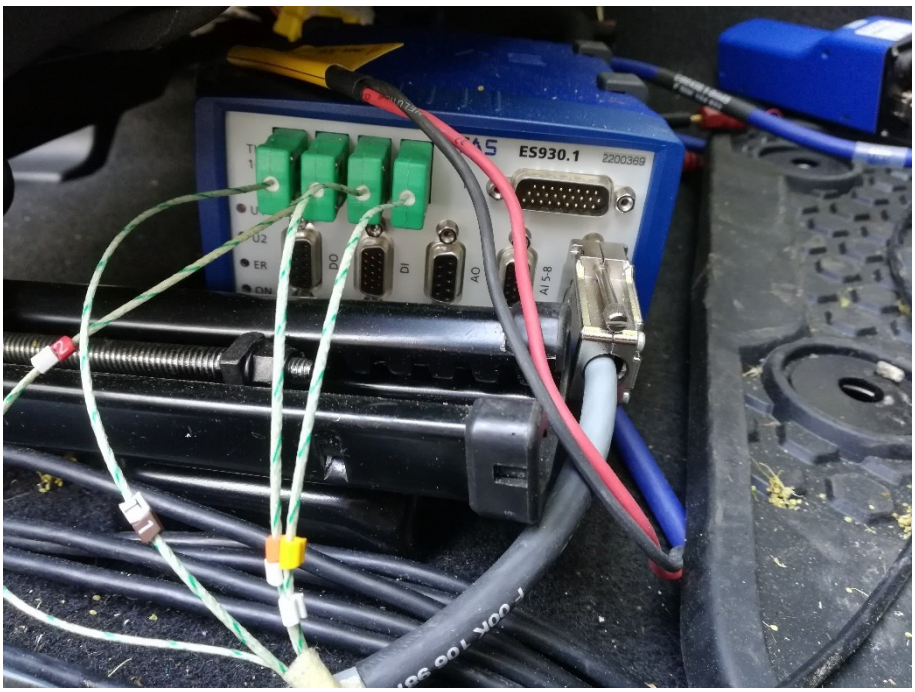

Figure 8-14. Image of the ES930.1 module with the channels actually used.

The main module ES930.1 is able to manage a wide variety of input signals. However, the main features noteworthy for this experimental study can be summarized as follows:

- The maximum voltage of the analog input signals is 60 V in DC, and 30 V in AC.
- The cut off frequency of the anti-aliasing filter is 10 kHz.
- The maximum sample rate of the analog inputs is 40 kHz.
- The maximum measuring range of the thermo inputs goes from -200°C to 1372°C for K-type thermocouples.
- The voltage of the power supply of transducers can be selected by the user within the range +5V / +15V (through the INCA interface).
- The sample rate is adapted automatically depending on the variability of the measured quantities. This setting is necessary if the recording of the quantities coming from the engine ECU wants to be performed simultaneously to the that of the sensors managed by the *daisy chain*. Hence, for high variable engine operating points, the module will increase the sample rate, whereas for steadier ones, the sample rate will be coarser.

Finally, it is worth noting that, while the thermo input connections are simply K-type plugs, the analog inputs are managed through a 15-pin high density DSUB socket (Figure 8-13 (a)), to which a specific cable (named CBAV420.1) can be connected (Figure 8-15). This cable has an open end with different colored sub-cables, that must be assigned to each pressure transducer according with the specifications reported in Table 8-8.

In this way, each pressure signal is assigned to the right pin of the analog input port. An image of the electronic board built to manage the analog channel inputs and the pressure transducers is reported in Figure 8-16.

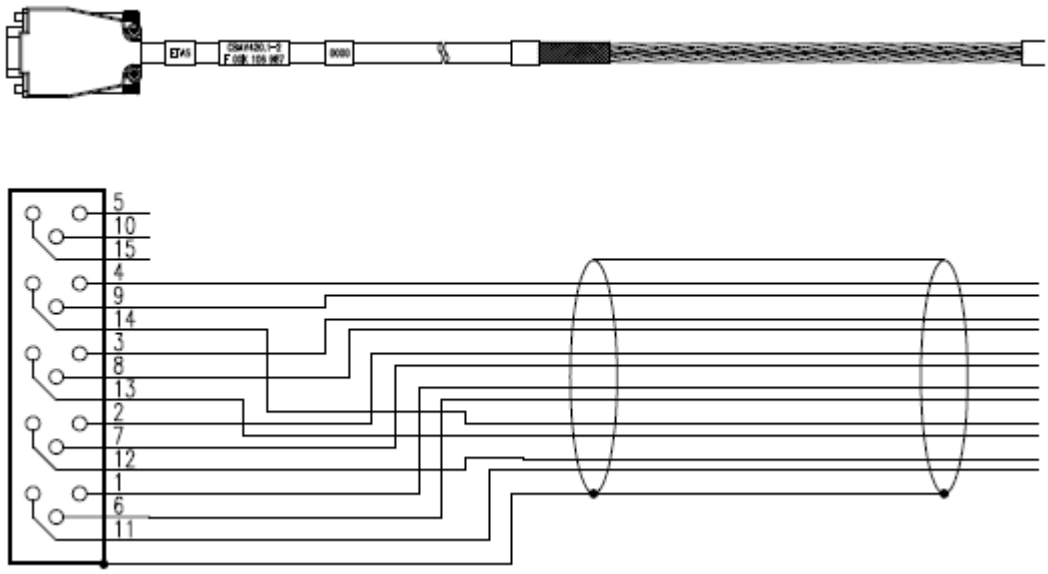

Figure 8-15. CBAV420.1 cable with wiring plan [272].

HD-SUBD PIN	Signal	Open cable end Pair	Color
4	AI_CH4	1	white
9	AI_CH4_GND	1	brown
3	AI_CH3	2	green
8	AI_CH3_GND	2	yellow
2	AI_CH2	3	gray
7	AI_CH2_GND	3	pink
1	AI_CH1	4	blue
6	AI_CH1_GND	4	red
14	SensorSupply_CH2_GND	5	black
13	SensorSupply_CH2	5	violet
12	SensorSupply_CH1_GND	6	gray/pink
11	SensorSupply_CH1	6	red/blue
5, 10, 15	N.C.		
Housing		Shield	

Table 8-8. Assignment of the CBAV420.1 cable when used at "AI 1-4" connection [272].

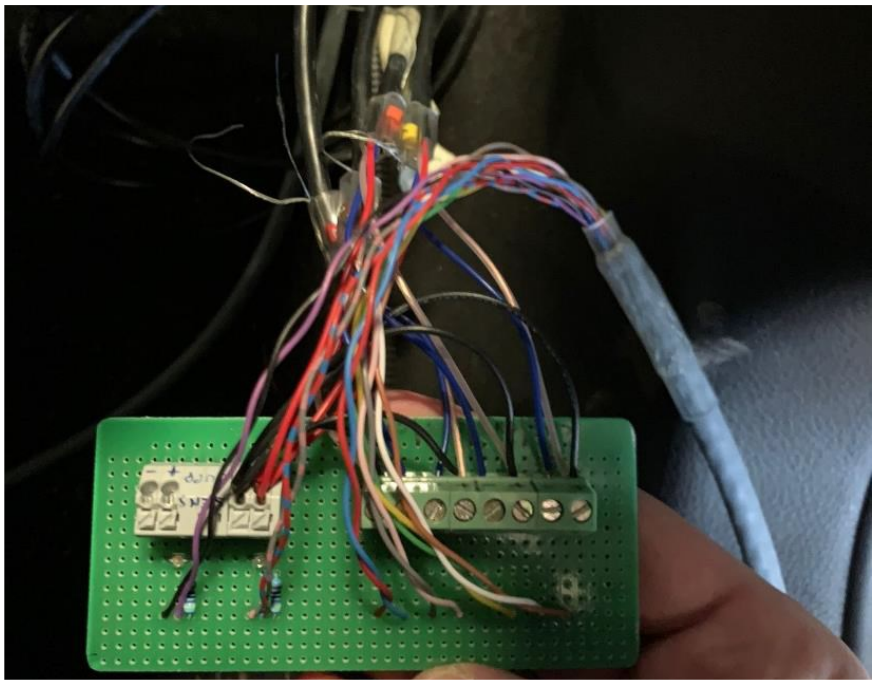

Figure 8-16. Image of the electronic board built to assign each pressure signal to the right pin of the analog input port.

To acquire all the sensors installed on the engine (Figure 8-6), the extension modules ES413.1 and ES421.1 have been added to the main one (the ES930.1), in order to form a *daisy chain*, i.e. a network of ETAS modules all connected to the same DAQ system.

The ES413.1 module allows to acquire four additional analog inputs (Figure 8-17 (a)). Every channel has its own power supply, and the same features already described for the main module ES930.1. Moreover, the module ES421.1 (Figure 8-17 (b)) adds eight K-type thermocouples to the *daisy chain*, with the same features of the thermo inputs available in the main module.

(a) (b)

Figure 8-17. ETAS ES413.1 (a) and ES421.1 (b) modules [273,274].

Each of these extension modules is connected with the main one through IN/OUT ports (Figure 8-18). Specifically, the three modules are daisy-chained together, linking the OUT port

of the main module with the IN port of the first extension module, and so on. This connection provides also the power supply to the extension modules, and thus to the attached sensors.

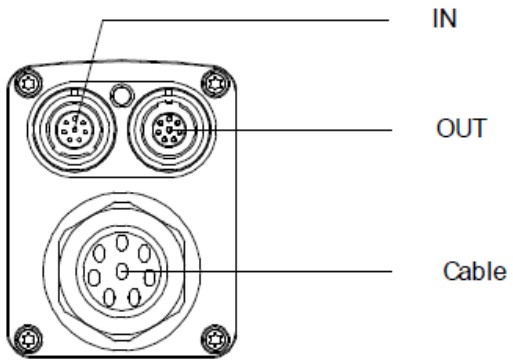

Figure 8-18. Frontal view of the additional modules: the ES421.1 has the connection cable for 8 thermocouples, whereas ES413.1 the cable with the pins for the four analog inputs [273].

In this way, a *daisy chain* for Measurement and Calibration applications has been realized. Generally, such DAQ systems can include also other components, as the Lambda module (Figure 8-19). However, in this experimental activity, only the main module (ES930.1) and two extension ones (ES413.1 and ES421.1) have been employed (Figure 8-20), with the addition of the stand-alone module ES582.1 to register the data coming from the engine ECU (described later in this Section). Specifically, the extension module ES413.1 allows to acquire the fifth pressure transducer (p_5 in Figure 8-6, set as an analog input), and the ES421.1 to acquire the remaining three thermocouples (T_5, T_6 and $T_{oil,sump}$, set as thermo inputs).

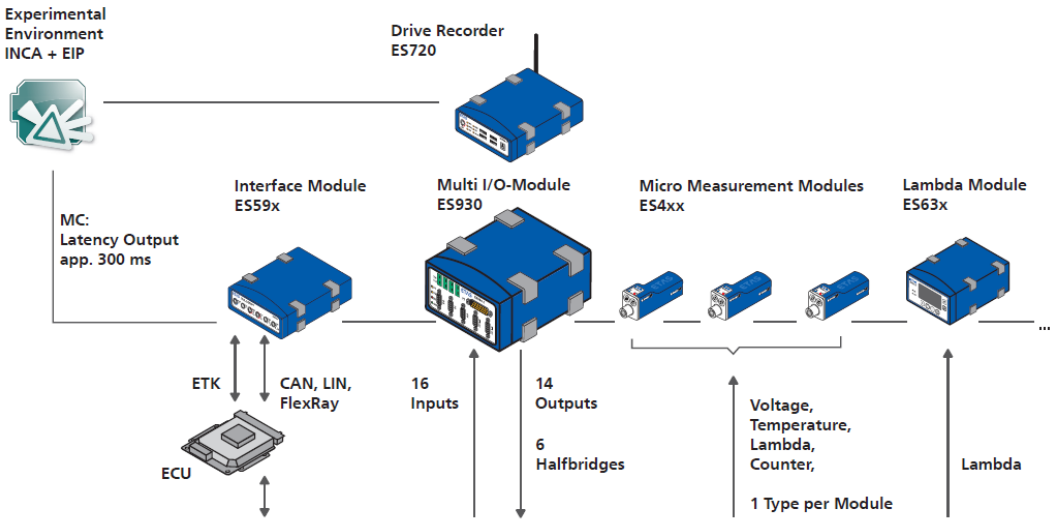

Figure 8-19. Example of *daisy chain* for Measurement and Calibration applications [273].

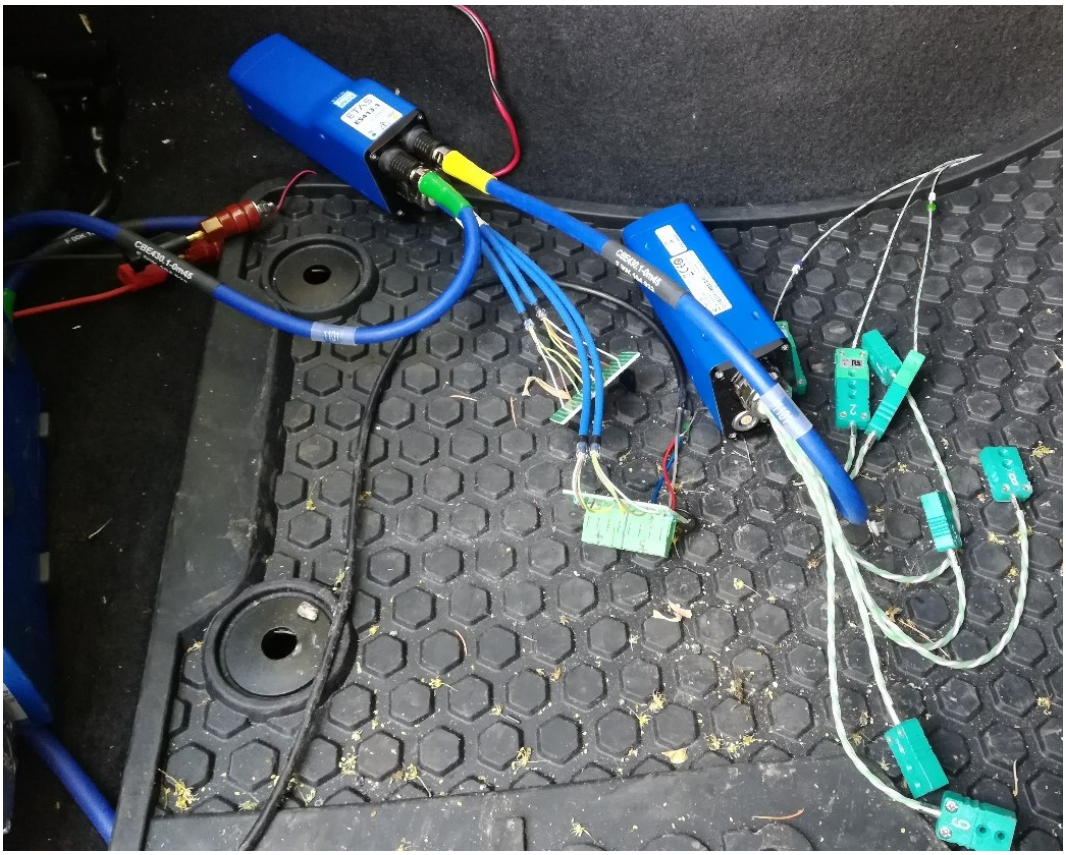

Figure 8-20. Image of the extension modules ES413.1 and ES421.1, connected together and with the main module ES930.1 (not visible in the figure) to form a *daisy chain*.

The ES582.1 is a CAN FD (Flexible Data Rate) Bus Interface USB module, which is stand-alone relatively to the *daisy chain* described above. It is used to transfer the data registered by the engine ECU to the PC, thus allowing to manage them through the INCA software. This module is equipped with two CAN/CAN FD interfaces for connection to the CAN bus of a vehicle or an ECU, as well as with a USB port for the connection with a PC or a drive recorder (Figure 8-21).

The CAN-bus (Controller Area Network) is the “language” used on board of a vehicle to exchange data from different control units. In this specific case, the ES582.1 module has been used for recording and acquiring calibration communication data from the engine ECU via the CAN bus interface. This has been accomplished by connecting the CAN FD port with an OBD by-pass port, made available by the vehicle manufacturer to access to a broader range of parameters registered by the engine ECU (Figure 8-22).

The operating states of the ES582.1 module are indicated by different LEDs placed directly on the module, whose meaning has been summarized in Table 8-9.

Figure 8-21. ETAS ES582.1 stand-alone module, with an USB port and a CAN FD Bus Interface [275].

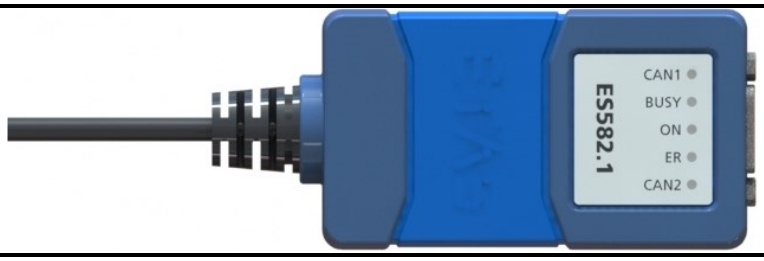

LED	Display	Description
CAN1	Flashing yellow	Communication at the CAN1 interface
	Off	Communication at the CAN1 interface interrupted
	Red	Communication error at the CAN1 interface
BUSY	Blue	Module is in the boot phase or a firmware update is being performed. Do not disconnect the module from the PC!
	Off	Normal operation
ON	Green	Module is switched on
	Off	Module is switched off
ER	Red	Booting was not successful or software error of module. Restart the module.
	Off	No error
CAN2	Flashing yellow	Communication at the CAN2 interface
	Off	Communication at the CAN2 interface interrupted
	Red	Communication error at the CAN2 interface

Table 8-9. Legend of the operating states of the ES582.1 module [275].

(a) (b)

Figure 8-22. Image of the ES582.1 module (a), and of the OBD by-pass port (b).

8.3.2.2 Acquired parameters

The DAQ system described in the previous Section allows to acquire the parameters coming from the additional sensors mounted in the engine, as well as from the engine ECU.

In Table 8-10, the parameters acquired from the Engine ECU through the ES582.1 module have been reported. It is worth noting that not all these parameters are measured, being some of them calculated by the ECU according to pre-loaded performance maps. Typical examples are the engine torque or the cylinder pressure. Moreover, the available software interface and OBD by-pass connection allowed to record a limited number of ECU parameters. Hence, Table 8-10 reports only those selected among all the others.

The parameters acquired by the additional sensors installed on the engine have been reported from Table 8-11 to Table 8-13. Those acquired by the main module ES930.1 have been summarized in Table 8-11. There are four pressure signals, set as analog inputs, which refer to the pressures of the coolant fluid at the positions identified in the engine cooling circuit reported in Figure 8-6. In particular, they are the pressures at the in/out sections of the cooling pump (p_3 and p_2), and those at the engine and radiator outlet pipes (p_1 and p_4). Moreover, four temperature signals corresponding to the four thermocouples installed in the engine block (Figure 8-7) have been set as thermo inputs.

The remaining sensors have been connected with the additional input channels made available by the extension modules. Specifically, the engine radiator inlet pressure (p_5) has been recorded by the ES413.1 module (Table 8-12). In addition, the ES421.1 module acquires the remaining three thermocouples as thermo inputs (Table 8-13). They are the coolant temperature at the Oil Cooler and Engine Radiator outlet sections (T_5 and T_6, respectively), and the oil temperature at the sump ($T_{oil,sump}$).

N°	Parameter name	Unit	Description
1	Time	[s]	
2	OIL_PRESSURE_ABS	[kPa]	Oil pressure
3	THR_INLET_GAS_TEMP	[°C]	Throttle Inlet Gas Temperature upstream turbocharger / downstream throttle
4	PTC_FW_TRQ_ACT	[Nm]	Actual static torque input to the transmission
5	PREM	[mbar]	Inlet manifold pressure
6	KNK_SENSOR_VOLTAGE_CYL	[V]	Knock sensor cylinder 2
7	DI_FUEL_PRESS_SCALED	[MPa]	Gasoline pressure
8	FUEL_MASS_CYL1	[mg/charge/cyl]	Steady state fuel mass required per cylinder
9	FAN_SPEED	[rpm]	Current Fan speed in RPM.
10	ANGFARLW	[deg]	Throttle angle
11	TRANS_CURRENT_GEAR	[count]	Current gear of transmission
12	ECT	[°C]	Scaled coolant temperature
13	RPM	[rpm]	Engine speed
14	TOILVVA	[°C]	Oil temperature MultiAir system
15	KNK_TOTAL_RETARD_CYL	[EngineDeg]	Spark ignition delay cylinder 2
16	PERAPDL	[%]	Gas pedal opening
17	PREUTH	[mbar]	Upstream throttle / compressor outlet pressure
18	BARO	[kPa]	Barometric pressure
19	QAH	[kg/h]	Intake air flow rate
20	ANGVVAEC	[EngineDeg]	Inlet valve closing angle
21	CYL_PRESS_1	[MPa]	Cylinder pressure
22	EXH_PRESS	[kPa]	Absolute (i.e. not the 'gauge') back pressure in the exhaust system
23	ENILMPRGMN_PowerTot	[kW]	Total Power
24	COMRX_VEH_SPEED	[km/h]	'Vehicle Speed' signal received on communication bus
25	FUEL_RATE_L_PER_HR	[l/hr]	Fuel Flow Rate in L per Hr
26	ACT	[°C]	Air temperature
27	GPFT_EXH_T2_TEMP	[°C]	Exhaust gas temperature downstream the GPF
28	ETH_HEAT_COIL_PWM	[%DC]	The desired control input for electric thermostat heat coil
29	AIR_PORT_MASS_FLOW_CYL1	[g/s]	Air mass flow into intake port of cylinder 1
30	WG_FDB_POS_DEG	[deg]	Wastegate actuator feedback position in degrees
31	TEXH	[°C]	Estimated Exhaust Gas Temperature
32	LV2_EngineFrictionTorque_FOR_BUS	[Nm]	Level 2 value of outgoing engine friction value
33	ANGVVAHB	[EngineDeg]	Inlet valve opening angle
34	GPFT_EXH_T1_TEMP	[°C]	Exhaust gas temperature upstream the GPF
35	FUEL_FLOW_RATE	[g/s]	Instant mass flow rate of fuel through the injectors

Table 8-10. Parameters acquired from the Engine ECU through the module ETAS ES582.1.

N°	Parameter name	Channel	Unit	Description (see labels in Figure 8-6)
		Pressures – Analog Inputs		
1	Time		[s]	
2	PP_OUT	ES930_AI1_CH2	[bar]	Pump outlet pressure (p_2)
3	PRad_OUT	ES930_AI1_CH4	[bar]	Engine radiator outlet pressure (p_4)
4	PICE_OUT	ES930_AI1_CH1	[bar]	Engine outlet pressure (p_1)
5	PP_IN	ES930_AI1_CH3	[bar]	Pump inlet pressure (p_3)
		Temperatures – Themo Inputs		
1	Time		[s]	
2	T3	ES930_TH1_CH3	[°C]	Engine block temperature (T_3)
3	T4	ES930_TH1_CH4	[°C]	Engine block temperature (T_4)
4	T1	ES930_TH1_CH1	[°C]	Engine block temperature (T_1)
5	T2	ES930_TH1_CH2	[°C]	Engine block temperature (T_2)

Table 8-11. Parameters acquired by the main module ETAS ES930.1.

N°	Parameter name	Channel	Unit	Description (see labels in Figure 8-6)
		Pressures – Analog Inputs		
1	Time		[s]	
2	PRad_IN	ES413_ADS1_CH3	[bar]	Engine radiator inlet pressure (p_5)

Table 8-12. Parameters acquired by the extension module ETAS ES413.1.

N°	Parameter name	Channel	Unit	Description (see labels in Figure 8-6)
		Temperatures – Themo Inputs		
1	Time		[s]	
2	TOC_OUT	ES421_TH1_CH1	[°C]	Oil Cooler outlet temperature (T_5)
3	TRad_OUT	ES421_TH1_CH2	[°C]	Engine radiator outlet temperature (T_6)
4	T_Coppa	ES421_TH1_CH3	[°C]	Oil sump temperature ($T_{oil,sump}$)

Table 8-13. Parameters acquired by the extension module ETAS ES421.1.

8.3.2.3 Software interface

The software used to manage the hardware described in the previous Section 8.3.2.1 is INCA™ (Integrated Calibration and Application Tool), also produced by ETAS™.

INCA is a measuring, calibration, and diagnostic system that provides comprehensive measuring support, aiding in all essential tasks during control unit calibration. It consists of modular hardware and software, and thus it can be customized for specific projects and applications.

The basic software is the outer framework that can be filled with exactly the "subsystems" the user requires (Figure 8-23). Each subsystem supports a specific phase in the work process of a user and has its own user interface, i.e. its own window with menus and dialog boxes.

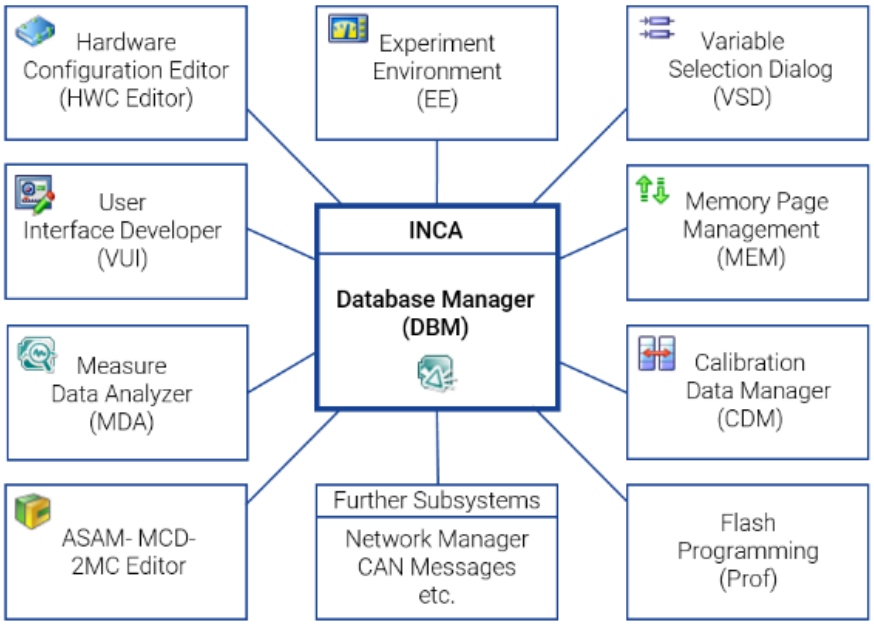

Figure 8-23. INCA and its subsystems [276].

The Database Manager (DBM) is at the heart of INCA. This is where the user starts the individual subsystems and sets user-specific options, such as the storage directories. The main purpose of the DBM is to systematically store all data created during the calibration process (workspaces, experiments, projects, and datasets) in a database, completely editable by the user.

The first step to use INCA is to configure the Hardware used in the experimental activity. This can be accomplished through the Hardware Configuration Editor (HWC) subsystem. The aim is to let the software know what kind of hardware (measuring hardware and control unit interface) is being used. In Figure 8-24 the HWC set for this experimental study is shown, where the *daisy chain* modules and the ES582.1 stand-alone module can be distinguished.

The HWC Editor allows also to configure the IN/OUT ports of each module. Among all, the measurement range and the type of output signal of the transducers can be set. An image of the HWC Editor for the ES930.1 module is reported in Figure 8-25.

Once set all the hardware, the Experiment Environment (EE) can be discussed. Basically, it contains the functionality required to perform a measurement and calibration task. These functionality can be summarized in four groups:

- Configuring. The user can select the settings required for the respective partial task, i.e. select variables to be measured and calibrated, and set sampling rate, measuring range, and display parameters for each variable.
- Measuring and recording. The user can customize the interface (measurement and calibration windows) to the task at hand. The measuring control information (recorders used for different recordings, measuring times, trigger conditions, repeat triggers, etc.) is displayed and the recordings are carried out.

- Calibrating control unit parameters. The user can modify characteristics graphically or numerically in a variety of different calibration windows (e.g., numerical editor, combined curve editor, etc.). Moreover, mathematical operations (such as addition or multiplication with a factor) can be performed. Measurement and calibration tasks can be performed simultaneously.
- Managing and Copying Data Versions. The user can load data versions into the control unit, copy them from the control unit to the hard disk and exchange them between different users.

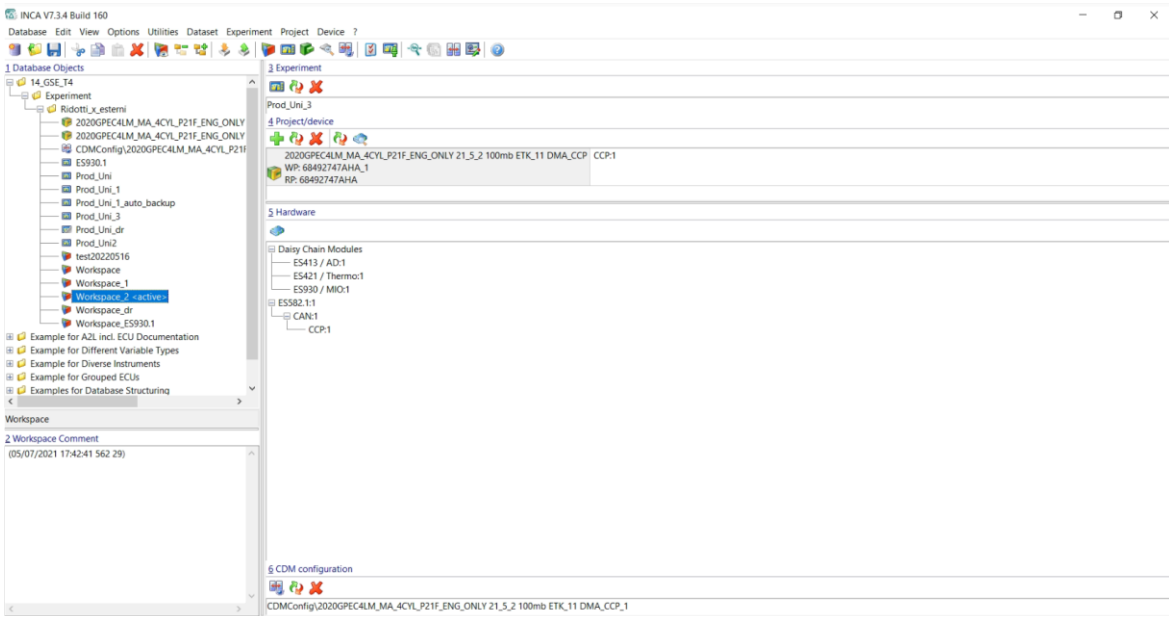

Figure 8-24. Screenshot of the Database Manager (DBM).

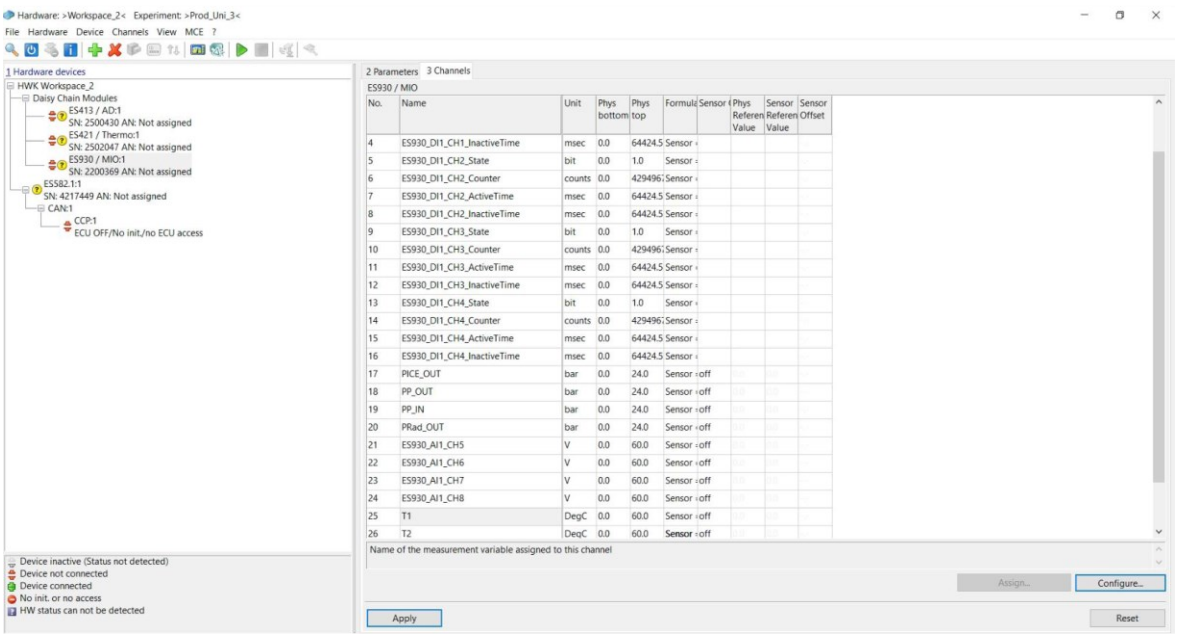

Figure 8-25. Screenshot of the Hardware Configuration Editor (HWD) relative to the ES930.1 module.

The EE programmed for this specific application is reported in Figure 8-26. The parameters relative to the engine ECU (summarized in Table 8-10) have been disposed in the left part of the Experiment, distinguishing the main pressures and temperatures in separate windows. Instead, the parameters relative to the additional sensors installed in the engine (summarized in Table 8-11, Table 8-12 and Table 8-13) have been reported in the right part of the Experiment interface. Specifically, the engine block temperatures, the coolant and oil temperatures, and the coolant pressures have been displayed in separate windows. Finally, some extra parameters have been calculated, such as the mean temperature of the engine block (Tmedia_Blocco in the figure), or the pressure losses in the main components of the engine cooling circuit (DP_Rad, DP_CabinH, DP_ICE, DeltaPP in the figure). The aim was to ease the visualization of such information during tests.

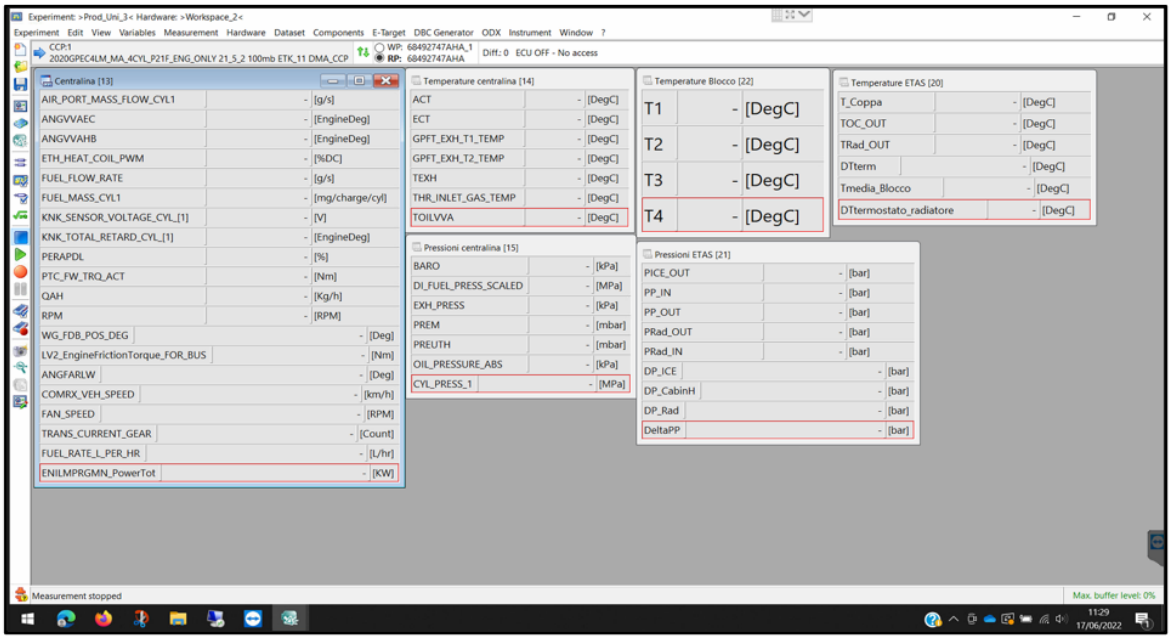

Figure 8-26. Screenshot of the Experiment Environment (EE), programmed for the specific application.

8.3.3 PEMS

To measure the emissions of the FireFly T4 engine during on-the-road tests, the *AVL M.O.V.E iS+™ PEMS* System has been installed on the Jeep Compass vehicle.

This PEMS system consists of several sub-components, each of which has a specific task. Generally, these components are (Figure 8-27):

- The *AVL M.O.V.E System Control*, which is the on-board computer responsible for the managing of all the other measuring devices.
- The *AVL M.O.V.E EFM*, which is the subsystem for the measurement of the exhaust gases flow rate.
- The *GAS PEMS iS+*, which is the subsystem for the measurement of pollutants and CO_2 emissions.
- The *PN PEMS iS*, which is the subsystem for the measurement of the Particulate Number (PN).
- A *GPS probe*, for the measurement of the GPS position of the vehicle and of the ambient conditions (pressure, temperature, humidity, etc.).
- An *ECU OBD II connection*, to connect with the OBD system of the vehicle and acquire the main parameters registered by the engine ECU (engine speed, coolant temperature, etc.).

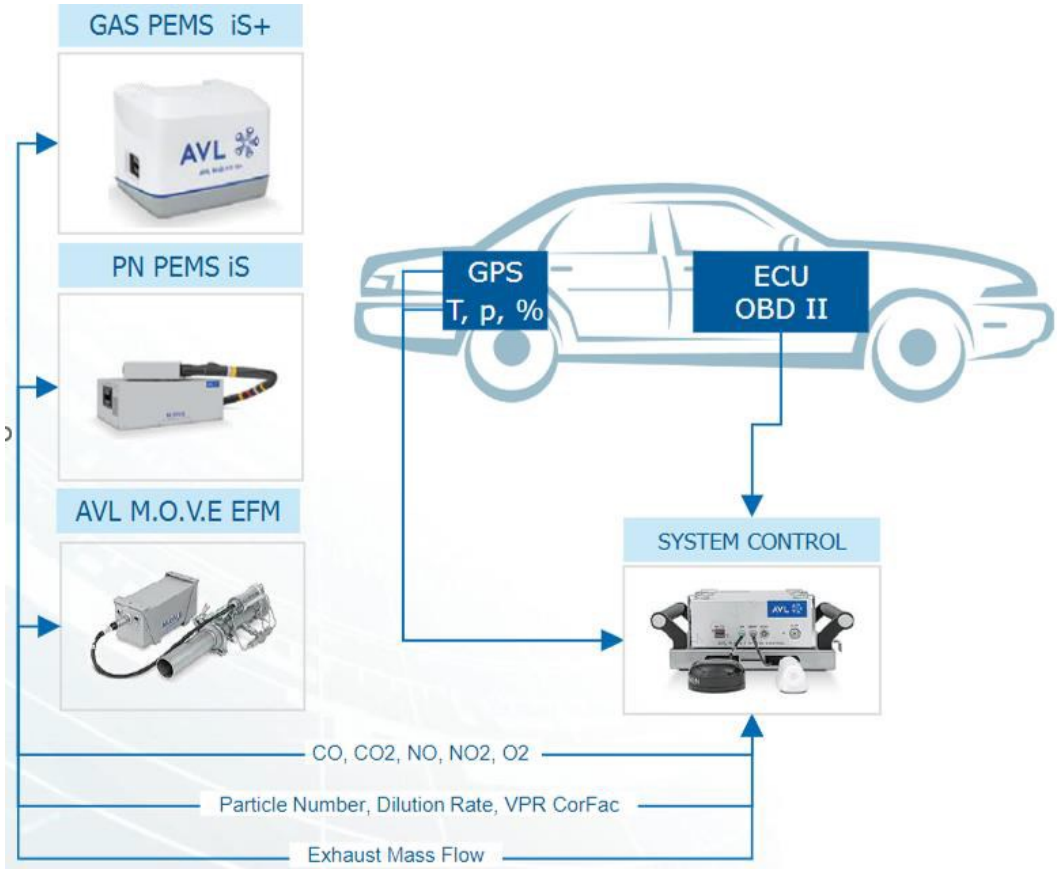

Figure 8-27. Overview of the AVL M.O.V.E iS+ PEMS System [38].

It is worth noting that advanced AVL PEMS systems include also a further component (called *FID iS*) dedicated to the measurement of Unburned Hydrocarbons (UHC), and a suitably modified version of the *GAS PEMS iS+* to measure also the Particulate Matter (PM) emissions.

The power is supplied to all these subsystems by an energy box (called *E-Box*), which is powered by a 24V-30Ah battery pack, or by a 24V-30A Charger in case the batteries are recharging (Figure 8-28).

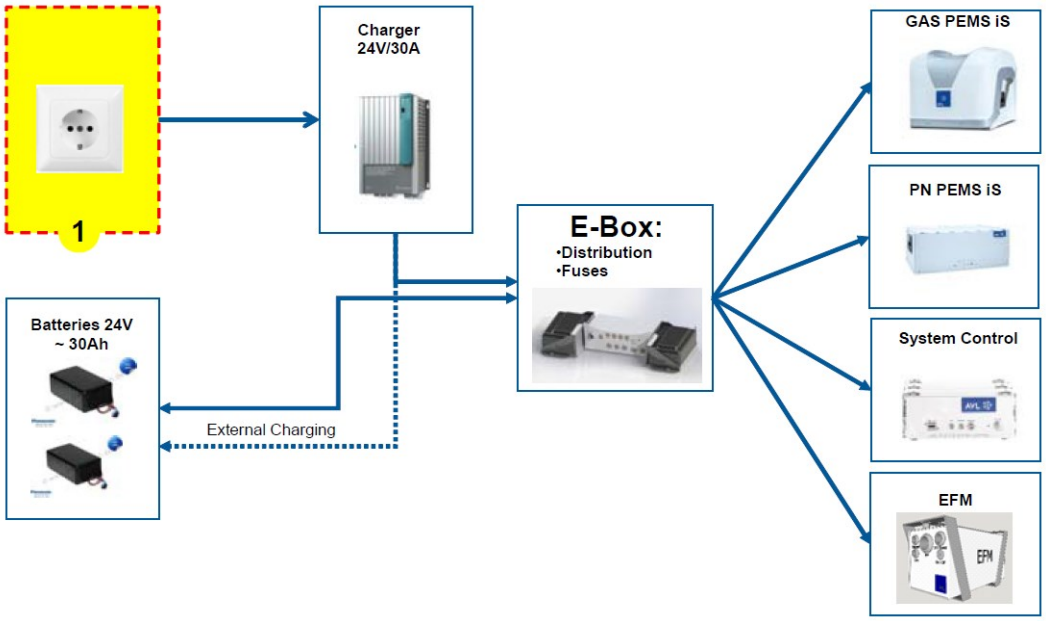

Figure 8-28. Power supply distribution among the components of the AVL M.O.V.E iS+ System [277].

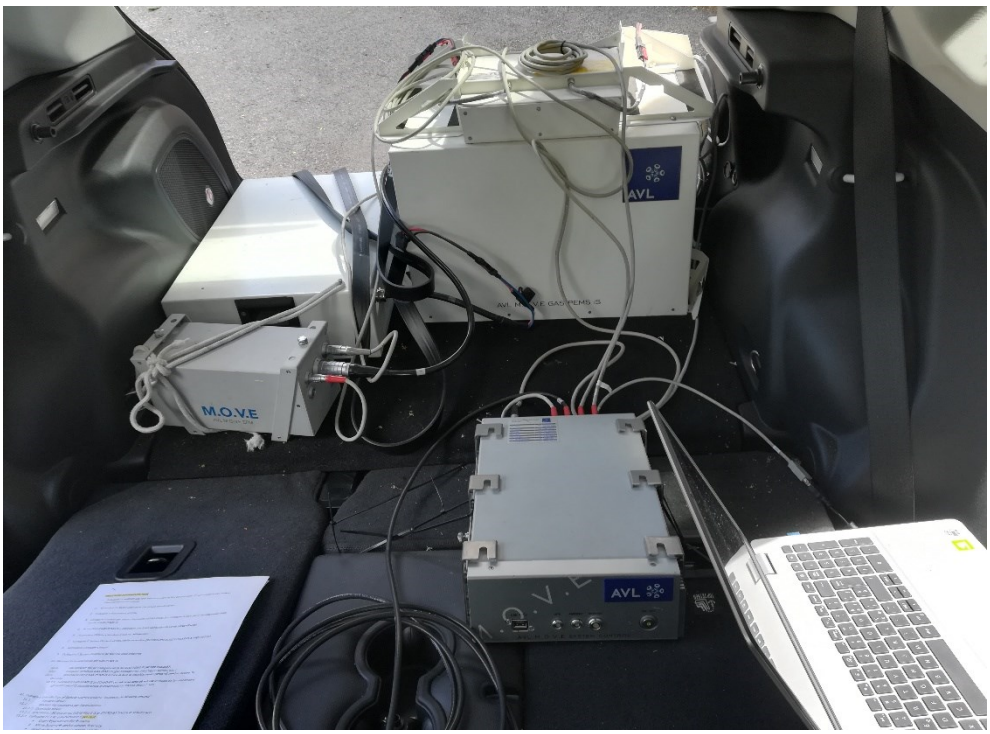

Figure 8-29. Overview of the AVL PEMS installed on the Jeep Compass, seen from the vehicle cabin.

(a)

(b)

Figure 8-30. Overview of the AVL PEMS installed on the Jeep Compass, with open (a) and closed (b) tailgate.

In this experimental activity, a simplified version of the *AVL M.O.V.E iS+ PEMS* System has been considered. Specifically, it does not include the *PN PEMS iS* and *FID iS* components. Moreover, the *GAS PEMS iS+* system is not equipped to measure Particulate Matter (PM) emissions. Hence, only CO, CO_2 and NO_x concentrations in the exhaust gases have been measured, along with their mass flow rate. An overview of this specific PEMS system from inside and outside the vehicle is shown in Figure 8-29 and Figure 8-30, respectively. The description of each component will be presented in the following section.

8.3.3.1 Hardware

The "brain" of the AVL PEMS system is the *AVL M.O.V.E System Control*. It is a robust, vehicle PC based system for controlling mobile measuring devices, for central data acquisition and for the calculation of the results. Devices and sensors can be easily connected via a multitude of integrated standard interfaces. The System Control software monitors and stores the data of all connected in-vehicle devices and sensors within a single file. Additionally, it features user-guided test sequences (pre, main, post-test) to make the operation as easy as possible and to prevent invalid or void test runs (see Section 8.3.3.2).

The *System Control* includes sensors for acquiring environmental conditions (pressure, temperature and relative humidity) as well as a GPS sensor. Moreover, further measurement devices can be connected via integrated Ethernet, CAN and USB interfaces. CAN interfaces enable the connection of vehicle Bus-systems (e.g.: ECU or vehicle CAN). Table 8-14 summarizes other important technical features.

	System Control
Dimensions [mm]	241 x 89 x 350
Temperature range	-20 … 60°C
IP security	IP44
Power supply	9…36 VDC Incl. puffer function for bridging short-term voltage drops
Power Consumption	50W
CPU	CoreDuo L2400
Clock	1.66 GHz
RAM	2 GB
Memory	32 GB SSD
USB 2.0	3
RS232	1
VGA	1
CAN 2.0 A & B	2
LAN [100MBit/s]	2 (extended to 5 by means of an internal switch)
I/O	4 x Digital I/O (galvanically not separated) Optional as extension: 3 x NiCrNi TC; 1 x PT100; 3 x Analog inlet +/- 10V (differential, galvanically not separated)
Ambient temperature	-40 °C … 80 °C
Ambient humidity	0 … 100% RH
Ambient pressure	0,5 … 1,5 bar
GPS	WAAS compatible. Position: <3 Meter, 95% typical

Table 8-14. Technical specifications of the AVL M.O.V.E System Control [278].

The System Control installed on the vehicle is shown in Figure 8-31. It has been connected with the vehicle OBD, in parallel with the OBD by-pass connection of the ES582.1 module for the ETAS DAQ system (Figure 8-22 (b)).

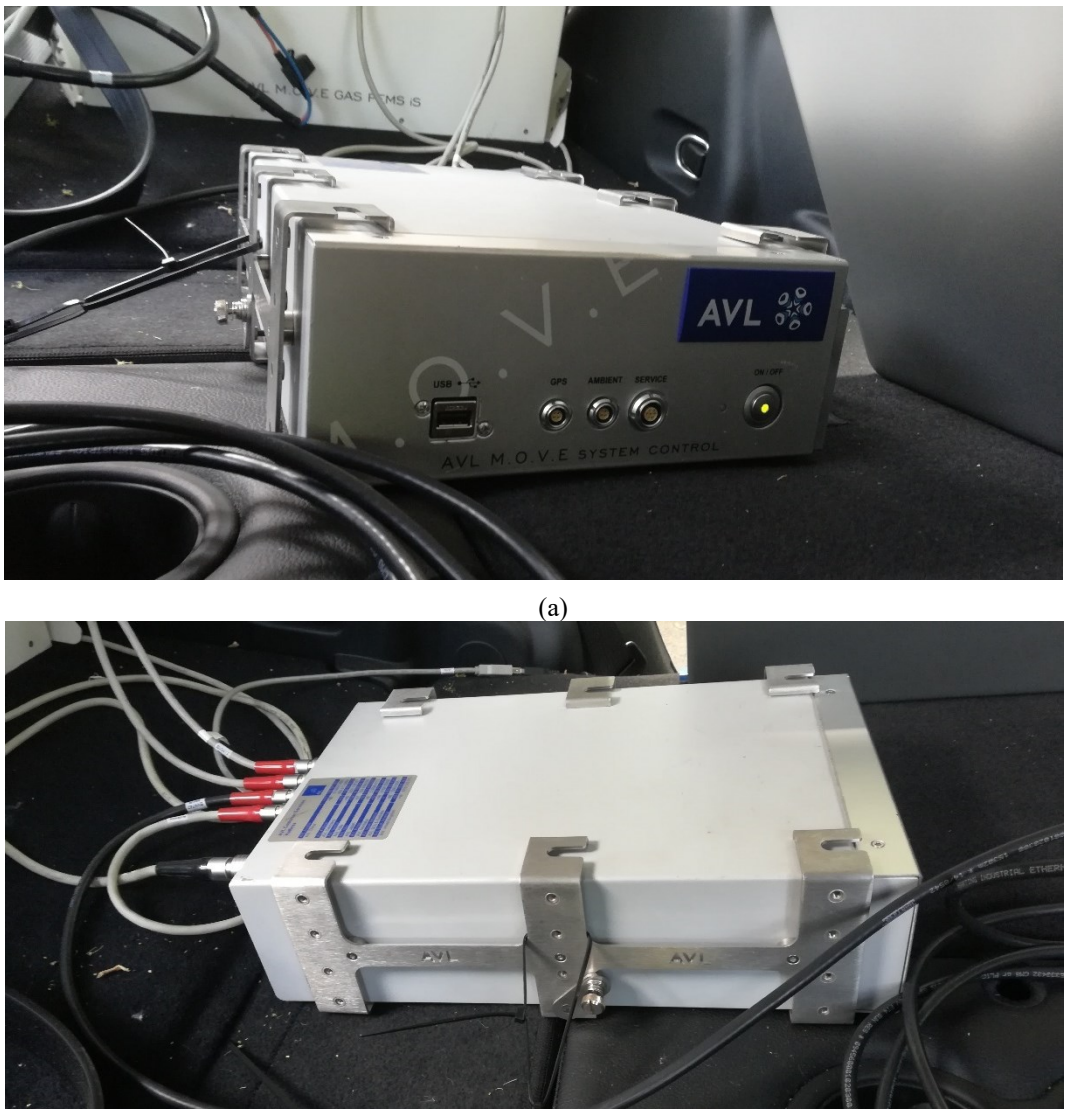

(a)

(b)

Figure 8-31. Front (a) and side (b) views of the AVL M.O.V.E System Control.

Among the measuring devices connected with the System Control, there is the AVL M.O.VE. EFM (Exhaust flowmeter). It is a compact and robust system for time resolved measurement of gas flow rates. It is optimized for the measurement of the exhaust flow rate of combustion engines and its design accounts for the influence of flow pulsations at low speed/load conditions. The main technical specifications of the EFM are summarized in Table 8-15.

EFM (Exhaust flowmeter)	
Power supply	Input range 22 … 28.8 VDC with max. 10 A
Power consumption	Typ. below 40 W (after warm-up when it is stabilized) Consumption during warm-up: approx. 120 W
Warm-up time	Approx. 15 min, depending on ambient temperature conditions
Max. exhaust temperature	Up to 700 °C at flow pipe (materials: pipe is 1.4301 steel, pitot is 1.4404 steel, fittings are 1.4401 steel)
Update recording frequency	Up to 10 Hz with System Control or via DUI measurement data logging; Up to 100 Hz via CAN
Electrical inputs/outputs	1 × power supply 1 × Ethernet (TCP/IP) 1 × CAN/ANALOG
Operating temperature	-10 … +45 °C ambient Corresponding to a maximum humidity of 95 % at 35 °C, non-condensing.
Storage temperature	-30 … +60 °C dry ambient conditions
Operation sea level	Up to 3000 m
Relative air humidity	≤ 95%, non-condensing
Degree of protection	Lemo K-series: IP 66; Power switch: IP 67; Control box with EMI sealing: IP 65; Pressure compensation element: IP 68
Noise load	<70 dB(A)
Interfaces	1 × 24 V Power 1 × TCP/IP Network (Ethernet) 1 × CAN/ANALOG (CAN) 1 × Flow pipe connection (EFM)

Table 8-15. Technical specifications of the AVL M.O.V.E EFM [279].

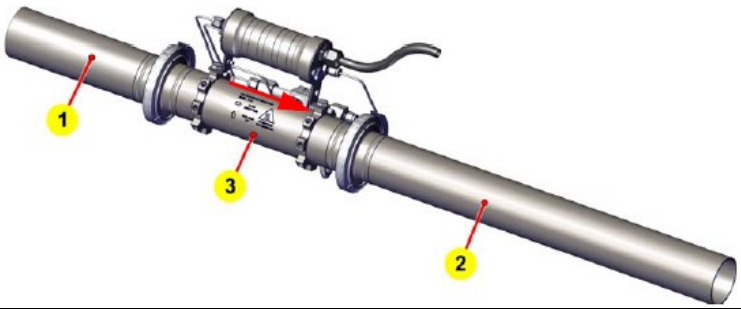

Pipe size	2"	2.5"	3"
Outer diameter [mm]	48.4	60.3	76.1
Length [mm]			
Extension 1	157.0	203.0	233.0
Extension 2	490.0	496.5	496.5
Main tube 3	252	270	330
Weight [kg]			
Control box	approx. 4 kg		
Flow pipe (without extensions)	~2.2	~2.7	~3.2
Flow measurement accuracy	±2.0% of reading or ±0.5% of full scale, whichever is greater		
Flow rate - Calibrated measurement range (@ ambient conditions)			
Flow [kg/h]	10…570	12…900	22…1050
Flow [m^3/min]	0.14 … 7.9	0.17 … 12.46	0.3 … 14.53
Linearity	$\lvert X_{min} \times (a_1 - 1) + a_0 \rvert < 1.0\%$ of full scale; Slope: $0.98 \leq a_1 \leq 1.02$; SEE: ≤ 2% max; R_2: ≥ 0.990		

Table 8-16. Flow Pipe specifications [279].

The EFM is constituted by two main components: a flow meter and a control box. The flow meter (Figure 8-32 (a)) must be placed along the engine exhaust line (Figure 8-32 (b)). To this end, a pipe with a 2.5 inches diameter has been added at the engine exhaust, and suitably shaped according with the specifications reported in Table 8-16. Hence, the flow meter gathers the up- and downstream dynamic pressures via a Pitot tube, as well as the static pressure inside the pipe and the gas temperature via a Thermoprobe. Then, it transfers the related pressure waves and voltage signals via a single EFM cable to the control box. The control box (Figure 8-32 (c)) measures the pressure and temperature signals, calculates the flow rate and communicates with the AVL M.O.V.E System Control. It also regulates its internal temperature at about 50°C. Finally, it can be mounted both in the vehicle cabin or externally, near the flow meter.

(a) (c)

(b)

Figure 8-32. AVL M.O.V.E EFM: flow meter (a) installed along the engine exhaust line (b), and control box (c).

The other measuring device connected with the System Control is the *AVL GAS PEMS iS+*. It is a compact and robust device for time resolved measurement of NO/NO_2, CO/CO_2 and O_2 concentrations in the exhaust gas of combustion engines.

The analyzers, which have proven their accuracy on test cells, are optimized for mobile application and are distinguished by a high level of accuracy and low drift. All analyzers are temperature conditioned to ensure reliable measurements even at extreme ambient conditions. Internal damping measures and special housing options, which also enable off-road applications, protect the device from vibrations/shocks and mechanical damage. The device is designed for tailpipe measurement, and it is controlled via TCP/IP. Data can be logged at up to 5 Hz (for the gaseous components, TEC pressures and temperatures).

According to the technical data summarized in Table 8-17, the device can be used in a range of ambient temperatures between -10°C and +45°C, and with a maximum humidity of 95% at 35°C, non-condensing. Moreover, it is worth noting that the device is designed for use on combustion engines whose exhaust gas does not contain substances harmful to the device, like NH_3, SO_2 or SO_3. Such substances lead to corrosion. Furthermore, the presence of urea determines decomposition products and salts of ammonia in the exhaust gases. These substances cause a traceable clogging of the gas and condensate paths due to condensation and crystallization, which leads to malfunctions and higher maintenance efforts.

AVL GAS PEMS iS+	
Power supply	22 … 28.8 V DC with max. 28 A
Power consumption	typ. below 300 W (at 20 °C with 1.25 m heated sampling line)
Warm-up time	45 … 120 min, depending on ambient temperature conditions
Sample flow rate	Approx. 2.0 l/min
Pneumatic inlets/outlets	ambient air, calibration unit, sample gas inlet, drain outlet
Max. exhaust temperature	Up to 500 °C at sample point with AVL Tailpipe Sampling Kit (flexible steel hose) Max. 200 °C at the heated line's entrance
Max. exhaust pressure	±50mbar rel.
Update recording frequency	Up to 5 Hz for gaseous components Up to 1 Hz for service data channels
Electrical inputs/outputs	1× power supply 1 × heated sampling line 1 × Ethernet (TCP/IP) 1 × calibration unit
Operating temperature	+15 … +45 °C: ventilation slide controls open -10 … +15 °C: ventilation slide controls closed Corresponding to a maximum humidity of 95% at 35 °C, non-condensing.
Storage temperature	-30 … 70 °C (oxygen sensor must be removed below 0 °C and above 50 °C)
Operation sea level	Up to 3000 m
Relative air humidity	≤ 95%, non-condensing
Degree of protection	IP24
Dimensions	~ 495 × 334 × 377 mm (W × H × D)
Weight	Approx. 30 kg without accessories
Noise load	<70 dB(A)
Communication interfaces	1 × Ethernet (TCP/IP)

Table 8-17. Technical specifications of the AVL GAS PEMS iS+ [277].

Basically, this device uses two analyzers to measure the concentrations of NO/NO_2 and CO/CO_2, that are the Non-dispersive Ultraviolet (NDUV) Analyzer and the Non-dispersive Infrared (NDIR) Analyzer, respectively. In addition, an O_2 sensor measures the concentration of Oxygen. The NDUV Analyzer is characterized by the following features:

- its measuring capabilities are very sensitive and stable with regard to NO;
- the nitrogen oxide components (NO and NO_2) are measured directly;
- it has a high level of selectivity towards accompanying components contained in the sample gas, and it has shown to have no effect on CO_2 and H_2O, in particular.

The UV Analyzer is a multi-component UV photometer with high zero-point and end-point stability. Its measuring effect is based on the properties of gases like NO and NO_2, which form discrete vibration absorption bands and absorb radiation in a wavelength range of 200 to 500 nm. At the heart of the analyzer is the UV radiation source, an electrodeless discharge lamp (EDL), which, induced by high-frequency, emits radiation specific to NO in an electromagnetic field, as shown in the following schematic reaction equations (Eq. 8-1 and Eq. 8-2):

$$N_2 + O_2 \rightarrow NO_2^* \rightarrow NO + hv \qquad \text{Eq. 8-1}$$

$$2\,NO \rightarrow N_2 + O_2 \qquad \text{Eq. 8-2}$$

The emitted NO lines are comparable to a fingerprint of the absorption lines specific to NO gas. Therefore, this measuring method is a resonant method, and it is referred to as DUV resonance absorption spectroscopy. Other gases absorbed in the UV, such as NO_2 and SO_2, are determined with the help of the interference filter correlation as non-dispersive UV method.

The radiation emitted by the UV radiation source is modulated using a filter wheel and split into a measuring beam and a reference beam in a semitransparent beam splitter (Figure 8-33 (a)). In one measurement cycle, a total of four signals are recorded for two interference filter positions via the measurement beam and the reference beam, and calculated with the formation of double quotients. This four-beam method forms the basis for the high measuring stability attained in the NO measurement. It makes the analyzer largely independent of any contamination in the measurement cuvette or aging of the radiation source.

The measurement principle of resonant NO absorption is represented in Figure 8-33 (b). The specific signal required is determined in two steps. Firstly, the full absorption signal is recorded in the measurement phase. Then, in the subsequent reference phase, a gas filter filled with NO is swiveled into position, and only those spectral portions that are not absorbable by NO reach the detector through the measurement cuvette. By comparing together these two recordings, the concentration of NO is measured.

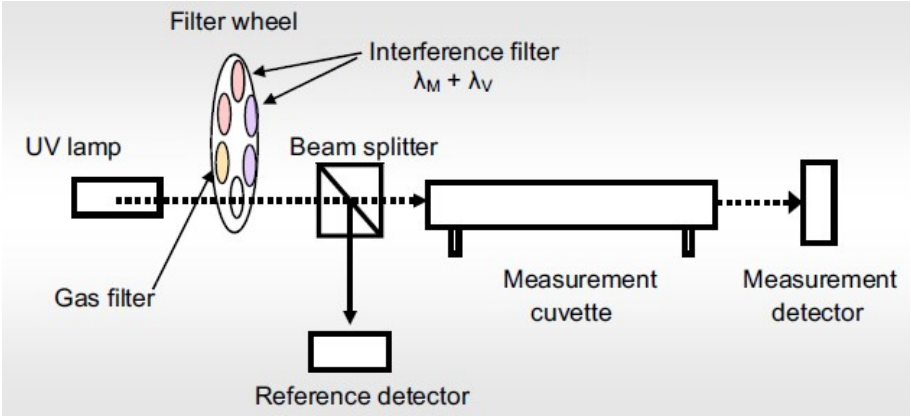

(a)

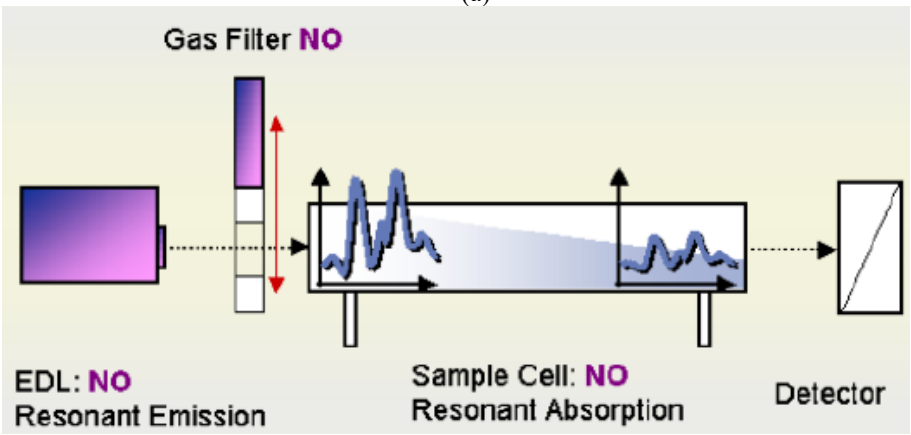

(b)

Figure 8-33. (a) Schematic of the NDUV Analyzer present in the AVL GAS PEMS iS+; (b) measurement principle of resonant NO absorption [277].

The NDIR analyzer is designed to obtain real time concentration data for carbon dioxide and carbon monoxide when present in an exhaust gas stream. Qualitative and quantitative molecular analysis is readily achieved using the principles and techniques of infrared spectrometry. Infrared radiation in the range from 1 to 100 μm is absorbed and converted by most molecules into molecular vibrational energy. Due to the quantum characteristics of molecules, the absorption characteristics of a molecule appear as discrete lines or bands in the infrared spectrum. The spectral location of these absorption bands are in general unique to a particular molecule. The frequency of the wavelength of absorption depends on the relative masses of the atoms, the force constants of the chemical bonds, and the geometry of the atoms.

The absorption strength or band intensities are expressed as transmittance (T) or absorbance (A). Transmittance is the ratio of the radiant power in a spectral band transmitted through a sample to the radiant power incident on the sample. Absorbance is the logarithm (base 10) of the reciprocal of the transmittance (Eq. 8-3).

$$A = \log\left(\frac{1}{T}\right) \qquad \text{Eq. 8-3}$$

The fundamental law of photometry (Beer-Lambert law) states that the transmittance of monochromatic radiation through a uniformly absorbing media is given by Eq. 8-4. In this

equation, I_0 is the intensity of the incident power to the absorbing medium, I is the intensity of the transmitted power, a is the absorption strength at a given wavelength (often referred to as extinction coefficient, cross section, oscillator strength or molar absorptivity), l is the length of the absorbing medium (sample cell length), and C is the sample concentration or gas density.

$$\frac{I}{I_0} = e^{-(a\,l\,C)} \qquad \text{Eq. 8-4}$$

Frequently, gas mixtures must be analyzed in a single photometer and the spectrum of these gases may be quite similar. Spectral overlap can occur, which leads to "cross channel interferences". With proper control, these cross channel interferences can be effectively eliminated using compensation calculations. Selection of an appropriate absorption band, measurement of the radiant power transmittance and correction for non-ideal behavior are the fundamental basis of infrared gas analysis.

Single-beam Infrared spectrometers consist of four principle sections (Figure 8-34):

- Radiation source. Infrared radiation is typically produced by electrically heating a source from 600 to 3000 °C. The spectral intensity distribution of these incandescent source is similar to a blackbody radiator. Variations from a true blackbody source are due to variations in the emissivity of the source material over the infrared spectral region.
- Monochromator. To achieve the greatest sensitivity for a given gas, and avoid interferences from other gases, the infrared radiation which is incident on the sample cell should spectrally overlap the absorption band of the analyzed gas. The selection of infrared wavelength (or frequency) to be transmitted through the sample cell can be achieved by several methods. Transmission filters exhibit high efficiency selection of radiation and are chosen in this NDIR analyzer application for wavelength selection.
- Sample cell. The chamber used to hold the gas sample is constructed of a cylindrical tube containing inlet and outlet plumbing. The ends of the cylinder are sealed with windows which transmit infrared radiation. The length of the sample cell is determined by considering the absorption strength of the desired gas and the concentration range expected. Sample cell lengths can range from 0.01 mm to several meters, depending on the application.
- Detector. The infrared radiation which is not absorbed by the sample gas is converted to an electrical signal using a thermopile detector.

It is worth noting that, for a better temperature stabilization, the whole analyzer is placed in a box. The temperature in the box is regulated to ±0.5 °C even during rapid changes in ambient temperature. Under these conditions, the NDIR provides stable signals. Very low zero drift is therefore observed over hours of operation.

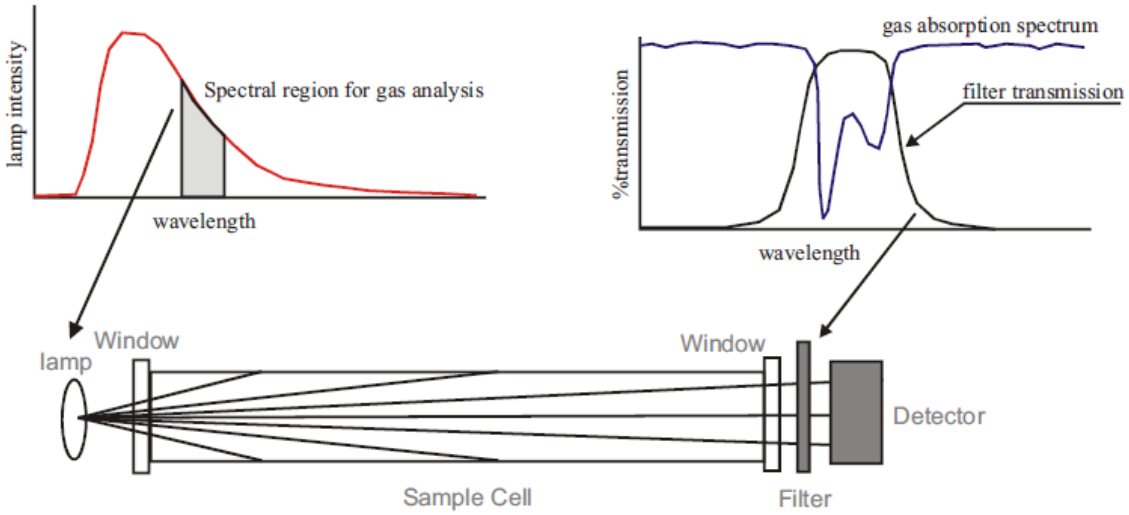

Figure 8-34. Single-beam non-dispersive spectrometer [277].

AVL GAS PEMS iS+				
	Range	Display Resolution	Accuracy	Linearity
CO	Linearized range: 0 … 49999 ppm Display range: 0 … 15 vol%	1 ppm	0 … 1499 ppm: ±30 ppm abs. 1500 … 49999 ppm: ±2% rel.	Slope: 0.99 ≤ Slope ≤ 1.01 Intercept = 0.5% SEE: ≤ 1% of range and R^2: ≥ 0.999
CO_2	0 … 20 vol%	0.01 vol%	0 … 9.99 vol%: ±0.06 vol% abs. 10 … 20 vol%: ±2% rel.	
NO	0 … 5000 ppm	0.1 ppm	0 … 5000 ppm: ±0.2% FS or ±2% rel.	Slope: 0.99 ≤ Slope ≤ 1.01 Intercept = 0.5% SEE: ≤ 1% of range and R2: ≥ 0.999
NO_2	0 … 2500 ppm	0.1 ppm	0 … 2500 ppm: ±0.2% FS or ±2% rel.	
O_2	0 … 25%	0.1 vol%	±1 vol% of full scale at constant temperature and pressure	-
Device fully warmed up, 24 V supply, laboratory conditions and using dry calibration gases				

Table 8-18. Measurement specifications of the AVL GAS PEMS iS+ [277].

AVL GAS PEMS iS+					
	Span Range	Repeatability	Span Drift	Zero Drift	Precision
CO	0.1 … 8.2 vol%	0 … 1000 ppm: ±20 ppm abs. 1000 … 10 vol%: ±1% rel.	≤20 ppm abs./8 h or 2% rel./8 h	20 ppm/8 h	1.0% FS
CO_2	7.5 … 20 vol%	0 … 10 vol%: ±0.1 vol% abs. 10 … 20 vol%: ±1% rel.	≤0.1% abs/8 h abs. or 2%rel./8 h rel.	0.1%/8 h abs.	1.0% FS
NO	250 …5000 ppm	0 … 100 ppm: ±1 ppm abs. 100 … 5000 ppm: ±0.5% rel.	≤4 ppm abs./8 h or 2% rel./8 h	2 ppm abs./8 h	0.5% FS
NO_2	125 …2500 ppm	0 … 100 ppm: ±1 ppm abs. 100 … 2500 ppm: ±0.5% rel.	≤6 ppm abs./8 h or 2% rel./8 h	4 ppm abs./8 h	0.5% FS
NO_x	-	-	≤10 ppm abs./8 h or 2% rel./8 h	6 ppm abs./8 h	-
Device fully warmed up, 24 V supply, laboratory conditions and using dry calibration gases					

Table 8-19. Span and drift ranges of the AVL GAS PEMS iS+ [277].

Overall, the measurement specifications of the chemical species concentrations (CO/CO_2, NO/NO_2 and O_2) measured by the *AVL GAS PEMS iS+* have been summarized in Table 8-18. Moreover, the span and drift ranges for each substance have been reported in Table 8-19. In fact, this device must be calibrated before each experimental measurement, as will be described in Section 8.3.3.2.

The *AVL GAS PEMS iS+* is composed of a base unit and a sampling probe (Figure 8-35 (a) and (b) respectively). These two elements are connected together through a heated sampling line (the black flexible tube in the figure), which warms up the sample gas prior to pass it to the analyzers. Moreover, a filter (1) between the heated sampling line (2) and the base unit (a) prevents particles small as PMs to poison the analyzers.

The *AVL GAS PEMS iS+* installed in the vehicle is shown in Figure 8-36, where the base unit (a), and the heated sampling line (b) can be distinguished.

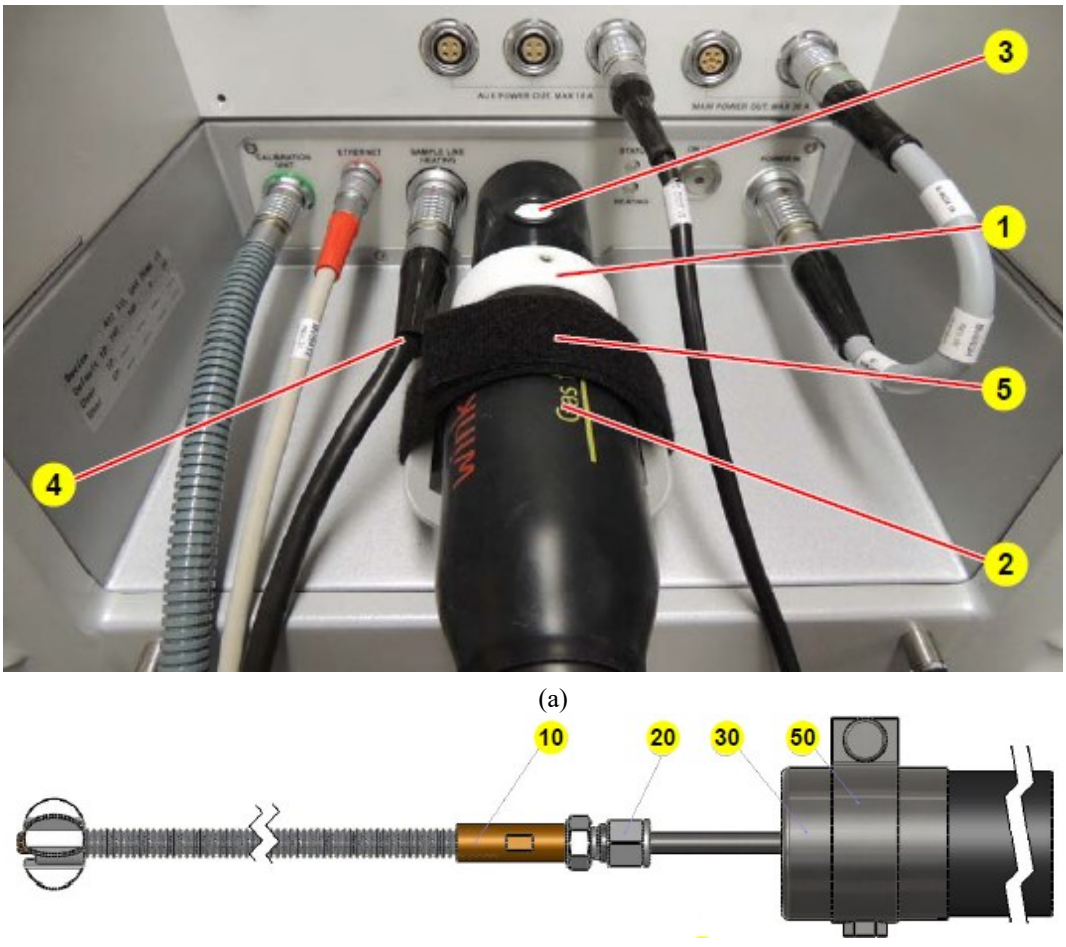

(a)

(b)

Figure 8-35. Base unit (a) and tailpipe sampling probe (b). Note the filter (1 in fig.(a)), the heated sampling line (2 in fig.(a) or 50 in fig.(b)), and the sampling probe (10 in fig.(b)) [277].

(a)

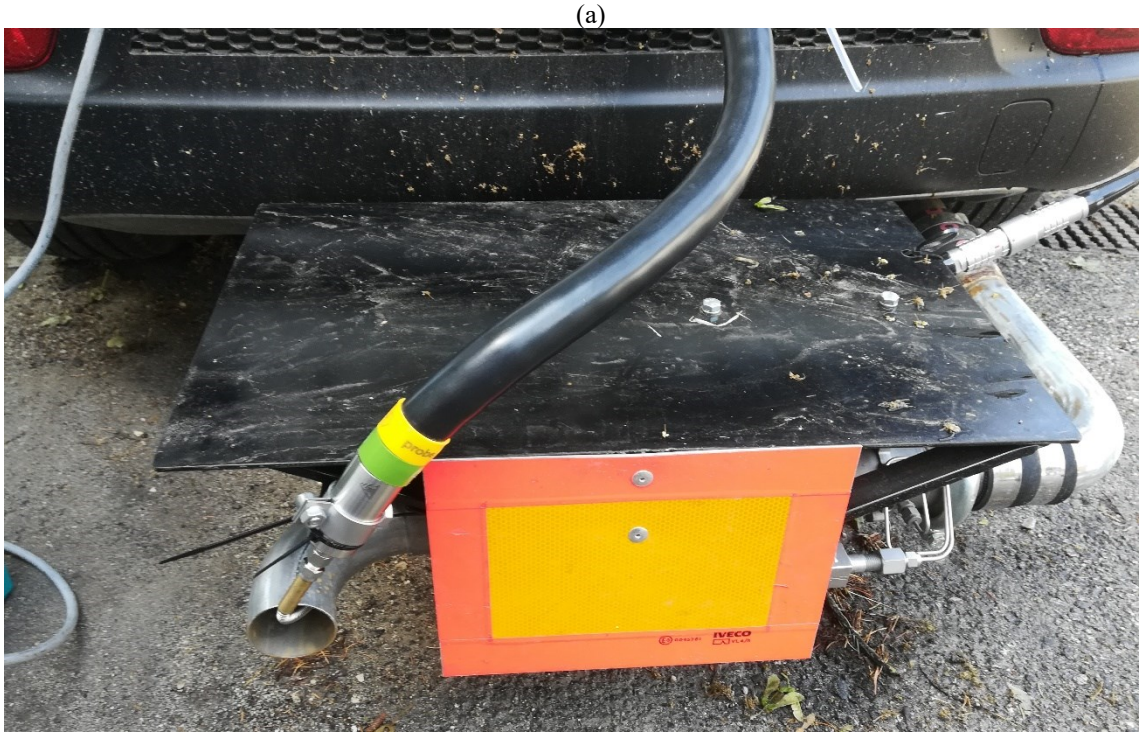

(b)

Figure 8-36. AVL Gas PEMS is: Base Unit (a), integrated with the Energy Box (at the top); sampling probe (b) installed at the exhaust pipe outlet.

In this specific version, the energy box (E-Box) is mounted directly on top of the base unit of the *GAS PEMS is+*, whereas the battery pack at the right side of the trunk (Figure 8-36 (a)). As mentioned above, the *E-Box* powers all the PEMS' components (Figure 8-28). Its main technical specifications have been summarized in Table 8-20. The power supply can come from the 24V/30Ah battery pack (Figure 8-37 (a)), or the 24V/30A Charger (Figure 8-37 (b)) when the whole system is powered by the grid.

More technical information about the single components, as well as prescriptions about installation, operation and maintenance of the system, can be found in [277–279].

E-Box	
Dimensions	~ 26 × 8 × 18 cm (W × H × D)
Weight	~ 2 kg
IP class	IP 24
Electrical outputs	2 × 24 V/30 A; 3 × 24 V/10 A
Electrical inputs	Power supply IN (max. 28 A) / External battery IN
Max. internal batteries current	30 A each (max. 2 batteries)
Max. external battery current	28 A (1 battery)
Communication interfaces	5 × Ethernet (TCP/IP)
Max. charging current	27.5 A per battery
Max. charging voltage	28.8 V
Max. output current	60 A (with 2 30 A batteries), 88 A (with 2 batteries + power supply connected)

Table 8-20. E-Box specifications [277].

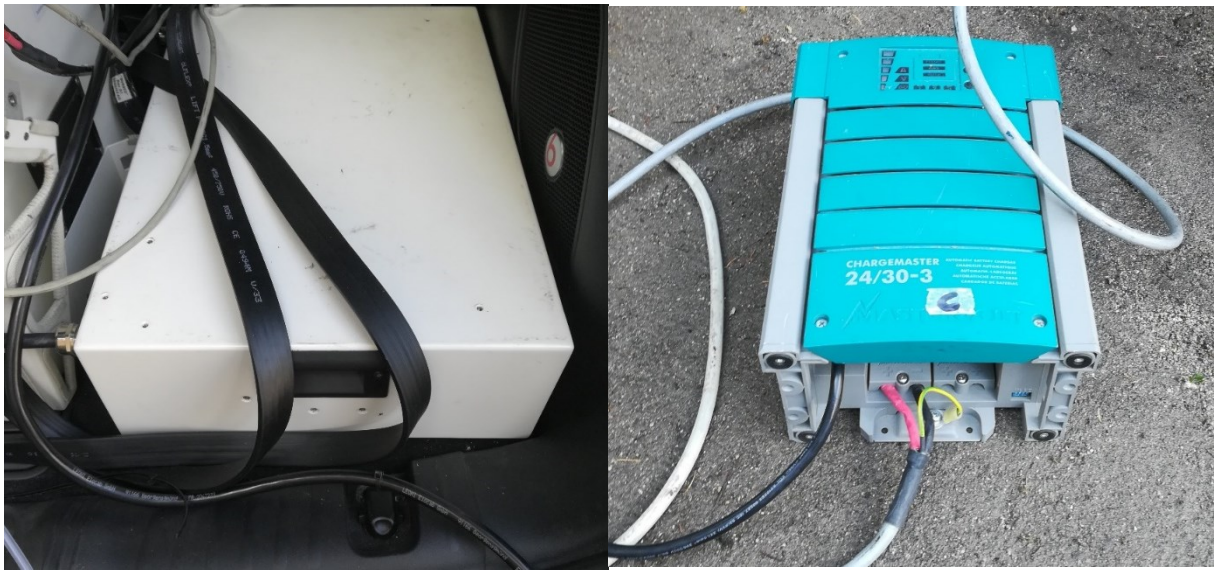

(a) (b)

Figure 8-37. Battery pack (a) and Chargemaster charger (b).

8.3.3.2 Test procedure

To guarantee high quality measurements, a specific workflow must be performed when using a PEMS system. For the *AVL PEMS*™, this procedure has been reported in Figure 8-38. Three main phases can be distinguished, i.e. the Pre-Test, Main-Test and Post-Test. Together, they define a specific on-the-road test.

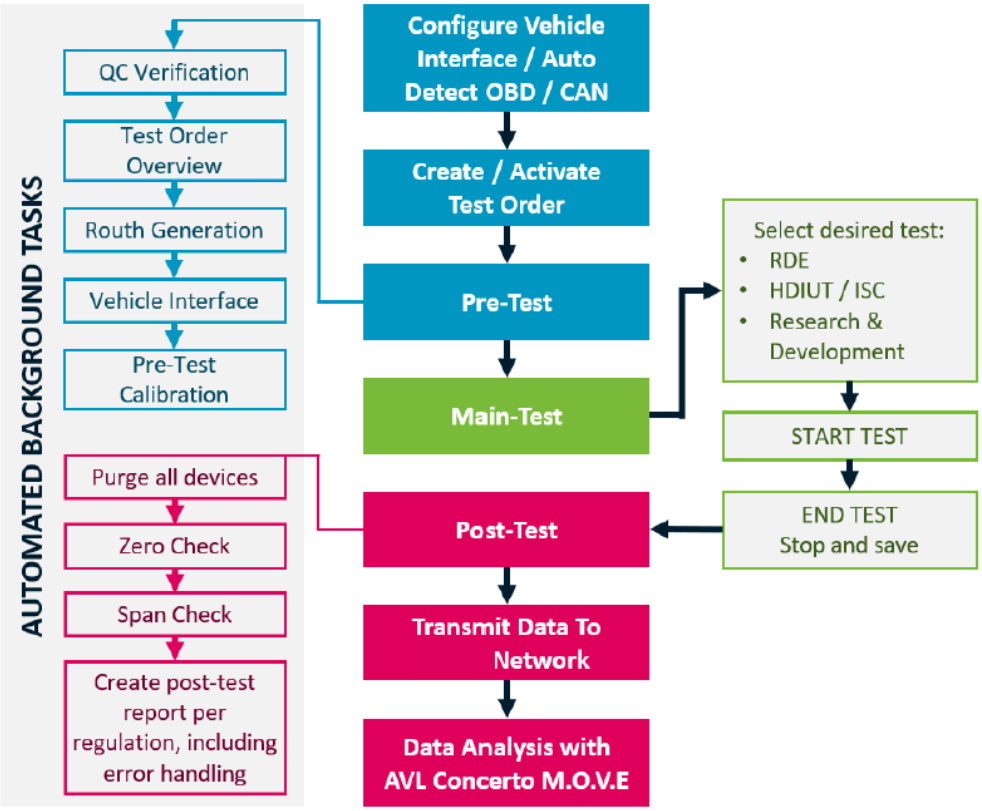

Figure 8-38. Schematic of the PEMS workflow, whose main phases are: Pre-Test, Main-Test and Post-Test [38].

The main scope of the Pre-Test is to calibrate the GAS PEMS, in order to set the zero point of the system. To this end, the *eCAL* module (Figure 8-39) must be connected to the base unit (Figure 8-35 (a)) and to calibration gas cylinders, each of which has a span gas with a specific concentration. For each gas, the span ranges summarized in Table 8-19 must be fulfilled.

Moreover, during the pre-test, the heating of all the PEMS' components must be performed, according with the specifications reported in Table 8-15 and Table 8-17. In addition, the leak check and purging of the *GAS PEMS is+* are recommended, according with the procedure detailed in [277]. Also, a check on the integrity of the filter (1) in Figure 8-35 (a) is suggested at the beginning of each test, to prevent the early clogging of the gas analyzers.

Subsequently, details about test and vehicle type must be specified inside the software interface running in the System Control. Among all, the user must indicate what kind of test is going to be performed. In case of an RDE, the system wants to know the Emission Regulation

the test is referring to. In this way, all the parameters will be calculated according with the specific regulation. Moreover, the System Control will perform on-line calculations during the Main-Test, in order to inform the user if the characteristics of the test (length, duration, etc.) comply with the validity requirements imposed by the specific regulation.

Figure 8-39. *AVL eCAL* module for the calibration of the *AVL GAS PEMS is+* [277].

At this point, the test can be started (Main-Test). During this phase, the System Control will register all the data coming from the measuring devices, i.e. the EFM and GAS PEMS in this case. These data will be stored in a separate file compared with the one created automatically during the Pre-Test.

At the end of the route, the user must stop and save the Main-Test, and begin the Post-Test. This latter must be completed within a certain period of time (about 45 min [280]) to consider valid the whole test. During the Post-Test, zero and span checks must be performed to verify if any drift of the analyzers' reference points occurred during the Main-Test. To this end, the *eCAL* module must be connected to the GAS PEMS along with the calibration gas cylinders, and repeat the procedure already performed during the Pre-Test.

Moreover, a purge of all devices (especially of the GAS PEMS) is recommended to expel any impurities formed inside the system during the Main-Test. All these steps are guided by the software interface running in the System Control, and the results are stored in a separate file relative to those previously created for the Pre and Main Tests.

Finally, the data relative to Pre, Main and Post Tests can be transferred from the System Control to another computer, and post-processed using the software AVL Concerto™. This tool allows to phase align the experimental data acquired by the different components of the PEMS. Moreover, it calculates variables deriving from the measured quantities, according with the specific Emission Regulation set at the beginning of the test. It also allows to export the experimental data at different steps of the post-processing phase, enabling the user to perform other calculations not implemented in the software.

In this thesis, the experimental measures of the PEMS have been post-processed by using the AVL Concerto™ interface. Then, they have been compared with those relative to the engine cooling system and the ECU, acquired through the INCA-ETAS™ DAQ system described in Section 8.3.2.

8.4 Experimental investigation over on-the-road tests

8.4.1 Road map of the tests

The measuring system installed on the vehicle (Section 8.3) allows to investigate experimentally how the engine thermal state impacts on fuel consumption and emissions. With this aim, two on-the-road tests have been realized, one at cold start conditions, and the other with the engine already warmed-up. In the following, these conditions will be referred to as *cold test* and *warm test*, respectively. Specifically, the cold test starts with the engine at ambient temperature, which is about 20°C in this specific case. In fact, the experimental activity was carried on in June. Instead, the warm test starts with the engine at about 75°C. This test was conducted the same day of the cold test, after about one hour, in order to limit the influence of weather conditions on the accuracy of the results, especially for what concerns the emissions measured through the PEMS.

Both tests have been realized on the same road trip nearby L'Aquila. The GPS map and the altitude profile of the trip are reported in Figure 8-40. The trip is long about 62.5 km, and includes urban and extra-urban sections. Specifically, starting from the University Fluid Laboratory *Carmelo Caputo* (Roio, AQ), a first 10.5 km urban section down to the L'Aquila-Ovest tollgate was covered. Then, a 17 km extra-urban segment up to Tornimparte (AQ) was taken, followed by a U-turn to go back down to the L'Aquila-Ovest toolgate, and proceed straight up to the L'Aquila-Est one, for a total of 21.8 km. Subsequently, the trip proceeded for the last 12 km down to the city, and then up again towards the University Lab.

Due to the topography of the area, the road trip was highly variable in terms of altitude (Figure 8-40 (b)). In fact, the University Lab is located in Roio (AQ), which is at about 1000 meters above the seal level (m.a.s.l.), whereas the L'Aquila-Ovest tollgate is at about 650 m.a.s.l., i.e. the altitude of the city. The highest point is Tornimparte (AQ), at about 1150 m.a.s.l., while the L'Aquila-Est tollgate is at about 760 m.a.s.l.

Moreover, it is worth noting that the highway section was slowed down by several roadworks, which had also a great impact on traffic conditions among the two tests. Hence, the highway segment was referred to as extra-urban section, due to the limited speeds reached, more proper of an extra-urban trip rather than a highway one.

Finally, the on-board auxiliary systems (air conditioning, infotainment system, etc.) were switched off during both tests, to eliminate their influence on the results.

With these characteristics, the RDE standards (Section 1.4.2.2) cannot be met. However, this is not the scope of this study, which instead is aimed at measuring the effects of the engine thermal state on fuel consumption and emissions during the warm-up phase.

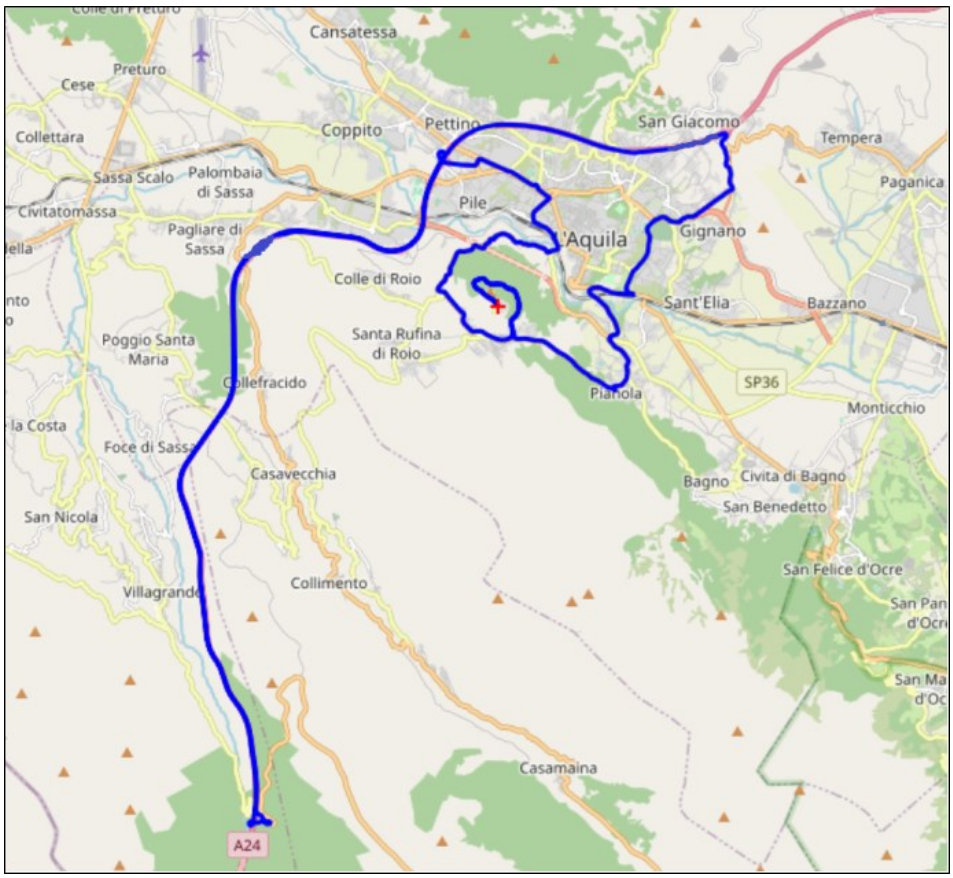

(a)

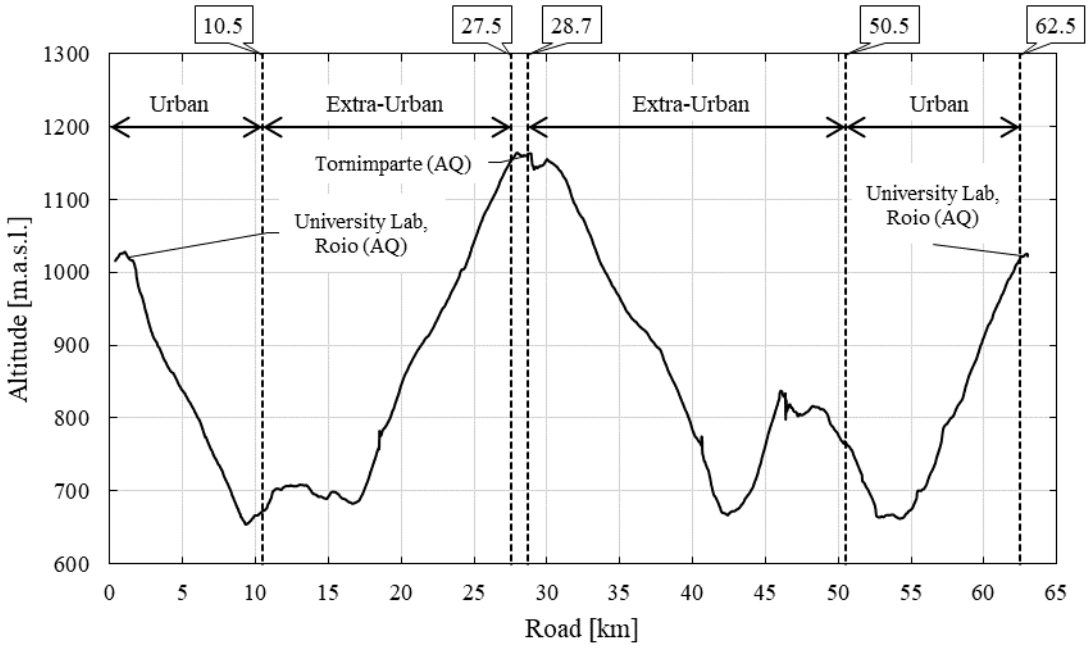

(b)

Figure 8-40. Map (a) and altitude profile (b) of the on-the-road test carried out with the instrumented vehicle.

8.4.2 Experimental results

8.4.2.1 Engine performances

As known, the experimental results of road tests are inevitably affected by the local and temporary driving conditions, which are not predictable a priori. However, the repeatability of the road test can be evaluated by comparing together the engine performances during each test conducted on the same road trip. If on average they can be approximatively overlapped together, then the two tests can be considered comparable in terms of emissions results.

Moreover, the results of both tests have been reported as a function of the road trip, instead of time. In fact, the time spent to carry on the two tests is different, due to variability on driving and traffic conditions. Instead, the length of the road trip is constant, and thus suitable to be considered as a common factor for the comparison of the results of the two tests.

In light of these considerations, firstly it is necessary to assess the comparability of the cold and warm tests performed on the same road trip described in Section 8.4.1. To this end, the vehicle speed profiles of both tests have been compared in Figure 8-41, distinguishing between urban and extra-urban sections. Clearly, the two profiles are almost overlapped during the urban sections, whereas some discrepancies can be observed during the extra-urban ones. This is due to the roadworks present along the highway (the A24), which slowed down significantly the traffic, with a great variability at different times of the day. As a result, the cold test has lower vehicle speeds than those achieved during the warm one, especially in the extra-urban segment between the L'Aquila-Ovest and Tornimparte tollgates (from 10.5 km to 27.5 km). The top speed was reached on a straight downhill road in the second extra-urban section, and it is equal to 138 km/h and 151 km/h for the cold and warm tests, respectively. Moreover, it can be clearly distinguished the U-turn dividing the two extra-urban sections of each test, in which the vehicle had to be stopped two times due to the out/in crossing of the Tornimparte tollgate.

To understand if the discrepancies in the vehicle speed can be accepted, the mechanical power supplied by the engine in both tests has been calculated (Figure 8-42). This has been possible thanks to the engine torque and speed acquired by the ECU during the tests (Figure 8-43 and Figure 8-44, respectively). In these figures, also the mean values have been reported for each segment, to catch more easily any differences between the two tests.

Clearly, the average power supplied by the engine is almost the same in both tests (Figure 8-42). The more significant discrepancies can be observed in the first urban and extra-urban sections. There, the average engine power supplied during the cold test is about 6.3 kW and 27.9 kW respectively, whereas that of the warm test is about 4.4 kW and 30.4 kW.

Similar differences can be observed also in the engine torque profiles (Figure 8-43). In fact, the engine torque supplied during the cold test was 34 Nm and 116 Nm over the first urban and extra-urban sections, respectively, whereas it was 26 Nm and 123 Nm during the warm test.

Instead, the engine speed differs among the two tests only during the first urban section, being equal to 1625 rpm for the cold test and 1396 rpm for the warm one, while no significant discrepancies can be noticed for the rest of the trip (Figure 8-44).

It is worth noting that, in both tests, the average engine torque and power supplied during the first urban section are almost halved compared to those of the last urban segment. Similarly, those registered during the first extra-urban section are almost doubled compared to the corresponding values acquired during the subsequent extra-urban one. This is mostly due to the altitude profile of the specific road trip (Figure 8-40 (b)). In fact, this profile has strong downhill and uphill paths following each other, that almost correspond to the sequence of urban and extra-urban sections. On the contrary, a similar behavior is not present in the engine speed profile. In fact, in both tests, the engine operates with almost the same average speed during the extra-urban segments, with slight differences only among the urban sections. In this regard, an important role is surely played by the automatic gearbox (Table 8-3), which has been left in the drive position without setting on the sport mode. The aim was to let the gearbox choose the right gear according to the standard logic implemented in the ECU, without any influence of the driver.

It is worth mentioning that only the engine speed is actually measured during the test. Instead, the engine torque is a parameter present in performance maps previously saved in the ECU, and just picked up by the ECU during the test according with other engine performance parameters. Consequently, the profile reported in Figure 8-43 is not a real time measurement of the engine torque, still extremely difficult to realize in an on-the-road test. However, it gives a good understanding of its variation during the test, allowing to estimate the instant mechanical power delivered by the engine with a good approximation.

The cumulated mechanical energy supplied by the engine over the cold and warm tests has been reported in Figure 8-45. Overall, the two tests required almost the same mechanical energy, specifically 15.6 kWh and 15 kWh for the cold and warm tests, respectively. Moreover, both the energy profiles show two almost constant segments, one occurring during the first 10 km, and the other between 28 km and 37 km. These are mainly due to the downhill road stretches of the first urban and second extra-urban sections (Figure 8-40 (b)), which have been covered with few engine power request (Figure 8-42).

In light of these results, if the intrinsic non-repeatability of a road test is taken into account, the variations of the main engine performance parameters among the cold and warm tests realized in this study can be considered acceptable. Hence, the two tests can be compared together for what concerns fuel consumption and pollutant and CO_2 emissions. The aim is to identify any correlation with the engine thermal dynamics measured thorough the DAQ system implemented in the vehicle. Such knowledge will be useful for future studies on the optimization of the engine thermal management, especially during the initial warm-up phase.

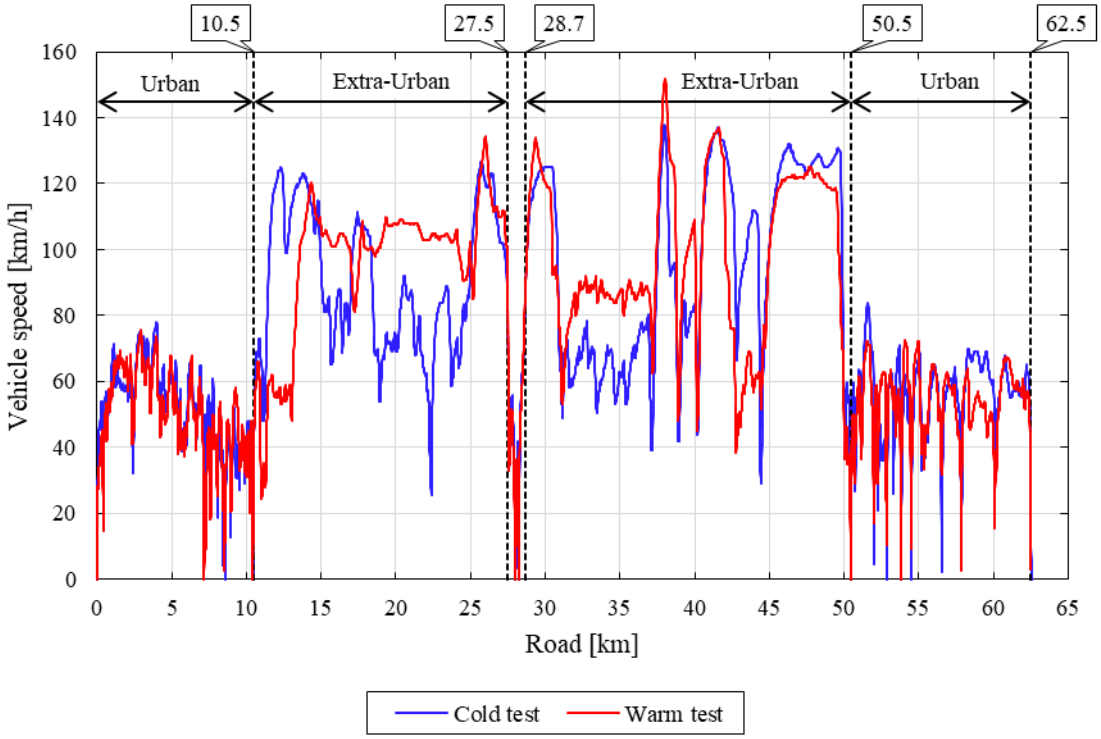

Figure 8-41. Vehicle speed profile during cold and warm tests.

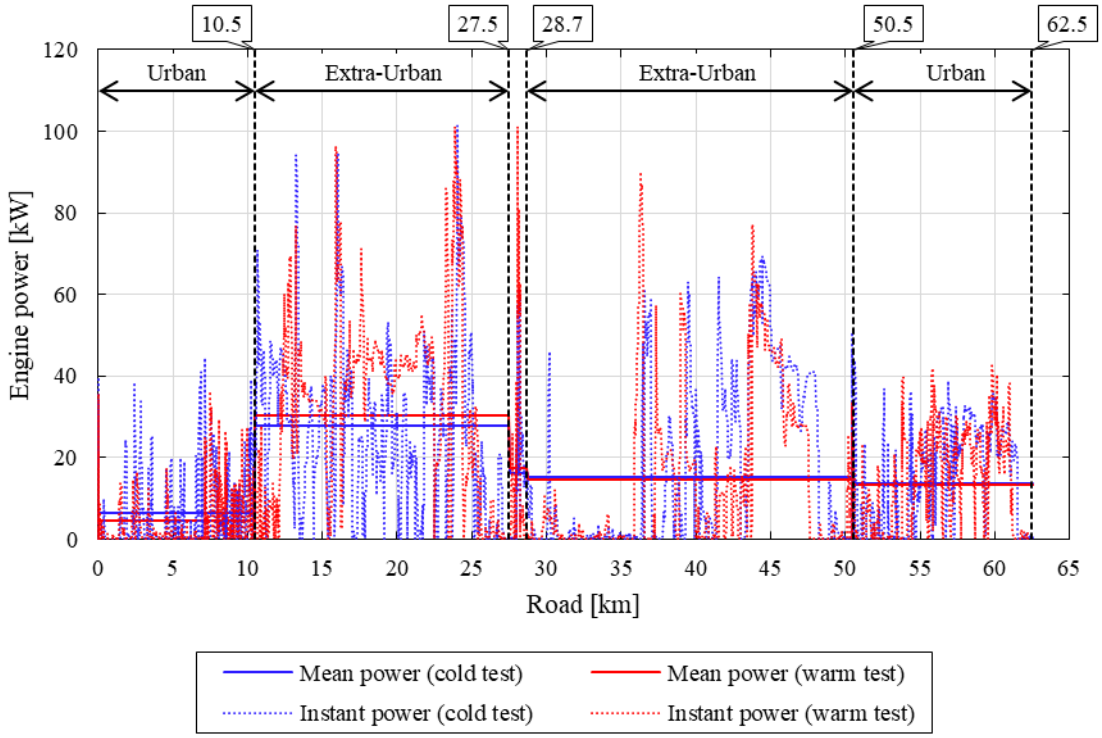

Figure 8-42. Mean and instant engine power during cold and warm tests.

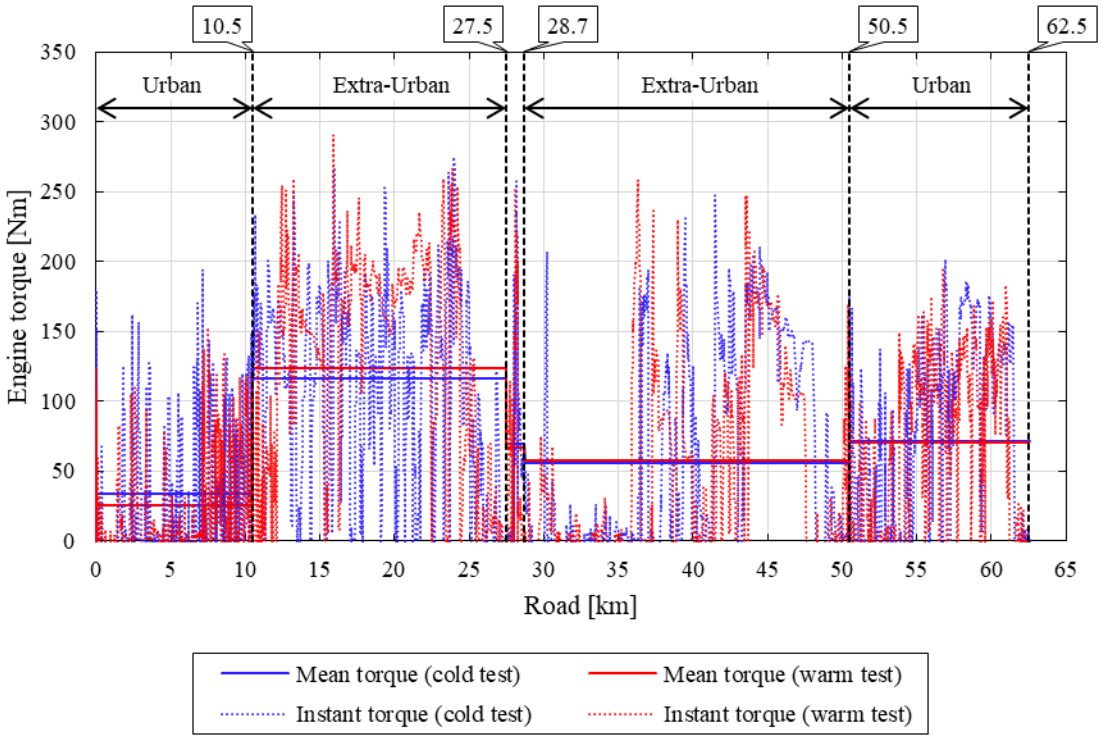

Figure 8-43. Mean and instant engine torque during cold and warm tests.

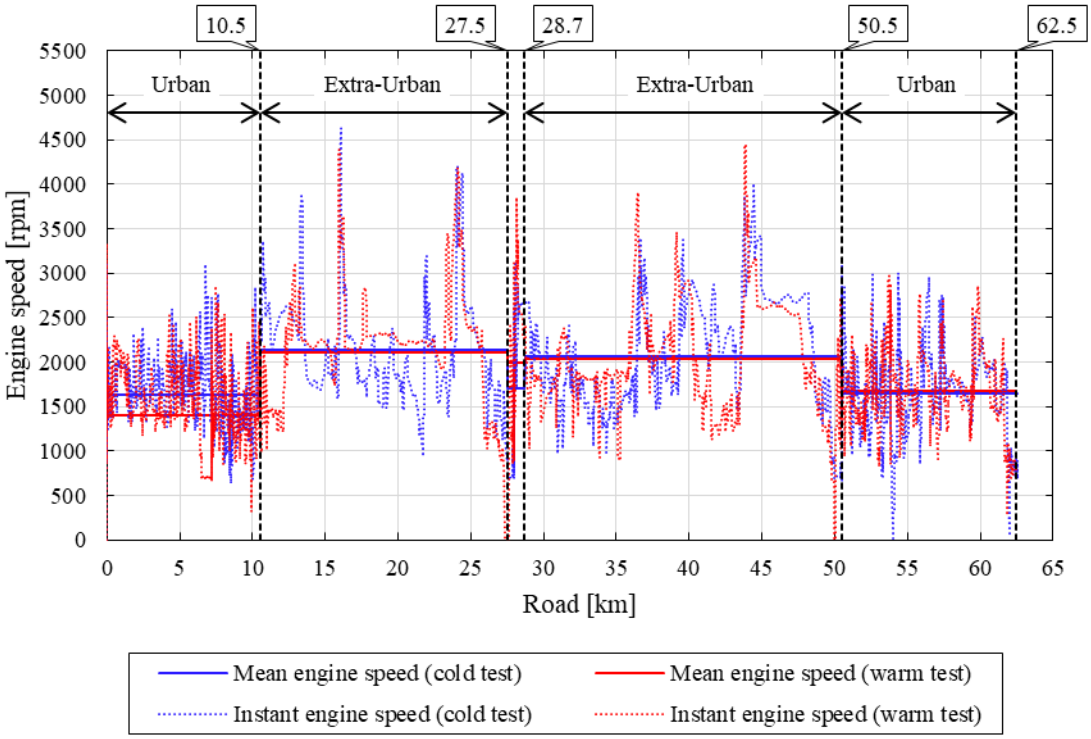

Figure 8-44. Mean and instant engine speed during cold and warm tests.

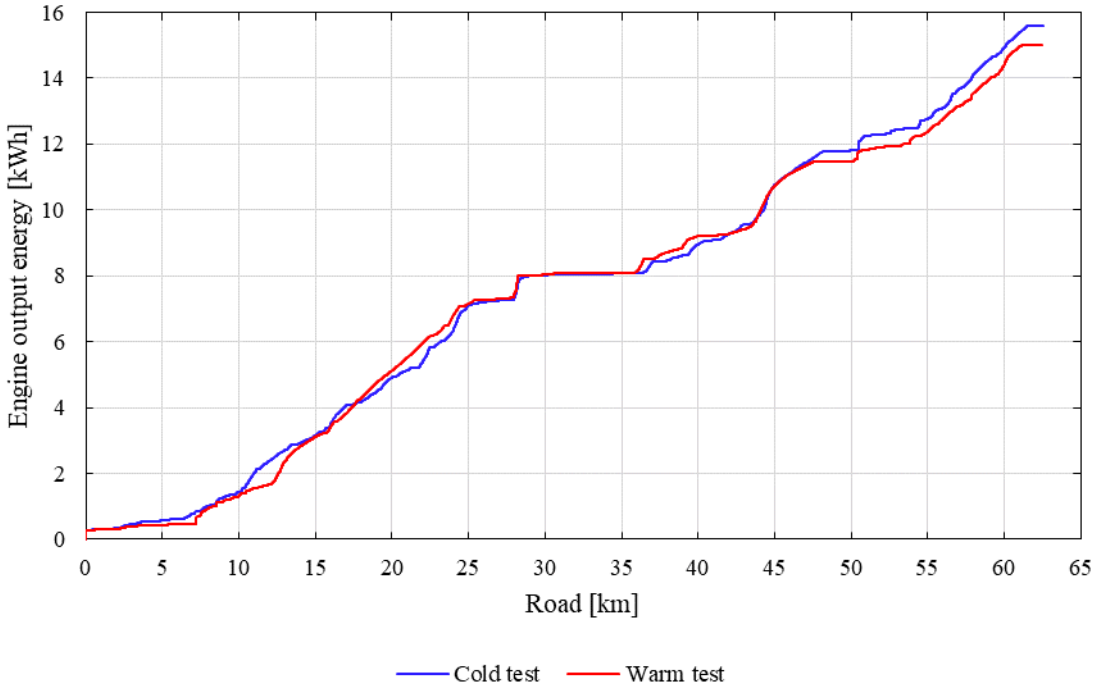

Figure 8-45. Engine output energy during cold and warm tests.

8.4.2.2 Engine thermal dynamics

To characterize experimentally the engine thermal dynamics, several temperatures have been investigated. Some of them are recorded directly by the ECU, thanks to the sensors standardly equipped on the engine. They are the coolant and oil temperatures, measured at the thermostat of the cooling circuit, and at the VVA system, respectively.

Moreover, some of the temperatures measured by the additional thermocouples installed in the engine have been considered. Specifically, they are the temperatures of the metallic masses measured at the engine block (Figure 8-7), and the oil temperature measured at the sump (Figure 8-6).

In this way, the thermal dynamics of engine coolant, oil and block has been characterized experimentally for the cold and warm tests. The results are reported in Figure 8-46 and Figure 8-47, respectively. In these figures, the engine block temperature has been calculated as the average among the temperatures measured by the four thermocouples mounted at different positions of the engine block (T_1, T_2, T_3 and T_4 in Figure 8-7).

In both tests, the temperatures of engine coolant, oil and block stabilize around the same values. Specifically, the coolant temperature oscillates between 85°C and 103°C, depending on the balance between the engine load and the thermostat valve opening. The same profile is followed by the engine block average temperature, which is simply shifted towards higher

values, thus varying between 90°C and 110°C. This almost simultaneous variation of coolant and engine block temperatures indicates a low thermal inertia of the engine. This has been accomplished thanks to the use of aluminum as material for head and block, and to an advanced topological optimization of the engine geometry. Moreover, the cooling system is filled with a small volume of coolant, which further reduces the thermal inertia of the overall system.

Similarly, the engine oil temperatures follow with a certain delay the dynamics of the coolant temperature, and stabilize in the range between 100-110°C at the VVA system, and between 95-110°C at the oil sump. Specifically, the time delay between oil and coolant temperatures is about 4 minutes during the warm-up phase. Moreover, the oil temperature at the sump is almost always lower by about 3-5°C than that at the VVA system, due to the higher distance from the combustion chamber.

In these figures, the warm-up phase can be also observed. In the cold test, the initial temperature of the engine, as well as of coolant and lubricant oil, is about 20°C. Starting from this point, these temperatures rise up to 90°C during the first 9 km, covered in about 13 minutes.

Instead, in the warm test, the initial temperatures range between 65°C and 80°C, and all reach about 90°C within the first 5 km, i.e. after about six and a half minutes.

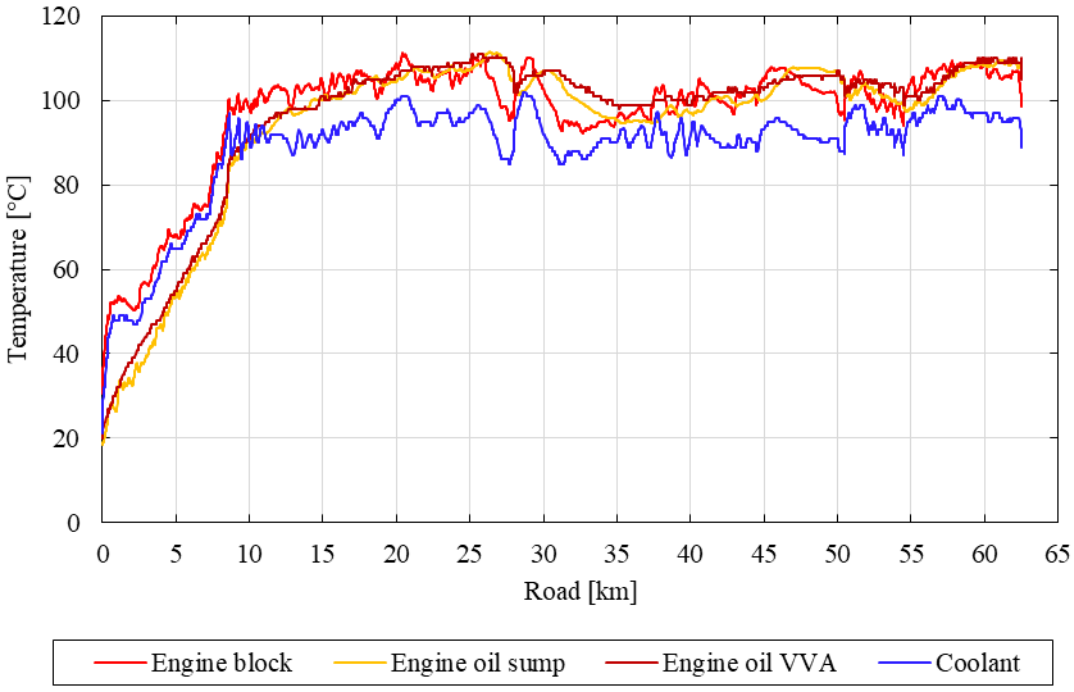

Figure 8-46. Temperatures of engine, oil and coolant during the cold test.

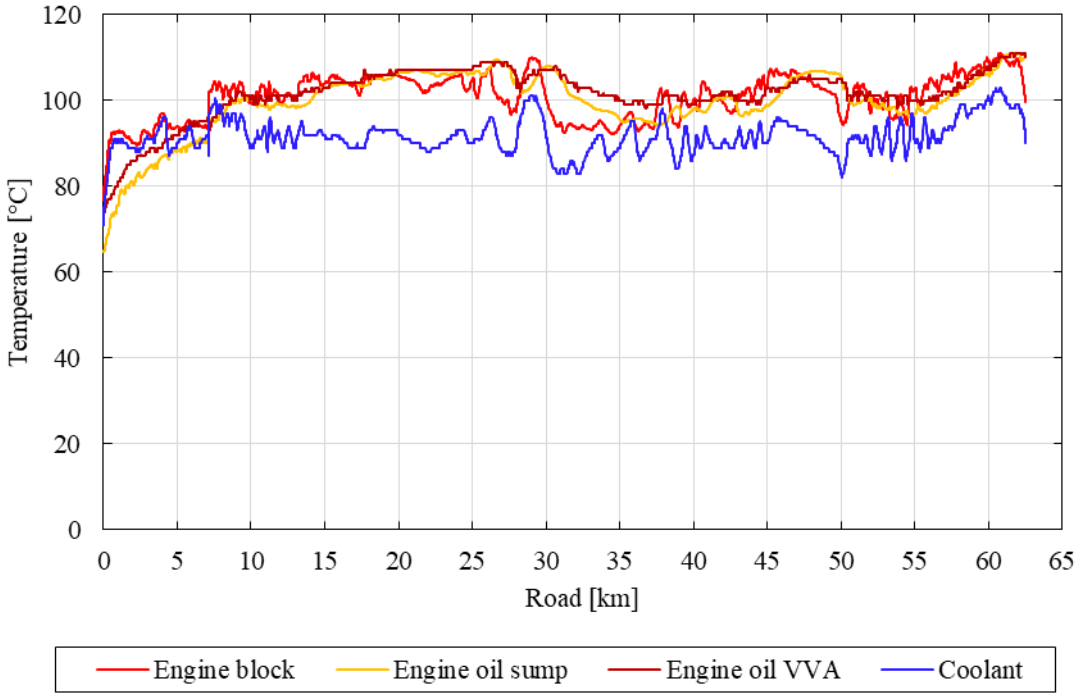

Figure 8-47. Temperatures of engine, oil and coolant during the warm test.

To better understand the engine thermal dynamics during the warm-up phase, the temperatures measured during the first 9 km of the cold test have been zoomed in Figure 8-48. In this figure, the thermostat opening can be clearly distinguished. In fact, the coolant temperature rises progressively up to 97°C at 8.6 km, i.e. after 11.7 minutes. Then, a sudden decrease occurs, due to the cooling effect induced by the engine radiator. The impact of the thermostat valve opening can be observed also in the engine block and oil temperatures, which stop rising almost suddenly, and become approximately steady.

Overall, the coolant and engine block temperatures rise almost simultaneously during the warm-up phase. Only short steady segments can be distinguished in the ranges 0.8-2 km, 4.7-5.4 km, and 6.6-7.1 km. These segments correspond to downhill road stretches, where very low engine power operating points have been experienced (Figure 8-40 (b) and Figure 8-42).

Instead, the engine oil temperatures increase with an almost linear trend, except for a sharper rise just before the thermostat valve opening, immediately followed by a steady segment. Moreover, the oil in the sump is always at a lower temperature (at most by 5°C) than that in the VVA system.

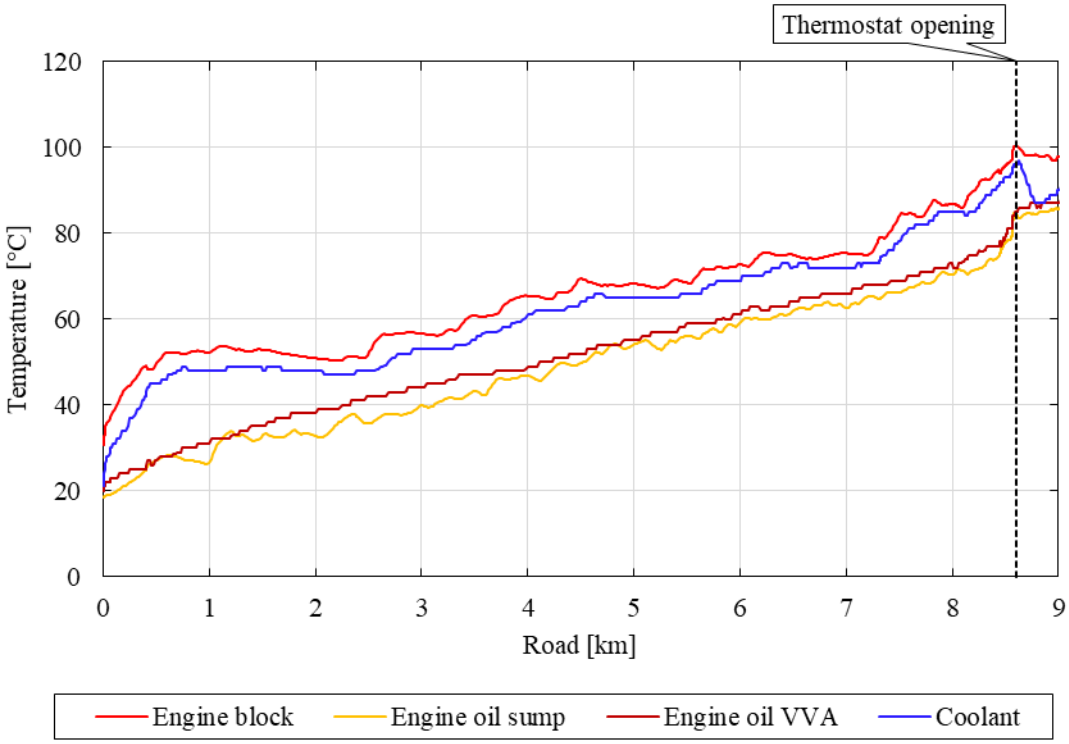

Figure 8-48. Temperatures of engine, oil and coolant during the warm-up phase of the cold test.

The engine block temperature represented in the previous figures is an average among those measured by the thermocouples installed in the engine block (Figure 8-7). These temperatures relative to the cold and warm tests can be observed in Figure 8-49 and Figure 8-50, respectively.

As expected, T_2 is the highest temperature, being it measured at the top of the cylinder liner of the second cylinder, at thus very close to the combustion chamber. Specifically, after the warm-up phase, this temperature varies between 90°C and 125°C, depending on the engine load.

Then, the second highest temperature is T_1, which is measured at the bottom of the cylinder liner of the same cylinder, and thus less exposed to the high temperatures of the combustion gases. This temperature oscillates between 95°C and 115°C after the warm-up phase, and follows the variations of T_2 with a time delay of about 1 minute.

A different discussion must be made when analyzing the temperatures T_3 and T_4. In fact, after the warm-up phase, T_3 is always lower than all the other temperatures. Moreover, it ranges between 89°C and 104°C, and follows the variations of T_2 almost simultaneously.

Instead, T_4 is generally between T_1 and T_3, and oscillates in the range 90-105°C. Moreover, it overlaps on T_2 for short segments where T_2 diminishes, mainly due to the higher time delay (about 1 minute) of T_4 relative to T_2.

This behavior can be explained considering the position of the thermocouples measuring T_3 and T_4. In fact, T_3 is measured at the external wall of the coolant flow passage near the top of the cylinder liner. Hence, it is representative of the temperature of the coolant flowing inside the engine, which has to be lower than the temperatures of the cylinder liner (T_1 and T_2) to

actually absorb the waste heat from combustion rejected by the engine. Moreover, T_3 is less subjected to the thermal inertia of the metallic masses diving the combustion chamber from the rest of the engine, and thus it is able to follow the variations of T_2 almost instantly.

Instead, T_4 is measured at the external cover of the block dividing the engine from the ambient air. Hence, it is less representative of the temperature of the coolant inside the engine. Moreover, it is subjected to a higher thermal inertia of the metallic masses, being more distant from the combustion chamber. Consequently, in this specific case, T_4 can be considered more influenced by local thermal conductivity phenomena, which make it higher than the temperature measured near the cooling passageways (T_3).

It is worth discussing also how the temperatures of the engine block evolve during the warm-up phase. In the cold test (Figure 8-49), these temperatures reach their nominal values in less than 9 km, i.e. about 11 minutes. Instead, in the warm test (Figure 8-50), they are already at about 70-80°C at the beginning of the test. Hence, they reach their steady state range (90-120°C) just after few hundred meters of road, i.e. few tens of seconds.

These results underline a fast warm-up phase of this engine, considering also the specificity of the road test. In fact, this phase takes place in the first urban section, which is substantially in downhill conditions, and thus covered with very low engine power requests (see Figure 8-40 (b) and Figure 8-42). Hence, the warm-up phase would have been even faster if a road trip requesting more power had been covered soon after the engine start-up.

Finally, it is worth noting the high responsiveness of the temperature measured at the top of the cylinder liner (T_2), which follows the engine load variations almost instantly. This can be observed by comparing together T_2 in Figure 8-49 and Figure 8-50, with the mechanical power supplied by the engine during the cold and warm tests reported in Figure 8-42.

Moreover, remarkably, the coolant temperature is almost simultaneous with the average temperature of the block in this specific engine (Figure 8-46 and Figure 8-47).

Both these features are particularly useful if an advanced actuation of the cooling pump wants to be performed to further speed-up the warm-up phase. In fact, the pump could be actuated only when needed, depending on the engine block temperature (T_2). This latter would be representative of the instant engine thermal state, which varies very quickly depending on the engine load. Specifically, thanks to the knowledge of the engine block temperature, the pump could be stopped during the warm-up phase, while maintaining a fail-safe system. This characteristic cannot be assured if the coolant temperature is taken as reference, because the absence of flow rate would determine a temperature measured at the thermostat valve not representative of the engine temperature.

Hence, these experimental results on the engine thermal state during on-the-road tests provide precious information on possible criteria to be used when introducing a speed-variable pump in the engine cooling system of a vehicle.

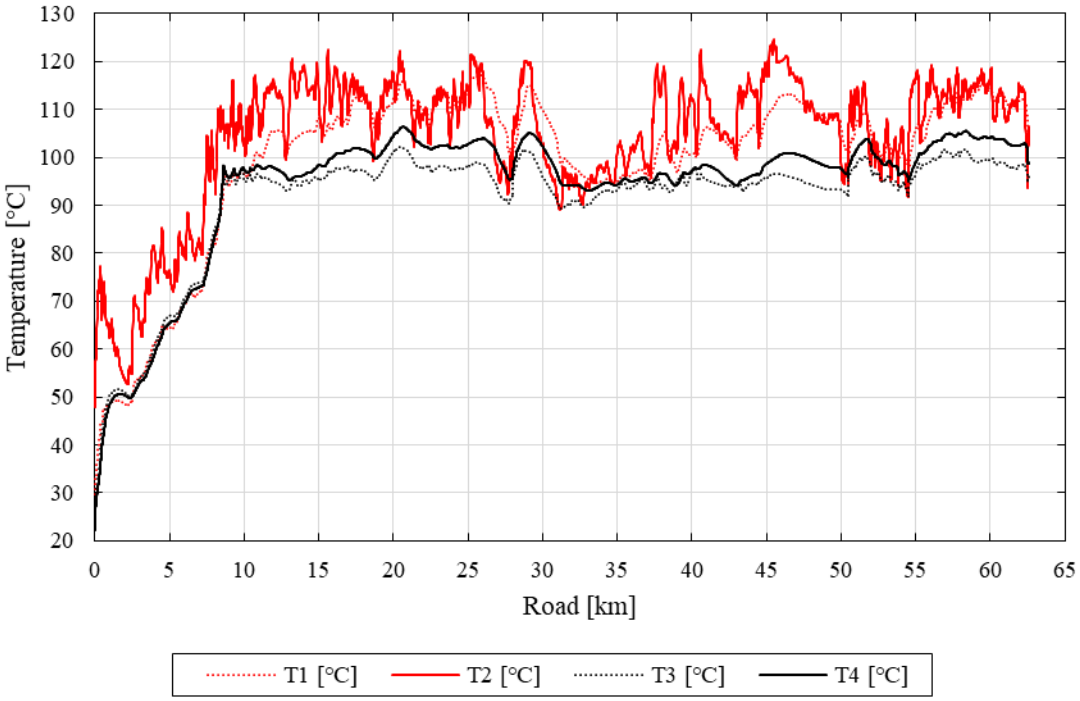

Figure 8-49. Temperatures of the engine block during the cold test.

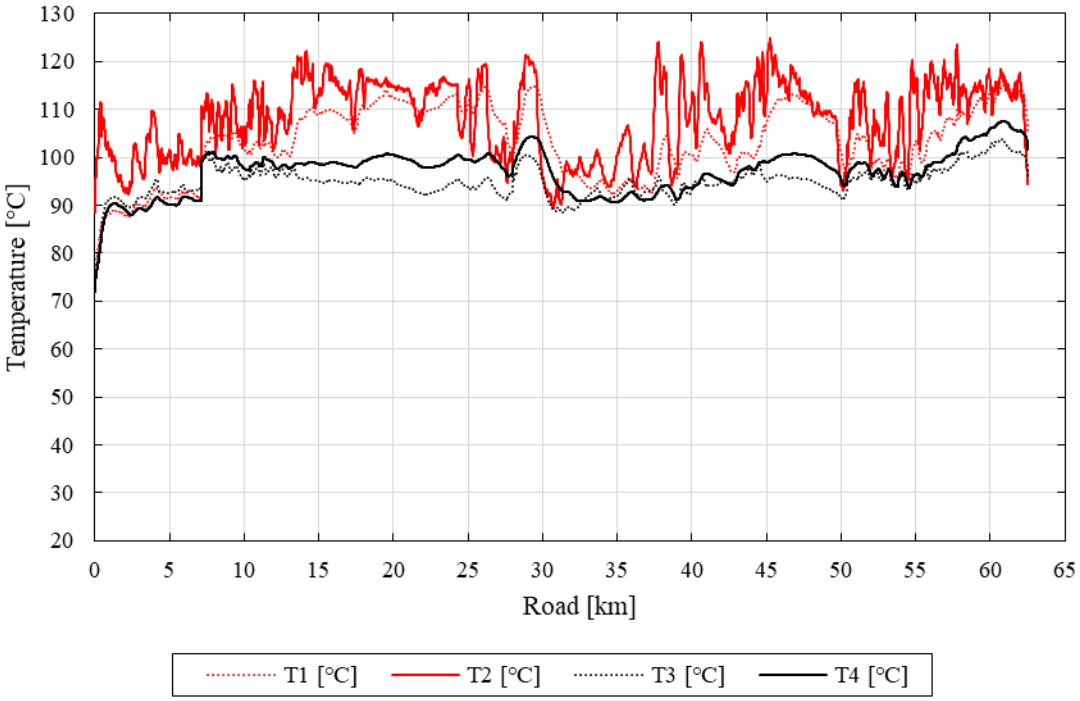

Figure 8-50. Temperatures of the engine block during the warm test.

The previous figures pointed out also a significant difference between the warm-up phase during the cold and warm tests. To better appreciate this aspect, the coolant temperature during the first 7 km of these tests has been reported in Figure 8-51. Clearly, during the warm test, the coolant reaches 90°C just after few hundred meters of road, i.e. in less than one minute. Instead, in the cold test, the warm-up time is far longer. In fact, after 7 km (i.e. 8 and a half minutes), the warm-up phase is still on-going, being the coolant temperature about 70°C.

This different warm-up time among cold and warm tests has an impact on fuel consumption and pollutant and CO_2 emissions, which will be discussed in detail in the following sections.

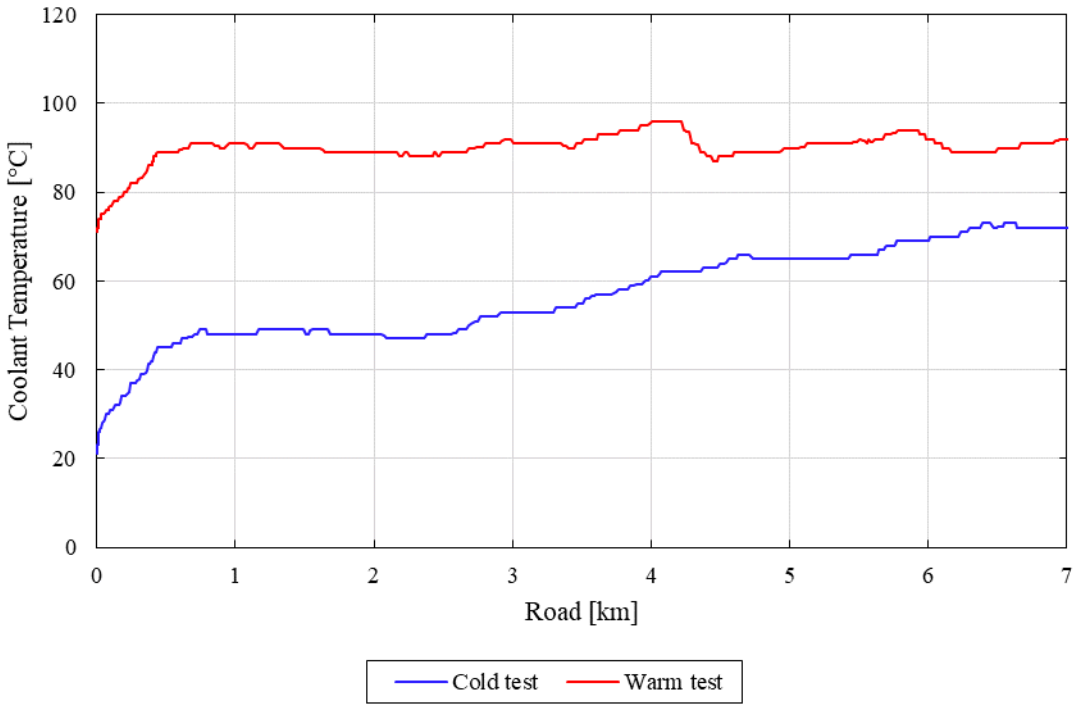

Figure 8-51. Coolant temperature during the warm-up phase of cold and warm tests.

8.4.2.3 Fuel consumption

The experimental results concerning fuel consumption have been obtained thanks to the instantaneous fuel flow rate recorded by the engine ECU during the tests. Specifically, the ECU stores a mass flow rate expressed in g/s (Table 8-10). Thus, by assuming a constant fuel density (730 g/l), the fuel consumption in l/s has been calculated.

The instant fuel consumptions relative to the cold and warm tests have been reported in Figure 8-52. This figure shows also the mean consumptions for each section of the road trip. Clearly, the fuel consumption profiles are aligned with those of the instant engine power, torque and speed (from Figure 8-42 to Figure 8-44).

On average, the highest fuel rates have been reached during the first extra-urban section, being about 2.5 and 2.8 ml/s for the cold and warm tests, respectively. This is due to the uphill highway road, which caused a high engine load especially in the warm test, in which higher vehicle speeds were reached. Instead, the lowest fuel rates (less than 1 ml/s on average) have been registered during the first urban section, due to its low-speed downhill path.

Moreover, the main discrepancies between cold and warm tests can be observed during the first urban and extra-urban sections, whereas the fuel consumptions of both tests are almost coincident for the remaining part of the road trip.

For what concerns the first extra-urban section, the higher fuel consumption registered during the warm test can be attributed mainly to the higher vehicle speeds reached in this segment (Figure 8-41), which determined a higher power demand to the engine (Figure 8-42).

Instead, the first urban section has been covered with about the same speed during both tests (Figure 8-41), but the cold test requested more engine power (Figure 8-42), thus determining a higher fuel consumption.

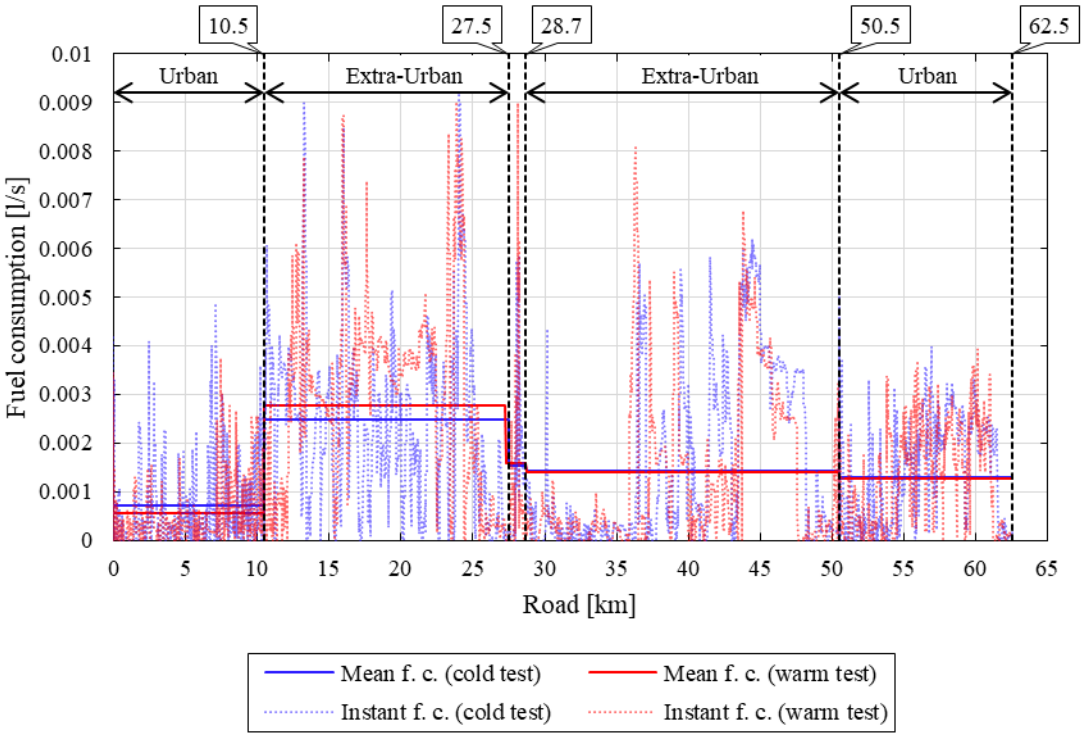

Figure 8-52. Mean and instant fuel consumption during cold and warm tests.

The higher fuel consumption of the cold test during the first urban section can be mainly attributed to the engine warm-up phase. To this end, the cumulative fuel consumptions of cold and warm tests during the first 7 km have been represented together with the coolant and engine block temperatures (Figure 8-53 and Figure 8-54, respectively). In these figures, the continuous lines are relative to the cold test, whereas the dashed lines to the warm test.

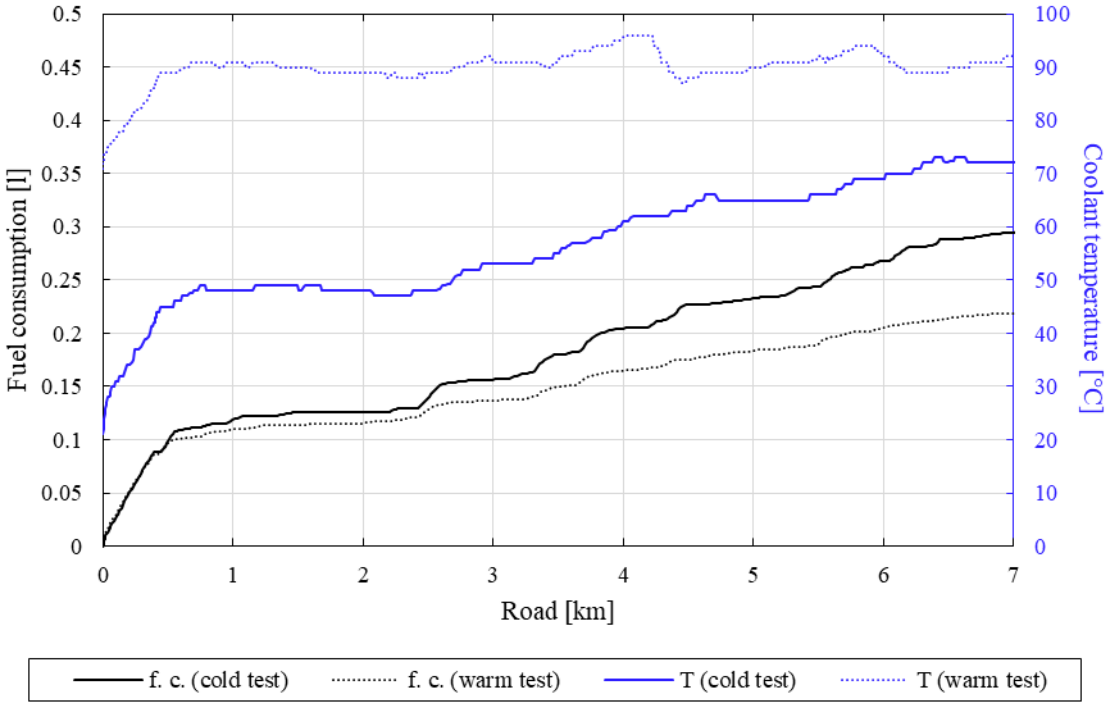

Figure 8-53. Fuel consumption (black) and coolant temperature (blue) during the warm-up phase, for cold (continuous lines) and warm (dashed lines) tests.

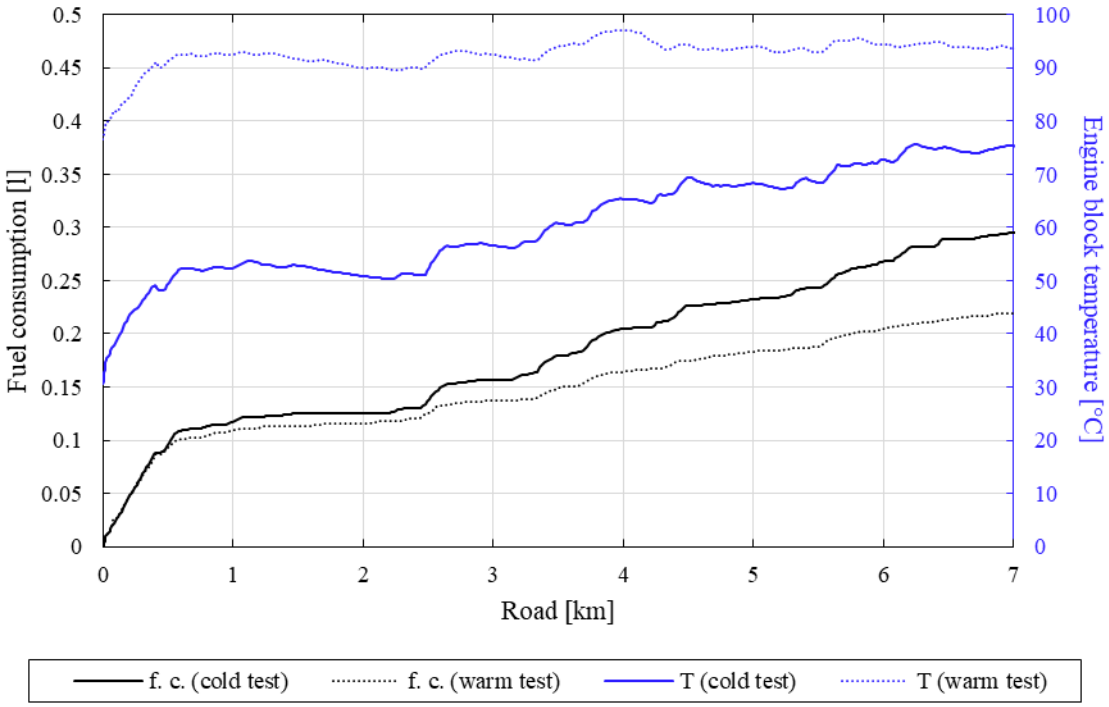

Figure 8-54. Fuel consumption (black) and engine block temperature (blue) during the warm-up phase, for cold (continuous lines) and warm (dashed lines) tests.

Clearly, the engine warm-up phase of the cold test determines a higher fuel consumption compared with that registered in the warm test. Specifically, about 295 ml of fuel was burned to cover the first 7 km when starting the engine at 20°C, against 219 ml when starting the engine already at 75°C. Consequently, in this specific test case, the engine warm-up phase determined an increase in fuel consumption by about 35%. This significant result corroborates the need to reduce as much as possible the engine warm-up phase, especially in short road trips, where it impacts more on the overall fuel consumption.

Finally, the total fuel consumption obtained over the cold and warm tests can be discussed (Figure 8-55). Here, the impact of the warm-up phase on the overall fuel consumption is mitigated by the length of the trip, which is equal to 62.5 km. In fact, the fuel consumption registered during the cold test (engine initial temperature at 20°C) is equal to 5.3 liters (i.e. 11.8 km/l), whereas during the warm test (engine initial temperature at 75°C) the engine has consumed 5.1 liters of fuel (i.e. 12.3 km/l). Consequently, in this specific case, the higher initial temperature of the engine in the warm test allowed to reduce fuel consumption by about 3.9%.

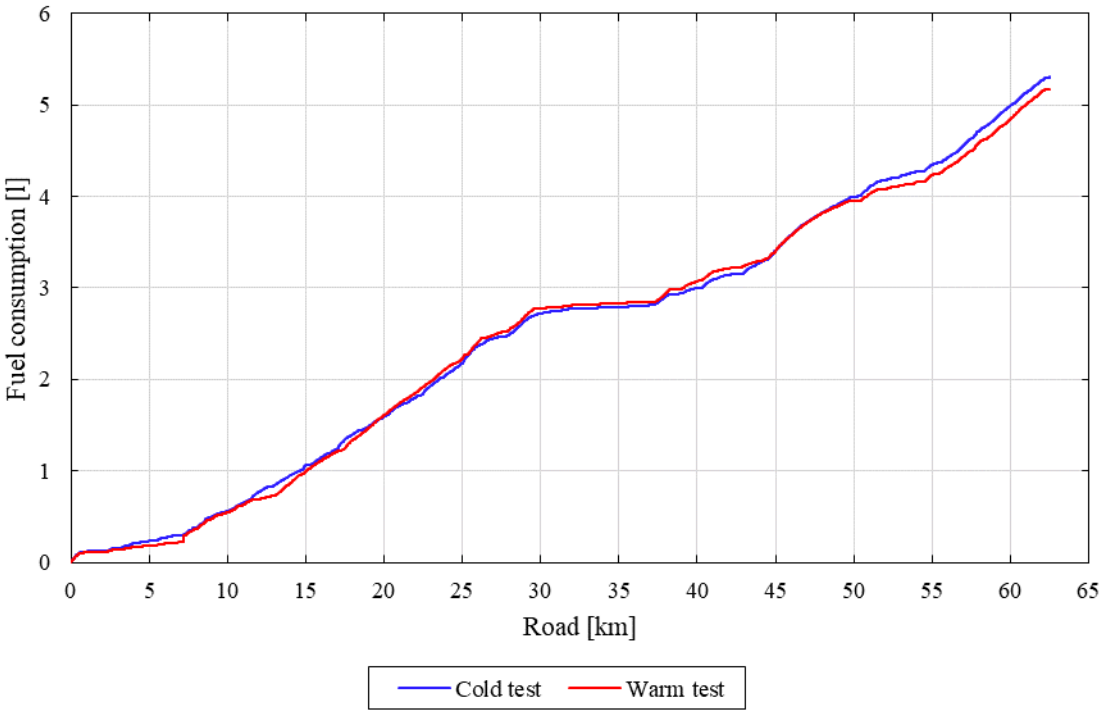

Figure 8-55. Total fuel consumption over cold and warm tests.

This fuel saving cannot be completely attributed to the reduced engine warm-up phase of the warm test. However, if the average fuel rates in each section are considered (Figure 8-52), then it appears clear that a faster engine warm-up determines surely a significant benefit in this sense. In fact, despite the higher fuel consumption registered in the warm test during the first extra-urban section, the overall fuel consumption of the warm test is lower than that of the cold one. This is possible only thanks to the reduced fuel consumption in the first urban section, being

the last extra-urban and urban sections covered almost with the same fuel consumption of the cold test. Hence, the reduction of the engine warm-up phase would have determined an even higher total fuel saving if the first extra-urban section had been covered with the same engine load of the cold test.

Finally, it is worth noting the discrepancy between the fuel consumption declared by the vehicle manufacturer, and those registered in these tests. In fact, the manufacturer declares an average fuel consumption of 14.29-15.15 km/l (Table 8-4), which is far from the results obtained in this experimental study. This depends on the specific regulation followed to homologate the vehicle, which in this case is based on the WLTP emission test procedure, being the vehicle a 2021 model-year version (see Section 1.5).

As known, a fuel saving has positive benefits also on CO_2 emissions. Moreover, the different engine temperature during the warm-up phase will likely have an impact also on pollutant emissions. Hence, a dedicated discussion on engine emissions will be presented in the following section.

8.4.2.4 CO_2 and pollutant emissions

In this section, the engine emissions measured through the PEMS during the cold and warm tests will be analyzed. As mentioned in Section 8.3.3, the specific PEMS installed on the vehicle allows to measure only the NO_x, CO and CO_2 emissions in the exhaust gases. Specifically, this system provides the concentrations of NO_x and CO in ppm (parts per million). Instead, the carbon dioxide CO_2 is expressed as a percentage of the exhaust gases, which are measured through the flow meter mounted at the tailpipe outlet.

To derive the mass flow rate of NO_x and CO emissions starting from their concentration in ppm, the criteria defined by the EU Regulation 2017/1151 [32] have been followed. Hence, the instantaneous mass emissions [g/s] have been determined by multiplying the instantaneous concentration of the pollutant under consideration [ppm], with the instantaneous exhaust mass flow rate [kg/s], and the respective *u* value of Table 8-21. Specifically (Eq. 8-5):

$$m_{gas,i} = u_{gas} \cdot c_{gas,i} \cdot q_{mew,i} \qquad \text{Eq. 8-5}$$

where:

- $m_{gas,i}$ is the mass of the exhaust component *gas* [g/s];
- u_{gas} is the ratio of the density of the exhaust component *gas* and the overall density of the exhaust, as listed in Table 8-21;
- $c_{gas,i}$ is the measured concentration of the exhaust component *gas* in the exhaust [ppm];
- $q_{mew,i}$ is the measured exhaust mass flow rate [kg/s];
- *gas* is the respective component;

- i is the number of the measurement.

Fuel	ρ_e [kg/m^3]	Component or pollutant i					
		NO_x	CO	HC	CO_2	O_2	CH_4
		ρ_{gas} [kg/m^3]					
		2,053	1,250	([1])	1,9636	1,4277	0,716
		u_{gas}[(2),(6)]					
Diesel (B7)	1,2943	0,001586	0,000966	0,000482	0,001517	0,001103	0,000553
Ethanol (ED95)	1,2768	0,001609	0,000980	0,000780	0,001539	0,001119	0,000561
CNG [(3)]	1,2661	0,001621	0,000987	0,000528 [(4)]	0,001551	0,001128	0,000565
Propane	1,2805	0,001603	0,000976	0,000512	0,001533	0,001115	0,000559
Butane	1,2832	0,001600	0,000974	0,000505	0,001530	0,001113	0,000558
LPG [(5)]	1,2811	0,001602	0,000976	0,000510	0,001533	0,001115	0,000559
Petrol (E10)	1,2931	0,001587	0,000966	0,000499	0,001518	0,001104	0,000553
Ethanol (E85)	1,2797	0,001604	0,000977	0,000730	0,001534	0,001116	0,000559

[(1)] depending on fuel
[(2)] at $\lambda = 2$, dry air, 273 K, 101.3 kPa
[(3)] u values accurate within 0,2 % for mass composition of: C=66-76 %; H=22-25 %; N=0-12 %
[(4)] NMHC on the basis of $CH_{2.93}$ (for THC the u gas coefficient of CH_4 shall be used)
[(5)] u accurate within 0,2 % for mass composition of: C_3 =70-90 %; C_4 =10-30 %
[(6)] u_{gas} is a unitless parameter; the u_{gas} values include unit conversions to ensure that the instantaneous emissions are obtained in the specified physical unit, i.e., g/s

Table 8-21. Raw exhaust gas u values depicting the ratio between the densities of exhaust component or pollutant i [kg/m^3] and the density of the exhaust gas [kg/m^3] [32].

In this way, the instantaneous and cumulative emissions of CO and NO_x have been calculated over the cold and warm tests. The results have been reported, for each gas, distinguishing between the emissions produced during the engine warm-up phase of the cold test (i.e. the first 7 km), and during the overall test (62.5 km long).

The results concerning the CO emissions are reported in Figure 8-56 and Figure 8-57. Generally, the cold test determined higher CO emissions compared with the warm one.

Specifically, the CO emissions produced in the first 7 km of the tests are reported in Figure 8-56. In this section, the engine emitted 2.98 g_{CO} of CO during the cold test, against 1.77 g_{CO} produced during the warm one. Consequently, the engine warm-up phase of the cold test determined an increase in CO emissions compared with the warm test equal to 68% during the first 7 km.

Moreover, it is worth noting that this significant increase occurred mainly soon after the engine start-up, i.e. during the first hundreds meters of the road trip. Then, this offset kept almost constant for the rest of the trip up to 7 km.

Such behavior can be explained considering two main aspects. The first one is the high difference between the initial engine temperature at the beginning of the cold test, compared with that of the warm test, which is about 50-60°C (Figure 8-51). This caused low temperatures in the combustion chamber, as well as “rich” air-fuel mixtures, soon after the engine start-up, which resulted inevitably in high CO emissions.

In addition, the very first meters of the tests took place in a uphill road (Figure 8-40 (b)), which worsens fuel consumption and emissions, being the engine still in the warm-up phase. However, after this short uphill segment, the rest of the test occurred in a downhill road up to 7 km. There, the engine load was low, and thus CO emissions remained almost constant.

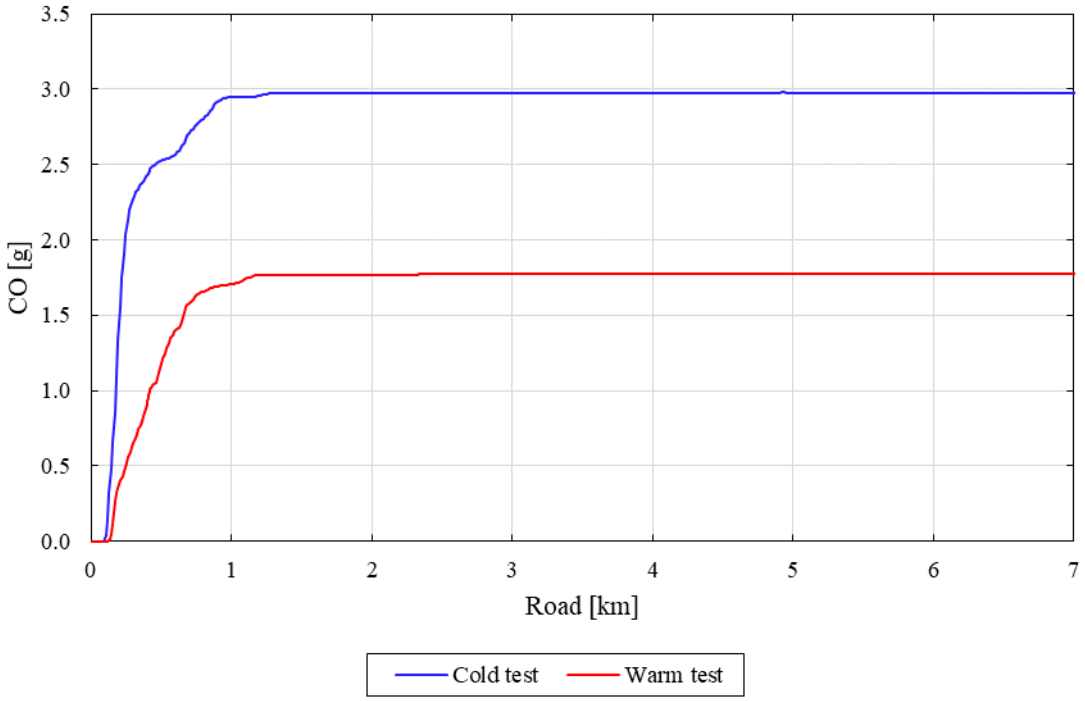

Figure 8-56. CO emissions during the engine warm-up phase of the cold test, compared with those emitted during the warm test.

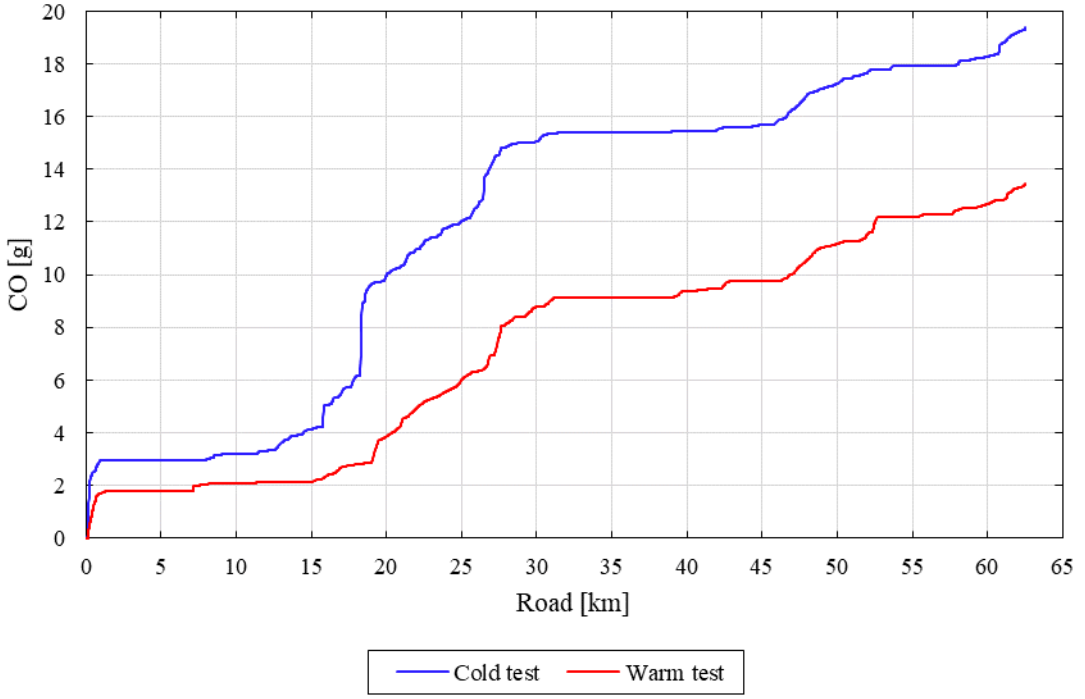

Figure 8-57. Total CO emissions during the cold and warm tests.

Overall, the total CO emissions of cold and warm tests are reported in Figure 8-57. At the end of the trip (62.5 km), this vehicle emitted 19.3 g_{CO} of CO in the cold test (i.e. with the engine initial temperature at 20°C), against 13.4 g_{CO} in the warm test (i.e. with the engine initial temperature at 75°C). Hence, the warm test allowed to reduce the CO emissions by about 30.6% compared with the cold one.

Moreover, it is worth analyzing how this gap established during the test. The first contribution derives from the initial engine warm-up phase of the cold test happened within the first hundred meters of road, as already observed in Figure 8-56. Then, several segments with no significant variations in CO emissions can be observed. They correspond to downhill road conditions, mainly concentrated in the first urban section (1-7 km), in the second extra-urban section (31-42 km) and in the last urban section (52-55 km). These segments have been covered with few engine power request, and thus they did not contribute significantly to the overall CO emissions.

Instead, between these constant segments, several sharp increases of CO emissions have been registered. They correspond to high engine load conditions, deriving from sharp accelerations and/or uphill driving conditions. Clearly, the cold test determined slightly higher increases in CO emissions during these short high engine load operations, compared with the warm test. These CO increments contributed to widen the gap initially set by the engine warm-up phase, although the initial offset appears to be the main contribution in the different CO emissions registered in the two tests.

The results concerning the NO_x emissions are reported in Figure 8-58 and Figure 8-59. Generally, the warm test determined higher NO_x emissions compared with the cold one. This can be attributed to the higher initial temperature of the engine, which produced higher temperatures in the combustion chamber, and thus higher NO_x emissions.

Specifically, in the first 7 km, the engine emitted 0.21 g_{NOx} of NO_x during the warm test, against 0.09 g_{NOx} produced during the cold test (Figure 8-58). In other words, the warm test determined NO_x emissions more than doubled compared to the cold one.

The great part of this gap occurred during the first kilometer of road, where the engine emitted 0.18 g_{NOx} of NO_x during the warm test, i.e. almost four times the emissions registered during the cold test, equal to 0.05 g_{NOx}. This is due to the higher initial temperature of the engine (75°C in the warm test, against 20°C in the cold test), which undoubtedly had an impact on the combustion temperature, and thus on the NO_x emissions measured soon after the engine start-up. Furthermore, it is worth noting that the FireFly T4 engine does not have a dedicated EGR system, but only an EGR strategy implemented through the VVA system [268]. This is another aspect that allowed higher NO_x emissions at the beginning of the warm test.

However, after this sharp initial increase, the engine emitted almost the same NO_x emissions during both tests. Moreover, these emissions are very low up to 7 km, due to the downhill road and the low vehicle speeds, which determined low engine loads.

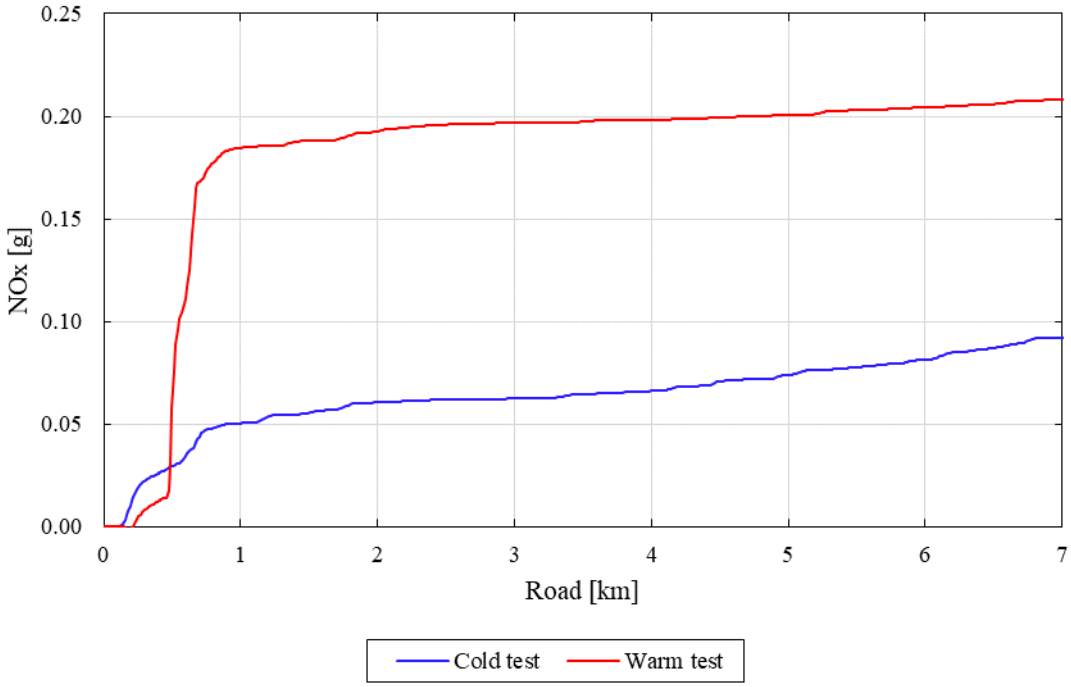

Figure 8-58. NO_x emissions during the engine warm-up phase of the cold test, compared with those emitted during the warm test.

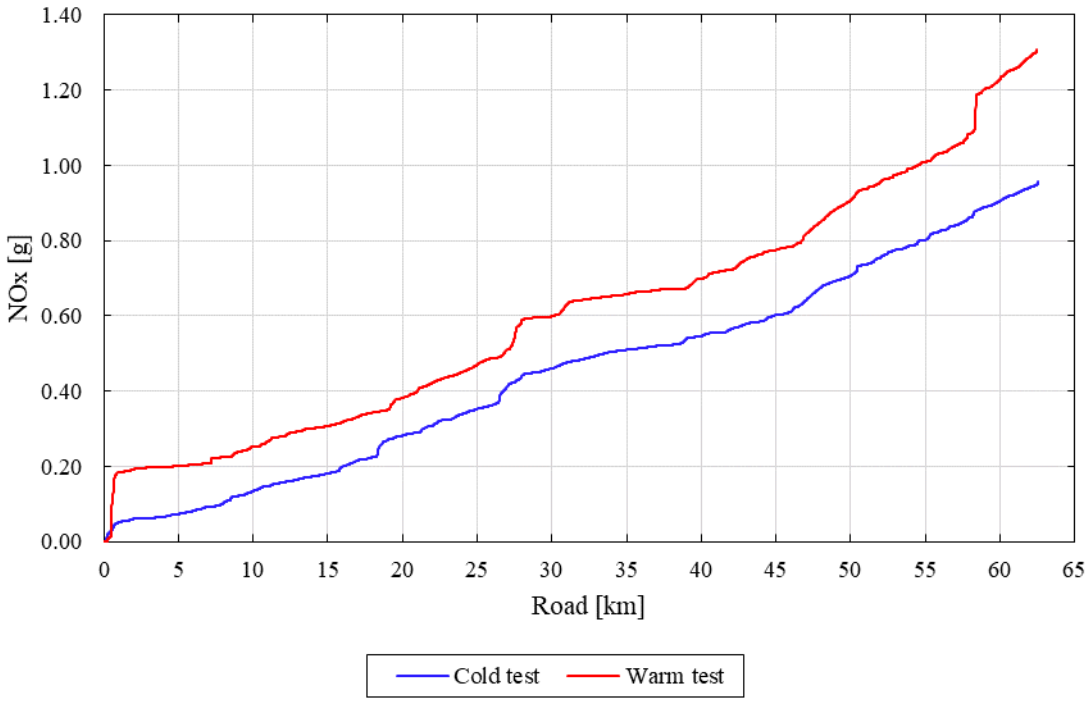

Figure 8-59. Total NO_x emissions during the cold and warm tests.

This behavior is maintained also during the rest of the road trip, as shown by Figure 8-59. In fact, the NO_x emissions curve of the warm test is simply shifter upwards compared with that of

the cold test, by an amount almost equal to the initial gap registered at the beginning of the warm test.

The only exception can be noticed at 58 km, where a further sharp increase in NO_x emissions has been registered during the warm test. This gap cannot be attributed to an actual variation of the engine load or thermal state. Instead, it appears to be correlated with a malfunctioning of the PEMS instrumentation at that point. This assumption is based on a careful evaluation of the main engine parameters registered in correspondence of the gap. Some of them have been reported in Figure 8-60. Specifically, they are the engine speed (a), the intake air flow rate (b), the gas pedal opening (c) and the boost pressure (d). None of these parameters present any sharp variation around 58 km, and their unsteady trend complies with the typical behavior that can be expected from an ICE operating in an on-board vehicle application. Hence, the gap measured at 58 km can be discarded.

Overall, the NO_x emissions measured during the entire cold test are equal to 0.97 g_{NOx}, whereas those measured during the warm test (without considering the gap at 58 km) are 1.18 g_{NOx}, i.e. about 21.6% higher.

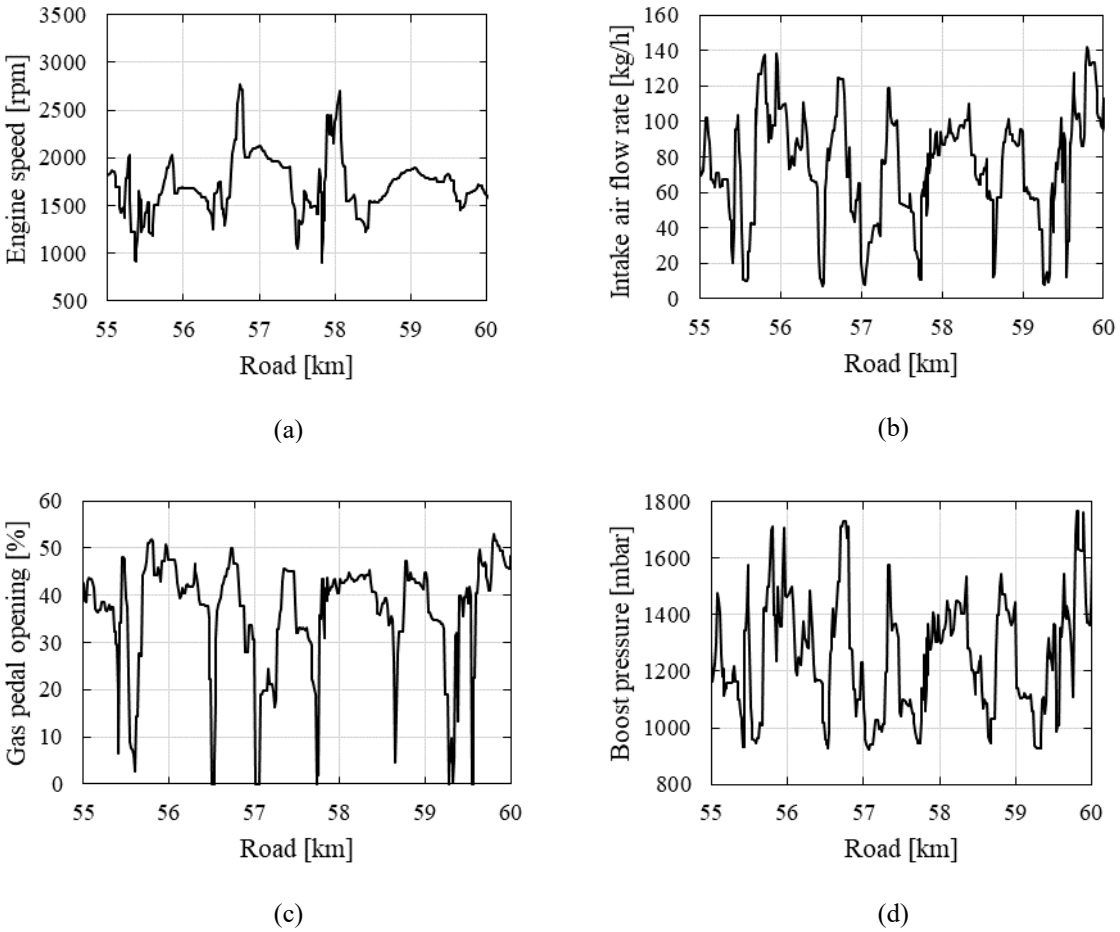

Figure 8-60. Engine parameters registered by the ECU in the range between 55 and 60 km of the warm test: (a) engine speed; (b) intake air flow rate; (c) gas pedal opening; (d) boost pressure.

The results concerning the CO_2 emissions are reported in Figure 8-61 and Figure 8-62. Generally, the cold test determined higher CO_2 emissions compared with the warm one. This result agrees with that obtained for fuel consumption, already discussed in Section 8.4.2.3.

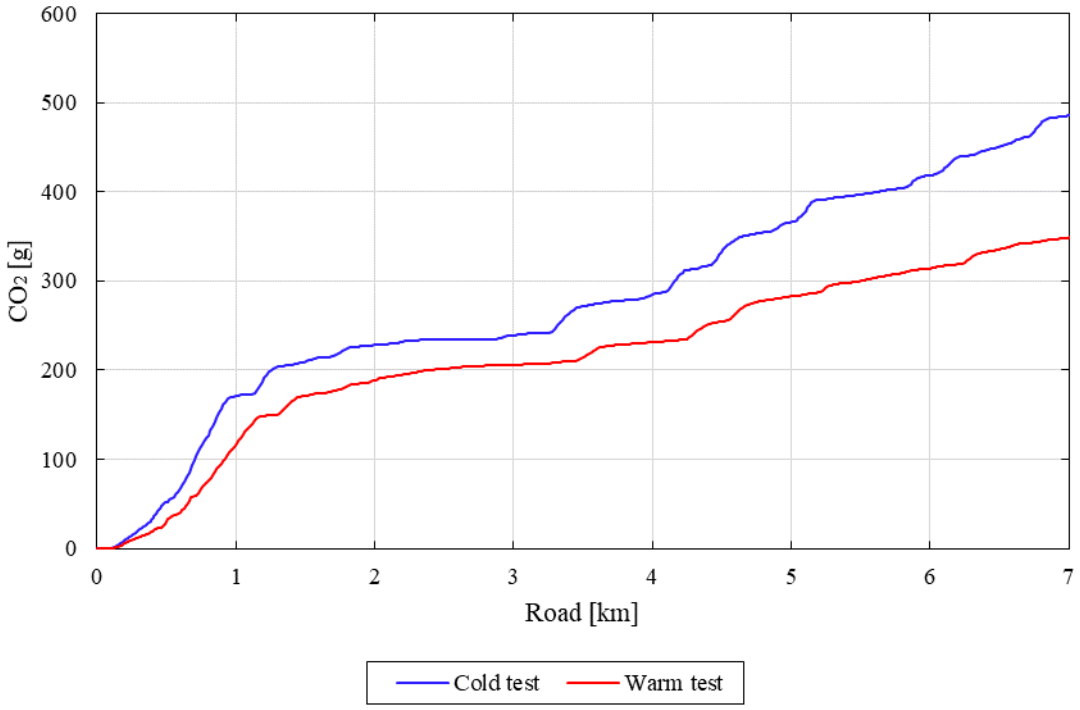

Figure 8-61. CO_2 emissions during the engine warm-up phase of the cold test, compared with those emitted during the warm test.

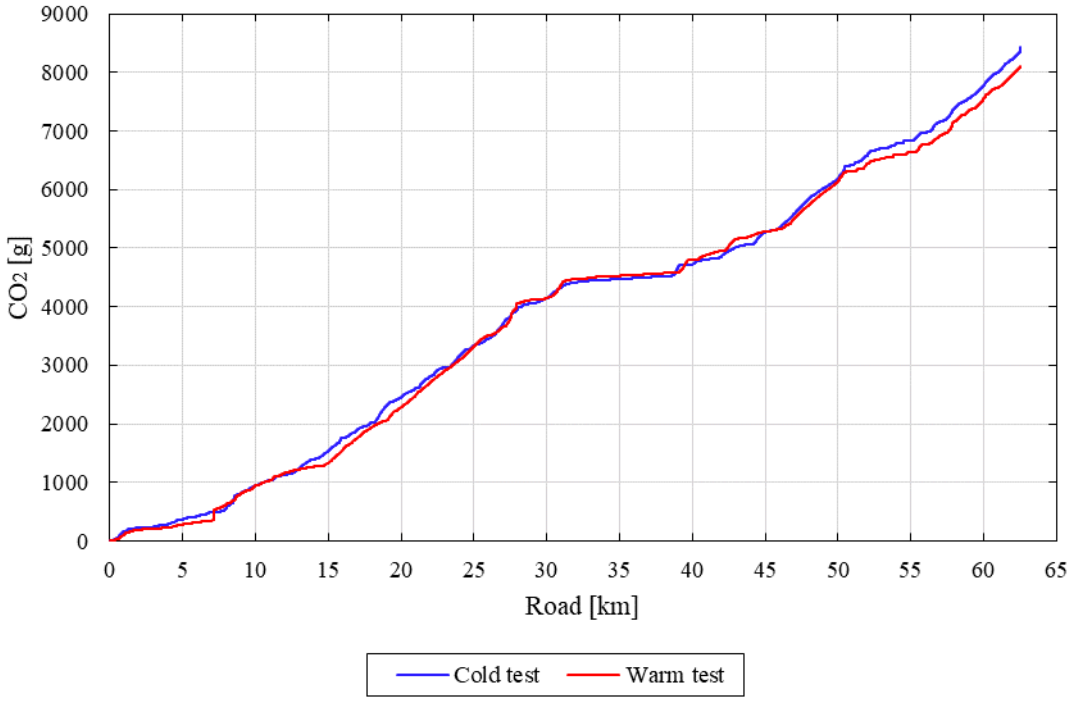

Figure 8-62. Total CO_2 emissions during the cold and warm tests.

Specifically, after the first 7 km, the engine emitted 486 g_{CO2} of CO_2 during the cold test, against 349 g_{CO2} produced during the warm test (Figure 8-61). Hence, the engine warm-up phase of the cold test determined an increase in CO_2 emissions compared with the warm one equal to 39%. This is strictly related to the higher fuel consumption registered in the same section (Figure 8-53 and Figure 8-54). In fact, when starting the engine at ambient temperature (20°C), the oil viscosity is higher than that reached when the engine is warmed-up, determining higher friction losses during the engine warm-up phase. This translates into higher fuel consumption and CO_2 emissions, if the same road trip has to be covered.

Moreover, in the CO_2 emissions' profiles reported in Figure 8-61, almost constant segments can be distinguished (as at 1.5-3.5 km). These corresponds to steep downhill roads, where the engine loads were almost negligible, and so also fuel consumption and CO_2 emissions. Between these segments, rapid increases of CO_2 emissions have been registered, which correspond to fast accelerations and/or uphill streets.

Similar trends can be observed also considering the overall road trip (Figure 8-62), which shows also the total amount of CO_2 emitted in both tests. Specifically, after 62.5 km, this engine produced about 8.5 kg_{CO2} of CO_2 in the cold test, against 8 kg_{CO2} in the warm one. Consequently, the CO_2 emissions are reduced by 5.9% if the engine is already warm (i.e. at 75°C instead of 20°C) at the beginning of the road trip.

Finally, the specific emissions and the average fuel consumptions measured in the cold and warm tests have been calculated for the warm-up phase (i.e. the first 7 km, Table 8-22) and for the overall test (i.e. 62.5 km, Table 8-23). Moreover, also the variations induced by the warm test relative to the cold one have been reported, as well as the emission limits imposed by the current EU regulation (Section 1.5) and the nominal fuel consumption declared by the manufacturer (Table 8-4).

Generally, compared with the cold test, the warm test has a better fuel economy and lower CO and CO_2 emissions, but higher NO_x emissions. Specifically, the fuel economy increased by 34.7% and 3.9% during the warm-up phase and the overall test, respectively. Consequently, also the CO_2 emissions reduced by 28.2% and 5.9% respectively, as well as the CO emissions (-40.6% in the warm-up phase and -30.6% in the overall test). Instead, the NO_x emissions increased by 133.3% and 21.6% after the first 7 km and 62.5 km, respectively.

These results can be mainly attributed to the different warm-up phase of the two tests, being them performed on the same road trip (Figure 8-40), with about the same engine power request (Figure 8-42). In fact, in the warm test, the engine initial temperature is already at about 75°C, instead of at the ambient temperature (20°C) as in the cold test. Hence, the engine warm-up phase is completed much faster than in the cold test (few hundred meters, against 7 km). Consequently, the engine operates with reduced friction losses since the beginning, and thus with significantly lower fuel consumption and CO_2 emissions. Similarly, less CO emissions are produced, because the engine operates almost immediately with higher temperatures in the combustion chamber and with a leaner air-fuel mixture. However, the higher initial engine

temperature of warm test worsens the NO_x emissions, creating an offset with the cold test soon after the engine start-up, which is maintained almost constantly till the end of road trip. It is worth noting that this increment in NO_x emissions could have been kept under control if more advanced after-treatment systems were installed. In that case, only benefits would have been introduced by the warm test.

Warm-up (7 km)	Warm test (w)	Cold test (c)	Variation (w)-(c)	Emission limit
Fuel Economy [km/l]	32,0	23,7	+ 34,7 %	15 km/l*
NO_x [g/km]	0,030	0,013	+ 133,3 %	0,06 g/km
CO [g/km]	0,253	0,426	- 40,6 %	1 g/km
CO_2 [g/km]	49,9	69,4	- 28.2%	95 g/km

Table 8-22. Average fuel consumption and specific emissions of warm and cold tests after the first 7 km, compared with the emission limits [32] and the *reference value declared by the vehicle manufacturer [267].

Total test (62,5 km)	Warm test (w)	Cold test (c)	Variation (w)-(c)	Emission limit
Fuel Economy [km/l]	12,3	11,8	+ 3,9 %	15 km/l*
NO_x [g/km]	0,019	0,016	+ 21,6 %	0,06 g/km
CO [g/km]	0,214	0,309	- 30,6 %	1 g/km
CO_2 [g/km]	128	136	- 5,9 %	95 g/km

Table 8-23. Average fuel consumption and specific emissions of warm and cold tests after 62.5 km, compared with the emission limits [32] and the *reference value declared by the vehicle manufacturer [267].

Table 8-22 and Table 8-23 allow to compare also the specific emissions obtained in these tests with the current limits. In all cases, CO and NO_x emissions comply with the corresponding emission limits thoroughly. Instead, the CO_2 emissions are under the limit of 95 g_{CO2}/km only during the first 7 km, whereas after the full test (62.5 km) they exceed it significantly. However, this is not a matter of concern if the actual method used to define the CO_2 emission target of each manufacturer is considered (see Section 1.5).

Finally, the average fuel economy obtained in these tests can be compared with the value declared by the vehicle manufacturer. During the warm-up phase (first 7 km), the fuel economy is higher than the nominal value both in the cold and warm tests. This is due to the steep downhill road of the first urban section, where the warm-up phase occurs (Figure 8-40 (b)). Instead, in both tests, the average fuel economy over the whole trip (62.5 km) is well below the one declared by the vehicle manufacturer. This can be attributed to the current method used by manufacturers to define such data, which is still based on a WLTP executed on a test bench.

However, such discrepancies can be accepted if the impossibility to fully reproduce a real road test on a test bench is taken into account.

8.5 Conclusions

In this Chapter, the warm-up phase of a passenger vehicle propelled by a spark ignition engine has been investigated experimentally. Specifically, road tests have been realized starting with the engine at ambient temperature and at warmed-up conditions. In these tests, engine performances, fuel consumption, and CO_2 and pollutant emissions have been measured. This has been possible thanks to the installation on the vehicle of suitable measurement systems. Specifically, they are a PEMS system for the measurement of the engine emissions, and a DAQ system to acquire the engine performance parameters from the ECU. Furthermore, the engine cooling system has been completely instrumented with additional sensors, to characterize thoroughly even the thermal dynamics of the engine block.

Hence, two tests on the same road trip of 62.5 km have been realized in the same day. The first one (named *cold test*) started with the engine initial temperature at 20°C. Instead, the second one (named *warm test*) started with the engine already almost warmed-up (about 75°C).

Firstly, the two tests have been compared together for what concerns the engine performances. The results show acceptable variations among them, if the intrinsic non-repeatability of a road test is taken into account. This allows to compare them also for what concerns fuel consumption, and pollutant and CO_2 emissions.

Then, the engine thermal dynamics measured in both tests has been analyzed. The warm test shows a very fast warm-up phase (few seconds, i.e. few hundred meters). Instead, the cold one shows a longer warm-up time, equal to about 10 minutes, i.e. 7 km. In addition, the results show that the average temperature of the engine block is almost simultaneous with the coolant temperature. Moreover, the temperature measured at the top of the cylinder liner follows the engine load variations almost instantly. Both these results are worthy of attention if a variable-speed cooling pump wants to be implemented to speed-up the engine warm-up phase. In fact, the engine block temperature could be used as a reference value to control the pump speed, which could be actuated only when needed. This would overcome the issues related to the use in such control systems of the coolant temperature measured at the thermostat, which is not representative of the engine temperature when the coolant flow rate is low or negligible.

Subsequently, fuel consumption, and pollutant and CO_2 emissions obtained in the two tests have been compared together. Generally, compared with the cold test, the warm test has a better fuel economy and lower CO and CO_2 emissions, but higher NO_x emissions. This happens eighter considering the first 7 km of road, where the engine warm-up phase occurs, or the overall trip (62.5 km). Moreover, in all cases, the emission limits are fulfilled for what concerns CO and NO_x. Instead, limit overruns have been found for CO_2 emissions, although not critical with respect to the current regulation. Furthermore, the fuel economy declared by the vehicle

manufacturer is met only during the first 7 km, thanks to the low engine loads in that section. Instead, considering the whole trip, both the cold and warm tests show higher fuel consumptions compared with the declared value.

Finally, it is worth remarking that this experimental activity has proven a significant reduction of fuel consumption, CO and CO_2 emissions when reducing the engine warm-up time of a passenger vehicle. This testifies the high potential benefits that advanced engine thermal management strategies could still provide to the automotive sector. Moreover, this study suggests to introduce more advanced after-treatment systems capable to minimize also the NO_x emissions. In this way, only advantages could be introduced by implementing innovative technologies able to accelerate the engine warm-up phase, as a speed-variable cooling pump.

Conclusions

In this thesis, methods to improve the thermal management of Internal Combustion Engines of road vehicles have been studied. In fact, the engine thermal management can contribute significantly to the reduction of fuel consumption an emissions in the road transport sector. Moreover, the engine cooling system still presents much room for improvement, especially regarding the technologies used for the cooling pump. Indeed, this latter is generally a centrifugal pump mechanically actuated by the crankshaft, without any system capable to vary their speeds independently. Furthermore, the cooling pump is typically oversized in order to guarantee the engine cooling even under extreme operating conditions, although they are almost never reached during everyday driving. Both these characteristics lead to a waste of energy and long engine warm-up times, being the pump operated far from its design point and the engine cooled even when not necessary.

Therefore, innovative pumps for engine cooling have been investigated in this work. Specifically, screw-type volumetric pumps have been studied to assess their potential to reduce the energy spent to cool the engine, and thus fuel consumption and CO_2 emissions.

To this end, a comprehensive mathematical model capable to predict the volumetric and mechanical performances of screw pumps has been developed. The model considers a triple-screw pump with a simple layout potentially appealing for the automotive sector, which generally requires reliable and low cost solutions. Specifically, this pump has one driver screw supported by a dedicated bearing, and two idler screws simply entrained inside cylindrical supports. Such layout does not prevent any screws' axes misalignments, and thus their effects on the pump performances had to be considered in the model.

Hence, the proposed mathematical model is composed by a volumetric, an indicated and a mechanical sub-model, and it calculates flow rate and mechanical power as main outputs, by giving as inputs pressure head and pump speed. Specifically, the volumetric sub-model estimates the backflow occurring inside the pump though a Poiseuille-Couette flow modeling, suitably redefined on the specific screws' geometry. Then, the indicated sub-model calculates the indicated power by estimating the power lost due to the filling and emptying processes of suction and discharge plenums, respectively. Finally, the mechanical sub-model estimates the power lost inside the pump due to friction phenomena, depending on the specific contact conditions realized between the idler screws and the pump case. Two progressively more complex approaches have been proposed to model these friction losses. The first one considers a constant friction coefficient between idlers and pump case. Instead, the second approach considers a friction coefficient variable with the pump operating point. The variation law was identified by suitably redefining a Petroff's equation, capable to adapt the friction coefficient to the specific hydro-dynamic conditions realized in the meatus between the idlers and the pump case.

Thus, the mathematical model has been validated experimentally. The flow rate is calculated with an average error equal to 0.6%, whereas the error in the mechanical power depends on the considered friction modeling. With a constant friction coefficient between idlers and pump case, the average error is equal to 13.5%. Instead, by using the redefined Petroff's equation, the error decreases to 6.1%, testifying the reliability of the proposed friction modeling.

Once validated, the model has been used to optimize the design of screw pumps for engine cooling applications. Firstly, the potential benefits in reducing the energy spent to cool the engine have been evaluated theoretically. Specifically, a triple-screw pump suitable for a light-duty application has been designed, and its performances compared with those of the standard centrifugal pump over a homologation cycle. The energy necessary to cool the engine reduced by 13.8%.

This significant result suggested to develop a model-based design approach of screw pumps for engine cooling. Hence, the main criteria optimizing the design point and the pump geometry have been outlined. Specifically, the design point should be chosen to match the maximum flow rate requested by the engine during a homologation cycle, while verifying the capability of the pump to deliver the flow rate requested by the engine operating at maximum power. This allows the pump to operate more frequently near its best efficiency point during everyday driving, thus reducing the energy absorbed to cool the engine.

Moreover, the screw pump efficiency can be maximized by optimizing its geometry. To this end, the performances of a wide set of pumps with different geometric proportions have been evaluated through the model, considering a specific design point defined in terms of flow rate and pressure head. The results show that triple-screw pumps with a geometric proportion between the screws given by the 5-3-1 series allow to reach the best values of efficiencies (up to 70%), compared to those obtained with other commonly used pump series. Furthermore, the efficiency of screw pumps decreases when the design speed increases, and thus the displacement on turn should be increased in order to have low design speeds, according with the space available on-board. Therefore, the design of screw pumps, in engine cooling applications, should be oriented towards a 5-3-1 series and low design speeds to optimize the overall pump efficiency. In addition, the influence of the aspect ratio of the pump on its efficiency has been investigated. It was found that finger-shaped screw pumps (with higher aspect ratios) should be preferred over disk-shaped ones to maximize the pump efficiency. For the considered design point, by increasing the aspect ratio from 1.94 to 3, the efficiency of a 5-3-1 series pump rose from 56.7% to 59.9%.

By putting together all these optimization criteria, the preliminary design of a screw pump for the cooling system of a small gasoline engine has been realized. The output was a 5-3-1 series triple-screw pump, with a displacement equal to 27 cm^3 and an aspect ratio equal to 3, which led to an efficiency at the BEP equal to 60%. Hence, the performances of this pump have been evaluated through the model when operating in a homologation cycle. Compared with the OEM centrifugal pump, the proposed one reduces the energy absorbed to cool the engine by

56.5%, which on turn reduces CO_2 emissions by about 2.08 g_{CO2}/km. It is worth remarking that this strong reduction is due to the combined effect of two main aspects: the optimization of the design point, and the capability of the screw pump to have an efficiency independent on the revolution speed. This makes the screw pump efficiency definitively higher than the centrifugal one, which suffers of low efficiency when operating far from the design point.

In light of these encouraging results, a complete model-based design of a screw pump for the considered engine cooling application has been realized. This pump introduces also other design improvements, mainly aimed at reducing friction, wear and vibration issues, occurring especially at high speeds. In particular, a mechanical support for the idler screws' axis has been designed, which improved significantly the durability of the pump, as well as its efficiency, which is now 61% at the BEP.

For the same engine cooling application and design point, also a centrifugal pump has been optimized through a corresponding model-based design approach. In this case, the efficiency at the BEP reached 47.7%. Then, both pumps have been built, and their performances compared experimentally over a homologation cycle. Even in this case, the results showed significant energy (-21%) and emissions (-0.28 g_{CO2}/km) savings when using the screw pump instead of a centrifugal counterpart optimized for the same application. Consequently, the triple-screw pump prototyped in this work appears to be the most efficient solution for the thermal management of the considered engine.

Subsequently, the mathematical model has been refined to predict more accurately the performances of screw pumps adopting the layout proposed by the prototype. In fact, its experimental characterization showed some discrepancies compared with the first screw pump used to validate the model, which suggested a modeling upgrade. Specifically, the characteristic curves at low pressure heads showed a non-linear trend, which had an impact also on the pump efficiency.

Hence, the volumetric sub-model has been suitably modified to predict also the blow-hole backflows. These were neglected in the previous modeling, because of their low impact on the overall backflow, due to the higher size of the screw pump considered in that case. Instead, in the prototyped pump, the blow-hole backflows are not negligible, especially at low pressure heads. This in mainly due to the smaller size of the prototype, which rises their impact on the volumetric efficiency.

Moreover, the mechanical sub-model has been upgraded to consider the new idler screws' axis support introduced by the prototype. In fact, this support fixes the idlers' axis, changing the reaction forces exchanged between them and the pump case. Moreover the idlers are now forced to rotate around a fixed axis, thus avoiding any direct contact of the screws' teeth with the pump case. Therefore, the friction model previously developed to calculate the power lost due to the screws rotation has been suitably modified, and different friction coefficients identified and experimentally calibrated.

Thus, the so-modified model has been validated experimentally, finding average errors in the flow rate and mechanical power calculations equal to 1.9% and 3.5%, respectively.

Subsequently, this model has been used to calculate the performances of the prototyped pump when operating under extreme conditions, difficult to measure experimentally. Such assessment is useful to explore the efficiency guaranteed by this type of pumps also for other tough cooling applications different from engine cooling.

Specifically, two pump speeds (1000-4000 rpm) and two pressure heads (1-5 bar) have been considered as extreme operating boundaries. Among them, the global efficiency (η_g) and its sub-components, i.e. the volumetric (η_v), indicated (η_i) and mechanical (η_m) efficiencies, have been calculated. Generally, for a given pump speed, an increase of the pressure head determines a decrease of η_v, but an increase of η_i and η_m. Instead, for the same pressure head, an increase of the pump speed determines a decrease of η_i and η_m, but an improvement of η_v.

As a result, the global efficiency (η_g) has a maximum value of about 60%, which is shifted towards higher pressure heads if the pump speed rises. However, in any cases, the efficiency is almost steady around the maximum value for a significant range of operating points, and still higher than 20% also when operating very far from the BEP, i.e. with low pressure heads and high pump speeds, or vice versa. This testifies the good versatility of this type of pumps, not only for engine cooling applications.

The availability of a screw pump prototype suggested to further investigate experimentally also the indicated cycle of this type of pumps. To this end, additional pressure sensors have been installed on the pump case to measure the pressure of the fluid inside the machine. Specifically, two of them have been placed at suction and discharge plenums, respectively, whereas a third at an intermediate position along the screws' axis. This position has been identified by taking into account how the chamber volumes evolve inside the machine as the screws rotate. Hence, an evolution law of the chamber volumes as a function of the screws' rotation angle has been derived theoretically thanks to a 3D geometrical model of the screws. This showed that the pump is able to process more chamber volumes simultaneously, each generated every half screws' revolution. Moreover, each chamber volume takes more than two screws' revolution to complete an entire pumping process, which is composed by a suction, a displacement and a discharge phase. In particular, the pumping process lasts $4\pi+\Delta\theta$, of which the first 2π are for the suction phase from the inlet plenum, the subsequent $\Delta\theta$ are for the displacement phase of the constant volume trapped among the screws, and the last 2π for the discharge phase towards the outlet plenum.

Therefore, the three pressure signals acquired experimentally have been correlated with the chambers' evolution law derived theoretically to reconstruct the indicated cycle of the machine. It was found that this pump ensures a smooth pumping process of each chamber volume, as well as of the entire pump displacement. Specifically, the suction and discharge phases take place with slight under and over pressure conditions relative to the in/out pressures, respectively. Moreover, the displacement phase occurs at an intermediate pressure among those

at suction and discharge plenums, without any pressure peaks. This behavior is due to the pressure losses occurring during the suction and discharge phases, which diminish and increase the fluid pressure at the corresponding plenums, respectively. Moreover, during the displacement phase, the existence of clearances among the screws creates easy way outs for the fluid trapped in the moving chambers in case of undesired volume restrictions, preventing the onset of pressure spikes. Hence, in this phase, the fluid pressure is determined only by the effect of the backflow existing inside the machine.

Furthermore, the indicated cycle was measured for other two operating points to understand their effect on it. One had the same pump speed of the first measurement (1500 rpm) but lower pressure head (0.13 bar against 0.5 bar), and the other had the same pressure head (0.5 bar) but lower pump speed (750 rpm). The results show that suction and discharge pressure losses depend on pump speed, but not on pressure head. Specifically, the higher is the pump speed, the higher are pressure losses. Consequently, their negative impact on the indicated power, i.e. on the indicated efficiency, is higher when the pump operates at low pressure heads and high pump speeds. This dependency of suction and discharge pressure losses (and thus of the indicated cycle) with the pump speed rather than the pressure head had been predicted by the model. However, the model generally underestimates these losses, thus resulting in good agreement with the experimental cycle for operating points with low pump speed and high pressure head.

Finally, the thermal management of a passenger vehicle propelled by a spark ignition engine has been investigated experimentally. The aim was to measure the impact of the engine thermal state on CO_2 and pollutant emissions under real driving conditions, and to identify any strategies to speed-up the engine warm-up phase.

To this end, a Jeep Compass propelled by a FireFly T4 engine has been instrumented with a PEMS system, capable to measure CO_2, CO and NO_x emissions. Moreover, additional sensors have been installed in the engine to completely characterize the thermal dynamics of coolant, oil and engine block. In particular, this latter has been instrumented with four thermocouples, installed in different positions around the combustion chamber to measure the thermal inertia of the main metallic masses of the engine. These sensors have been acquired though a DAQ system installed in the vehicle cabin, which allowed to record also the main engine parameters registered by the engine ECU.

With this so-instrumented vehicle, on-the-road tests have been realized starting with the engine at ambient temperature and at warmed-up conditions. Specifically, two tests on the same road trip of 62.5 km around L'Aquila have been realized in the same day. The first one (named *cold test*) started with the engine initial temperature at 20°C. Instead, the second one (named *warm test*) started with the engine already almost warmed-up (about 75°C).

Firstly, these tests have been compared together for what concerns the engine performances. Acceptable variations among the cold and warm tests have been found, if the intrinsic non-

repeatability of a road test is taken into account. This allowed to compare them also for what concerns the engine thermal dynamics, fuel consumption and pollutant and CO_2 emissions.

Thus, the engine thermal dynamics have been analyzed. Generally, this engine shows fast warm-up times, especially if the specificity of the first road segment is considered (low speeds and downhill conditions). In fact, in the cold test, the engine takes about 10 minutes, i.e. 7 km, to reach the nominal temperature, whereas in the warm one only few seconds, i.e. few hundred meters.

In addition, the temperature profiles acquired during the tests showed relevant features of this engine. Specifically, the average temperature of the engine block is almost simultaneous with that of the coolant, indicating a low thermal inertia of the engine block and of the entire cooling system. Furthermore, the temperature measured at the top of the cylinder liner follows the engine load variations almost instantly. Both these results are extremely relevant if a variable-speed cooling pump wants to be implemented. In fact, the engine block temperature could be used as a reference value to control the pump speed, overcoming the issues related to the use in such control systems of the coolant temperature measured at the thermostat valve, which is not representative of the engine temperature when the coolant flow rate is low or negligible. In this way, the coolant pump could be actuated only when necessary, stopping it (or slowing it down) during the engine warm-up phase.

Finally, fuel consumption and emissions of the cold and warm tests have been compared together. Generally, the warm test has a better fuel economy and lower CO_2 and CO emissions, but higher NO_x emissions. This happens eighter considering the first 7 km of road, where the engine warm-up phase of the cold test occurs, or the overall trip (62.5 km).

Specifically, after the first 7 km, the fuel economy increased by 34.7% in the warm test compared with the cold one. Consequently, CO_2 and CO emissions decreased by 28.2% and 40.6%, respectively, whereas NO_x emissions increased by 133.3%.

Similarly, after the whole trip, in the warm test the fuel economy increased by 3.9%, CO_2 and CO emissions decreased by 5.9% and 30.6%, respectively, but NO_x emissions increased by 21.6%.

These results can be mainly attributed to the different warm-up phases of the two tests, being them comparable in terms of road trip and engine load. In fact, the higher initial temperature of the engine in the warm test reduces friction losses since the beginning, resulting in lower fuel consumption and CO_2 emissions compared with the cold test. Similarly, less CO emissions are produced, because the engine operates almost immediately with higher temperatures in the combustion chamber and with a leaner air-fuel mixture. Instead, these higher temperatures determine higher NO_x emissions just after the engine start-up, creating an offset relative to the cold test which is maintained almost constantly till the end of road trip. However, this is not a matter of concern, if more advanced after-treatment systems capable to control NO_x emissions are installed in the engine. In that case, only benefits could be introduced by a faster engine warm-up phase.

It is worth noting that the limits imposed by the current EU regulation are fulfilled for what concerns CO and NO_x emissions in both the cold and warm tests. Instead, in the whole trip, the CO_2 emissions of this vehicle exceed the limit, but this is not relevant being the target of each manufacturer set on a fleet-based approach.

Finally, the fuel economy declared by the vehicle manufacturer is met only during the first 7 km, thanks to the low engine loads in that section. Instead, considering the whole trip, both tests show higher fuel consumptions compared with the declared value. These results can be attributed to the current method used by manufacturers to define such data, still based on tests executed on a chassis dynamometer, which inevitably introduces discrepancies compared with real driving conditions.

In conclusion, this manuscript offers several contributions to the scientific research in the field of the engine thermal management.

The first one is an unprecedented study on screw-type volumetric pumps when used in the engine cooling system of road vehicles. Their potential benefits in terms of energy saved to cool the engine have been assessed theoretically and experimentally. Moreover, a model-based design approach of such pumps for this type of application has been proposed, and put into practice by building a physical prototype for a specific engine. Furthermore, the indicated cycle of screw pumps has been investigated experimentally, advancing the knowledge on the intrinsic complex fluid-dynamic phenomena occurring inside these machines.

In addition, this thesis provides significant suggestions to develop innovative actuation systems for the cooling pump, in order to further optimize the engine thermal management, especially during the warm-up phase. This has been accomplished thanks to a comprehensive experimental campaign on a passenger vehicle, which allowed to characterize thoroughly the engine thermal dynamics and its impact on CO_2 and pollutant emissions over on-the-road tests.

In light of these promising results, future investigations should be oriented towards the implementation in engine cooling systems of screw-type volumetric pumps, suitably optimized with the proposed model-based design approach. Combined with variable-speed actuation strategies, these pumps could optimize also the engine thermal management in most everyday driving conditions, reducing significantly CO_2 and pollutant emissions.

Appendix A

Considering the frontal view of the screws, ψ is defined as the maximum meshing angle (Eq. A. 1), while ξ is the corresponding angle relative to the idler screw's axis (Eq. A. 2, Figure A. 1).

$$\psi = cos^{-1}\left(\frac{(R_1^2 + (R_1 + R_2 - t)^2 - R_2^2)}{2\,R_1\,(R_1 + R_2 - t)}\right) = \varphi_{MAX} \qquad \text{Eq. A. 1}$$

$$\xi = sin^{-1}\left(\frac{R_1}{R_2}\,sin\,(\psi)\right) \qquad \text{Eq. A. 2}$$

The angles α and β describe the angular extension of the driver and the idler screws' teeth, respectively (Figure A. 1). The specific application adopts a ratio between β and α equal to 2.65, where α is calculated through simple geometrical considerations (Eq. A. 3).

$$\alpha = \frac{\pi - 2\gamma}{1 + {}^{\beta}/_{\alpha}} \qquad \text{Eq. A. 3}$$

The angle γ is called the epicycloid angle and it depends on the meshing angle φ, which is equal to the maximum meshing angle ψ (Eq. A. 4, Figure A. 1).

$$\gamma = sin^{-1}\left(\frac{R_1\,sin\,\varphi}{R_2}\right) - \varphi \qquad \text{Eq. A. 4}$$

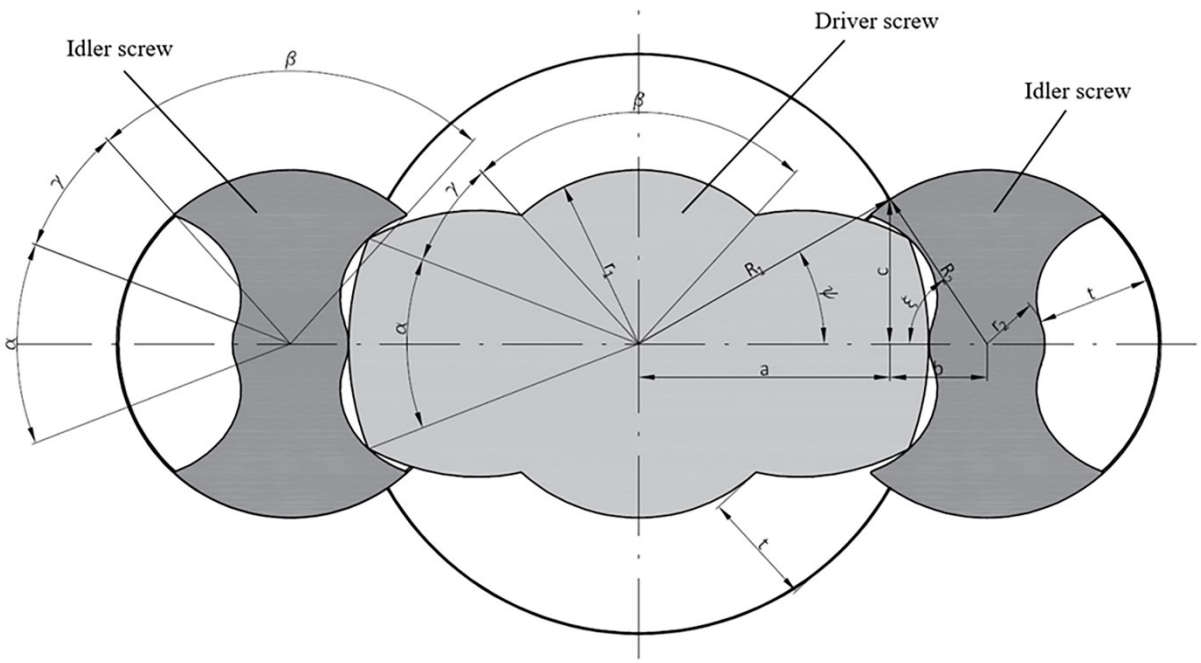

Figure A. 1. Geometrical parametrization of the driver and the idler screws.

The theoretical fluid flow section can be calculated distinguishing between the driver and the idler screws' cross sections, and the case cross section. Thus, the geometrical parameters *a*,

b and c are evaluated through simple trigonometric considerations: $a = R_1\, cos\,(\psi)$, $b = R_2\, cos\,(\xi)$, $c = R_1\, sin\,(\psi)$ (Figure A. 1).

This allows to calculate the cross-sectional area of the case, the driver and the idler screws (from Eq. A. 5 to Eq. A. 10).

$$A_{CASE} = \pi\, R_1^2 + n_{idl}\,(\pi\, R_2^2 - A_{cs}) \quad \text{Eq. A. 5}$$

$$A_{DRIVER} = \alpha R_1^2 + \beta\,(R_1 - t)^2 + 2\gamma\left(R_1 - \frac{t}{2}\right)^2 \quad \text{Eq. A. 6}$$

$$A_{IDLER} = (\alpha + 2\gamma)(R_2 - t)^2 + \beta\, R_2^2 - 4A_\gamma R_2^2 \quad \text{Eq. A. 7}$$

$$A_{cs1} = \frac{2\psi R_1^2}{2} - \frac{2ac}{2} = \psi R_1^2 - ac \quad \text{Eq. A. 8}$$

$$A_{cs2} = \xi\, R_2^2 - bc \quad \text{Eq. A. 9}$$

$$A_{cs} = A_{cs1} + A_{cs2} \quad \text{Eq. A. 10}$$

Note that a slight approximation is adopted in the calculation of the idler screws' cross sectional area (Eq. A. 7). In fact, the subtracted term in this equation depends on A_γ [256]. It is calculated numerically with a trapezoidal Riemann sum for the main series. For the 5-3-1 series, A_γ/R_2^2 is equal to 0.0265, determining a 6% error in the area estimation. This error will have an impact in the theoretical flow rate and, consequently, in the volumetric efficiency calculations. Moreover, the driver and the idler perimeters, as well as the case perimeter, can be calculated as follows (Eq. A. 11, Eq. A. 12, Eq. A. 13):

$$p_{DRIVER} = 2\pi R_1 - 2n_{idl}\psi R_1 \quad \text{Eq. A. 11}$$

$$p_{IDLER} = 2\pi R_2 - 2\xi R_2 \quad \text{Eq. A. 12}$$

$$p = R_1(2\pi - 2n_{IDLER}\psi) + n_{IDLER}R_2(2\pi - 2\xi) \quad \text{Eq. A. 13}$$

The axial length of the screws' tooth Δx can be expressed by simple geometrical relations (Eq. A. 14, Eq. A. 15, Figure A. 2, Figure A. 3):

$$\Delta x_{DRIVER} = \frac{\alpha}{2\pi} L \quad \text{Eq. A. 14}$$

$$\Delta x_{IDLER} = \frac{\beta}{2\pi} L \quad \text{Eq. A. 15}$$

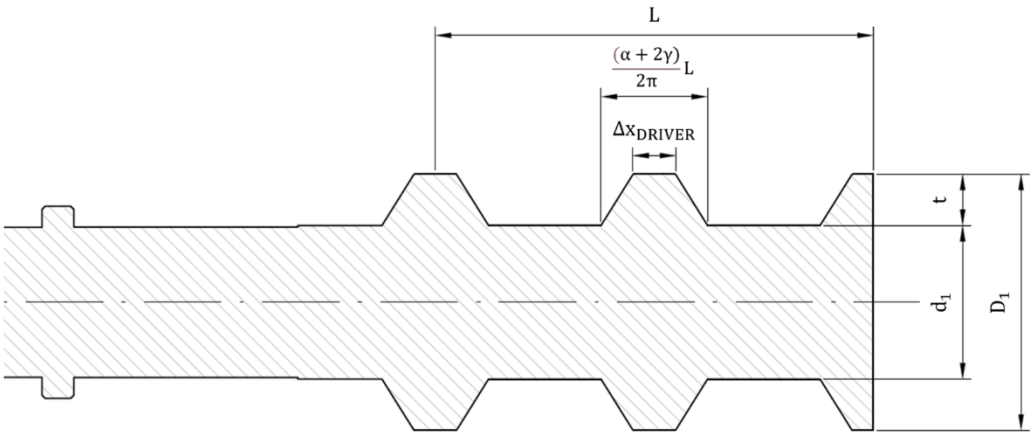

Figure A. 2. Sectional view of the driver screw.

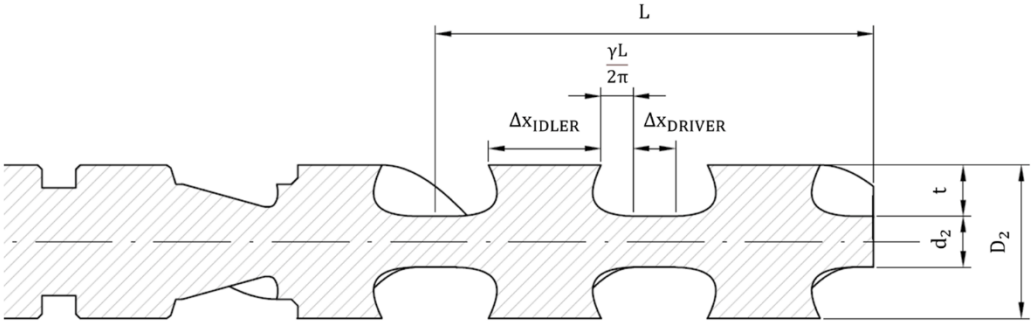

Figure A. 3. Sectional view of the idler screw.

This length Δx can be projected along the direction perpendicular to the screws' flank, obtaining ΔX_{DRIVER} and ΔX_{IDLER} (Eq. A. 16, Eq. A. 17, Figure A. 4).

$$\Delta X_{DRIVER} = \frac{\alpha}{2\pi} L \ sin\,\sigma = \alpha \ R_1 \ cos\,\sigma \qquad \text{Eq. A. 16}$$

$$\Delta X_{IDLER} = \frac{\beta}{2\pi} L \ sin\,\sigma = \beta \ R_2 \ cos\,\sigma \qquad \text{Eq. A. 17}$$

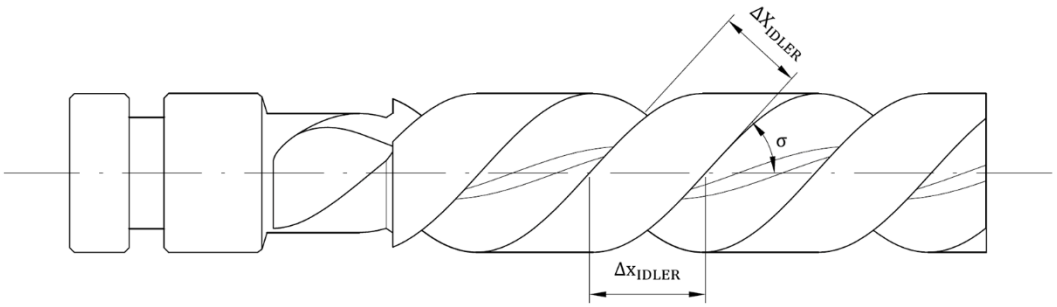

Figure A. 4. Lateral view of the idler screw, with the difference between the axial lengths of the screws' tooth Δx and ΔX.

Appendix B

The idler screw profile observed on a cross section of the pump is formed by a succession of curves. Specifically, an inner and an outer circumference with radius r_2 and R_2, respectively, are linked together through an epitrochoid curve, which constitutes the idler screw's tooth profile (Figure B. 1).

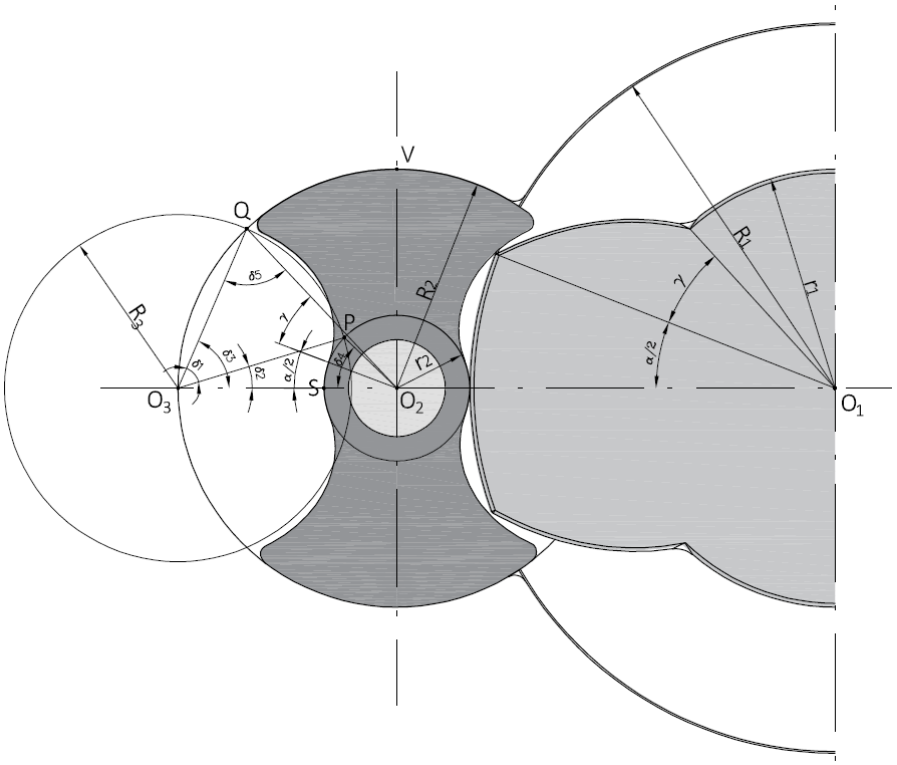

Figure B. 1. Geometrical parametrization of the idler screw to calculate its perimeter.

The perimeter P_{IDLER} of the cross section of the idler screw can be calculated by approximating the epitrochoid curve with a sequence of circular arcs. These can be identified by defining a circumference centered in O_3, i.e. in the interception between the horizontal axis and the pump case (Figure B. 1), and with radius equal to R_3, defined to let the circumference pass through the idler screw's ideal tooth tip Q (Eq. B. 1).

$$R_3 = \sqrt{2\,R_2^2 - 2\,R_2^2\;cos\left(\gamma + \frac{\alpha}{2}\right)} \qquad \text{Eq. B. 1}$$

In this way, the interception point P between this circumference and the idler inner one (centered in O_2 and with radius r_2) can be found analytically. The coordinates of point P are expressed by Eq. B. 2 and Eq. B. 3, obtained considering an x-y orthogonal system centered in O_2.

$$x_P = \frac{R_3^2 - R_2^2 - r_2^2}{2\,R_2} \qquad \text{Eq. B. 2}$$

$$y_P = \sqrt{r_2^2 - \left(\frac{R_3^2 - R_2^2 - r_2^2}{2\,R_2}\right)^2} \quad \text{Eq. B. 3}$$

The point P allows to define three circular arcs $\widehat{QV}$, $\widehat{QP}$ and $\widehat{PS}$ (Figure B. 1), whose sum approximates well the idler screw's perimeter P_{IDLER} (Eq. B. 4).

$$P_{IDLER} = 4\left(\widehat{QV} + \widehat{QP} + \widehat{PS}\right) \quad \text{Eq. B. 4}$$

The circular arcs $\widehat{QV}$, $\widehat{QP}$ and $\widehat{PS}$ are calculated through the equations Eq. B. 5, Eq. B. 6 and Eq. B. 7, respectively.

$$\widehat{QP} = R_3\,\delta_1 \quad \text{Eq. B. 5}$$

$$\widehat{PS} = r_2\,\delta_4 \quad \text{Eq. B. 6}$$

$$\widehat{QV} = R_2\left(\frac{\beta}{2}\right) \quad \text{Eq. B. 7}$$

In these equations, the angles δ_1 and δ_4 can be obtained through simple geometrical considerations, which have been summarized from Eq. B. 8 to Eq. B. 12.

$$\delta_4 = tan^{-1}\left(\frac{y_P}{|x_P|}\right) \quad \text{Eq. B. 8}$$

$$\delta_2 = sin^{-1}\left(\frac{r_2}{R_3} sin\,\delta_4\right) \quad \text{Eq. B. 9}$$

$$\delta_5 = sin^{-1}\left(\frac{R_2}{R_3} sin\left(\gamma + \frac{\alpha}{2}\right)\right) \quad \text{Eq. B. 10}$$

$$\delta_3 = \pi - \delta_5 - \left(\gamma + \frac{\alpha}{2}\right) \quad \text{Eq. B. 11}$$

$$\delta_1 = \delta_3 - \delta_2 \quad \text{Eq. B. 12}$$

Nomenclature

Symbols

D_1	Outer diameter of the driver screw
D_2	Outer diameter of the idler screw
d_1	Inner diameter of the driver screw
d_2	Inner diameter of the idler screw
f	Scale factor
t	Tooth height
α	Angle of outer radius of driver screw tooth
β	Angle of outer radius of idler screw tooth
γ	Epicycloid angle
ψ	Maximum meshing angle of the driver screw
ξ	Maximum meshing angle of the idler screw
σ	Screw angle
n_{STAGE}	Number of stages of the pump
n_{START}	Number of screws starts
L	Screw pitch length
L_{tot}	Overall length of the screws
n_{IDLER}	Number of idler screws
$n_{CHAMBERS}$	Number of sealing chambers
δ_{DRIVER}	Clearance between the driver screw and the pump case
δ_{IDLER}	Clearance between the idler screw and the pump case
δ	Equivalent clearance for the backflow calculation
A_γ	Epicycloid Area
A_{PUMP}	Flow area of the screw pump
A_{CASE}	Cross sectional area of the pump case
A_{DRIVER}	Cross sectional area of the driver screw
A_{IDLER}	Cross sectional area of the idler screw
S_{DRIVER}	Backflow across driver-screw's tooth tips and pump case
S_{IDLER}	Backflow across idler-screws' tooth tips and pump case
$S_{DR/IDL}$	Blow-hole backflow across the contact regions between the screws
S_{TOT}	Overall backflow
$D_{SUCTION}$	Diameter of the suction pipe
$D_{DISCHARGE}$	Diameter of the discharge pipe
N, ω	Rotation speed
Q	Theoretical flow rate
Q_{REAL}	Actual flow rate
Δp_{tot}	Outlet-inlet pressure difference
Δp_{ind}	Discharge-suction pressure difference
τ	Shear stress of the fluid in contact with the screws
A	Action area of the fluid shear stress
P_t	Theoretical power output
P_i	Indicated power
P_h	Hydraulic power output
P_m	Mechanical power
P_{FR}	Friction power losses
$P_{FR\ VISC}$	Viscous power losses
$P_{FR\ SCREW}$	Power losses between the screws
$P_{FR\ DISK}$	Power losses at the disk coupling elements
$P_{FR\ AUX}$	Power losses in the auxiliary elements (sealings and bearings)
η_v	Volumetric efficiency
η_i	Indicated efficiency
η_m	Mechanical efficiency
η_g	Global efficiency
μ	Dynamic viscosity of the fluid
ρ_{FLUID}	Density of the fluid
ρ_{IDLER}	Density of the idler screw material
f_{SCREW}	Friction coefficient between driver and idler screws
f_{STAT}	Friction coefficient between idler screws and pump case
f_{DISK}	Friction coefficient between the disk coupling elements

Acronyms

GHG	Greenhouse gas
ICE	Internal Combustion Engine
PEMS	Portable Emissions Measurement Systems
WLTP	Worldwide Harmonized Light Vehicles Test Procedure
ECU	Engine control unit
EGR	Exhaust Gases Recirculation
VVA	Variable Valve Actuation
VCR	Variable Compression Ratio
OEM	Original Equipment Manufacturer
BEP	Best Efficiency Point

List of figures

List of tables

Bibliography

1. IPCC *Climate Change 2021 The Physical Science Basis Summary for Policymakers Working Group I Contribution to the Sixth Assessment Report of the Intergovernmental Panel on Climate Change*; 2021; ISBN 9789291691586.
2. NOAA. Trends in Atmospheric Carbon Dioxide Global CO2 monitoring. Available online: https://www.esrl.noaa.gov/gmd/ccgg/trends/gl_gr.html (accessed on Apr 29, 2022).
3. Huang, J. Bin; Wang, S.W.; Luo, Y.; Zhao, Z.C.; Wen, X.Y. Debates on the causes of global warming. *Adv. Clim. Chang. Res.* **2012**, *3*, 38–44, doi:10.3724/sp.j.1248.2012.00038.
4. Anderson, T.R.; Hawkins, E.; Jones, P.D. CO2, the greenhouse effect and global warming: from the pioneering work of Arrhenius and Callendar to today's Earth System Models. *Endeavour* **2016**, *40*, 178–187, doi:10.1016/j.endeavour.2016.07.002.
5. NASA. Global Climate Change, Vital signs of the Planet, Carbon Dioxide. Available online: https://climate.nasa.gov/vital-signs/carbon-dioxide/ (accessed on Apr 19, 2022).
6. Lindsey, R. If carbon dioxide hits a new high every year, why isn't every year hotter than the last? Available online: https://www.climate.gov/news-features/climate-qa/if-carbon-dioxide-hits-new-high-every-year-why-isn't-every-year-hotter-last (accessed on Apr 19, 2022).
7. Masson-Delmotte, V.; Portner, H.O.; Roberts, D. *IPCC Global warming of 1.5 C*; 2018; ISBN 9788578110796.
8. Nulman, E. Brief History of Climate Change Policy and Activism. *Clim. Chang. Soc. Movements* **2015**, 8–23, doi:10.1057/9781137468796_2.
9. United Nations. *The paris agreement*; 2015; pp. 1–27;.
10. MCC. MCC aligns Carbon Clock with new IPCC figures. Available online: https://www.mcc-berlin.net/en/news/information/information-detail/article/mcc-aligns-carbon-clock-with-new-ipcc-figures.html (accessed on May 1, 2022).
11. Ritchie, H. Overview of Global Energy. Available online: https://ourworldindata.org/energy-overview#citation (accessed on May 6, 2022).
12. Ritchie, H. CO_2 and Greenhouse Gas Emissions. Available online: https://ourworldindata.org/emissions-by-sector (accessed on May 6, 2022).
13. *EU Transports in Figures*; 2021; ISBN ISBN 978-92-76-40101-8.
14. United States Environmental Protection Agency. Learn About Volkswagen Violations.

Available online: https://www.epa.gov/vw/learn-about-volkswagen-violations (accessed on May 9, 2022).

15. Senecal, K.; Leach, F. *Racing Toward Zero: The Untold Story of Driving Green*; 2021; ISBN 9781468601473.
16. Engeljehringer, K. *AVL Emission Handbook V2.1*; 2022;
17. United Nations Environment Programme *Used Vehicles and the Environment*; 2021;
18. Abdoun, A. Fuel Quality and Emission Standard Developments in Africa. *Strat. Advis.* **2018**.
19. Moskalik, A. Using Transmission Data to Isolate Individual Losses in Coastdown Road Load Coefficients. *SAE Tech. Pap.* **2020**, *2020-April*, doi:10.4271/2020-01-1064.
20. Liu, Z.; Ortmann, W.J.; Nefcy, B.; Colvin, D.; Connolly, F. Methods of Measuring Regenerative Braking Efficiency in a Test Cycle. *SAE Int. J. Altern. Powertrains* **2017**, *6*, 103–112, doi:10.4271/2017-01-1168.
21. *Regulation No83 of the Economic Commission for Europe of the United Nations (UN/ECE) — Uniform provisions concerning the approval of vehicles with regard to the emission of pollutants according to engine fuel requirements*; 2007; Vol. 7;.
22. Weiss, M.; Bonnel, P.; Hummel, R.; Manfredi, U.; Colombo, R.; Lanappe, G.; Le Lijour, P.; Sculati, M. Analyzing on-road Emissions of Light-duty Vehicles with Portable Emission Measurement Systems (PEMS). *Eur. Comm. Jt. Res. Centre, Inst. Energy* **2011**, *JRC 62639*, 54.
23. Marotta, A.; Pavlovic, J.; Ciuffo, B.; Serra, S.; Fontaras, G. Gaseous Emissions from Light-Duty Vehicles: Moving from NEDC to the New WLTP Test Procedure. *Environ. Sci. Technol.* **2015**, *49*, 8315–8322, doi:10.1021/acs.est.5b01364.
24. Tsiakmakis, S.; Fontaras, G.; Cubito, C.; Pavlovic, J.; Anagnostopoulos, K.; Ciuffo, B. *From NEDC to WLTP: effect on the type-approval CO2 emissions of light-duty vehicles*; 2017; ISBN 9789279716423.
25. United Nation *GTR 15 - Global technical regulation on Worldwide harmonized Light vehicles Test Procedure*; 2014; p. 234;.
26. Peter MockI; Uwe Tietge; Vicente Franco; John German; Anup Bandivadekar; Norbert Ligterink; Udo Lambrecht; Jörg Kühlwein; Iddo Riemersma *From laboratory to road: A 2014 update | International Council on Clean Transportation*; 2014;
27. Emission Test Cycles - Worldwide Harmonized Light Vehicles Test Cycle (WLTC) Available online: https://www.dieselnet.com/standards/cycles/wltp.php (accessed on May 25, 2022).

28. Pavlovic, J.; Ciuffo, B.; Fontaras, G.; Valverde, V.; Marotta, A. How much difference in type-approval CO2 emissions from passenger cars in Europe can be expected from changing to the new test procedure (NEDC vs. WLTP)? *Transp. Res. Part A Policy Pract.* **2018**, *111*, 136–147, doi:10.1016/j.tra.2018.02.002.
29. US EPA Dynamometer Drive Schedules Available online: https://www.epa.gov/vehicle-and-fuel-emissions-testing/dynamometer-drive-schedules#FTP (accessed on Aug 4, 2022).
30. European Commission *Commission Regulation (EU) 2016/427*; 2016;
31. European Commission *Commission Regulation (EU) 2016/646*; 2016;
32. European Commission *Commission Regulation (EU) 2017/1151*; 2017;
33. European Commission *Commission Regulation (EU) 2017/1154*; 2017;
34. European Commission *Commission Regulation (EU) 2018/1832*; 2019;
35. UNECE UNECE endorses stringent new vehicle emissions regulation Available online: https://unece.org/transport/press/unece-endorses-stringent-new-vehicle-emissions-regulation (accessed on Aug 4, 2022).
36. The International Council on Clean Transportation *Real-Driving Emissions Test Procedure for Exhaust Gas Pollutant Emissions of Cars and Light Commercial Vehicles in Europe*; 2017;
37. Andrych-Zalewska, M.; Chlopek, Z.; Merkisz, J.; Pielecha, J. Research on exhaust emissions in dynamic operating states of a combustion engine in a real driving emissions test. *Energies* **2021**, *14*, doi:10.3390/en14185684.
38. Schoggl, M. Mastering the global Real Driving Emission challenge - AVL M.O.V.E iS+ 2020, 44.
39. DieselNet EU Cars and Light Trucks: RDE Testing Available online: https://dieselnet.com/standards/eu/ld_rde.php (accessed on Aug 4, 2022).
40. ACEA European Automobile Manufacturers' Association Average age of the EU vehicle fleet, by country Available online: https://www.acea.auto/figure/average-age-of-eu-vehicle-fleet-by-country/ (accessed on Aug 5, 2022).
41. Suarez-Bertoa, R.; Valverde, V.; Clairotte, M.; Pavlovic, J.; Giechaskiel, B.; Franco, V.; Kregar, Z.; Astorga, C. On-road emissions of passenger cars beyond the boundary conditions of the real-driving emissions test. *Environ. Res.* **2019**, *176*, 108572, doi:10.1016/j.envres.2019.108572.
42. Joshi, A. Review of Vehicle Engine Efficiency and Emissions. *SAE Tech. Pap.* **2020**, *2*, 2479–2507, doi:10.4271/2022-01-0540.

43. Valverde Morales, V.; Clairotte, M.; Pavlovic, J.; Giechaskiel, B.; Bonnel, P. On-Road Emissions of Euro 6d-TEMP Vehicles: Consequences of the Entry into Force of the RDE Regulation in Europe. *SAE Tech. Pap.* **2020**, 1–12, doi:10.4271/2020-01-2219.
44. Demuynck, J.; Favre, C.; Bosteels, D.; Bunar, F.; Spitta, J.; Kuhrt, A. Diesel Vehicle with Ultra-Low NOx Emissions on the Road. *SAE Tech. Pap.* **2019**, *2019-Septe*, doi:10.4271/2019-24-0145.
45. Leach, F.; Kalghatgi, G.; Stone, R.; Miles, P. The scope for improving the efficiency and environmental impact of internal combustion engines. *Transp. Eng.* **2020**, *1*, doi:10.1016/j.treng.2020.100005.
46. Demuynck, J.; Kufferath, A.; Kastner, O.; Brauer, M.; Fiebig, M. Improving Air Quality and Climate through Modern Diesel Vehicles. *MTZ Worldw.* **2020**, *81*, 52–59, doi:10.1007/s38313-020-0266-y.
47. Pavlovic, J.; Marotta, A.; Ciuffo, B. CO2 emissions and energy demands of vehicles tested under the NEDC and the new WLTP type approval test procedures. *Appl. Energy* **2016**, *177*, 661–670, doi:10.1016/j.apenergy.2016.05.110.
48. Lee, H.; Lee, K. Comparative evaluation of the effect of vehicle parameters on fuel consumption under NEDC and WLTP. *Energies* **2020**, *13*, doi:10.3390/en13164245.
49. Woo, J.R.; Choi, H.; Ahn, J. Well-to-wheel analysis of greenhouse gas emissions for electric vehicles based on electricity generation mix: A global perspective. *Transp. Res. Part D Transp. Environ.* **2017**, *51*, 340–350, doi:10.1016/j.trd.2017.01.005.
50. Leach, F.; Lewis, A.; Akehurst, S.; Turner, J.; Richardson, D. Sub-23 nm Particulate Emissions from a Highly Boosted GDI Engine. *SAE Tech. Pap.* **2019**, *2019-Septe*, doi:10.4271/2019-24-0153.
51. Yang, Z.; Bandivadekar, A. *2017 Global update: Light-duty vehicle greenhouse gas and fuel economy standards*; 2017;
52. European Union. *Regulation (EU) 2019/631 of the European Parliament and of the Council*; 2019; pp. 1–50;.
53. European Parliament *REGULATION (EC) No 443/2009 OF THE EUROPEAN PARLIAMENT AND OF THE COUNCIL*; 2009; Vol. 140, pp. 1–15;.
54. European Union *REGULATION (EU) No 510/2011 OF THE EUROPEAN PARLIAMENT AND OF THE COUNCIL*; 2011; Vol. 2011, p. 18;.
55. ICCT Market Monitor. European Passenger Car and Light Commercial Vehicle Registrations : January – December 2021. 2022.
56. Tietge, U.; Mock, P.; Dornoff, J. Overview and evaluation of eco-innovations in

European passenger car CO2 standards. *ICCT* **2018**.

57. Wappelhorst, S.; Tietge, U.; Bieker, G.; Mock, P. *Europe's CO2 emission performance standards for new passenger cars: Lessons from 2020 and future prospects*; ICCT; 2021;
58. ICCT US Passenger Vehicle CAFE and GHG Regulations: the basics Available online: https://theicct.org/stack/us-passenger-vehicle-cafe-and-ghg-regulations-the-basics/ (accessed on Aug 16, 2022).
59. Bui, A.; Yang, Z. U.S. light-duty vehicle greenhouse gas standards for model years 2023–2026 and corporate average fuel economy standards for model years 2024–2026. *ICCT Policy Updat.* **2022**.
60. Hula, A.; Maguire, A.; Bunker, A.; Rojeck, T.; Harrison, S.; Agency, E.P. *The 2021 EPA Automotive Trends Report: Greenhouse Gas Emissions, Fuel Economy, and Technology since 1975*; 2021;
61. EPA - NHTSA *Light-Duty Vehicle Greenhouse Gas Emission Standards and Corporate Average Fuel Economy Standards; Final Rule*; 2010; pp. 25324–25728;.
62. United States Environmental Protection Agency (EPA). EPA Federal Test Procedure (FTP). Available online: https://www.epa.gov/emission-standards-reference-guide/epa-federal-test-procedure-ftp (accessed on May 9, 2022).
63. Hill, N. Determining the environmental impacts of conventional and alternatively fuelled vehicles through LCA. *Ricardo* **2020**, 1–456.
64. Transport & Environment How clean are electric cars? **2020**, 1–33.
65. Both, D.; Steinfort, T. Cradle-to-Grave Life-Cycle Assessment in the Mobility Sector. *FVV* **2020**.
66. IEA Global EV Outlook 2022. Securing supplies for an electric future. **2022**, 221.
67. Olabi, A.G.; Ali, M.; Wilberforce, T.; Alkhalidi, A.; Salameh, T.; Abo-khalil, A.G.; Mutasim, M.; Taha, E. Battery electric vehicles: Progress, power electronic converters, strength (S), weakness (W), opportunity (O), and threats (T). *Int. J. Thermofluids* **2022**, *16*, 100212, doi:10.1016/j.ijft.2022.100212.
68. İnci, M.; Büyük, M.; Demir, M.H.; İlbey, G. A review and research on fuel cell electric vehicles: Topologies, power electronic converters, energy management methods, technical challenges, marketing and future aspects. *Renew. Sustain. Energy Rev.* **2021**, *137*, doi:10.1016/j.rser.2020.110648.
69. Verhelst, S. Recent progress in the use of hydrogen as a fuel for internal combustion engines. *Int. J. Hydrogen Energy* **2014**, *39*, 1071–1085, doi:10.1016/j.ijhydene.2013.10.102.

70. Kalghatgi, G. Is it really the end of internal combustion engines and petroleum in transport? *Appl. Energy* **2018**, *225*, 965–974, doi:10.1016/j.apenergy.2018.05.076.
71. Hombach, L.E.; Doré, L.; Heidgen, K.; Maas, H.; Wallington, T.J.; Walther, G. Economic and environmental assessment of current (2015) and future (2030) use of E-fuels in light-duty vehicles in Germany. *J. Clean. Prod.* **2019**, *207*, 153–162, doi:10.1016/j.jclepro.2018.09.261.
72. Internal Combustion Engine - The road ahead Available online: https://www.industr.com/en/internal-combustion-engine-the-road-ahead-2357709 (accessed on Sep 21, 2022).
73. ICCT Vision 2050: A strategy to decarbonize the global transport sector by mid-century. **2020**.
74. Reitz, R.D.; Ogawa, H.; Payri, R.; Fansler, T.; Kokjohn, S.; Moriyoshi, Y.; Agarwal, A.K.; Arcoumanis, D.; Assanis, D.; Bae, C.; et al. IJER editorial: The future of the internal combustion engine. *Int. J. Engine Res.* **2020**, *21*, 3–10, doi:10.1177/1468087419877990.
75. OPEC *World Oil Outlook 2045*; 15th editi.; 2021; ISBN 9783950489026.
76. Duleep, K.G. Internal Combustion Engine Vehicles. In *Encyclopedia of Energy*; 2004; Vol. 3, pp. 497–513.
77. Petruzzelli, A.M. A story of breakthrough. The case of common rail development. *Int. J. Innov. Manag.* **2015**, *19*, 1–35, doi:10.1142/S1363919615500346.
78. Where the Energy Goes: Gasoline Vehicles Available online: http://www.fueleconomy.gov/feg/atv.shtml (accessed on Sep 23, 2022).
79. Lutsey, N.; Meszler, D.; Isenstadt, A.; German, J.; Miller, J. Efficiency Technology and Cost Assessment for U.S. 2025-2030 Light-Duty Vehicles. *ICCT* **2017**.
80. Ahmad, H.; Markina, A.A.; Porotnikov, M. V.; Ahmad, F. A review of carbon fiber materials in automotive industry. *IOP Conf. Ser. Mater. Sci. Eng.* **2020**, *971*, doi:10.1088/1757-899X/971/3/032011.
81. Ligterink, N.; van Mensch, P.; Cuelenaere, R. Correction algorithms for WLTP chassis dynamometer and coast-down testing. *TNO Rep.* **2014**, 66.
82. Hamada, A.T.; Orhan, M.F. An overview of regenerative braking systems. *J. Energy Storage* **2022**, *52*, 105033, doi:10.1016/j.est.2022.105033.
83. le Good, G.; Johnson, C.; Clough, B.; Lewis, R. The Aesthetics of Low Drag Vehicles. *SAE Int. J. Engines* **2011**, *4*, 2638–2658, doi:10.4271/2011-37-0016.
84. Kühlwein, J. Driving Resistances of Light-Duty Vehicles in Europe: Present Situation,

Trends and Scenarios for 2025. *ICCT* **2016**, 1–46.

85. Edmunds, D. Do Stop-Start Systems Really Save Fuel? Available online: https://www.edmunds.com/car-reviews/features/do-stop-start-systems-really-save-fuel.html.
86. Dornoff, J.; German, J.; Ashok, D.; Athanasios, D. Mild-Hybrid Vehicles: a near term technology trend for CO2 emissions reduction. *ICCT* **2022**, 47.
87. German, J. Hybrid vehicles: Technology development and cost reduction. *ICCT* **2015**, 1–18.
88. McGuckin, N.; Fucci, A. *Summary of Travel Trends: 2017 National Household Travel Survey*; 2018;
89. Plötz, P.; Link, S.; Ringelschwendner, H.; Keller, M.; Moll, C.; Bieker, G.; Dornoff, J.; Mock, P. Real-World Usage of Plug-in Hybrid Vehicles in Europe. A 2022 Update on Fuel Consumption, Electric Driving, and CO2 Emissions. *ICCT* **2022**.
90. US Department of Energy. Plug-in Hybrids. Available online: https://www.fueleconomy.gov/feg/phevtech.shtml#:~:text=Plug-in hybrids use roughly,greenhouse gas than conventional vehicles. (accessed on Sep 28, 2022).
91. Islam, E.; Moawad, A.; Kim, N.; Rousseau, A. An Extensive Study on Sizing, Energy Consumption, and Cost of Advanced Vehicle Technologies. *Argonne Natl. Lab.* **2018**, 100, doi:https://doi.org/10.2172/1463258.
92. Mock, P.; Díaz, S. Pathways to decarbonization: the European passenger car market in the years 2021-2035. *ICCT* **2021**.
93. Szybist, J.P.; Busch, S.; McCormick, R.L.; Pihl, J.A.; Splitter, D.A.; Ratcliff, M.A.; Kolodziej, C.P.; Storey, J.M.E.; Moses-DeBusk, M.; Vuilleumier, D.; et al. What fuel properties enable higher thermal efficiency in spark-ignited engines? *Prog. Energy Combust. Sci.* **2021**, *82*, doi:10.1016/j.pecs.2020.100876.
94. Schenk, C.; Butters, K. 2014 Mazda 2.0L SKYACTIV-G Engine Tier 2 Fuel - Test Data Package. Version 2018-02. *U.S. Environ. Prot. Agency Natl. Veh. Fuel Emiss. Lab.* **2018**, 2–5.
95. Matsuo, S.; Ikeda, E.; Ito, Y.; Nishiura, H. The New Toyota Inline 4 Cylinder 1.8L ESTEC 2ZR-FXE Gasoline Engine for Hybrid Car. *SAE Tech. Pap.* **2016**, *2016-April*, doi:10.4271/2016-01-0684.
96. Hakariya, M.; Toda, T.; Sakai, M. The New Toyota Inline 4-Cylinder 2.5L Gasoline Engine. *SAE Tech. Pap.* **2017**, *2017-March*, doi:10.4271/2017-01-1021.
97. Ralf, B.; Rainer, W.; Günther, M.; Thomas, H. The New Audi 2.0-l I4 TFSI Engine.

Innov. ENGINES 16–23.

98. Iyer, C.O.; Yi, J. Spray pattern optimization for the Duratec 3.5L EcoBoost engine. *SAE Tech. Pap.* **2009**, *2*, doi:10.4271/2009-01-1916.
99. Richards, P. *Automotive Fuels Reference Book*; Third Edit.; SAE International, 2014; ISBN 978-0-7680-0638-4.
100. Dale, J.D.; Checkel, M.D.; Smy, P.R. Application of high energy ignition systems to engines. *Prog. Energy Combust. Sci.* **1997**, *23*, 379–398, doi:10.1016/s0360-1285(97)00011-7.
101. Carney, D. Mazda Has Improved the Gasoline Engine to a Level That Even Tesla Should Respect. *IEEE Spectr.* **2018**, 20–25, doi:https://doi. org/10.1109/MSPEC.2018.8423579.
102. Sellnau, M.; Hoyer, K.; Moore, W.; Foster, M.; Sinnamon, J.; Klemm, W. Advancement of GDCI Engine Technology for US 2025 CAFE and Tier 3 Emissions. *SAE Tech. Pap.* **2018**, *2018-April*, 1–16, doi:10.4271/2018-01-0901.
103. Hanson, R.; Salvi, A.; Redon, F.; Regner, G. Experimental Comparison of Gasoline Compression Ignition and Diesel Combustion in a Medium-Duty Opposed-Piston Engine. *ICEF2018, ASME* **2018**, *141*, 1–8, doi:10.1115/1.4043825.
104. Dahham, R.Y.; Wei, H.; Pan, J. Improving Thermal Efficiency of Internal Combustion Engines: Recent Progress and Remaining Challenges. *Energies* **2022**, *15*, 6222, doi:10.3390/en15176222.
105. Splitter, D.; Reitz, R.; Hanson, R. High efficiency, low emissions RCCI combustion by use of a fuel additive. *SAE Tech. Pap.* **2010**, *3*, 742–756, doi:10.4271/2010-01-2167.
106. Curran, S.; Prikhodko, V.; Cho, K.; Sluder, C.; Parks, J.; Wagner, R.; Kokjohn, S.; Reitz, R. In-cylinder fuel blending of gasoline/diesel for improved efficiency and lowest possible emissions on a multi-cylinder light-duty diesel engine. *SAE Tech. Pap.* **2010**, doi:10.4271/2010-01-2206.
107. Zhu, S.; Hu, B.; Akehurst, S.; Copeland, C.; Lewis, A.; Yuan, H.; Kennedy, I.; Bernards, J.; Branney, C. A review of water injection applied on the internal combustion engine. *Energy Convers. Manag.* **2019**, *184*, 139–158, doi:10.1016/j.enconman.2019.01.042.
108. Wan, J.; Zhuang, Y.; Huang, Y.; Qian, Y.; Qian, L. A review of water injection application on spark-ignition engines. *Fuel Process. Technol.* **2021**, *221*, 106956, doi:10.1016/j.fuproc.2021.106956.
109. Alvarez, C.E.C.; Couto, G.E.; Roso, V.R.; Thiriet, A.B.; Valle, R.M. A review of prechamber ignition systems as lean combustion technology for SI engines. *Appl. Therm. Eng.* **2018**, *128*, 107–120, doi:10.1016/j.applthermaleng.2017.08.118.

110. Sens, M.; Binder, E. Pre-Chamber Ignition as a Key Technology for Future Powertrain Fleets. *MTZ Worldw.* **2019**, *80*, 44–51, doi:10.1007/s38313-018-0150-1.
111. Duan, W.; Huang, Z.; Chen, H.; Tang, P.; Wang, L.; Chen, W. Effects of passive pre-chamber jet ignition on combustion and emission at gasoline engine. *Adv. Mech. Eng.* **2021**, *13*, 1–10, doi:10.1177/16878140211067148.
112. Covini, G. Maserati Nettuno: il V6 che nobilita la MC20. *Auto Tec.* **2020**, 1–7.
113. Kasseris, E.; Heywood, J.B.; Seitz, S.; Kolakaluri, R. Real World Performance of an Onboard Gasoline/Ethanol Separation System to Enable Knock Suppression Using an Octane-On-Demand Fuel System. *SAE Tech. Pap.* **2018**, *2018-April*, 1–14, doi:10.4271/2018-01-0879.
114. Putrasari, Y.; Lim, O. A review of gasoline compression ignition: A promising technology potentially fueled with mixtures of gasoline and biodiesel to meet future engine efficiency and emission targets. *Energies* **2019**, *12*, 1–27, doi:10.3390/en12020238.
115. Alger, T.; Mangold, B. Dedicated EGR: A new concept in high efficiency engines. *SAE Tech. Pap.* **2009**, *2*, 620–631, doi:10.4271/2009-01-0694.
116. Shelby, M.H.; Leone, T.G.; Byrd, K.D.; Wong, F.K. Fuel Economy Potential of Variable Compression Ratio for Light Duty Vehicles. *SAE Int. J. Engines* **2017**, *10*, 817–831, doi:10.4271/2017-01-0639.
117. Stuhldreher, M. Fuel Efficiency Mapping of a 2014 6-Cylinder GM EcoTec 4.3L Engine with Cylinder Deactivation. *SAE Tech. Pap.* **2016**, doi:10.4271/2016-01-0662.
118. Wilcutts, M.; Switkes, J.; Shost, M.; Tripathi, A. Design and benefits of dynamic skip fire strategies for cylinder deactivated engines. *SAE Int. J. Engines* **2013**, *6*, 278–288, doi:10.4271/2013-01-0359.
119. Abani, N.; Nagar, N.; Zermeno, R.; Chiang, M.; Thomas, I. Developing a 55% BTE Commercial Heavy-Duty Opposed-Piston Engine without a Waste Heat Recovery System. *SAE Tech. Pap.* **2017**, *2017-March*, doi:10.4271/2017-01-0638.
120. Kojima, S.; Kiga, S.; Moteki, K.; Takahashi, E.; Matsuoka, K. Development of a New 2L Gasoline VC-Turbo Engine with the World's First Variable Compression Ratio Technology. *SAE Tech. Pap.* **2018**, *2018-April*, 1–10, doi:10.4271/2018-01-0371.
121. Hoang, A.T. Waste heat recovery from diesel engines based on Organic Rankine Cycle. *Appl. Energy* **2018**, *231*, 138–166, doi:10.1016/j.apenergy.2018.09.022.
122. Heywood, J.B. *Internal combustion engine fundamentals*; Second edi.; McGraw-Hill Education, 2018; ISBN 007028637X.

123. Aghaali, H.; Ångström, H.E. A review of turbocompounding as a waste heat recovery system for internal combustion engines. *Renew. Sustain. Energy Rev.* **2015**, *49*, 813–824, doi:10.1016/j.rser.2015.04.144.
124. Millo, F.; Mallamo, F.; Pautasso, E.; Ganio Mego, G. The potential of electric Exhaust Gas Turbocharging for HD diesel engines. *SAE Tech. Pap.* **2006**, doi:10.4271/2006-01-0437.
125. Thompson, I.G.M.; Spence, S.W.; Thornhill, D.; McCartan, C.D.; Talbot-Weiss, J.M.H. The technical merits of turbogenerating shown through the design, validation and implementation of a one-dimensional engine model. *Int. J. Engine Res.* **2014**, *15*, 66–77, doi:10.1177/1468087412458383.
126. Burnete, N.V.; Mariasiu, F.; Depcik, C.; Barabas, I.; Moldovanu, D. Review of thermoelectric generation for internal combustion engine waste heat recovery. *Prog. Energy Combust. Sci.* **2022**, *91*, 101009, doi:10.1016/j.pecs.2022.101009.
127. Hewawasam, L.S.; Jayasena, A.S.; Afnan, M.M.M.; Ranasinghe, R.A.C.P.; Wijewardane, M.A. Waste heat recovery from thermo-electric generators (TEGs). *Energy Reports* **2020**, *6*, 474–479, doi:10.1016/j.egyr.2019.11.105.
128. Jaziri, N.; Boughamoura, A.; Müller, J.; Mezghani, B.; Tounsi, F.; Ismail, M. A comprehensive review of Thermoelectric Generators: Technologies and common applications. *Energy Reports* **2020**, *6*, 264–287, doi:10.1016/j.egyr.2019.12.011.
129. Di Battista, D.; Carapellucci, R.; Cipollone, R. Integrated evaluation of Inverted Brayton cycle recovery unit bottomed to a turbocharged diesel engine. *Appl. Therm. Eng.* **2020**, *175*, 115353, doi:10.1016/j.applthermaleng.2020.115353.
130. Di Battista, D.; Fatigati, F.; Carapellucci, R.; Cipollone, R. Inverted Brayton Cycle for waste heat recovery in reciprocating internal combustion engines. *Appl. Energy* **2019**, *253*, 113565, doi:10.1016/j.apenergy.2019.113565.
131. Imran, M.; Haglind, F.; Asim, M.; Zeb Alvi, J. Recent research trends in organic Rankine cycle technology: A bibliometric approach. *Renew. Sustain. Energy Rev.* **2018**, *81*, 552–562, doi:10.1016/j.rser.2017.08.028.
132. Bianchi, M.; De Pascale, A. Bottoming cycles for electric energy generation: Parametric investigation of available and innovative solutions for the exploitation of low and medium temperature heat sources. *Appl. Energy* **2011**, *88*, 1500–1509, doi:10.1016/j.apenergy.2010.11.013.
133. Shi, L.; Shu, G.; Tian, H.; Deng, S. A review of modified Organic Rankine cycles (ORCs) for internal combustion engine waste heat recovery (ICE-WHR). *Renew.*

Sustain. Energy Rev. **2018**, *92*, 95–110, doi:10.1016/j.rser.2018.04.023.

134. Fatigati, F.; Di Battista, D.; Di Bartolomeo, M.; Di Giovine, G.; Mariani, L. Steady and transient operations of small-scale ORC-based power unit for low-grade thermal sources. In Proceedings of the 6th International Seminar on ORC Power Systems; Munich, Germany, 2021; pp. 1–10.
135. Fatigati, F.; Di Giovine, G.; Cipollone, R. Feasibility Assessment of a Dual Intake-Port Scroll Expander Operating in an ORC-Based Power Unit. *Energies* **2022**, *15*, doi:10.3390/en15030770.
136. Di Battista, D.; Di Bartolomeo, M.; Villante, C.; Cipollone, R. On the limiting factors of the waste heat recovery via ORC-based power units for on-the-road transportation sector. *Energy Convers. Manag.* **2018**, *155*, 68–77, doi:10.1016/j.enconman.2017.10.091.
137. Chatzopoulou, M.A.; Simpson, M.; Sapin, P.; Markides, C.N. Off-design optimisation of organic Rankine cycle (ORC) engines with piston expanders for medium-scale combined heat and power applications. *Appl. Energy* **2019**, *238*, 1211–1236, doi:10.1016/j.apenergy.2018.12.086.
138. Marchionni, M.; Bianchi, G.; Karvountzis-Kontakiotis, A.; Pesyridis, A.; Tassou, S.A. An appraisal of proportional integral control strategies for small scale waste heat to power conversion units based on Organic Rankine Cycles. *Energy* **2018**, *163*, 1062–1076, doi:10.1016/j.energy.2018.08.156.
139. Chatzopoulou, M.A.; Lecompte, S.; Paepe, M. De; Markides, C.N. Off-design optimisation of organic Rankine cycle (ORC) engines with different heat exchangers and volumetric expanders in waste heat recovery applications. *Appl. Energy* **2019**, *253*, 113442, doi:10.1016/j.apenergy.2019.113442.
140. Fatigati, F.; Di Giovine, G.; Cipollone, R. Model-based characterization of a dual intake-port scroll expander operating in an ORC-based power unit. In Proceedings of the 16th Conference on Sustainable Development of Energy, Water and Environment Systems; Dubrovnik, Croatia, 2021; pp. 1–21.
141. Fatigati, F.; Di Bartolomeo, M.; Cipollone, R. Dual intake rotary vane expander technology: Experimental and theoretical assessment. *Energy Convers. Manag.* **2019**, *186*, 156–167, doi:10.1016/j.enconman.2019.02.026.
142. Fatigati, F.; Di Bartolomeo, M.; Di Battista, D.; Cipollone, R. A dual-intake-port technology as a design option for a Sliding Vane Rotary Expander of small-scale ORC-based power units. *Energy Convers. Manag.* **2020**, *209*, 112646, doi:10.1016/j.enconman.2020.112646.

143. Dietsche, K.-H.; Reif, K. *Automotive Handbook*; 11th Editi.; Bosch, 2022; ISBN 9781119911906.
144. Burke, R.D.; Brace, C.J.; Hawley, J.G.; Pegg, I. Review of the systems analysis of interactions between the thermal, lubricant, and combustion processes of diesel engines. *Proc. Inst. Mech. Eng. Part D J. Automob. Eng.* **2010**, *224*, 681–704, doi:10.1243/09544070JAUTO1301.
145. Brace, C.J.; Burnham-Slipper, H.; Wijetunge, R.S.; Vaughan, N.D.; Wright, K.; Blight, D. Integrated cooling systems for passenger vehicles. *SAE Tech. Pap.* **2001**, doi:10.4271/2001-01-1248.
146. Pang, H.H.; Brace, C.J. Review of engine cooling technologies for modern engines. *Proc. Inst. Mech. Eng. Part D J. Automob. Eng.* **2004**, *218*, 1209–1215, doi:10.1243/0954407042580110.
147. Wang, Z.; Liu, H.; Reitz, R.D. Knocking combustion in spark-ignition engines. *Prog. Energy Combust. Sci.* **2017**, *61*, 78–112, doi:10.1016/j.pecs.2017.03.004.
148. Abu-Nada, E.; Al-Hinti, I.; Al-Sarkhi, A.; Akash, B. Effect of piston friction on the performance of SI engine: A new thermodynamic approach. *J. Eng. Gas Turbines Power* **2008**, *130*, doi:10.1115/1.2795777.
149. Tung, S.C.; McMillan, M.L. Automotive tribology overview of current advances and challenges for the future. *Tribol. Int.* **2004**, *37*, 517–536, doi:10.1016/j.triboint.2004.01.013.
150. Taylor, R.I. Engine friction: The influence of lubricant rheology. *Proc. Inst. Mech. Eng. Part J J. Eng. Tribol.* **1997**, *211*, 235–246, doi:10.1177/135065019721100306.
151. Shayler, P.J.; Allen, A.J.; Leong, D.K.W.; Pegg, I.; Brown, A.J.; Dumenil, J.-C. Characterising Lubricating Oil Viscosity to Describe Effects on Engine Friction. *SAE Int.* **2007**, doi:https://doi.org/10.4271/2007-01-1984.
152. Gao, J.; Tian, G.; Sorniotti, A.; Karci, A.E.; Di Palo, R. Review of thermal management of catalytic converters to decrease engine emissions during cold start and warm up. *Appl. Therm. Eng.* **2019**, *147*, 177–187, doi:10.1016/j.applthermaleng.2018.10.037.
153. Gong, C.; Huang, K.; Deng, B.; Liu, X. Catalyst light-off behavior of a spark-ignition LPG (liquefied petroleum gas) engine during cold start. *Energy* **2011**, *36*, 53–59, doi:10.1016/j.energy.2010.11.026.
154. El-Sharkawy, A.; Arora, D.; Huxford, M.W. Optimization of catalytic converter design to improve Under-Hood thermal management. *SAE Tech. Pap.* **2019**, *2019-April*, 1325–1332, doi:10.4271/2019-01-1263.

155. Clough, M.J. Precision cooling of a four valve per cylinder engine. *SAE Tech. Pap.* **1993**, doi:10.4271/931123.
156. Kobayashi, H.; Yoshimura, K.; Hirayama, T. A study on dual circuit cooling for higher compression ratio. *SAE Tech. Pap.* **1984**, doi:10.4271/841294.
157. Finlay, I.C.; Tugwell, W.; Biddulph, T.W.; Marshall, R.A. The influence of coolant temperature on the performance of a four cylinder 1100 cc engine employing a dual circuit cooling. *SAE Int.* **1988**, *paper 8802*.
158. Ap, N.S.; Jouanny, P.; Potier, M.; Genoist, J. UltimateCooling™ system for new generation of vehicle. *SAE Tech. Pap.* **2005**, doi:10.4271/2005-01-2005.
159. Kim, Y.J.; Song, Y.S. HIGH/LOW TEMPERATURE WATER COOLING SYSTEM. *United States - Pat. Appl. Publ.* 2004.
160. Mokire, M.K.; Ma, J. ENGINE COOLING SYSTEM HAVING TWO COOLING CIRCUITS. *United States Pat.* 2010.
161. Naderi, A.; Qasemian, A.; Shojaeefard, M.H.; Samiezadeh, S.; Younesi, M.; Sohani, A.; Hoseinzadeh, S. A smart load-speed sensitive cooling map to have a high- performance thermal management system in an internal combustion engine. *Energy* **2021**, *229*, 120667, doi:10.1016/j.energy.2021.120667.
162. Castiglione, T.; Falbo, L.; Perrone, D.; Bova, S. Cooling on-demand for knock prevention in spark-ignition engines: An experimental analysis. *Appl. Therm. Eng.* **2021**, *195*, 117161, doi:10.1016/j.applthermaleng.2021.117161.
163. Castiglione, T.; Morrone, P.; Bova, S. A Model Predictive Approach to Avoid Coolant After-Boiling in ICE. *SAE Tech. Pap.* **2018**, *2018-April*, 1–9, doi:10.4271/2018-01-0779.
164. Basir, H.; Hosseini, S.A.; Nasrollahnezhad, S.; Jahangiri, A.; Rosen, M.A. Investigation of engine's thermal management based on the characteristics of a map-controlled thermostat. *Int. Commun. Heat Mass Transf.* **2022**, *135*, doi:10.1016/j.icheatmasstransfer.2022.106156.
165. Chalgren, R.D.; Allen, D.J. Light duty diesel advanced thermal management. *SAE Tech. Pap.* **2005**, doi:10.4271/2005-01-2020.
166. Li, J.; Deng, Y.; Wang, Y.; Su, C.; Liu, X. CFD-Based research on control strategy of the opening of Active Grille Shutter on automobile. *Case Stud. Therm. Eng.* **2018**, *12*, 390–395, doi:10.1016/j.csite.2018.05.009.
167. Perrone, D.; Rodinò, S.; Curcio, E.; Castiglione, T.; Bova, S.; Maletta, C.; Brandizzi, M. Numerical and Experimental Characterization of Active Grille Shutter Loads for

Automotive Applications. *SAE Tech. Pap.* **2022**, 1–10, doi:10.4271/2022-37-0022.

168. El-Sharkawy, A.E.; Kamrad, J.C.; Lounsberry, T.H.; Baker, G.L.; Rahman, S.S. Evaluation of Impact of Active Grille Shutter on Vehicle Thermal Management. *SAE Int. J. Mater. Manuf.* **2011**, *4*, 1244–1254, doi:10.4271/2011-01-1172.
169. Chiara, F.; Canova, M. A review of energy consumption, management, and recovery in automotive systems, with considerations of future trends. *Proc. Inst. Mech. Eng. Part D J. Automob. Eng.* **2013**, *227*, 914–936, doi:10.1177/0954407012471294.
170. Pizzonia, F.; Castiglione, T.; Bova, S. A Robust Model Predictive Control for efficient thermal management of internal combustion engines. *Appl. Energy* **2016**, *169*, 555–566, doi:10.1016/j.apenergy.2016.02.063.
171. Castiglione, T.; Bova, S.; Belli, M. A Novel Approach to the Thermal Management of Internal Combustion Engines. *Energy Procedia* **2017**, *126*, 883–890, doi:10.1016/j.egypro.2017.08.300.
172. Ferrari, G. *Motori a combustione interna*; Esculapio, Ed.; Seconda ed.; 2016; ISBN 978-8874889716.
173. Liu, Z.; Li, L.; Deng, B. Cold start characteristics at low temperatures based on the first firing cycle in an LPG engine. *Energy Convers. Manag.* **2007**, *48*, 395–404, doi:10.1016/j.enconman.2006.07.011.
174. Dardiotis, C.; Martini, G.; Marotta, A.; Manfredi, U. Low-temperature cold-start gaseous emissions of late technology passenger cars. *Appl. Energy* **2013**, *111*, 468–478, doi:10.1016/j.apenergy.2013.04.093.
175. Gumus, M. Reducing cold-start emission from internal combustion engines by means of thermal energy storage system. *Appl. Therm. Eng.* **2009**, *29*, 652–660, doi:10.1016/j.applthermaleng.2008.03.044.
176. Shayler, P.J.; Belton, C. In-cylinder fuel behaviour and exhaust emissions during the cold operation of a spark ignition engine. *Proc. Inst. Mech. Eng. Part D J. Automob. Eng.* **1999**, *213*, 161–174, doi:10.1243/0954407991526775.
177. Lee, S.; Bae, C. The application of an exhaust heat exchanger to protect the catalyst and improve the fuel economy in a spark-ignition engine. *Proc. Inst. Mech. Eng. Part D J. Automob. Eng.* **2007**, *221*, 621–628, doi:10.1243/09544070JAUTO190.
178. Al-Hasan, M. Evaluation of fuel consumption and exhaust emissions during engine warm-up. *Am. J. Appl. Sci.* **2007**, *4*, 106–111, doi:10.3844/ajassp.2007.106.111.
179. Favez, J.Y.; Weilenmann, M.; Stilli, J. Cold start extra emissions as a function of engine stop time: Evolution over the last 10 years. *Atmos. Environ.* **2009**, *43*, 996–1007,

doi:10.1016/j.atmosenv.2008.03.037.

180. Rakopoulos, C.D.; Dimaratos, A.M.; Giakoumis, E.G. Investigation of turbocharged diesel engine operation, exhaust emissions, and combustion noise radiation during starting under cold, warm, and hot conditions. *Proc. Inst. Mech. Eng. Part D J. Automob. Eng.* **2011**, *225*, 1118–1133, doi:10.1177/0954407011400155.
181. Tauzia, X.; Maiboom, A.; Karaky, H.; Chesse, P. Experimental analysis of the influence of coolant and oil temperature on combustion and emissions in an automotive diesel engine. **2018**, doi:10.1177/1468087417749391.
182. Trapy, J.D.; Damiral, P. An investigation of lubricating system warm-up for the improvement of cold start efficiency and emissions of S.I. automotive engines. *SAE Tech. Pap.* **1990**, *99*, 1635–1645, doi:10.4271/902089.
183. Korin, E.; Reshef, R.; Tshernichovesky, D.; Sher, E. Reducing cold-start emission from internal combustion engines by means of a catalytic converter embedded in a phase-change material. *Proc. Inst. Mech. Eng. Part D J. Automob. Eng.* **1999**, *213*, 575–583, doi:10.1243/0954407991527116.
184. Roberts, A.; Brooks, R.; Shipway, P. Internal combustion engine cold-start efficiency: A review of the problem, causes and potential solutions. *Energy Convers. Manag.* **2014**, *82*, 327–350, doi:10.1016/j.enconman.2014.03.002.
185. Shayler, P.J.; Baylis, W.S.; Murphy, M. Main Bearing Friction and Thermal Interaction During the Early Seconds of Cold Engine. *J. Eng. Gas Turbines Power Copyr. © 2005 by ASME* **2005**, *127*, 197–205, doi:10.1115/1.1804538.
186. Zammit, J.P.; Shayler, P.J.; Pegg, I. Thermal coupling and energy flows between coolant, engine structure and lubricating oil during engine warm up. *IMechE/SAE Int. Conf. VTMS 10* **2011**, 177–188, doi:10.1533/9780857095053.3.177.
187. Boretti, A. Improving the efficiency of turbocharged spark ignition engines for passenger cars through waste heat recovery. *SAE Tech. Pap.* **2012**, doi:10.4271/2012-01-0388.
188. Will, F.; Boretti, A. A New Method to Warm Up Lubricating Oil to Improve the Fuel Efficiency During Cold Start. *SAE Int. J. Engines* **2011**, *4*, 175–187, doi:10.4271/2011-01-0318.
189. Grimaldi, C.N.; Poggiani, C.; Cimarello, A.; De Cesare, M.; Osbat, G. An Integrated Simulation Methodology of Thermal Management Systems for the CO2 Reduction after Engine Cold Start. *SAE Tech. Pap.* **2015**, *2015-April*, doi:10.4271/2015-01-0343.
190. Kim, J.H.; Kim, T.; Park, S.J.; Han, J.J.; Jung, C.; Chung, Y. rock; Pae, S. Effect of Engine Oil Heater Using EGR on the Fuel Economy and NOx Emission of a Full Size

Sedan during Cold Start. *SAE Int. J. Engines* **2016**, *9*, 719–728, doi:10.4271/2016-01-0656.

191. Vittorini, D.; Di Battista, D.; Cipollone, R. Engine oil warm-up through heat recovery on exhaust gases – Emissions reduction assessment during homologation cycles. *Therm. Sci. Eng. Prog.* **2018**, *5*, 412–421, doi:10.1016/j.tsep.2018.01.010.
192. Di Battista, D.; Cipollone, R. Improving engine oil warm up through waste heat recovery. *Energies* **2018**, *11*, doi:10.3390/en11010010.
193. Andrews, G.E.; Ounzain, A.M.; Li, H.; Bell, M.; Tate, J.; Ropkins, K. The use of a water/lube oil heat exchanger and enhanced cooling water heating to increase water and lube oil heating rates in passenger cars for reduced fuel consumption and CO2 emissions during cold start. *SAE Tech. Pap.* **2007**, doi:10.4271/2007-01-2067.
194. Di Battista, D.; Cipollone, R. Experimental and numerical assessment of methods to reduce warm up time of engine lubricant oil. *Appl. Energy* **2016**, *162*, 570–580, doi:10.1016/j.apenergy.2015.10.127.
195. Cipollone, R.; Di Battista, D.; Mauriello, M. Effects of oil warm up acceleration on the fuel consumption of reciprocating internal combustion engines. *Energy Procedia* **2015**, *82*, 1–8, doi:10.1016/j.egypro.2015.11.870.
196. Hamedi, M.R.; Doustdar, O.; Tsolakis, A.; Hartland, J. Thermal energy storage system for efficient diesel exhaust aftertreatment at low temperatures. *Appl. Energy* **2019**, *235*, 874–887, doi:10.1016/j.apenergy.2018.11.008.
197. Sara, H.; Chalet, D.; Cormerais, M.; Hetet, J.F. Evaluation of hot water storage strategy in internal combustion engine on different driving cycles using numerical simulations. *Proc. Inst. Mech. Eng. Part D J. Automob. Eng.* **2018**, *232*, 1019–1035, doi:10.1177/0954407017724637.
198. Di Battista, D.; Fatigati, F.; Di Bartolomeo, M.; Vittorini, D.; Cipollone, R. Thermal Management Opportunity on Lubricant Oil to Reduce Fuel Consumption and Emissions of a Light-Duty Diesel Engine. *E3S Web Conf.* **2021**, *312*, 07023, doi:10.1051/e3sconf/202131207023.
199. Rundo, M.; Nervegna, N. Lubrication pumps for internal combustion engines: a review. *Int. J. Fluid Power* **2015**, *16*, 59–74, doi:10.1080/14399776.2015.1050935.
200. Di Battista, D.; Cipollone, R.; Fatigati, F. Engine oil Thermal Management: Oil Sump Volume Modification and Heating by Exhaust Heat during ICE Warm Up. *SAE Tech. Pap.* **2018**, *2018-April*, 1–8, doi:10.4271/2018-01-1366.
201. Di Battista, D.; Vittorini, D.; Fatigati, F.; Cipollone, R. Technical review of opportunities

to reduce the warm-up time of lubricant oil in a light-duty diesel engine. *AIP Conf. Proc.* **2019**, *2191*, doi:10.1063/1.5138798.

202. Lan, S.; Smith, A.; Stobart, R.; Chen, R. Feasibility study on a vehicular thermoelectric generator for both waste heat recovery and engine oil warm-up. *Appl. Energy* **2019**, *242*, 273–284, doi:10.1016/j.apenergy.2019.03.056.
203. Osborne, S.; Kopinsky, J.; Norton, S.; Sutherland, A.; Lancaster, D.; Nielsen, E.; Isenstadt, A.; German, J. *Automotive Thermal Management Technology - ICCT*; 2016;
204. Brace, C.J.; Hawley, G.; Akehurst, S.; Piddock, M.; Pegg, I. Cooling system improvements - Assessing the effects on emissions and fuel economy. *Proc. Inst. Mech. Eng. Part D J. Automob. Eng.* **2008**, *222*, 579–591, doi:10.1243/09544070JAUTO685.
205. Bent, E.; Shayler, P.; La Rocca, A.; Rouaud, C. The effectiveness of stop-start and thermal management measures to improve fuel economy. *Inst. Mech. Eng. - VTMS 2011, Veh. Therm. Manag. Syst. Conf. Proc.* **2013**, 27–39, doi:10.1533/9780857094735.1.27.
206. Gardiner, R.; Zhao, C.; Addison, J.; Shayler, P.J. The effects of thermal state changes on friction during the warm up of a spark ignition engine. *Inst. Mech. Eng. - VTMS 2011, Veh. Therm. Manag. Syst. Conf. Proc.* **2013**, 307–317, doi:10.1533/9780857094735.7.307.
207. Zammit, J.P.; Shayler, P.J.; Gardiner, R.; Pegg, I. Investigating the Potential to Reduce Crankshaft Main Bearing Friction During Engine Warm-up by Raising Oil Feed Temperature. *SAE Int. J. Engines* **2012**, *5*, 1312–1319, doi:10.4271/2012-01-1216.
208. Goettler, H.J.; Vidger, L.J.; Majkrzak, D.S. The Effect of Exhaust-to-Coolant Heat Transfer on Warm-up Time and Fuel Consumption of Two Automobile Engines. *SAE Tech. Pap. Ser.* **1986**.
209. Kaltakkıran, G.; Akif Ceviz, M.; Bakirci, K. Instantaneous energy balance and performance analysis during warm up period of a spark ignition engine under several thermal energy management strategies. *Energy Convers. Manag.* **2022**, *269*, doi:10.1016/j.enconman.2022.116102.
210. Kauranen, P.; Elonen, T.; Wikström, L.; Heikkinen, J.; Laurikko, J. Temperature optimisation of a diesel engine using exhaust gas heat recovery and thermal energy storage (diesel engine with thermal energy storage). *Appl. Therm. Eng.* **2010**, *30*, 631–638, doi:10.1016/j.applthermaleng.2009.11.008.
211. Rakov, V.; Pikalev, O.; Bogomolov, A.; Dymov, N. Modeling of engine warm-up with the use of an exhaust gas recuperator at low ambient temperatures. *Transp. Res. Procedia* **2021**, *57*, 547–552, doi:10.1016/j.trpro.2021.09.083.

212. Cipollone, R.; Di Battista, D. Performances and opportunities of an engine cooling system with a double circuit at two temperature levels. *SAE Tech. Pap.* **2012**, doi:10.4271/2012-01-0638.
213. Cipollone, R.; Di Battista, D.; Gualtieri, A. Head and block split cooling in ICE. *IFAC Proc. Vol.* **2012**, *45*, 400–407, doi:10.3182/20121023-3-FR-4025.00056.
214. Cipollone, R.; Di Battista, D.; Gualtieri, A. A novel engine cooling system with two circuits operating at different temperatures. *Energy Convers. Manag.* **2013**, *75*, 581–592, doi:10.1016/j.enconman.2013.07.010.
215. Cipollone, R.; Di Battista, D.; Gualtieri, A.; Massimi, M. Development of thermal modeling in support of engine cooling design. *SAE Tech. Pap.* **2013**, *6*, doi:10.4271/2013-24-0090.
216. Broatch, A.; Olmeda, P.; Martín, J.; Dreif, A. Improvement in engine thermal management by changing coolant and oil mass. *Appl. Therm. Eng.* **2022**, *212*, doi:10.1016/j.applthermaleng.2022.118513.
217. Wang, S.; Li, Y.; Fu, J.; Liu, J.; Dong, H. Numerical research on the performance, combustion and energy flow characteristics of gasoline-powered vehicle under WLTC. *Fuel* **2021**, *285*, 119135, doi:10.1016/j.fuel.2020.119135.
218. Mohamed, E.S. Development and analysis of a variable position thermostat for smart cooling system of a light duty diesel vehicles and engine emissions assessment during NEDC. *Appl. Therm. Eng.* **2016**, *99*, 358–372, doi:10.1016/j.applthermaleng.2015.12.099.
219. Haghighat, A.K.; Roumi, S.; Madani, N.; Bahmanpour, D.; Olsen, M.G. An intelligent cooling system and control model for improved engine thermal management. *Appl. Therm. Eng.* **2018**, *128*, 253–263, doi:10.1016/j.applthermaleng.2017.08.102.
220. Zhou, B.; Lan, X.D.; Xu, X.H.; Liang, X.G. Numerical model and control strategies for the advanced thermal management system of diesel engine. *Appl. Therm. Eng.* **2015**, *82*, 368–379, doi:10.1016/j.applthermaleng.2015.03.005.
221. Kang, H.; Ahn, H.; Min, K. Smart cooling system of the double loop coolant structure with engine thermal management modeling. *Appl. Therm. Eng.* **2015**, *79*, 124–131, doi:10.1016/j.applthermaleng.2014.12.042.
222. Castiglione, T.; Pizzonia, F.; Piccione, R.; Bova, S. Detecting the onset of nucleate boiling in internal combustion engines. *Appl. Energy* **2016**, *164*, 332–340, doi:10.1016/j.apenergy.2015.11.083.
223. Castiglione, T.; Pizzonia, F.; Bova, S. A novel cooling system control strategy for

internal combustion engines. *SAE Int. J. Mater. Manuf.* **2016**, *9*, 294–302, doi:10.4271/2016-01-0226.

224. Castiglione, T.; Perrone, D.; Algieri, A.; Bova, S. A contribution to improving the thermal management of powertrain systems. *SAE Int. J. Engines* **2020**, *13*, 35–48, doi:10.4271/03-13-01-0003.
225. Castiglione, T.; Morrone, P.; Falbo, L.; Perrone, D.; Bova, S. Application of a Model-Based Controller for Improving Internal Combustion Engines Fuel Economy. *Energies* **2020**, *13*, 22, doi:10.3390/en13051148.
226. Di Bartolomeo, M.; Fatigati, F.; Di Battista, D.; Cipollone, R. A New Approach for Designing and Testing Engine Coolant Pump Electrically Actuated. *SAE Tech. Pap.* **2020**, 1–12, doi:10.4271/2020-01-1161.
227. Kim, J.H.; Lee, H.C.; Kim, J.H.; Kim, S.; Yoon, J.Y.; Choi, Y.S. Design techniques to improve the performance of a centrifugal pump using CFD. *J. Mech. Sci. Technol.* **2015**, *29*, 215–225, doi:10.1007/s12206-014-1228-6.
228. Mariani, L.; Di Bartolomeo, M.; Di Battista, D.; Cipollone, R.; Fremondi, F.; Roveglia, R. Experimental and numerical analyses to improve the design of engine coolant pumps. *E3S Web Conf.* **2020**, *197*, doi:10.1051/e3sconf/202019706017.
229. Mariani, L.; Di Giovine, G.; Di Battista, D.; Cipollone, R. Design, optimization, and testing of a high-speed centrifugal pump for motorsport application. *E3S Web Conf.* **2021**, *312*, 11006, doi:10.1051/e3sconf/202131211006.
230. Mariani, L.; Di Giovine, G.; Fremondi, F.; Di Battista, D.; Carminati, A.; Cipollone, R.; Fatigati, F.; Di Bartolomeo, M.; Camagni, U. Model Based Design, Prototyping and Testing of a Small Size High Speed Electrically Driven Centrifugal Pump. *SAE Tech. Pap.* **2022**, doi:10.4271/2022-37-0025.
231. Shin, Y.H.; Kim, S.C.; Kim, M.S. Use of electromagnetic clutch water pumps in vehicle engine cooling systems to reduce fuel consumption. *Energy* **2013**, *57*, 624–631, doi:10.1016/j.energy.2013.04.073.
232. Cipollone, R.; Di Battista, D. Sliding vane rotary pump in engine cooling system for automotive sector. *Appl. Therm. Eng.* **2015**, *76*, 157–166, doi:10.1016/j.applthermaleng.2014.11.001.
233. Cipollone, R.; Di Battista, D.; Contaldi, G.; Murgia, S.; Mauriello, M. Development of a sliding vane rotary pump for engine cooling. *Energy Procedia* **2015**, *81*, 775–783, doi:10.1016/j.egypro.2015.12.083.
234. Cipollone, R.; Bianchi, G.; Di Battista, D.; Fatigati, F. Fuel economy benefits of a new

engine cooling pump based on sliding vane technology with variable eccentricity. *Energy Procedia* **2015**, *82*, 265–272, doi:10.1016/j.egypro.2015.12.032.

235. Bianchi, G.; Cipollone, R. Theoretical modeling and experimental investigations for the improvement of the mechanical efficiency in sliding vane rotary compressors. *Appl. Energy* **2015**, *142*, 95–107, doi:10.1016/j.apenergy.2014.12.055.
236. Fatigati, F.; Di Battista, D.; Cipollone, R. Design improvement of volumetric pump for engine cooling in the transportation sector. *Energy* **2021**, *231*, 120936, doi:10.1016/j.energy.2021.120936.
237. Fatigati, F.; Di Battista, D.; Di Bartolomeo, M.; Mariani, L.; Cipollone, R. On the optimal design of sliding rotary vane pump for heavy-duty engine cooling systems. *E3S Web Conf.* **2021**, *312*, 07017, doi:10.1051/e3sconf/202131207017.
238. Fatigati, F.; Bartolomeo, M. Di; Cipollone, R. Development and experimental assessment of a Low Speed Sliding Rotary Vane Pump for heavy duty engine cooling systems. *Appl. Energy* **2022**, *327*, 120126, doi:10.1016/j.apenergy.2022.120126.
239. Li, W.; Lu, H.; Zhang, Y.; Zhu, C.; Lu, X.; Shuai, Z. Vibration analysis of three-screw pumps under pressure loads and rotor contact forces. *J. Sound Vib.* **2016**, *360*, 74–96, doi:10.1016/j.jsv.2015.09.013.
240. Kovacevic, A.; Stosic, N.; Smith, I. *Screw Compressors - Mathematical Modelling and Performance Calculation*; Springer, 2005; ISBN 9781119130536.
241. Stosic, N.; Smith, I.K.; Kovacevic, A. Optimisation of screw compressors. *Appl. Therm. Eng.* **2003**, *23*, 1177–1195, doi:10.1016/S1359-4311(03)00059-0.
242. Read, M.; Stosic, N.; Smith, I.K. Optimization of Screw Expanders for Power Recovery From Low-Grade Heat Sources. *Energy Technol. Policy* **2014**, *1*, 131–142, doi:10.1080/23317000.2014.969454.
243. Buckney, D.; Kovacevic, A.; Stosic, N. Consideration of clearances in the design of screw compressor rotors. *Inst. Mech. Eng. - 7th Int. Conf. Compressors Their Syst. 2011* **2011**, 401–410, doi:10.1533/9780857095350.8.401.
244. Three-screw pumps aid power plant. *World Pumps 2017*, 20,22-23, doi:10.1016/S0262-1762(18)30067-1.
245. Yan, D.; Tang, Q.; Kovacevic, A.; Rane, S.; Pei, L. Rotor profile design and numerical analysis of 2–3 type multiphase twin-screw pumps. *Proc. Inst. Mech. Eng. Part E J. Process Mech. Eng.* **2018**, *232*, 186–202, doi:10.1177/0954408917691798.
246. Xu, J.; Feng, Q.; Wu, W. Geometrical design and investigation of a new profile of the three screw pump. *J. Mech. Des. Trans. ASME* **2011**, *133*, 1–5, doi:10.1115/1.4004588.

247. Tang, Q.; Zhang, Y. Screw optimization for performance enhancement of a twin-screw pump. *Proc. Inst. Mech. Eng. Part E J. Process Mech. Eng.* **2014**, *228*, 73–84, doi:10.1177/0954408913478602.
248. Wang, J.; Wu, M.; Cui, F.; Tan, Q.; Wang, Z. Research of a novel eccentric involute rotor and its performance analysis for twin-screw vacuum pumps. *Vacuum* **2020**, *176*, 109309, doi:10.1016/j.vacuum.2020.109309.
249. Zhang, S.; Zhang, Z.; Xu, C. Virtual design and structural optimization of dry twin screw vacuum pump with a new rotor profile. *Appl. Mech. Mater.* **2009**, *16–19*, 1392–1396, doi:10.4028/www.scientific.net/AMM.16-19.1392.
250. Hsieh, C.F.; Hwang, Y.W.; Fong, Z.H. Study on the tooth profile for the screw claw-type pump. *Mech. Mach. Theory* **2008**, *43*, 812–828, doi:10.1016/j.mechmachtheory.2007.06.011.
251. Mujic, E.; Kovacevic, A.; Stosic, N.; Smith, I. Advanced Design Environment for Screw Machines. In Proceedings of the International Compressor Engineering Conference; 2010.
252. Kovačević, A.; Stošić, N.; Smith, I.K. Numerical simulation of combined screw compressor-expander machines for use in high pressure refrigeration systems. *Simul. Model. Pract. Theory* **2006**, *14*, 1143–1154, doi:10.1016/j.simpat.2006.09.004.
253. Kim, S.; Piepenstock, U.; Murrenhoff, H. Effects of manufacturing deviation on the pressure pulsation of three screw pumps. *Int. J. Fluid Power* **2011**, *12*, 41–50, doi:10.1080/14399776.2011.10781021.
254. Thurner, J.; Corneli, T.; Pelz, P. Development of a Hydrostatic Load Balancing System for 3-Spindle Screw Pumps. *9th Int. Fluid Power Conf.* **2014**.
255. Thurner, J.; Pelz, P.F.; Holz, F. Dynamics of a hydrodynamic supported screw PUMP rotor. *ISROMAC 2012 - 14th Int. Symp. Transp. Phenom. Dyn. Rotating Mach.* **2012**, 1–5.
256. Putira, A. Parametrization of Triple Screw Pumps for Aerospace Applications, Embry-Riddle Aeronautical University, 2018.
257. Schlichting, H.; Gerten, K. *Boundary-Layer Theory.*; Ninth Edit.; Springer, 2017; ISBN 9783662529171.
258. Feng, C.; Yueyuan, P.; Ziwen, X.; Pengcheng, S. Thermodynamic performance simulation of a twin-screw multiphase pump. *Proc. Inst. Mech. Eng. Part E J. Process Mech. Eng.* **2001**, *215*, 157–163, doi:10.1243/0954408011530406.
259. Dong, P.; Zhao, S.; Zhao, Y.; Zhang, P.; Wang, Y. Design and experimental analysis of

end face profile of tri-screw pump. *Proc. Inst. Mech. Eng. Part A J. Power Energy* **2020**, *234*, 481–489, doi:10.1177/0957650919870373.

260. Mimmi, G.C.; Pennacchi, P.E. Design of three-screw positive displacement rotary pumps. *Trans. Eng. Sci.* **1995**, *7*.
261. Mimmi, G.C.; Pennacchi, P.E. Computation of pressure loads in three screw pump rotors. *J. Mech. Des. Trans. ASME* **1998**, *120*, 581–588, doi:10.1115/1.2829318.
262. Mimmi, G.C.; Pennacchi, P.E. Dynamic effects of pressure loads in three screw pump rotors. *J. Mech. Des. Trans. ASME* **1998**, *120*, 589–592, doi:10.1115/1.2829319.
263. Karassik, I.J.; Messina, J.P.; Cooper, P.; Heald, C.C. *Pump Handbook*; McGraw-Hill, 2001; ISBN 0-07-034032-3.
264. Richard G. Budynas and J. Keith Nisbett *Shigley's Mechanical Engineering Design*; Ninth Edit.; McGraw-Hill, 2011; ISBN 9780073529288.
265. Baart, P.; Lugt, P.M.; Prakash, B. Review of the lubrication, sealing, and pumping mechanisms in oil- and grease-lubricated radial lip seals. *Proc. Inst. Mech. Eng. Part J J. Eng. Tribol.* **2009**, *223*, 347–358, doi:10.1243/13506501JET473.
266. Romano, D.; Arcarese, C.; Bernetti, A.; Caputo, A. *Italian Greenhouse Gas Inventory 1990 - 2015 (R261/2017)*; ISPRA;
267. 2021 Jeep Compass II (facelift 2021) 1.3 GSE T4 (150 Hp) DCT Available online: https://www.auto-data.net/en/jeep-compass-ii-facelift-2021-1.3-gse-t4-150hp-dct-43187 (accessed on Feb 8, 2023).
268. Daudo, F. FCA FireFly: l'erede del FIAT FIRE Available online: https://www.autotecnica.org/fca-firefly-t3-t4-turbo-benzina/ (accessed on Feb 8, 2023).
269. Schede tecniche motori FireFly (internal source).
270. Gefran TK Pressure Transmitter - Datasheet.
271. ETAS ES930.1 Multi-I/O Module User Guide.
272. ETAS ES930.1 Multi-I/O Module - Pin Assignment and Accessories 1–38.
273. ETAS ES413.1 - A/D Module with Sensor Supply - User Guide 1–92.
274. ETAS ES421.1-K - Thermo Module - User Guide 1–84.
275. ETAS ES582.1 - CAN FD Bus Interface USB Module - User Guide 1–41.
276. ETAS INCA V7.3 Getting Started 2022.
277. AVL M.O.V.E Gas PEMS iS - Product Guide 2017, 1–164.
278. AVL M.O.V.E System Control - Product Description 1–5.
279. AVL M.O.V.E Exhaust Flow Meter 495 - Product Guide 2020, 1–102.
280. AVL M.O.V.E Data Toolbox, Application Guide 2021.

Acknowledgments

I apologize to English readers, but I allow myself to write the acknowledgements in Italian, my native language.

Desidero ringraziare profondamente il Professor Roberto Cipollone per avermi guidato in modo impeccabile durante tutto il percorso di Dottorato. Mente geniale e personalità eccellente, è stato, e rimarrà sempre per me, un esempio da seguire sia dal punto di vista professionale che umano. Sono felice ed onorato di averlo avuto come mio Tutor, e spero di essere stato un allievo all'altezza del suo così alto profilo.

Un sentito ringraziamento va anche agli ingegneri di Metelli S.p.a. e Stellantis N.V., per il supporto tecnico fornito nell'ambito delle attività in comune con quelle previste dal Progetto Hyper.

Un ringraziamento speciale va anche al gruppo di ricerca al quale ho avuto la fortuna di appartenere: il ricercatore Marco Di Bartolomeo, ed i Professori Fabio Fatigati e Davide Di Battista. Li ringrazio infinitamente per il supporto tecnico e morale che mi hanno offerto in questi anni, e per avermi aiutato nei momenti più difficili.

E poi ci sono i miei colleghi, Luigi Mariani e Simona Abbate. Sono contento di aver condiviso con loro questo viaggio, e li ringrazio per il supporto (anche indiretto) che mi hanno fornito durante alcune delle prove più ardue che si sono presentate, prima tra tutte la Pandemia da Covid-19.

Un ringraziamento va anche agli altri dottorandi (Luca, Domenico, Arianna, Elia), ai tecnici del laboratorio (Cesare, Loris, Giovanni), ed a tutte le persone che ho incontrato durante questo percorso (ricercatori, tesisti, collaboratori), per aver contribuito alla mia crescita professionale ed umana.

Il più grande ringraziamento va però alla mia Famiglia, mamma, papà e mio fratello. A voi devo tutto, ed è a voi che dedico e restituisco questo importante risultato.

Voglio conservare memoria di tutte le esperienze che questo Dottorato mi ha offerto. Dai momenti di gioia ed euforia della prima pubblicazione, fino ai momenti di frustrazione di fronte a risultati che inizialmente non arrivavano, nonostante mesi di lavoro. Tanti sono stati gli insegnamenti ricevuti. Ma il più prezioso di tutti è stato quello di non arrendersi mai, di non stancarsi mai di risolvere i problemi complessi che la vita spesso ci pone innanzi. Cercherò di farne tesoro e di non dimenticarlo mai.